

AD 745427

FTD-MT-24-1462-71

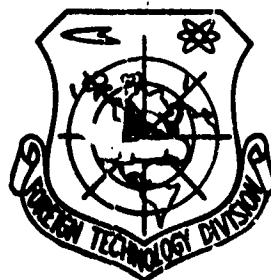
## FOREIGN TECHNOLOGY DIVISION



DESIGN AND STRESS ANALYSIS OF EXTRA-  
TERRESTRIAL ELECTRIC ROCKET ENGINES

by

A. F. Gurov, D. D. Sevruck, and D. N. Surnov



DDC  
RECEIVED  
JUL 27 1972  
B

Approved for public release;  
Distribution unlimited.

Reproduced by  
NATIONAL TECHNICAL  
INFORMATION SERVICE  
U S Department of Commerce  
Springfield VA 22151

UNCLASSIFIED

Security Classification

## DOCUMENT CONTROL DATA (R &amp; D)

(Security classification of title, body of abstract and indexing notation must be entered when the overall report is classified)

1. ORIGINATING ACTIVITY (Corporate author) Foreign Technology Division Air Force Systems Command U. S. Air Force		2a. REPORT SECURITY CLASSIFICATION UNCLASSIFIED	
		2b. GROUP	
3. REPORT TITLE DESIGN AND STRESS ANALYSIS OF EXTRATEPRESTRIAL ELECTRIC ROCKET ENGINES			
4. DESCRIPTIVE NOTES (Type of report and inclusive dates) Translation			
5. AUTHOR(S) (First name, middle initial, last name) A. F. Gurov, D. D. Sevrjuk, and D. N. Surnov			
6. REPORT DATE 1970		7a. TOTAL NO. OF PAGES 657	7b. NO. OF REFS 52
8a. CONTRACT OR GRANT NO.		8b. ORIGINATOR'S REPORT NUMBER(S) FTD-MT-24-1462-71	
9. PROJECT NO.			
10. DIA Task No. T69-04-9		9b. OTHER REPORT NO(S) (Any other numbers that may be assigned this report)	
10. DISTRIBUTION STATEMENT Approved for public release; distribution unlimited.			
11. SUPPLEMENTARY NOTES		12. SPONSORING MILITARY ACTIVITY Foreign Technology Division Wright-Patterson AFB, Ohio	
13. ABSTRACT Given are general data on the design of electric rocket engines calculation of their strength and vibrations, evaluation of their reliability. Considerable attention is given to power generators of cosmic engine installations. Analyzed are structural diagrams of nuclear reactors, isotopic power supply sources, solar concentrators and chemical fuel elements. Given are methods for calculation of strength of various generator parts; housings, casings, and walls, perforated plates under load. Discussed is the calculation of temperature stresses in heat-releasing reactor elements. The calculation is based on safety factors taking into account length of operation of units under thermal load conditions. The calculation methods are simplified due to the assumption that the calculation is made in initial structural development of these units at the level of a preliminary design. Described are designs of various power converters of cosmic engine installations; machine, thermoemission, thermoelectric and photoelectric converters. After the discussion of characteristics of various structural diagrams, we give methods for calculation of strength and vibrations of turbine blades and disks, carrying capacity of hydrostatic bearings and critical velocities of turbogenerator shafts installed on liquid-metal bearings. Given are methods for calculation of the anodic pack of the thermoemission converter.			

DD FORM 1473  
NOV 68

UNCLASSIFIED

Security Classification

UNCLASSIFIED  
Security Classification

14. KEY WORDS	LINK A		LINK B		LINK C	
	ROLE	WT	ROLE	WT	ROLE	WT
Thermal Thermoemission Liquid Propellant Rockets Solid Propellant Rockets Extraterrestrial Electric Rocket Nuclear Reactor Atomic Reactor Stress Analysis						

10

UNCLASSIFIED  
Security Classification

**FTD-MT-** 24-1462-71

## **EDITED MACHINE TRANSLATION**

FTD-MT-24-1462-71

DESIGN AND STRESS ANALYSIS OF EXTRATERRESTRIAL  
ELECTRIC ROCKET ENGINES

By: A. F. Gur'yev, D. D. Sevruck, and D. N. Surnov

English pages: 657

Source: Konstruktsiya i Raschet na Prochnost'  
Kosmicheskikh Elektoraketnykh  
Dvigatelyey, Izd-vo Mashinostroyeniye,  
Moscow, 1970, pp. 1-491.

Requester: FTD/PDTN

This document is a SYSTRAN machine aided translation post-edited for technical accuracy by:  
Louise Heenan

Approved for public release;  
Distribution unlimited.

THIS TRANSLATION IS A RENDITION OF THE ORIGINAL FOREIGN TEXT WITHOUT ANY ANALYTICAL OR EDITORIAL COMMENT. STATEMENTS OR THEORIES ADVOCATED OR IMPLIED ARE THOSE OF THE SOURCE AND DO NOT NECESSARILY REFLECT THE POSITION OR OPINION OF THE FOREIGN TECHNOLOGY DIVISION.

PREPARED BY:

TRANSLATION DIVISION  
FOREIGN TECHNOLOGY DIVISION  
WP-AFB, OHIO.

**FTD-MT-** 24-1462-71

Date 27 April 1972



## TABLE OF CONTENTS

U. S. Board on Geographic Names Transliteration System...	iv
Designations of the Trigonometric Functions.....	v
Preface.....	viii
Chapter I. Extraterrestrial engines.....	1
1.1. Classification of ERE.....	1
1.2. Requirements for extraterrestrial electric rocket engines.....	3
1.3. Structural diagrams of ERE.....	10
1.4. ERE reliability problems.....	19
1.5. Problems of ERE stress analysis.....	49
Chapter II. ERE power generators.....	88
2.1. Nuclear reactor unit.....	88
Structural diagrams of nuclear reactors.....	90
The construction of reactor elements.....	93
Stress analysis of reactor parts.....	108
Thermal stresses in fuel elements.....	113
Stress analysis of reactor shells.....	126
Stress analysis of the load-bearing plate of a reactor.....	161
2.2. Radioactive isotopic sources of energy for extraterrestrial rocket engines.....	189
Design of an ampoule for an isotopic heat source.....	191
Ampoule stress analysis.....	193
2.3. Solar energy concentrators for an ERE.....	201
Structural diagrams of solar concentrators.....	202

2.4. Fuel elements.....	206
Structural diagrams of fuel elements.....	208
Chapter III. Converters.....	221
3.1. Mechanical converters.....	221
Selection of basic parameters for the circulating part of turbines.....	222
Structural diagrams and designs for bracing the working blades to the rotor.....	225
The effect of the supersaturation of vapor and its condensation on turbine operations.....	239
Some features of electric generators.....	240
Stress analysis of working blades.....	245
Vibrational analysis of blades.....	258
Stress analysis of turbine disks.....	289
Analysis of critical shaft speed.....	351
Vibrations in rotors on hydrostatic bearings....	386
3.2. Thermoemission energy converter.....	406
Structural diagrams and design of converters....	408
Stress analysis of converter parts.....	416
3.3. Thermoelectric and photoelectric converters.....	421
Structural diagrams and design of converters....	423
Chapter IV. Heat exchangers.....	433
4.1. Radiator-coolers.....	433
Structural diagrams of radiator-coolers.....	434
Radiator element design.....	440
Stress analysis of radiator elements.....	442
4.2. Heat exchange equipment.....	463
Structural diagrams of heat exchange equipment.....	466
Materials for heat exchange equipment.....	475
Stress analysis of the elements of heat exchange equipment.....	478
Chapter V. Motors.....	500
5.1. Plasma motors.....	500
Structural diagrams and designs of the motors...	501
Stress analysis of motor elements.....	512

5.2. Ion motors.....	579
Principal and structural diagrams of motors.....	580
Motor element design.....	587
Stress analysis of motor elements.....	596
Appendix. Strength characteristics of materials used in extraterrestrial engines.....	635
Bibliography.....	656

# U. S. BOARD ON GEOGRAPHIC NAMES TRANSLITERATION SYSTEM

Block	Italic	Transliteration	Block	Italic	Transliteration
А а	<i>А а</i>	A, a	Р р	<i>Р р</i>	R, r
Б б	<i>Б б</i>	B, b	С с	<i>С с</i>	S, s
В в	<i>В в</i>	V, v	Т т	<i>Т т</i>	T, t
Г г	<i>Г г</i>	G, g	У у	<i>У у</i>	U, u
Д д	<i>Д д</i>	D, d	Ф ф	<i>Ф ф</i>	F, f
Е е	<i>Е е</i>	Ye, ye; E, e*	Х х	<i>Х х</i>	Kh, kh
Ж ж	<i>Ж ж</i>	Zh, zh	Ц ц	<i>Ц ц</i>	Ts, ts
З з	<i>З з</i>	Z, z	Ч ч	<i>Ч ч</i>	Ch, ch
И и	<i>И и</i>	I, i	Ш ш	<i>Ш ш</i>	Sh, sh
Й й	<i>Й й</i>	Y, y	Щ щ	<i>Щ щ</i>	Shch, shch
К к	<i>К к</i>	K, k	Ъ ъ	<i>Ъ ъ</i>	"
Л л	<i>Л л</i>	L, l	Ы ы	<i>Ы ы</i>	Y, y
М м	<i>М м</i>	M, m	Ь ь	<i>Ь ь</i>	'
Н н	<i>Н н</i>	N, n	Э э	<i>Э э</i>	E, e
О о	<i>О о</i>	O, o	Ю ю	<i>Ю ю</i>	Yu, yu
П п	<i>П п</i>	P, p	Я я	<i>Я я</i>	Ya, ya

\* ye initially, after vowels, and after ъ, ь; e elsewhere.  
 When written as ѣ in Russian, transliterate as ye or ѣ.  
 The use of diacritical marks is preferred, but such marks  
 may be omitted when expediency dictates.

FOLLOWING ARE THE CORRESPONDING RUSSIAN AND ENGLISH  
DESIGNATIONS OF THE TRIGONOMETRIC FUNCTIONS

Russian	English
sin	sin
cos	cos
tg	tan
ctg	cot
sec	sec
cosec	csc
sh	sinh
ch	cosh
th	tanh
cth	coth
sch	sech
csch	csch
arc sin	sin <sup>-1</sup>
arc cos	cos <sup>-1</sup>
arc tg	tan <sup>-1</sup>
arc ctg	cot <sup>-1</sup>
arc sec	sec <sup>-1</sup>
arc cosec	csc <sup>-1</sup>
arc sh	sinh <sup>-1</sup>
arc ch	cosh <sup>-1</sup>
arc th	tanh <sup>-1</sup>
arc cth	coth <sup>-1</sup>
arc sch	sech <sup>-1</sup>
arc csch	csch <sup>-1</sup>
rot	curl
lg	log

General information on the design of electric rocket engines, their stress analysis, and reliability evaluation are stated.

Considerable attention is given to the power generator of an extraterrestrial engine (HAY) [ERE]. The structural diagrams of nuclear reactors, isotopic power sources, solar concentrators and chemical fuel elements are examined. Methods of stress analysis for generator parts are given: housings, shells, end walls, perforated loaded plates. The calculation of thermal stresses in reactor fuel elements is examined. Calculation is conducted on strength reserves, taking into account the operating time under conditions of thermal loading. Design procedure has been simplified because it is assumed that calculation is conducted in the primary structural study of these units at the level of sketch planning.

Designs are described for various power converters in an ERE: machine, thermoemission, thermal, and photoelectric. After considering the features of various structural diagrams, methods are stated for calculating strength and vibrations of turbine blades and disks, the bearing capacity of hydrostatic bearings, and the critical speed of shafts of turbogenerators installed on liquid-metal supports. The design procedure for the anode package of the thermoemission converter is given.

Fundamental questions of planning and stress analysis for heat-exchange equipment used in ERE as well as plasma and ion motors are stated. The structural diagram, unit design, and stress analysis of most stressed elements are examined. Characteristic for these units

is the calculation of thermal stress in the tubes of the radiators cooling the panels and ribs, and in the cylindrical and conical shells. Considerable attention is given to the calculation of thermal stress in the electrodes of motors and parts of the feed system. In the appendix is given information on the rupture strength of the materials most widely used in extraterrestrial engines.

This book is a manual for senior students in courses of related specialties. It can also be useful to engineers and designers who work in the sphere of space technology. 30 tables, 350 illustrations, bibliography of 52 titles.

## PREFACE

This manual is written in accordance with the program of a course in the design of extraterrestrial electric rocket engines (ERE), and is to be read in schools of higher education.

In the press a number of problems connected with ERE have been widely discussed. However, the questions examined in this book of their design, strength, vibrations, have not as yet been properly systematized and much time should be spent on their study.

In this manual we have made an attempt at the systematic presentation of the indicated information. In its preparation the authors took into account the fact that the students are already familiar with courses on the strength of materials and the theory of extraterrestrial electric rocket engines.

The book consists of five chapters. Chapter I presents general information on extraterrestrial engines and requirements imposed on them; ERE classification is given, their fundamental and structural diagrams are presented, and also the general problems of reliability and strength are examined.

Chapter II contains fundamental information on design and stress analysis of the ERE power generator. The greatest attention is here given to nuclear reactors; their classification, structural diagram, and design of separate units and parts are examined.



In stress analysis the calculation of thermal stress in reactor parts is of considerable interest.

Further discussed are the areas of applicability, the design and stress analysis of radioactive isotopic power sources, solar concentrator, and fuel elements.

Chapter III has been dedicated to the energy converters in an ERE. Along with mechanical energy converters which include the turbine, generator, shafts, bearings, we examine thermoemission, thermal, and photoelectric converters. Chapter IV deals with the problems of strength and design of heat exchange equipment.

Chapter V has been dedicated to motors. Plasmas and ion motors, their classification, structural diagram, design and stress analysis, particularly thermal stress, make up the basic content of this chapter.

In the manual are used materials published in the press. The given examples of design and calculation have a methodical character and are not connected with specific engines.

The section dedicated to the problem of reliability of an extraterrestrial engine (Chapter I) is written by Doctor of the Technical Sciences, Professor D. D. Sevruck, the section on "Machine Converters" (Chapter III) and "Heat-Exchange Equipment" (Chapter IV) by Docent D. N. Surnov, the section "Vibration of a Rotor on Hydrostatic Bearings" (Chapter III) is written by Doctor of the Technical Sciences Professor A. F. Gurov and Teacher V. I. Bykov; the remaining material is by Doctor of the Technical Sciences, Professor A. F. Gurov.

The manuscript was looked over by Doctor of the Technical Sciences Professor A. V. Kvasnikov and his colleagues who made a number of valuable remarks. Many useful indications have been

made by the reviewers. The authors express their sincere gratitude to them. Furthermore, the authors are grateful to Doctor of Technical Sciences Professor G. S. Skubachevskiy who was of great aid during the work on this book.

All remarks and requests for this book should be directed to the Mashinostroyeniye Publishing House (Moscow, B-66, 1st Basmannyy per., 3).

## CHAPTER I

### EXTRATERRESTRIAL ENGINES

The purpose of a course in the design and stress analysis of extraterrestrial electric rocket engines is to study designs of engines (ERE), their units and parts, stress and vibration analysis, the development of experience in planning and designing units and parts, and research on the dynamic phenomena which accompany engine operation.

Various engines can be used in space. Today widely used are chemical propellant rockets — liquid propellant rockets (LPRE) and solid propellant rockets (SPRE).

In this course are studied designs of extraterrestrial electric rocket engines and the thrust which they create as a result of interaction of electromagnetic and electrostatic fields with the ionized working medium. Such an engine consists of two fundamental parts: the airborne power installation and the engine itself, which can be called a motor (predominantly low thrust).

#### 1.1. CLASSIFICATION OF ERE

All electric rocket space engines, *based on type of power plant* can be divided into ERE:

- with nuclear reactor (or reactors);
- with the use of radioactive isotope power;
- with the use of solar energy;
- with the use of chemical energy.

Based on the method of energy conversion into electrical, they can be divided into motors:

- with mechanical power conversion;
- with thermoemission power conversion;
- with thermoelectric and photoelectric power conversion;
- with thermodynamical power conversion + by fuel element;
- with magnetohydrodynamic power conversion.

Based on type of motor:

- ionic (electrostatic);
- plasma;
- electrothermal.

Based on purpose:

- sustainer;
- correction;
- short-life one-shot use.

Engines are divided also into multimode and single mode.

Let us examine the classification based on purpose because in courses on engine theory this classification has not been thoroughly studied.

Sustainer engines are intended to provide interplanetary flight into outer space. These motors can be both single mode and multimode. In the latter case, they can change the value and the direction of the thrust sector. A gradual variation in the thrust level can be accomplished by switching the motors in the power installation on and off or by continuously variable control. Sustainer motors can be designed for manned or unmanned flight. The piloted spacecraft

requires special protection of the crew from cosmic radiation and radiation from the nuclear reactor. For some space programs such motors can operate for 10,000 h or more.

Correction motors are intended for correcting the trajectory (orbit) of spaceflight vehicles. The operating time of these motors can reach 100 h.

Short-life motors are single mode motors of one-shot use for pilotless flight vehicles and for man-made satellites of various purposes. The duration of their operation does not exceed 5 h.

## 1.2. REQUIREMENTS FOR EXTRATERRESTRIAL ELECTRIC ROCKET ENGINES

The specific mass of the motor

The motor should have the very lowest specific mass.

The specific mass of the motor  $\gamma$  is the ratio of the mass  $M$  of a "drive" motor (without the expended working medium) to its thrust  $R$  (in kg/N) or to the electrical power  $N_e$  (in kg/kW):

$$\gamma = \frac{M}{R}; \text{ or } \gamma = \frac{M}{N_e}. \quad (1.1)$$

The parameter  $\gamma$  estimates the degree of weight perfection of the motor.

In designing motors we start from an assignment in which thrust level, as well as the size and mass (weight) engine characteristics, have been shown. In this case, it is advantageous that a motor of given thrust have minimum overall size and mass.

Sometimes overall size and mass of the motor are given and it is necessary to obtain a motor with the maximum possible thrust.

This task appears frequently in planning as the result of the modification of designs already built. The parameters of a motor, its characteristics - thrust and power - are connected with its overall size and mass.

The specific mass of a motor is one of the important quality criteria in engine design. In proportion to the perfection of the design its specific mass is decreased.

Extraterrestrial electric rocket motors are not produced in serial production; they have not acquired final forms. This is why their specific mass fluctuates within a wide range and depends upon the type of design, purpose, and power of this system.

Table 1.1 and Fig. 1.1 show the specific mass of various power units for space engines and their power.

Table 1.1.

NAME OF SYSTEM	$N_e$ kW	$\gamma$ kg/kW
Turbogenerator with nuclear reactor	10,000	3
	5	100
Thermoemission with nuclear reactor	2500	4
	8	80
Thermoelectric with nuclear reactor	5	200
and protection	0.3	1000
Thermoemission with solar power	3	50
concentrator	0.1	45
Thermoelectric on radioactive	1	120
isotopes	0.1	300

As can be seen from the table and Fig. 1.1, the specific mass of power units depends upon electrical power. A particularly noticeable reduction in specific mass is seen with an increase in the power of the power plant with nuclear reactors. This is explained by the fact that specific mass is defined as the ratio of the ERE's mass to the

electrical power of the power installation. This is convenient because the thrust of the motor  $R$  and the electrical power of the power installation  $N_e$  (W) are connected by the ratio

$$N_e = \frac{mw^2}{2\eta} = \frac{Rw}{2\eta},$$

where  $m$  — the per-second mass flow of the working medium, kg/s;  
 $w$  — the discharge velocity, m/s;  $R$  — thrust, N;  $\eta$  — the efficiency of the motor.

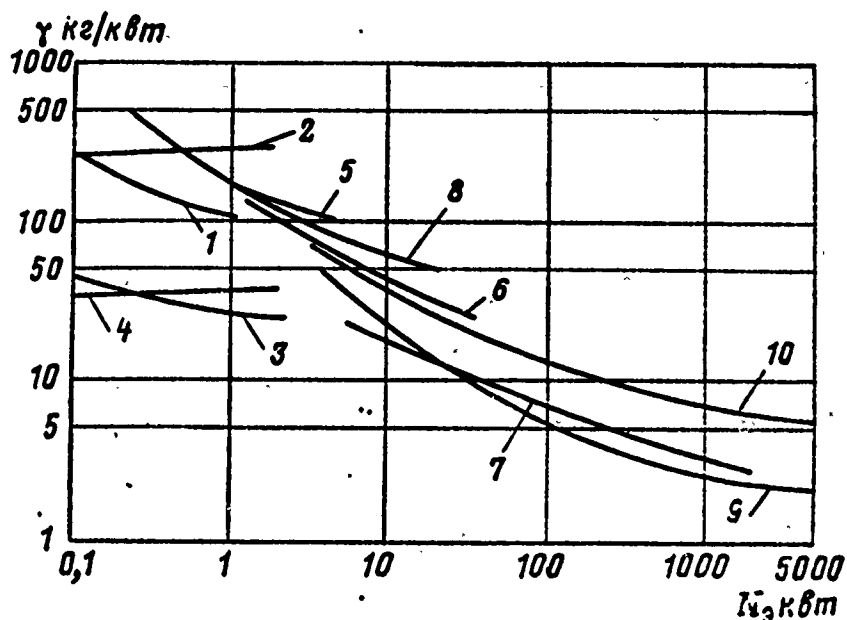


Fig. 1.1. The dependence of the specific mass of power units on electrical power: 1 — thermoelectric system on radioisotopes; 2 — solar photoelectric batteries; 3 — thermoemission system on solar energy; 4 — thermoelectric system with atomic reactor without protection; 5 — thermoelectric system with atomic reactor with protection; 6 — turbogenerator system on solar energy; 7 — thermoemission system with atomic reactor without protection; 8 — thermoemission system with atomic reactor with protection; 9 — turbogenerator system with atomic reactor without protection; 10 — turbogenerator system with atomic reactor.

Designations:  $\gamma_e/\gamma_{em} = \text{kg/kW}$ ,  $\gamma_{em} = \text{kW}$ .

The mass of the nuclear reactor and the mass of the protection unit, making up the major portion of the mass of the power plant, vary little with an increase in the power of the power plant. Therefore, at high power levels the specific mass of installations with nuclear reactors is the smallest and these installations are preferable for use in space engines.

Turbogenerator installations have less specific mass as compared with thermoemission beginning with a power of approximately 50 kW because of the higher efficiency which is evident from Fig. 1.2.

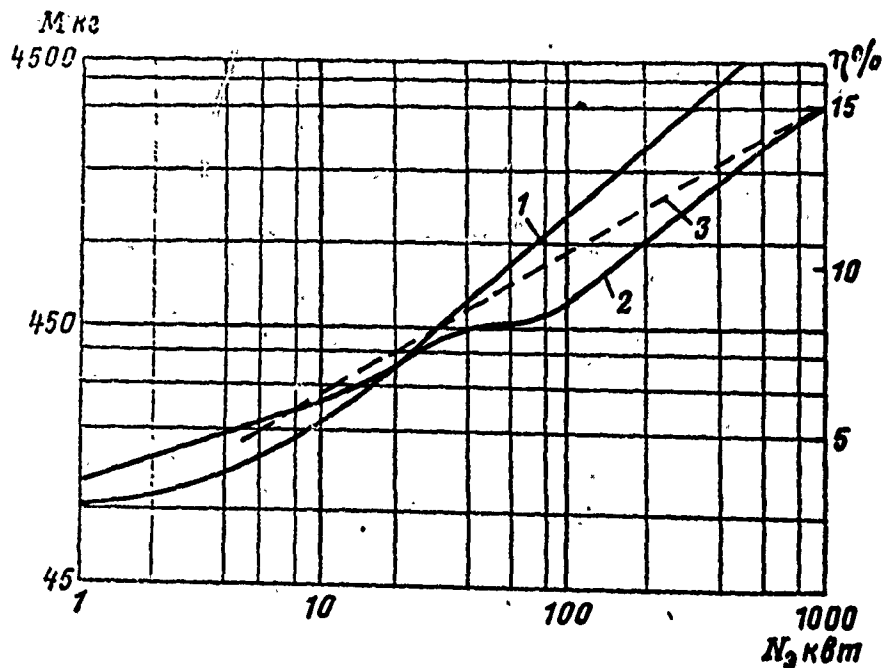


Fig. 1.2. The dependence of mass and efficiency of nuclear power units upon electrical power (without protection): 1 - the mass of thermoemission installations with efficiency equal to 10; 2 - the mass of turbogenerator installations with efficiency changing according to curve 3; 3 - the efficiency of turbogenerator power installations.

Designations:  $kg = kg$ ,  $kW = kW$ .



Extraterrestrial motors in power from 1 to 50 kW are promising with thermoemission, thermoelectric energy conversion with any nonnuclear heat source. Radioisotope power sources are effective for systems with thermoelectric energy converters for low-power motors (from 30 W to 50 kW).

#### The economy of extraterrestrial motors

The second important requirement for an ERE is minimum expenditure of working medium during its operation, i.e., the best economy factor. This is determined by the specific function of the working medium.

Specific consumption is the ratio of the flow rate per second of the working medium to the thrust level of the motor (kg/N·s):

$$C_{ys} = \frac{m_r}{R}. \quad (1.2)$$

In an electrical ERE the entire reserve of the working medium is located aboard the ship; therefore, we determine the economy factor of a motor based on the specific impulse.

The specific impulse of a motor is the ratio of its thrust to the flow rate per second of the working medium:  $J = R/m_r$ . This value is inverse to the specific flow rate of the working medium.

Specific impulse in the International System is

$$[J] = \left[ \frac{R}{m_r} \right] \text{ N} \cdot \text{s/kg} \quad (1.3)$$

Table 1.2 gives a comparison of the specific impulses of plasma extraterrestrial engines (PEE), ion extraterrestrial engines (IEE), and liquid propellant rocket engines (LPRE).

Table 1.2.

Impulse J	LPRE	PEE	IEE
m/s	$(2.2-3.5) \cdot 10^3$	$(50-100) \cdot 10^3$	up to $600 \cdot 10^3$

Extraterrestrial electrical rocket motors have a specific impulse higher than LPRE. This explains the preferred use of electrical rocket motors for interstellar flights. The value of specific impulse in each concrete case should be optimal.

#### Reliability and service life of ERE

Reliability is usually understood as the property of the product to execute assigned functions, preserving its operating indexes within assigned limits during the required time interval or required operating time.

The reliability of a product is explained by its "dependability," "maintainability," "storage stability," and also by the "longevity" of its parts.

In this section we examine only problems relating to longevity. A broader discussion of the problem of reliability is given in section 1.4.

*Longevity* is the property of a part to preserve efficiency up to a limiting condition with the necessary interruptions for maintenance and repair.

The indexes of longevity are life and service period.

Life is characterized by the length of operating time up to a limiting condition specified in the technical specifications and records. The service period is the length of time by the calendar

that a part operates before the limiting condition sets in or before write-off.

Identical motors during operation will have different longevity since damage and breakdowns are possible in various elements of the motor and at different times and occur as a result of scarcely noticeable differences in material, manufacturing procedures, etc.

The life (service) is established by the supplier plant as the time of guaranteed faultless operation of the engine. After working its full life the engine is removed from operation.

Longevity is different for engines of different purposes. For example, for liquid and solid propellant rocket engines (LPRE and SPRE) it is less than 5 h, for aviation turbojet (TJE) 100-1500 h, and for extraterrestrial electrical rocket engines (ERE) 5-10,000 h.

Life of ordinary rocket engines (LPRE and SPRE) for one-shot use is made up of the useful operating time, the plant inspection time, and the acceptance testing time.

The life of engines for repeated use is easily established, based on the trouble-free service time of the most stressed critical part of the engine. Such engines have the concept of full or amortized life, which is established from several intermediate lives. After operating for a period corresponding to an intermediate lifetime the motor undergoes complete dismantling, replacement of stressed parts which are dangerous in an emergency, and then the second operation on the following lifetime. There can be several such lifetimes. Amortized or full life can consist of two or three intermediate lifetimes after overhauls. Only after working out the amortized or full lifetime does an engine go for remelting.

The longevity of ERE can be different depending upon their purpose.

## Radiation safety for an ERE

Radiation safety is especially important for systems whose power source is a nuclear reactor or radioactive isotopes.

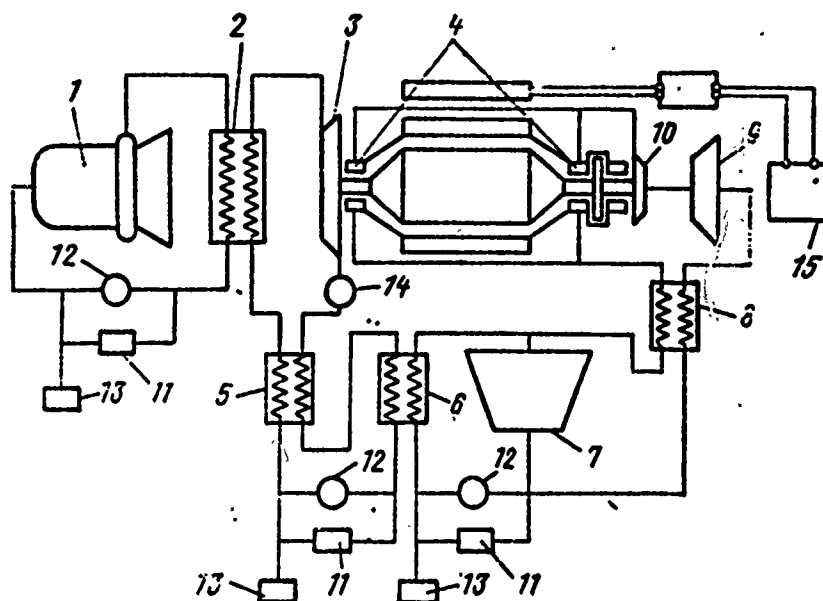
The requirements for safety techniques for emergency states are different depending upon the time and place of the emergency. If the emergency is at the start, in the immediate proximity of the earth's surface (altitude of failure no more than 50 km), the power plant should be allowed to fall and not be destroyed (it can not have time to burn). If the emergency occurs upon start at a significant distance from earth, the ERE should be destroyed into such fine particles as to ensure that the installation will burn up at a distance of 100-150 km from earth. If such destruction does not occur, or if the destruction or emergency occurs in the zone of earth orbits, it should be shot off to the side of orbits exceeding 400 km where its radiation is not dangerous and where it can remain for a long period of time.

### 1.3. STRUCTURAL DIAGRAMS OF ERE

Let us examine an ERE with an ion motor and a power installation with an energy conversion machine. Figure 1.3 shows the structural diagram of such an ERE. It consists of two fundamental parts - the power installation 1-14 and the ion motor itself 15.

The power installation is a three-circuit system and each circuit is a sealed independent system where liquid metal circulates. Despite the apparent complexity, a three-circuit diagram is preferable to a single-circuit or a two-circuit.

One of the substantial advantages of the three-circuit installation is the fact that in the reactor and the cooler-radiator the working medium is in a single-phase working state.



In the single-circuit installation the reactor should be a boiling reactor. In the two-circuit installation we can not avoid the two-phase state of the working medium in the radiator.

The second circuit of the installation consists of a steam generator 2, a turbine 3 of the turbogenerator, turbine control 14, regenerative heat exchanger 5, condensation heat exchanger 6, and units 11, 12 and 13.

Table 1.3. Possible parameters of working media in power plants.

(1) контур				(1) контур				(1) контур						
(2) Рабочее тело	(3) Реактор		Парогенератор (4)		(2) Рабочее тело	(4) Парогенератор	(5) Турбина		(2) Рабочее тело	(6) Конденсатор		(7) Излучатель		
	$t^{\circ}\text{C}$	$P \cdot 10^{-3} \frac{\text{H}}{\text{M}^2}$	$t^{\circ}\text{C}$	$P \cdot 10^{-3} \frac{\text{H}}{\text{M}^2}$			$t^{\circ}\text{C}$	$P \cdot 10^{-3} \frac{\text{H}}{\text{M}^2}$		$t^{\circ}\text{C}$	$P \cdot 10^{-3} \frac{\text{H}}{\text{M}^2}$			
(8) Na вход	480—590	1—2	2	510—700	(8) Hg вход	360	1,5—2	670	1,5—2	(8) Na—K вход	258	1—1,2	351	1,1—1,2
(9) Na выход	510—700	1—2	2	480—590	(9) Hg выход	670	1,5—2	360	1,09	(9) Na—K выход	351	1—1,2	258	1,1—1,2
(8) Na вход	600—680	2—1	2—1	800—1000	(8) K вход	630	2—3	830	2,3	(8) Na вход	420	1,5	550	1,4
(9) Na выход	800—1000	2—1	2—1	600—650	(9) K выход	830	2—3	630	0,3	(8) Na выход	550	1,4	420	1,5
(8) Li вход	860—1100	2—2,5	2—2,5	1000—1200	(8) K вход	700	5	1030	5	(9) Li вход	556—720	1,5—2	700—1200	1,5—2
(9) Li выход	1000—1200	2—2,5	2—2,5	800—1100	(9) K выход	1030	5,0	700	0,5	(6,9) Li выход	700—1200	1,5—2	550—750	1,5—2

KEY: (1) circuit (outline); (2) Working medium; (3) Reactor; (4) Steam generator; (5) Turbine; (6) Condenser; (7) Radiator; (8) Input; (9) output.

Designation:  $\text{H} / \text{M}^2 = \text{N} / \text{m}^2$ .

Table 1.3 shows the working media, temperatures, and pressures which may be encountered in designing such an installation. As can be seen from the table, mercury, potassium, and sodium eutectic make possible the designing of a comparatively low-temperature power plant. Its advantage lies in the possible use of simple stainless steel of type Kh18N9T. The low level of temperature for the heat carrier simplifies the finishing of this installation and operation. The shortcoming of these working media is the low temperature of the radiator. A cycle with elevated radiator temperature under equal conditions gives a lighter installation.

An installation where the working media are lithium and potassium, other conditions being equal, has less mass because of the decrease in size of the radiator. However, here we should consider the necessity of using the more expensive materials niobium and molybdenum in circuits with lithium.

Installations with sodium and potassium have a more intermediate position with respect to their advantages.

Let us examine the interaction of elements of the installation (see Fig. 1.3). Sodium or lithium eutectic from the reactor enters the steam generator 2 forming the steam of the working medium for the secondary circuit of the installation. Steam entering turbine 3 turns the rotor of the turbogenerator, installed, as a rule, on hydrostatic bearings. The working medium enters regenerator 5 where part of the heat is given off to the condensed working medium and further into condenser 6 where the steam is completely condensed.

The condensation of vapor in the secondary circuit is accomplished by the cold liquid metal of the third circuit which is usually selected to be the same as the metal of the first circuit. In the third circuit the heat is expended by the condenser-radiator 7.

The pumping of metal in each circuit is done by pump 12 and the cleaning by filter 11; the compensation of metal expansion during

heating is accomplished by capacitor 13. Turbine revolution is controlled by regulator 14.

Part of the liquid metal in the third circuit enters the bearings of the turbine generator. Usually the temperature of this metal coming out of the radiator is higher than the optimum temperature of the bearing. It should be lowered to  $t = 150-200^{\circ}\text{C}$ . Pressure in the circuit, defined only by resistance in the circuit and the cavitation characteristics of pump 12 (usually not exceeding  $(1.0-2) \times 10^5 \text{ N/m}^2$ ), is insufficient for bearing efficiency. This is why in a parallel circuit of the third outline there is installed, besides an additional cooler 9, a centrifugal pump 10 which pressurizes the metal in the bearing to  $(4-6) \cdot 10^5 \text{ N/m}^2$ .

There is one more circuit in this installation, the fourth circuit, the cooling circuit of the turbogenerator windings.

The advantage of such an installation lies in the fact that in all its parts elements of known technical solutions are used and, in this sense, it is nearer than any other to accomplishment. It is also known that for an ERE of high power the specific mass of such an installation is the least. The shortcomings of such an installation are its complexity and bulkiness.

Let us give one of the possible versions of the starting of such installation.

The installation is vacuumized and serviced with the working medium. After filling, the metal is cleaned by the filters. After servicing in the heated state, the installation enters the carrier rocket and in this state is placed in orbit. In orbit, after dropping the aerodynamic and heat shields, the reactor is turned on. The temperature of the working medium is raised. The radiator, unfolded into working position, ensures the cooling of the working medium. The turbine of the turbogenerator makes its first revolution. The ERE after a certain time goes into operating mode.



The schematic of a nuclear thermoemission power plant with a plasma motor

The motor installation shown in Fig. 1.4 consists of power plant 1-11 and the motor itself 12.

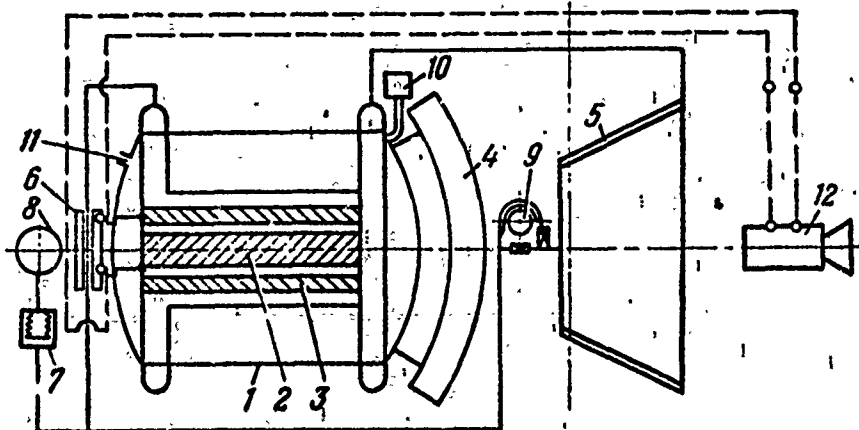


Fig. 1.4. Diagram of an ERE with a thermoemission energy converter.

The power plant is a single-circuit type and includes the subassembly of the reactor 1 in which the heat-releasing element (HRE) has been combined with cathode 2 and anode 3 and the units for protection 4, radiator 5, pump 6, compensating capacitor 7, tank with inert gas 8, and starting pump 9 complete the installation.

The figure also shows the arbitrary placement of capacitor 10 with cesium, the discharging jet 11 for dumping cesium and slag products.

During the starting of the reactor and its heating, there proceeds the emission of electrons from the heated cathode to the comparatively cold anode. Heat is removed from the anode by the liquid metal which circulates in the circuit and the radiator. The current being obtained is used for the power supply of the motor, pumps and units.

The advantage of such an arrangement is the simplicity (there are no rotating parts), compactness, and the possibility of obtaining high currents directly, which simplifies the power supply of the plasma motor. The shortcomings of the arrangement are the complexity of finishing the reactor unit with a converter, and the difficulty involved with studying and adjusting these two fundamental elements.

The subassembly works under conditions of elevated temperatures when large neutron fluxes exist, and prolonged time, which complicates the selection of adequate materials.

The installation is started similarly to the installation in the previous example. After filling, heating, and cleaning, the installation is ready to start. Circulation of liquid metal is ensured by starting pump 9 which, after the reactor is started, is disconnected.

#### Diagram of an extraterrestrial power plant with thermoelectric energy conversion

Figure 1.5 shows this type of two-circuit unit. The first circuit consists of the reactor 1, the pump 3, and the thermoelectric converter unit 4. The second circuit consists of the converter 4 and the radiator 5. Each circuit has a compensating capacitor 6 (shown here only in the radiator circuit). The unit can have one pump 3 on both circuits. The cooling of such a pump can require an additional cooler-radiator 2.

When the reactor is started there occurs heating of the hot junction of the thermoelectric (semiconductor) converter of the unit. The cooling of the converter is accomplished by the liquid metal of the secondary circuit. Current obtained as a result is used for the power supply of the space engine system.

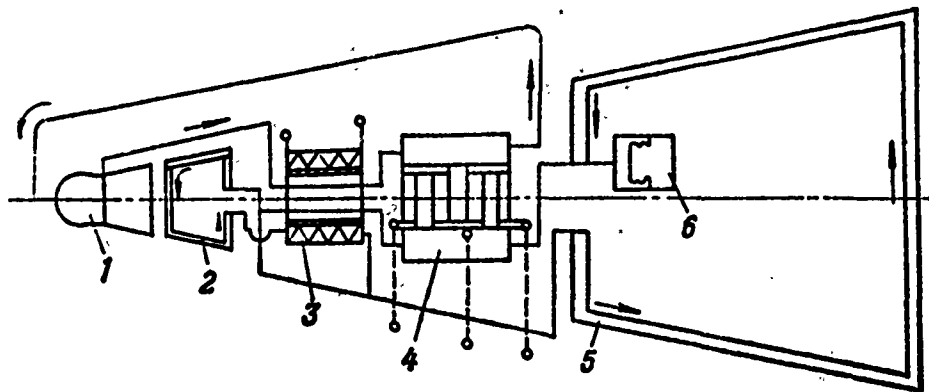


Fig. 1.5. Diagram of an ERE with a thermoelectric energy converter.

The advantages of the unit are simplicity and lightness with limited power levels; a shortcoming is less efficiency than in the other two examined units.

Semiconductors have low temperatures for the cold-soldered joint, which makes a heavier radiator.

The unit is started similarly to the unit examined above.

#### Diagram of a solar extraterrestrial power plant with fuel elements

This system consists of three circuits (Fig. 1.6). The first circuit includes the solar concentrator 1 with thermal trap 2, heat exchanger 4, and units 7, 8, 9 being the pump, filter and compensator.

The second circuit includes the generator, the fuel element itself 3, the evaporator and regenerative phase separator 4, and the condenser 5. The third circuit consists of the condenser 5, the cooler-radiator 6, and units 7, 8, and 9.

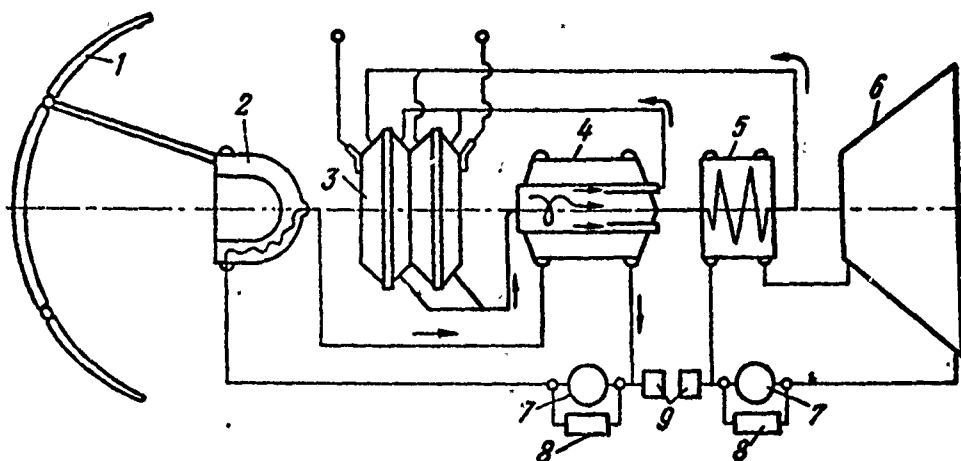


Fig. 1.6. Diagram of a solar extraterrestrial power plant with fuel elements.

In guiding the installation into orbit, the orientation system insures flux concentration of solar emission in trap 2. The liquid metal is heated by the heat of the trap, for example, the lithium which enters the generator 4 for the separation of the reaction products of the fuel element into the basic components.

In the fuel element the anode working medium, for example, sodium, enters the ion-exchange membrane, is ionized, giving off electrons to the anode, penetrates the membrane to the cathode area where it is connected with the cathode working medium, for example, tin. The cathode working medium, while dissolving the positive anode ions, releases energy close to the heat effect of reaction. Electrons which have completed operation in the external circuit participate in the formation of a reaction product alloy, in our example, Na-Sn.

Subsequently, the reaction product enters the regenerator and the process is repeated. In the installation in question the anode working medium, for example, metal, is condensed in the heat-exchanger 5 with the help of the metal of the third circuit and cooler 6.

The advantage of this arrangement is its simplicity, cheapness, lightness, and efficiency; the shortcoming is the difficulty of selecting design materials for the fuel element which works for a prolonged time.

#### 1.4. ERE RELIABILITY PROBLEMS

##### Initial assumption

In extraterrestrial motors various types of propellant rockets can be used. However, the most effective are the nuclear electric rocket motors. The electrical power of such installations can be thousands of kilowatts and, subsequently, even many tens of thousands of kilowatts. ERE for piloted interplanetary flights must work reliably for 10-25 thousands of hours.

To provide reliable operation for this long a period of time with a large number of on and off switchings, we must solve a number of complex problems. Therefore, we shall present only the general problems of ERE reliability and, in a number of cases, show some possible approaches to the solutions of specific questions of ERE reliability.

For *reliability criteria* values are taken with which reliability is estimated quantitatively; they include the probability of breakdown-free operation, failure rate, etc.

As a reliability criterion we take the *probability of breakdown-free operation*, i.e., the fact that in a given period of time or in the limits of a given mission failures do not occur; then based on the available experience in building foreign liquid propellant rocket engines, the average reliability of a LPRE, 0.9, is achieved after approximately 300-400 firing tests. In this sense, the work on a single-chamber LPRE with a thrust of 690 t (the F-1 engine, USA) is very characteristic. This engine operates on a propellant which

consists of kerosene (RP-1 fuel) and liquid oxygen. It was developed during the period 1960-1965 with 1545 bench starts and an overall average operating time of ~8200 s for each engine. Fifty-eight motor samples were spent on the first thousand starts. In use on a rocket this motor should work reliably for ~150 s. If we assume<sup>1</sup> that at the moment of the beginning of motor operation its reliability P was equal to zero (in actuality, probability of breakdown-free operation of this type engine with the first start can scarcely be lower than 0.2) and then it built up according to exponential law

$$P = 1 - e^{-\alpha N}, \quad (1.4)$$

where N is the number of tests,  $\alpha$  is a certain coefficient which characterizes the rate of reliability rise (see example at the end of section), then after conducting 310 tests the reliability calculated thus was 0.7-0.75, and after conducting 1545 tests it became no less than 0.9975. By reliability we mean the lower confidence limit of the probability of breakdown-free operation during a preset period of time under given conditions with a confidence coefficient of 0.95.<sup>2</sup>

As concerns ERE, because of their extremely high cost they can only be manufactured in single samples. However, the quantitative forecast of reliability and its experimental confirmation are necessary; special items are not isolated for confirmation of reliability, but everything necessary for this is obtained simultaneously with operation and acceptance tests of working samples.

---

<sup>1</sup>Barlow P., Proshan F., Mathematic reliability theory, translated from English, 1zd-vo "Sovetskoye radio," 1969, str. 334.

<sup>2</sup>Confidence range is the interval limited by the confidence boundaries in which, with a given confidence coefficient, lie the parameter being evaluated. Confidence parameter is the probability of the fact that the parameter being evaluated lies within a given confidence interval (GOST 13216-67).

A complex system or any part of it, with the advent of the science of reliability, became possible to estimate as a certain number which quantitatively characterizes the reliability of each specific item. However, it is necessary to know fully that this number (if it is near enough to one) can be an actual characteristic of the reliability of the specific example of the product only under the condition of continuous effective action to maintain (perfect) the quality of the part in all stages of its manufacture and operation. The reliability of any product combines into one very many different elements, units, instruments, systems and processes.

At the ERE planning stage as a measure of reliability it is possible to use conditionally the probability of breakdown-free operation in the execution of a problem. Breakdown-free operation must be provided during the guidance of the spacecraft with the ERE to the start orbit, during the start in this orbit, during operation in the transfer phases, in the stopping and starting processes for these phases, and in the trajectory returning the crew to earth orbit.

Statistical data on such installations are still scarcely available; therefore in predicting reliability we use various factors whose selection depends upon tests and engineering intuition of the designers. These factors are useful in the early stage of planning since they enable the distribution of reliability requirements between component parts of the complex. Calculations of reliability decrease the subjectivity of the approach for the definition of technical specifications under development and make it possible to simplify the agreement of inconsistent requirements. Furthermore, reliability calculations are necessary to define the program necessary to provide reliability. Actually calculations connected with the prediction of reliability concern only the reference line of incorrect execution. They do not include uncertainties and indeterminacies characteristic for new developments,

especially for installations intended for prolonged operation under new conditions. As noted, these uncertainties are estimated subjectively. Prediction and confirmations of reliability should consider and estimate the results of all conditions: the bases for development, the qualification for developers, the level of production, physical phenomena leading to failures, operation, the possibility of designing a product able to resist at all stages the conditions which deteriorate product qualities. In this case, an approximation should be selected correctly. One ought also to remember that the test conditions never completely correspond to actual service conditions, especially as this relates to complex ERE. The proper use of weighted tests, just as natural tests, in determining weak points in projects requires especially large experiments. Therefore, forecasting the reliability of a complex system which has been created can be done only by highly skilled specialists. High reliability can be achieved by performing a group of operations including the following:

- analytical investigations;
- generalization of the experiment of developers and utilization of statistics;
- mathematical simulation in analog-digital computers (ADC):
- complex simulation (the ADC together with natural units or systems);
- deep exploratory investigations and careful adjustment in laboratory conditions, on stands with the simulation of space conditions as well as in-flight conditions;
- equipment providing for the maintenance of reliability and functioning during operation;
- strict and continuous support, procedural, industrial and organizational measures which ensure faultless production and the operation of the item;
- positive solutions, equipment, and measures which ensure adaptability of an ERE to self-maintenance in working during the entire period of operation.



## Stages and content of operation

The creation and use of complex products generally, and with an ERE especially, is divided into the following stages:

- scientific research and the introduction of proposals concerning the creation of an ERE of a specific purpose;
- preliminary planning, compilation and agreement of technical tasks;
- sketch and engineering design;
- experimental adjustment in full scale and the manufacture of experimental models;
- bench tests under conditions of space simulation, flight design tests, and government tests;
- the manufacture of the working part;
- program application (utilization, operation).

The quantity and sequence of stages during the creation of an ERE can change based on specific problems.

To provide and evaluate reliability as a parameter of an ERE the development and utilization of special procedures is required at all stages of creation and product application (special methods of study, calculation, adjustment of construction and technology, measurement, provision for faultless production, etc).

Coordination and general organization of work in creating an ERE with the assigned level of reliability should be carried out on the basis of the following assumptions:

- concerning the order of development, tests, experimental manufacture, manufacture for use, and input of ERE into operation;
- concerning the order of the agreement of specifications on the supply of component parts (elements), materials and their supply with the reliability evaluation;

- concerning the evaluation and current marginal testing of products in production;
- concerning a single system of information about the technical state and the reliability of all parts and the ERE as a whole;
- concerning reclamation work;
- concerning the reliability services of all organizations which participate in the creation of the ERE.

Requirements for methods of standardizing and evaluating the reliability of individual forms of systems and complex products making up the ERE should be specified in special documentation.

Reliability requirements for an ERE and its parts are introduced into technical assignments and then into technical specifications and manufacturing records.

Reliability at the stages of product manufacture is ensured and confirmed (measured, demonstrated) on the basis of the common plan for the creation (development, manufacture) of the product with the assigned level of reliability and the program for providing engineering data and reliability of the component parts of product.

Methods and means of confirming (measuring, demonstrating) reliability are established by general and specific procedures or by specifications for manufacture, test and inspection of component parts and the ERE as a whole. During the creation of such a complex system as an ERE, especially at the initial stages, it is not always possible to estimate quantitatively its reliability. In these cases it is advantageous to use its merit rating. By merit rating for reliability we mean the evaluation of the suitability of the product for use with respect to its purpose, based predominantly upon qualitative analysis. This includes:

- the correctness of the operating principles selected, volume and depth of design and theoretical substantiation, modes of operation,

the use of earlier systems and units, the advisability of using basic materials and component parts, stability against service failure in the least reliable elements, the correctness of the accepted structural solutions and product strength reserves;

- procedural and industrial provision for solutions arrived at during planning;

- the necessary volume of tests during the experimental check of designs, circuits, modes of operation, stability to external effects, critical characteristics and conditions;

- the sufficiency of complex tests and checks of the correctness of a combination of systems under various possible emergency situations.

During the compilation and coordination of works based on programs to ensure ERE reliability, it is necessary to keep in mind:

- reliability as a given value can be achieved only after conducting a series of adjustment stages for all parts and the ERE as a whole;

- achievement of the assigned level of reliability with the correct work setting is determined by the number of valid experiments made while conducting a given stage of adjustment for the part of the structure being examined or the ERE complex;

- the value which characterizes the reliability rises sharply with the use of special airborne apparatus for monitoring, maintenance, and optimization of ERE efficiency as a whole or an extraterrestrial vehicle which uses an ERE as the basic motor.

This latter can guarantee adaptability of an ERE to supporting itself in working order during its entire life.

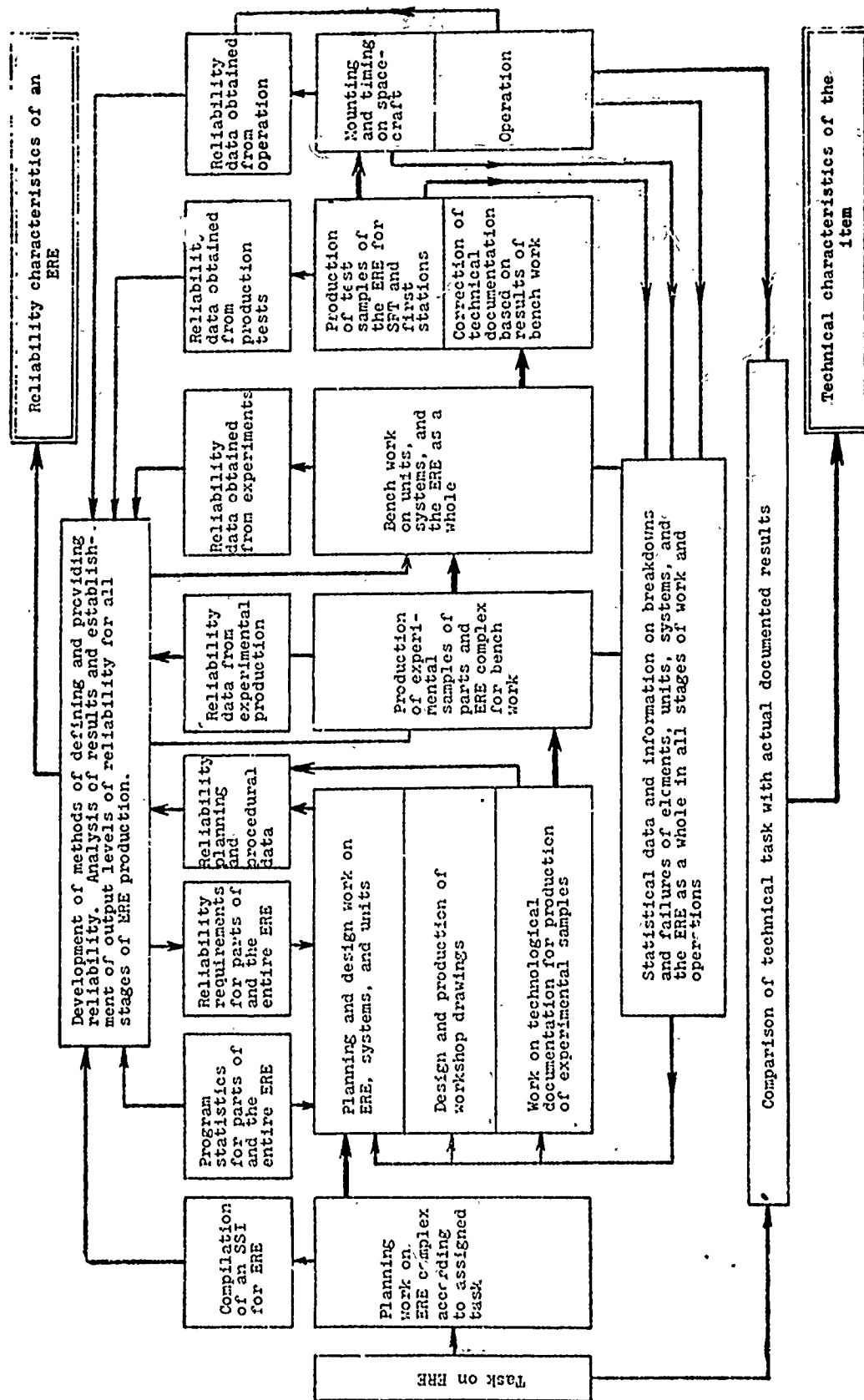


Fig. 1.7. Flowchart for reliability work on an ERE.

## Structural diagram of operations

The reliability of elements, units, systems, and the ERE as a whole, as with any complex product, is set at the planning and designing stage, is ensured and supported at the subsequent stages of manufacture, experimental adjustment, production of flight samples, and during their operation. Figure 1.7 depicts the structural diagram of operations with respect to ERE reliability. Figure 1.8 shows the results of calculations in a fully simplified analytical model of reliability. They show how reliability of a complex ERE depends upon the levels of the reliability of the main operating parts. This reliability is given taking into account the different levels of the effect of subsystems involved in the structural diagram of ERE reliability along with the main operating parts. To compile a curve of reliability growth, as depicted in Fig. 1.8, it is necessary to examine the entire structural diagram of the ERE. Such branched schematics must be composed for a series of structural solutions being examined and the optimum version should be selected (including the accepted redundancy, maintainability, etc.). From the approximation chart in Fig. 1.8 it is evident that in the initial stages of finishing the decisive influence on reliability is the various links. In the process of finishing their effect is almost excluded. In spite of this, the reliability of the entire complex in practice has not been acceptable even with high reliability for the main operating parts. Above has been shown the complex of operations in establishing reliability which must be accomplished to achieve an assigned reliability for a real ERE.

Since creating an ERE is the joint work of a large number of specialized organizations, the responsibility for providing reliability is distributed among the chief developer of the ERE complex and the organizations making the component parts, materials, units, and systems. The correct distribution of reliability requirements between developers forces them to make an evaluation

and analysis. It is evident that with the assigned (or accepted) reliability of an ERE the reliability criteria of its components should be very high. Therefore, to provide the required reliability all developer organizations should create specific routines for providing reliability and fulfill them. The chief developer must find and accept such diagrams and structural solutions as will allow, with the reliability of all component parts somewhat less than unity, the fulfillment of the functions of a given ERE while preserving its operational criteria within assigned limits for the necessary period of time.

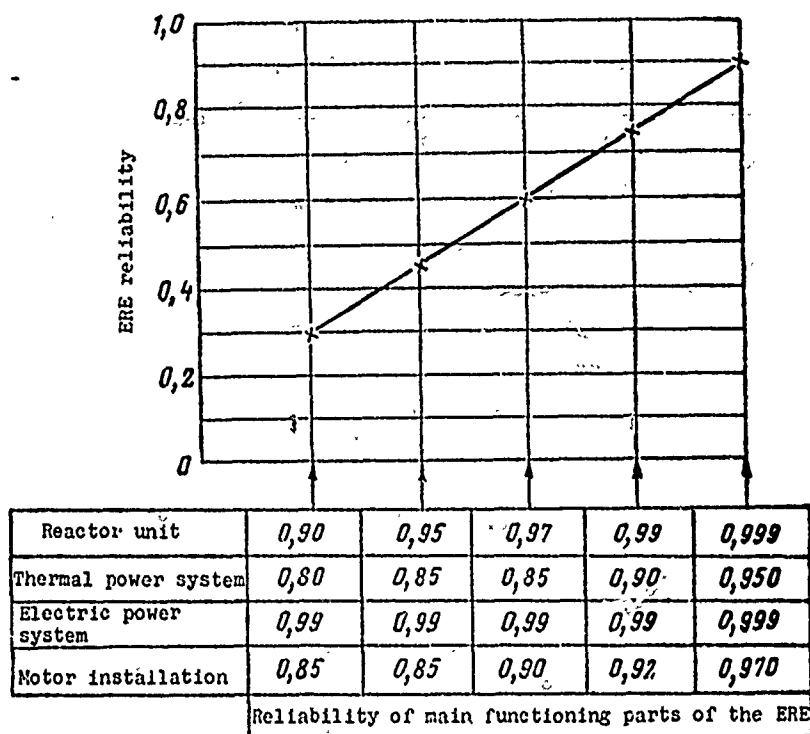


Fig. 1.8. Possible projected reliability (probability of breakdown-free operation) for an ERE complex under different levels of reliabilities for the main functioning parts.

## Reliability program

An ERE, as any item of space technology, must have high reliability under the condition of the systematic fulfillment of specific operations (programs). Below is a list of operations which ensure the reliability programs.

1. A study of technical and reliability characteristics of parts of analogs and prototypes. An acquaintance with items at their production sites (design, preparation, adjustment) and operating sites. Recognition of breakdowns and emergencies; recognition of factors determining these breakdowns and emergencies; a study of methods used to eliminate them; examination of methods used to adjust item to the necessary reliability.

2. Compilation and analysis of the reliability of versions of enlarged structural diagrams and mathematical models of items to be developed, taking into account the conditions of their use. In compiling the diagrams, it is necessary to apply the principle of self-adaptation, which in its practical application reduces to the automatic detection of deviations in the operation of the item (or a part, system, unit of it), their identification (establishment of reasons), choice of correcting actions (or operations), and application of the selected operation to eliminate the failure noted (disturbance of operational capability).

A self-adapting ERE, because of the presence in it of means for breakdown compensation, can ensure great longevity with optimal characteristics of each condition of flight. Self-adaption makes it possible to use for achieving almost absolutely reliability elements which are not absolutely reliable. From the point of view of ERE production and adjustment, the use of self-adapting devices means that for adjustment tests considerably less self-adapting items than the ordinary nonself-adapting items are necessary.

3. The first optimization of self-adapting systems and the ERE as a whole is based on the following parameters:

- reliability of structural diagram;
- weight characteristics;
- cost.

4. Preliminary standardization of the reliability of elements, units, instruments, aggregates, and systems.

5. Development and bases for requirements on complex reliability, more precise definition of reliability norms for systems, taking into account requirements on operation, cost and weight.

6. Selection of completing elements; solution to problems of specialized development of new completing elements and materials with respect to engineering level which is expected in the operating period of the future ERE.

7. Second optimization of ERE reliability, taking into account the work of in-flight systems for checking and maintaining reliability and ERE control. Determining the basic data and compiling the technical task for developing this in-flight system which must also be built according to the self-adaptation principle and fulfill the following basic operative functions:

- multiple check (sometimes hundreds or even thousands per second) according to several values (indices) of each tested parameter;

- evaluation (automatic) of the reliability of the check results based on all tested parameters, for each moment of the check;



- indication of state, transmission of command to turn on reserve elements or systems or automatic maintenance of reliability on the prescribed level;

- prediction of state and optimization of the possibilities of fulfilling the program at each checked moment of flight in the presence of a reserve, after its exhaustion and after each breakdown of ERE parts in the absence of their possible replacement;

- delivery of prediction data with respect to the provision of breakdown-free flight or return to base.

8. Development of reliability of methodology for the ERE and its systems applicable to all stages.

9. Determining the nomenclatures of bench equipment. Compiling working methodology, programs, and graphs for finishing the ERE and all its parts up to required reliability. Determining the number of samples necessary for tests. Developing systems and forms of gathering, handling, and using information on reliability for all stages of ERE production and operation. Organization of the exchange of reliable information between all development and operational sections.

10. Refined optimization (with respect to characteristics indicated in paragraph 3). Correction, completion, or reworking of technical documentation as work is fulfilled on the stages depending upon the applicability of the approximation achieved for the prescribed values of working parameters, weight, life, reliability. Achievement and maintenance of reliability - this process is for the entire period of the item's existence - from the moment of the agreement on a technical task for its development to the end of the operating period.

## Organization of work

A piloted spacecraft for flights to the planets is, of course, unique in its complexity. The ERE for such a craft will be a powerful installation on a high engineering level. Insuring its reliability is the greatest problem, not only scientific and technical but also organizational.

After receiving the technical task (TT) and establishing time periods for development, it is necessary to plan all the work. One of the well-known progressive methods of organizational guidance in the creation of complex systems is the method of network planning and administration (NTA). The main value of this method lies in the fact that it allows us to distinguish the optimal version of planning and administration in all stages.

To illustrate this method we shall graph the creation of a hypothetical ERE for a piloted spacecraft. We assume that work is carried out in five stages and ten phases; for each phase one year is set aside. The stages and phases are illustrated on the graph (Fig. 1.9).

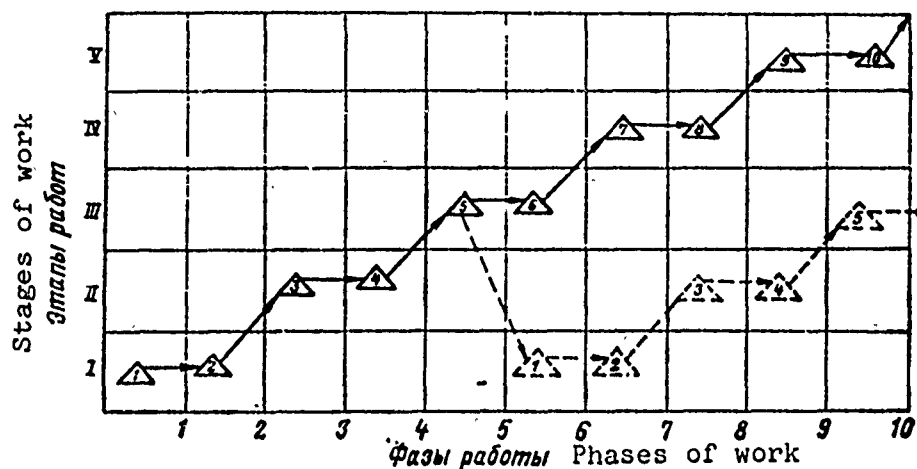


Fig. 1.9. Main stages and phases of operation in the NTA system in the creation of a hypothetical ERE for a piloted spacecraft (solid line); dashes show the development of work on the creation of an ERE for a flight which would land astronauts on a planet and return them to earth.

### *Stages*

I. Analysis of the technical task, planning sketches of the ERE, and experimental work on the systems.

II. Development and testing of experimental samples of ERE.

III. Acceptance tests for systems, the beginning of the finishing work on the ERE complex.

IV. Completion of finishing, acceptance tests and production of an ERE working model.

V. Combined (complex) bench tests of a spacecraft with an ERE; delivery of samples of the ERE working model.

### *Phases*

1. Analysis of the technical task, beginning of preliminary ERE drafting, development of experimental samples of aggregates and systems, beginning of experimental work on aggregates and systems.

2. Obtaining initial experimental results on aggregates and systems, finishing preliminary draft on ERE complex.

3. Finishing experimental work on aggregates and systems, making experimental samples of ERE.

4. Introducing necessary changes, finishing aggregates and systems, experimental work on ERE complex.

5. Completion of finishing work on aggregates and systems, completion of experimental work on ERE complex, introduction of necessary changes.

6. Beginning of finishing work on ERE complex, conducting experimental flight tests of some systems, conducting acceptance tests on systems.

7. Completion of finishing work on the ERE complex, introduction of necessary changes, preparation of working samples of the complex.

8. Conducting experimental flight tests of the complex, beginning acceptance tests of the complex, production of ERE working model.

9. Completion of acceptance test of ERE complex, introduction of necessary changes, check of bench tests, and delivery of samples of ERE working model.

10. Combined complex bench and flight tests of spacecraft with ERE.

Similar, but considerably more detailed, graphs should be compiled for systems and their separate parts.

The listed stages and phases show only the development and completion of the basic cycle of research and development work, after which we proceed to space flight tests (SFT) of the sample spacecraft with all the airborne and ground flight support equipment.

*Component diagram (of component parts)  
of the ERE*

At the beginning of ERE planning its systems, component parts, operating principles, operating processes, operating modes, materials, etc., should be selected. All interrelations must be determined; problems involved in ensuring the stability of parameters, lifetime, reserves, self-adaptation, and reliability must be solved. Also problems in the organization of work, accomplishment periods, and cost should be solved.

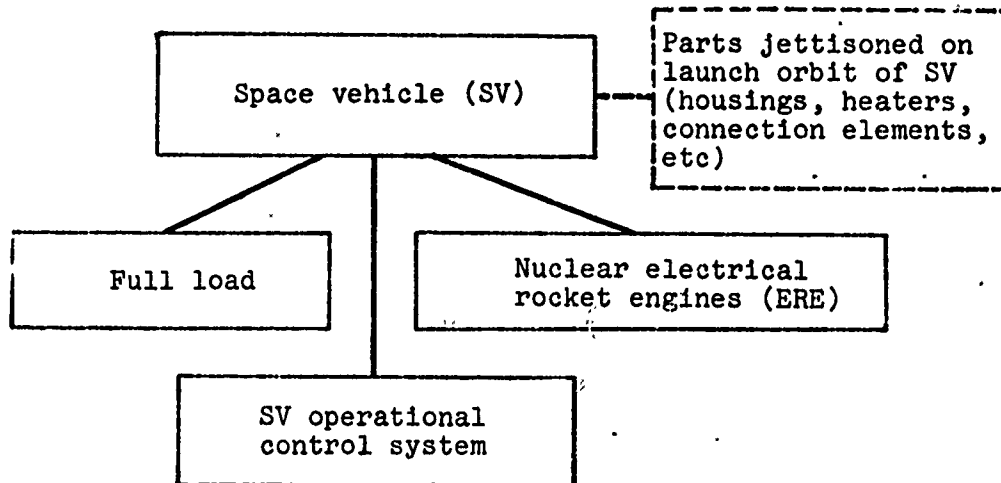


Fig. 1.10. Diagram characterizing the component parts of a hypothetical piloted space vehicle with an ERE.

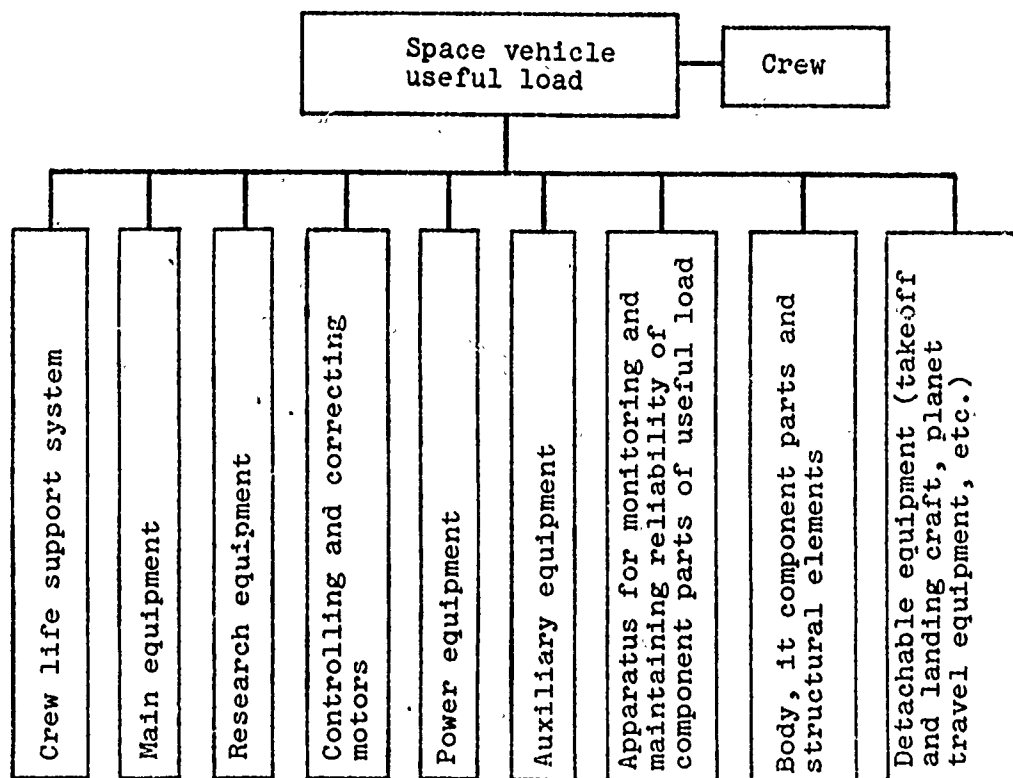


Fig. 1.11. Component parts of useful load for a space vehicle.

The first of these works is to draw up an ERE composition diagram. For general orientation, Fig. 1.10 presents a composition diagram of a hypothetical piloted space vehicle with an ERE, broken down into its main parts; Fig. 1.11 presents the component parts of useful load, and Fig. 1.12 the component parts of the control system of this vehicle.

In the development of an ERE based on a technical task, the composition diagrams must comply with all conditions imposed by the buyer. Therefore, below, in Fig. 1.13-1.16 diagrams are presented which characterize the composition of an ERE only with respect to the large systems used in any ERE. For example, Fig. 1.16 shows a more detailed breakdown of only one nuclear electric ERE with a turbogenerator system for obtaining electrical power. The composition of a nuclear electrical system and other ERE systems depends upon a huge number of possible general and particular solutions with respect to each of the systems used in the ERE. A list of aggregates and instruments, presented in Fig. 1.16, reflects the approximate nomenclature of aggregates, instruments, units, and subsystems. It is assumed that all the main systems and their parts are created on the principle of self-adaptation.

#### Composition of ion engine

For example, let us examine the composition diagram of an ion engine presented in Fig. 1.15. From the diagram it is apparent that the electrical rocket engine includes:

- a system of converting parameters of electrical power for the electrical rocket engines;
- automatic electrical equipment, circuit breakers, and emergency electrical power release;
- cooling system for electrical rocket engines;
- module unit of electrical rocket engines;
- automatic control equipment for the engine unit;
- equipment for monitoring and maintaining reliability;
- structural parts: power frame, attachment devices, electrical supply line, etc.

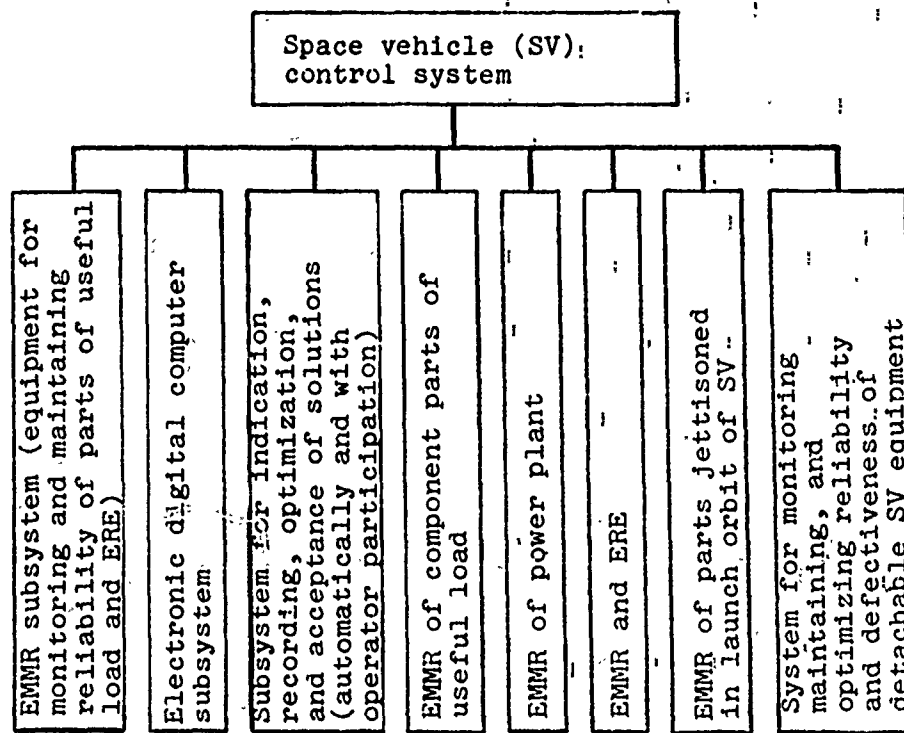


Fig. 1.12. Component parts of space vehicle control system.

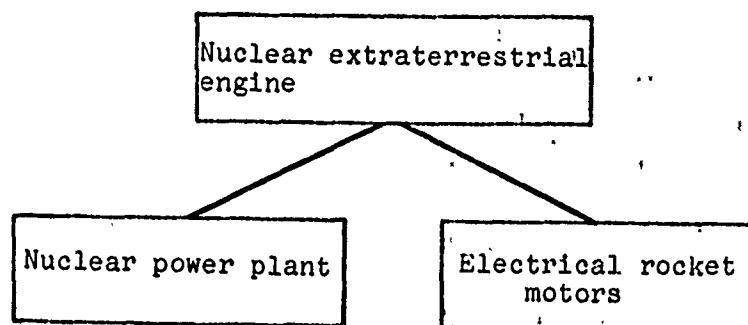


Fig. 1.13. Diagram characterizing component parts of nuclear ERE.

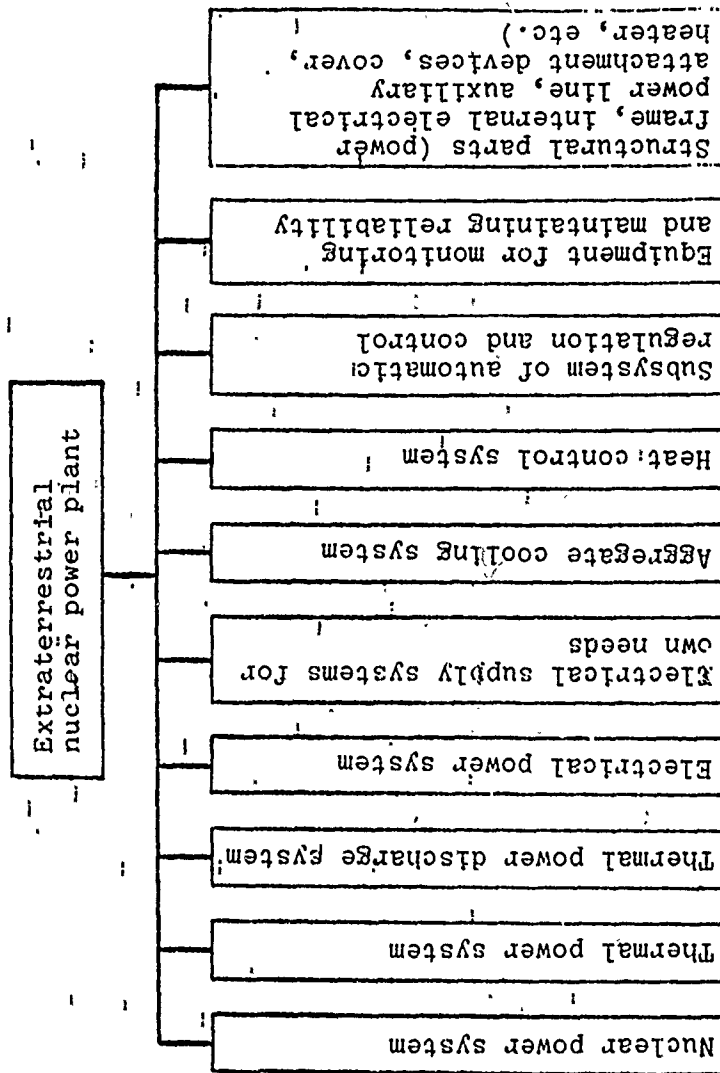


Fig. 1.14. Component parts of extraterrestrial nuclear power plant.



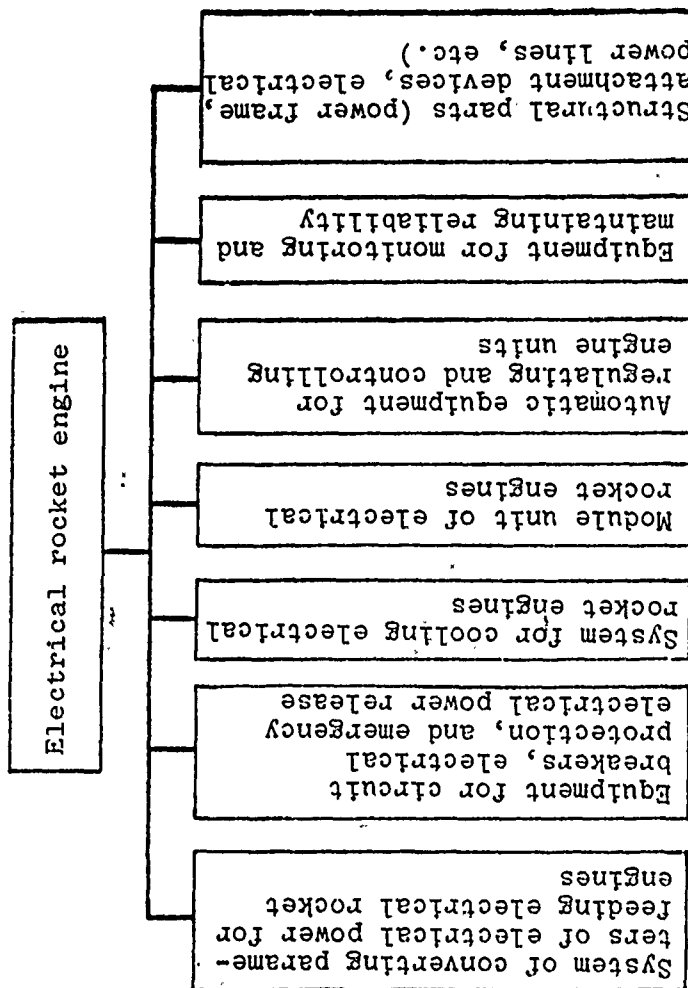


Fig. 1.15. Component parts of an electrical rockets engine.

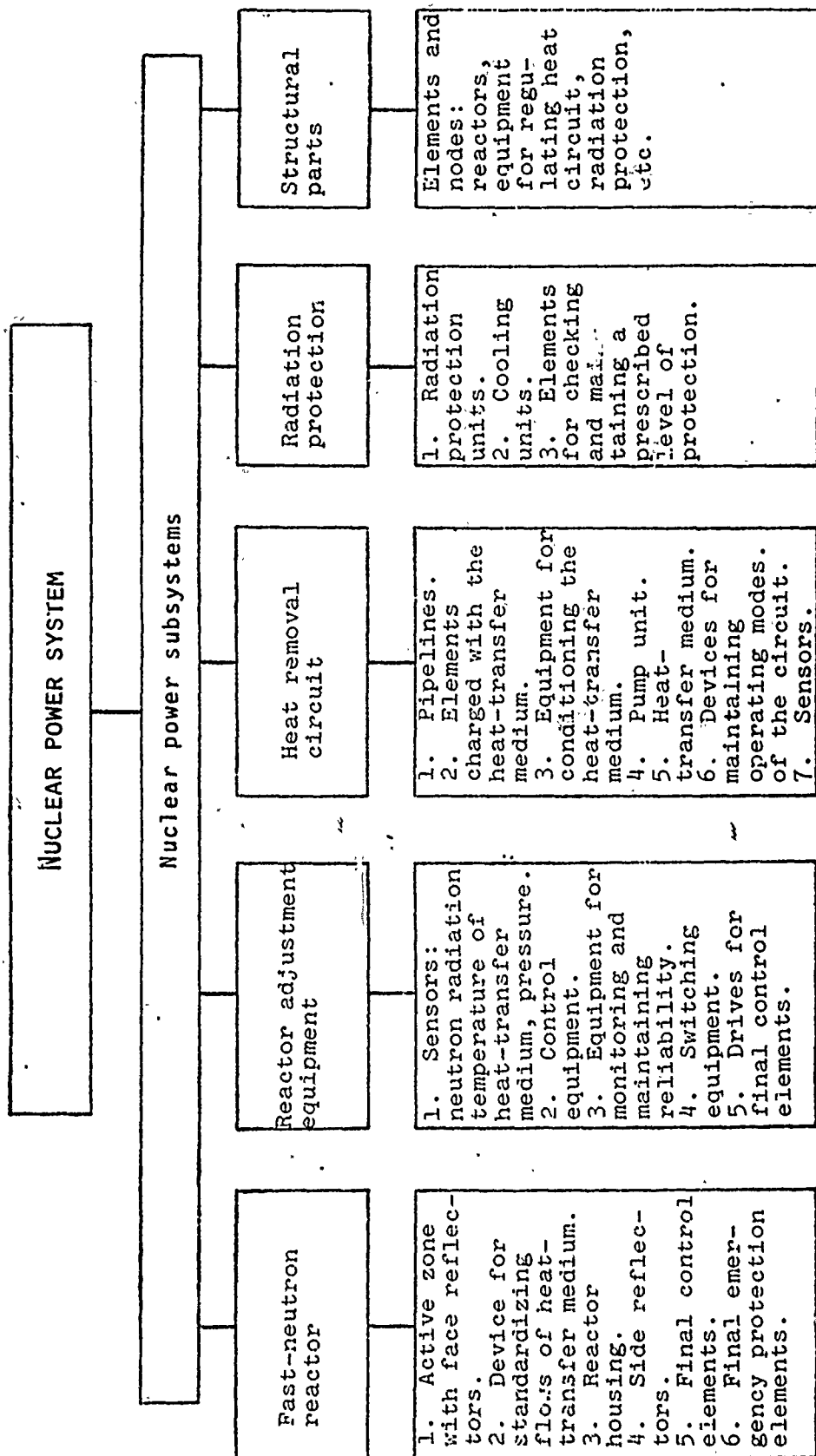


Fig. 1.16. Example of a diagram characterizing the component parts of a nuclear power plant.

However, this list can be changed depending upon the engine's operating principle or structural decisions made with respect to any part. For example, if the electrical power plant is a type of reactor-transformer, it is advisable to use a low-voltage plasma engine. The use of this engine is more expedient if the electrical voltage of the reactor-transformer is equal to the working voltage of the engine and it is installed directly on the switching unit of the reactor-transformer. Such a decision substantially changes the nomenclature and content of the entire ERE composition indicated in Fig. 1.15, while the ERE itself can be optimal for this case both with respect to the working parameters and reliability. Therefore, below we have presented only the overall requirements on ERE reliability and the particular case examined is to solve the problem of electrical rocket engine reliability with an ion engine.

#### Engine reliability requirements

The engine of a piloted spacecraft for long-range flights must have very high, practical 100% reliability. The length of the operating period is measured in years. Electrical rocket engines in general and ion engines in particular are being built for the first time and, therefore, it is impossible to expect 100% reliability for an ERE with only one engine. The tested engineering approach to the solution of such a problem is the joint use of two paths:

- the creation of a highly reliable electrical rocket motor which is a module of the engine;
- the use of reserve modules.

In the case of an ion engine the module system is obviously more applicable. It is a unit composed of modules of ion motors, a complex of necessary equipment and devices, also with corresponding reserves.

From the point of view of reliability, the engine in the ERE system is that part whose breakdown can entail, in the best case, an emergency or nonfulfillment of task, and in the worst, a catastrophe for the entire space vehicle. Therefore, the engine must provide the necessary impulse in all operating modes, including damage of certain elements, systems or motors.

Diagrams of ERE systems must exclude the possibility of the occurrence of operation modes which are not permissible in safe flight or conditions of ERE controlling sections where failures occur in the systems themselves or any part of the ERE.

Equipment for inspecting and maintaining ERE reliability must switch off, in a timely manner, places with reduced reliability, switch on reserves, and send the primary commands to the space vehicle control system for a general solution to the question of the possibility of meeting the flight program or correcting it.

Engineering methodology for calculations must be set up in the planning and development process.

However, even in the initial stage of development it is necessary to solve approximately general problems of evaluating reliability of modules, systems, the main parts of the ERE, and also the entire ERE. Let us consider an example.

Example 1.1. We shall estimate the reliability of a module of a ion rocket engine for the initial stage of its experimental work. We shall keep in mind that in this stage there is as yet no control system for the space vehicle (see Fig. 1.12) nor a part of it - the equipment for inspecting and maintaining reliability of the ERE (see Fig. 1.14). Unsolved also are problems of self-adaptation and as yet incompletely researched are the physical processes involved. No evaluation has been made of the effect of external factors on the operation of the electrical rocket engine; no production technology has been worked out and new structural materials have not been

developed. Of course, there are no statistics on the operational ability of the elements, nodes, aggregates, and systems of the engine module. In this stage of work the operating time achieved (lifetime) is hundreds or even thousands of times less than that required.

For the subsequent study the following selections are made:

- an ion engine (IE) with ionization of the working medium by oscillating discharge (Fig. 1.17);
- an ion motor with ionization of the working medium on a heated porous surface (Fig. 1.18).

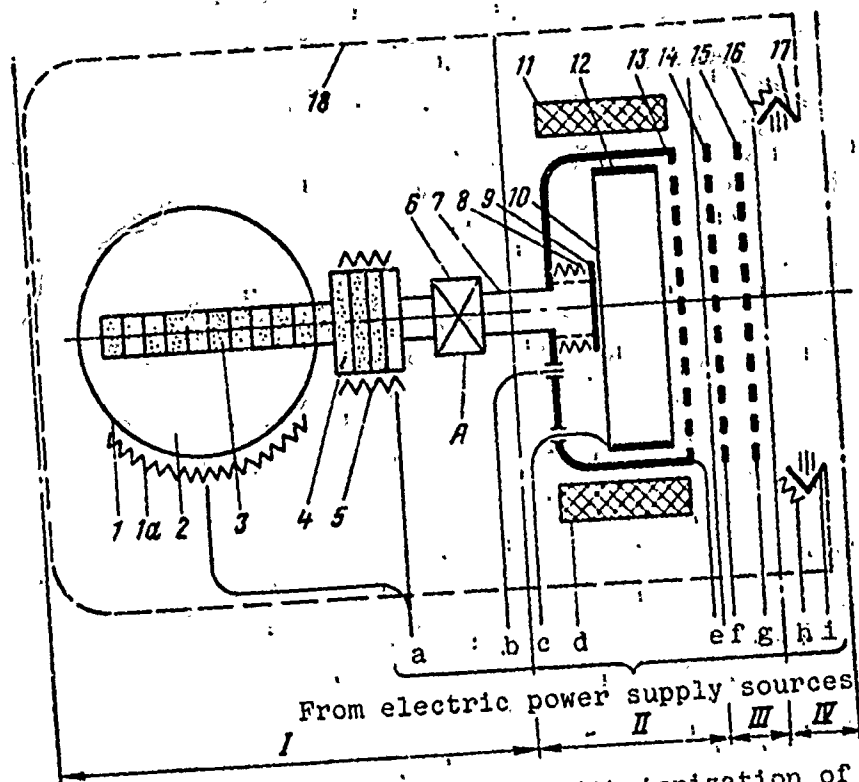


Fig. 1.17. Diagram of ion motor module with ionization of working medium by oscillating discharge: 1 - working medium tank; 1a - tank heater; 2 - working medium; 3 - supplying "wick" (porous medium); 4 - vaporizers; 5 - heat for vaporizers; 6 - cutoff valve; 7 - steam pipe; 8 - cathode heater; 9 - cathode; 10 - discharge chambers; 11 - solenoid; 12 - anode; 13 - extending grid; 14 - intermediate grid or grid systems; 15 - accelerating grid; 16 - neutralizer heater; 17 - neutralizer; 18 - electrostatic shield; a-i - inlets from electric power supply sources; A - inlet from engine automatic system.

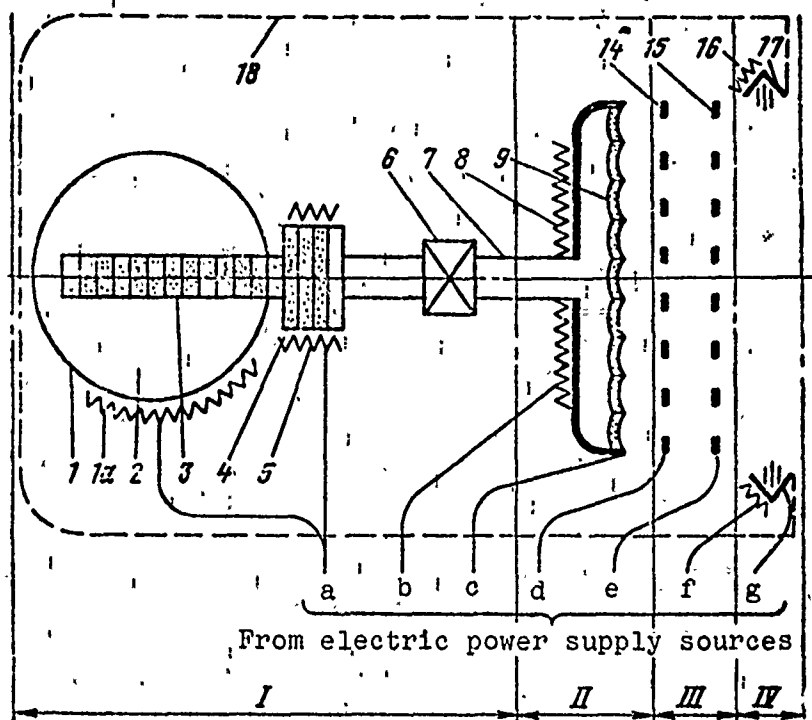


Fig. 1.18. Diagram of ion motor module with ionization of working medium on heated porous surface: 1 - working medium tank; 1a - tank heater; 2 - working medium; 3 - supplying "wick" (porous medium); 4 - vaporizer; 5 - vaporizer heater; 6 - cutoff valve; 7 - steam type; 8 - ion emitter heater; 9 - porous ion emitter; 14 - intermediate grid or grid system; 15 - accelerating grid; 16 - neutralizer heater; 17 - neutralizer (electron source); 18 - electrostatic shield; a-g - inlets from electric power supply sources; A - inlet from engine automatic system.

For convenience the common elements of both diagrams are shown on the figures and designated identically, while the diagrams themselves are divided into four systems which are common to them:

- I - a supply system for the working medium,
- II - ion source,
- III - ion optical system,
- IV - space charge neutralization system.

From the design and operational points of view, these two diagrams differ mainly in the thermal stress of the main elements. A comparison of the working processes for these diagrams show that the ion motor with a three-dimensional ion source can be made so that none of its parts will be heated above 700°C. At the same time an ion motor with a surface ionizer, all other things being equal, requires the ionizer temperature and the temperature of elements connected with it to be approximately 1400°C. Therefore, in the second diagram it is considerably more difficult to achieve a high level of reliability than it is in the first. In addition, the first type of motor is less sensitive to contamination, the quality of material processing, and fabrication precision for a considerable number of parts; it does not require highly oxidation-resistant metals and insulators. In it can be used quite a variety of working media, while in the ion motor with a surface ionizer virtually only cesium and rubidium can be used. Thus, a comparison of module diagrams gives the designer many starting points for solving reliability problems.

Structurally it is advisable to build an ERE with an ion motor on the basis of modules. For the current reliability evaluations of an ion motor module, in the process of experimental work, we can use the assumption made in calculating reliability that the planned module, which must have a long lifetime, can have two types of failures:

- sudden failures, which can be caused by the effect of random factors (in the presence of equipment for checking and maintaining reliability, there can be virtually no sudden failures);

- gradual failures, which are due to irreversible processes (material aging, electrode erosion, various types of wear, irremovable contamination, etc.). In this case, we can take as a reliability criterion probability  $P_M$  of failure-free work of the ion motor module during given period of time  $\tau$ . In other words  $P_M(\tau)$

is the probability that the average time before breakdown occurs (T) will be greater than prescribed:

$$P_M(\tau) = \text{Bep}(T \geq \tau). \quad (1.5)$$

It is obvious that the reliability diagram plotted as a logical functional diagram of module system connections for Figs. 1.17 and 1.18 is a series of the above four systems. The compilation of a more detailed structural diagram is necessary and possible in the development of the module and its systems.

For the indicated structural diagram of the module the probability of stability in the main parameters of the module  $P_M$  during tests (current reliability) can be expressed as the product:

$$P_M = \prod_{i=1}^k P_i = \prod_{i=1}^{k-4} P_I P_{II} P_{III} P_{IV}, \quad (1.6)$$

where  $P_M$  is the current probability of successful test results, i.e., such that the main parameters of the module (and similarly of the system) do not go beyond the permissible limits for any reason.

Taking the division of failures into sudden and gradual and their mutual independence, the probability of breakdown-free operation for the module

$$P_M = \prod_{i=1}^k (P_{BH} P_{\Gamma})_i, \quad (1.7)$$

where  $P_{BH}$  and  $P_{\Gamma}$  are the probability of breakdown-free operation for the i-th component of the structural diagram defined respectively according to sudden and gradual failures; k is the number of the component parts of structural diagram.



As the number of tests builds up and the operational ability of the module improves, a failure distribution law is distinguished; in the first approximation we can assume it is exponential. Then the current probability of the  $N_1$ -th test being successful is written in the following manner:

$$P_M = 1 - ae^{-\alpha N_1} = 1 - \alpha n_k \frac{e^{-\alpha N_1}}{1 - e^{-\alpha N_k}}, \quad (1.8)$$

where  $a$  and  $\alpha$  are coefficients determined exponentially;  $n_k$  is the total number of failures;  $N_k$  is the total number of tests examined.

To determine coefficients  $a$  and  $\alpha$  a graph of the accumulated failures has been plotted. Failures lead to single standardized test conditions. In this case, failures caused by random factors (industrial defects, errors in the bench system, rough deviations in tests conditions, etc.) are not taken into account. An example of such a graph is given in Fig. 1.19. Bends of the curve at points a-d correspond to the proper solutions made in the process of development, which lead to an increase in the number of failures. The spot where the curve stops climbing corresponds to the end of the finishing tests; the module of the ion motor is brought up to a given requirement of failure-free operation. The curve in sections is approximated by an exponent, for each section of which the value of coefficient  $\alpha$  is found.

For each section, coefficient

$$a = \alpha n_k \frac{1}{1 - e^{-\alpha N_k}}. \quad (1.9)$$

Based on the obtained results of processing experimental data, a graph of current reliability is plotted for the module of the ion motor or its systems  $P_M = f(N_1)$ .

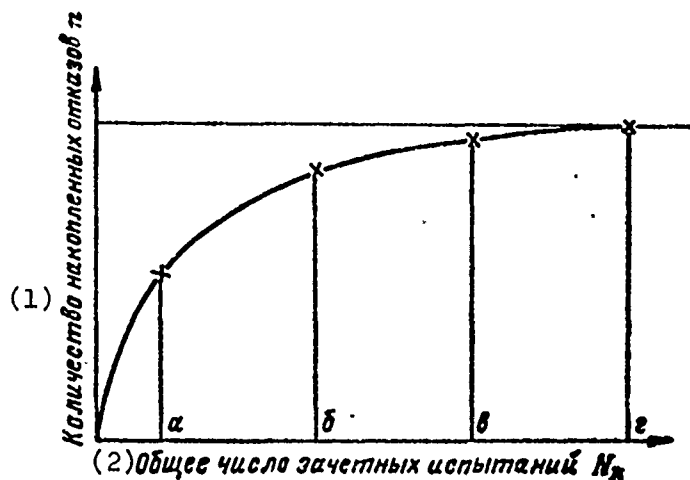


Fig. 1.19. Bar graphs of accumulated failures. Points a-d correspond to the acceptance of solutions which improved the work of the module; point d corresponds to the end of finishing.

KEY: (1) Quantity of accumulated failures,  $n$ ; (2) Total number of tests examined,  $N_k$ .

With the aim of rapidly revealing the weakest spots in the motor during experimental processing, it is advisable to plot such curves for individual units, aggregates, processes, techniques, bench test conditions, and for other reasons affecting reliability in the module development process as shown in Fig. 1.20.

Thus, the quantity  $P_M$  characterizes the validity of the reference data at the  $N_1$ -th moment of testing. At the end of the development work, when failures for any reasons cease, the module achieves the full required reliability  $P_M$ .

Using the graph in Fig. 1.20, we can, in certain limits, predict the future course of finishing work and, if necessary, pose the problems of the necessity for accepting specific solutions capable of increasing the reliability level.

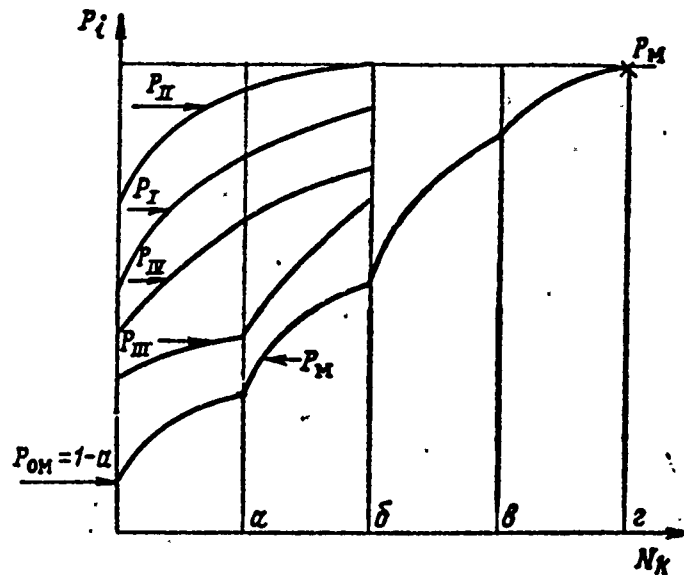


Fig. 1.20. Curves showing buildup of current reliability for ion motor systems and module (buildup of probability for successful  $N_1$ -th test of system and module):

$P_{0M} = 1 - a$  - initial reliability (probability);  $P_M$  - module reliability achieved.

### 1.5. PROBLEMS OF ERE STRESS ANALYSIS

Questions of ERE strength in this course are examined with respect to the preliminary sketching of parts and structural nodes. In this stage of planning we assume that a node in the first approach is made up of components and its main dimensions are selected. We also assume that the designer has selected the basic thicknesses of the walls of the parts bearing the load; the basic loads are determined for critical parts; heat flux and wall temperature are determined for heated parts.

A check of the correctness of the selected design dimensions, in the first approach, and a check of the strength of critical parts of a node in the preliminary sketch are the main tasks of the proposed

stress analysis. The correctness criterion will be the amount of strength reserve or plasticity of the part.

At this stage of planning stress analysis is generally conducted as an elastic problem, which makes it possible to obtain comparatively simple relationships which are also convenient to use. Such a calculation is a verification. It does not exclude and, in some cases, requires a more detailed calculation using special methods which we shall not discuss in this book because of space limitations.

#### Strength reserve. Plasticity reserve

Stress analysis for parts consists of three stages.

*First stage* - determining forces and moments acting on the part and its unsafe section.

*Second stage* - calculation of stresses which occur in the part from the effect of forces and moments. This stage, as a rule, is the most difficult.

*Third stage* - comparison of stress obtained with limiting stresses of the stress-strain diagram for the material from which the part is made or with stress in similar designs which operate successfully.

Let us clarify the terminology which we shall be using in our study.

The strength of a part is the ability of the part to resist the loads acting on it. Strength is a function of many factors: temperature and length of operation, the character of stress variation, the shape of the part, its dimensions, surface condition, the design of junction and couplings, the orientation of the fibers of the metal and its structure, etc. The proper evaluation of the effect of each of these factors on strength is one of the tasks of calculation.

Stress is the intensity of the internal forces of elasticity, corresponding to a given elementary area of a certain cross section. Stress is calculated for this area as the ratio of the absolute value of force to the size of the area on which it acts, i.e., as the force which occurs per unit of area.

Normal stress  $\sigma_k$  is that component of stress which acts perpendicularly to the area; the subscript  $k$  designates the direction of normal to the area. For example, if the area is perpendicular to axis  $x$ , normal stress acting on this area is designated  $\sigma_x$ .

Tangential stress  $\tau_{ik}$  is the component of stress acting along the area; the subscript  $k$  also indicates the direction of normal to the area, while the subscript  $i$  is the direction of the vector of tangential stress; the dimension of stress  $N/m^2$  (or  $kg/cm^2$ ).

Under the effect of external forces and stress which occur, the dimensions of the part change somewhat; it is deformed.

Deformation is the change in linear or angular dimensions of a part; usually these changes are very insignificant as compared with the part's dimensions.

Absolute elongation, i.e., change in the linear dimensions  $l_k$ , is designated  $\Delta l_k$ . It is positive during extension and negative during compression.

Relative elongation  $\epsilon_k$  is the ratio:  $\epsilon_k = \Delta l_k / l_k$ ; the subscript  $k$  indicates in what direction elongation is occurring.

Relative shear  $\gamma$  is the angle by which the original right angle between two selected directions in the part changes during its deformation. If these mutually perpendicular directions are designated  $x$  and  $y$ , relative shear  $\gamma$  is given the subscript  $xy$ .

The mechanical properties of the material under static loading are characterized by a stress-strain diagram which represents the relationship between the conditional normal stresses  $\sigma$  and the relative elongations  $\epsilon$ .

The arbitrariness of normal stresses  $\sigma$  and the relative elongation  $\epsilon$  which corresponds to them lies in the fact that stresses  $\sigma$  pertain to the original area of sample cross section while elongation  $\epsilon$  pertains to its original length.

In the range of low elastic and elasto-plastic deformations, arbitrary stresses and elongations differ little from true ones calculated with the contraction of the sample cross section during its testing taken account, and for ordinary engineering calculations are used as reference values.

One of the peculiarities of the deformation diagram examined is the standard method of obtaining it. The diagram is determined experimentally on standard machines in a comparatively short period of time (less than two minutes). The standardness of the method of finding the deformation diagram is an obligatory condition in determining the properties of the material; otherwise it would be impossible to use these results.

A typical arbitrary deformation diagram is presented in Fig. 1.21a. The deformation process can be illustrated also by a simplified stress-strain diagram consisting of two straight lines (Fig. 1.21b).

On the deformation diagram characteristic points  $y$ ,  $T$ , and  $b$  are determined, each of which correspond to a certain limiting stress.

The plastic limit  $\sigma_y = \sigma_{0.002}$  is that stress at which the first sign of plastic deformation appear. This limit is defined as the stress responsible for a given small permanent set. Usually the residual relative elongation  $\epsilon = 0.002-0.005\%$ . Plastic limit is a

strength criterion only when even small residual deformation can not be permitted during operation.

The modulus of elasticity  $E$  is the coefficient of stress and strain proportionality in the limits of elasticity:

$$\sigma = E\epsilon,$$

where

$$E = \operatorname{tg} \alpha = \frac{d\sigma}{d\epsilon} = \frac{\sigma}{\epsilon}.$$

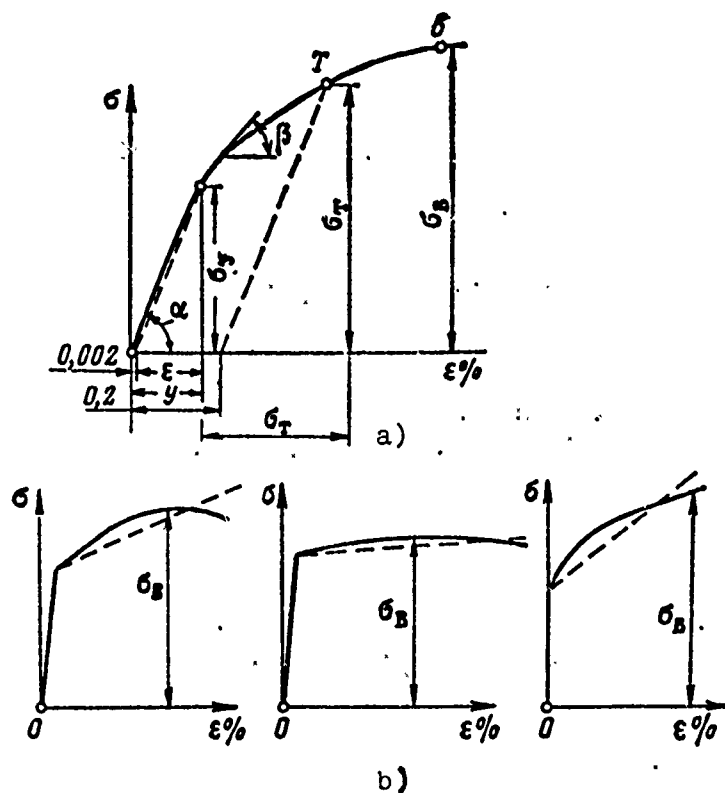


Fig. 1.21. Material deformation diagram:  
a) typical arbitrary diagrams; b) simplified diagrams.

Yield limit  $\sigma_T = \sigma_{0.2}$  is the stress which corresponds to the appearance of permanent sets of a certain magnitude. Usually yield limit is defined as the stress at which residual relative elongation  $\epsilon = 0.2\%$  occurs. Yield limit is widely used in calculations as a characteristic of the material's resistance to static loads when the operating capability of the part or design element is determined by its deforming properties, for example, when rotating parts interfere with nonrotating parts or when the elongation of an element leads to the overlapping of important ducts for passage of the working medium.

Beyond the plastic limit is the hardening modulus  $D$ , which characterizes the resistance of the material to small elastic-plastic deformations:

$$\sigma = D\epsilon,$$

where

$$D = \operatorname{tg} \beta = d\sigma/d\epsilon.$$

The substantial difference between  $D$  and  $E$  is the fact that the quantity  $D$  is a variable. In approximate calculations it is frequently assumed to be constant.

The hardening modulus  $D$  with an increase in stresses from  $\sigma_y$  to  $\sigma_T$  can be decreased by a factor of 100 and more.

The strength limit or tensile strength of the material  $\sigma_B$  is the arbitrary stress corresponding to maximum load during extension or compression tests on the sample.

For most structural materials tensile strength is the main strength characteristic of metal during static loading, the quantity determining strength reserve of the structure.



Strength reserve is the ratio of the strength limit of the material to the maximum stress rising in the material of a part when it is in operation:

$$n = \frac{\sigma_n}{\sigma_{max}} \quad (1.10)$$

Plasticity reserve can be determined from formula

$$n_{0,2} = \frac{\sigma_{0,2}}{\sigma_{max}}, \quad \text{or} \quad n_{0,2} = \frac{P_{npx}}{P_{max}}, \quad (1.11)$$

if the stresses are expressed in loads. This calculation is called the limiting load calculation.

The conditions for the operating capability of a part are  $n > 1$ ;  $n_{0,2} \geq 1$ .

As seen from the formulas, a substantial factor determining strength reserve is the quality of the material. Obviously, the higher  $\sigma_B$ , the higher the strength reserve will be and the easier, all other things being equal, it will be to make a part or structural element from it with the required properties.

What requirement should be imposed on materials to ensure high structural strength reserve with the least weight? The following requirements are imposed on structural materials used in extraterrestrial electrical rocket engines and, particular, in reactor units:

- high strength (strength limit must be the highest possible);
- high-temperature strength;
- oxidation resistance - high resistance to interaction with air and other gases at high temperatures;
- good weldability;
- small cross sections for capture (absorption) of neutrons;

- capable of resistance to neutron fluxes without substantial change in deformation diagrams;
- compatibility with corrosive working media;
- low evaporation rate in the vacuum of space.

How do the materials actually behave?

The strength limit of structural materials rapidly drops with an increase in temperature and length of operation (Fig. 1.22a) and scarcely changes from the irradiation of neutron fluxes. Viscosity of the material is reduced and the cold brittleness threshold rises. In the deformation pattern, as it were, the scale is reduced along the axis of the abscissas (Fig. 1.22b). Therefore, the calculation of strength reserve for structural materials in neutron fluxes differs little from ordinary calculations. Plasticity reserve, however, should be determined while taking the distortion of the deformation diagram into account.

The selection of structural materials depends upon the working medium and its compatibility with certain materials.

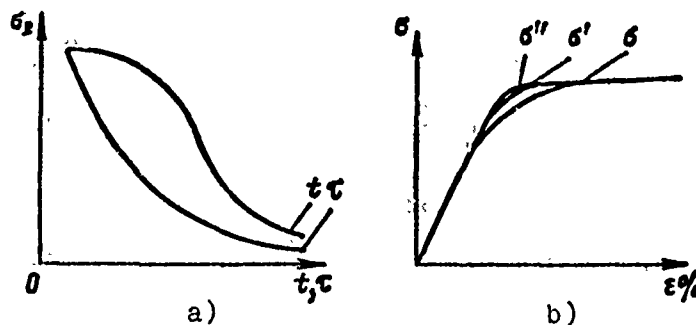


Fig. 1.22. Variation in material strength limit: a) as a function of time and temperatures; b) as a function of irradiation by neutrons.

We know that liquid metals, widely used in power plants, are corrosive media. They actively affect structural materials, destroying them. Noncorroding chromium-nickel alloys, under conditions of compatibility, can be used at temperatures up to 800°C with all liquid metals except lithium. At higher temperatures of liquid metals, including lithium, the use of niobium and molybdenum is required.

All structural materials sublime and evaporate in space and do so more intensely the higher their surface temperature. Figure 1.23 shows that at temperatures above 1000°C the evaporation rate of carbon and chromium-nickel alloys reaches several millimeters a year. In evaluating the strength of thin-walled structures, we must keep in mind their thinning due to sublimation. These properties of materials make it possible to refine the formulas (1.10) and (1.11). If material tests are carried out on a standard machine (i.e., test time is not long), the formula of strength and plasticity reserve will be:

$$n = \frac{\sigma_n^t}{\sigma_{\max}}; \quad n_{0.2} = \frac{\sigma_{0.2}^t}{\sigma_{\max}}, \quad (1.12)$$

where the subscript t indicates the temperature of the material during the tests.

With these formulas we can design parts for short-life engines. If the parts operate for a long time, we should use a reserve of stress-rupture strength and creep.

#### Stress-rupture strength reserve. Creep

Elasticity theory considers the stress and strain state of a part as a linear relationship between stresses and strains. With short test duration, low levels of temperature and stresses, the application of formulas of the theory of elasticity and thermoelasticity to actual bodies and designs composed of these bodies, does not result

in significant errors, which is usually substantiated by experiments. Such calculation is also advisable in the stage of preliminary sketching for the first evaluation of the stressed and strained state of a part and to enable the proper choice of its main dimensions.

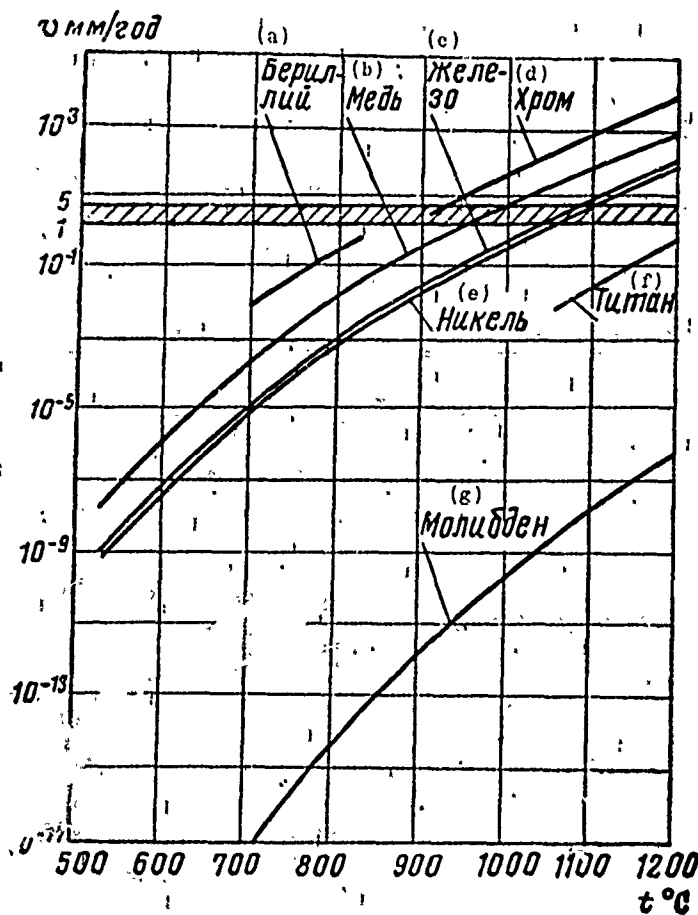


Fig. 1.23. Evaporation rate of metals in a vacuum.

KEY: (a) Berillium, (b) Copper, (c) Iron, (d) Chromium, (e) Titanium, (f) Nickels, (g) Molybdenum.

Designation: мм/год = mm/yr.

However, when the operating time is increased, as well as the temperature level and stresses, the difference in the behavior of ideally elastic bodies and the actual body becomes greater and greater and more or less significant corrections must be introduced into the calculations, taking into account the characteristics of the behavior of the actual materials under working condition.

It is necessary to calculate parts in the stage of creep and stress relaxation, in three cases.

1) For parts operating a long time at high temperatures, the change in geometric dimensions must be strictly monitored due to the effect of these dimensions on the working process of the engine, its efficiency, or parameters. For example, impairment of cooling in nozzles of the engines because of a decrease in the flow-through sections for the coolant.

2) For parts operating a long time at high temperatures with large stress gradients due to thermal or external loading. Stress relaxation substantially levels off the nonuniformities of stress in the part, as a result of which structural relief is manifest.

3) For parts operating in compression. Compression stresses arising in structural elements which are safe when calculating elasticity can become dangerous with plastic deformations during long operation and lead to loss of structural stability.

As we know, there are two concepts concerning nonelastic behavior of materials: plasticity and creep. The difference in these two similar concepts lies in the fact that plastic deformation weakly or scarcely depends on time, while creep deformation develops with time. Thus, creep can be defined as the state of a material at which with constant stresses in the part deformation develops depending upon its operating time. Time is one of the main characteristics of creep. In the presence of creep there occurs a redistribution of stresses which changes with time.

As indicated above, the operational capability of material is determined by the deformation diagram. The deformation diagram of a material is experimentally determined on standard machines in a comparatively short period of time — less than 2 min (curve 0 in Fig. 1.24).

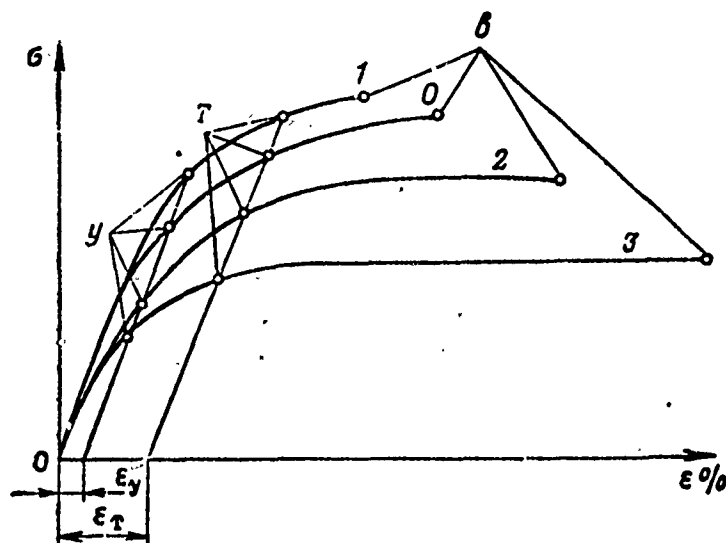


Fig. 1.24. Diagram of material deformation versus length of testing.

However, it has long been noted that a deformation diagram is substantially distorted if testing time changes. If testing time is reduced, line  $\sigma = f(\epsilon)$  moves to a higher level. The limiting values of stress  $\sigma_{0.002}$ ,  $\sigma_{0.2}$ ,  $\sigma_B$  are high (curve 1 on Fig. 1.24) as compared with the standard deformation curve (curve 0 on the same figure).

The strain diagram is even more distorted if the testing time is increased (curve 2) as compared with standard. Distortion proceeds toward a decrease in maximum stresses  $\sigma_{0.002}$ ,  $\sigma_{0.2}$ ,  $\sigma_B$  and toward an increase in the section of the diagram from plasticity limit  $\sigma_{0.2}$  (point T on the diagram) to point  $\sigma_B$  — the point of sample fracture. This effect is intensified if the sample is subjected to additional heating.

Plastic deformations in the latter case can achieve such significant values that we can not disregard them where it is important to conserve the geometric dimensions of an item.

To evaluate the supporting power of material operating for a long time under elevated temperatures, it would be best to take the deformation diagram of this material under conditions of actual operating time and temperature. However, machines for experiments under such conditions would have to be built. The conditions themselves cannot be a limitless quantity; some tests cannot be set up at all. Therefore, tests are carried out on the simplest machines. Constant pull  $P$  is applied to a sample and elongation and rupture stress are measured as a function of time and temperature. As a result of such tests, we can plot curves  $\sigma = f(\tau)$  at  $t = \text{const}$  or  $\sigma = f(t)$  at  $\tau = \text{const}$  (Fig. 1.25a, b).

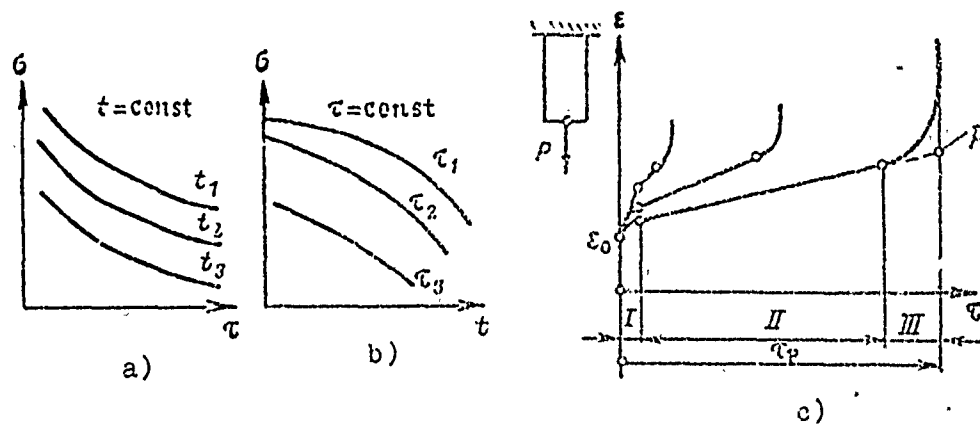


Fig. 1.25. Typical creep diagram.

However, it is best to obtain the function  $\epsilon = f(\tau)$ , which we call the creep curve (Fig. 1.25c).

If stresses are low and the time for taking the deformation diagram is short, relative elongation of a rod will be determined from formula  $\epsilon = \sigma/E = P/EF$ .

According to this formula, at constant stress, elongation maintains a constant value and does not depend on time. (At low temperatures and stresses, change in  $\epsilon$  will be slow and small and can be disregarded.) In Fig. 1.25c this stress corresponds to point  $\epsilon_0$ .

At high temperatures and stresses, the rise in  $\epsilon$  will be significant; it will substantially depend upon time (Fig. 1.25c). On this curve we can distinguish three stages of creep (I, II, and III). Stage I is characterized by a variable growth rate in creep flow  $\dot{\epsilon} = d\epsilon/dt$ . At the beginning of the stage the growth rate is not high; then it drops to a minimum value, remaining approximately constant in the II stage.

The area of creep I with decreasing rate is called unstable creep. This stage is usually brief, although, in certain cases, it can reach several tens of hours. This area of creep is manifested in calculations for parts of short-life rocket engines. In designing parts for long-life rocket engines it can be disregarded.

The area of creep II, characterizing constant deformation rate is called steady creep. Depending upon temperature and stress level, it can last from tens of minutes to many hundreds of hours. In materials for extraterrestrial electrical rocket engines this zone can reach 10,000 and more hours. It is fundamental in analyzing parts for creep.

The third, brief stage of creep is characterized by the formation of a neck in the sample and fracture. The sharp increase in  $\epsilon$  at the end of stage III is explained by the increase in sample stress. It is difficult to keep stress constant in an ordinary experimental machine. If we create such conditions, then creep stage III becomes less pronounced (dashes on Fig. 1.25c) and also terminates in the fracture of the sample at point p. Time  $\tau_p$  characterizes the full operating time of the material up to its fracture.



Let us examine the basic design relationships under creep and subsequent rupture.

Any material having the property of elasticity and creep can, in the first approach, be represented in the form of the elementary model shown in Fig. 1.26. The model consists of two different types of parts connected in series - an elastic element having rigidity  $C$  and a cylinder filled with a viscous liquid which can overflow through small holes in a piston. Resistance to the piston displacement is proportional to the speed of its displacement and the coefficient of viscous friction  $\alpha$  of the liquid.

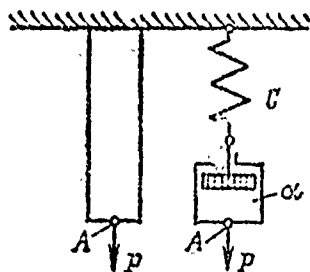


Fig. 1.26. Model of elastic viscous body.

The displacement of point A of the element can be made up of the displacements of the elastic (subscript "1") and viscous parts of the element (subscript "2"). For the elastic part of the element

$$P = Cx_1; \quad x_1 = \frac{P}{C}; \quad \dot{x}_1 = \frac{\dot{P}}{C} \quad (1.13)$$

(the derivative of the time function is designated by the dot).

For the viscous part of the element

$$\left. \begin{aligned} P &= \alpha \dot{x}_2; \quad \dot{x}_2 = \frac{P}{\alpha}, \quad \text{or} \quad dx_2 = \frac{P}{\alpha} d\tau \\ \text{and} \quad x_2 &= \frac{P}{\alpha} \tau. \end{aligned} \right\} \quad (1.14)$$

Total deflection and total displacement rate of point A will be

$$\left. \begin{aligned} x_A &= x_1 + x_2, \text{ or } x_A = \frac{P}{C} + \frac{P}{a} \tau; \\ \dot{x}_A &= \dot{x}_1 + \dot{x}_2, \text{ or } \dot{x}_A = \frac{\dot{P}}{C} + \frac{P}{a}. \end{aligned} \right\} \quad (1.15)$$

It is easy to see that formulas (1.15) describe qualitatively, rather well, the behavior of a linear elastic plastic body. Actually, if time  $\tau$  is brief, i.e.,  $\tau \rightarrow 0$ , deformation of the element is determined only by the first term after the equal sign in the expression (1.15). At high values of  $\tau$  plastic flow increases with constant elastic deformation. The deformation rate of point A is determined only by the viscosity of the body since with a constant value for force  $P$  the derivative of this quantity is zero.

A large number of materials possess viscosity. For them the deformation change rate with uniaxial deformation will be determined from formulas similar to (1.15):

$$\epsilon = \frac{\sigma}{E} + \frac{\sigma}{a} \tau; \quad \dot{\epsilon} = \frac{\dot{\sigma}}{E} + \frac{\sigma}{a},$$

where  $E$  and  $a$  are constants of the material.

A somewhat different relationship gives better agreement with experiment for metals:

$$\dot{\epsilon} = \frac{\dot{\sigma}}{E} + \left( \frac{\sigma}{\lambda} \right)^n,$$

where  $\lambda$  is the constant of the metal. If we assume  $1/\lambda^n = B$ , we finally obtain

$$\dot{\epsilon} = \frac{\dot{\sigma}}{E} + B \sigma^n. \quad (1.16)$$

The constants  $B$  and  $n$  are determined in processing the experimental creep curve. For example, on Fig. 1.27a the dependence of creep deformation  $\epsilon$  on time and stress is shown for steel. The section of unsteady creep is disregarded.

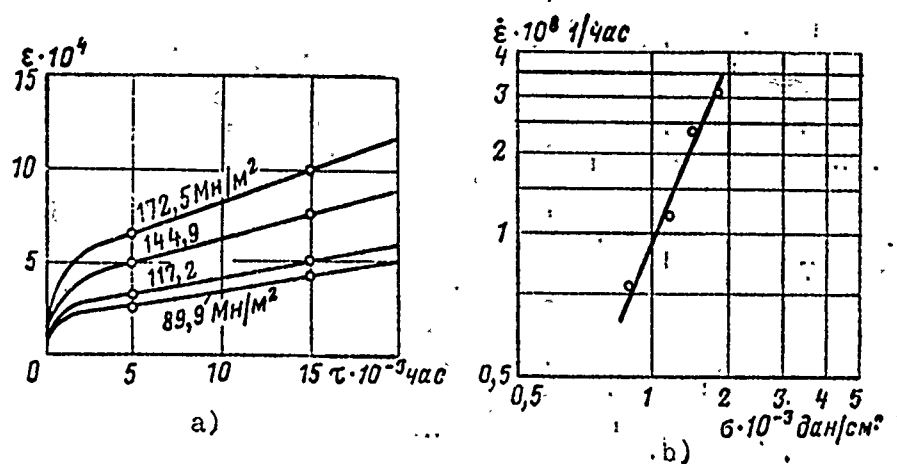


Fig. 1.27. Determining constants of the creep curve. Steel content:  $C = 0.31$ ;  $Mn = 0.54$ ;  $Ni = 2.05$ ;  $Cr = 0.83$ .

Designations:  $\text{MN/m}^2 = \text{MN/m}^2$ ;  $\text{vac} = \text{h}$ ;  $\text{daN/cm}^2 = \text{daN/cm}^2$ .

From these curves we determine the rates corresponding to steady creep  $\dot{\epsilon} = \dot{\epsilon}_{\min}$  (the subscript "min" will be dropped in the future). The value of creep rate is presented in Table 1.4. We map these points on a logarithmic grid (Fig. 1.27b) and draw a straight line so that it occupies, as nearly as possible, the "average" position between them. Since relationship (1.16) for steady creep has the form

$$\dot{\epsilon} = B\sigma^n, \quad (1.17)$$

the tangent of the slope angle of a straight line  $\ln \dot{\epsilon} = \ln B + n \ln \sigma$  agrees with index  $n$ ; from Fig. 1.27b we find  $n = 2.3$ . After this, from the points of the straight line we find  $B$ . The values of

$n$  and  $B$ , even for single-type metals, vary within a wide range. Table 1.5 presents some values of these quantities for various steels.

Table 1.4.

Stress $\sigma$ MN/m <sup>2</sup>	89,9	117,2	141,9	172,5
Creep rate $\dot{\epsilon} \cdot 10^8$ 1/h	0,77	1,26	2,35	3,17

Table 1.5.

(1)	(2)			(1)	(2)		
Марка стали	Температура, °C	$n$	$B(\text{дан/см}^2)^n \cdot \text{час}$	Марка стали	Температура, °C	$n$	$B(\text{дан/см}^2)^n \cdot \text{час}$
20	500	6,1	$2,3 \cdot 10^{-23}$	Kh18N9T	650	5,9	$1,34 \cdot 10^{-22}$
25	400	6,9	$1,58 \cdot 10^{-30}$	Kh13N16E	700	5,0	$6,9 \cdot 10^{-20}$
12G2A	454	4,4	$4,6 \cdot 10^{-23}$	KhNVM12	500	7,76	
12KhMF	600	12,7	$3,3 \cdot 10^{-44}$		600	10,3	
					700	5,21	

KEY: (1) Brand of steel; (2) Temperature, °C.

Designation:  $(\text{дан/см}^2)^n \cdot \text{час} = (\text{даN/см}^2)^n \cdot \text{h}$

Constant  $B$  in equation (1.17) is sometimes called the Baily constant. For the best approximate description of the creep processes under slow and monotonically changing stress, L. M. Kachanov [21] has proposed that we consider coefficient  $B$  a function of time. In accordance with this, equation (1.16) is rewritten as

$$\dot{\epsilon} = \frac{\dot{\sigma}}{E} + B(\tau) \sigma^n. \quad (1.18)$$

Equation (1.18) is called the basic equation of flow theory.

Along with equation (1.18) we use equation

$$\varepsilon = \frac{\sigma}{E} + \Omega(\tau) \sigma^n, \quad (1.19)$$

where

$$\Omega(\tau) = \int_0^{\tau} B(\tau) d\tau \quad (1.20)$$

and, consequently,

$$B(\tau) = \frac{d\Omega}{d\tau}. \quad (1.21)$$

Sometimes for a comparative evaluation of the resistance of a given material to creep, the so-called creep limit is introduced. By creep limit we mean the stress at which in a given period of time  $\tau$  a given creep flow  $\varepsilon$  is achieved.

For extraterrestrial electric rocket engines this time reaches 4000-10,000 h. Elongation  $\varepsilon = 1-2\%$ .

The value of creep limit is established by processing a set of creep curves (Fig. 128a). Assuming the quantities  $n$  and  $B$  are known in equation  $\varepsilon = B\sigma^n$  and substituting them into relationship

$$\varepsilon = \int_0^{\tau} B\sigma^n d\tau,$$

we find for a given  $\varepsilon$  (for example,  $\varepsilon = 1\%$ ) time  $\tau$  at which with a given stress this deformation is achieved, i.e., we examine the relationship

$$\varepsilon = B\tau\sigma^n, \text{ or } \sigma^n = \frac{\varepsilon}{B\tau} = \frac{A}{\tau},$$

or after taking the logarithm

$$n \lg \sigma = \lg A - \lg \tau. \quad (1.22)$$

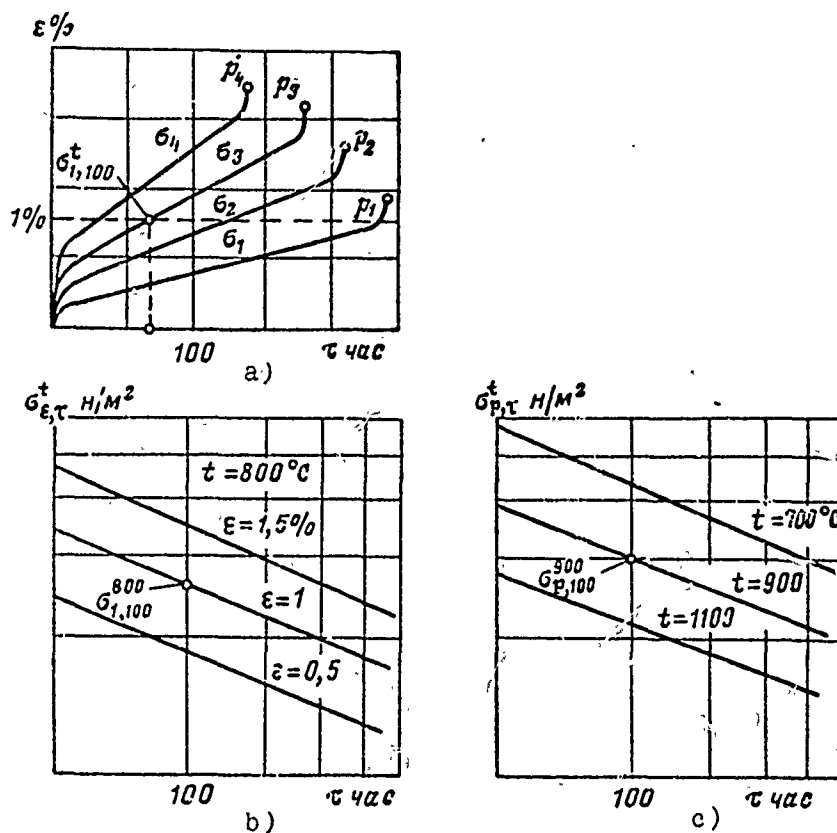


Fig. 1.28. Determining creep limit and stress-rupture strength.

Designation:  $\text{vac} = h$ ;  $\text{H/M}^2 = \text{N/m}^2$ .

The form of this dependence is shown in Fig. 1.28b where the creep limit is designated  $\sigma_{\varepsilon,\tau}^t$  ( $\varepsilon$  indicates deformation in %,  $\tau$  test time,  $t$  test temperature).

Reserve of stress-rupture strength in material

As mentioned, the strength limit of materials substantially depends upon operation time and temperature.

If testing continues, as shown in Fig. 1.25b, creep stage III ends in material rupture. Stress at which rupture occurs will depend upon the material, the testing time, and the temperature. Limiting value of stress at which sample rupture appears in a set period of time is called the stress-rupture strength of the material and is designated by  $\sigma_{B,\tau}^t$  or  $\sigma_{p,\tau}^t$  (the subscript  $\tau$  indicates the operating time before rupture). This time is usually 100, 1000, 5000, 10,000 h and is determined by both the design operating time and the capabilities of the test machine on which these values are achieved. The superscript  $t$  indicates the sample testing temperature since it is the second factor, after operating time, which determines the value of the strength limit of a given material.

In many cases of stress analysis, just as the strength limit  $\sigma_B$  of a standard strain diagram, the stress-rupture strength is a criterion for the operational capability of a design. The principal difference between stress-rupture strength and strength limit  $\sigma_B$  lies in its dependence on operating time. In the same way as graph  $\sigma_{B,\tau}^t = f(\tau)$  is plotted in determining creep limit, so graph

$\sigma_{B,\tau}^t$  is plotted in determining stress-rupture strength as a function of material operating time. Figure 1.28c shows a typical stress-rupture strength curve.

The supply of stress-rupture strength is determined similarly to the supply with short-term loading:

$$n = \frac{\sigma_{p,\tau}^t}{\sigma_{\max}}, \quad (1.23)$$

where  $\sigma_{\max}$  is the maximum stress in a part or the maximum intensity of stresses under a complex stressed state (see below). Since in logarithmic coordinates the graph showing the dependence of stress-rupture strength on time is linear, the dependence of time before rupture on stress-rupture strength is exponential:

$$\tau = A\sigma^{-m} \quad (1.24)$$

This relationship serves for finding the coefficient of operating time reserve.

The coefficient of time reserve  $n_t$  is the ratio of sample rupture time to material operating time for a part:

$$n_t = \frac{\tau_{p,\sigma}^t}{\tau} \quad (1.25)$$

(superscript  $t$  and subscript  $\sigma$  indicate temperature and stress of test). This expression is used to find the operating time reserve of an item.

The exponential dependence (1.22) of stress-rupture strength on material operating time makes it possible to evaluate strength limit in a wide range of material operating time. However, the interpolation method examined below should be used with caution only for a first rough estimate of strength limit in the absence of other more reliable data.

We shall assume that we have diagram  $\sigma_B = f(\tau, t)$  and diagram of maximum states  $\sigma = f(\epsilon, t, \tau)$ . The shape of these diagrams is shown in Fig. 1.29b and a.

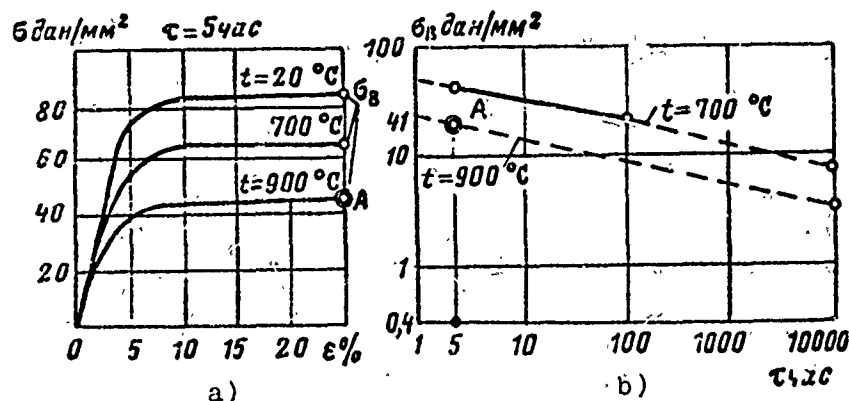


Fig. 1.29. Diagram of strength limit: a)  $\sigma = f(\epsilon, t, \tau)$ ; b)  $\sigma_B = f(t, \tau)$ .

Designations:  $\text{daN/mm}^2 = \text{daN/mm}^2$ ;  $\text{vac} = \text{h}$ .



Based on the known deformation diagram of the material with short-term testing (Fig. 1.29a) and the known dependence of stress-rupture strength for any temperature (Fig. 1.29b - solid line), the curves of strength limit are interpolated.

Line  $t = 700^{\circ}\text{C}$  is extended to  $\tau \geq 10,000$  h. Line  $t^{\circ} = 900^{\circ}\text{C}$  is drawn wholly based on one point A, taken from Fig. 1.29a. Such a plotting is not complex since curve  $\sigma_B = f(\tau)$  in a logarithmic grid is illustrated by a straight line.

In limiting load calculations we can encounter another case; we have a stress-rupture strength diagram - in Fig. 1.30a it is presented in the form  $\sigma_B = f(t)$  - and a deformation diagram in the form of  $\sigma = f(\tau)$  (Fig. 1.30b) for the usual testing time, for example,  $\tau = 5$  h (curves are indicated by solid lines). It is necessary to find the deformation diagram for another operating time. In the approximate calculation we use a method of completing the diagram in Fig. 1.30b. For example, if there is a diagram of the type shown in Fig. 1.30a for a long operating time, for example,  $\tau = 1000$  h, and there is a deformation diagram of the type shown in Fig. 1.30b for a brief operating time, for example  $\tau = 5$  h, then, by drawing on the diagram in Fig. 1.30b the point of long operation for the corresponding temperature (for example, point B at  $t = 800^{\circ}\text{C}$ ), we plot all the missing branches of the diagram, proportionally varying the distance between branches for other temperatures. The obtained network of curves (illustrated by dashes) can be used for the approximate calculation of plasticity reserve during long operation of a material.

### Intensity of stresses

When a part is in uniaxial stressed state, in the denominator of formula (1.23) is the maximum value of stress and the answer, if  $\sigma_B$  is known, is obtained immediately since the deformation diagrams of the material are obtained on samples subjected to uniaxial load.

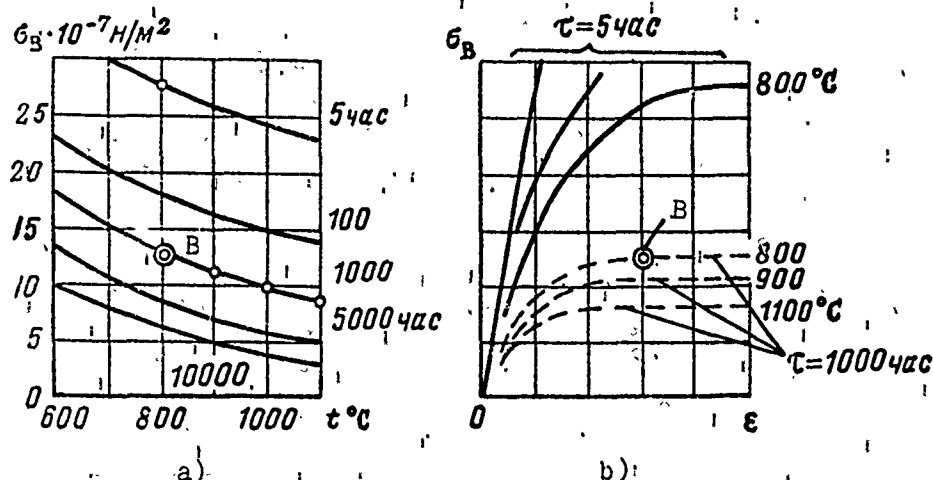


Fig. 1.30. Plotting curve  $\sigma_B = f(\epsilon, t)$  by the approximate method.

Designations:  $\text{H/M}^2 = \text{N/m}^2$ ;  $\mu\text{ac} = \text{h}$ .

However, can stress, in the direction of any axis in a complexly stressed element be compared with that obtained according to the usual deformation diagram? Obviously, this can not be done. The effect of stress in a perpendicular direction, strongly distorts the supporting power of the element. This is easily established in Fig. 1.31a. For a uniaxial state  $\sigma_x = E\epsilon_x$ , or  $\epsilon_x = \sigma_x/E$ , while in a biaxial state

$$\epsilon_x = \frac{1}{E} (\sigma_x - \mu\sigma_y).$$

Obviously we can plot the deformation diagram while stretching a sample in two mutually perpendicular directions (Fig. 1.31b). However, this is not simple since the ratio of stresses  $\sigma_x$  and  $\sigma_y$  can be very different and, in principle, infinitely large.

It is also important to use material accumulated in experiments in a uniaxial state for new tasks and not to do all the experimental work again.

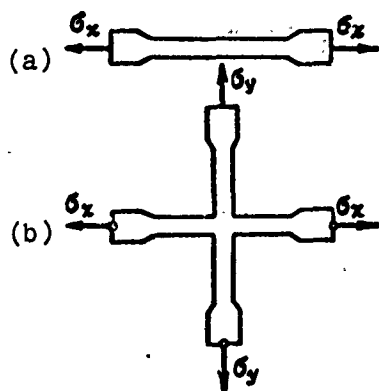


Fig. 1.31. Uniaxial (a) and two-dimensional (b) stressed state of a sample.

Strict analysis indicates that the diagram of deformation for a sample in a uniaxial stressed state, according to law  $\sigma = E\varepsilon$  can be used for determining the supporting power of an element in a two-dimensional or three-dimensional stressed state if, instead of  $\sigma_x$  and  $\varepsilon_x$  or  $\sigma_y$  and  $\varepsilon_y$ , we compare generalized or equivalent stress  $\sigma_1$ , which is called intensity of stresses, and generalized or equivalent deformations  $\varepsilon_1$ , obtained in accordance with one of the theories of material strengths. Then the basic relationship between stress and deformation will have the form

$$\sigma_1 = E\varepsilon_1, \quad (1.26)$$

where

$$\sigma_1 = f(\sigma_x, \sigma_y); \quad \varepsilon_1 = \varphi(\varepsilon_x, \varepsilon_y).$$

Equivalent stress  $\sigma_1$ , i.e., stress which should be created in an extended sample so that its stressed state correspond to a given state, is most frequently in accordance with one of two strength theories, the theory based on equality of the largest tangential stresses and the theory of the equality of distortion energy. The first is widely used in tasks, where the limiting stage is characterized by a transition of the elastic state to

plastic, i.e., if  $\sigma_{0.002} < \sigma_{\max} < \sigma_{0.2}$ . It, however, is used if we encounter in the calculation a complex stressed state of design elements when the largest and smallest of the main stresses have different signs. The second is used in tasks, where the limiting state is characterized by the beginning of rupture, i.e., if  $\sigma_{0.2} < \sigma_{\max} < \sigma_B$ .

The formula for determining equivalent stress in accordance with the first theory

$$\sigma_i = \sigma_1 - k\sigma_3, \quad (1.27)$$

where  $\sigma_1, \sigma_2, \sigma_3$  are the main stresses;  $k = \sigma_{T.p}/\sigma_{T.c}$  is the ratio of the yield point of the materials during extensions to the yield point during contraction  $k = \sigma_{B.p}/\sigma_{B.c}$  for brittle materials; for the majority of structural materials  $k = 1$ .

Formulas for determining the equivalent stressed state in accordance with the second theory will be different depending upon whether the element is in elastic ( $\mu = 0.3$ ) or plastic ( $\mu = 0.5$ ) state.

Equivalent stress for a three-dimensional stressed state is

$$\sigma_i = \sqrt{0.5[(\sigma_x - \sigma_y)^2 + (\sigma_y - \sigma_z)^2 + (\sigma_z - \sigma_x)^2]}. \quad (1.28)$$

We find equivalent stress for a two-dimensional stressed state. The element is in elastic state ( $\mu = 0.3$ ):

$$\left. \begin{aligned} \varepsilon_i &= \frac{1}{1+\mu} \sqrt{\varepsilon_x^2 + \varepsilon_x \varepsilon_y + \varepsilon_y^2} \\ \sigma_i &= \sqrt{\sigma_x^2 - \sigma_x \sigma_y + \sigma_y^2} \end{aligned} \right\} \quad (1.29)$$

The element is in plastic state ( $\mu = 0.5$ ):

$$\left. \begin{aligned} \varepsilon_l &= \frac{2}{\sqrt{3}} \sqrt{\varepsilon_x^2 + \varepsilon_x \varepsilon_y + \varepsilon_y^2}; \\ \varepsilon_x &= \frac{4}{3} \frac{\sigma_l}{\sigma_f} (\varepsilon_x + 0.5 \varepsilon_y); \\ \varepsilon_y &= \frac{4}{3} \frac{\sigma_l}{\sigma_f} (\varepsilon_y + 0.5 \varepsilon_x). \end{aligned} \right\} \quad (1.30)$$

Example 1.2. Find the equivalent stress for three stressed states indicated in Fig. 1.32. Stresses are given in  $\text{daN/cm}^2$ .<sup>1</sup> Material under extension and contraction operates identically ( $k = 1$ ).

The value of equivalent stress according to formula (1.27) is

$$\sigma_l = \sigma_1 - \sigma_3$$

- a)  $\sigma_l = 800 - 100 = 700$ ; ( $\sigma_1 = 800$ ,  $\sigma_2 = 300$ ,  $\sigma_3 = 100$ );  
 b)  $\sigma_l = 600 - (-100) = 700$  ( $\sigma_1 = 600$ ,  $\sigma_2 = 0$ ,  $\sigma_3 = -100$ );  
 c)  $\sigma_l = 750 - 0 = 750$ ; ( $\sigma_1 = 750$ ,  $\sigma_2 = 100$ ,  $\sigma_3 = 0$ ).

The value of equivalent stress according to formula (1.28) is

$$\sigma_l = \sqrt{0.5 [(\sigma_1 - \sigma_2)^2 + (\sigma_2 - \sigma_3)^2 + (\sigma_3 - \sigma_1)^2]};$$

- a)  $\sigma_l = \sqrt{0.5 [(800 - 300)^2 + (300 - 100)^2 + (100 - 800)^2]} = 623$ ;  
 b)  $\sigma_l = \sqrt{0.5 [(600 - 0)^2 + (0 - 100)^2 + (-100 - 600)^2]} = 654$ ;  
 c)  $\sigma_l = \sqrt{0.5 [(750 - 0)^2 + (100 - 0)^2 + (0 - 750)^2]} = 805$ .

As seen from the example, the values of equivalent stresses, calculated according to different strength theories, are not the same.

<sup>1</sup>1 daN = 10 N; 1 daN/cm<sup>2</sup> = 1000 N/m<sup>2</sup> = 1 kN/m<sup>2</sup>.

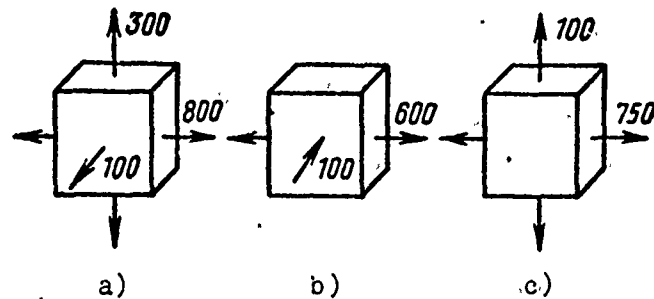


Fig. 1.32. Finding equivalent stresses.

### Stress-rupture strength of material under nonstationary loading

A considerable number of engine parts operate under nonstationary stress and nonstationary heating. Let us examine the samples whose temperature and loading is shown in Fig. 1.33.

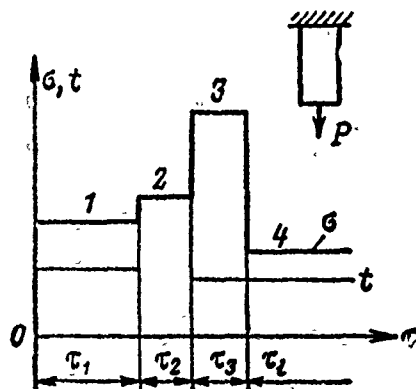


Fig. 1.33. Determining stress-rupture strength limit for material under nonstationary loading.

As seen from the figure, the material of the sample was first heated to  $t_1$  and stressed  $\sigma_1$  to, during time period  $\tau_1$ ; then on section  $\tau_2$  temperature and stress were changed to values  $t_2$ ,  $\sigma_2$ , etc., until complete rupture. At the end of such variable loading the sample experienced stress  $\sigma_k$  at temperature  $t_k$  and ruptured with time lapse  $\tau_k$ .

Total operating time of the sample before rupture was

$$\tau_p = \sum_{i=1}^k \tau_i.$$

Let us designate in terms of  $\tau_{1p}, \tau_{2p}, \dots, \tau_{kp}$  the time intervals necessary for rupture under stresses  $\sigma_1, \sigma_2, \dots, \sigma_k$ . These quantities are determined from the stress-rupture strength curves at various temperatures  $t_1, t_2, \dots, t_k$ . We shall call the ratios  $\tau_1/\tau_{1p}, \tau_2/\tau_{2p}, \dots, \tau_k/\tau_{kp}$  material damage in first, second, etc., modes.

Experimental studies on stress-rupture strength of samples operating under nonstationary stresses and heating have enabled us to establish the fact that total damage for a given material is equal to one:

$$\sum_{i=1}^k \frac{\tau_i}{\tau_{ip}} = 1. \quad (1.31)$$

This assumption is called the law of linear damage summation.

Under continuous stress variation

$$\int_0^{\tau_p} \frac{d\tau}{\tau_{p,\sigma}} = 1, \quad (1.32)$$

where  $\sigma$  and  $t$  are subscript and superscript indicating that rupture time  $\tau_p$  is determined for a given stress  $\sigma$  and a given temperature  $t$ .

Let us find the coefficient of operating time reserve, which, as before, we shall designate  $n_\tau$ .

We increase the loading time of a part in each segment  $\tau_1, \tau_2, \dots, \tau_k$  an identical number of times so that at the end of the k-th loading stage the part ruptures. Then the quantity indicating how many times the time segments  $\tau_1, \tau_2, \dots, \tau_k$  must be increased so that rupture occurs at the end of the mode is the coefficient of longevity reserve. We designate this new loading time for each segment with an asterisk:

$$\tau_1^* = n_\tau \tau_1; \tau_2^* = n_\tau \tau_2; \dots, \tau_k^* = n_\tau \tau_k.$$

Then

$$\tau_p = \sum_{i=1}^k \tau_i^* = n_\tau \sum_{i=1}^k \tau_i = n_\tau \tau, \quad (1.33)$$

where  $\tau$  is the operating time of the part. Hence, substituting relationships (1.33) into (1.31), we obtain the formula for the coefficient of longevity reserve:

$$n_\tau = \frac{1}{\sum_{i=1}^k \frac{\tau_i}{\tau_{ip}}}. \quad (1.34)$$

To determine a coefficient of strength reserve under nonstationary loading we assume that stresses  $\sigma_1, \sigma_2, \dots, \sigma_k$  are increased an identical number of times  $n_\sigma$  so that at the end of the new mode rupture occurs. Then in expression (1.31), taking into account formula (1.24),

$$\left. \begin{aligned} \tau_{ip} &= A_i (n_\sigma \sigma_i)^{-m_i}; \\ \tau_i^* &= A_i (\sigma_{ip})^{-m_i}, \end{aligned} \right\} \quad (1.35)$$

where  $\tau_{ip}$  is the stress necessary for rupture after time  $\tau_i^*$ . It is found from the stress-rupture strength curve of the material under various temperatures.



Substituting expression (1.35) into formula (1.31), we obtain the equation for determining the coefficient of strength reserve:

$$\sum_1^k n_p^{m_l} \left( \frac{\sigma_l}{\sigma_{lp}} \right)^{m_l} = 1. \quad (1.36)$$

This equation is solved graphically. In the particular case of constant temperature, formula (1.36) is simplified. Assuming  $m_1 = m_2 = m_k = m$ , we obtain

$$n_p = \frac{1}{\sqrt[m]{\sum_1^k \left( \frac{\sigma_l}{\sigma_{lp}} \right)^m}}, \quad (1.37)$$

where  $n_p$  is the stress-rupture strength reserve of a part when it is under nonstationary loading.

### Stress relaxation

A change in the stressed state of a part during a period of time under constant load is called stress relaxation.

Equation (1.18) enables us to calculate stress relaxation. We assume that the element is in a stressed state and thus it is established that its subsequent deformation is limited. Then from equation (1.18), assuming  $\epsilon = \text{const}$  and  $\dot{\epsilon} = 0$ , we obtain  $d\sigma/\sigma^n = -EB(\tau)d\tau$ , or on the basis of expression (1.21),

$$\frac{d\sigma}{\sigma^n} = -E d\Omega. \quad (1.38)$$

Integrating this expression, we find

$$\frac{1}{1-n} (\sigma^{1-n} - \sigma_0^{1-n}) = -E\Omega. \quad (1.39)$$

Designating  $Q = \frac{\sigma}{\sigma_0}$ , we obtain

$$Q = \frac{1}{\sqrt[n-1]{1 + (n-1) E \sigma_0^{n-1} \Omega}} \quad (1.40)$$

or

$$Q = [1 + (n-1) E \sigma_0^{n-1} \Omega]^{-\frac{1}{n-1}}$$

Since  $n > 1$  and  $\Omega$ , with unlimited time increase, grows without restriction,  $Q$  is a diminishing function. The shape of the function  $Q$  is indicated in Fig. 1.34.

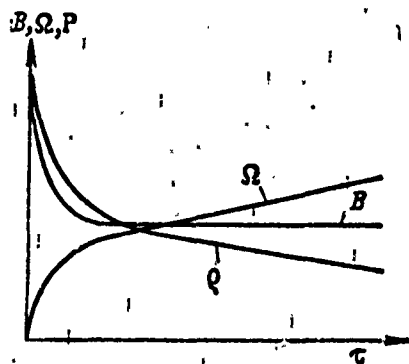


Fig. 1.34. Determining stress relaxation.

A graph of functions  $B(\tau)$  and  $Q$  can be found from the main dependences of plastic flow

$$\varepsilon = \sigma^n \Omega \quad \text{and} \quad \dot{\varepsilon} = B(\tau) \dot{\sigma}^n. \quad (1.41)$$

We note that since when  $t = 0$  deformation  $\varepsilon = 0$ ; therefore, when  $\tau = 0$   $\Omega = 0$ .

The value of the exponent  $n$  is known from the experimental creep curves. Function  $\Omega$  is found from equation (1.41) based on the known  $\varepsilon$ ,  $\sigma$ , and  $n$ . We obtain a graph of function  $\Omega$  (Fig. 1.34).

Function  $B(\tau)$  is found after determining function  $\Omega$  by graphic and numerical differentiation.

As seen from the figure, the value of coefficient  $B(\tau)$  is variable in a certain segment — it corresponds to the segment of unsteady creep and is constant in the remaining segment — the segment of steady creep. Function  $\Omega$  after a certain value grows monotonically. Function  $\rho$  decreases sharply when  $t$  is near zero and then, monotonically.

### Thermal stresses

In studying thermal stresses we face two different problems.

The first problem is finding the thermal stresses which appear as a result of rapid heating or cooling of a junction or part. This mode, although brief, corresponds to the maximum temperature gradients and, consequently, stresses. Decrease in these stresses can be achieved by increasing unit firing time or starting time. For an installation where the time must be minimal, stresses must be designed for.

The second problem is to calculate stresses which occur in parts as a result of the effect of steady thermal fluxes and their corresponding steady temperature gradients.

For very many elements this calculation is fundamental if deformations corresponding to these stresses do not go beyond the limits of elastic. This calculation can be a reference for stress analysis if thermal stresses exceed the elasticity limit of the material when plastic deformations accompanying these stresses can not be disregarded. Strength calculation for parts, in this case, must be made with relaxation phenomena taken into account.

If we heat a three-dimensional element of an elastic body to temperature  $t_1$  and in no way hinder its free expansion, the element expands in all directions and its thermal deformations are expressed by the following formulas:

$$\left. \begin{aligned} \varepsilon_{xt} = \varepsilon_{yt} = \varepsilon_{zt} &= \alpha \Delta t; \\ \gamma_{xyt} = \gamma_{yzt} = \gamma_{zxt} &= 0, \end{aligned} \right\} \quad (1.42)$$

where  $\Delta t = t_1 - t_0$  ( $t_0$  is initial temperature of the body);  $\alpha$  is the coefficient of linear expansion (relative elongation of the material under heating per  $1^\circ\text{C}$ ).

The disappearance of shear components of pure thermal deformations  $\gamma$  comes from the absence of any distortions of units with this deformation.

If the body is heated nonuniformly or any segment of its surface is connected with another body, the elements of the body can not freely expand and thermal or temperature stresses occur in it. In this case, deformation of each body element is made up of thermal deformation of a free element and elastic deformation caused by thermal stresses. If these stresses are designated, as they usually are, in terms of  $\sigma_x, \sigma_y, \sigma_z, \tau_{xy}, \tau_{yz}, \tau_{zx}$ , then deformations

$$\left. \begin{aligned} \varepsilon_x &= \frac{1}{E} [\sigma_x - \mu (\sigma_y + \sigma_z)] + \alpha \Delta t; \\ \varepsilon_y &= \frac{1}{E} [\sigma_y - \mu (\sigma_z + \sigma_x)] + \alpha \Delta t; \\ \varepsilon_z &= \frac{1}{E} [\sigma_z - \mu (\sigma_x + \sigma_y)] + \alpha \Delta t; \\ \gamma_{xy} &= \frac{1}{G} \tau_{xy}; \quad \gamma_{yz} = \frac{1}{G} \tau_{yz}; \quad \gamma_{zx} = \frac{1}{G} \tau_{zx}, \end{aligned} \right\} \quad (1.43)$$

where

$$G = \frac{E}{2(1 + \mu)}.$$

We shall express stresses in terms of deformation. Adding the first three equations, we obtain

$$\varepsilon = \varepsilon_x + \varepsilon_y + \varepsilon_z = \frac{1-2\mu}{E} (\sigma_x + \sigma_y + \sigma_z) + 3\alpha\Delta t, \quad (1.44)$$

where  $\varepsilon$  is the relative three-dimensional expansion of an element.

The first equation (1.43) is then transformed as:

$$\begin{aligned} \varepsilon_x &= \frac{1}{E} [\sigma_x (1+\mu) - \mu (\sigma_x + \sigma_y + \sigma_z)] + \alpha\Delta t = \\ &= \frac{\sigma_x}{2G} - \frac{\mu}{1-2\mu} \varepsilon + \frac{1+\mu}{1-2\mu} \alpha\Delta t. \end{aligned} \quad (1.45)$$

Hence we determine  $\sigma_x$ ,  $\sigma_y$ , and  $\sigma_z$ :

$$\left. \begin{aligned} \sigma_x &= \frac{E}{1+\mu} \left( \varepsilon_x + \frac{\mu}{1-2\mu} \varepsilon - \frac{1-\mu}{1-2\mu} \alpha\Delta t \right), \quad \tau_{xy} = G\gamma_{xy}; \\ \sigma_y &= \frac{E}{1+\mu} \left( \varepsilon_y + \frac{\mu}{1-2\mu} \varepsilon - \frac{1+\mu}{1-2\mu} \alpha\Delta t \right), \quad \tau_{yz} = G\gamma_{yz}; \\ \sigma_z &= \frac{E}{1+\mu} \left( \varepsilon_z + \frac{\mu}{1-2\mu} \varepsilon - \frac{1+\mu}{1-2\mu} \alpha\Delta t \right), \quad \tau_{zx} = G\gamma_{zx}. \end{aligned} \right\} \quad (1.46)$$

The obtained general expressions for strains and stresses are simplified for the case of two-dimensional and uniaxial stressed states.

For the two-dimensional stressed state

$$\left. \begin{aligned} \varepsilon_x &= \frac{1}{E} (\sigma_x - \mu\sigma_y) + \alpha\Delta t; \\ \varepsilon_y &= \frac{1}{E} (\sigma_y - \mu\sigma_x) + \alpha\Delta t; \\ \gamma_{xy} &= \frac{1}{G} \tau_{xy} \end{aligned} \right\} \quad (1.47)$$

and relationships (1.46) assume the form

$$\left. \begin{aligned} \sigma_x &= \frac{E}{1-\mu^2} [\varepsilon_x + \mu\varepsilon_y - (1+\mu)\alpha\Delta t]; \\ \sigma_y &= \frac{E}{1-\mu^2} [\varepsilon_y + \mu\varepsilon_x - (1+\mu)\alpha\Delta t]; \\ \tau_{xy} &= G\gamma_{xy}. \end{aligned} \right\} \quad (1.48)$$

For the uniaxial stressed state

$$\varepsilon_x = \frac{1}{E} \sigma_x + \alpha\Delta t; \quad \sigma_x = E(\varepsilon_x - \alpha\Delta t). \quad (1.49)$$

The results obtained have simple physical meaning.

In generalized form they can be presented as

$$\varepsilon = \varepsilon_t + \varepsilon_y; \quad \sigma = E\varepsilon_y, \quad (1.50)$$

where  $\varepsilon_t$  is the thermal deformation of a free part;  $\varepsilon_y$  is elastic deformation of a part occurring due to contained thermal deformation.

Thus, the total deformation of the heated part is made up of its free thermal expansion and elastic deformation due to the containment of this deformation.

Thermal stresses are determined only by the elastic component of deformation. Finding it is the basic difficulty in analysis.

Thermal deformation  $\varepsilon_t$  is always known; for example, for a rod

$$\varepsilon_t = \alpha\Delta t. \quad (1.51)$$

This simplifies obtaining a numerical result. The rules of the stressed state of a heated part show a substantial difference

between it and the stressed state of an unheated part under loading where, as we know, any relative deformation corresponds to a certain stress. Let us examine, for example, the stress and strains in a part free from attachment (Fig. 1.35a).

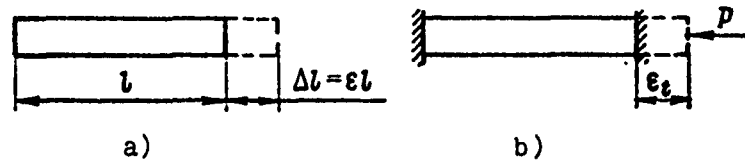


Fig. 1.35. Thermal deformation under uniaxial loading.

The quantities  $\alpha$  and  $\Delta t$  are given. Deformation is

$$\begin{aligned}\epsilon &= \epsilon_x + \epsilon_y = \epsilon_x, \text{ since } \epsilon_y = 0; \\ \epsilon &= \epsilon_x = \alpha \Delta t; \quad \sigma = E \epsilon_y = 0.\end{aligned}$$

Let us note that  $\epsilon \neq 0$ , while  $\sigma = 0$ , i.e., full deformation of a part does not characterize its stressed state.

We shall examine stress and strains in a part having rigid attachment (presented, for example, in Fig. 1.35b).

Quantities  $\alpha$  and  $\Delta t$  are given. Deformation

$$\begin{aligned}\epsilon &= \epsilon_x + \epsilon_y = 0; \quad \epsilon_y = -\epsilon_x = -\alpha \Delta t; \\ \sigma &= E \epsilon = -E \alpha \Delta t.\end{aligned}$$

Let us note that  $\epsilon = 0$ , while  $\sigma \neq 0$ .

The stressed state of a part having a rigid attachment has one more important quality — the rigid attachment is a single attachment, with which the thermal deformation of the part is precisely equal to its elastic deformation with opposite sign.

In parts having an elastic attachment, conditions for rigid attachment are mentally created to evaluate the maximum thermal stresses which can occur.

Example 1.3. Find the thermal stresses in a part made of steel and installed rigidly as shown in Fig. 1.35b, if  $\alpha = 10 \cdot 10^{-5} \text{ 1/}^\circ\text{C}$ ;  $E = 2 \cdot 10^{11} \text{ N/m}^2$ ;  $\Delta t = 100^\circ\text{C}$ , are known.

Stress

$$\sigma = E\alpha\Delta t = -2 \cdot 10^{11} \cdot 10 \cdot 10^{-5} \cdot 100 = -20 \cdot 10^7 \text{ N/m}^2$$

As seen from the example, even this relatively little preheating of a rigidly attached part causes great stresses.

The appearance of stresses when heating a part with an attachment (Fig. 1.35b) is sometimes given such a physical interpretation as the following: if there were no limiting attachment, the part would expand under heating by quantity  $\epsilon_t = \alpha\Delta t$ , but since there is a rigid attachment, this elongation does not occur. This can be represented as the inverse deformation of a free part as a result of the action of force  $P$  which occurs at the site of the rigid attachment.

The introduction of reactive force  $P$ , occurring at the site of deformation confinement, makes possible simple methods of finding thermal stresses in the most varied cases. We shall examine a common engineering method of finding thermal stresses.

We have a part (Fig. 1.36a) whose deformation is confined. Quantities  $\alpha$ ,  $\Delta t$ , and  $E$  are given. If this part is deformed freely, its deformation  $\epsilon_t = \alpha\Delta t$ . Since the deformation of the part is confined, its deformation is equal to  $\epsilon$ ; this quantity is less than  $\epsilon_t$  by quantity  $\epsilon_y$ , as shown in Fig. 1.36a. We find the value of deformation  $\epsilon_y$  in the following manner.



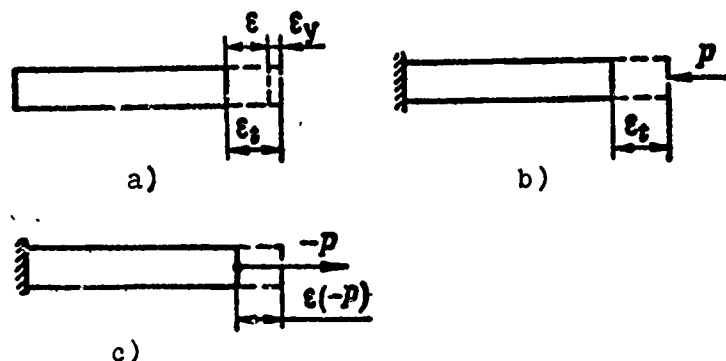


Fig. 1.36. Determining thermal stresses.

Before heating, the part is installed in a rigid housing which does not allow expansion during heating (Fig. 1.36b). Reactive force  $P$  occurs during heating. We find it from the thermal deformation, which is known; for this case it is equal to elastic deformation:  $\epsilon_y = -\epsilon_t = -\alpha \Delta t$ . Hence  $P = \epsilon_y EF$ .

Stresses and strains obtained in this state differ from actual ones since there is no rigid attachment of the part. To obtain true thermal deformations we must apply to the part load  $P$ , which occurs in the attachment of the part, but is directed in the opposite direction, i.e., with negative sign (Fig. 1.36c).

The sum of part deformations with rigid attachment (Fig. 1.36b) and deformations from reaction forces  $P$ , taken with opposite sign (Fig. 1.36c), gives the true elastic deformation. Finally, we obtain

$$\epsilon_y = -\alpha \Delta t + \epsilon(-P). \quad (1.52)$$

This method of finding elastic thermal deformation and, consequently, stresses will be used in even more complex problems.

## CHAPTER II

### ERE POWER GENERATORS

#### 2.1. NUCLEAR REACTOR UNIT

A nuclear reactor is the most promising source of power of an extraterrestrial rocket engine. It exhibits high power capabilities, makes it possible to obtain sufficiently high temperatures for the working medium, and has a constant mass characteristic during its entire operating time. Disadvantages of a reactor include its high cost, construction difficulties, necessity for crew protection from nuclear radiation during operation, repair limitations, and the danger present during emergencies. The problem of obtaining the best structural materials for the core is presently in the stage of solution.

*Based on the energy of neutrons* which determine the nuclear fission, reactors are broken down into those operating on fast, intermediate, and thermal neutrons. Reactors on fast neutrons are simple in construction and have comparatively small size and mass. They are also simple technologically, have a small number of parts, are not sensitive to the use of structural materials which absorb neutrons in the core. A disadvantage is the large load of fissionable material that they require and, therefore, in many cases, they are more expensive than other reactors.

Reactors on thermal neutrons are more complex in construction, have greater mass and size with the same power, and are more sensitive to the use of structural materials in the core. However, these reactors have a number of merits. They are usually cheaper since,

other conditions being equal, the charge of fissionable material is less. To moderate the neutron from the energy which they have during fission ( $\sim 2$  MeV), moderating material (a moderator) is used for example, hydrogen, which contains material mixed uniformly in the core or separately from the fissionable material.

Reactors on intermediate neutrons have a number of disadvantages and advantages somewhere between the two previous types of reactors.

Thermal and intermediate reactors are divided into homogeneous and heterogeneous *based on the principle of the core layout*. Homogeneous reactors have a moderator which is uniformly mixed with the fissionable material; in heterogeneous reactors the moderator and the fissionable material can be in different phases in the core.

*Based on the physical state of the heat-transfer agent*, reactors are divided into those with liquid and those with gas heat exchange. Reactors in which the heat-transfer agent passes from liquid phase to vapor phase are called "boiling." Reactors with liquid and gas heat exchange are divided, based on the working medium's pattern of motion, into direct-flow and loop reactors. In direct-flow reactors the heat-transfer agent moves in the same direction in all sections of the reactor. Communications, in this case, have a simple form; the reactor is comparatively simple in construction. In reactors with loop (or counter-current) flow the heat-transfer agent is first used for cooling the housing of the reactor and then enters the core. The loop pattern is sometimes determined by the location of the reactor in the power plant.

*Based on length of operation*, reactors are divided into long-use and relatively short-use reactors.

In addition, based on the character of the contact between the working medium and the surface of the fuel elements of the core, reactors are divided into reactors with solid, liquid, or gaseous fuel element surfaces. The last two types of reactors allow the working medium's temperature to rise beyond the limits of solid state. However, they have not gone beyond the experimental or

research stage. Reactors with a solid wall have preference in extraterrestrial rocket engines.

## Structural diagrams of nuclear reactors

### Direct-flow nuclear reactor on fast neutrons

One of the possible reactor designs (Fig. 2.1a) consists of a housing (1, 2, 3), fuel elements 4, a radial reflector 5, regulating cylinders 6 and 7, and a protection unit 8.

The housing 1 is the main structural part of the reactor. It braces the core and the control system; it absorbs and transmits loads arising during the start of the engine and during its normal operation. The housing unit includes the load-bearing panel 2, a perforated plate which is also called the tube panel. This braces the fuel elements and absorbs the loads from them during start and operation.

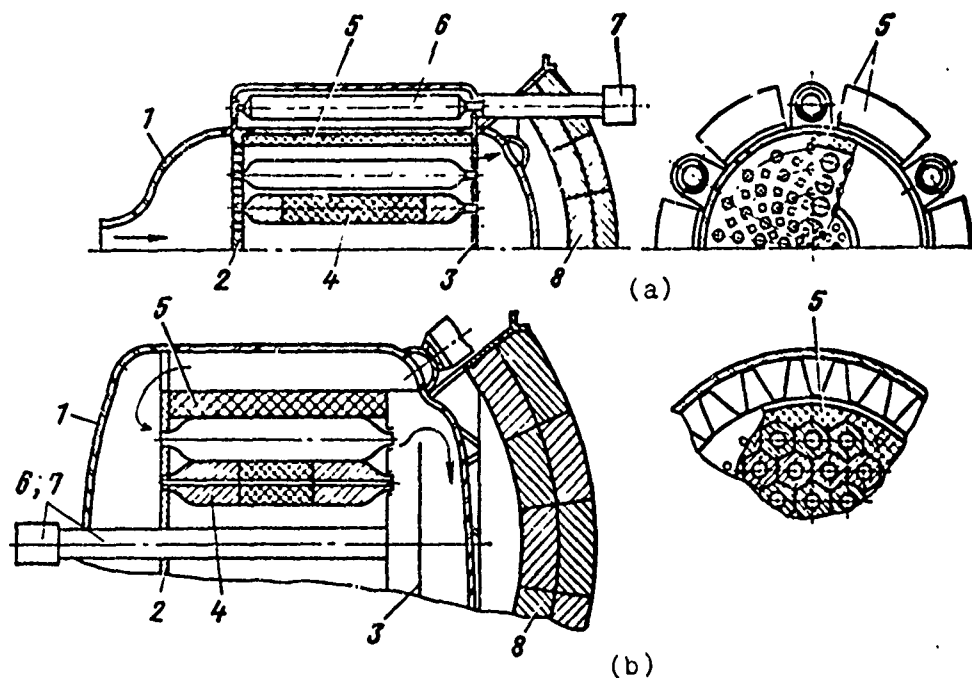


Fig. 2.1. Structural diagrams of nuclear reactors: a - direct-flow on fast neutrons; b - homogeneous on thermal neutrons.

The fuel elements also rest on a light thin diaphragm 3, whose purpose is to hold the fuel elements and deflect the heat-transfer agent during reactor operation. Fuel element 4 consists of a shell with which it is braced through the shank to the load-bearing panel of the reactor, an active fissionable substance, and two end reflectors. The radial reflector 5, in this example, consists of two parts - a fixed part in the form of a thin layer adjoining the inner surface of the housing 1 and an external part, which is removed to stop the reactor in the case of an emergency situation.

The reactor is controlled by cylinder 6, which is started in motion by mechanism 7; emergency turn-off is accomplished by moving reflectors 5.

Liquid metal, as indicated by the arrow, enters the reactor from a conduit in the head of the reactor, passes through the openings in the tube panel between the fuel elements, and emerges from the collector on the rear wall of the reactor.

Diagram of a homogeneous thermal neutron reactor with loop motion of the working medium

This reactor (Fig. 2.1b) consists of a housing unit (1, 2, 3); a fuel element unit 4 consisting of a shell, an end reflector, and the fissionable material mixed with the moderator; a radial reflector 5; regulating and emergency rods 6 and 7; and a protection unit 8. The heat-transfer agent entering the reactor passes between the outer shell of housing and the thin wall connected by a fluted adapter. Then, as shown by the arrow, the heat-transfer agent passes through the openings in the load-bearing panel to the core and then to the exhaust outlet. The fuel elements are installed in the core with very small thermal clearances. To decrease the absorption of neutrons, structural material - steel shells - is used only for the emergency and regulating rods 6 and 7, located in the core.

### Diagram of intermediate reactor

This diagram (Fig. 2.2a) is similar to the previous two diagrams. The housing (1, 2, 3) is the same as in the thermal neutron reactor. The fuel elements 4 are installed in a shell of structural material just as in a rapid neutron reactor. The radial reflector 5 is similar to that in a fast neutron reactor as is the control, carried out by cylinder 6 located in reflector 5. Here also are the cylinders for emergency cut-off.

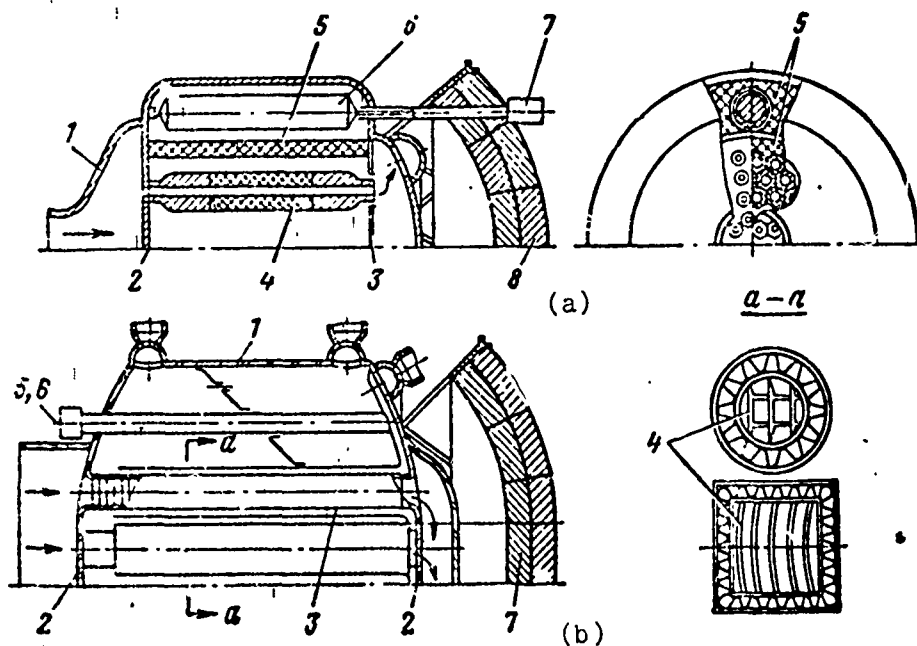


Fig. 2.2. Structural diagrams of nuclear reactors: a - on intermediate neutrons; b - heterogeneous on thermal neutrons.

Figure 2.2b gives a structural diagram for a heterogeneous reactor with a gaseous working medium.

The housing 1 of the reactor, the end walls 2, and the pipes for the fuel elements and the passage of the heat-transfer agent 3 are a rigid all-welded design of the direct-flow type. The fuel elements 4, in the form of plates, shown in the figure on the right, are set by sections into the pipes 3. The controlling and emergency rods 5 and 6 are made similarly to the diagram of a thermal reactor.

As the reflector and moderator in this reactor, one of the possible variants is water, which enters the right upper branch connection of the housing and occupies the entire free space between the fuel elements and the housing. In order to provide a uniform mixing of the water during the operation of the reactor, diaphragms with openings are installed in the housing. To ensure the necessary cooling of the structural elements there is a special water supply into the jacket which covers the fuel element shell.

The gas, for example, helium, passing along the internal channel, is heated from the plates, which can be made from a uranium alloy. The form of the channel can be different depending upon the pressure of the heat-transfer agent.

## THE CONSTRUCTION OF REACTOR ELEMENTS

### Means of connecting elements

Many reactor parts are made from sheet material and are joined by welding or soldering. Let us outline the welding technique used for reactor elements and then show examples.

Electric argon-arc welding - the fundamental form of welding in the construction of a reactor - ensures a durable pressurized seam. This procedure can be completely automated.

Resistance welding ensures a durable unpressurized seam. This is used for the connection of uncritical parts.

Spot welding does not provide a durable pressurized seam. It is used for clamping in intermediate operations and also for bracing uncritical parts.

Electron-beam welding provides a durable pressurized seam of the highest quality. It allows the welding of different types of materials, for example, nonferrous metal to steel, tungsten, etc., i.e., materials which do not ordinarily undergo welding well. It should be noted that this form of welding is not always used; it is expensive and requires special equipment.

In addition to these methods, sometimes rare welding techniques of great promise are used. These include friction welding, thermal diffusion welding, ultrasonic welding, laser beam and blast welding.

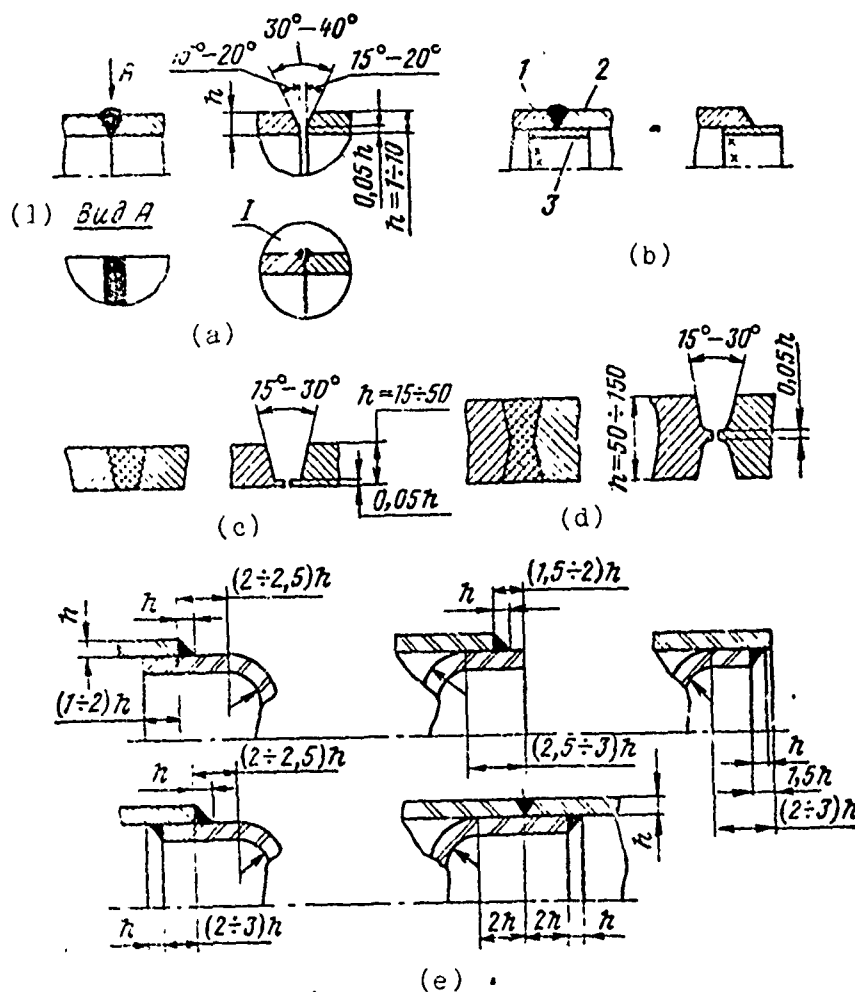


Fig. 2.3. Weld seams obtained by argon-arc welding.  
KEY: (1) View.

Soldering is also widely used in the construction of reactor elements. In many elements, for example, the connection of multi-layer shells, the bracing of power units, etc., soldering is used successfully along with welding. In certain cases - the connection of structural materials with ceramics it is irreplaceable and is a unique means of connecting the elements.



Let us examine the examples of welding reactor elements in the drawing. Figure 2.3 shows examples of argon-arc electric welding of housing elements with butt welding and overlapping.

The edges of the shells under the weld must be processed by a specific method (Fig. 2.3a); for thin materials the edges are cut along a plane at an angle of  $\beta \sim 20^\circ$ . The thickness of the uncut material is  $\sim 0.05h$ , where  $h$  is the thickness of the sheet. Such a joint is used if the design allows it to be examined from two sides. In the figure it is apparent that butt welding cannot be depicted on a drawing (see sketch I).

Figure 2.3b shows a seam when its inspection from the side is ruled out because of the inaccessibility or complexity of the design. On the inside, before the welding of parts 1 and 2, deflector 3, which is a plate or a thin ring (depending upon the size), is installed by spot welding. Such a deflector ensures the uniform penetration of the joint and guarantees the quality of the seam, averting accidental overshoots of molten metal during welding.

With an increase in the thickness of the welded plate to 50 mm or more, the edges of the sheet are processed as shown in Fig. 2.3c and d. Here such seams are shown in the drawing in profile or cross section.

When shell designs are overlapped (Fig. 2.3e) the seam should be removed from the edge of the shell or from other deformations; this is a necessary condition for strengthening the structure.

Figure 2.4 shows connection methods which are rarely encountered in reactor design. Resistance welding is successfully used in overlapping sheets (Fig. 2.4a) where durable but not pressurized seams are required, for example, in welding the bracing collar to the shell.

Deflectors, jackets, shields and auxiliary parts can be welded by electric spot welding. The location of electrodes and the form of welding are shown in the drawing on Fig. 2.4b.

In the illustration of electron-beam welding (Fig. 2.4c) the filling of the seam with metal is not shown or is shown in the form of a wedge with a  $3^{\circ}$ - $5^{\circ}$  angle.

The seam, without shading, is shown on the drawing of friction welding (Fig. 2.4d).

Figure 2.4e is an illustration of soldering single-type or different-type materials.

The two-layer shells 1, 2, 3, shown in Fig. 2.4f, are widely used in reactor construction. The shells 1 and 3 are connected with adapter 2 between them by soldering. The shape of the adapter differs. An adapter with steep pitch is used in elements where the load on the shell 3 is small.

Extreme differences in the thicknesses of welded parts should be avoided for argon-arc welding in butt and overlap welded units. Figure 2.5a shows examples of correctly and incorrectly (circled sketches) welded units.

Figure 2.5b gives an example of argon-arc welding of sheet-metal elements of the reactor's housing with elements not made from sheet metal. In the housing there are parts which connect several such elements, for example, a frame flange. The thicknesses of the walls of the welded elements must be the same at the welding points. The welding seams of parts 4 and 5 are made on different levels to provide for assembling from the same side.

On the four drawings in Fig. 2.5c we see the end finishing of two-layer shells. Usually, two-layer shells consist of a thick-walled power shell having minimum temperature, a thin hot shell, and the adapter between them which connects the shells with soldering.

Between these shells passes a fluid which either completely or partially fills the space between them. Sometimes the working medium passes in the opposite direction along the fluted adapter as shown in the first sketch.

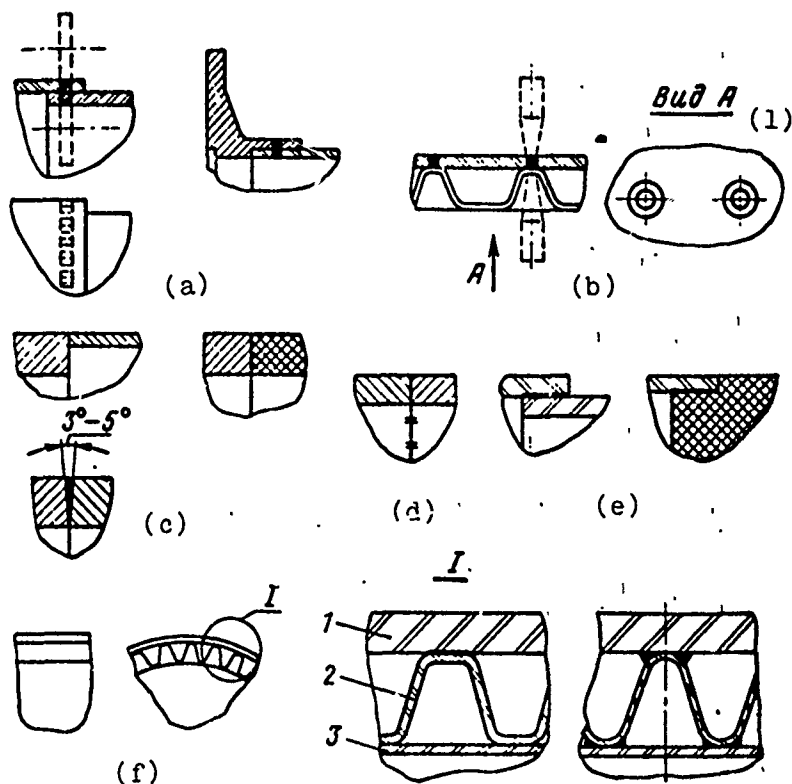


Fig. 2.4. Methods of joining reactor elements.  
KEY: (1) View.

At the inlet points for the working fluid in the inner-shell space, the end finishing of the internal thin shells can be performed by different methods. In the second sketch the end of the internal shell is deformed so as to allow the blind soldering of the internal to the external shell, completely closing off the exit of the internal fluid. In the third sketch this same effect is achieved by soldering the end of the internal shell by means of a ring which can be made from the soldering material if the distance between the shells is small. The fourth sketch shows the partial soldering of the fluted adapter on the end. Such soldering allows the overflow of part

of the fluid from the space between the shells to the adjacent section if this is necessary.

As with any other construction, we know that it is expedient to assemble reactor elements in units. For example, hood 1 and hood 3 of the reactor (Fig. 2.5d) must be welded to the central part 2 of the reactor when each part is completely or almost completely assembled. Such assembly is complicated if the shells of these parts consist of two or more layers. The figure illustrates a method of connecting such multi-layered units.

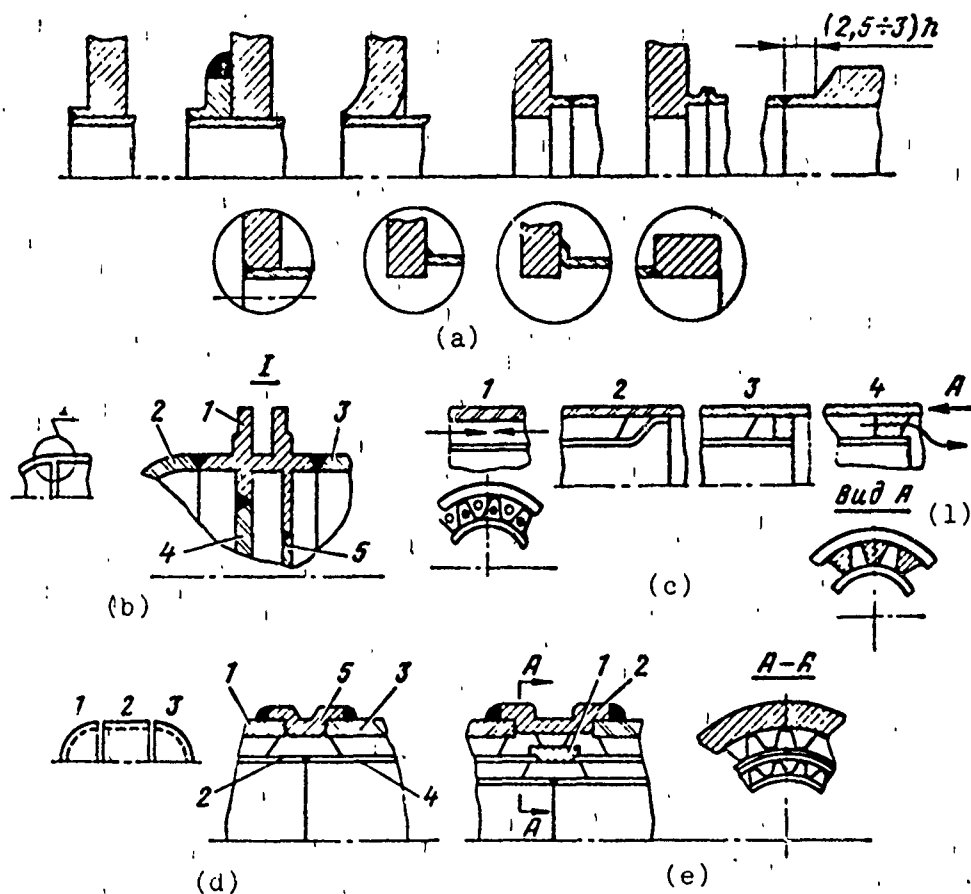


Fig. 2.5. Methods of joining reactor elements.  
KEY: (1) View.

The procedure for welding a two-layer shell is as follows: the internal shells 2 and 4 are welded. This is easy to do since the outer shell projects beyond the edge. After welding, seam cleaning and inspection, the external ring 5, consisting of two-halves, is welded on.

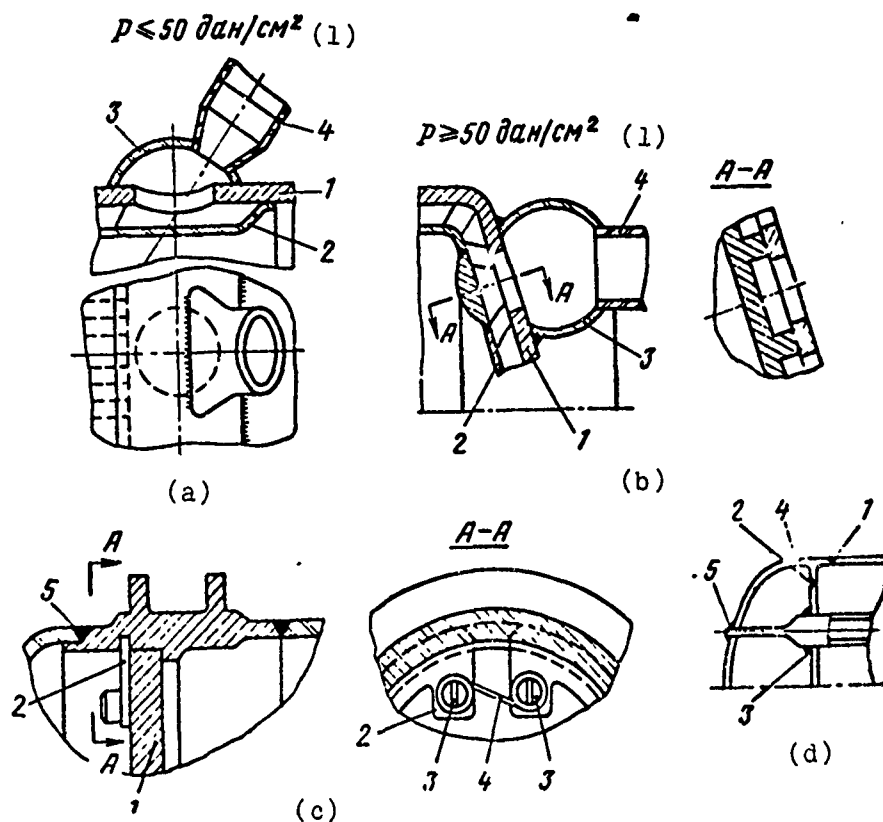


Fig. 2.6. Construction of reactor housing elements.

KEY: (1)  $p \leq 50 \text{ daN/cm}^2$ .

It should be kept in mind that the distance between shells 1 and 3 must not be very big since it determines the size of the section of internal shells 2 and 4 which are not reinforced by an adapter. This is essential for designs having a large pressure drop on the internal shells 2 and 4.

Figure 2.5e shows the same design procedure for connecting two parts of three-layer shells. In this construction the middle split collar 1 is held by the flanges of split collar 2.

The working fluid must be fed into and drained from the reactor housing. Figure 2.6a is a sketch of a supply pipe for moderate pressures (not exceeding  $50 \text{ daN/cm}^2$ ). The power housing 1 has openings which connect the cavity of tank 3 with the intershell space. These openings are made before soldering shells 1 and 2. The working medium is fed along pipe 4 which is flattened here. If the pressure of the working fluid exceeds  $50 \text{ daN/cm}^2$  (Fig. 2.6b), the branch pipe and tanks must be stronger. The internal shell 2 in the section located opposite the openings in housing 1 is reinforced. Tank 3 and pipe 4 have a circular cross section; this design is typical for gas reactors.

In some cases, the reactor core is installed as an independent unit. The core is fully assembled on the pipe panel of the reactor. Figure 2.6c shows one of the possible designs of such a pipe panel. The pipe panel 1 is installed before the support to the bead on the reactor flange and is held motionless by an elastic ring 2 which is attached by screws 3 and wire 4. The seam 5 is made after the core is installed.

Usually reactor construction is all-welded; therefore, the location of the weld seams must agree with the sequence of its assembly. The last seam on the diagram in Fig. 2.6d can only be seam 5. This diagram enumerates the most probable sequence of weld seams.

#### Construction of the fuel element for a fast neutron reactor

In some cases, for engineering reasons, a fuel element can be mounted unassembled. Figure 2.7a shows a design which allows the installation and removal of a fuel element.

A fuel element is a closed pressurized thin-walled design, consisting of shells 2 covered on two sides by end pieces 1 and 5. Inside the shell with a small gap is placed part of the end reflector 3 and the pellet of fissionable material 4. Depending upon the heat-transfer agent, its temperature, and the type of fissionable material, shell 2 and end pieces 1 and 5 are made from stainless steel, for example, Kh16N9T, ZhSK, molybdenum, niobium alloys. The fissionable material is made from uranium alloys, uranium carbide oxide. The reflector is made from beryllium, beryllium oxide. End piece 1 of the fuel element freely enters the opening of the pipe panel 6 and the rectangular notch of fixing plate 7. Then by turning the fuel element 90° it is fixed axially to plate 7 and the flange of end piece 1. Then the end piece is restrained from freely turning during the transporting and operating of plate 8 in which there are rectangular notches for the end piece and openings for the passage of the heat-transfer agent. Plate 8 is screwed to the pipe panel 6. In figure 2.7a the B - B cross section is given without plate 8, and view A is given with this plate installed.

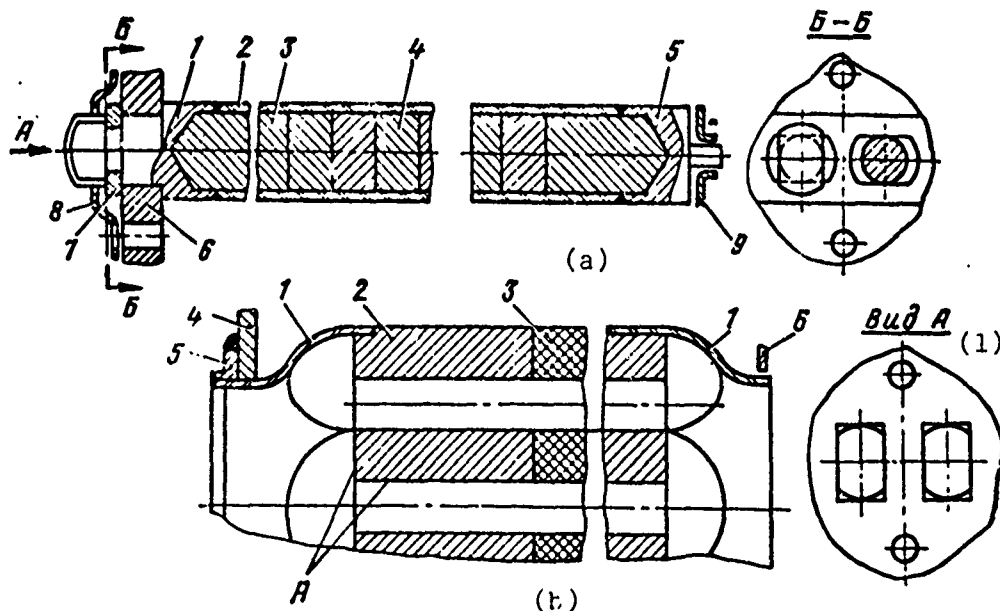


Fig. 2.7. Construction of a fuel element for reactors: a - on fast neutrons; b - on thermal neutrons.  
KEY: (1) View.

The second end piece 5 fixes the fuel element to the lightweight diaphragm 9 of the reactor.

The shell of the fuel element is the most loaded element in the reactor and, consequently, in the entire power plant. The shell operates under the highest possible temperature. It is subjected to the action of gas forces arising as a result of uranium fission. Gaseous fission products can collect under the shell. If the reactor has various alternating modes of operation, this leads to cyclic loading of the shell.

The fuel element unit of a thermal reactor (Fig. 2.7b) includes end piece 1, part of end reflector 2, and the fissionable material 3.

Depending upon the heat-transfer agent and the temperature of the fuel element, the end pieces are made from stainless steel, for example, Kh18N9T, molybdenum, niobium. The reflector can be beryllium oxide, beryllium; the fuel in a homogeneous reactor can be a blend of uranium with graphite, beryllium oxide, hydrides.

A fuel element, thus, is a structure of various materials assembled into one unit. A connection between the separate elements, the steel end pieces, and the outer shell, if there is one, is accomplished by welding or soldering.

The fuel elements form the core of a homogeneous reactor. The end piece 1 in the form of a tube then becomes hexagonal, which ensures a tight fit for the core. The heat-transfer agent passes through the openings inside the fuel element or between the units. The fuel element is welded to the load bearing panel 4 through ring 5, providing a uniform wall for the welded parts. The second ring of the fuel element rests on a diaphragm 6.



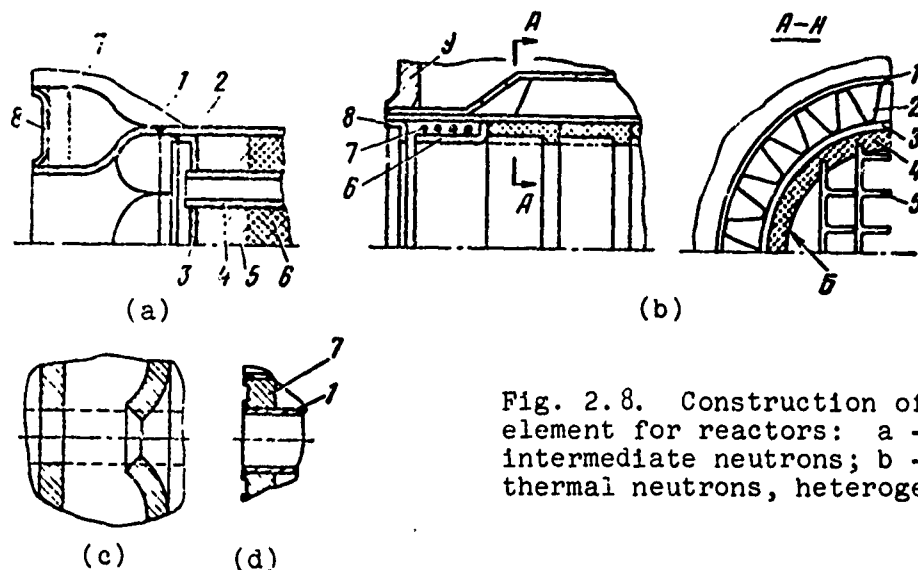


Fig. 2.8. Construction of a fuel element for reactors: a - on intermediate neutrons; b - on thermal neutrons, heterogeneous.

Presented in Fig. 2.8a, the fuel element for an intermediate neutron reactor is made as that of a fast neutron reactor, in the shape of a closed thin-walled welded shell (1, 2, 3, 4) inside of which is located part of the end of reflector 5, the fissionable material 6, mixed, as in a thermal reactor, with a moderator. The shells of the fuel element are made from stainless steel, molybdenum, niobium; the reflector from beryllium oxide; the core from a mixture of uranium with beryllium oxide, hydrides. The cross-sectional shape of a fuel element in the core can be circular or hexagonal. The heat-transfer agent can pass along the channels inside the fuel element or can wash over the surface of the fuel element on the outside. The end piece 1 of the fuel element and the load-bearing panel 7, in this example, are attached by a thin pressed plate 8 welded to plate 7 by spot welding. Figure 2.8b shows a version of fuel element attachment to the load-bearing panel 7. The uniform wall of the welded surfaces is achieved by boring or milling plate 7 at the bracing point of the fuel element shell 1.

Figure 2.8b illustrates the construction of a fuel element of a heterogeneous reactor. The fuel element consists of a two-layer shell 1, 2, 3 inside of which the core units are located. Each unit consists of a graphite base 4 and plates of fissionable material 5 made from uranium alloy.

The units are fixed in the shell 3 with a spacer ring 6, a spring 7, and a support ring 8. The external shell of the fuel element is welded to the load-bearing panel 9. The plate is tapered at the bracing point of the fuel element by a comparatively simple engineering method. The plate is drilled, stamped as shown in sketch c, and then stretched to the necessary size. This ensures identical thickness for the welded elements. The material of shells 1, 2, 3 is stainless steel.

### Construction of adjusting cylinder for a fast neutron reactor and an intermediate reactor

The unit (Fig. 2.9a) consists of a housing 1, which is held by flange 2 to the projection of the housing flange. The adjusting cylinder (4, 5, 6) is located on bearings 3 and 7 in the housing 1.

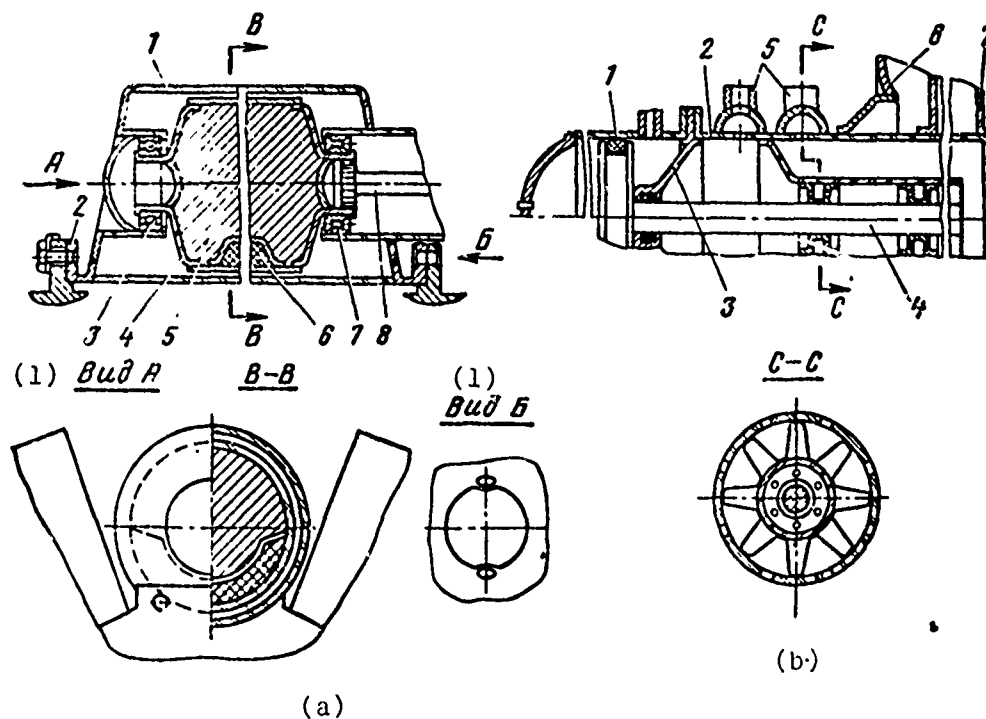


Fig. 2.9. Construction of the regulating rod of a reactor: a - on fast neutrons and intermediate neutrons; b - on thermal neutrons.  
KEY: (1) View.

The reflector material 5 (beryllium, beryllium oxide) is packed into the pressurized shell 4. A segment of boron steel 6, which exhibits powerful neutron absorbance, is set in the lugs to the internal surface of the shell 4, which occupies approximately  $180^\circ$ . It must be cooled to prevent overheating. The adjusting cylinder is turned by spring 8. The journal-thrust bearing 3 and the journal bearing 7 operate with a dry lubricant or are lubricated with the cooling fluid if the cylinder is of such construction.

The housing of the adjusting cylinder 1 is attached so as to ensure free thermal deformation of the more highly heated reactor housing and the installation is light because of the pin connection. The locking of the pin is shown in the figure (view 5).

One of the possible designs of the adjusting rod in a thermal reactor (Fig. 2.9b) consists of a controlling cylinder 1, a housing 2, support devices 3, and the rod 4. These elements of the rod are made from stainless steel, except for rod 4 which is made from boron steel.

The adjustment is performed by the moving of the rod into the core of the reactor using a piston and cylinder; the rod must be cooled during operation. The coolant is fed to tanks 5.

The working fluid controlling the rod, in this case, is the same as the cooling fluid. The housing of the adjustment rod 1 is welded to the load-bearing plate of the reactor 6 and the support diaphragm 7. The disadvantage of this design is its porosity.

#### Protection unit

The protection unit (Fig. 2.10) of the studied reactor has a mass which sometimes exceeds the mass of the reactor itself. The protection unit consists of a bracing frame 1 which connects the protection with the reactor and with other elements of the installation, load-bearing rings 2, diaphragms 3, shells 4, pipes 5 for introducing the adjusting rod into the reactor. The protective

material is sheet tungsten 6 for protecting the installation from  $\gamma$ -radiation; metal hydride and layers of boron steel 8 or other material protect the installation from neutron radiation.

The entire unit is a welded pressurized structure. Pressurization is necessary to contain the hydrogen given off as a result of the neutron bombardment of metal hydride.

The release of hydrogen during operation requires that the protective shell be designed for strength and stability. A decrease in hydrogen pressure can be achieved by creating a vacuum when filling the shells with metal hydride.

In designing this shell we should also keep in mind the heating of the protection unit during the operation of the reactor.

Figure 2.11 shows an overall view of a homogeneous nuclear reactor whose energy is effected in a thermal electric converter. The reactor has 37 fuel elements which are cooled by the eutectic Na-K at  $t_{\text{bx}} = 455^\circ\text{C}$  and  $t_{\text{btx}} = 518^\circ\text{C}$  [bx = input; btx = output].

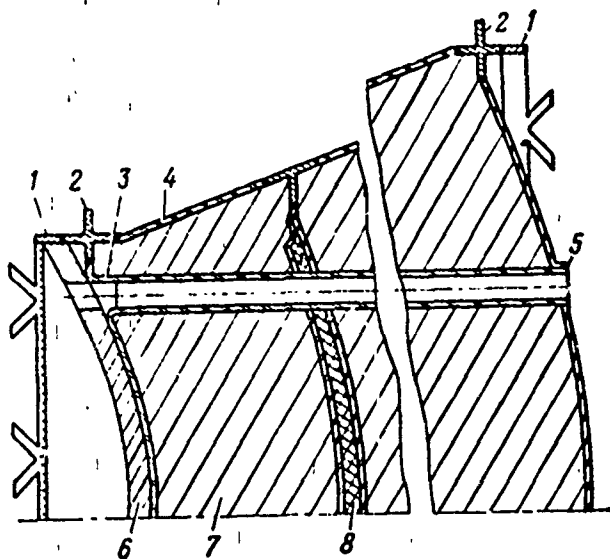


Fig. 2.10. Reactor protection unit.

Figure 2.12 is a sketch of a fast neutron reactor. The working medium is the eutectic Na-K, the nuclear fuel uranium carbide, the reflector beryllium, the material of the regulating cylinders beryllium. The heat-transfer agent has a loop-type feed.

The eutectic, passing through the two-layer shell 1 of the housing, enters the reactor core through the openings in the pipe panel 2. Part of the heat-transfer agent goes through the central channel in the fuel element 3 and part into the cavity between the fuel elements and then into the branch pipes of the reactor housing. Thermal deformation of the core is compensated by installing the pipe panel 4 on syphon bellows 5.

Figure 2.13 shows a heterogeneous reactor on intermediate neutrons. This reactor consists of a housing with branch pipes (1, 2, 3), a core (4, 5, 6), regulating devices (7, 8, 9) and shield 10.

The liquid metal enters the reactor housing through branch pipe 2, passes through the core and exits from the reactor through branch pipe 3. The core is made up of disks 4 with openings through which the pipes pass which connect it with the pipe panels 5 and 6.

The reactor is regulated by cylinders 7; emergency control is accomplished by tilting reflectors 8 and the reflectors 8 are moved by mechanism 9. The shield 10 is of multilayer construction. Shadow shielding is used; therefore, the outlines of the reactor must be inscribed in it.

Figure 2.14 illustrates a reactor of the "Romashka" type, in which heat transfer from the core is accomplished without a heat-transfer agent.

The reactor is cylindrical. The heat releasing elements 1 are made in the form of plates of uranium dicarbide with 90% enrichment by the uranium isotope  $U^{235}$ . The core consisting of the fuel elements and graphite plates 2 with a maximum temperature in the center of

1770°C is surrounded on all sides by reflector 3 of beryllium, in the side sections of which are four regulating rods 4.

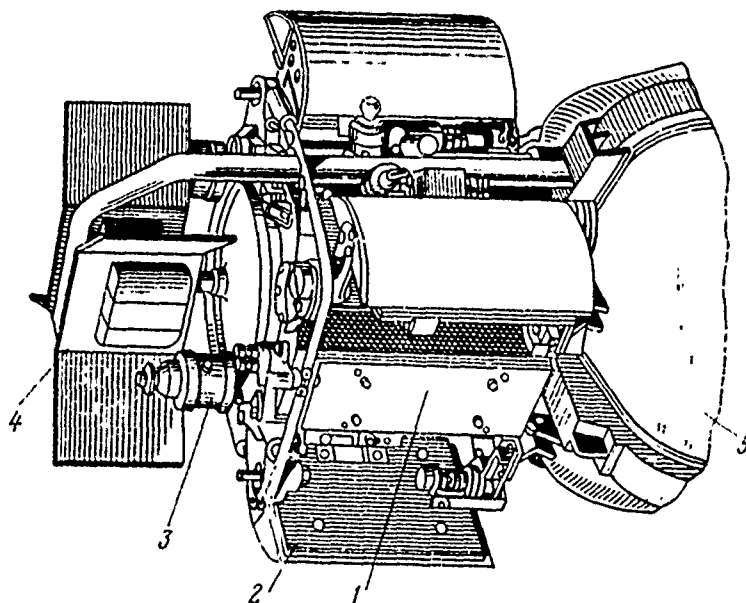


Fig. 2.11. Construction of a nuclear reactor on thermal neutrons: 1 - housing; 2 - regulating rods; 3 - electric drive of the rod; 4 - pump; 5 - shield.

A thermal electric converter 5 of germanium-silicon alloy is located directly on the surface of the radial reflector, having a temperature of 1000°C. The electrical power of the converter 5 is 500W. The figure shows fins 6 installed on the converter for cooling.

#### Stress analysis of reactor parts

Let us consider a minimum stress analysis for the reactor part.

The following basic elements should be analyzed: cores and shells of heat-releasing elements, housing and other shells, and the load-bearing panel.

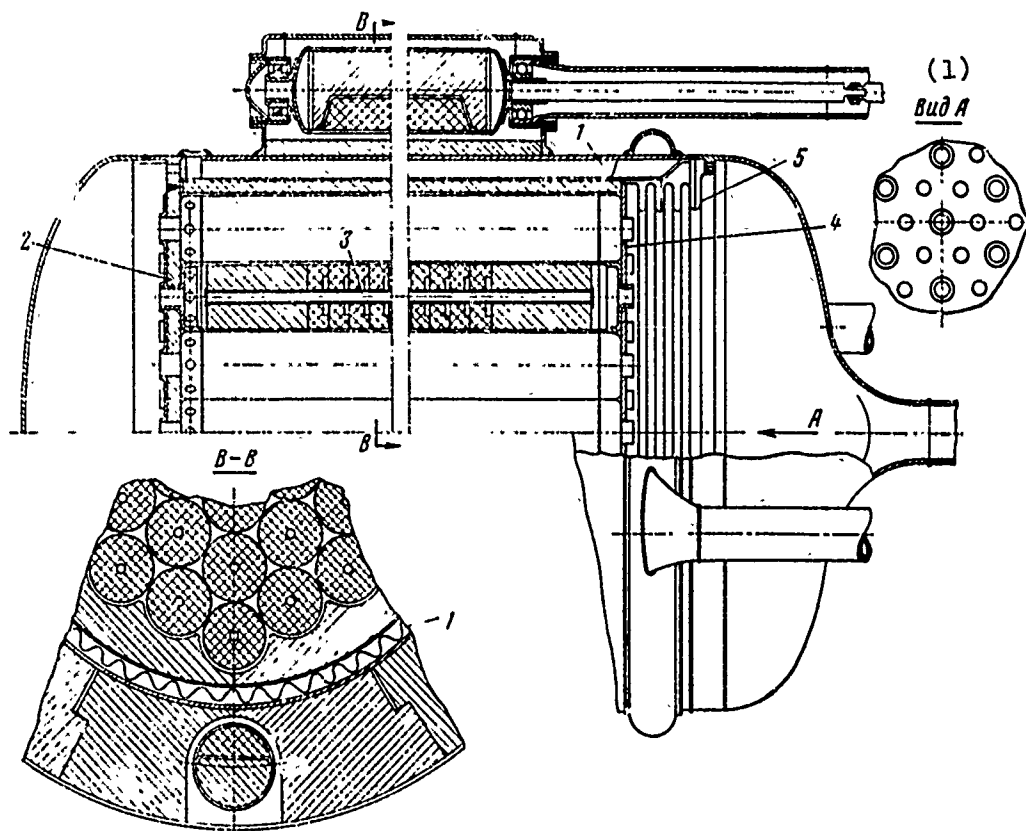


Fig. 2.12. Construction of a fast neutron nuclear reactor.  
KEY: (1) View.

The heat-releasing elements in the form of solid circular rods or plates experience thermal stresses due to the nonuniform heating of the material. The greatest nonuniformity of heating and, consequently, the highest temperature gradient occurs in the cross section of a fuel element when along its axis the temperature changes more or less smoothly.

If heat release in uranium or its compounds occurs uniformly and the heat is uniformly drained from a cylindrical or flat surface, then the temperature field is symmetric with respect to the axis of

the fuel element's core and the temperature gradient can be a function of the radius  $r$  of a circular fuel element or the distance from the axis of symmetry of a flat fuel element. In this case, in the first evaluation of strength we disregard the effect of end sections of the core on the intensity and we find the stresses in the fuel element at any point removed from the ends. A more precise evaluation of thermal stresses is obtained if we take into account the deformation of the end sections.

As a result of the temperature gradient in the core, there are radial, circular, and axial stresses corresponding to the thermal deformations of the core, i.e., it is in a three-dimensional stressed state which should be taken into account in stress analysis.

To decrease the thermal stresses, cores are frequently made in the form of pellets of fissionable material placed in a cylindrical shell. Cracking and crushing of pellets during operation is undesirable; therefore, temperature stresses should be checked. If the pellet is thin-walled, it will be in a two-dimensional stressed state and will experience loading in circular and radial directions; stresses in the direction of the fuel element's axis will be small and are not taken into account.

The shell surrounding the pellets of the fuel elements will be loaded by the pressure of gases given off during uranium fission. To check the strength of the shell involves a number of calculations concerning the strength of the reactor unit.

Then in a number of minimum calculations for the reactor the calculation of the reactor housing and the support plate is involved.

To determine thermal stresses we shall assume that the temperature gradient along the element of the part is known and given. Also known are the main characteristics of the reactor material (some of them are presented at the end of the book).



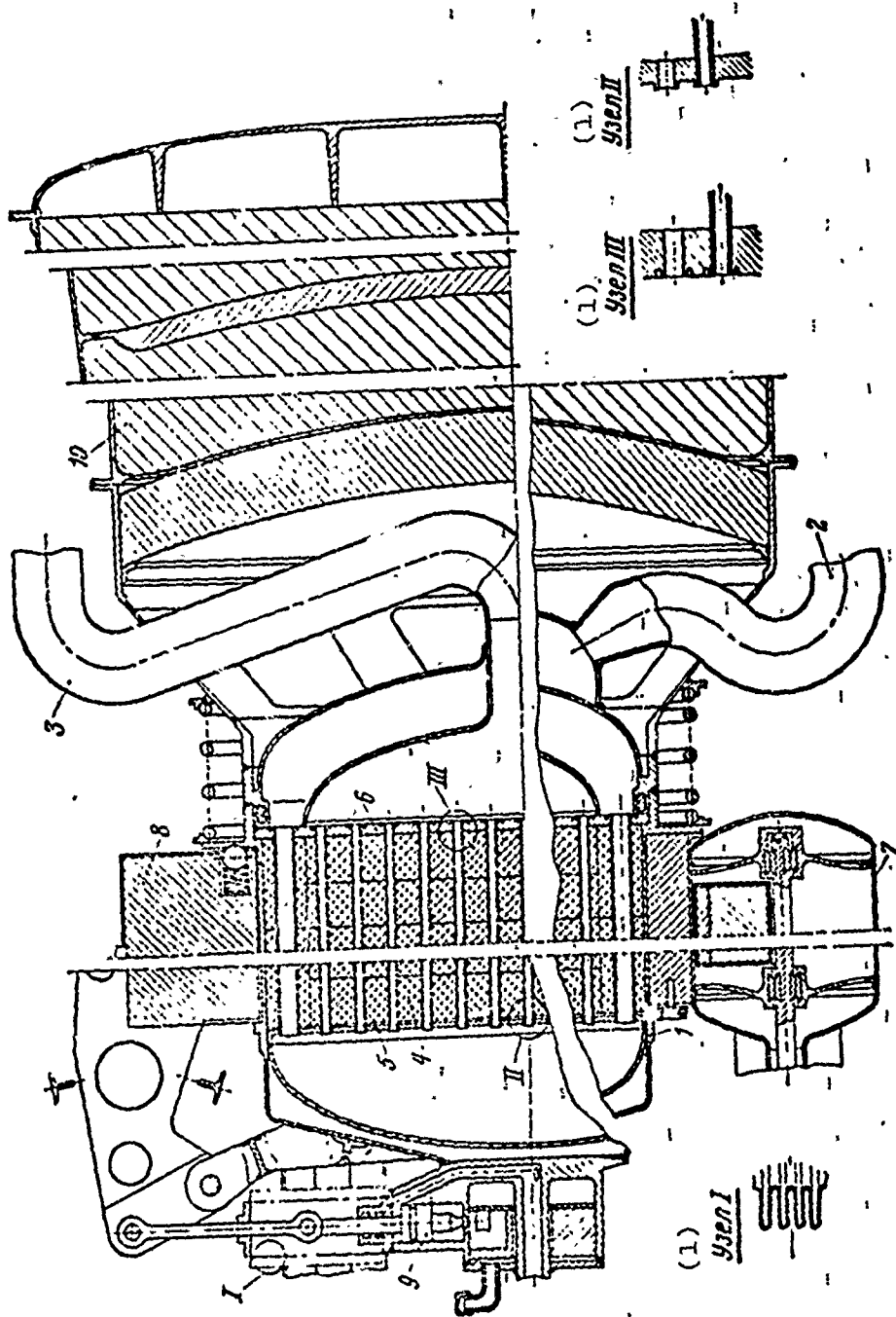


Fig- 2.13. Construction of an intermediate neutron nuclear reactor.  
KEY: (1) Node.

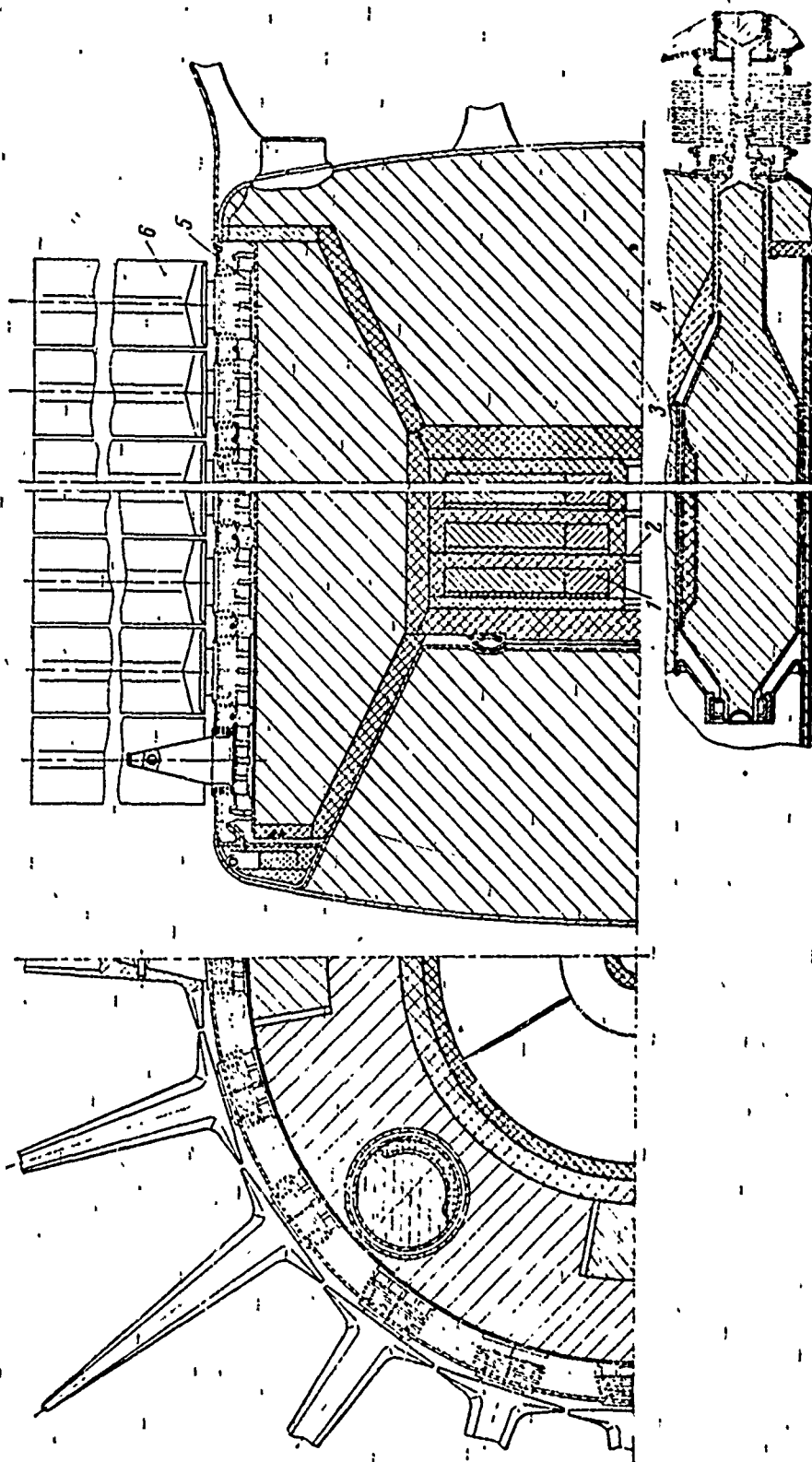


Fig. 2.14. Construction of a nuclear reactor with a solid core.

## THERMAL STRESSES IN FUEL ELEMENTS

### Thin cylindrical pellets

The rods of a fuel element are made in the form of flat thin pellets - disks (Fig. 2.15a). The disk is in a two-dimensional stressed state. Stress in the direction of the x-axis is zero.

The quantities  $\alpha$ ,  $\Delta t = f(r)$ ,  $E$ ,  $\sigma_{B.T.}^t$  are given. We must find  $\sigma_r$  and  $\sigma_\varphi$ , where  $\sigma_r$  are radial and  $\sigma_\varphi$  are circular stresses.

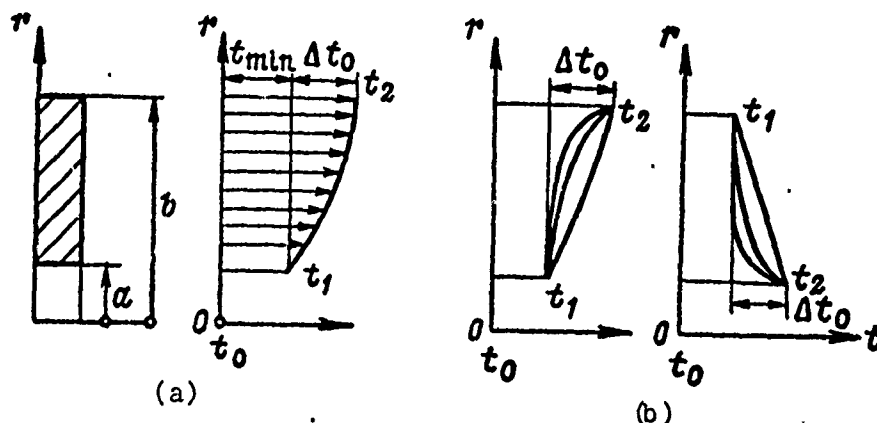


Fig. 2.15. Temperature gradients.

From the symmetry of the problem it follows that radial displacements  $u$  depend only on radius  $r$  while circular displacements  $v$  in the direction  $\varphi$  are zero. Then the main deformations have the form:

$$\left. \begin{aligned} \epsilon_r &= \frac{du}{dr} = \frac{1}{E} (\sigma_r - \mu \sigma_\varphi) + \alpha \Delta t; \\ \epsilon_\varphi &= \frac{u}{r} = \frac{1}{E} (\sigma_\varphi - \mu \sigma_r) + \alpha \Delta t, \end{aligned} \right\} \quad (2.1)$$

hence

$$\left. \begin{aligned} \sigma_r &= \frac{E}{1-\mu^2} \left[ \frac{du}{dr} + \mu \frac{u}{r} - (1+\mu) \alpha \Delta t \right]; \\ \sigma_\varphi &= \frac{E}{1-\mu^2} \left[ \frac{u}{r} + \mu \frac{du}{dr} - (1+\mu) \alpha \Delta t \right]. \end{aligned} \right\} \quad (2.2)$$

We substitute  $\sigma_r$  and  $\sigma_\varphi$  into the equation of equilibrium<sup>1</sup>:

$$\sigma_r - \sigma_\varphi + r\sigma_r' = 0.$$

We find the differential equation for radial displacement

$$u'' + \frac{1}{r}u' - \frac{u}{r^2} = (1 + \mu)a(\Delta t)'. \quad (2.3)$$

For integration it is conveniently represented in the form

$$\left[ \frac{1}{r}(ru)' \right]' = (1 + \mu)a(\Delta t)'. \quad (2.4)$$

The first integration gives

$$(ru)' = (1 + \mu)a\Delta t r + C_1 r, \quad (2.5)$$

and the second

$$u = \frac{1 + \mu}{r} \int_a^r r a \Delta t dr + \frac{1}{2} C_1 r + \frac{C_2}{r}. \quad (2.6)$$

Here  $C_1$  and  $C_2$  are constants.

Substituting equation (2.6) in (2.2), we find the formulas for stresses:

$$\left. \begin{aligned} \sigma_r &= -\frac{E}{r^2} \int_a^r r a \Delta t dr + \frac{EC_1}{2(1 - \mu)} - \frac{EC_2}{(1 + \mu)r^2}; \\ \sigma_\varphi &= \frac{E}{r^2} \int_a^r r a \Delta t dr - E a \Delta t + \frac{EC_1}{2(1 - \mu)} + \frac{EC_2}{(1 + \mu)r^2}. \end{aligned} \right\} \quad (2.7)$$

Let us find the constants  $C_1$  and  $C_2$ . We know that

---

<sup>1</sup>This equation (2.82) is derived in section 2.2.

$$\sigma_{ra} = 0 \text{ when } r = a;$$

$$\sigma_{rb} = 0 \text{ when } r = b. \quad (2.8)$$

Substituting these conditions into equations (2.7), we obtain

$$\begin{aligned} C_1 &= \frac{2(1-\mu)}{(b^2-a^2)} \int_a^b r a \Delta t dr; \\ C_2 &= \frac{(1+\mu)a^2}{(b^2-a^2)} \int_a^b r a \Delta t dr. \end{aligned} \quad (2.9)$$

Finally, we obtain

$$\begin{aligned} \sigma_r &= \frac{r^2-a^2}{b^2-a^2} \frac{E}{r^2} \int_a^b a \Delta t r dr - \frac{E}{r^2} \int_a^r a \Delta t r dr; \\ \sigma_z &= \frac{r^2+a^2}{b^2-a^2} \frac{E}{r^2} \int_a^b a \Delta t r dr + \frac{E}{r^2} \int_a^r a \Delta t r dr - E a \Delta t. \end{aligned} \quad (2.10)$$

For a disk without an opening in these formulas we should assume  $a = 0$ . Then

$$\begin{aligned} \sigma_r &= \frac{E}{b^2} \int_0^b a \Delta t r dr - \frac{E}{r^2} \int_0^r a \Delta t r dr; \\ \sigma_z &= \frac{E}{b^2} \int_0^b a \Delta t r dr + \frac{E}{r^2} \int_0^r a \Delta t r dr - E a \Delta t. \end{aligned} \quad (2.11)$$

Let us find the deflection of the pellet. We substitute into expression (2.6) the value of constants  $C_1$  and  $C_2$ :

$$u = \frac{(1-\mu)r^2 + (1+\mu)a^2}{r(b^2-a^2)} \int_a^b a \Delta t r dr + \frac{1+\mu}{r} \int_a^r a \Delta t r dr. \quad (2.12)$$

In these formulas  $\Delta t$  is the temperature gradient. In the earlier examined problems it is determined from formula

$$\Delta t = t_1 - t_0,$$

where  $t_0$  is the temperature of part manufacture or assembly, usually 20°C;

$t_1$  is the temperature which exists in the part as a result of heating.

For this problem this equality can be conveniently presented in the form

$$\Delta t = t_{\min} + \Delta t_0 f(r) - t_0 = \Delta t_{\min} + \Delta t_0 f(r),$$

i.e., in the form of a constant component of gradient  $\Delta t_{\min}$  and a variable component of a gradient depending upon the radius,  $\Delta t_0 f(r)$ . If we substitute this expression of the gradient into the stress formula (2.10), we find that the integrals of the constant component of the gradient  $t$  will be equal to zero and the stress will be a function of only  $\Delta t_0$  and the law of temperature variation along the radius  $f(r)$ . The main technological stresses we shall disregard. Therefore, it is advisable to determine the temperature gradient  $\Delta t$  by the formula  $\Delta t = \Delta t_0 f(r)$ .

In many cases, it is advisable to replace the true law of temperature variation with approximate functions. Figure 2.15b shows the temperature gradients which can be encountered in these calculations.

The linear law of temperature variation is

$$t = \Delta t_0 \left( \frac{b-r}{b-a} \right).$$

The hyperbolic law of temperature variation is

$$t = \Delta t_0 \frac{a}{b-a} \left( \frac{b-r}{r} \right).$$

The exponential logarithmic dependence is

$$t = \Delta t_0 \frac{\ln(b/r)}{\ln(b/a)}.$$

The law of temperature gradient variation along the radius  $f(r)$  can be represented, in many cases, in the form of a power dependence

$$\Delta t = \Delta t_0 \left( \frac{b-r}{b-a} \right)^n, \quad (2.13)$$

where  $n = 1, 2, 3, \dots, n$ .

If we substitute expression (2.13) into (2.10), we obtain the calculation formulas for computing stresses:

$$\begin{aligned} \sigma_r = E\alpha\Delta t_0 & \left\{ \frac{r^2 - a^2}{b^2 - a^2} \frac{1}{r^2 (b-a)^n} \left[ \frac{b(b-a)^{n+1}}{n+1} - \frac{(b-a)^{n+2}}{n+2} \right] - \right. \\ & \left. - \frac{1}{r^2 (b-a)^n} \left[ \frac{(b-r)^{n+2}}{n+2} - \frac{(b-a)^{n+2}}{n+2} - \frac{b(b-r)^{n+1}}{n+1} + \frac{b(b-a)^{n+1}}{n+1} \right] \right\}; \\ \sigma_\varphi = E\alpha\Delta t_0 & \left\{ \frac{r^2 + a^2}{b^2 - a^2} \frac{1}{r^2 (b-a)^n} \left[ \frac{b(b-a)^{n+1}}{n+1} - \frac{(b-a)^{n+2}}{n+2} \right] - \right. \\ & \left. - \frac{1}{r^2 (b-a)^n} \left[ \frac{(b-r)^{n+2}}{n+2} - \frac{(b-a)^{n+2}}{n+2} - \frac{b(b-r)^{n+1}}{n+1} + \frac{b(b-a)^{n+1}}{n+1} \right] - \right. \\ & \left. - \left( \frac{b-r}{b-a} \right)^n \right\}. \end{aligned} \quad (2.14)$$

If the heat removal in the fuel element is accomplished from the surface of the internal opening, then the gradient will be

$$\Delta t = \Delta t_0 \left( \frac{r-a}{b-a} \right)^n, \quad (2.15)$$

where  $n = 1, 2, 3, \dots, n$ .

If we substitute expression (2.15) into (2.10), we obtain the calculation formulas for this case also. The result is presented in Chapter V, relation (5.89).

Example 2.1. Find the thermal stresses in the disk, assuming

$$n=1 \text{ and } \Delta t = \Delta t_0 \left( \frac{b-r}{t-a} \right)^n.$$

As a result of calculation, we obtain

$$r=a; \quad \sigma_r=0; \quad \sigma_\varphi = -E\alpha\Delta t_0 \cdot 0,55; \quad r=b; \quad \sigma_r=0; \quad \sigma_\varphi = E\alpha\Delta t_0 \cdot 0,13.$$

A stress diagram is shown in Fig. 2.16b. The crosshatched lines show the stresses if  $a = 0$ .

#### Thick-walled cylindrical fuel elements

The quantities  $E, \alpha, \Delta t, \sigma_{B.T.}^t$  are given (Fig. 2.17). Find  $\sigma_r, \sigma_\varphi, \sigma_x$ . We assume that temperature distribution  $\Delta t$  is symmetric relative to the axis of the cylinder and does not change in the direction of its axis.

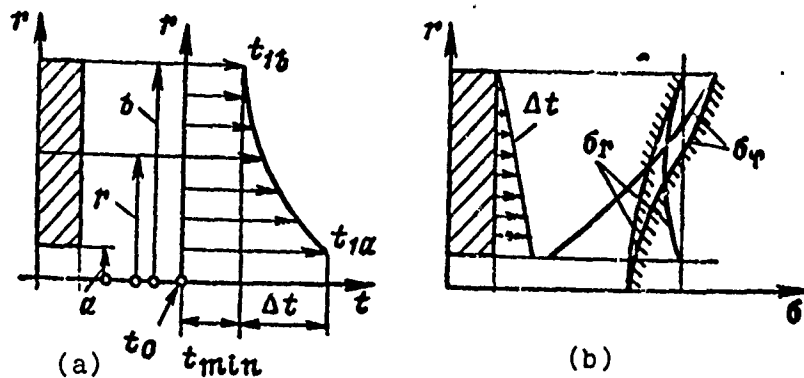


Fig. 2.16. Thermal stresses.

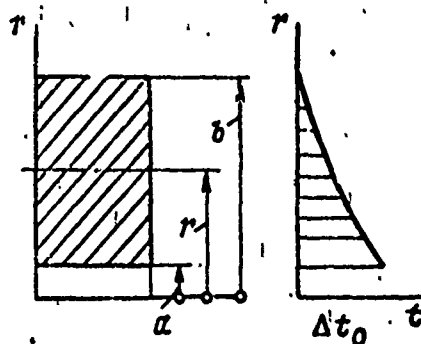
We assume that at a sufficient distance from the ends the cross sections of the cylinder are flat, i.e., we shall consider the part



of the cylinder between two adjacent cross sections as a disk experiencing plane strain. Normal stresses  $\sigma_r$ ,  $\sigma_\varphi$  and  $\sigma_x$  also occur. The latter are distributed along the faces of this disk so that the faces are kept flat. The stresses which arise in the cylinder are determined from formulas [40]:

$$\begin{aligned}\sigma_r &= \frac{1}{1-\mu} \left( \frac{r^2 - a^2}{b^2 - a^2} \frac{E}{r^2} \int_a^b u \Delta t r dr - \frac{E}{r^2} \int_a^r u \Delta t r dr \right); \\ \sigma_\varphi &= \frac{1}{1-\mu} \left( \frac{r^2 + a^2}{b^2 - a^2} \frac{E}{r^2} \int_a^b u \Delta t r dr + \frac{E}{r^2} \int_a^r u \Delta t r dr - E u \Delta t \right); \\ \sigma_x &= E \varepsilon_x + \frac{1}{1-\mu} \left( \frac{2\mu E}{b^2 - a^2} \int_a^b u \Delta t r dr - E u \Delta t \right).\end{aligned}\quad (2.16)$$

Fig. 2.17. Thermal stresses.



If there are no openings in the cylinder, then  $a = 0$  and the stress formulas acquire the form:

$$\begin{aligned}\sigma_r &= \frac{1}{1-\mu} \left( \frac{E}{b^2} \int_0^b u \Delta t r dr - \frac{E}{r^2} \int_0^r u \Delta t r dr \right); \\ \sigma_\varphi &= \frac{1}{1-\mu} \left( \frac{E}{b^2} \int_0^b u \Delta t r dr + \frac{E}{r^2} \int_0^r u \Delta t r dr - E u \Delta t \right); \\ \sigma_x &= \frac{1}{1-\mu} \left( \frac{2\mu E}{b^2} \int_0^b u \Delta t r dr - E u \Delta t \right) + E \varepsilon_x.\end{aligned}\quad (2.17)$$

Constant axial relative strain  $\epsilon_x$  in each particular case must be chosen so that the equally acting forces, distributed along the cross section of the cylinder, vanish, i.e.,

$$2\pi \int_0^b \sigma_x r dr = 0. \quad (2.18)$$

A joint solution of equations (2.17) and (2.18) gives

$$\epsilon_x = \alpha \left( t_{\min} + \frac{\Delta t_0}{2} \right),$$

where  $\Delta t_0 = t_a - t_b$  is the maximum value of the temperature gradient along the cross section of the fuel element.

If  $t_a$  is the temperature on the internal surface of the cylinder and the temperature on the external surface is zero, the temperature at any distance  $r$  from center is

$$\Delta t = t_a \ln \frac{b}{r} / \ln \frac{b}{a}.$$

Substituting this value into formulas (2.17), we find the following expressions for thermal stresses:

$$\begin{aligned} \sigma_r &= \frac{E\alpha t_a}{2(1-\mu) \ln b/a} \left[ -\ln \frac{b}{r} - \frac{a^2}{b^2-a^2} \left( 1 - \frac{b^2}{r^2} \right) \ln \frac{b}{a} \right]; \\ \sigma_\varphi &= \frac{E\alpha t_a}{2(1-\mu) \ln b/a} \left[ 1 - \ln \frac{b}{r} - \frac{a^2}{b^2-a^2} \left( 1 + \frac{b^2}{r^2} \right) \ln \frac{b}{a} \right]; \\ \sigma_x &= \frac{E\alpha t_a}{2(1-\mu) \ln b/a} \left[ 1 - 2 \ln \frac{b}{r} - \frac{2a^2}{b^2-a^2} \ln \frac{b}{a} \right]. \end{aligned} \quad (2.19)$$

If  $t_a$  is positive, radial stress for all points is compressive and vanishes on the internal and external surfaces of the cylinder. The stress components  $\sigma_\varphi$  and  $\sigma_x$  reach their highest absolute values on the inner and outer surfaces of the cylinder. Assuming  $r = a$ , we find

$$\sigma_r = \sigma_x = \frac{E\alpha t_a}{2(1-\mu) \ln b/a} \left( 1 - \frac{2b^2}{b^2 - a^2} \ln \frac{b}{a} \right). \quad (2.20)$$

When  $r = b$

$$\sigma_r = \sigma_x = \frac{E\alpha t_a}{2(1-\mu) \ln b/a} \left( 1 - \frac{2a^2}{b^2 - a^2} \ln \frac{b}{a} \right). \quad (2.21)$$

If the wall thickness is small as compared with the external radius of the cylinder, formulas (2.20) and (2.21) can be simplified, assuming

$$\frac{b}{a} = 1 + m; \quad \ln \frac{b}{a} = m - \frac{m^2}{2} + \frac{m^3}{3} - \dots$$

and considering  $m$  a small quantity. Then when  $r = a$

$$\sigma_r = \sigma_x = -\frac{E\alpha t_a}{2(1-\mu)} \left( 1 + \frac{m}{3} \right), \quad (2.22)$$

and when  $r = b$

$$\sigma_r = \sigma_x = \frac{E\alpha t_a}{2(1-\mu)} \left( 1 - \frac{m}{3} \right). \quad (2.23)$$

If the walls of the cylinder are very thin, we disregard the term  $m/3$  in expressions (2.22) and (2.23). Then for surfaces  $r = a$  and  $r = b$  we obtain, respectively,

$$\begin{aligned} \sigma_{ra} = \sigma_{xa} &= -\frac{E\alpha t_a}{2(1-\mu)}, \\ \sigma_{rb} = \sigma_{xb} &= \frac{E\alpha t_a}{2(1-\mu)}. \end{aligned} \quad (2.24)$$

These thermal stresses will be distributed throughout the thickness the same as in a two-dimensional plate or a thin shell with a linear law of temperature distribution.

Thermal stresses are the main factor to keep in mind when designing a fuel element for a reactor. This is easy to show if we express the temperature of fuel element through the heat-release function  $q_v$ , called the three-dimensional state of thermal stress:

$$t = t_{\min} + \Delta t = t_{\min} + \frac{q_v R^2}{4k} \left[ 1 - \left( \frac{r}{R} \right)^2 \right].$$

If  $\alpha = 0$ , then

$$\begin{aligned} \sigma_r &= \frac{E\alpha}{1-\mu} \frac{\Delta t}{4} \left[ \left( \frac{r}{R} \right)^2 - 1 \right]; \\ \sigma_\theta &= \frac{E\alpha}{1-\mu} \Delta t \left\{ \left( \frac{r}{R} \right)^2 - \frac{1}{4} \left[ 1 + \left( \frac{r}{R} \right)^2 \right] \right\}; \\ \sigma_x &= \frac{E\alpha}{1-\mu} \frac{\Delta t}{2} \left[ 2 \left( \frac{r}{R} \right)^2 - 1 \right]. \end{aligned} \quad (2.25)$$

In the temperature range 50-600°C the quantity  $E\alpha/(1-\mu)$  for uranium, for example, has virtually a constant value:

$$\frac{E\alpha}{1-\mu} \approx 0,35 \text{ daN/(M.M}^2 \text{ }^\circ\text{C)}.$$

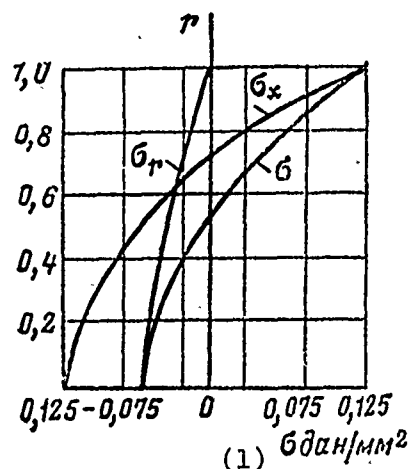
Figure 2.18 shows the stress distribution in the core of a uranium heat-releasing element with a temperature difference of  $\Delta t = 1$ . Circular and axial stresses have the highest value. On the surface of the core both of these stresses are maximum and equal to

$$\sigma_{rb} = \sigma_{xb} = 0,5 \frac{E\alpha}{1-\mu} \Delta t \approx 0,175 \Delta t. \quad (2.26)$$

These formulas are useful for evaluating the correctness of the fuel element core dimensions.

Fig. 2.18. Thermal stresses in the core of a fuel element.

KEY: (1)  $5 \text{ daN/mm}^2$ .



The maximum temperature gradient (1. °C) along the cross section of a heat-releasing element for a cylinder with an internal heat source can be determined from formula [30]

$$\Delta t = \frac{q_v d^2}{1 \lambda},$$

where  $\lambda$  is the thermal conductivity coefficient in  $\text{W/m} \cdot \text{deg}$ ;

$q_v$  is the three-dimensional state of thermal stress in  $\text{W/m}^3$ ;

$\Delta t$  is the temperature difference on the axis and the surface of the core in °C;

$d$  is the core diameter in m.

If we replace the temperature difference between the center and the surface of the core  $\Delta t$  in formula (2.26) with the cited expression, we obtain

$$\sigma_{rb} = \sigma_{xb} = 11 \cdot 10^{-3} \frac{q_v d^2}{\lambda}.$$

From this formula it is apparent that a decrease in core diameter is an effective method of reducing maximum thermal stresses since these stresses are proportional to the square of the diameter.

Example 2.2. Find the maximum thermal stress in a fuel element of the reactor if the following are known: core diameter 5 mm,  $\lambda = 30 \text{ W/m} \cdot \text{deg}$ ;  $q_v = 0.435 \cdot 10^9 \text{ W/m}^3$ . Obviously

$$\sigma_{\tau b} = 11 \cdot 10^{-3} \frac{q_v d^2}{\lambda} = 11 \cdot 10^{-3} \frac{0,435 \cdot 109 \cdot 25 \cdot 10^{-6}}{39} = 4 \text{ daN/mm}^2.$$

This example shows that significant thermal stresses arise with comparatively small dimensions of the fuel element rod.

Naturally an increase in the dimensions of the fuel element increases its thermal loading and can cause stresses which exceed the yield point. In this case, calculations should be performed with allowance for plastic flow.

The physical picture of the stressed state will be as follows.

Since the stresses exceed the yield point, plastic flow of the metal will occur in the fuel element core, due to which plastic deformations will appear and the excess thermal stresses will be relaxed. When the heat-releasing element is cooled, there will appear in its core residual stresses of opposite sign which can also be called metal flow if the yield point is exceeded. Since the temperature field is axisymmetrical, the form of the fuel element remains unchanged, but its rupture resistivity will be weakened due to the cyclic nature of the loading.

In each individual case the stress level is determined by the degree of the fuel element's thermal intensity  $N_{yA}$ . In low-power unstressed reactors  $N_{yA} \leq 1 \text{ kW/kg}$ . After finding  $\sigma_r$ ,  $\sigma_\varphi$ ,  $\sigma_x$ , the strength of the fuel element core should be evaluated from formula (1.23)

$$n = \frac{\sigma_{b,\tau}^t}{\sigma_{l \max}},$$

where

$$\sigma_l = \sqrt{0,5[(\sigma_r - \sigma_\varphi)^2 + (\sigma_\varphi - \sigma_x)^2 + (\sigma_x - \sigma_r)^2]}.$$

It is necessary that  $n \geq 1$ . If this is not the case, calculations should be performed in greater detail with allowance for the plastic flow of the material.

#### Laminated fuel elements

A laminated fuel element whose diagram is presented in Fig. 2.19 is installed freely in a housing. The quantities  $E$ ,  $\alpha$ ,  $\Delta t = t_1 - t_0$  are given. Find  $\sigma_x$ .

As is apparent from the figure, the temperature gradient is symmetric with respect to the axis of the fuel element. According to the common method of finding thermal stresses, we fix the fuel element rigidly in the axial direction (Fig. 2.19b) and find stress  $\sigma_1$  from the reactive forces arising from such a bracing:

$$\sigma_1 = -\frac{1}{1-\mu} E \alpha \Delta t. \quad (2.27)$$

The factor  $1/(1-\mu)$  is introduced because of the two-dimensional stressed state of the plate. A detailed derivation of this formula for a plate will be given in Chapter V.

The application of a bond leads to a violation of the boundary conditions of the freely installed plate. We reproduce the conditions by the application of a force which is equal and opposite to the reactive force in the fixing:

$$P = \int_{-h/2}^{h/2} E \alpha \Delta t b dy.$$

Stress from this force is

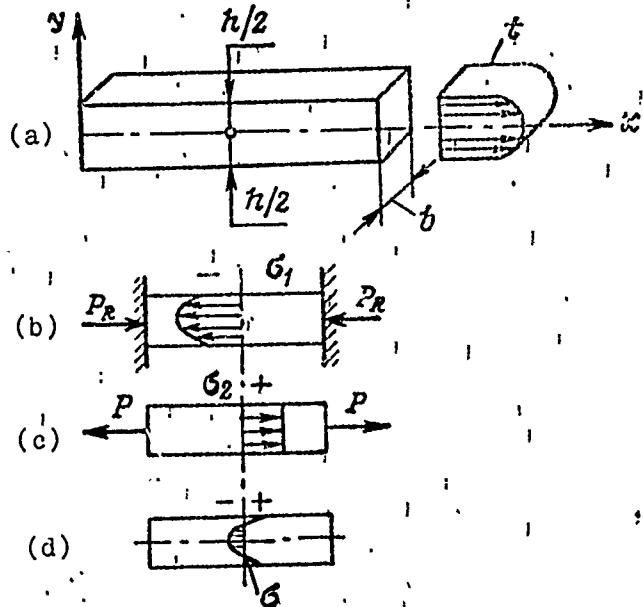
$$\sigma_2 = \frac{1}{1-\mu} \frac{P}{bh} = \frac{1}{(1-\mu)bh} \int_{-h/2}^{h/2} E \alpha \Delta t b dy. \quad (2.28)$$

Finally, stresses in the free plate, are

$$\sigma = \sigma_1 + \sigma_2 = -\frac{1}{1-\mu} E \alpha \Delta t + \frac{1}{(1-\mu) b h} \int_{-h/2}^{h/2} E \alpha \Delta t b t y. \quad (2.29)$$

Figure 2.19b, c, and d show the stress diagrams for  $\sigma_1$ ,  $\sigma_2$  and the total stress diagram of the plate.

Fig. 2.19. Finding thermal stresses in a laminated fuel element.



Sometimes stress equations are expressed in terms of thermal fluxes. If  $q_v$  is three-dimensional heat released in  $W/m^3$ , and  $\lambda$  is the thermal conductivity coefficient in  $W/m \cdot \text{deg}$ , formula (2.29) will have the form

$$\sigma = \frac{E \alpha q_v \left(\frac{h}{2}\right)^2}{(1-\mu) \lambda} \left[ \frac{1}{3} - \frac{1}{2} \left(1 - \frac{y^2}{(h/2)^2}\right) \right].$$

### Stress analysis of reactor shells

Let us mention several common concepts relating to shells.

By a shell we mean a body which has one of three measurements considerably smaller than the other two. The two surfaces of the shell having the largest dimensions are called the main surfaces.



The locus of points equidistant from the main surfaces of the shell is called the middle surface. The geometric shapes of a shell are completely determined by the shape of the middle surface and the law of variation for the shell thickness. As a rule, this thickness is constant.

The most widely used are shells of revolution, i.e., shells which have a middle surface formed by the rotation of any plane curve around an axis lying in the plane of this curve and called the generatrix.

If the middle surface is a plane, the shell is called a plate.

The curve formed on the surface of the shell by the intersection of it by the plane passing through the axis is called the meridian. Obviously the meridians agree with the generatrices of the shell. The meridian's radius of curvature at any point is called the first principal radius of curvature  $R_1$  of the surface at a given point; the radius of curvature of the curve obtained from the intersection of the surface by a plane perpendicular to the meridian is called the second principal radius  $R_2$  of the surface at a given point. Sometimes the word "principal" is omitted.

The radii  $R_1$  and  $R_2$  are variable quantities characterizing the geometry of a shell of rotation. Completely geometric forms of a shell of revolution are characterized by these two radii and the angle  $\theta$ , formed by the normal to the middle surface and the axis of symmetry. Figure 2.20 presents these parameters for various types of single-layer shells.

In engines, in addition to simple single-layer shells, complex two- and multilayer shells are used, which have, as a rule, the shape of a body of revolution. Between the walls of the shells flows liquid or gas, frequently used for cooling the walls. Various types of complex multilayer shells are shown in Fig. 2.21.

In many cases, we can assume that the stresses arising in the shell are uniformly distributed throughout the thickness. Shell theory constructed on this assumption is called momentless theory. This corresponds to cases when the shell has no sharp transitions or rigid attachments if it is not loaded with concentrated boundary forces and moments.

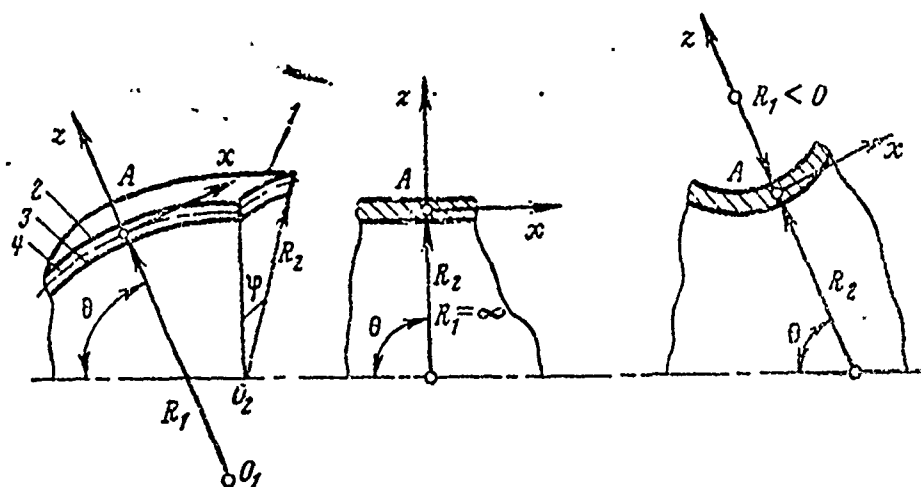


Fig. 2.20.

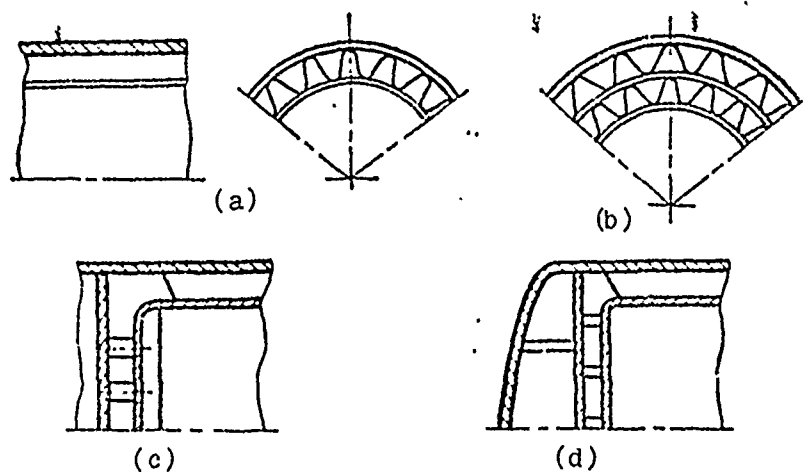


Fig. 2.21. Types of multilayer shells.

# Equations of equilibrium for an axisymmetric single-layer shell

We shall examine the equilibrium of an element of an axisymmetric shell (Fig. 2.22) cut by two meridional and conical surfaces.

We assume that the x-axis and the displacement along this axis  $u$  are directed along a tangent to an arc of the meridian, the y-axis and  $v$ , respectively, along a tangent to an arc of the circle, and the z-axis and  $w$  along the normal. If the strain of the shell is axisymmetric, displacement  $v$  is absent.

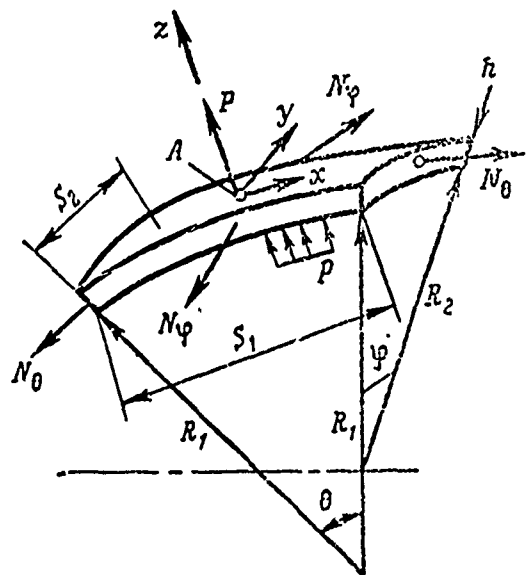
We apply to the faces of this element internal forces, and at point A external forces.

We designate with the symbols  $\bar{N}_\theta$  and  $\bar{N}_\varphi$  the pull which occurs per unit length of an arc of corresponding cross section (in  $\text{N/m}^2$ ):

$$\bar{N}_\theta = \frac{N_\theta}{S_2}; \quad \bar{N}_\varphi = \frac{N_\varphi}{S_1};$$

where  $S_1, S_2$  is the length of the arc of the element.

Fig. 2.22. Derivation of equilibrium equations for shell element.



The quantities  $R_1$ ,  $R_2$ ,  $h$ ,  $p$  ( $N/m^2$ ) are known, where  $p$  is the pressure of the working medium,  $h$  is the thickness of the element. Find  $\sigma_\theta$ ,  $\sigma_\varphi$ ,  $n$ .

Obviously, the meridional  $\sigma_\theta$  and peripheral  $\sigma_\varphi$  stresses will be

$$\sigma_\theta = \frac{\bar{N}_\theta}{h} = \frac{N_\theta}{hS_2}; \quad \sigma_\varphi = \frac{\bar{N}_\varphi}{h} = \frac{N_\varphi}{hS_1}.$$

We project all forces onto the  $z$ -axis; their sum must be equal to zero:

$$\begin{aligned} \sum N_{\theta z} &= -2N_\theta \sin \frac{\theta}{2} = -N_\theta \theta = -N_\theta \frac{S_1}{R_1}; \\ \sum N_{\varphi z} &= -N_\varphi \frac{S_2}{R_2}; \quad p = pS_1S_2. \end{aligned}$$

The equilibrium condition is written as

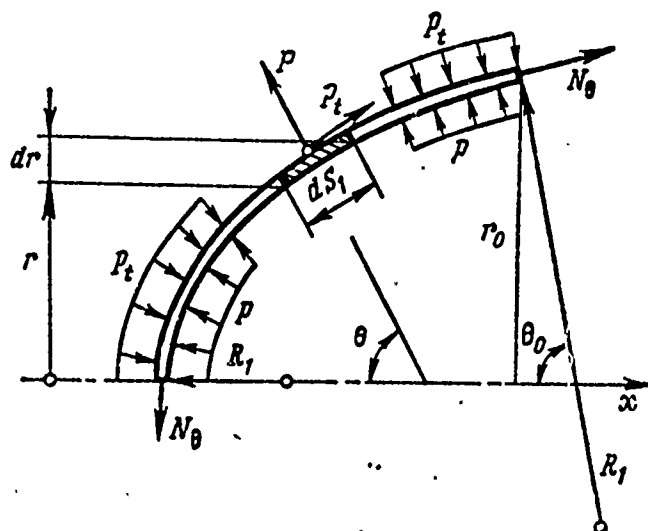
$$-N_\theta \frac{S_1}{R_1} - N_\varphi \frac{S_2}{R_2} + pS_1S_2 = 0.$$

Hence, after dividing the entire equation by  $S_1S_2h$ , we obtain

$$\frac{\sigma_\theta}{R_1} + \frac{\sigma_\varphi}{R_2} = \frac{p}{h}. \quad (2.30)$$

Here the two unknowns are  $\sigma_\theta$  and  $\sigma_\varphi$ . The second equilibrium equation of the system is set up for part of the shell (Fig. 2.23) cut off by the normal conical section. To add to the available load  $p$  we allow for the possible internal distributed load  $p_t$  applied indicated in Fig. 2.23.

Fig. 2.23. Equilibrium of a shell element.



The sum of the projections of the forces onto the x-axis must be equal to zero. The projections of these forces onto the x-axis are

$$N_{t,x} = \bar{N}_t 2\pi r_0 \sin \theta_0; \quad dP_x = p 2\pi r dS_1 \cos \theta; \quad dS_1 = \frac{dr}{\cos \theta}.$$

After integration we obtain

$$P_x = - \int_0^{\theta} p 2\pi r dr$$

and, analogously,

$$P_{t,x} = \int_0^{\theta} p_t 2\pi r \sin \theta dS_1 = \int_0^{\theta} p_t 2\pi r \operatorname{tg} \theta dr.$$

The equilibrium condition is written as:

$$\bar{N}_t 2\pi r_0 \sin \theta_0 = \int_0^{\theta} p 2\pi r dr - \int_0^{\theta} p_t 2\pi r \operatorname{tg} \theta dr,$$

where

$$\bar{N}_t r_0 \sin \theta_0 = \int_0^{\theta} (p - p_t \operatorname{tg} \theta) r dr. \quad (2.31)$$

If the external load is zero, then  $\bar{N}_\theta r_0 \sin \theta_0 = \int_0^\theta p r dr$  or after integration  $N_\theta \sin \theta_0 = p \pi r^2$ . Equations (2.30) and (2.31) enable us to obtain the unknown stresses  $\sigma_\theta$  and  $\sigma_\phi$  in an axisymmetric shell.

The supporting power of a single-layer spherical shell

Spherical shells are found in auxiliary devices for the reactor unit. Stress in a single-layer spherical shell, filled with gas or liquid at pressure  $p$ , is determined from expression (2.30). For the sphere  $R_1 = R_2 = R$ ,  $\sigma_\theta = \sigma_\phi = \sigma$  and

$$\sigma = pR/2h. \quad (2.32)$$

The walls of the sphere are in a plane-stressed state but this does not affect its supporting capacity since

$$\sigma_t = \sqrt{\sigma_\theta^2 - \sigma_\theta \sigma_\phi + \sigma_\phi^2} = \sigma$$

and the coefficient of safety is

$$n = \frac{\sigma_{n,\tau}^t}{\sigma_{l \max}} = \frac{\sigma_{n,\tau}^t}{\sigma}.$$

A spherical shell is the most reasonable design for volumes found under high pressure. In the systems encountered we should assume  $n = 1.1-1.2$ . Figure 2.24 shows the formation of a welded seam in a spherical shell.

The supporting capacity of a single-layer cylindrical shell

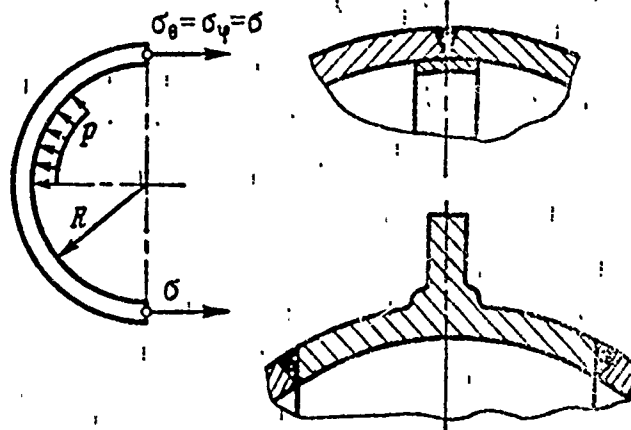
Cylindrical single-layer shells are frequently encountered in various design elements (Fig. 2.25). Based on the known quantities  $R$ ,  $h$  and  $p$ , let us find  $\sigma_\theta$ ,  $\sigma_\phi$  and  $n$ .

The first equilibrium equation for an element cut out of a cylindrical wall is obtained from expression (2.30) by substituting  $R_1 = \infty$  and  $R_2 = R$ :

$$\sigma_{\varphi} = pR/h. \quad (2.33)$$

The stress  $\sigma_{\theta} = \sigma_x$  we find by dividing the forces acting on the bottom by the cross section of the shell. As we know, if uniformly distributed pressure acts on any surface, then, regardless of the shape of the surface (see 1, 2, 3 on Fig. 2.25b), the projection of the equally acting forces of pressure onto a given axis is equal to the product of the pressure  $p$  times the area of the surface projection onto a plane perpendicular to the axis.

Fig. 2.24. Formation of a welded seam in a spherical shell.



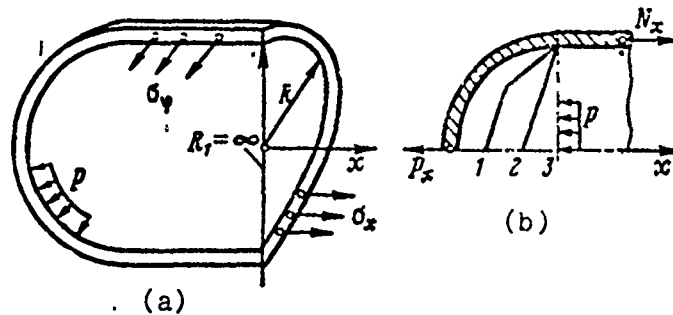
Consequently, regardless of the shape of the bottom, the force pulling the shell in the direction of the  $x$ -axis,

$$N_x = \pi R^2 p,$$

and the stress

$$\sigma_r = \frac{p \pi R^2}{2 \pi R h} = \frac{p R}{2 h}. \quad (2.34)$$

Fig. 2.25. A cylindrical single-layer shell.



Thus, the peripheral stress  $\sigma_\phi$  in the walls of a cylindrical shell is twice as great as the axial stress  $\sigma_x$ . Also important is the fact that this peripheral stress is almost equal to the equivalent stress which determines the strength and the supporting capacity of the shell. Actually, equivalent stress

$$\sigma_l = \sqrt{\sigma_x^2 - \sigma_x \sigma_\phi + \sigma_\phi^2} \approx 0.87 \sigma_\phi \approx \sigma_\phi,$$

since  $\sigma_x = 0.5 \sigma_\phi$ .

The formula (2.33) is widely used in rough calculations of more complex design.

The safety coefficient of the shell is found by the usual method:

$$n = \frac{\sigma_{n,\tau}^l}{\sigma_\phi}; \quad (2.35)$$

depending upon the purpose of the element  $n = 1.2-1.5$ .

#### End plate of a cylindrical shell

Frequently single-layer cylindrical shells have a closed shape. One of the possible forms of the end part is a sphere with a radius equal to the radius of the cylinder, i.e.,  $r = R$  (Fig. 2.26).



The wall stress of this sphere is determined from formula (2.32):

$$\sigma_x = \sigma_\varphi = \frac{pr}{2h}.$$

The wall stress of the cylinder  $\sigma_\varphi = pr/h = \sigma_{\varphi c}$ . The spherical end plate of a cylindrical shell with the radius of the sphere equal to the radius of the cylinder is not a reasonable design with respect to either weight or dimensions. As seen from Fig. 2.26a, if the thicknesses of the cylinder material and the end plate are identical, stresses  $\sigma_1$  in them will be different;  $\sigma_{1c\phi} = pr/2h = 0.5\sigma_{\varphi c}$ ;  $\sigma_{1\text{цил}} = 0.87 pr/h$  [цил = cylinder]; the structure will be too heavy. A decrease in the thickness of the end plate by a factor of two (Fig. 2.26b) does not lead to an equally strong construction. There is a new disadvantage - the weld seam is located at the point where the cylinder changes into a sphere. A change in the thickness of the material in the design is also technologically undesirable. The dimensions are as large as before.

The two designs of end plates, presented in Figs. 2.27a and b, are also not reasonable since in them bending moments load the transitional parts of the shells.

If we assume that the radius of a spherical end plate is  $r = 2R$ , the additional maximum pulling stress from bending  $\sigma_x = \sigma_{x \max}$  at point A, which is found on the internal surface of the element (Fig. 2.27), exceeds  $\sigma_{\varphi c}$  in the two indicated cases (a and b) by a factor of 30 and by a factor of 6, respectively, i.e.,  $\sigma_{x \max} = 30\sigma_{\varphi c}$  and  $\sigma_{x \max} = 6\sigma_{\varphi c}$ .

Considerably more reasonable is an end plate of elliptical shape.

#### Stress analysis of an elliptical end plate

The elliptical shape is taken for an end plate of reactor housings and of various volumes. We know that for an ellipse with semiaxes  $a$  and  $b$  the principal radii of curvature (Fig. 2.28a) will be expressed by formulas:

$$R_1 = \frac{a^2 b^2}{(a^2 \sin^2 \alpha + b^2 \cos^2 \alpha)^{3/2}};$$

$$R_2 = \frac{a^2}{(a^2 \sin^2 \alpha + b^2 \cos^2 \alpha)^{1/2}}. \quad (2.36)$$

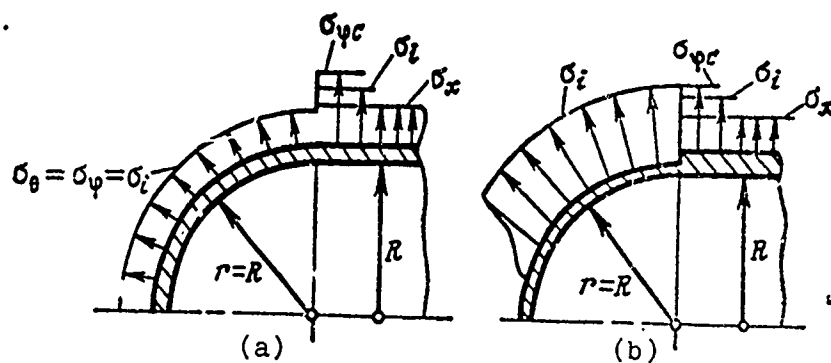


Fig. 2.26.

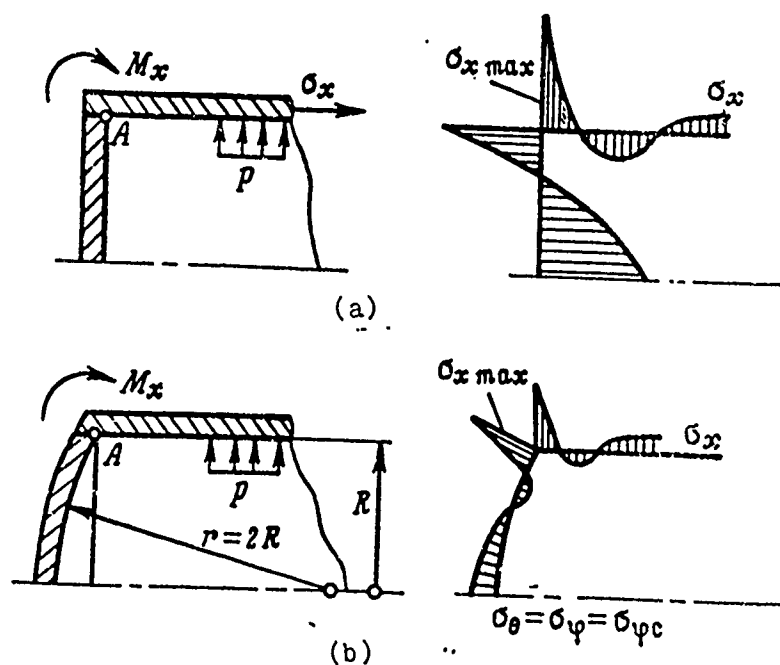


Fig. 2.27.

These formulas enable us to plot the elliptical surface. Given the angle  $\alpha$  of the vector's radius (this angle agrees with angle  $\theta$ ), we find the radii of curvature  $R_1$  and  $R_2$ , after which we plot the ellipse. For example,

$$\alpha = 0, R_1 = R_2 = a^2/b; \alpha = \pi/2, R_1 = b^2/a; R_2 = a.$$

We find stresses  $\sigma_\theta$  acting on the element in a meridional direction. Let us project the forces acting on the shell element onto the x-axis. We obtain (Fig. 2.28a)  $\bar{N}_\theta \sin \alpha 2\pi r = p\pi r^2$ , where  $r = R_2 \sin \alpha$ , or

$$\sigma_\theta = \frac{\bar{N}_\theta}{h} = \frac{pr}{2 \sin \alpha h} = \frac{pR_2}{2h}. \quad (2.37)$$

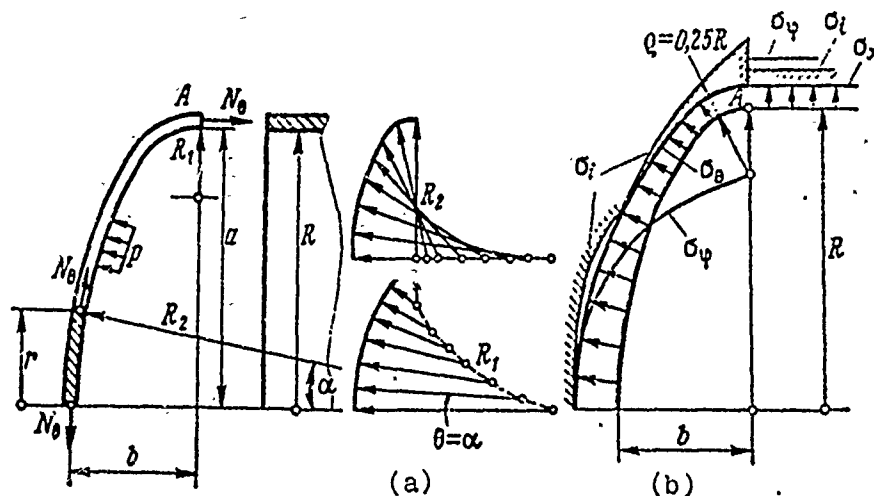


Fig. 2.28. Determining stresses in an elliptical end plate.

Substituting (2.37) into the basic equation (2.30), we find the stress  $\sigma_\phi$  acting in a peripheral direction:

$$\frac{\sigma_{\theta}}{R_1} + \frac{\sigma_{\varphi}}{R_2} = \frac{p}{h};$$

$$\sigma_{\varphi} = R_2 \left( \frac{p}{h} - \frac{\sigma_{\theta}}{R_1} \right) = R_2 \frac{p}{h} \left( 1 - \frac{R_2}{2R_1} \right). \quad (2.38)$$

Formulas (2.37) and (2.38) enable us to compute the stress in an elliptical end plate or an elliptical vessel.

**Example 2.3.** Find the stress in an elliptical end plate at points O and A if its dimensions  $a = R$ ;  $b = 0.5R$  of a cylindrical shell. The stresses in the end plate depend upon the radii of curvature  $R_1$  and  $R_2$ , which, in turn, depend upon the dimensions  $a$  and  $b$  of the ellipse.

The stress at point O (lying on the axis of symmetry):

$$u = 0; \quad R_1 = R_2 = \frac{a^2}{b} = \frac{R^2}{0.5R} = 2R;$$

$$\sigma_{\theta} = \sigma_{\varphi} = \frac{pR_2}{2h} = \frac{pR}{h}.$$

Thus, the stress at point O of the elliptical end plate is equal to the peripheral stress of a cylindrical shell.

The stress on the equator at point A:

$$a = \frac{\pi}{2}; \quad R_1 = \frac{b^2}{a} = \frac{(0.5R)^2}{R} = 0.25R; \quad R_2 = a = R;$$

$$\sigma_{\theta} = \frac{pR_2}{2h} = \frac{pR}{2h}; \quad \sigma_{\varphi} = \frac{p}{h} R_2 \left( 1 - \frac{R_2}{2R_1} \right) = -\frac{pR}{h}.$$

The meridional stresses at point A are equal to the axial stresses in a cylindrical shell. Peripheral stress, however, on the equator achieves negative values. A stress diagram is shown in Fig. 2.28b. Here, however, the diagram is drawn for generalized

stresses. Maximum generalized stresses in the equatorial cross section are

$$\sigma_1 = \sqrt{\sigma_\theta^2 - \sigma_\theta \sigma_\varphi + \sigma_\varphi^2}$$

Substituting  $\sigma_\theta = -0.5\sigma_{\varphi c}$ , we obtain at point A stress  $\sigma_1 = 1.32\sigma_{\varphi c}$ . The stress  $\sigma_1$  is equal to  $\sigma_\theta$  where  $\sigma_\varphi$  on the end plate is equal to zero.

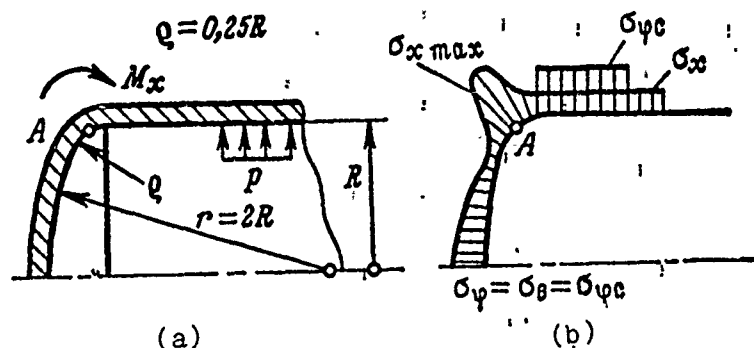


Fig. 2.29. Bending stress at coupling points.

Thus, in the central part of the end plate the generalized stresses are almost equivalent to stresses in a cylindrical shell. Consequently, an elliptical end plate can be made of almost equal strength with a cylindrical shell by varying the dimensions  $a$  and  $b$  of the ellipse.

The disadvantage of an elliptical end plate is the variable value of the radius of curvature with respect to angle  $\alpha$ . Sometimes the end plate is formed similarly to an elliptical one but with the radii of two circumferences (Fig. 2.29).

The maximum stress at point A as a result of the appearance of bending moment  $M_x$  will be [43]  $\sigma_{x \max} = (r/6.6\rho)\sigma_{\varphi c}$ , and if  $\rho = 0.25R$ , as is frequently the case, then  $\sigma_{x \max} \approx 1.25\sigma_{\varphi c}$ , i.e., very nearly the maximum stress of a cylindrical shell.

In critical structures the small overstressing at point A can be compensated by structural methods. An effort is made not to locate the welding seams of the end plate at a bending point of the shells (Fig. 2.30a); sometimes the reinforcing ring is introduced at a sharp angle (Fig. 2.30b).

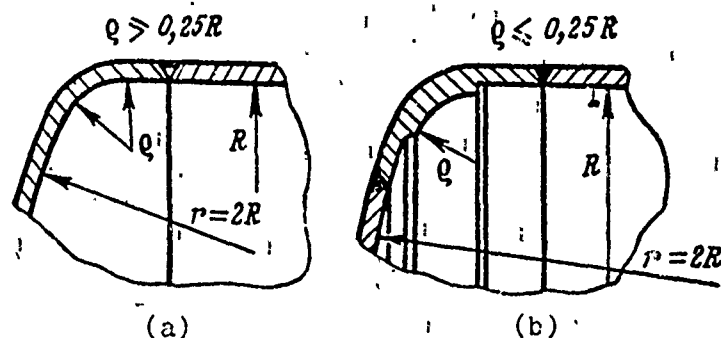


Fig. 2.30. Structural diagram of couplings.

Such structural methods provide a uniformly strong structure for the end plate and eliminate the need for additional stress analyses. If, however, additional stresses cannot be avoided, the safety coefficient must be evaluated according to the usual formula

$$n = \frac{\sigma_n^t}{\sigma_{l \max}}$$

where  $n = 1.2-1.5$  depending upon the specific conditions.

#### Supporting capacity of a two-layer cylindrical shell

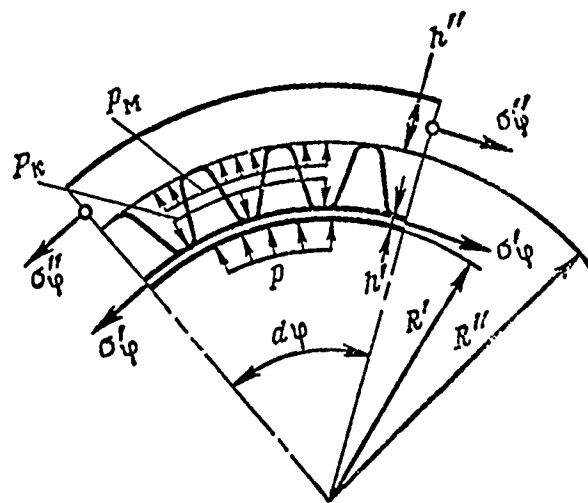
We analyze the two-layer shell whose element is shown in Fig. 2.31 for supporting ability based on zero-moment theory. We shall examine the joint deformation of nonidentically heated shells, connected by rigid longitudinal bonds. The type of bond has no effect on the total supporting capacity. Usually the rigidity of bonds is comparatively high although structurally they can be made quite differently.

Shells in the reactors which we shall examine below experience force and temperature effects. The temperature of the heat-transfer agent in the reactor can be quite high. The wall temperature of the shell, which touches the hot working medium, will be substantially lower due to cooling; however, it remains nevertheless so high that this has a noticeable effect on the mechanical and strength properties of the shell material. The most severely heated is the wall touching the hot working medium. It can have a temperature of 800-1000°C and, in some cases, even higher.

The wall temperature depends greatly on its thickness. The thicker the wall the higher its heat resistance and the higher, consequently, its temperature and the lower the strength indices of the material.

At high temperatures, which working media have, it is impossible to increase the strength of the hot shell by increasing its thickness. This would lead to overheating, local fusion, and washing out of metal.

Fig. 2.31. Diagram of an element of a two-layer cylindrical shell.



Thus, the shell touching the hot working medium must be rather thin in order to provide the necessary heat transfer and to maintain a low temperature. On the other hand, it must be sufficiently strong in order to maintain a pressure drop between the interhousing and the working spaces.

The second shell is the main load-bearing element which receives both the full pressure drop of the working medium and the ambient medium and the load of the unit as a whole. The temperature of this shell is considerably less than the first and does not exceed the temperature of the cooling liquid. Its thickness is determined not by the conditions of heat transfer but is dictated wholly by strength considerations.

Figure 2.32 shows the probable pressures and temperatures of two-layer shells of reactors in a working mode. This is the main design mode for which careful check of shell strength is required [26], [30].

As seen from Fig. 2.32, the first shell experiences a small pressure drop but is severely heated. The second shell, on the other hand, is moderately heated but is loaded with a large pressure drop. The pressure drop is not great if in the interhousing space a liquid metal is flowing. The pressure drop is great if the cooling working medium is fluid and particularly gas.

The second design mode is the mode of hydrocompression. Into the interhousing space of the shells a cold engineering fluid is fed under full pressure for a short test. This technological loading of a shell is a very grave task since the thin-walled first shell, which does not experience such drops in the working mode, is under the full pressure drop in this test. Neither the shells themselves, nor the connection between them, nor the solder should be damaged as a result of the hydrocompression.

The low temperatures and short duration of this mode should be kept in mind. Such a test is not only a strict technological check of design quality; such modes can occur when an ERE is started.

Analysis of a two-layer cylindrical shell without allowance for axial load

In this analysis only peripheral stresses in the shell are examined, assuming that there are no other stresses, for example,



axial stresses. Simplicity fully justifies the errors which will be present in the calculations.

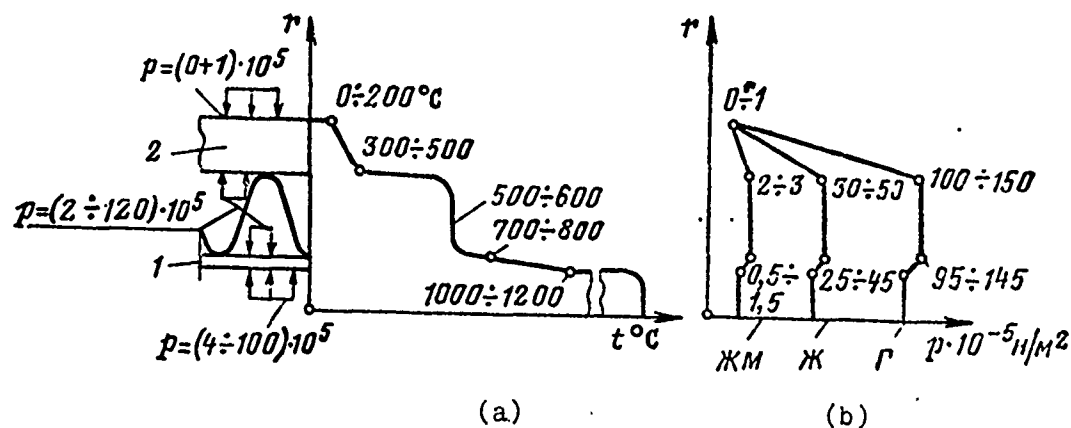


Fig. 2.32. Example of temperature gradient and pressure gradient in two-layer shells: ЖМ - liquid metal; Ж - liquid; Г - gases; 1 - hot shell; 2 - cold shell.

One of the peculiarities of this analysis is also the fact that ordinarily analysis is made on the ductility reserve since two-layer shells, in most cases, are used as pipes for carrying the working fluid where the pass-through sections must preserve their basic parameters throughout the operation of the design.

We know:  $p_r$  is the pressure of the gas for the liquid in the working cavity of the unit in  $N/m^2$ ;  $p_m$  is the pressure in the inter-housing space in  $N/m^2$ ; the geometric dimensions of the shells and the unit are  $h$ ,  $R$ ; the coefficient of linear expansion for the shell material  $\alpha$  and their mean temperature  $t$ ; operating time  $\tau$ , shell strain diagram  $\sigma = E\epsilon$ . Find  $\sigma'_\phi$ ,  $\sigma''_\phi$ ,  $n_{0.2}$ .

All parameters relating to the inner shell we shall designate with one prime, and parameters relating to the outer shell with two primes. Let us assume that the radii of the shells are near each other, i.e.,  $R' \approx R'' \approx R$ . We shall also keep in mind that the connections of the shells are undeformable in a radial direction and pliable in a peripheral direction.

Let us examine the equilibrium of an element taken from a shell (see Fig. 2.31) with central angle  $d\varphi$ , for which within this element we separate the inner shell from the outer shell. Gas pressure  $p$ , pressure in the inner shell space  $p_m$ , and contact pressure  $p_H$ , which is an averaged pressure of the forces of the connection between the shells, act on the internal shell.

Pressures  $p_m$  and  $p_H$  act on the external shell; we disregard the pressure on the external surface (if it is substantial, it must be taken into account). If we applied the vectors of the peripheral stresses  $\sigma'_\varphi$  and  $\sigma''_\varphi$ , we write the condition for shell element equilibrium, indicated in Fig. 2.31, according to formula (2.33). We obtain

$$h'\sigma'_\varphi = (p - p_m - p_H)R; \quad h''\sigma''_\varphi = (p_m + p_H)R,$$

where  $p$  is the current value of the gas or liquid pressure.

Eliminating  $(p_m + p_H)$  from these equations we obtain

$$h'\sigma'_\varphi + h''\sigma''_\varphi = pR. \quad (2.39)$$

In this equation there are two unknowns  $\sigma'_\varphi$  and  $\sigma''_\varphi$ ; we supplement equation (2.39) with the strain compatibility equation.

A peculiarity of strains in an axisymmetric (in this case, cylindrical) element is the inter-relationship (usually called compatibility) of the strains in radial and peripheral directions. Let us examine the elongation of element  $ab$  (Fig. 2.33) up to the dimensions  $a_1b_1$ ; in view of the axial symmetry, points  $a$  and  $a_1$ ,  $b$  and  $b_1$  remain on the radii of this element.

The full relative strain of the element in a peripheral direction  $\epsilon_{\varphi n}$  is easily determined:

$$\varepsilon_{\varphi''} = \frac{\widetilde{a_1 b_1 - ab}}{ab} = \frac{(R + \Delta R) d\varphi - R d\varphi}{R d\varphi} = \frac{\Delta R}{R}. \quad (2.40)$$

This full relative peripheral strain of each shell will be made up of elastic and thermal strains and if we allow for the fact that we have assumed  $R' = R'' = R$ , the second missing equation will have the following form:

$$\varepsilon_{\varphi n} = \varepsilon_{\varphi}' + \alpha' t'_{cp} = \varepsilon_{\varphi}'' + \alpha'' t''_{cp} = \frac{\Delta R}{R}. \quad (2.41)$$

Here  $\varepsilon_{\varphi}'$  and  $\varepsilon_{\varphi}''$  are only the elastic strains of the shells in the peripheral direction and  $\alpha' t'_{cp}$  and  $\alpha'' t''_{cp}$  [ $cp$  = average] are their thermal strains.

Let us show the order of the numerical stress analysis based on formulas (2.39) and (2.41).

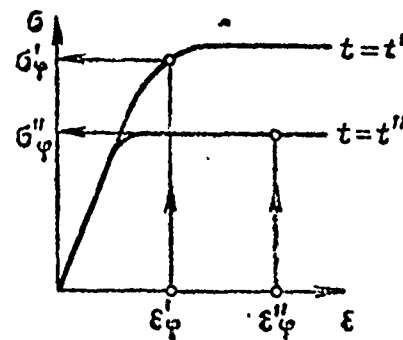
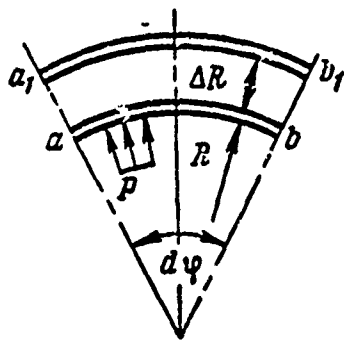


Fig. 2.33. Derivation of strain Fig. 2.34. Determining  $\sigma_{\varphi}$ . equations.

We shall assign the quantity  $\varepsilon_{\varphi n} = \varepsilon_{\varphi}' = \varepsilon_{\varphi}'' = \Delta R/R$ . Based on this quantity and the known  $\alpha' t'_{cp}$  and  $\alpha'' t''_{cp}$ , we find

$$\varepsilon_{\varphi}' = \varepsilon_{\varphi n} - \alpha' t'_{cp}; \quad \varepsilon_{\varphi}'' = \varepsilon_{\varphi n} - \alpha'' t''_{cp}.$$

Then, according to the diagram  $\sigma = f(\varepsilon)$  we determine  $\sigma_{\varphi}'$  and  $\sigma_{\varphi}''$  (Fig. 2.34). Here, based on the known  $\sigma_{\varphi}'$  and  $\sigma_{\varphi}''$ , we find

$$p = \frac{1}{R} (h' \sigma_{\varphi}' + h'' \sigma_{\varphi}'')$$

and plot the function  $p = f(\Delta R)$  (Fig. 2.35). On the curve we locate the point of the given  $p_r$  (point 3) and determine the reserve of the total supporting capacity of the shell - the ratio of limiting pressure of the working gas or liquid  $p_{\text{пред}}$  to their working pressure  $p_r$ .

The quantity  $p_{\text{пред}}$  is determined according to the graph of function  $p = f(\Delta R)$  (Fig. 2.35). On this graph we note point 4, at which the straight line drawn from the origin of coordinates is tangent to the curve  $p = f(\Delta R)$ . This point determines the beginning of large strains which are dangerous with respect to a change in the geometric dimensions of the shells. The pressure corresponding to the point 4 we shall call limiting pressure  $p_{\text{пред}}$ . If on this diagram we plot the calculated working fluid pressure  $p_r$ , then the ratio of  $p_{\text{пред}}$  to  $p_r$  will be the safety coefficient (loading capacity)  $n_{0.2}$  of the shell:

$$n_{0.2} = p_{\text{пред}} / p_r. \quad (2.42)$$

The quantity  $n_{0.2}$  must be within 1.3-1.8.

On this same diagram we plot the stress curves  $\sigma_{\varphi}'$  and  $\sigma_{\varphi}''$  and note the characteristic points.

Point 1 corresponds to the position where the outer shell is stretched due to the heating of the inner shell. The external pressure  $p$  on the shell is zero.

Point 2 illustrates the extension of the outer shell by pressure  $p$  and by the inner shell due to its thermal elongation. The compressive stresses of the inner shell during its thermal expansion are completely compensated by its extension as a result of the application of pressure  $p$ .

Point 3 corresponds to the stressed state of shells in working mode. They are loaded by pressure  $p_r$  so that both shells are stretched and both participate in the operation.

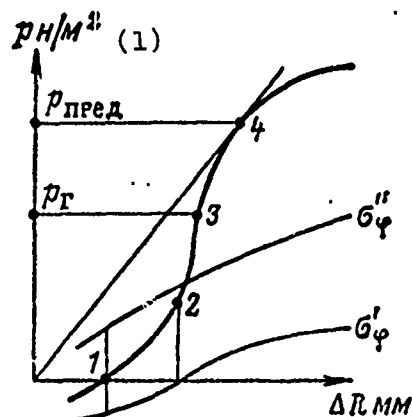


Fig. 2.35. Stresses and safety coefficient in two-layer shells.  
KEY: (1)  $p \text{ N/m}^2$ .

Point 4 is the point of maximum pressure after which deformation of shells cannot be permitted. This is the plasticity limit of shells. Further loading can lead to inadmissible changes in the cooling channel.

The breaking pressure corresponding to design strength is easy to find on the diagram. This is the maximum pressure  $p$ .

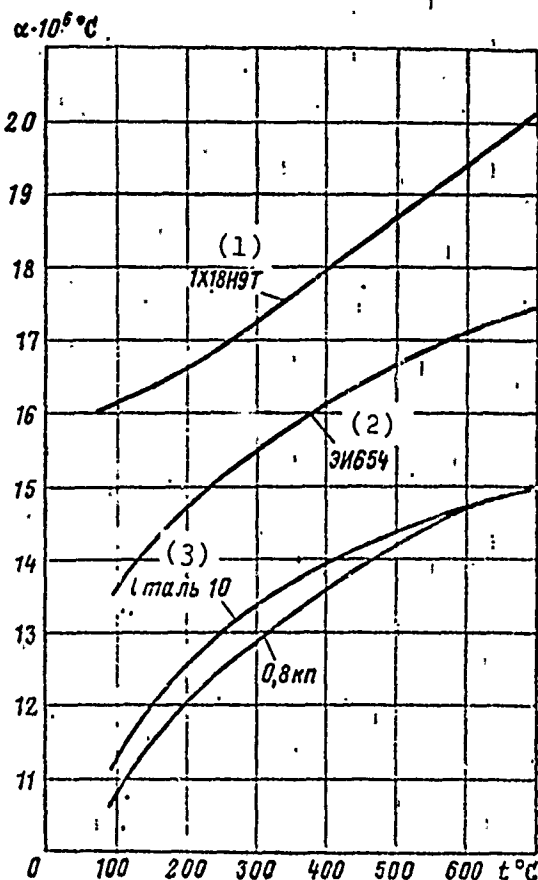


Fig. 2.36. Variation in the coefficient of linear expansion for steels versus heating temperature.  
KEY: (1) 1Kh18N9T; (2) EI654; (3) Steel.

Example 2.4. Let a two-layer shell be given with dimensions:  
 $R = 9.2 \text{ cm} = 9.2 \cdot 10^{-2} \text{ m}$ ,  $h' = h'' = 1.5 \text{ mm} = 1.5 \cdot 10^{-3} \text{ m}$ .

The mean temperatures of the inner and outer walls are  
 $t_{cp}' = 575^\circ\text{C}$ ;  $t_{cp}'' = 100^\circ\text{C}$ ; shell material is Kh18N9T steel. Thermal elongations are determined from the graphs presented in Fig. 2.36, from which it is apparent that  $\alpha' t_{cp}' = 0.0104$ ;  $\alpha'' t_{cp}'' = 0.0016$ .

The stretch diagrams for Kh18N9T steel at temperatures of 575 and  $100^\circ\text{C}$  are presented in Fig. 2.37. We assume that at negative values of  $\epsilon_\varphi$  the diagram  $\sigma_\varphi, \epsilon_\varphi$  has the same shape as at positive values but the sign of  $\sigma_\varphi$  reverses. The working pressure  $p_r = 40 \cdot 10^5 \text{ N/m}^2$ . We assigned the value  $\Delta R = 0.25 \cdot 10^{-3} \text{ m}$ .

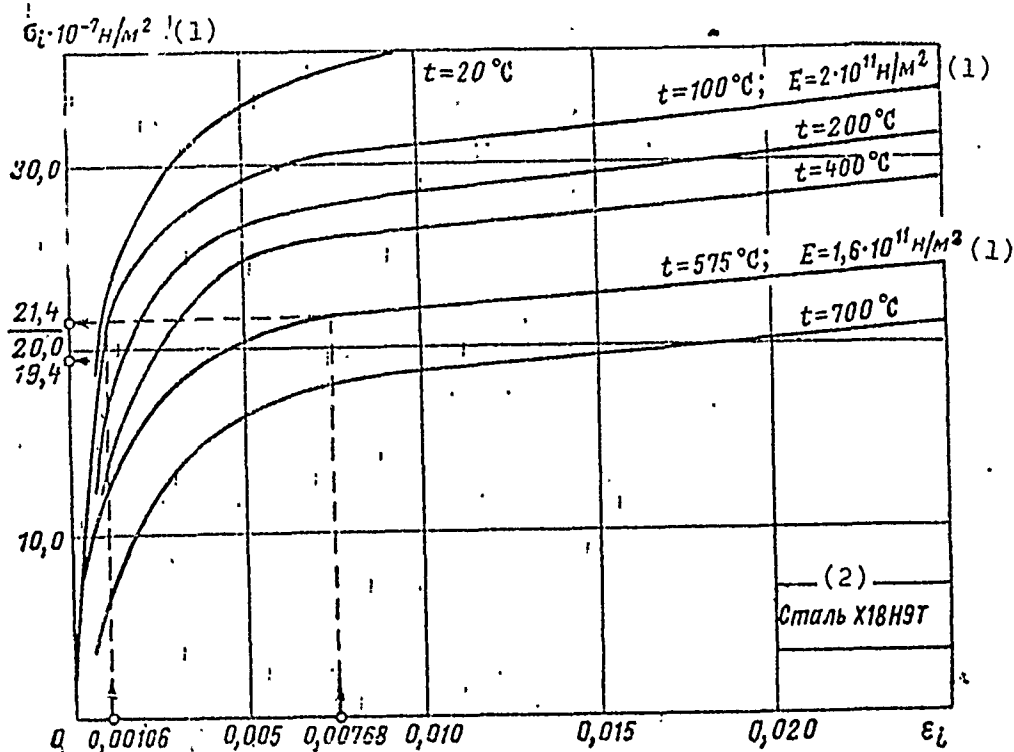


Fig. 2.37. Strain diagram for stainless steel.  
 KEY: (1)  $\text{N/m}^2$ ; (2) Kh18N9T steel.

Now we seek the pressure of the gases which cause this radial strain. For this we find from formula (2.41)  $\epsilon_{\varphi n} = \Delta R/R = 0.25/92 = 2.72 \cdot 10^{-3}$ . Next we find  $\epsilon'_{\varphi}$  and  $\epsilon''_{\varphi}$ :

$$\epsilon'_{\varphi} = \epsilon_{\varphi n} - \alpha' t' = 2.72 \cdot 10^{-3} - 10.4 \cdot 10^{-3} = -7.68 \cdot 10^{-3};$$

$$\epsilon''_{\varphi} = \epsilon_{\varphi n} - \alpha'' t'' = 2.72 \cdot 10^{-3} - 1.56 \cdot 10^{-3} = 1.06 \cdot 10^{-3}.$$

According to the known values of relative strains  $\epsilon'_{\varphi}$  and  $\epsilon''_{\varphi}$  from the graph  $\sigma = f(\epsilon_{\varphi})$  presented in Fig. 2.37, we find the value of the stresses

$$\sigma'_{\varphi} = -21.4 \cdot 10^7 \text{ N/m}^2 \text{ and } \sigma''_{\varphi} = 9.4 \cdot 10^7 \text{ N/m}^2.$$

As mentioned above, we assume that with negative values of  $\epsilon_{\varphi}$  the diagram  $\sigma = f(\epsilon)$  has the same form as at positive values, only the sign of  $\sigma_{\varphi}$  changes.

At low values of  $\epsilon_{\varphi}$  the stress  $\sigma_{\varphi}$  can be directly calculated from formula  $\sigma_{\varphi} = E \epsilon_{\varphi}$ , where the Young's modulus for each temperature is taken from the graph presented in Fig. 2.38.

$$\text{In our case, } E' = 1.6 \cdot 10^{11} \text{ N/m}^2; E'' = 2 \cdot 10^{11} \text{ N/m}^2.$$

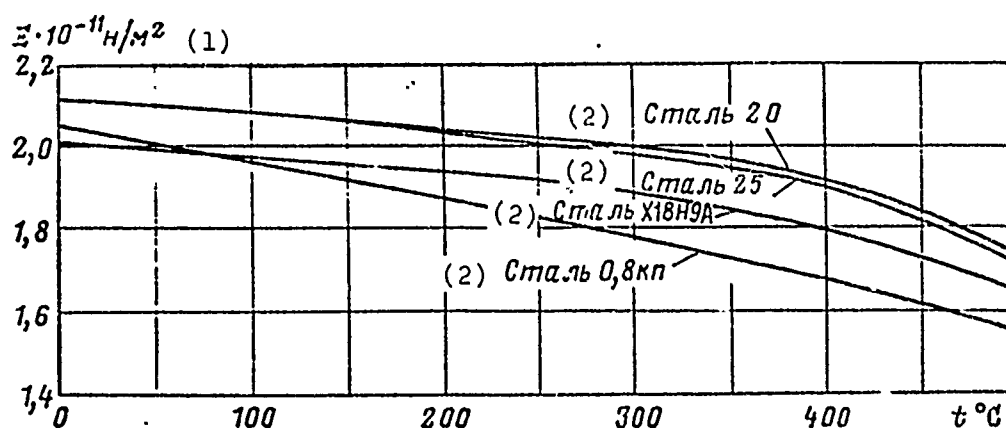


Fig. 2.38. Variation in the Young's modulus of various materials.  
KEY: (1)  $\text{N/m}^2$ ; (2) Steel.

Finally, from formula (2.39) we determine

$$p = \frac{1}{R} (h' \sigma_{\varphi}' + h'' \sigma_{\varphi}'').$$

The obtained value  $p = 3.3 \cdot 10^5 \text{ N/m}^2$  indicates that the selection of  $\Delta R$  has been unsuccessful since the pressure inside the shells  $p_r = 40 \cdot 10^5 \text{ N/m}^2$ . Let us continue calculations until we obtain the full curve  $p = f(\Delta R)$ , after assigning other values for  $\Delta R$  (see Table 2.1).

Table 2.1.

(1) № строки	(2) Функция	(3) Множитель	$\Delta R \cdot 10^3 = 0,25$	$\Delta R \cdot 10^3 = 0,5$	$\Delta R \cdot 10^3 = 0,75$	$\Delta R \cdot 10^3 = 0,875$	$\Delta R \cdot 10^3 = 1,0$	$\Delta R \cdot 10^3 = 1,25$	$\Delta R \cdot 10^3 = 1,5$
1	$\varepsilon_{\varphi} = \Delta' R$	$10^{-3}$	2,72	5,44	8,16	9,52	10,90	13,61	16,32
2	$\varepsilon_{\varphi}' = \varepsilon_{\varphi} - \alpha' t'$	$10^{-3}$	-7,68	-4,96	-2,24	-0,88	0,50	3,21	5,92
3	$\varepsilon_{\varphi}'' = \varepsilon_{\varphi} - \alpha'' t''$	$10^{-3}$	1,06	3,78	6,50	7,86	9,24	11,95	14,66
4	$\sigma_{\varphi}'$	107	-21,4	-20,4	-16,8	-10,8	8	18,8	20,8
5	$\sigma_{\varphi}''$	107	19,4	27,8	29,4	30	30,4	31,2	31,8
6	$h' \sigma_{\varphi}'$	104	-32,1	-30,6	-25,2	-16,2	12	28,2	31,2
7	$h'' \sigma_{\varphi}''$	104	29,1	41,7	44,1	45	45,6	46,8	47,7
8	(6)+(7)	104	-3	11,1	18,9	28,8	57,6	75	78,9
9	$p = (8)' R$	105	-3,3	12,1	20,6	31,3	62,5	81,5	85,5

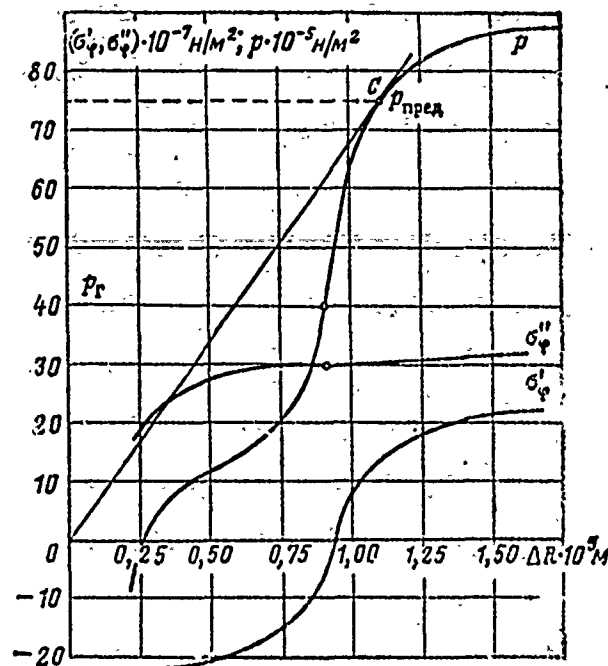
KEY: (1) Line number; (2) Function; (3) Factor.

The results of calculation are presented in the form of a curve (Fig. 2.39). On the figure we see the variations of  $\sigma_{\varphi}'$  and  $\sigma_{\varphi}''$  as the function of  $\Delta R$ . Note on these curves the points corresponding to the pressure  $p_r = 40 \cdot 10^5 \text{ N/m}^2$ .



As is apparent from Fig. 2.39, the increase in shell radius at working pressure is  $0.9 \cdot 10^{-3}$  m. The stress in the outer shell is  $\sigma''_{\phi} = 30 \cdot 10^7$  N/m<sup>2</sup> and in the inner shell is  $\sigma'_{\phi} = -6 \cdot 10^7$  N/m<sup>2</sup>; the latter stress is compressive which is explained by the great thermal elongation of the inner shell. If the working pressure were higher the stress in the inner shell would be tensile stress.

Fig. 2.39. The stressed state of shells as a function of radial strain.



The curves presented in Fig. 2.39 show that when  $p = 0$  there is a certain strained state caused by the thermal expansion of the inner shell.

It is important to note that on the pressure variation curve two sections of sharp increase are observed. The first section with low  $\Delta R$  and the second with  $\Delta R \approx 0.9 \cdot 10^{-3}$  m. This is explained as follows. If the pressure is low, the external shell operates elastically and with a rise in pressure, strains slowly increase. If the pressure is greater than a certain magnitude, in the outer shell plastic flow will occur; now it will be loaded not only by the forces of pressure but also by forces from the direction of the inner and more severely heated shell. A rapid increase in  $\Delta R$  occurs with an insignificant rise in pressure.

At high pressures shell resistance again grows (sharp rise in pressure curve). This occurs when elongation under the effect of pressure exceeds thermal elongation. Then the inner shell begins to extend and is put into operation.

Finally, as is apparent from the curve presented in Fig. 2.39, at pressures above  $p = 70 \cdot 10^5 \text{ N/m}^2$ , a sharp increase in plastic flow occurs in the shells.

Supporting capacity of the shell is  $n_{0.2} = 75 \cdot 10^5 / 40 \cdot 10^5 = 1.87$  where  $p_{\text{пред}} = 75 \cdot 10^5 \text{ N/m}^2$  and is determined by the above method.

Analysis of a two-layer shell with allowance for axial loading

Let us cut an element out of the shell and apply to it all the known loads (Fig. 2.40). As in the preceding case, we know the pressures  $p_r$ ,  $p_m$ , the geometric dimensions of the shells  $h$ ,  $R$ , the coefficients of linear expansion for the material  $\alpha$ , the mean heating temperature  $t$ , the shell operating time  $\tau$ , and the strain diagram of the material  $\sigma = E\varepsilon$ . We must find  $\sigma_x$ ,  $\sigma_\varphi$  and  $n_{0.2}$ .

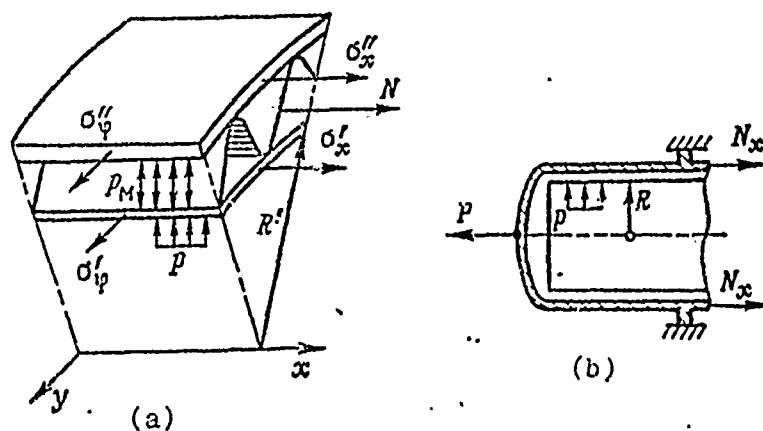


Fig. 2.40. An element of a two-layer axisymmetric shell.

We shall assume, as before, that the shell is in the zero-moment state. The main difficulty lies in the fact that the supporting

capacity of a shell in a two-axis stressed state is determined with the strain diagrams obtained for single-axis stressed state.

Axial loading, which is conditionally illustrated in Fig. 2.40b by vector  $N_x$ , can have various origins. Usually it is proportional to the pressure of the working fluid and can be determined from formula

$$N_x = kp, \quad (2.42)$$

where  $k$  is the coefficient of proportionality depending upon the construction of the unit and the method of bracing. For example, for the diagram shown in Fig. 2.40b,

$$N_x = \pi R^2 p = kp, \text{ отсюда } k = \pi R^2.$$

Let us examine the equilibrium of this element. Proceeding as before, we obtain the equilibrium condition in a peripheral direction and the strain compatibility condition:

$$h' \varepsilon_{\varphi}' + h'' \varepsilon_{\varphi}'' = pR;$$

$$\varepsilon_{\varphi n} = \varepsilon_{\varphi}' + a' t' = \varepsilon_{\varphi}'' + a'' t'' = \frac{\Delta R}{R},$$

similar to conditions (2.39) and (2.41):

Four equations are necessary to solve the problem since there are four unknowns. From the condition of strained compatibility in the direction of the  $x$ -axis we obtain

$$N_x = kp = 2\pi R (\varepsilon_x' h' + \varepsilon_x'' h''). \quad (2.43)$$

Let us transform equation (2.43) for simplicity's sake. From it we find what  $p$  equals, we substitute into the equation (2.39), and we finally obtain

$$(h'\sigma_\varphi + h''\sigma_\varphi^*) = \frac{2\pi R^2}{k} (\sigma_x' h' + \sigma_x'' h''). \quad (2.44)$$

Let us establish the difference

$$\Delta = (h'\sigma_\varphi + h''\sigma_\varphi^*) - \frac{2\pi R^2}{k} (\sigma_x' h' + \sigma_x'' h''). \quad (2.45)$$

The condition for the proper selection of  $\epsilon_x$  and  $\epsilon_\varphi$  will be  $\Delta = 0$ .

From the condition that the relative strains of the shells in the x-axis direction will be equal, we obtain the last necessary equation

$$\epsilon_{x\pi} = \epsilon_x' + a't' = \epsilon_x'' + a''t''. \quad (2.46)$$

The calculation procedure is similar to the procedure presented in example 2.4. Only we should allow for the fact that both shells are in a two-axis stressed state and operate in a stage of plastic flow. For this, in the strain diagram of the shell material we must replace the stresses and strains  $\sigma$  and  $\epsilon$  plotted along the axes with the quantity  $\sigma_1$  and  $\epsilon_1$ , determining the latter from formulas (1.30).

Let us consider the sequence of calculations.

We assign the quantity  $\epsilon_{\varphi\pi} = \Delta R/R$  and determine the elastic deformations  $\epsilon_\varphi'$  and  $\epsilon_\varphi''$ :

$$\epsilon_\varphi' = \epsilon_{\varphi\pi} - a't'; \quad \epsilon_\varphi'' = \epsilon_{\varphi\pi} - a''t''.$$

We also assign the values of  $\epsilon_{x\pi 1}$  and  $\epsilon_{x\pi 2}$ . For these two values we find elastic deformations  $\epsilon_x'$  and  $\epsilon_x''$ :

$$\varepsilon'_{x1} = \varepsilon_{x1} - a't', \quad \varepsilon'_{x2} = \varepsilon_{x2} - a't';$$

$$\varepsilon''_{x1} = \varepsilon_{x1} - a''t'', \quad \varepsilon''_{x2} = \varepsilon_{x2} - a''t''.$$

Then from the first formula of the system (1.30) we compute the generalized strains  $\varepsilon'_1$  and  $\varepsilon''_1$  for two values of  $\varepsilon'_x$  and  $\varepsilon''_x$ :

$$\varepsilon'_{11} = \frac{2}{\sqrt{3}} \sqrt{(\varepsilon'_{x1})^2 + \varepsilon'_{x1}\varepsilon'_\varphi + (\varepsilon'_\varphi)^2};$$

$$\varepsilon'_{12} = \frac{2}{\sqrt{3}} \sqrt{(\varepsilon'_{x2})^2 + \varepsilon'_{x2}\varepsilon'_\varphi + (\varepsilon'_\varphi)^2};$$

$$\varepsilon''_{11} = \frac{2}{\sqrt{3}} \sqrt{(\varepsilon''_{x1})^2 + \varepsilon''_{x1}\varepsilon''_\varphi + (\varepsilon''_\varphi)^2};$$

$$\varepsilon''_{12} = \frac{2}{\sqrt{3}} \sqrt{(\varepsilon''_{x2})^2 + \varepsilon''_{x2}\varepsilon''_\varphi + (\varepsilon''_\varphi)^2}.$$

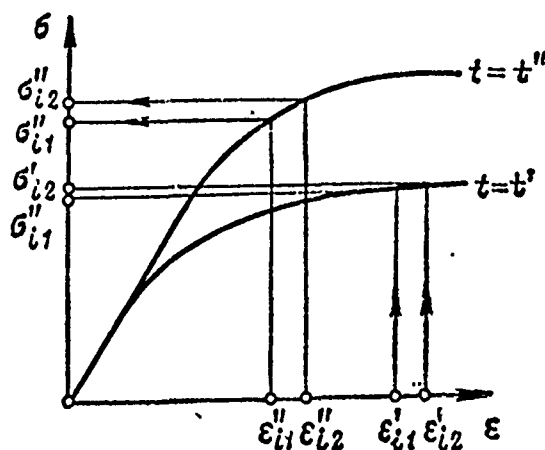


Fig. 2.41. Finding  $\sigma_{11}$  and  $\sigma_{12}$ .

Based on these values of generalized strains, from the strain diagram of the material  $\sigma = f(\varepsilon)$  we find  $\sigma'_{11}$ ,  $\sigma'_{12}$ ,  $\sigma''_{11}$ , and  $\sigma''_{12}$  (see Fig. 2.41) and then from expression (1.30) we determine:

$$\sigma'_{x1} = \frac{4}{3} \frac{\sigma'_{11}}{\varepsilon'_{11}} (\varepsilon'_{x1} + 0.5\varepsilon'_\varphi); \quad \sigma'_{x2} = \frac{4}{3} \frac{\sigma'_{12}}{\varepsilon'_{12}} (\varepsilon'_{x2} + 0.5\varepsilon'_\varphi).$$

$$\sigma_{x1} = \frac{4}{3} \frac{\sigma_{i1}}{\varepsilon_{i1}} (\varepsilon_{x1} + 0,5 \varepsilon_{\varphi}); \quad \sigma_{x2} = \frac{4}{3} \frac{\sigma_{i2}}{\varepsilon_{i2}} (\varepsilon_{x2} + 0,5 \varepsilon_{\varphi}).$$

$$\sigma_{\varphi 1} = \frac{4}{3} \frac{\sigma_{i1}}{\varepsilon_{i1}} (\varepsilon_{\varphi} + 0,5 \varepsilon_{x1}); \quad \sigma_{\varphi 2} = \frac{4}{3} \frac{\sigma_{i2}}{\varepsilon_{i2}} (\varepsilon_{\varphi} + 0,5 \varepsilon_{x2}).$$

$$\sigma_{\varphi 1} = \frac{4}{3} \frac{\sigma_{i1}}{\varepsilon_{i1}} (\varepsilon_{\varphi} + 0,5 \varepsilon_{x1}); \quad \sigma_{\varphi 2} = \frac{4}{3} \frac{\sigma_{i2}}{\varepsilon_{i2}} (\varepsilon_{\varphi} + 0,5 \varepsilon_{x2}).$$

Now we substitute the values of the stresses into equation (2.45) and find whether or not they satisfy this equation. Since the values of  $\varepsilon_{\varphi n}$  and  $\varepsilon_{x n}$  are chosen arbitrarily, equation (2.45) will not be satisfied. Let us plot a graph of dependence  $\Delta = f(\varepsilon_{x n})$  based on the two points, where

$$\Delta_1 = h' \sigma_{\varphi 1} + h'' \sigma_{x1} - \frac{2\gamma R^2}{k} (\sigma_{x1} h' + \sigma_{\varphi 1} h'');$$

$$\Delta_2 = h' \sigma_{\varphi 2} + h'' \sigma_{x2} - \frac{2\gamma R^2}{k} (\sigma_{x2} h' + \sigma_{\varphi 2} h'').$$

We shall try, graphically, to find the value of  $\varepsilon_{x n}$ , at which  $\Delta = 0$  (Fig. 2.42). Based on the given value of  $\varepsilon_{\varphi n}$  and on the obtained value of  $\varepsilon_{x n}$ , we shall find the unknown  $p$  from formula (2.39). We repeat the calculation for new values of  $\varepsilon_{\varphi n}$  and  $\varepsilon_{x n}$ .

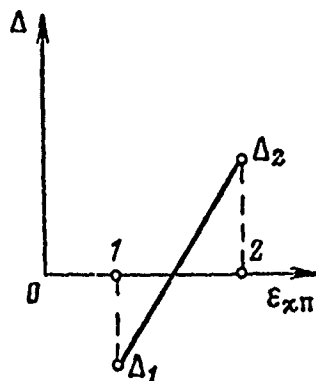


Fig. 2.42. Finding  $\varepsilon_{x n}$ .

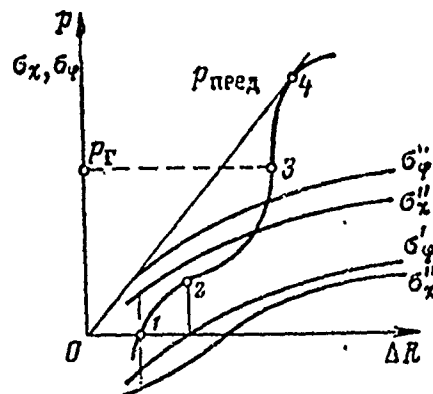


Fig. 2.43. Dependence of stresses in shells on radial strain.

We plot the unknown curve  $p = f(\Delta R)$  and, as before, seek the supporting capacity of the shell  $n = p_{\text{пред}}/p_r$ . Figure 2.43 shows the curve  $p = f(\Delta R)$  and the stress curves for both shells.

Point 1 corresponds to loading of the outer cold shell from the thermal expansion of the inner shell. Point 2 corresponds to loading of the outer shell as a result of pressure created by the forces of gases and the thermal expansions of the inner shell. This point is of interest because of the elastic equilibrium of the inner shell, obtained as a result of the pressure and its thermal expansion. Point 3 is the point of the given pressure of the working medium inside the shells. Point 4 is the point for the limiting value of pressure when the shell yields.

Usually the ductility reserve for reactor elements should be selected within the range  $n_{0.2} = 1.1-1.3$ .

Example 2.5. Let us calculate the shell examined in example 2.4, with allowance for axial loading from the shell bracing according to the diagram indicated in Fig. 2.40b. In this case, the axial force is  $N = p\pi R^2$ , and the coefficient of proportionality is  $k = \pi R^2$ .

Equation (2.44) assumes the following form:

$$h' \varepsilon_{\varphi}' + h'' \varepsilon_{\varphi}'' = 2 (h' \varepsilon_x' + h'' \sigma_x''). \quad (2.47)$$

The stretch diagram of the material for the inner and outer shells is presented in Fig. 2.37. We must only remember that now  $\varepsilon$  is replaced by the quantity  $\varepsilon_1$  and  $\sigma$  by the quantity  $\sigma_1$ .

We assign the values of  $\Delta R$  and select for each of them  $\varepsilon_{x\pi}$  such that equation (2.45) is satisfied. The results of the calculations are presented in Table 2.2.

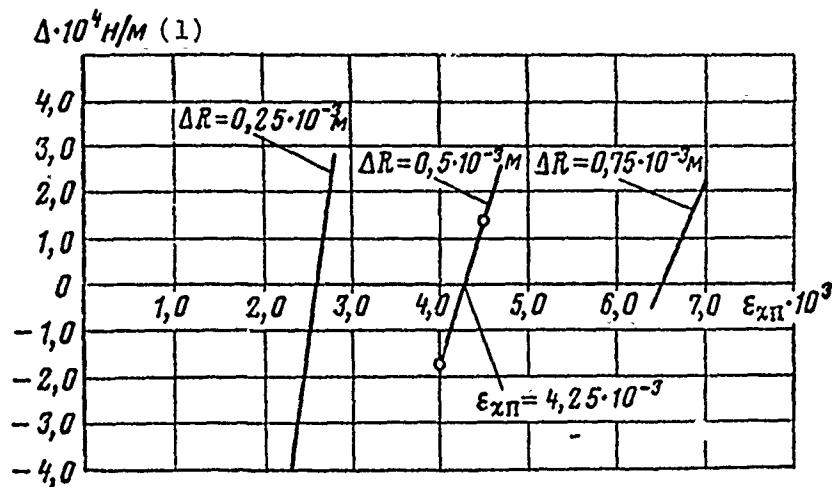


Fig. 2.44. A graphic solution of the relationship.  
KEY: (1) N/m.

With  $\epsilon_{x\Pi}$  selected and  $\Delta R$  given, for example,  $\Delta R = 0.5 \cdot 10^{-3} m$ , we shall use the graph of  $\Delta = f(\epsilon_{x\Pi})$ . After assigning the values  $\epsilon_{x\Pi} = 4.0 \cdot 10^{-3}$  and  $4.5 \cdot 10^{-3}$ , we find, graphically, the value  $\Delta = 0$  and, corresponding to it,  $\epsilon_{x\Pi} = 4.25 \cdot 10^{-3}$ , as shown in Fig. 2.44.

Now, according to the obtained value  $\epsilon_{x\Pi} = 4.25 \cdot 10^{-3}$ , completely repeating the calculation, we find  $p$ . In some cases, we can omit the second calculation. For this, when we have verified that  $\Delta$  changes sign in line 37 of Table 2.2, we can immediately find  $p$  graphically (Fig. 2.45).

If we plot  $p = f(\Delta R)$ , we find the unknown value of  $p_{пред}$  and the supporting capacity from Fig. 2.46:

$$n = \frac{p_{пред}}{p_2} = \frac{88.5 \cdot 10^5}{40 \cdot 10^5} = 2.2.$$

Here the values of the stresses  $\sigma_x$  and  $\sigma_\varphi$  are plotted as a function of  $\Delta R$ .



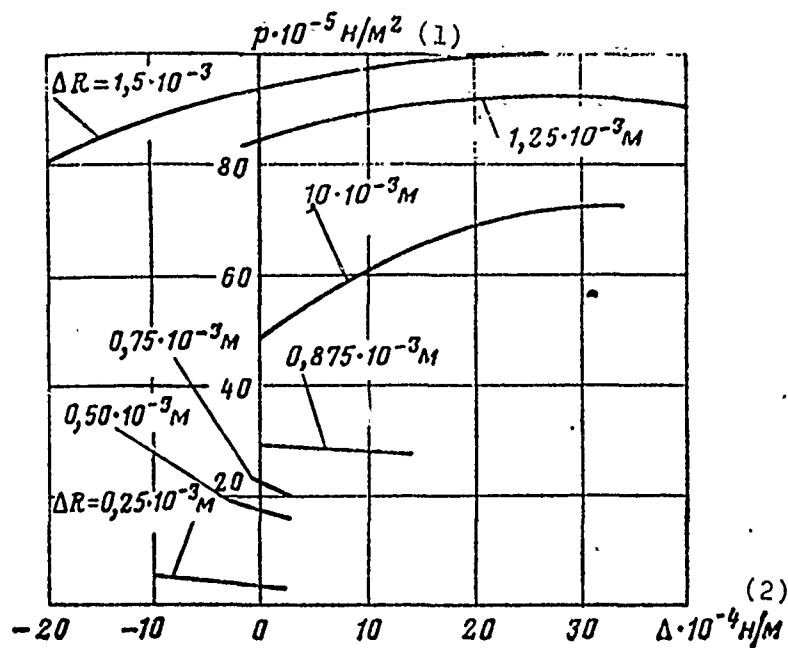


Fig. 2.45. A graphic method of finding  $p$ .  
KEY: (1)  $N/m^2$ ; (2)  $N/m$ .

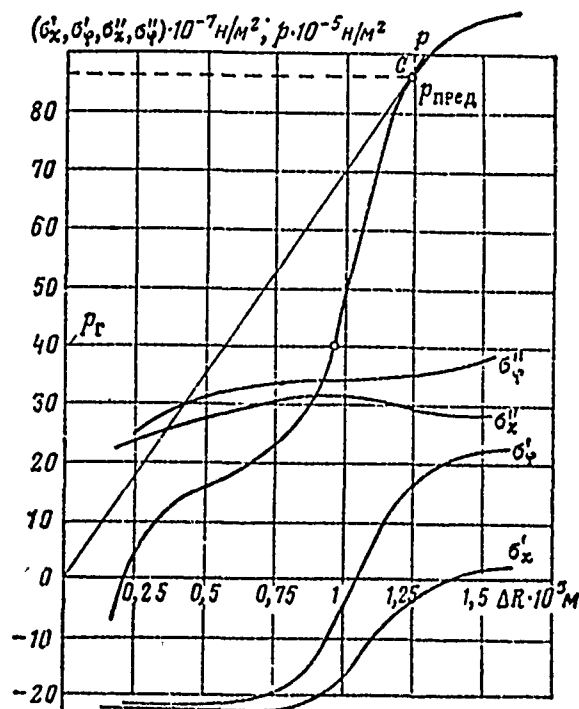


Fig. 2.46. The state of stress in shells as a function of pressure.

Table 2.2.

(1) № строки	(2) Функция	(3) Множитель	(4) Значения функций при			
			$\Delta R=0,5 \cdot 10^{-3} \mu;$ $\varepsilon_{\varphi n}=5,44 \cdot 10^{-3}$		$\Delta R=0,75 \cdot 10^{-3} \mu;$ $\varepsilon_{\varphi n}=8,16 \cdot 10^{-3}$	
1	$\varepsilon_{x n}$	$10^{-3}$	4,0	4,5	6,4	6,6
2	$\varepsilon'_x = \varepsilon_{x n} - \alpha' t'$	$10^{-3}$	-6,4	-5,9	-4	3,8
3	$\varepsilon'_x = \varepsilon_{x n} - \alpha' t'$	$10^{-3}$	-4,96	-4,96	-2,24	-2,24
4	$\varepsilon_x = \varepsilon_{x n} - \alpha'' t''$	$10^{-3}$	2,34	2,84	4,74	-4,94
5	$\varepsilon_x = \varepsilon_{x n} - \alpha'' t''$	$10^{-3}$	3,78	3,78	6,5	6,5
6	(2)	$10^{-6}$	40,96	34,81	16	14,44
7	(3) <sup>2</sup>	$10^{-6}$	24,6	24,6	5,02	5,02
8	(2)(3)	$10^{-6}$	31,74	29,26	8,96	8,51
9	(3)+(7)+(8)	$10^{-6}$	97,3	88,67	29,98	27,97
10	$(2 \sqrt{3}) \sqrt{(9)} = \varepsilon'_i$	$10^{-3}$	11,39	10,88	6,32	6,11
11	(4) <sup>2</sup>	$10^{-6}$	5,47	8,07	22,47	24,4
12	(5) <sup>2</sup>	$10^{-6}$	14,29	14,29	42,25	42,25
13	(4)·(5)	$10^{-6}$	8,85	10,73	30,81	32,11
14	(11)+(12)+(13)	$10^{-6}$	28,61	33,09	95,53	98,76
15	$(2 \sqrt{3}) \sqrt{(14)} = \varepsilon'_i$	$10^{-3}$	8,18	6,64	11,29	11,48
16	$\sigma'_i$	107	22,25	22,10	21,25	21,2
17	$\sigma'_i$	107	30	30,2	31,25	31,3
18	(3) 0,5	$10^{-3}$	-2,48	-2,48	-1,12	-1,12
19	(2)+(18)	$10^{-3}$	-8,88	-8,33	-5,12	-4,92
20	$(4 \cdot 3) [(16)'(10)] (2) = \sigma'_x$	107	-23,11	-22,68	-22,91	-22,75
21	0,5 (2)	$10^{-3}$	-3,2	-2,95	-2	-1,9
22	(3)+(21)	$10^{-3}$	-8,16	-7,91	-4,24	-4,14
23	$(4 \cdot 3) [(16)'(10)] (2) = \sigma'_\varphi$	107	-21,24	-21,41	-19	-19,15
24	0,5 (5)	$10^{-3}$	1,89	1,89	3,25	3,25
25	(4)+(24)	$10^{-3}$	4,23	4,73	7,99	8,19
26	$(4 \cdot 3) [(17)'(15)] (25) = \sigma'_x$	107	27,37	28,68	29,47	29,73

KEY: (1) Line number; (2) Function; (3) Factor; (4) Values of function, when.

Table 2.2. (Cont'd)

(1) № стр-ки	(2) Функция	(3) Множит-ель	(4) Значения функций при			
			$\Delta R = 0,5 \cdot 10^{-3} \text{ м};$ $\epsilon_{\varphi 0} = 5,14 \cdot 10^{-3}$		$\Delta R = 0,75 \cdot 10^{-3} \text{ м};$ $\epsilon_{\varphi 0} = 8,16 \cdot 10^{-3}$	
27	0,5 (4)	$10^{-3}$	1,17	1,42	2,37	2,47
28	(5)+(27)	$10^{-3}$	4,95	5,2	8,87	8,97
29	(4.3) [(17) (15)] (28) = $c_{\varphi}$	107	32,03	31,52	32,71	32,00
30	(20) $h'$	104	-34,67	-34,02	-33,41	-34,13
31	(26) $h'$	104	41,05	43	44,20	44,64
32	(30)+(32)	104	6,38	8,98	9,79	10,51
33	(23) $h'$	104	-31,86	-32,11	-32,28	-28,5
34	(29) $h'$	104	48,05	47,28	49,07	49,91
35	(33)+(34)	104	18,19	15,17	20,57	10,17
36	0,5 (35)	104	8,09	7,59	10,29	10,09
37	(32)-(35) = $\Delta$	104	-1,71	1,39	-0,5	0,42
38	$p = (35)/R$	105	17,59	16,49	22,35	21,92

## Stress analysis of the load-bearing plate of a reactor

In the design of reactors and other engine units we frequently encounter single-layer and multi-layer plates, as well as disks, which operate in a bend from the forces of fluid pressure and concentrated loads.

Support plates and end pieces are usually found to have a constant thickness of asymmetric form with asymmetrically located openings and bracing rods. They can be greatly or moderately heated and, in certain cases, there can be a temperature gradient along the radius of a disk and some variation in its thickness. The latter case can include two-layer plates shielded from hot fluids by a thin wall. The support plate has openings for the passage of fluids; the openings are used for attaching pipes which connect both plates. The perforations in the support plate lead to the fact that in a radial direction it usually has variable rigidity, particularly at its bracing point to the walls of the cylinder part of the shell.

In the first approximation we can assume the plate to be rigidly fixed in the peripheral part during its operation in a bend and non-rigidly fixed during its operation under radial strains (when radial strains are scarcely contained due to the thin-wall nature of the cylindrical shell's construction).

In some cases, the plate is considered freely supported along the peripheral section and thus the stressed state is determined in the most unfavorable case. Actually, a support plate is attached elastically. The elasticity of the attachment should be allowed for in more detailed calculations.

### Stresses and bending moments

If we assume that the bending strain of a section of plate follows the hypothesis of the invariability of the normal and take the system of coordinates shown in Fig. 2.47, we shall find the stresses  $\sigma_r$ ,  $\sigma_\phi$ , which occur in the plate, its strain  $w$  and safety coefficient  $n$ .

Let us examine a plate of constant thickness  $h$  loaded with forces which are symmetrically located with respect to the  $z$ -axis. Strains, displacements, and stresses arising in the plate will also be symmetric relative to the  $z$ -axis.

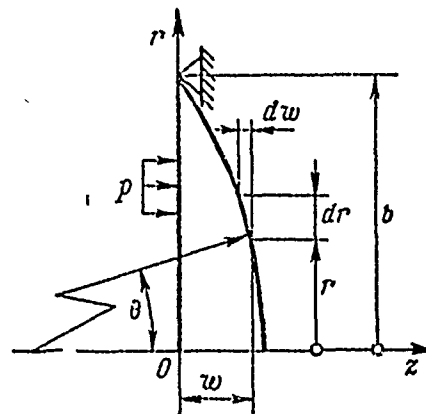


Fig. 2.47. Coordinate axes.

We designate the bend of the plate  $w$  and the turn angle of the normal  $\theta$ . The quantities  $w$  and  $\theta$  are functions of only the radius  $r$  and are related to each other by relation

$$\theta = -\frac{dx}{dr} = -w'. \quad (2.48)$$

The sign is negative because with an increase in bend the slope angle decreases.

A plate element removed from the central axis  $O - r$  a distance  $z$  is in a two-dimensional stressed state. The strains of this element (Fig. 2.48) are

$$\varepsilon_r = \frac{1}{E}(\sigma_r - \mu\sigma_\varphi); \quad \varepsilon_\varphi = \frac{1}{E}(\sigma_\varphi - \mu\sigma_r),$$

and the stresses

$$\left. \begin{aligned} \sigma_r &= \frac{E}{1-\mu^2}(\varepsilon_r + \mu\varepsilon_\varphi); \\ \sigma_\varphi &= \frac{E}{1-\mu^2}(\varepsilon_\varphi + \mu\varepsilon_r). \end{aligned} \right\} \quad (2.49)$$

These stresses determine the supporting capacity of the plate.

Let us find  $\varepsilon_r$  and  $\varepsilon_\varphi$ . We shall examine the strain of the plate element.

Figure 2.48 shows a plate element  $dr$  before and after strain. The normal which occupied position  $AB$  before plate deflection turns angle  $\theta$  and occupies position  $A'B'$  according to the hypothesis of the invariability of the normal. The normal  $A_1B_1$  turns angle  $\theta + d\theta$ . Segment  $CC_1$ , located distance  $z$  from the middle surface in a radial direction, achieves elongation

$$C_1C'_1 - CC' = z(\theta + d\theta) - z\theta = zd\theta.$$

The dimension of element  $CC_1$  before strain is  $dr$ . Thus, relative elongation of the plate in a radial direction is

$$\varepsilon_r = z \frac{d\theta}{dr} = z\theta'. \quad (2.50)$$

Let us find the relative strain of an element in the peripheral direction. Before the plate bends the length of the circumference passing through point C will be  $2\pi r$ , and after the bend  $2\pi(r + z\theta)$ . Consequently, relative elongation in a peripheral direction is

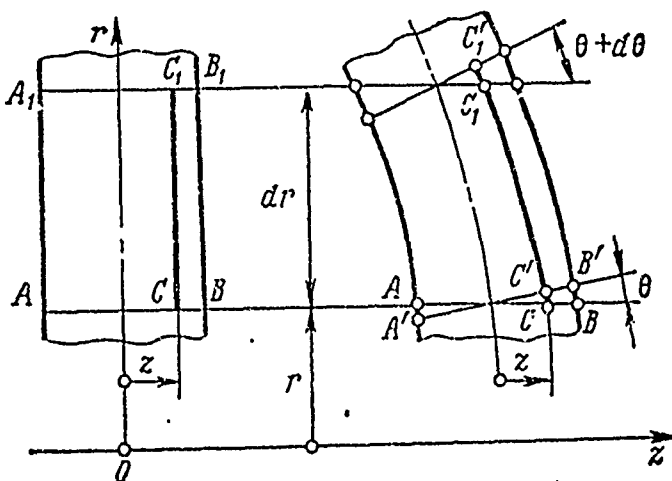
$$\varepsilon_\varphi = \frac{2\pi(r + z\theta) - 2\pi r}{2\pi r} = z \frac{\theta}{r}. \quad (2.51)$$

Substituting expressions (2.50) and (2.51) into (2.49), we finally obtain the stresses in the plate

$$\left. \begin{aligned} \sigma_r &= \frac{Ez}{1-\mu^2} \left( \theta' + \mu \frac{\theta}{r} \right); \\ \sigma_\varphi &= \frac{Ez}{1-\mu^2} \left( \frac{\theta}{r} + \mu \theta' \right). \end{aligned} \right\} \quad (2.52)$$

Figure 2.49 shows the stresses  $\sigma_r$  applied to a strip taken from an elementary prism. Based on the known stresses  $\sigma_r$  and  $\sigma_\varphi$  we find the bending moments applied to the faces.

Fig. 2.48. Strain of a plate element.



We designate the relative moments occurring on the faces of the elements (moments reduced to a unit length of the cross section),  $\bar{M}_r$  and  $\bar{M}_\varphi$ , respectively.

Obviously,  $d\bar{M}_r = \sigma_r z dz$ ; then  $\bar{M}_r = \int_{-h/2}^{h/2} \sigma_r z dz$ .

Using expressions (2.52), we obtain

$$\bar{M}_r = \frac{E}{1-\mu^2} \left( \theta' + \mu \frac{\theta}{r} \right) \int_{-h/2}^{h/2} z^2 dz.$$

However,  $\int_{-h/2}^{h/2} z^2 dz = \frac{h^3}{12}$ , consequently,

$$\bar{M}_r = \frac{Eh^3}{12(1-\mu^2)} \left( \theta' + \mu \frac{\theta}{r} \right) = D \left( \theta' + \mu \frac{\theta}{r} \right), \quad (2.53)$$

$$\text{where } D = \frac{Eh^3}{12(1-\mu^2)} \quad (2.54)$$

Here D is the rigidity of the plate to a bend in N·m; this is called the cylindrical rigidity.

Analogously, we obtain the bending moment:

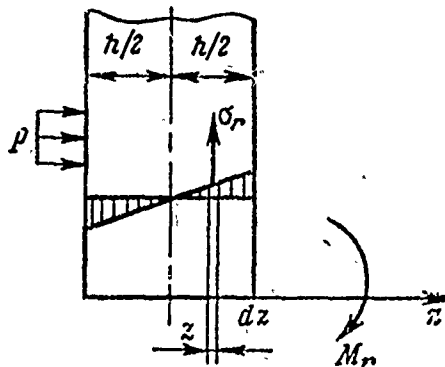
$$\bar{M}_\varphi = D \left( \frac{\theta}{r} + \mu \theta' \right). \quad (2.55)$$

Sometimes the bar over the designation for moments is omitted. Only we should never forget that in these expressions the moments relate to a unit length of the plate cross section.

We obtain the simple formulas connecting the bending moments and the stresses:

$$\sigma_r = \frac{\bar{M}_r}{h^2}; \quad \sigma_\varphi = \frac{6\bar{M}_\varphi}{h^2}. \quad (2.56)$$

Fig. 2.49. Determining bending moment.



### Equations of plate equilibrium

We shall examine, finally, the equilibrium of an element. We apply to the faces all equally effective forces and moments.

Figure 2.50 shows the positive forces and moments. When the plate is rotated in the direction of the  $z$ -axis, the positive moment is directed clockwise, and the intersecting forces along the positive direction of the  $z$ -axis.

On the  $abcd$  face (see Fig. 2.50) the tangent stresses give an equally effective shearing force  $Q$ , directed along the  $z$ -axis. Its intensity, i.e., force, arriving per unit arc  $r d\varphi$ , we designate  $\bar{Q}$ . The shearing force  $Q$  on the  $abcd$  face will be equal to  $\bar{Q} r d\varphi$ , and on the  $a_1 b_1 c_1 d_1$  face will be  $(\bar{Q} + d\bar{Q})(r + dr) d\varphi$ .

Since the stresses in layers to the right and left of the neutral plane of the element are identical but unlike in sign, there are no normal forces on the faces of the element.

Thus, the moments and forces expressed through the corresponding intensities will be:

$$Q = \bar{Q} r d\varphi; \quad Q + dQ = (\bar{Q} + d\bar{Q})(r + dr) d\varphi;$$

$$M_r = \bar{M}_r r d\varphi; \quad M_r + dM_r = (\bar{M}_r + d\bar{M}_r)(r + dr) d\varphi;$$



$$M_\varphi = \bar{M}_\varphi dr; \quad P = pr dr d\varphi;$$

$$M_p = P \frac{dr}{2} = pr dr d\varphi \frac{dr}{2};$$

$$M(Q + dQ) = (\bar{Q} + d\bar{Q})(r + dr) dr d\varphi.$$

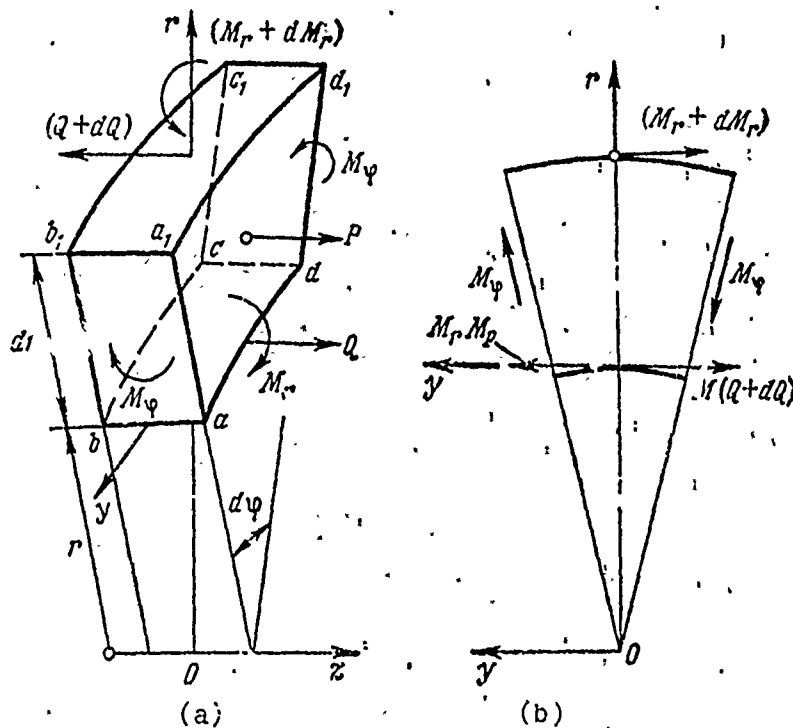


Fig. 2.50. A plate element.

Projecting all forces acting on the element (see Fig. 2.50a) onto the  $z$ -axis, we obtain

$$\bar{Q}r d\varphi - [(\bar{Q} + d\bar{Q})(r + dr) dz] + pr d\varphi dr = 0,$$

hence

$$(\bar{Q}r)' = pr. \quad (2.57)$$

We establish the sum of the moments of forces applied to the element relative to the y-axis, tangent to an arc of a circle with radius  $r$  and the middle plane (see Fig. 2.50b):

$$\begin{aligned} \bar{M}_r r d\varphi - [(\bar{M}_r + d\bar{M}_r)(r + dr) d\varphi] + pr dr d\varphi \frac{dr}{2} + \\ + 2\bar{M}_\varphi dr \sin \frac{d\varphi}{2} - (\bar{Q} + d\bar{Q})(r + dr) d\varphi dr = 0, \end{aligned}$$

or, disregarding quantities of the highest order, we obtain

$$\bar{M}_\varphi - (\bar{M}_r)' = \bar{Q}r. \quad (2.58)$$

If we substitute  $\bar{M}_r$  and  $\bar{M}_\varphi$  from expressions (2.53) into (2.58) and assume that plate rigidity  $D$  is constant, we obtain

$$r\theta'' + \theta' - \frac{\bar{Q}}{r} = -\frac{\bar{Q}r}{D},$$

or

$$\left[ \frac{1}{r} (\theta r)' \right]' = -\frac{\bar{Q}}{D}, \quad (2.59)$$

which can be checked by simple differentiation.

If we allow for dependence (2.48)  $\theta = -w'$ , equation (2.59) can be represented in the form

$$\left[ \frac{1}{r} (rw')' \right]' = \frac{\bar{Q}}{D}. \quad (2.60)$$

Finally if we substitute  $\bar{Q}$  from equation (2.56) into the right side of equation (2.60) then after certain transformation we find, finally

$$\frac{1}{r} \left\{ \left[ \frac{1}{r} (rw')' \right] \right\}' = \frac{p}{D}, \quad (2.61)$$

or in shortened form,

$$\nabla^2 \nabla^2 w = \frac{p}{D},$$

where the Laplacian operator

$$\nabla^2 w = w'' + \frac{1}{r} w' = \frac{1}{r} (rw')'.$$

Frequently we use the integral form of writing equation (2.61). We shall integrate equation (2.61) four times.

The first integral

$$\begin{aligned} r \left[ \frac{1}{r} (rw')' \right] &= \int_0^r \frac{pr}{D} dr + C_1; \\ \frac{1}{r} (rw')' &= \int_0^r \frac{1}{r} \int_0^r \frac{pr}{D} dr + C_1 \ln r + C_2. \end{aligned}$$

Integrating once more, we obtain

$$rw' = \int_0^r r \int_0^r \frac{1}{r} \int_0^r \frac{pr}{D} dr^3 + \frac{1}{2} C_1 r^2 \left( \ln r - \frac{1}{2} \right) + \frac{1}{2} C_2 r^2 + C_3.$$

And finally

$$\begin{aligned} w &= \int_0^r \frac{1}{r} \int_0^r r \int_0^r \frac{1}{r} \int_0^r \frac{pr}{D} dr^4 + \frac{1}{4} C_1 r^2 (\ln r - 1) + \\ &\quad + \frac{1}{4} C_2 r^2 + C_3 \ln r + C_4. \end{aligned} \quad (2.62)$$

## Deflection of a solid plate with constant cross section

Expression (2.62), valid for any plate with a constant cross section and any loading, is simplified for a plate without openings (Fig. 2.51). From the condition that when  $r = 0$  the quantity  $w$  must be final, we obtain  $C_1 = C_3 = 0$ .

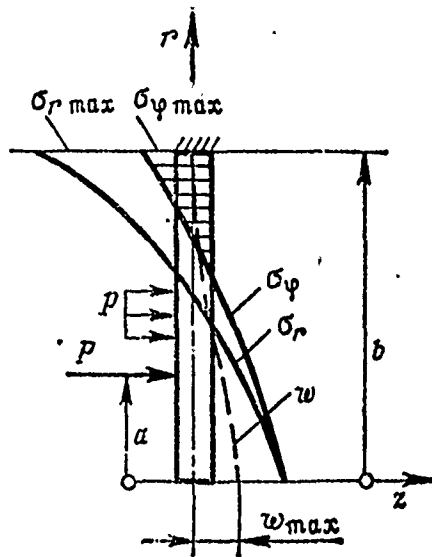


Fig. 2.51. Plate with sealed edges.

Thus, for a plate without a central opening,

$$w = \int_0^r \frac{1}{r} \int_0^r r \int_0^r \frac{1}{r} \int_0^r \frac{pr}{D} dr^4 + \frac{r^2}{4} C_2 + C_4. \quad (2.63)$$

In the particular case when  $p = \text{const}$ ,

$$w = \frac{pr^4}{64D} + \frac{r^2}{4} C_2 + C_4. \quad (2.64)$$

We shall examine two basic particular cases in analyzing solid plates.

Case 1. The plate is rigidly sealed along the outer contour and loaded uniformly with a distributed load.

In this case, the constant  $C_2$  in formula (2.64) must be determined from the condition  $w' = 0$  when  $r = b$ . After differentiating equation (2.64) once and equating the result to zero, we obtain

$$w' = -\left(\frac{pb^3}{16D} + \frac{b}{2}C_2\right) = 0,$$

Hence  $C_2 = -(pb^2)/(8D)$  and finally

$$w' = \frac{pr}{16D}(b^2 - r^2). \quad (2.65)$$

The constant  $C_4$  is found from condition  $w = 0$  when  $r = b$ ; we obtain

$$w = \frac{pb^4}{64D} - \frac{pb^4}{32D} + C_4 = 0,$$

hence  $C_4 = (pb^4)/(64D)$  and finally,

$$w = \frac{p}{64D}(b^2 - r^2)^2. \quad (2.66)$$

The greatest bend of the plate will be in its center

$$w_{\max} = \frac{pb^4}{64D}.$$

Bending moments are

$$\left. \begin{aligned} \overline{M}_r &= \frac{p}{16}[(1 + \mu)b^2 - (3 + \mu)r^2]; \\ \overline{M}_\varphi &= \frac{p}{16}[(1 + \mu)b^2 - (1 + 3\mu)r^2]. \end{aligned} \right\} \quad (2.67)$$

In the center of the plate  $\overline{M}_r = \overline{M}_\varphi = \frac{pb^2}{16}(1 + \mu)$ .

On the supported contour  $\overline{M}_r = -\frac{pb^2}{8}$ ;  $\overline{M}_\varphi = -\frac{pb^2}{8}\mu$ .

The relative moments are in N·m/m.

Let us find the stresses in the plate. As already mentioned,

$$\sigma_r = \frac{6\bar{M}_r}{h^2}; \quad \sigma_\varphi = \frac{6\bar{M}_\varphi}{h^2}.$$

Substituting the maximum values of the moments into these formulas, we obtain

$$(\sigma_r)_{\max} = -\frac{3}{4} \frac{pb^2}{h^2}; \quad (\sigma_\varphi)_{\max} = -\frac{3}{4} \frac{pb^2}{h^2}. \quad (2.67a)$$

A variation in stress along the radius of the plate is shown in Fig. 2.51.

Let us examine the values of plate deflection when it is loaded with a concentrated concentric load  $P$  (see Fig. 2.51).

Solving the initial equation (2.64), we obtain the bend of the plate:

$$w = \frac{P}{8\pi D} \left[ (a^2 + r^2) \ln \frac{a}{b} + \frac{(b^2 + r^2)(b^2 - a^2)}{2b^2} \right] \varepsilon_1 + \\ + \frac{P}{8\pi D} \left[ (a^2 + r^2) \ln \frac{r}{b} + \frac{(b^2 - r^2)(b^2 + a^2)}{2b^2} \right] \varepsilon_2, \quad (2.68)$$

where the unit functions are

$$\varepsilon_1 = \begin{cases} 1, & r < a; \\ 0, & r \geq a, \end{cases} \quad \varepsilon_2 = \begin{cases} 1, & r \geq a; \\ 0, & r < a. \end{cases}$$

The value of the bending moment on the plate contour is

$$M_r = -\frac{P}{4\pi} \left( \frac{b^2 - a^2}{b^2} \right). \quad (2.69)$$

If the external force is concentrated in the center, plate bend will be

$$w = \frac{P}{8\pi D} \left( r^2 \ln \frac{r}{b} + \frac{b^2 - r^2}{2} \right). \quad (2.70)$$

The current value of the bending moments is

$$\left. \begin{aligned} \overline{M}_r &= \frac{P}{4\pi} \left[ (1+\mu) \ln \frac{b}{r} - 1 \right]; \\ \overline{M}_\varphi &= \frac{P}{4\pi} \left[ (1+\mu) \ln \frac{b}{r} - \mu \right]; \end{aligned} \right\} \quad (2.71)$$

and the maximum bending moment is obtained in the seal of the plate:  
 $\overline{M}_r = -P/4\pi$ .

In this case, we usually assume that the load  $P$  is applied not along the circumference but to a certain ring-shaped area whose width is no less than the thickness of the plate.

Case 2. A plate is freely supported along the outer contour and is loaded uniformly by a distributed load (Fig. 2.52). In this case, the constant  $C_2$  in equality (2.69) must be determined from the condition  $M_r = 0$  when  $r = b$ . Omitting the intermediate transformations, we obtain

$$w = \frac{p(b^2 - r^2)}{64D} \left( \frac{5+\mu}{1+\mu} b^2 - r^2 \right). \quad (2.72)$$

Bending moments are

$$\left. \begin{aligned} \overline{M}_r &= \frac{p}{16} (3+\mu)(b^2 - r^2); \\ \overline{M}_\varphi &= \frac{p}{16} [(3+\mu)b^2 - (1-3\mu)r^2]. \end{aligned} \right\} \quad (2.73)$$

Bending moments achieve their maximum values in the center of the plate:

$$\overline{M}_r = \overline{M}_\varphi = \frac{p(3+\mu)}{16} b^2.$$

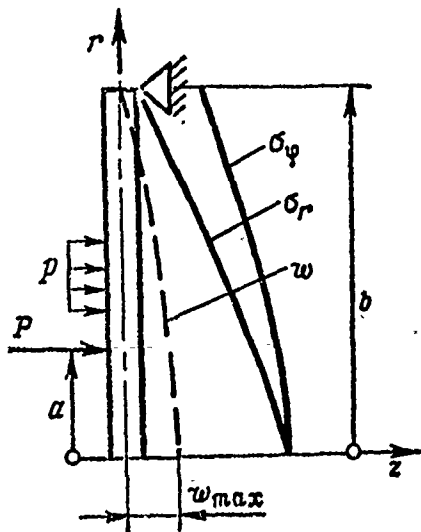


Fig. 2.52. Plate with freely supported edges.

Let us substitute the values of the moments into these formulas.

In the center of the plate  $(\sigma_r)_{\max} = (\sigma_\varphi)_{\max} = \frac{3(3+\mu)pb^2}{8h^2}$ .

On the outer contour  $\sigma_r = 0$ ;  $\sigma_\varphi = \frac{3}{4}(1-\mu)pb^2$ .

Obviously, this type of plate attachment is less desirable than the former.

The variation in stresses for the studied case is shown in Fig. 2.52.

Let us examine the loading of a plate with a concentrically located power loading (see Fig. 2.52). Solving equations (2.63); we obtain



$$w = \frac{P}{8\pi D} \left[ (a^2 + r^2) \ln \frac{a}{b} + (b^2 - a^2) \frac{(3 + \mu)b^2 - (1 - \mu)r^2}{2(1 + \mu)b^2} \right] \varepsilon_1 + \\ + \frac{P}{8\pi D} \left[ (a^2 + r^2) \ln \frac{r}{b} + (b^2 - r^2) \frac{(3 + \mu)b^2 - (1 - \mu)a^2}{2(1 + \mu)b^2} \right] \varepsilon_2,$$

where

$$\varepsilon_1 = \begin{cases} 1, & r \leq a; \\ 0, & r > a; \end{cases} \quad \varepsilon_2 = \begin{cases} 1, & r \geq a; \\ 0, & r < a. \end{cases}$$

The bend in the center will be maximum:

$$w = \frac{P}{8\pi D} \left[ \frac{3 + \mu}{2(1 + \mu)} (b^2 - a^2) + a^2 \ln \frac{a}{b} \right].$$

In these formulas it has been assumed that the concentric loading is applied to radius  $a$ , somewhat removed from the center. If radius  $a$  is constricted to a point or more accurately, to a circumference equal or nearly equal to the thickness of the plate, then bending moments will be

$$\left. \begin{aligned} \overline{M}_r &= \frac{P}{4\pi} \left[ (1 + \mu) \ln \frac{b}{r} \right]; \\ \overline{M}_\varphi &= \frac{P}{4\pi} \left[ (1 + \mu) \ln \frac{b}{r} + (1 - \mu) \right]. \end{aligned} \right\} \quad (2.74)$$

The bend of the plate is

$$w = \frac{P}{16\pi D} \left[ 2r^2 \ln \frac{r}{b} + \frac{3 + \mu}{1 + \mu} (b^2 - r^2) \right] \quad (2.75)$$

$$\text{In the center of the plate } w = \frac{P(3 + \mu)b^2}{16\pi D(1 + \mu)}$$

Let us find the safety coefficient of the plate:

$$n = \frac{\sigma_{nt}}{\sigma_{l \max}}; \quad \sigma_l = \sqrt{\sigma_r^2 - \sigma_r \sigma_\varphi + \sigma_\varphi^2}.$$

We should select  $n = 1.3-1.5$ .

### Peculiarities in analyzing braced and flexible reactor plates

In certain cases, it is immediately apparent that a plate, if it is not braced, will either be very heavy or will have an extremely large deflection under loading. A deflection is called large when it exceeds the thickness of the plate. In order to avoid this, we can rigidly connect, by welding the rods, the load-bearing plate with the end plate, which has great rigidity due to its shape and lower heating temperature (Fig. 2.53).

Two end plates connected thus are analyzed as follows. An elliptical end plate to which rods are braced we shall consider absolutely rigid. Only the plate and the bracing rods are deformed in operation. We shall assume that the rods are placed axisymmetrically forming a continuous force ring for a plate attachment.

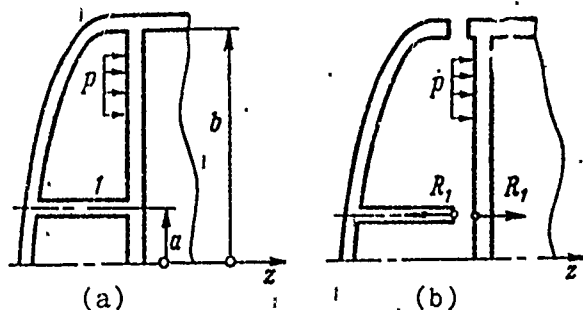


Fig. 2.53. Diagram of a braced plate.

The problem is statically indeterminate. We shall solve it by the structural mechanics method of forces. Let us cut the system at the spot where the rods join the plate; we compensate for the effect of the rods by force  $R$ . An equation is set up using the method of forces (see Fig. 2.53).

$$\sum M = M + M_{R1}; \quad \sum \tau = \tau + \tau_{R1}; \quad \sum w = w + w_{R1}.$$

If we find that  $w_{\max} < h$ , the problem is solved. Sometimes, for this, we should install two or three rows of bracing rods.

In some cases, there can be no bracing.

With normal stresses we shall obtain large deflections which shift the entire core along the axis. In these cases, we should refine the calculation, using equipment which will take into account the flexibility of the plate.<sup>1</sup> The main refinement would be to examine the deflection and strain of the plate not only as a result of the effect of bending moment  $M_p$  and  $M_\varphi$  but also as a result of the tensile forces in the plate T.

With small deflections the effect of T is small. With large deflections the solution to the plate equation reduces to the dependence

$$\frac{\rho b^4}{E h^4} = A \left( \frac{w}{h} \right) + B \left( \frac{w}{h} \right)^3. \quad (2.76)$$

It is easy to show that the first term after the equality sign corresponds to the bending of the plate as a result of the effect of bending moments; the second term after the equality sign refers to the effect of tensions T.

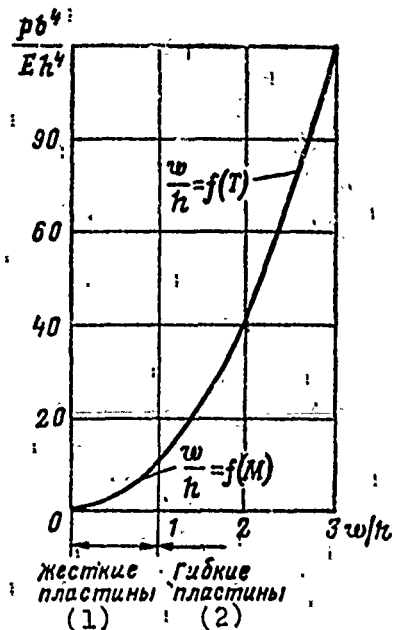
Examining figure 2.54, we see that when  $(w/h) < 1$ , the nonlinear contribution of the load creating the deflection is small. The deflection is wholly determined by bending moment. When  $(w/h) \geq 1$  the nonlinear contribution of the load causing the bending is great.

---

<sup>1</sup>This will be discussed in greater detail in Chapter V.

In this case, the plate must be considered flexible and analysis is performed with the formulas for flexible plates.

Fig. 2.54. Calculation of a flexible plate.  
KEY: (1) Rigid plate; (2) Flexible plates.



Example 2.6. Find the stress and deflection of a circular, rigidly sealed plate, braced by axisymmetric rods (Fig. 2.55) if the following is given:

$$a_1 = 0.45 \text{ m}; \quad a_2 = 0.8 \text{ m}; \quad h = 1.7 \text{ m}; \quad h = 1.5 \cdot 10^{-2} \text{ m}; \quad l_1 = 0.28 \text{ m}; \\ l_2 = 0.22 \text{ m}; \quad F = 70 \cdot 10^{-4} \text{ m}^2; \quad F_2 = 44 \cdot 10^{-4} \text{ m}^2; \quad p = 4.2 \cdot 10^5 \text{ N/m}^2; \\ E = 2.2 \cdot 10^{11} \text{ N/m}^2.$$

We assume that the elliptical end plate to which the rods are attached is rigid.

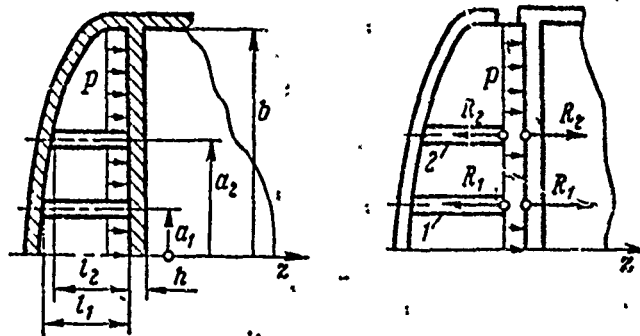


Fig. 2.55. Example of calculation.

We cut the system along the attachment points of rods 1 and 2, we compensate for the effect of the rods by the forces  $R_1$  and  $R_2$  and we set up the canonical equation for the method of forces used in structural mechanics:

$$\begin{aligned} \delta_{10}p + (\delta_{11} + \delta_1) R_1 + \delta_{12} R_2 &= 0; \\ \delta_{20}p + \delta_{21} R_1 + (\delta_{22} + \delta_2) R_2 &= 0. \end{aligned}$$

If we designate

$$\delta_{11} + \delta_1 = \delta(11); \quad \delta_{22} + \delta_2 = \delta$$

from system of equation

$$\begin{aligned} \delta(11) R_1 + \delta_{12} R_2 &= -\delta_{10}p; \\ \delta_{21} R_1 + \delta(22) R_2 &= -\delta_{20}p \end{aligned}$$

we find  $R_1 = \frac{\Delta_1}{\Delta}; \quad R_2 = \frac{\Delta_2}{\Delta},$

where

$$\Delta_1 = \begin{vmatrix} \delta_{10} & p\delta_{12} \\ \delta_{20} & p\delta(22) \end{vmatrix}; \quad \Delta_2 = \begin{vmatrix} \delta(11) & \delta_{10}p \\ \delta_{21} & \delta_{20}p \end{vmatrix}; \quad \Delta = \begin{vmatrix} \delta(11) & \delta_{12} \\ \delta_{21} & \delta(22) \end{vmatrix}.$$

Let us find the stresses, pliability, and bends.

If the plate were unbraced, the stress in its unsafe section  $r = b$  would be determined from formula (2.68) and would be equal to

$$\sigma_{\max} = -\frac{0,75 \, p b^2}{h^2} = -\frac{0,75 \cdot 4,2 \cdot 10^5 \cdot 1,7^2}{1,52 \cdot 10^{-4}} = -40 \, 600 \cdot 10^5 \, \text{N/m}^2.$$

This stress is extremely high. Let us evaluate what kind of stress occurs in a plate after we allow for the unloading action of the rods.

The bend of the plate at the first and second points from pressure  $p$  will be

$$\delta_{10} p = 0,17 \frac{p (l^2 - a_1^2)^2}{Eh^3} = 0,17 \frac{4,2 \cdot 10^5 (1,7^2 - 0,45^2)^2}{2,2 \cdot 10^{11} \cdot 1,5^3 \cdot 10^{-6}} = 0,66 \mu;$$

$$\delta_{20} p = 0,17 \frac{4,2 \cdot 10^5 (1,7^2 - 0,82^2)^2}{2,2 \cdot 10^{11} \cdot 1,5^3 \cdot 10^{-6}} = 0,484 \mu.$$

The bending rigidity of the plate will be

$$D = \frac{Eh^3}{12(1-\mu^2)} = \frac{2,2 \cdot 10^{11} \cdot 1,5^3 \cdot 10^{-6}}{12(1-0,3^2)} = 6,8 \cdot 10^4 \text{ N}\cdot\text{m}.$$

The power pliability of the plate will be

$$\begin{aligned} \delta_{11} &= \frac{1}{8\pi D} \left[ (a_1^2 + r^2) \ln \frac{a_1}{b} + \frac{(b^2 + r^2)(l^2 - a_1^2)}{2b^2} \right] = \\ &= \frac{1}{8,3,14,6,8 \cdot 10^4} \left[ 20,452 \ln \frac{0,45}{1,7} + \frac{1,7^2 - 0,45^2}{2 \cdot 1,7^2} \right] = \\ &= 0,525 \cdot 10^{-6} \mu/\mu; \end{aligned}$$

$$\delta_{12} = \frac{1}{8\pi D} \left[ (a_2^2 + a_1^2) \ln \frac{a_2}{b} + \frac{(l^2 + a_1^2)(l^2 - a_2^2)}{2b^2} \right] = 0,33 \cdot 10^{-6} \text{ m/N};$$

$$\delta_{22} = \frac{1}{8\pi D} \left[ (a_1^2 + r^2) \ln \frac{a_2}{b} + \frac{(l^2 + r^2)(b^2 - a_2^2)}{2l^2} \right] = 0,239 \cdot 10^{-6} \text{ m/N};$$

$$\delta_{21} = \delta_{12}.$$

The pliability of the bracing rods will be

$$\delta_1 = \frac{l_1}{EF_1} = \frac{0,28}{2,2 \cdot 10^{11} \cdot 70 \cdot 10^{-5}} = 0,0182 \cdot 10^{-5} \text{ m/N};$$

$$\delta_2 = \frac{l_2}{EF_2} = \frac{0,22}{2,2 \cdot 10^{11} \cdot 44 \cdot 10^{-4}} = 0,0227 \cdot 10^{-5} \text{ m/N}.$$

Let us find the unknown forces of the bonds  $R_1$  and  $R_2$ ;

$$\begin{aligned} \Delta &= \delta_{11} \delta_{22} - \delta_{12}^2 = (0,525 \cdot 10^{-6} + 0,0182 \cdot 10^{-5})(0,239 \cdot 10^{-6} + \\ &+ 0,0227 \cdot 10^{-5}) - 0,33 \cdot 10^{-12} \approx 0,017 \cdot 10^{-12} \text{ m/N}^2; \end{aligned}$$

$$\Delta_1 = -[\delta_{10} p \delta_{22} - \delta_{20} p \delta_{12}] =$$

$$= -(0,666 \cdot 0,239 \cdot 10^{-6} - 0,484 \cdot 0,33 \cdot 10^{-6}) = 0,05 \cdot 10^{-8} \text{ (m/N)}_n;$$

$$\Delta_2 = -[b_{20} p^2 (11) - b_{10} p^2 b_{21}] = -3,45 \cdot 10^{-8} \text{ (m/N)}_m;$$

$$R_1 = \frac{\Delta_1}{\Delta} = \frac{0,05 \cdot 10^{-8}}{0,017 \cdot 10^{-12}} = 2,9 \cdot 10^4 \text{ N};$$

$$R_2 = \frac{\Delta_2}{\Delta} = -203 \cdot 10^4 \text{ N}.$$

Hence the moments from the forces in the bonds will be

$$\overline{M}_{R1} = \frac{R_1}{4\pi} \cdot \frac{b^2 - a_1^2}{b^2} = \frac{2,9 \cdot 10^4}{4\pi} \left[ 1 - \left( \frac{0,45}{1,7} \right)^2 \right] = -0,22 \cdot 10^4 \text{ N} \cdot \text{m/m};$$

$$\overline{M}_{R2} = \frac{R_2}{4\pi} \cdot \frac{b^2 - a_2^2}{b^2} = 12,6 \cdot 10^4 \text{ N} \cdot \text{m/m}.$$

The bending moment from the outer load will be

$$\overline{M}_{r0} = -\frac{p b^2}{8} = -\frac{4,2 \cdot 10^5 \cdot 1,7^2}{8} = -15 \cdot 10^4 \text{ N} \cdot \text{m/m}.$$

Total bending moment is

$$\overline{M}_2 = (-15 - 0,22 + 12,6) 10^4 = -2,62 \cdot 10^4 \text{ N} \cdot \text{m/m}.$$

Maximum stress is

$$\sigma_r = \frac{6M_z}{b^2} = -\frac{6 \cdot 2,62 \cdot 10^4}{2,25 \cdot 10^{-4}} = -7000 \cdot 10^5 \text{ N/m}^2.$$

Comparing these stresses with those obtained earlier, we see that the bracing of a plate reduces the level of stresses by more than a factor of five.

Peculiarities in the analysis of perforated reactor plates

The load-bearing plate of a reactor is a discontinuous perforated plate of constant thickness. In a considerable part it is weakened by the openings for attaching the fuel elements and for the passage

of the heat-transfer agent or the coolant. This affects the value of the full load acting on the plate, as well as the rigidity and supporting capacity, and must be allowed for in calculations.

Let us estimate the pressure decrease of the plate due to its perforations. If the pressure drop on the plate  $p$  is known, then the force on a continuous plate (Fig. 2.56)  $P = p\pi b^2$ .

The force acting on part of the plate, with allowance for the decrease in its surface due to perforations, is

$$P_n = p\pi(b_n^2 - nr^2),$$

where  $r$  and  $n$  are the radius and number of openings in the fuel elements for the passage of the heat transfer agent.

Equivalent to this force, the conditional pressure which acts on the perforated part of the plate, if we assume it is continuous, we find from the expression  $P_n = p\pi(b_n^2 - nr^2) = p_n\pi b_n^2$ :

$$p_n = p \left(1 - \frac{nr^2}{b_n^2}\right). \quad (2.77)$$

If the entire load-bearing plate is covered with openings, then

$$p_n = p \left(1 - \frac{nr^2}{b_n^2}\right).$$

The diagram of pressures on the load-bearing plate, thus, has a stepped character, and we shall deal with the analysis of a plate with variable loading. Usually the radius at  $b_n$  is near  $b$ ; therefore, pressure  $p$  is assumed constant.

Let us evaluate the reduction in plate rigidity.



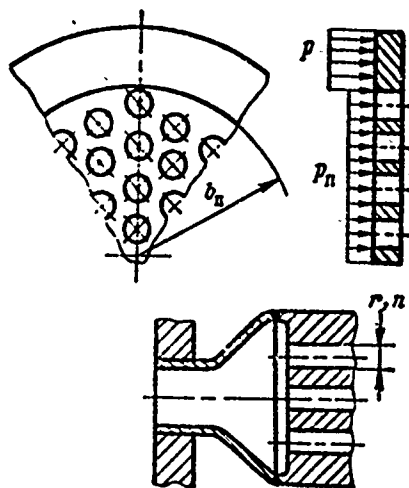


Fig. 2.56. Determining the force acting on a perforated plate.

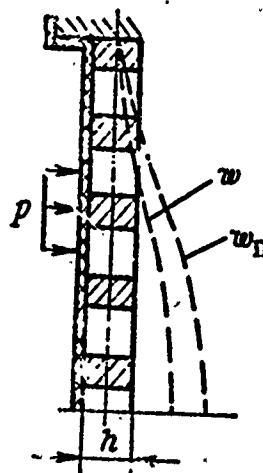
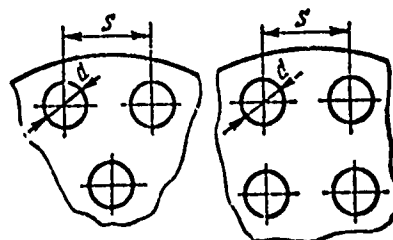


Fig. 2.57. Bend curves of solid and perforated plates.

A characteristic of its strain under loading, established by multiple experiments of various scientists, is important in evaluating the reduction in rigidity of a perforated plate. This characteristic is the fact that the shape of the deflection in a loaded perforated plate is similar to the shape of a deflection in a solid plate.

Figure 2.57 illustrates the bend curves for solid and perforated plates under identical loading. In order to ensure identical loading on a plate, a pliable field insert is used.

Fig. 2.58. Plate perforation diagram.



The degree of bending for a perforated plate depends substantially upon the dimensions  $s$ ,  $d$ ,  $h$  (Fig. 2.58). A perforated plate, just as a solid one, is in a two-dimensional stress state; its deflection is similar to the deflection of a solid plate; its supporting capacity

is determined by the principal stresses  $\sigma_r$  and  $\sigma_\phi$ , which reach their highest value on its surface.

Near the openings there is a certain concentration of stresses, which is substantial for plates of brittle materials. For the materials of plates used in reactors this concentration of stresses can be disregarded.

Based on the similarity of bending curves for the plates, we can write

$$\frac{w}{w_n} = \gamma, \quad (2.77)$$

where  $\gamma$  is the coefficient of proportionality allowing for the reduction in plate rigidity due to its perforation.

Let us find the value of  $\gamma$  from a comparison of the deflections of perforated and solid plates. For the plate shown in Fig. 2.57 the deflections

$$w = \frac{p(h^2 - r^2)^2}{64D}; \quad w_n = \frac{p(h^2 - r^2)^2}{64D_n},$$

hence  $(w)/(w_n) = \gamma = (D_n)/(D)$ .

Thus, the cylindrical rigidity of a perforated plate is equal to the rigidity of a nonperforated plate multiplied by the coefficient of perforations  $\gamma$ . This makes it possible, in the first approach, to find the stresses of a perforated plate from formulas for a solid plate, correcting for the reduction in rigidity due to perforation.

Cylindrical rigidities are

$$D = \frac{Eh^3}{12(1-\mu^2)}; \quad D_n = \frac{Eh_n^3}{12(1-\mu^2)}.$$

In some cases, it is assumed that the reduction in rigidity for a perforated plate occurs as a result of the variation in  $E$  and  $\mu$  of the plate. For the problems which we are studying, it is feasible to attribute the decrease in rigidity to the decrease in plate thickness, which we shall designate  $h_n$ , and we shall find from the relation  $\frac{D_n}{D} = \gamma = \frac{h_n^3}{h^3}$ :

$$h_n = h^3 \sqrt{\gamma}. \quad (2.78)$$

As has been mentioned, the value of  $\gamma$  depends upon the geometric dimensions of the perforated plate and is determined from formula [26]

$$\gamma = 0,25(3+k) \left(1 - \frac{d}{s}\right) (1 - \mu^2), \quad (2.79)$$

where  $d$  is the diameter of the opening;  
 $s$  is the step of the opening;  
 $k$  is the plate rigidity coefficient;

$$k = \frac{1,41}{1 + \left(\frac{h}{s-d}\right)^2}. \quad (2.80)$$

The variation in the coefficient  $k$  as a function of ratio of plate thickness  $h$  to width of connecting neck ( $s - d$ ) is shown in Fig. 2.59a. As is apparent from formula (2.80), it varies from zero to  $\sim 1$ .

The variation in the coefficient  $\gamma$  as a function of the ratio of the diameters of the perforation opening to their step is shown in Fig. 2.59b. Usually the values of  $\gamma$  fall within 0.1 to 0.5, which corresponds to the ratio  $(d/s) = 0.2-0.9$ .

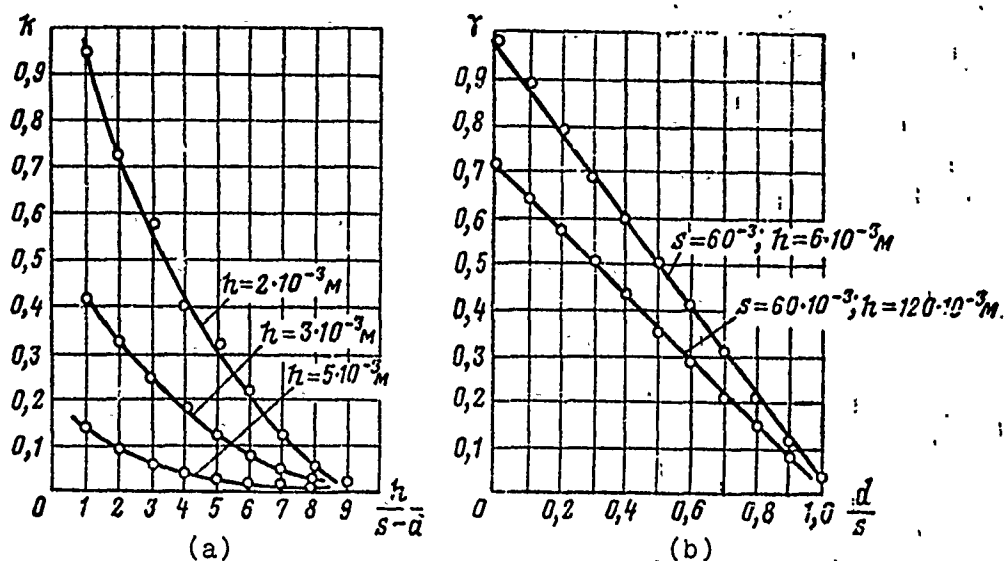


Fig. 2.59. Variation in coefficients  $k$ ,  $h$ ,  $\gamma$ .

Thus, knowing the values of  $\gamma$ , we obtain the final equation for calculating circular perforated plates. The initial equations (2.64) and (2.53) for the calculation will have the following form

$$\left. \begin{aligned} w_n &= \frac{pr^4}{64D\gamma} + \frac{C_2 r^2}{4} + C_4; \\ \bar{M}_{r_n} &= -D\gamma \left( w'' + \mu \frac{w'}{r} \right); \\ \bar{M}_{\varphi_n} &= -D\gamma \left( \frac{w'}{r} + \mu w'' \right). \end{aligned} \right\} \quad (2.81)$$

When the bending moments of an unperforated plate are computed and it is necessary to determine the stresses in it after perforation, in the formula of stresses (2.56) we should take the thickness of the plate, with allowance for perforation,  $h_n = h\sqrt{\gamma}$ , and compute the stresses from the formulas

$$\sigma_{r_n} = \frac{6\bar{M}_r}{h^2\gamma^{2/3}}; \quad \sigma_{\varphi_n} = \frac{6\bar{M}_{\varphi}}{h^2\gamma^{2/3}}.$$

For example, the stresses in a perforated plate, whose seal has a diagram similar to the one presented in Fig. 2.57, will be:

$$\sigma_{r n} = \frac{6pb^2}{16h^2\nu^{2/3}} \left[ (1+\mu) - (3+\mu) \frac{r^2}{b^2} \right];$$

$$\sigma_{\varphi n} = \frac{6pb^2}{16h^2\nu^{2/3}} \left[ (1+\mu) - (1+3\mu) \frac{r^2}{b^2} \right].$$

The safety coefficient of a perforated plate is determined from the usual formula

$$n = \frac{\sigma_{s, f}}{\sigma_{l \max}},$$

where

$$\sigma_l = \sqrt{\sigma_{r n}^2 - \sigma_{r n} \sigma_{\varphi n} + \sigma_{\varphi n}^2}.$$

The value of  $n$  should be selected within the range  $n = 1.1-1.3$ .

## 2.2. RADIOACTIVE ISOTOPIC SOURCES OF ENERGY FOR EXTRATERRESTRIAL ROCKET ENGINES

It is common knowledge that a large amount of heat is given off in the decay of radioactive materials. This heat can be successfully used in a space power plant.

Most radioactive isotopes used are obtained artificially as a result of neutron bombardment in ordinary energy reactors. As a result of isotope decay, a monotonic decrease in thermal energy occurs according to exponential law. These isotopes are simple and operationally reliable. The great difference in decay rates allows us a wide choice of energy sources for the most varied purposes.

However, power plants on radioactive isotopes have several disadvantages. They are expensive as compared with reactor installations since in order to obtain the isotope, uranium must be consumed in reactors: isolation of the isotope is also a complex and costly process.

Therefore, radioisotopic power plants are advisable only at low powers (less than a kilowatt). The use of isotopic elements requires a number of safety measures.

Although the radiation of  $\alpha$  particles (protons) is comparatively safe for man since it is extinguished in the materials of the isotope itself and the ampoule,  $\gamma$ -radiation (electromagnetic) and  $\beta$ -radiation (electrons), which gives off  $\gamma$ -bremsstrahlung during collision with particles of matter, require protection.

An ampoule with an isotope must be hermetically sealed in such a way that the seal is not destroyed in the event of a crash.

All  $\alpha$ -radioactive isotopes in their decay products have gaseous helium whose pressure, at the end of the service period, can reach huge values which complicates the construction of the source.

In designing a source it is necessary to reduce this pressure to permissible values.

Frequently the isotope must be alloyed with other metals to improve its heat conductivity and strength.

Curium-242 is obtained artificially by bombarding americium-241 with neutrons. The specific thermal capacity is 122 W/g. It can be used in generators with a service period from 3 to 6 months. The problems of protection during the use of this isotope are related to the suppression of incidental  $\alpha$ -decay of neutron and  $\gamma$ -radiations.

In decay curium-242 changes into plutonium-238, which causes the severe corrosion of ordinary stainless steels; only tantalum is not corroded. Curium-242 is used as an alloy with americium-241 (45% Cm and 55% Am) and is further alloyed with a stabilizing metal, for example, gold (1 part Cm + Am + 5 parts Au), which improve heat transfer in the alloy.

Helium is separated as a result of the decay of curium-242. If we place an isotope in a hermetically sealed ampoule without extra space, by the end of the service period the pressure of the helium accumulating in the ampoule rises to 550 daN/cm<sup>2</sup> (240 days after closing the isotope in the ampoule).

Table 2.3 presents data on the main isotopes used in extra-terrestrial power plants.

As is apparent from the table, we can design a source which will operate for different periods of time. Short-life sources are used for research purposes.

Let us examine the structural diagrams of isotopic energy sources.

Table 2.3.

Наименование (1)	Формула (2)	Способ распада (3)	Период полураспада (4) (лет, суток)	Топливное соединение (5)	Плотность г/см <sup>3</sup> (6)	Тепловая мощность вт/г (7)
(8) Плутоний	Pu <sup>238</sup>	$\alpha$	86,4л.	PuC; PuO <sub>2</sub>	12,5	0,55
(9) Цезий	Cs <sup>137</sup>	$\beta, \gamma$	33л.	CsCl	3,9	0,325
(10) Стронций	Sr <sup>90</sup>	$\beta, \gamma$	28л.	SrTiO <sub>3</sub>	4,8	0,112
(11) Кюрий	Cm <sup>244</sup>	$\alpha, n$	18л.	Cm <sub>2</sub> O <sub>3</sub>	11,8	2,54
(12) Кобальт	Co <sup>60</sup>	$\beta, \gamma$	5,3л.	Co	9	0,3
(13) Прометий	Pm <sup>147</sup>	$\beta, \gamma$	2,6л.	PmO <sub>3</sub>	6,6	0,167
(14) Церий	Ce <sup>144</sup>	$\beta, \gamma$	28,5с.	CeO <sub>2</sub>	6,4	1,96
(15) Кюрий	Cm <sup>242</sup>	$\alpha, n$	162с.	Cm <sub>2</sub> O <sub>3</sub>	11,75	110—122
(16) Полоний	Po <sup>210</sup>	$\alpha$	138с.	Po	9,3	140—170

KEY: (1) Name; (2) Formula; (3) Decay process; (4) Half-life (years, days); (5) Fuel compound; (6) Density g/cm<sup>3</sup>; (7) Thermal capacity W/h; (8) Plutonium; (9) Cesium; (10) Strontium; (11) Curium; (12) Cobalt; (13) Promethium; (14) Cerium; (15) Curium; (16) Polonium.

Designations: л = years; с = days.

#### Design of an ampoule for an isotopic heat source

A typical design is shown in Fig. 2.60. The isotopic source 1 is placed in a shell 2 of steel, molybdenum or tantalum. This shell can be covered inside with a protective material (tantalum carbide, tungsten).

A peculiarity of isotopes is that immediately after they are obtained in the breeding channel of a reactor, they continuously radiate particles and heat. Therefore, after enclosing the isotope in a shell and welding, which is done automatically using a manipulator, it must be placed in a medium with intense heat



removal, for example, in a container with water, dry ice, etc. If this is not done, the temperature of the isotope can reach such values that transporting the ampoule will be extremely difficult. It can lose hardness or completely melt.

In the container the isotope enters the installation, where it is installed in the housing of the ampoule 4, screwed in by the plug 5, and welded. The combination of threading and welding ensures a strong and hermetic seal.

The thick-walled housing of the ampoule 4 is made of heat-resistant material. The outer surface of the ampoule is conical, which provides for simplicity of installation into the housing of the station 6.

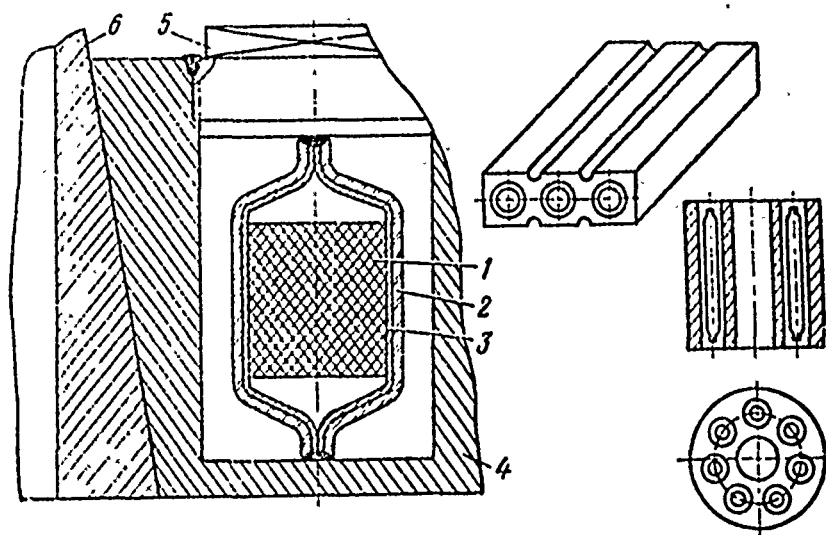


Fig. 2.60. Ampoule of an isotopic heat source.

The figure also shows other designs of ampoules which differ only in the shape of housing.

The thick-wall design is determined by the strength requirement. The ampoule must not break upon impact with the ground.

Figure 2.61 shows the design of a 210 W isotope installation. The working medium is the isotope strontium-90, the temperature of the hot junction of the converter is 530°C, and the temperature of the cold junction is 380°C. The installation consists of a source of energy 1, 2, thermal converters 3, 4, 5, and a thermal capacity control system 6, 7, 8, 9.

The isotopic source 1 and the thick-walled housing 2 heats the liquid metal between the two shells 3 and 4 of the installation's housing and the hot junction of the thermal converter 5. In the initial stage of operation excess thermal capacity is discarded into space, for which the control system is designed. This system consists of a movable radiator-screen 6, supports 7, and flaps which are turned relative to the immovable axes 8. The flaps are opened by supports 7 during movement of the radiator-screen as a result of thermal expansion of the liquid metal and deformation of the sylphon bellows 10.

Figure 2.62 shows one of the possible designs of low-power isotope installations.

#### Ampoule stress analysis

The analyzed modes of the ampoule housing are:

- operating mode; the principal loading of the ampoule is due to the helium pressure at the end of operations;
- technological mode; thermal stresses arising with the cooling process in the ampoule walls during transport are examined;
- emergency mode; the strength of the ampoule during fall is examined.

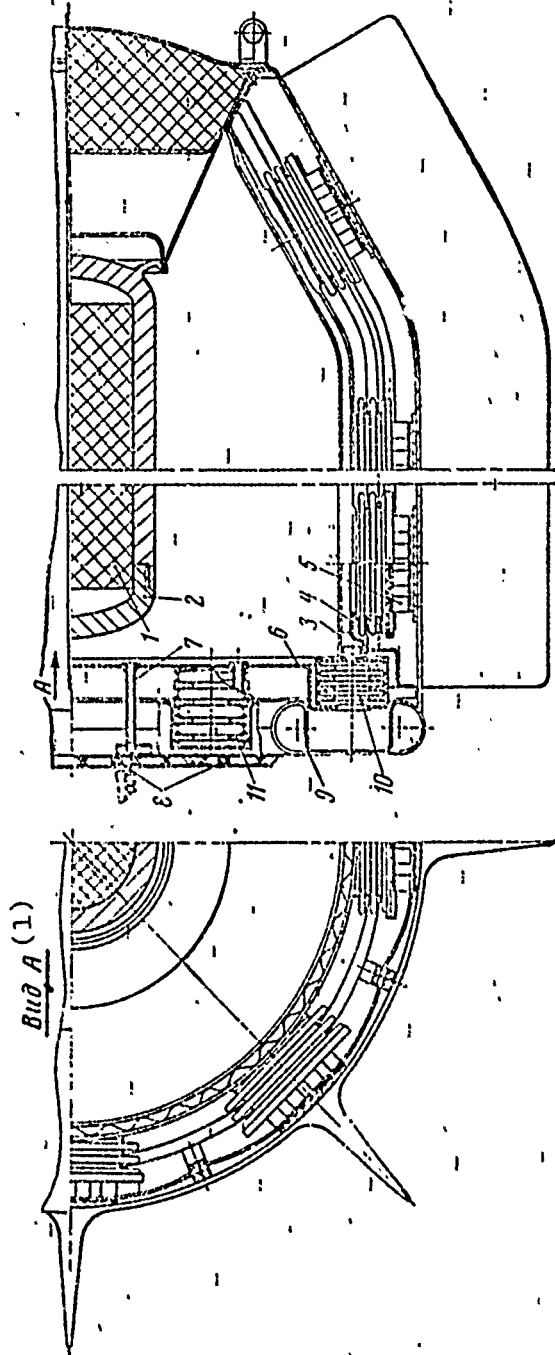


Fig. 2.61. Design of isotope installation.  
KEY: (1) View.

Let us consider the strength of the ampoule in the operating mode. We shall assume that the ampoule is uniformly heated, i.e., the temperature gradient along the housing is ignored. For wall thickness we take not only the thickness of an ampoule housing itself (this is shown by the dotted line on Fig. 2.63b) but also the thickness of the installation housing due to its diffusion welding.

The rated helium pressure in the ampoule is determined from the diagram of its dependence on source radiation time.

As is seen from Fig. 2.63a, helium pressure depends also on the free space  $v$  remaining in the ampoule after installation of the isotope. If this volume is small ( $v = v_1$ ) and is determined only by the clearance with which the isotope is installed in the ampoule, the pressure can be extremely high and the ampoule becomes heavy. If the volume is large ( $v = v_3$ ), the ampoule can also be heavy.

This diagram makes it possible to solve the problem in another manner. By assigning the pressure in the ampoule (no more than 100-120 daN/cm<sup>2</sup>), we can determine from the diagram the required free space and thus design a source.

#### Ampoule elasticity equilibrium equations

Figure 2.63b shows an ampoule of an isotopic source and an element cut out of the ampoule with the stress vectors  $\sigma_r$ ,  $\sigma_\varphi$ ,  $\sigma_z$  applied to it.

We know the dimensions of the ampoule  $a$ ,  $b$ ,  $l$ , the parameters  $p$ ,  $t$ ,  $\tau$ , and the diagram  $\sigma = E\varepsilon$ . Find  $\sigma_r$ ,  $\sigma_\varphi$ ,  $\sigma_z$ ,  $n$ .

Let us take an element from the wall of the ampoule and apply to its faces elasticity force vectors (Fig. 2.64):

$$\begin{aligned}
 N_r &= \sigma_r l r d\varphi; \\
 N_r + dN_r &= \sigma_r l r d\varphi + d(\sigma_r l r d\varphi); \\
 N_\varphi &= \sigma_\varphi l dr; \\
 N_z &= \sigma_z r d\varphi dr.
 \end{aligned}$$

We shall project these forces onto the vertical axis:

$$-\sigma_r l r d\varphi + \sigma_r l r d\varphi + d(\sigma_r l r d\varphi) - 2\sigma_\varphi l dr \frac{\sin d\varphi}{2} = 0.$$

After reducing all terms by  $l$  and  $d\varphi$ , and replacing  $\sin d\varphi \approx d\varphi$  and  $d(\sigma_r r) = d\sigma_r r + \sigma_r dr$ , we obtain the equation

$$\sigma_r - \sigma_\varphi + \sigma_r r = 0, \quad (2.82)$$

which connects the two unknown stresses. We have three unknowns; therefore, we shall seek a second equation. Let us proceed to the strain of this element.

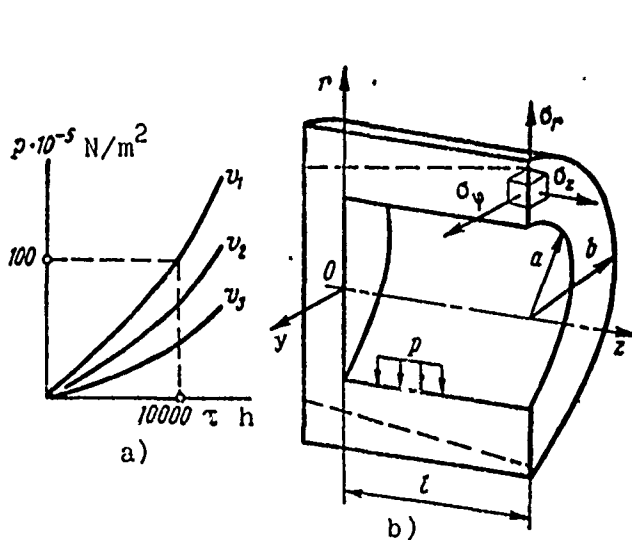


Fig. 2.63. Ampoule analysis.

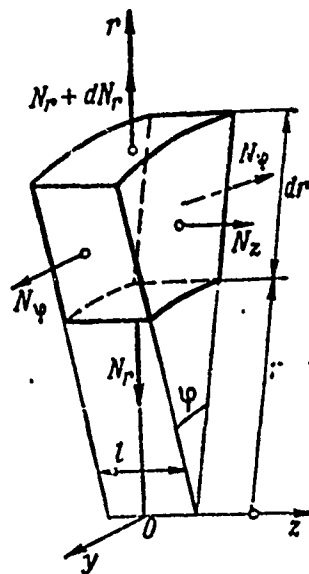


Fig. 2.64. Ampoule element.

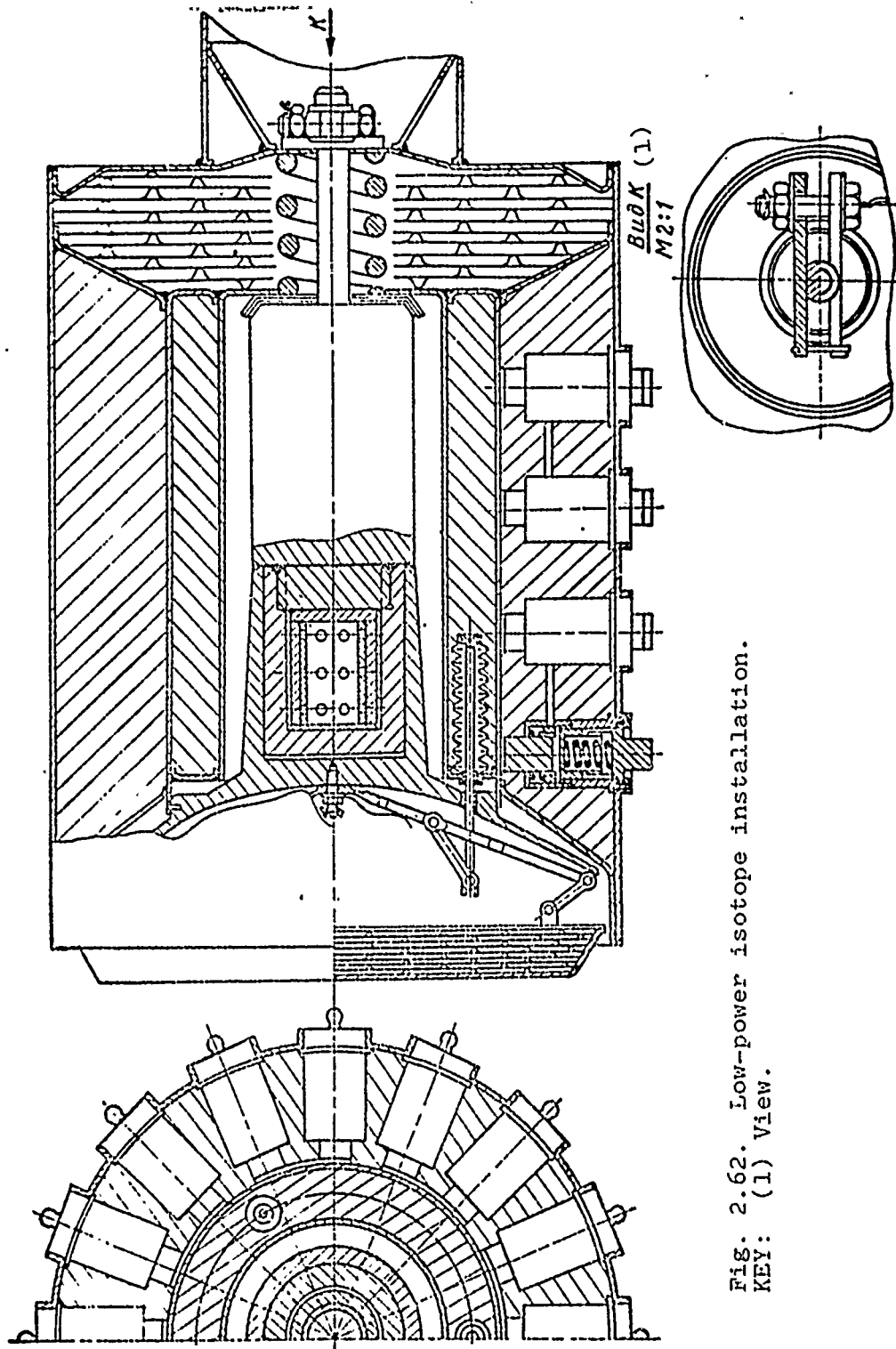


Fig. 2.62. Low-power isotope installation.  
KEY: (1) View.

It is perfectly obvious that the element is in a three-dimensional stressed state. The following dependences are valid:

$$\varepsilon_r = \frac{1}{E} (\sigma_r - \mu \sigma_\varphi - \mu \sigma_z);$$

$$\varepsilon_\varphi = \frac{1}{E} (\sigma_\varphi - \mu \sigma_r - \mu \sigma_z);$$

$$\varepsilon_z = \frac{1}{E} (\sigma_z - \mu \sigma_r - \mu \sigma_\varphi).$$

We examined the strains of the element  $\varepsilon_r$  and  $\varepsilon_\varphi$ : its elongation and the radial displacement of all points of its cross sections. The radial displacement of points of the inner surface of the element is designated by  $u$ . The points of the outer surface are displaced along the radius  $u + du$ ; thus, the thickness of this element increases by  $du$  and the relative elongation of the material in a radial direction.

$$\varepsilon_r = \frac{dr + du - dr}{dr} = \frac{du}{dr}.$$

In the direction of peripheral stresses  $\sigma_\varphi$  the relative elongation is

$$\varepsilon_\varphi = \frac{\overset{\sim}{a_1 b_1} - \overset{\sim}{ab}}{\overset{\sim}{ab}} = \frac{(r+u)d\varphi - r\varphi}{r\varphi} = \frac{u}{r};$$

hence

$$\varepsilon_r = \frac{1}{E} (\sigma_r - \mu \sigma_\varphi - \mu \sigma_z) = \frac{du}{dr};$$

$$\varepsilon_\varphi = \frac{1}{E} (\sigma_\varphi - \mu \sigma_r - \mu \sigma_z) = \frac{u}{r}.$$

Since  $\epsilon_r$  and  $\epsilon_\varphi$  are determined through the same function  $u$ , we find the strain equation. Let us differentiate  $\epsilon_\varphi$  with respect to  $r$ :

$$\frac{d}{dr}(r\epsilon_\varphi) = \frac{d}{dr}\left(r \frac{u}{r}\right) = \frac{du}{dr} = \epsilon_r.$$

We introduce into this equality the values of  $\epsilon_r$  and  $\epsilon_\varphi$ :

$$\frac{d}{dr}\left[\frac{r}{E}(\sigma_\varphi - \mu\sigma_r - \mu\sigma_z)\right] = \frac{1}{E}(\sigma_r - \mu\sigma_\varphi - \mu\sigma_z). \quad (2.83)$$

After differentiating the left side and reducing similar terms, we obtain

$$\frac{d}{dr}\left[\frac{1}{E}(\sigma_\varphi - \mu\sigma_r - \mu\sigma_z)\right] = \frac{1}{r} \frac{1+\mu}{E}(\sigma_r - \sigma_\varphi), \quad (2.84)$$

or, if we assume  $E = \text{const}$  and  $\sigma_z = \text{const}$

$$\frac{d\sigma_\varphi}{dr} - \mu \frac{d\sigma_r}{dr} = \frac{1+\mu}{r}(\sigma_r - \sigma_\varphi). \quad (2.85)$$

Substituting into (2.84) the relation (2.82), we find

$$\frac{d\sigma_\varphi}{dr} - \mu \frac{d\sigma_r}{dr} = -(1+\mu) \frac{d\sigma_r}{dr},$$

or

$$\frac{d\sigma_\varphi}{dr} + \frac{d\sigma_r}{dr} = 0. \quad (2.86)$$

For a joint solution to equations (2.82) and (2.86) we shall differentiate the first with respect to  $r$  and substitute into it the value of  $d\sigma_\varphi/dr$  from the equation (2.86):



$$\begin{aligned}\frac{d\sigma_\varphi}{dr} &= 2 \frac{d\sigma_r}{dr} + \frac{d^2\sigma_r}{dr^2} r; & \frac{d^2\sigma_r}{dr^2} r + 3 \frac{d\sigma_r}{dr} &= 0; \\ \frac{d^2\sigma_r}{dr^2} + \frac{3}{r} \frac{d\sigma_r}{dr} &= 0.\end{aligned}\quad (2.87)$$

The integral of this equation will be  $\sigma_r = A + (B)/(r^2)$ , which can be checked by direct substitution. Analogously, we find  $\sigma_\varphi = A - (B)/(r^2)$ .

The constants A and B are found from the conditions for the internal and external surfaces of a cylinder:

$$\sigma_r = -p \quad \text{при } r=a; \quad \sigma_r = 0 \quad \text{при } r=b.$$

при = when

Then

$$A = \frac{pa^2}{(b^2 - a^2)}; \quad B = -\frac{pa^2b^2}{(b^2 - a^2)}.$$

Using these values for the constants, we finally obtain formulas for  $\sigma_r$ ,  $\sigma_\varphi$  and  $\sigma_z$ :

$$\left. \begin{aligned}\sigma_r &= \frac{ra^2}{(b^2 - a^2)} \left(1 - \frac{b^2}{r^2}\right); & \sigma_\varphi &= \frac{pa^2}{(b^2 - a^2)} \left(1 + \frac{b^2}{r^2}\right); \\ \sigma_z &= \frac{pa^2}{b^2 - a^2};\end{aligned}\right\} \quad (2.88)$$

the stress  $\sigma_z$  we find from the condition of ampoule loading in an axial direction by internal pressure p.

Figure 2.65 shows diagrams of stresses in the walls of the ampoule. Maximum stresses develop on the internal surface

of the ampoule. It is important to note that radial stresses are negative.

The ampoule safety coefficient is

$$n = \frac{\sigma_{n,\tau}}{\sigma_{l \max}};$$

generalized stress  $\sigma_l$  is found from the formula for the three-dimensional stressed state:

$$\sigma_l = \sqrt{0.5[(\sigma_r - \sigma_\varphi)^2 + (\sigma_\varphi - \sigma_z)^2 + (\sigma_z - \sigma_r)^2]}. \quad (2.89)$$

The safety coefficient should be  $n = 1.1-1.2$ .

### 2.3. SOLAR ENERGY CONCENTRATORS FOR AN ERE

We know that the sun radiates tremendous energy. The density of the solar energy flux beyond the earth's atmosphere (called the solar constant) is  $S = 1.4 \text{ kW/m}^2$ , and near the earth's surface at the equator reaches  $1 \text{ kW/m}^2$ .

A flat surface is the simplest solar energy receiver. Mirror concentrators give great density of solar energy and, particularly, of thermal solar energy.

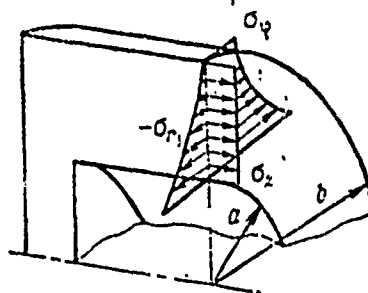


Fig. 2.65. Diagrams of stresses in ampoule walls.

The effectiveness of a concentrator is determined by the solar-ray concentration coefficient  $\gamma$ , which is equal to the ratio of the thermal flux in the collector trap to the solar flux  $S$  incoming from space. The value of  $\gamma$  is 80-2000.

The quality of the device for concentration and reception of solar energy is defined as the quantity of efficiency  $\eta_{c,h}$ , which is the product of the efficiency of the mirror and the efficiency of the concentrator trap. The efficiency of the mirror is equal to the ratio of the energy incident on the trap to the energy incident on the mirror. The energy of the trap is equal to the ratio of the outgoing trap energy to the incident trap energy. The energy of the solar concentrator for various designs and conditions is  $\eta_{c,h} = 0.2-0.8$ .

We can show the following values for the specific masses of metal concentrators:  $\gamma = 0.9-4.6 \text{ kg/m}^2$ .

The specific power of solar concentrators for these types at a trap wall temperature of  $800-2000^\circ\text{C}$  is  $N_{yA} = 0.1-0.4 \text{ kW/kg}$ .

The construction of solar concentrators is simple but they do have some shortcomings: the basic design element - the mirror - loses reflecting capacity during operation due to surface damage; the concentrator does not operate when shaded; it is not expedient to use such construction for powers above 20 kW because of its large mass and cumbersome nature.

Based on structural form, all solar concentrators can be divided into nonfolding and folding. Based on the shape of the mirror's surface, concentrators are broken down into parabolic, conical (Fresnel mirror) and spherical.

#### Structural diagrams of solar concentrators

Figure 2.66a is a diagram of a nonfolding solar concentrator with a conical mirror surface.

The concentrator consists of a mirror 1 which is formed by ring-shaped conical surfaces, a mirror base 2 which is the structural force element holding the mirror to the steel power plant, a force ring 3, three rods 4, and a thermal trap 5. This design is the simplest and can serve as an auxiliary, comparatively low-power, energy source.

Figure 2.66b is a diagram of the folding parabolic mirror for a high-power solar concentrator. The concentrator consists of mirror surfaces 1 and 2, a mirror base with a force ring 3, three rods 4, and a thermal trap 5.

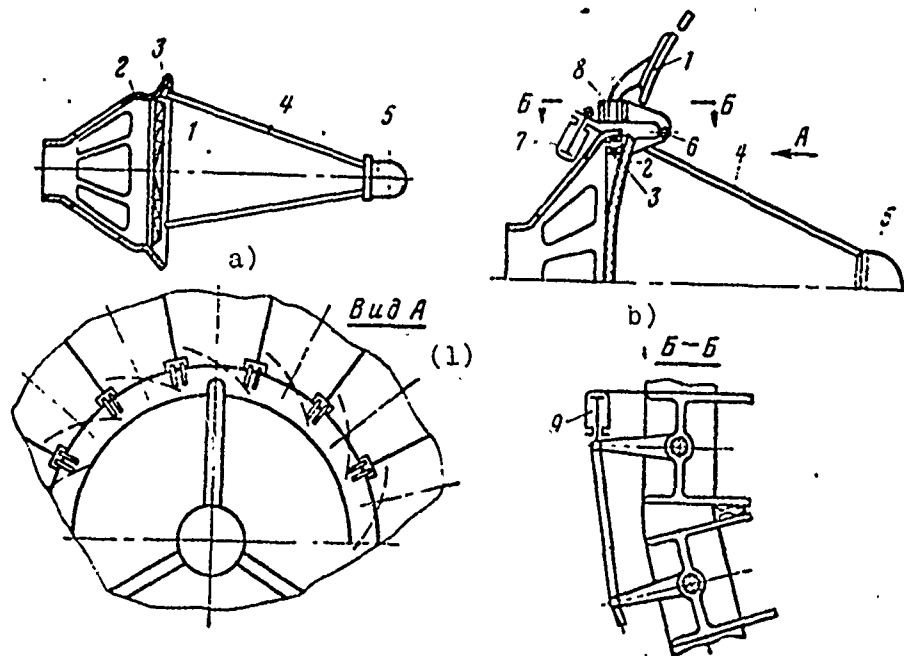


Fig. 2.66. Structural diagram of solar concentrator.  
KEY: (1) View.

To reduce the size of the mirror on launch, its upper part is made in the form of leaves which can be turned on a joint 6 by the hydraulic system and the power cylinders 7; in addition, each leaf of the mirror can be turned relative to its own axis 8 (see View A). After the leaves are turned to the working position relative to hinge 6, they are unfolded to the working position relative to axis 8 by hydraulic cylinder 9.

The dimensions of concentrators can reach 25-30 m in diameter and create power for the power plant of up to 30 kW. An example of solar concentrator mirror construction is shown in Fig. 2.67.

The mirror surface, in this case, is conical (Figure 2.67a), a multilayer rigid design. On the main force ring 1, soldered to the ring base 2, a stainless steel profiled surface 3 is installed. To improve the reflecting capacity of the surface, a layer of aluminum 4 (layer thickness 0.05-0.01 mm) is applied to it and, to strengthen this layer, another layer 5, which is similar in composition to glass ( $\text{SiO}_2$ ), with a thickness of less than 0.2 mm is also applied.

On the nonoperating side of the surface 3 a honeycomb 6 of thin aluminum (wall thickness less than 0.1 mm, view A) is soldered. Packed in the cells is fibre glass 7, a strong light insulating material. The entire structure is connected by soldering. In this way, a mirror surface is achieved which ensures high insulation efficiency.

Figure 2.67b shows the design of the joints for unfolding the mirror. To a leaf of mirror 1 is connected bracket 2 with a pivot on the end. Bracket 2 is attached to rigid frame 3 which has swing axis 4. Support 5 with axis 4 is attached to the rigid force ring 6 on the mirror, which with the mirror base 7 comprises the main structural system of the solar concentrator.

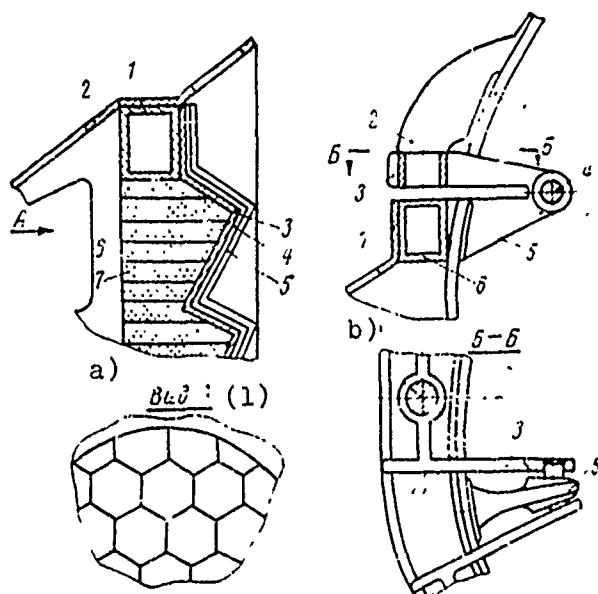


Fig. 2.67. Mirror construction.  
KEY: (1) View.

Figure 2.68 shows the design of the thermal trap, joined with the thermoemission converter. The power of the installation is 500 kW; voltage is 28 V. The trap consists of a housing unit 1, 2, 3, 4, a heat deflector 5, 6, cesium tanks 7, 8, 9, and forty converters 10, 11, 12.

The housing is made in the form of a multilayer pentagonal pyramid, between the shells 1 and 2 of which is mercury 3 and between the other two 2 and 4 are the thermoemission converters. The welded heat deflector 5 with a packing of heat-insulating material 6 is welded to the force ring 7 filled with porous nickel 8 and, at the same time, serving as one of the cesium tanks. Spherical cesium storage 9 of similar construction is attached to the summit of the trap housing. The thermoemission converter consists of a cathode tin heated with mercury, and anode 11 cooled by radiation from the surface of the trap, and a pipe 12 for channeling the cesium vapors.

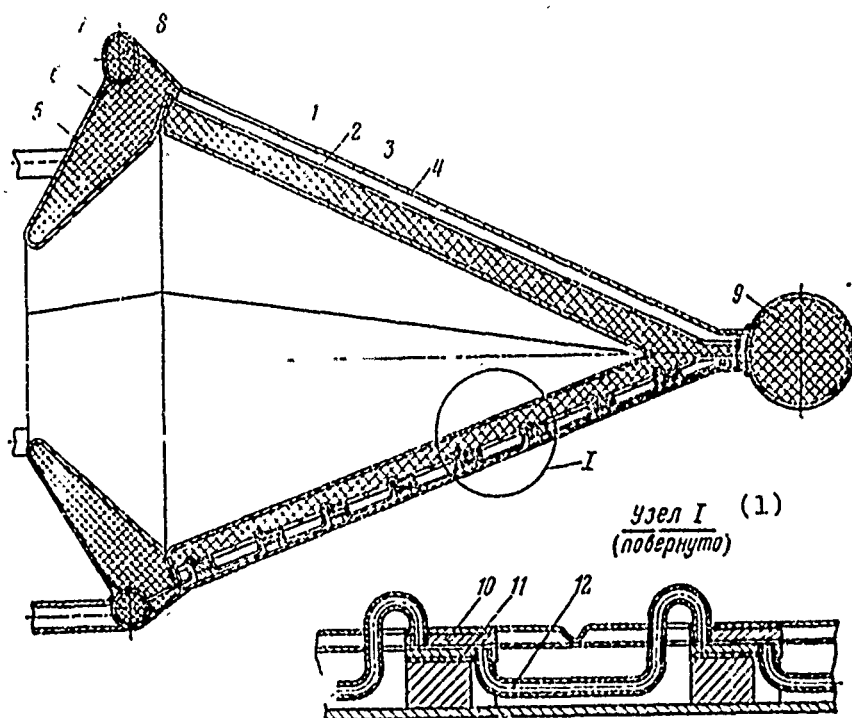


Fig. 2.68. Thermal trap.  
KEY: (1) Node I (inverted).

Fig. 2.69. Thermal trap with controllable flaps.

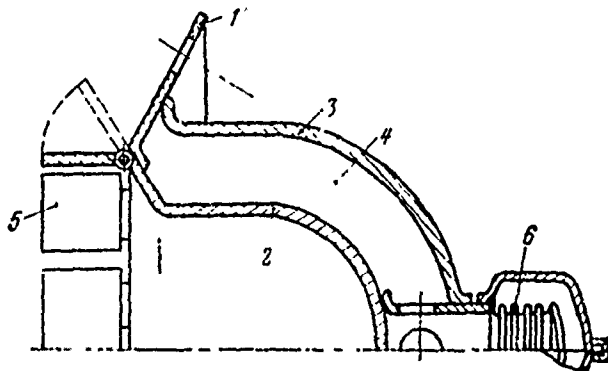


Figure 2.69 shows the design of the thermal trap with flaps for controlling the thermal flux. The trap consists of a ring 1 for attaching to the concentrator the housing parts 2, 3, which form the cavity 4 through which the liquid metal is pumped. A peculiarity of this design is the possibility of controlling the amount of thermal flux by the flaps 5. The dashes show the position of the flaps when the thermal flux is maximum. The device 6 which compensates for the variation in the volume of metal in the trap during heating is shown in the inset.

#### 2.4. FUEL ELEMENTS

A fuel element is the electrochemical device in which the chemical energy of the fuel is converted directly into electrical energy without intermediate conversion into thermal and mechanical energy.

The advantages of thermal elements are:

- high efficiency. Theoretically the efficiency of thermal elements is double the efficiency of installations with mechanical power conversion and can reach 60%;
  - low specific weight of the power installation on fuel elements, it is considerably lower than a turbogenerator converter;
  - comparatively simple structural shapes for the installation.
- There are no revolving parts as exist in installations, for example, with mechanical power conversion.

However, many aspects of fuel element operation have not as yet been studied and, particularly the problems of long performance have not been solved for the materials from which they are made.

Fuel elements with catalysts for accelerating reaction lose efficiency during operation due to irreversible processes which arise.

Let us consider fuel element classification.

*Based on the method of using the working medium* fuel elements can be divided into two groups; simple fuel elements or direct-reaction elements and regenerative elements.

In the first, as a result of a chemical reaction, electric energy, thermal energy, and reaction products are obtained. The reaction products are not used again in the fuel element. Such elements must have tanks with a working medium and tanks for the reaction products. A typical example can be oxygen-hydrogen and oxygen-carbon fuel elements. The reaction product in them is water and carbon dioxide.

In regenerative fuel elements the reaction products after regeneration are returned to the fuel element for reuse.

*Based on the type of working medium,* fuel elements can be divided into oxygen and liquid-metal. In oxygen fuel elements the process is based on the oxidation reaction of the fuel (hydrogen or carbon). These are low-temperature devices. In liquid-metal fuel elements the reaction occurs in the metal alloys; these are high-temperature devices. They have appreciably higher specific indices than the oxygen fuel elements. However, the higher temperatures and sometimes pressure make their construction somewhat difficult.

The chief difference in the construction of a fuel element is the *physical state of the working medium* entering the fuel element.



Based on this factor, fuel elements can be designated gas-gas (for example, hydrogen-oxygen fuel element), gas-liquid (lithium-hydrogen fuel element), liquid-liquid (element on metal alloys).

All fuel elements have a medium which separates the electrodes and assists the free transfer of ions from one electrode to another but prevents the transfer of neutral atoms. This medium is the electrolyte, which has in its composition atoms of the working medium of the fuel element but does not dissolve the electrodes.

Based on the type of electrolyte, fuel elements are divided into oxygen, alkaline, and liquid-metal. Electrolytes can be used in a liquid or solid (quasi-solid) state. In the latter case the fuel element has an ion-exchange membrane.

#### STRUCTURAL DIAGRAMS OF FUEL ELEMENTS

Hydrogen-oxygen and carbon-oxygen elements with a liquid electrolyte

This type of fuel element includes several designs which differ in material and shape of electrode, electrolyte, and output. The structural diagram of such a fuel element is shown in fig. 2.70.

This fuel element consists of a fuel chamber 1, an oxidizer chamber 2, porous electrodes 3 and 4 (a cathode and anode, respectively), an electrolyte 5. This is a direct-reaction element. It has a low or medium working reaction temperature; the electrolyte is a solution or melt of salts, for example, potassium (KOH), soda ( $\text{Na}_2\text{CO}_3$ ); the fuel is hydrogen or carbon and the oxidizer is oxygen.

In the example of this fuel element, operating with working media which are in various phase states (gas-liquid-gas), we find the main difficulties in creating a fuel element.

For the direct reaction of converting chemical energy into electrical, just as in a galvanic cell, in a fuel element it is:

necessary to establish direct contact between the three critical parts: the working medium (for example, hydrogen), the electrode and the electrolyte (for example, KOH salt solution). Obviously, contact between such different types of media is impossible without separating devices. In fuel elements with gas-liquid-gas working media separation is accomplished by electrodes which are made in the form of a porous body.

A sketch of such an electrode is shown in Fig. 2.70b. The central problem in designing the electrode is the evaluation and selection of pore dimensions.

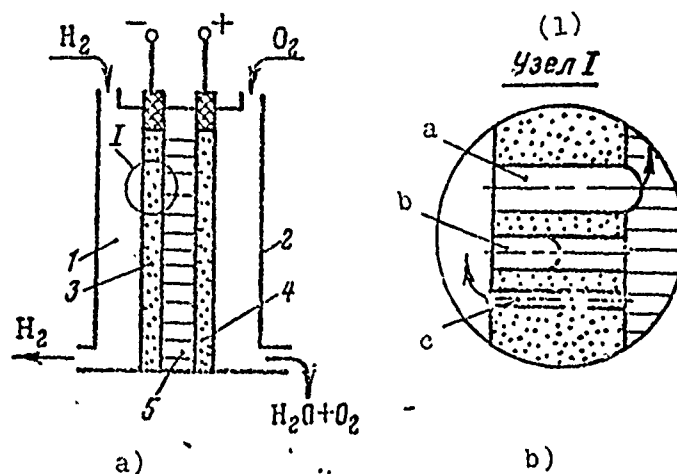


Fig. 2.70. Diagram of a hydrogen-oxygen fuel element.  
KEY: (1) Node I.

The electrode pore dimensions must be such that in the working mode of the fuel element the equilibrium of forces in the pores is preserved: the capillary pressure of the liquid, the pressure due to the surface tension of the liquid film, and the gas pressure.

In pores of extremely large dimensions (pore a) the electrolyte does not penetrate to the electrode because of the low capillary pressure. Gas, for example,  $H_2$  and  $O_2$ , can penetrate through the pore to the electrode and form a dangerously explosive mixture.

In extremely small pores (pore c) the gas does not penetrate to the electrode because of high capillary pressure. The electrolyte "leaks" into the gas cavity of the working medium, which disrupts the stable operation of the fuel element.

Only the necessary pore size (pore b), as a result of the proper selection of forces acting on the liquid and gas separating surface, ensures the stable contact of gas-reagent, electrolyte and electrode and, consequently, reliable operation.

The reason for the great structural differences of numerous hydrogen-oxygen and carbon-oxygen elements becomes perfectly clear. In addition to their difference in the electrode-electrolyte node they have other differences in the design and output parameters of the fuel element. One of the first fuel elements is the Bacon element (Fig. 2.71a). The most important difference here is the construction of the electrodes, which are designed in the form of porous nickel plates with different pore cross sections. In zone 2 of the plate, which is in contact with the gases, the pore dimensions is increased and reaches 30  $\mu\text{m}$ . In zone 3 of the plate, which is in contact with the electrolyte (KOH), the pores are reduced to 15  $\mu\text{m}$ .

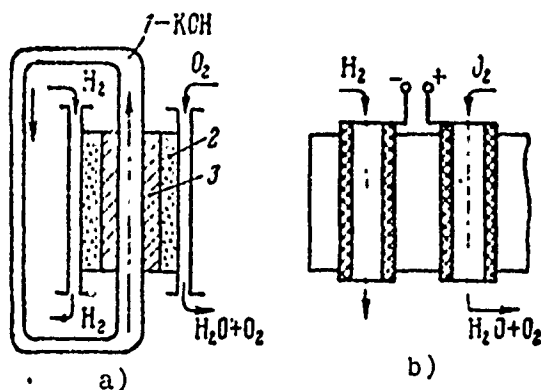


Fig. 2.71. Hydrogen-oxygen elements.

The electrolyte 1 circulates as a result of natural convection. The fuel element operates at approximately 230°C and 30-70 at. (It must exceed the vapor pressure of the electrolyte; otherwise, the latter will boil and evaporate).

Gas pressure exceeds electrolyte pressure by 0.2-0.5 at. The high working medium pressures are a disadvantage of this fuel element. Heating is accomplished by the thermal reaction which occurs in the element. An advantage of the element is its high current density, which is  $0.8 \text{ A/cm}^2$ . Voltage in the circuit is  $U = 0.7 \text{ V}$ .

Figure 2.71b shows a simplified diagram of a fuel element with activated graphite electrodes. In literature it is known as the Korden diagram.

The element is made in the form of a cylindrical sealed vessel, in which two tube electrodes are placed. Gaseous hydrogen and oxygen pass along the electrodes. The electrodes are of pressed porous activated graphite. Pores provide both a separation between the gaseous reagents and the liquid electrolyte and the diffusion necessary in order to obtain ions, electric current, and water.

This fuel element operates at  $50-70^\circ\text{C}$  and atmospheric gas pressure. The output characteristics of the element are current density  $i = 1 \text{ A/cm}^2$  at  $U = 0.7 \text{ V}$ .

The design of a carbon-oxygen element differs little from the elements examined. We know of such an element where soda  $\text{Na}_2\text{CO}_3$  serves as the electrolyte. It operates at high temperatures ( $1000-1100^\circ\text{C}$ ). The operating time element is several hours. Melted soda is aggressive. It even corrodes platinum. The element is also dangerously explosive and is inferior to an oxygen-hydrogen element in current density.

#### Hydrogen-oxygen element with an ion-exchange membrane

Liquid electrolyte in a fuel element (Fig. 2.72) creates a number of specific difficulties with its location. The need to provide a hermetic seal and packing, as well as the possibility of the electrolyte mixing with the working medium, complicates construction, makes it heavy and reduces reliability. This is

why fuel elements with a solid electrolyte in the form of a ion-exchange membrane have a considerable advantage.

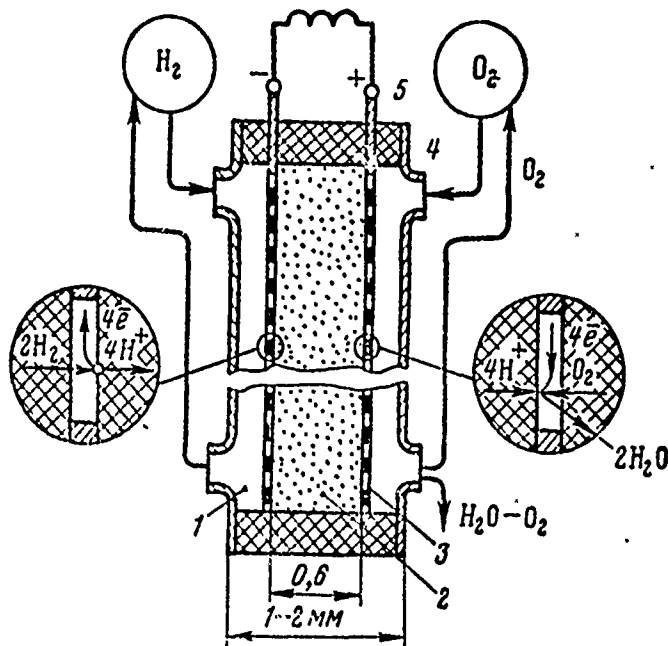


Fig. 2.72. Structural diagram of a hydrogen-oxygen element.

The ion-exchange membrane is an acid electrolyte in a quasi-solid state. Its properties, just as the properties of the electrolyte, include the fact that the hydrogen ions can move from one side of the membrane to the other and the neutral atoms cannot. Each side of the membrane is covered with a layer of platinum grid, which is the electrode of the fuel element and its catalyst. Current density  $i = 0.3-0.5 \text{ A/cm}^2$  at  $U = 0.7 \text{ V}$ . Membrane thickness can reach 0.8 mm, including the electrodes.

As seen from the drawing, the ion-exchange membrane 2 is covered with a platinum grid 3, which passes to the electrodes. The water which is in the oxygen chamber does not wet or penetrate through the electrolyte since it admits only positive hydrogen ions.

The membrane consists of a porous ceramic, mixed with a polymer, into which sulfuric acid is introduced.

The electrodes are made in either the form of solid platinum foil up to  $\Delta = 0.2$  mm thick, or, to improve the diffusion of gas through the foil, in the form of a grid of nickel wire,  $d = 76 \mu\text{m}$  in diameter (60 openings per  $1 \text{ cm}^2$ ), coated with platinum. This ensures the simultaneous contact of electrolyte, electrode, and gas.

The disadvantages of this fuel element are as follows: the element is expensive, has low current densities as compared with other elements, particularly during long-duration loading ( $j = 0.3 \text{ mA/cm}^2$  when  $U = 0.75 \text{ V}$ , which is one order less than other fuel elements).

The lifetime of a fuel element depends upon the operation of the membrane. Cracks in the membrane put the element out of service. The hydrogen used must be very pure. The operation of the element is improved if its operating temperature is above  $40^\circ\text{C}$ , but this impairs the operating conditions for the ion-exchange membrane and, consequently, the lifetime of the fuel element. The advantage of this element is its small size. One element can be 1 mm thick.

#### Regenerative fuel elements

Very advantageous is the type of fuel element where the chemical reaction products are regenerated for repeated use.

According to the diagram presented in Fig. 2.73, a fuel element can be connected with a regenerator in which the reaction products formed in the element are restored to the initial reagents and fed again to the element.

Obviously, the same amount of energy as is produced in the fuel element is fed to the regenerator. Usually regenerative devices are thermal and, therefore, they are called thermal regenerators. Also possible are other types of regenerators, for example, chemical and electrochemical.

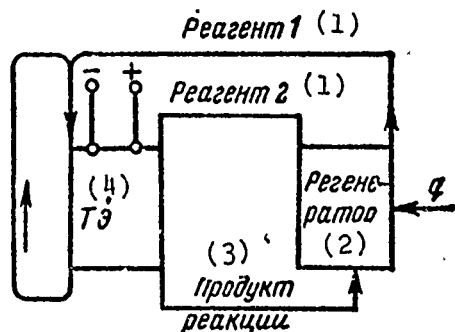


Fig. 2.73. A regenerative fuel element.  
KEY: (1) Reagent; (2) Regenerator; (3) Reaction product; (4) Fuel element.

Thermal regeneration lies in the heating of the alloy which has been formed during energy production to a temperature at which the component possessing the lowest boiling point evaporates from the alloy. Then the vapor is condensed in the condenser, collected as is the depleted alloy, and returned along separate lines to the fuel element.

It is assumed that the components have thermal and physical properties which make their separation technically possible.

#### A fuel element with thermal regeneration (lithium-hydrogen)

This is one of the simple elements with thermal regeneration (Fig. 2.74). The system consists of a fuel element 1, 2, 3, 4 (in which lithium is hydrogenized) operating at 450°C and a regenerator 5 operating at a temperature above 850°C, in which the lithium hydride disassociates into its component parts. The electrolyte is a melted eutectic mixture LiF-Li; the cathode is a porous metal electrode 3, and the anode the housing of the fuel element (1).

The structural diagram of the element is shown in Fig. 2.74. This is an example of a fuel element where the working media are in different aggregate states - liquid and gas.

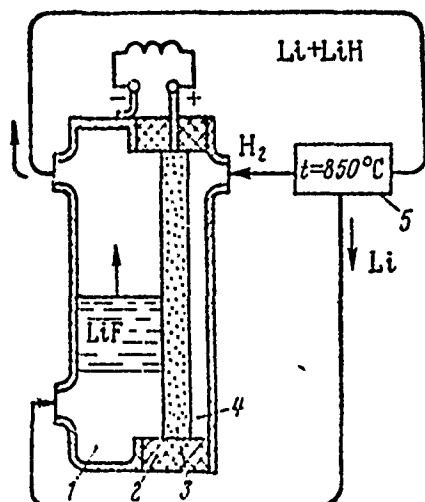


Fig. 2.74. Structural diagram of a regenerative fuel element.

#### Liquid-metal fuel element (mercury-mercury amalgam)

Sodium amalgam and mercury enter into an electrochemical reaction in the fuel element (5, Fig. 2.75). The reaction products are then thermally divided into the initial reagents by means of distillation in the regenerator 2; heat for separation is obtained from heat source 1.

The basis of the fuel element consists of a porous ceramic ion membrane saturated by an electrolyte of liquefied sodium salt. The melt is held in the pores of the membrane by capillary forces. When the sodium flows through the element, its atoms are transformed into ions on the surface of the membrane, giving a negative charge to the electrode.

Simultaneously the sodium ions are transformed into atoms on the surface of the second electrode where they react with the mercury, forming an intermetallic compound of the  $\text{Na}_x\text{Hg}$  type. As a result of the overflow of sodium ions, the sodium concentration near the negatively charged surface of the membrane decreases; near the positively charged surface the mercury is saturated by a weak solution of sodium.



As a result of the process, the depleted sodium and mercury amalgam leave the element. Then both of these flows are united and, an electromagnetic pump, are pumped into the regenerator 2.

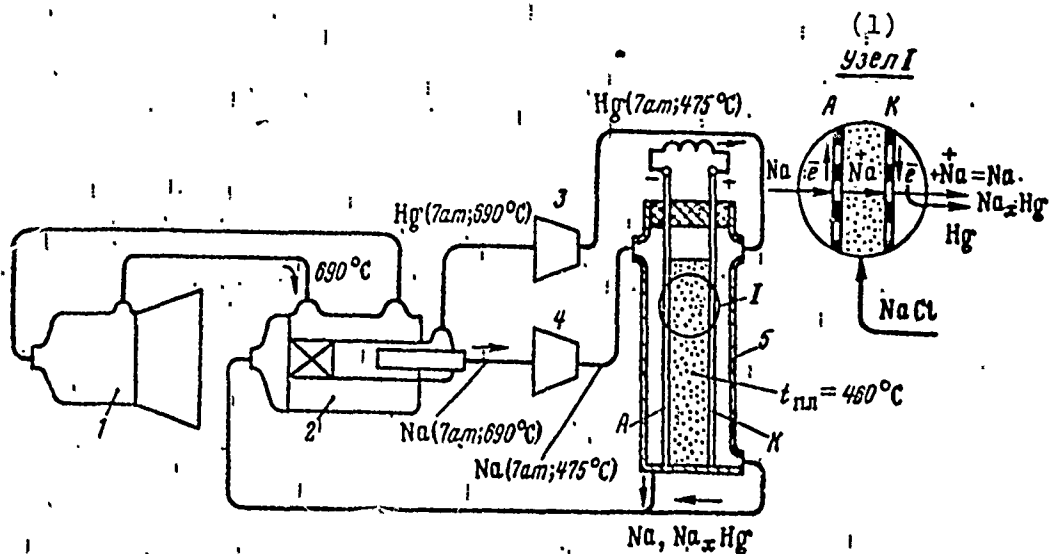


Fig. 2.75. Structural diagram of a mercury fuel element.  
KEY: (1) Node.

[am = at;  $t_{mn}$  = melting point].

In the separator of regenerator 2, while being heated from an extraneous heat source 1 (reactor, heat trap, solar concentrator), the amalgam is enriched with sodium.

The more easily evaporating part, - mercury - passes into the condenser 3; hence liquid mercury moves to the fuel element. Enriched with sodium, the alloy moves to condenser 4 and, thence, after reaching temperatures of  $\sim 475^\circ\text{C}$ , to the fuel element.

A peculiarity of the electric energy regeneration process is the fact that the transformation of chemical energy into electrical is accompanied by the absorption of heat during the regeneration of an alloy and the release of heat during the condensation of mercury vapor and the cooling of enriched alloy.

Since heat release is best carried out at the maximum possible reagent temperature, the temperature of the radiator is set at  $475^{\circ}\text{C}$  (according to the working medium); this temperature, with which the alloy and the mercury enter the fuel element, is determined by the efficiency of the electrolyte. Actually, the optimal temperature of the electrolyte is its melting point. In this example, the melting point is  $460^{\circ}\text{C}$ .

The pressure of the mercury vapor leaving the separator is  $\sim 7$  at. With the same pressure the enriched alloy of mercury amalgam enters the fuel element. Thus, the membrane in the element bears no loading from reagent pressure.

Figure 2.76 shows the construction of a hydrogen-oxygen element. The ion-exchange membrane 1 is covered with a thin platinum grid. Hydrogen is fed to the membrane through pipe 3, oxygen through pipe 4. The closed cavity 5 holds the coolant supply. Elements 6 fix the wall and hold the wick 7 which collects and drains the water formed as a result of the element's operation. The membranes 1 are insulated by insulators 8.

Figure 2.77 shows the construction of a liquid-metal fuel element. The ion-exchange membrane 1 is soldered to the steel rim 2; it separates two cavities of active metal A and B formed by thin plates 4. The membrane is attached with wires 3; they ensure a uniform opening for cavities A and B. Parts 2 and 4 of the element are insulated by a layer of  $\text{Al}_2\text{O}_3$  5. The metal alloy is drained through pipe 6.

Figure 2.78 is a drawing of a lithium-nitrogen fuel element and a unit of such elements. The element consists of a cathode 1 of vanadium, a magnesium electrode 2, and an electrolyte - lithium-nitrogen 3. The reaction product nitrogen is eliminated with filter 4. The change in the dimensions of the element during operation is compensated by spring 5. Heater 6 is provided to warm up the element.

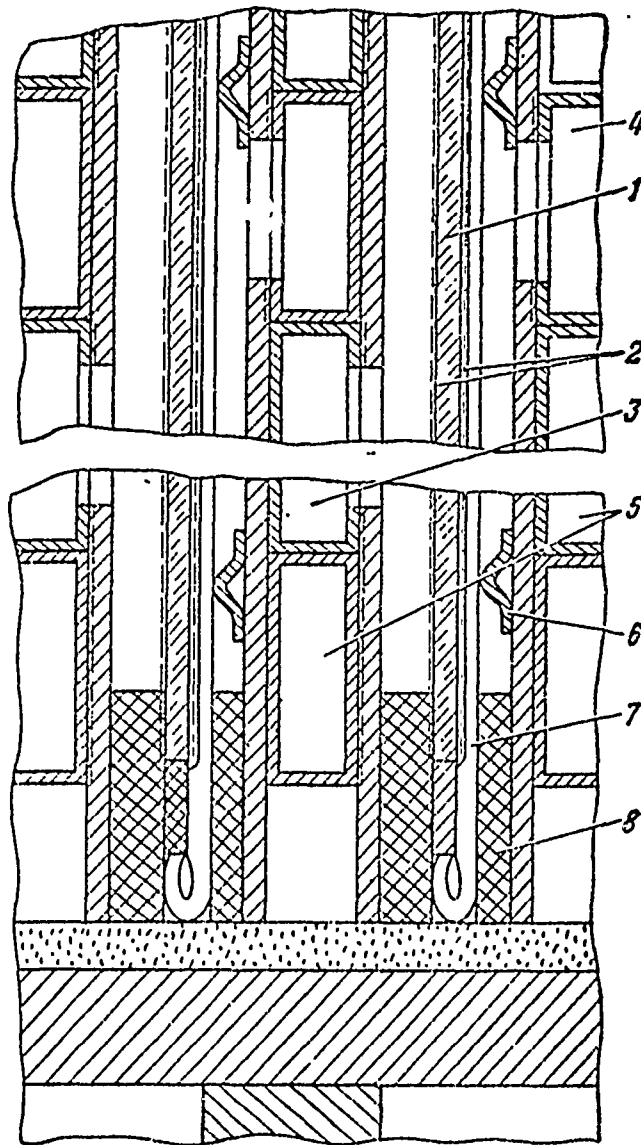


Fig. 2.76. Construction of a hydrogen-oxygen fuel element.

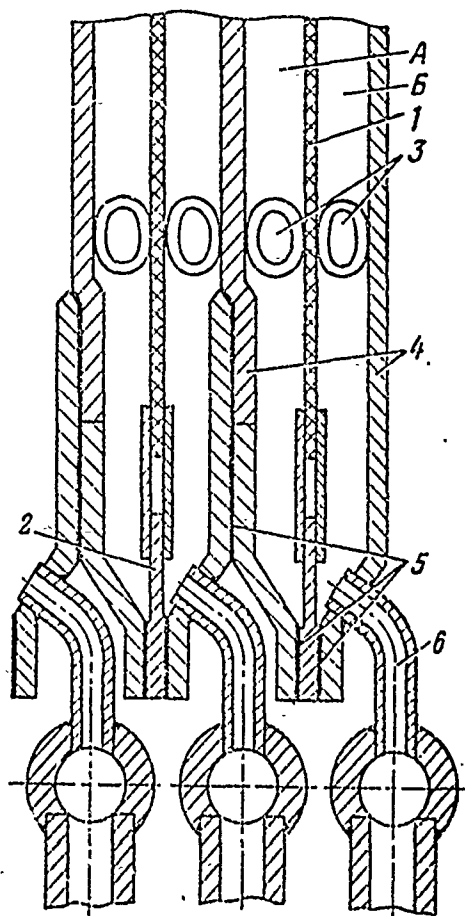


Fig. 2.77. Construction of a liquid-metal fuel element.

In this fuel element the functions of the fuel and the anode (lithium), as well as the oxidizer and the electrolyte (nitrogen) are combined, which appreciably simplifies construction and decreases the weight of the installation.

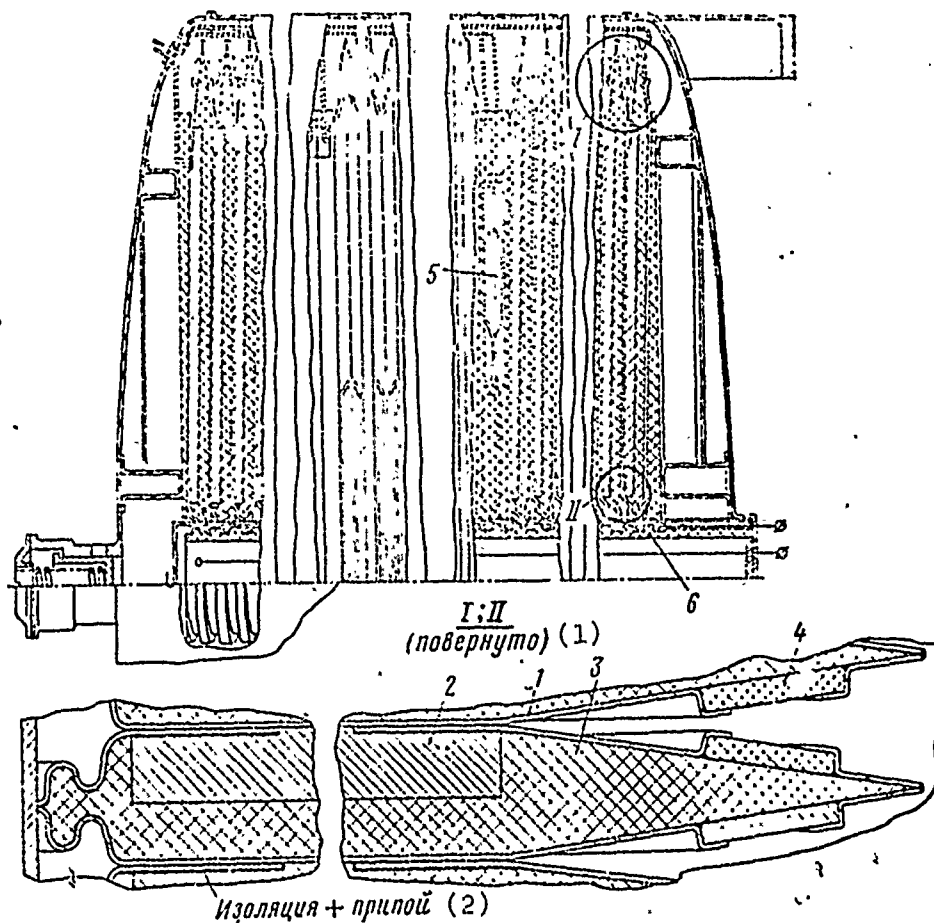


Fig. 2.78. Construction of a liquid-metal regenerative fuel element.  
KEY: (1) Inverted; (2) Insulation + solder.

## CHAPTER III

### CONVERTERS

#### 3.1. MECHANICAL CONVERTERS

Of the familiar methods of converting thermal energy into electrical, the turbogenerator method occupies a peculiar position. This method of obtaining electrical energy is historically established and there has been considerable design and operational experience in this area of technology.

Thermal energy obtained, for example, from the combustion of a chemical fuel or from the decay of a nuclear fuel in a reactor, goes to heat the working medium and obtain the vapor which brings the turbine into operation.

A turbine is the lightest and most compact of all known machines for transforming thermal energy into mechanical. The mechanical energy of a turbine, in turn, is converted, by a generator connected to the turbine, into dc or ac current of various frequencies. Such converters make it possible, with limited size factors, to obtain high-power electrical current (100 kW and higher). In addition, with the mechanical conversion of energy we obtain the highest conversion efficiency (40-50%).

In extraterrestrial power plants with mechanical energy converters, the use of turbines operating on the Rankine steam cycle is proposed (the efficiency of the Rankine cycle approaches the efficiency of the ideal Carnot cycle).

Figure 1.3 shows one of the possible ERE systems with a power plant operating on the Rankine cycle [34].

As working media in the turbine of an extraterrestrial power plant, we proposed the use of the vapors of such metals as mercury, potassium, sodium, sodium and potassium alloys, etc. Liquid-metal heat-transfer agents have high boiling points with comparatively low pressures, which makes it possible to maintain low pressure in the power plants. This is particularly important for an extraterrestrial plant, where the heat removal of the cycle (heat release into the ambient medium) is only effective at high temperatures. The characteristic processes of boiling and condensation for such heat-transfer agents and the high heat-transfer coefficients make it possible to transfer considerable amounts of heat in small and light weight heat-exchange devices.

On the other hand, the use of these heat-transfer agents poses the problem of the selection of structural materials which will preserve sufficiently high strength and corrosion properties at high temperatures in a medium of liquid metals and their vapors.

Because of the low viscosity of liquid-metal heat-transfer agents, comparatively low powers are required to pump them in extraterrestrial power plants. This permits the location of the heat-exchange apparatus away from the energy converter (which is advantageous from the installation point of view); of course, it should be kept in mind that the mass of the heat-transfer agent in the pipelines can appreciably affect the specific mass of the entire system.

#### Selection of basic parameters for the circulating part of turbines

A turbine must have high efficiency, be reliable in operation, compact, and light-weight. These requirements govern the selection of working medium parameters and the basic dimensions of a turbine.

For extraterrestrial power plants we usually use axial (single- and multi-stage) turbines since they do not limit power, have high efficiency, and insignificant weight.

The main dimensions of a turbine include the diameter of the rotor wheel along the average cross section of the blades ( $d_{cp}$ ) and the length of the blade ( $l$ ).

The diameter of the rotor wheel

$$d_{cp} = \frac{60u_{cp}}{\pi n}, \quad (3.1)$$

where  $n$  is the number of revolutions per minute (selected by gas-dynamics analysis of the turbine based on the magnitude of stresses in the root section of the blades);

$u_{cp}$  is the circular velocity on the average diameter of the turbine.

Although for gas turbines the value of  $u_{cp}$  reaches 350 and even 450 m/s (when  $d_{cp}/l = 5-6$ ) and is limited only by the condition of rotor part strength (blades, disks), for steam turbines the circular velocity should be limited to a value of no more than 275 m/s (when  $d_{cp}/l < 5$ ) because of the erosion of blades and other rotor parts due to vapor condensation during expansion in the turbine and the impact of the rapidly moving parts with the condensate.

The length of the blades (in m) is determined from the mass-per-second flow rate  $G$  of the working medium:

$$l = \frac{G}{\pi d_{cp} C_d \rho}, \quad (3.2)$$

where  $\rho$  is the density of the working medium at the nozzle output in  $\text{kg/m}^3$ ;



$C_a$  is the axial velocity of the working medium in m/s. We can assume  $C_a = 140-170$  m/s.

The working part of the blades is designed according to the velocity triangles known from gas-dynamics analysis.

With short blades ( $l = 10-20$  mm) it is expedient to use active turbines. The longer blades are a better design according to the principle of reactive turbines since higher efficiency can thus be obtained.

The chord of the blade  $b$  and the pitch  $t$  are matched with the length of the blade. As blade length increases  $l/b$  the axial dimensions of the turbine stage decrease; however, the stresses from bending and vibrations also increase. First-stage blades operating under more difficult conditions are usually shorter ( $l/b = 1.5-2.5$ ) than last-stage blades.

By cascade solidity we mean the ratio  $b/t$ . To reduce weight an attempt is made to increase the cascade solidity by decreasing the pitch. Minimum blade pitch is usually determined by the spacing of the blade shafts on the crown of the disk. The maximum value of  $b/t$  in the root lies within 2-2.2.

The chord most frequently is constant along the length of the blade.

An increase in the chord  $b$  toward the periphery increases the efficiency of the turbines; however, the vibrational reliability of the blade foil is reduced. Decreasing the thickness of the profile sections of a blade improves the gas-dynamic qualities and reduces the weight of the rotor wheel; however, stresses in the blades grow.

Usually blades are made with a variable cross-sectional area; for long and highly loaded blades the ratio of the area  $F(r_0)$  of the root to the area  $F(R)$  of the end is  $F(r_0)/F(R) = 4-6$ , and for short and less loaded blades  $F(r_0)/F(R) = 2-3$ .

The areas of the intermediate sections change exponentially (see below, "Stress Analysis of Working Blades").

Structural diagrams and designs for bracing the working blades to the rotor

The bracing node holding the working blades to the rotor experiences considerable loads mainly from the centrifugal forces of the blades.

The requirements imposed on the bracing nodes include the following: the spacing of a given number of blades with sufficient bracing strength, blade installation accuracy, identity of blade seal (ensuring a small spread of free oscillation frequencies), the least weakening of the disk's crown by the bracing, the least loading of the disks from the bracing, and ease of installation.

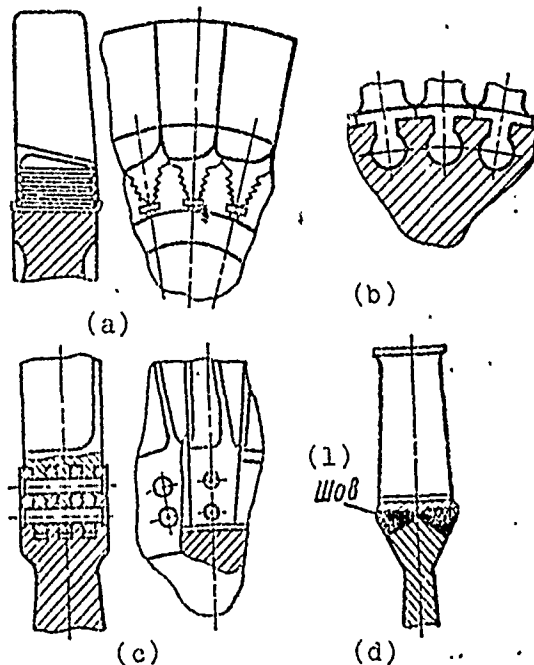


Fig. 3.1. Various methods of bracing working blades to turbine disks: a - with a "tree" lock; b - with a cylindrical lock; c - with a "fork" lock; d - welded. KEY: (1) Seam.

Figure 3.1 shows working blades of turbines and various methods of attaching them to the disks.

Of the dismountable bracings the most widely used is the one with the "tree" lock (Fig. 3.1a). This is a union in which the material of both the lock part of the blade and the disk is used well; the small dimensions of the lock along the circumference of the disk enable the placement of a large number of blades on the crown. Thanks to the free fit of the blade shaft in the groove of the disk, the possibility of additional thermal stresses occurring in the disk is reduced (due to the freedom of thermal strains). Centrifugal force presses the blade shaft to the projection of the disks all along the supporting surfaces; thus the blade is self-aligning and a high degree of uniformity in load distribution is ensured. These advantages of a "tree" lock are achieved by a high degree of purity and precision in its manufacture (the disk grooves are processed by drawing; the blade locks are obtained by accurate milling or stretching with subsequent polishing). The free fit of the blades facilitates their installation.

Other types of dismountable bracings include cylindrical (Fig. 3.1b) and forced locks (Fig. 3.1c). However, these bracings are not widely used.

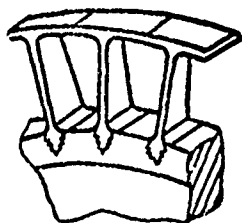


Fig. 3.2. Moving blades of a turbine with bandage webs.

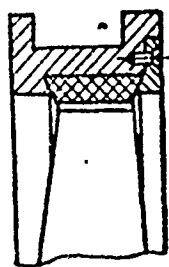


Fig. 3.3. Metal-ceramic inserts in turbine housing to reduce the radial gap between housing and blade ends (on working revolutions).

In a number of cases a nondismountable rigid bracing of the blades to the disk is accomplished by welding (Fig. 3.1d). Such bracing has high strength characteristics. However, we must correctly select blade and disk materials from the welding point of view and also check the quality of the weld and the accuracy of the blade installation before welding.

Blades can be attached to the disk by soldering with high-temperature solder. With small turbine dimensions blades can be cast together with the disks according to the models to be smelted. To reduce gas overflows through the radial gap and increase turbine efficiency, blades with bandage webs are used (Fig. 3.2). Bandage webs increase the rigidity of the blade and improve its vibrational character. However, they increase the stresses in the blade foil from centrifugal forces. Sometimes with long blades bandaging can be replaced by metal-ceramic inserts on the turbine housing (Fig. 3.3), which, on working revolutions, enable the radial gap between the turbine housing and the blade ends to be reduced to a minimum..

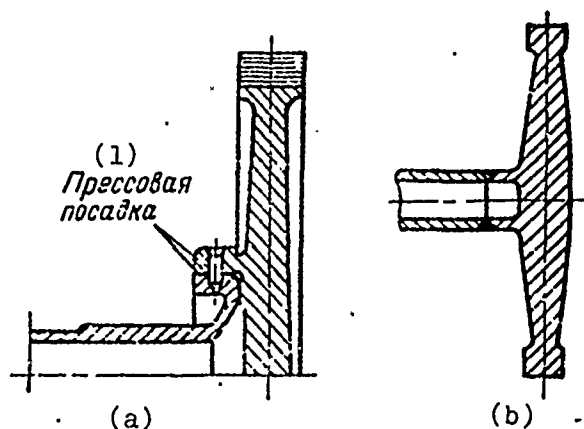
#### Turbine disks and connection with the shaft

Turbine rotors operate at high circular velocities and working temperatures. For these operating conditions, disk-type rotors with one crown are usually used (two-crown disks are used sometimes in quiet turbines or in turbines with very short blades to reduce weight).

In multistage turbines drum-disk rotors are used since lateral stiffness in such turbines is high.

For reasons of strength, an attempt is made to make disks without central openings (see "Stress Analysis of Disks"). When central openings cannot be avoided, disks are strengthened by thickening them near the openings.

Fig. 3.4. Union of disk with shaft: a - with a centering band and radial pins; b - by welding.  
KEY: (1) Force fit.



Joints between disks (in multistage turbines) and between a disk and the shaft are critical points in turbine design. These nodes must have high mechanical strength in order to transmit torque and axial forces and ensure the reliable installation of adjacent parts under all operating conditions as well as sufficient flexural stiffness for the rotor.

Connections of disks to each other or to the shaft can be dismountable. However, for simplicity and reliability these joints are better made nondismountable, for example, pressing the disk to a central collar on the shaft (Fig. 3.4a) or another disk and installing radial pins on the force fit.

The simplest is the connection of a disk to the shaft by welding (Fig. 3.4b) or by forging the disk and the shaft as one piece (with small rotor dimensions).

Nozzles consist of nozzle blades forming a circular cascade and bands forming the outer and inner walls of a ring-shaped system for the working medium.

The dimensions and shape of nozzle blades are determined on the basis of gas-dynamic analysis.

Nozzles must have sufficient stiffness during turbine operation, in order that the output angle of the working medium flow does not change (the efficiency of the turbine, its power and flow rate through the nozzle depend on this); the attachment must provide freedom of thermal strains to avoid the appearance of thermal stresses and warping. Therefore, nozzles are not included in the turbine housing diagram as load-bearing elements connecting the internal and external housing of the turbine.

The attachment of the nozzle blades can be double-seat or cantilever.

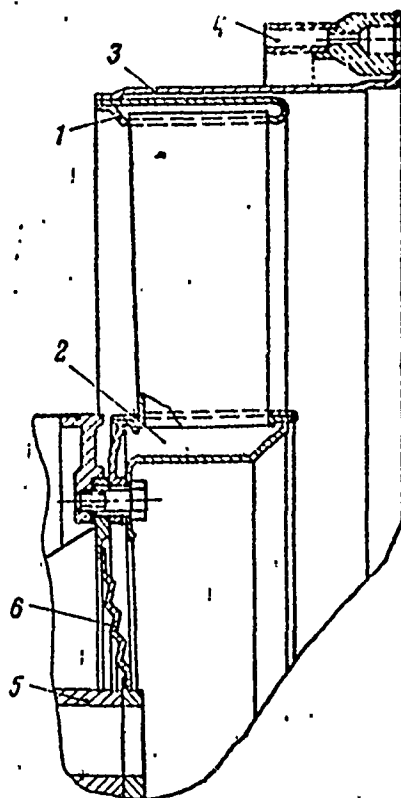
With double-seat attachment blades can be rigidly attached in both binding bands (in this case, cuts are made in the band every 4-6 blades), rigidly fixed in one band while in the other they are free, or, finally, freely set in both bands.

Usually nozzles are permanent - made by precision casting of sections with 2-4 blades each or in the form of a common casting, as well as welded, by welding the blades to the bands. An example of a welded nozzle is shown in Fig. 3.5.

The housing of a gas turbine absorbs the loads from the rotor (through bearings) and nozzle apparatuses and transfers them to the adjacent housings and the thermal power plant system. The housing should have high flexural rigidity, which does not allow the contact of the rotor and the stator during strain. The structural form of turbine casings depends upon the location of the rotor support, the means of bracing the nozzle apparatuses, and the means of housing manufacture. The primary structure of the housing must be shielded from the effect of the aggressive vapors of the working medium by means of installing single or double shields and channels along which the coolant should be pumped. This also pertains to the load-bearing elements which transmit the forces from the bearings to the external housing. The coupling points of adjacent elements of the housing should have centering collars. In order to avoid

warping, the material of the housing being joined is selected with the necessary coefficients of linear expansion and cooling is provided. For the purpose of pressurization, joints are usually welded.

Fig. 3.5. Welded nozzle apparatus with the welding of blades to an internal binding band: 1 - external band; 2 - internal band; 3 - elastic rim; 4 - external housing; 5 - bearing housing; 6 - elastic diaphragm.



#### Rotor mounts

Up to 500 kW the rotor of a turbogenerator is usually made to be permanent; i.e., the rotors of the generator and turbine are rigidly connected to each other. In this case, the rotor is double-seat. At high powers it is necessary to place the turbine and generator on independent supports and transfer the moment from the turbine to the generator with the aid of a clutch.

The reliability and service life of turbomachines depend to a considerable degree upon the bearings.

Under conditions of interstellar flight, gravitational forces are absent (this is the common state of an extraterrestrial flight vehicle). A steady load does not fall on the bearings. Instead of this, the bearings absorb forces which are variable in magnitude and direction and appear as a result of the misbalance of the rotor (which always takes place despite the careful manufacture of the parts), variable forces which appear with a variation in the parameters of the steam in the circulatory part of the turbine, and, finally, magnetic forces due to the eccentricity of the rotor relative to the stator. Time-variable loads on bearings can cause fatigue.

Gravitational forces can be created by revolving a spacecraft around certain axes to get a constant centrifugal force. If this force is sufficiently great as compared with the forces of disbalance and other variable forces, the service conditions of the bearings are almost the common conditions when bearings absorb static load.

Especially large loads appear on the bearings at the insertion of a spacecraft into orbit when the accelerations exceed terrestrial by several times. In this case, large vibrational accelerations can also arise. If the converter system does not work during the insertion into orbit, the problem of bearings is reduced to the solution of common questions connected with strain and fatigue.

At elevated temperatures in a medium of a liquid-metal heat-transfer agent, common antifriction bearings cannot be used. Even if these bearings are precision bearings and manufactured from special heat-resistant alloys, their lifetime is short.

Bearings of dry and semiliquid friction with graphite inserts (Fig. 3.6a) also cannot be used due to their rapid wear. Sleeve bearings from titanium carbides and tungsten (Fig. 3.6b) have a somewhat longer lifetime but are very brittle and during operation, due to the friction of the working surfaces, they wear and change their geometric dimensions. In order that the bearings be not superheated, it is necessary to cool them; this is possible by using the good cooling properties of liquid metal.



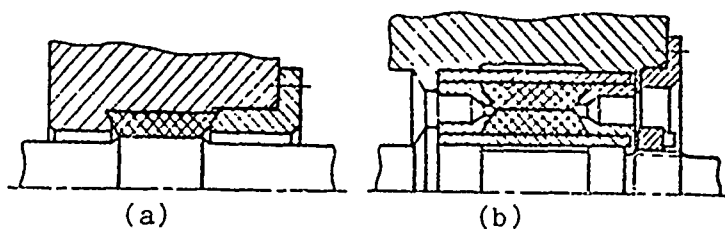


Fig. 3.6. Dry-friction bearings: a - with graphite inserts; b - with inserts made of tungsten and titanium carbides.

Slider-type bearings, in which the friction surfaces are separated by a layer of liquid, are more promising for use in the turbogenerator of extraterrestrial power plants. Two types of these bearings, differing in the means of obtaining bearing power in the liquid layer, are used today. The best known is the hydrodynamic bearing, whose carrying capacity in the carrying layer of liquid is created during the rotation of the central shaft which traps (because of viscosity) the lubricating liquid and drives it into the wedge-shaped clearance between the center shaft and the bearing insert (the housing).

During the rotation of the shaft, under the effect of the difference in the hydrodynamic pressures of the lubricating liquid in the clearance, the shaft comes up and the center line of the shaft neck turns angle  $\varphi$  in the direction of rotation (Fig. 3.7); purely fluid friction is thus ensured. Figure 3.7 shows the typical distribution of surplus hydrodynamic fluid pressure in the bearing clearance. The resultant forces of the pressure during purely fluid friction are equal in magnitude but reverse in direction to the carrying capacity  $P$  of the bearing.

It should be noted that the necessary load-lifting capacity of such a bearing is obtained with fully defined rotational velocity of the shaft (which should be lower than operating), a determined clearance, and a determined viscosity of the lubricating liquid.

With a low shaft rotation rate the bearing touches and dry friction appears. In order to eliminate misalignments and non-coaxiality (which also leads to metal-to-metal contact and dry friction), it is advantageous to use self-adjusting bearings.

The working medium is used as the lubricating liquid in the bearings of ERE turbogenerators, i.e., the same liquid-metal heat carriers as used in the main system. A number of difficulties arise with the use of common oils, in the first place, in creating gaskets capable of preventing, over a long period of time, the break-through of working medium vapors into the cavity of the bearings or the flow of the lubricant into the cavity with the working medium, as well as lubricant leakage.

As we know, the viscosity of liquid metal is very low (absolute viscosity of liquid-metal heat carriers is approximately 10-100 times less than common lubricating oils). Therefore, the working clearances in the fluid-friction bearing should be approximately 10% of the clearance in common oil bearings. In order to prevent the metal-to-metal contact which is destructive to the bearing, erosion, and the phenomenon of fatigue, we must strictly maintain this clearance during the operation of the turbogenerator.

Figure 3.8 shows the construction of a hydrodynamic bearing which handles liquid-metal lubrication. The bearing is a bushing with a ring groove installed in a spherical seat. To prevent the turning of the bushing, a pin has been installed. A bushing without a pin (the floating type) is also possible. The clearances between shaft and bearing and also between spherical ring and housing are set by selection.

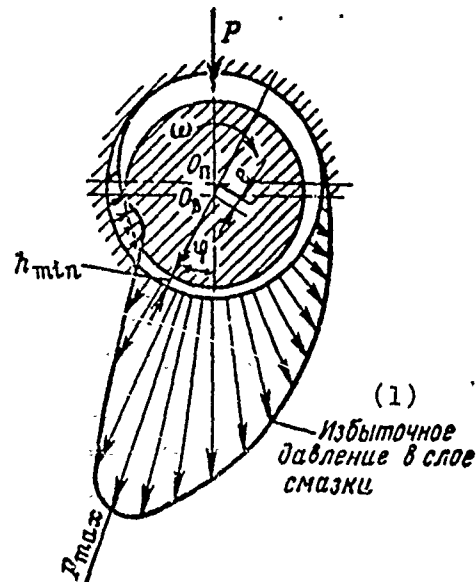
The bearing and the housing are made from an alloy of molybdenum with tungsten and titanium.

Pressed to the shaft is a bushing of tungsten carbide. The lubricant feeds through the opening in the housing, falls into the

ring groove, and through the inclined opening in the bearing toward the circular channel on the inner side of the bearing.

Fig. 3.7. The typical pressure distribution in the lubricant film of a hydrodynamic bearing during shaft rotation.

KEY: (1) Surplus pressure in the lubricant film,



From the channel the lubricant enters the working clearance between the center shaft and the bearing. Such a bearing can work at a temperature up to approximately 900°C. With a reduction in temperature the viscosity of the working liquid and the bearing capacity increase.

Less known yet is the so-called hydrostatic bearing. External load in such a bearing at any speed (even at  $n = 0$ ) is balanced basically by the hydrostatic pressure in the carrying layer of the liquid, ensured by the external (relative to the bearing) source of pressure - a pump.

In hydrostatic bearings any liquids, including liquid metal, can be used.

The external load in the normal operation of a hydrostatic bearing is absorbed by a continuous layer of liquid, which eliminates the possibility of dry contact.

The ability of hydrostatic bearings to absorb loads of different magnitudes is favorably combined with an extremely low coefficient of friction, on the order of  $4 \cdot 10^{-6}$  -  $7 \cdot 10^{-6}$  [47].

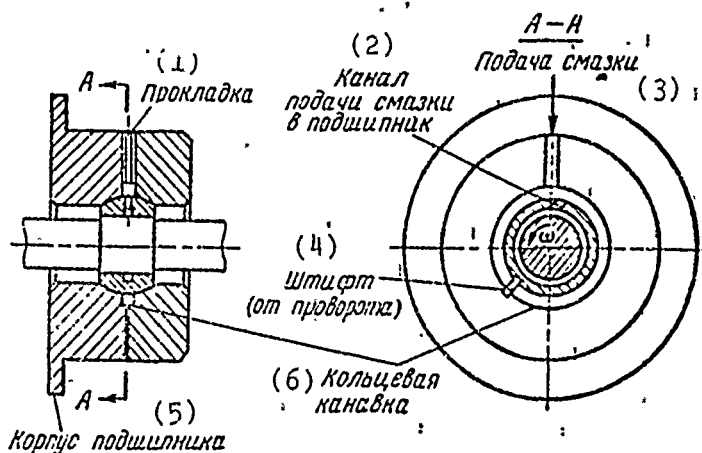


Fig. 3.8. Hydrodynamic bearing.

KEY: (1) Operator; (2) Channel of lubricant supply to bearing; (3) Lubricant supply; (4) Pin (from turning); (5) Bearing housing; (6) Ring groove.

To explain the principle of the operation of a hydrostatic bearing, let us examine Fig. 3.9. The center shaft is rotated in a fixed bushing which has on the side turned toward the center shaft several insulated chambers. The working liquid under initial pressure  $p_H$  is fed into the chambers from outside through proportioning openings (discharging jets). When eccentricity  $e = 0$ , clearances at the output of all chambers are equal, the fluid pressure in all chambers is equal, and the bearing capacity is equal to zero.

With a displacement of the shaft a certain distance from the axis, pressure in the chamber changes. In the chambers toward which the center shaft approaches, hydrodynamic drag during the outflow of liquid from them increases, as well as pressure. In the opposite chamber the pressure, on the contrary, decreases as a result of the reduction in hydrodynamic resistance at the output from the chambers.

Along with the variation in hydrodynamic resistance during the outflow of liquid from the chambers, the flow rate through the chambers and the discharging jet at the input to every chamber also changes. Thus, in the chambers where the clearance at output is decreased, the flow rate is also decreased and, together with this, resistance is reduced during the flow of lubricant through the discharging jet, and vice versa. All this gives rise to a pressure increment in some chambers and to a reduction in others, which creates the carrying capacity which balances the external load.

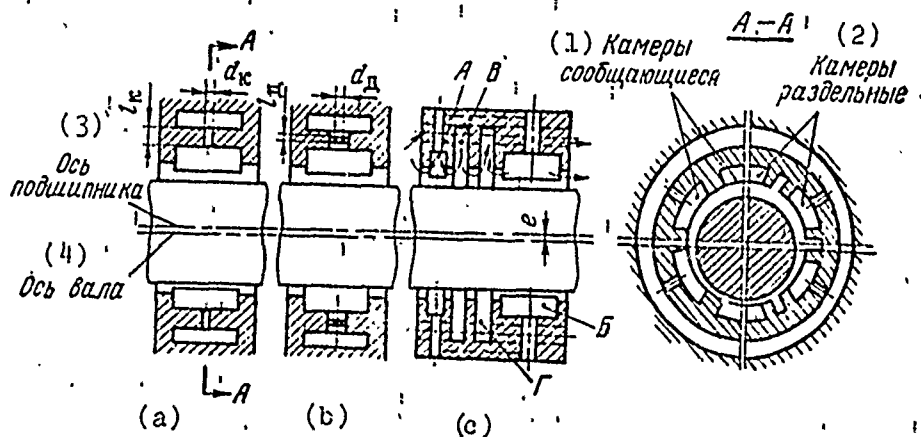


Fig. 3.9: Structural diagram of hydrostatic radial bearings: a - with capillary compensation [ $(l_k)/(d_k) > 10$ ]; b - with diaphragm compensation [ $(l_d)/(d_d) < 3$ ]; c - with slot compensation (with reverse slot choking).  
KEY: (1) Communicating chambers; (2) Separated chambers; (3) Bearing axis; (4) Shaft axis.

Figure 3.9 shows several structural diagrams of radial hydrostatic bearings: with capillary compensation (a), with diaphragm compensation (b), and with slot controllable compensation (c). The operation of bearings with capillary and diaphragm compensation is understandable from the foregoing:

Let us examine the work of bearings with slot controllable compensation (c). The working liquid in such a bearing first enters the chambers A, from which along the radial drillings and the helical

flutings on the outside diameter of the housing, it falls into the diametrically opposite working chambers 5. Circular channel 8 serves for the additional feeding of chambers A. The circular channel 7 is provided with a drainage cavity.

With the displacement of the shaft downward the upper clearance between the shaft and the bearing housing will increase and the lower will decrease. In this case the filling of the upper chambers A with liquid is facilitated and, correspondingly, the resistance at input to the lower chambers A increases. Simultaneously, the resistance at output from the upper working chambers 5 decreases and at the output from the lower working chambers 5 increases. All this leads to the appearance of a greater pressure differential in the working chambers 5 and to the creation of lift.

The described diagram of a hydrostatic bearing with reverse choking is more effective than a bearing with capillary or diaphragm compensation.

It is necessary to note that with the misalignment of a bearing its load-lifting capacity will fall because, in this case, the relationship between the throttling of the liquid at input and output is disturbed.

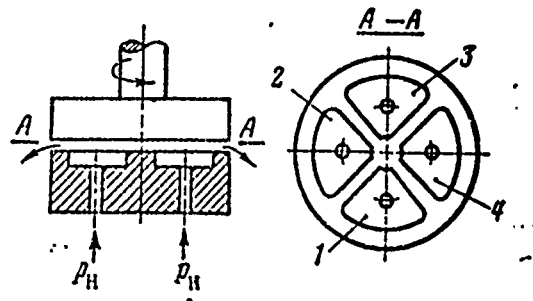
The operating principle of a thrust step bearing (Fig. 3.10) is analogous. In the case of misalignment of the bearing, clearance in the zone of chamber 1 is decreased and, accordingly, clearance in the zone of chamber 3 is increased. Hydrodynamic drag at input and output changes; pressure  $p_1$  increases and pressure  $p_3$  decreases. The appearing moment of force will align the position of the rotor. If the face of the bearing under the effect of axial force moves strictly along the axis, then, in this case pressure will increase simultaneously in all chambers and balancing force will arise in the step bearing.

The operation of oil-film bearings is connected with the circulation of a certain quantity of working liquid (the lubricant).

Friction and wear in such a bearing are very low. However, the expenditure of power on the circulation of the lubricant is rather high (special pumps are necessary). The supply of liquid to the bearing should begin before the start of rotor rotation.

The use of a liquid-metal lubricant can damage the bearing and shaft material. Erosion can be the result of the incompatibility of structural materials with the liquid-metal lubricant or can be caused by the washing of the surface of parts by the flow of high-density lubricating material, for example, mercury. This is connected with the low viscosity of liquid-metal lubricant, as a consequence of which the flow can be turbulent despite a small clearance. Turbulent flow gives rise to the onset of a high dynamic pressure for the lubricant on the surface of the part and to the washing out of material with the fluid flow.

Fig. 3.10. Diagram of a hydrostatic thrust bearing.



To reduce the effect of turbulence, it is necessary to increase the purity of the working parts of the bearing (by polishing). To reduce wear, obviously, special coatings are useful.

Fluid-friction bearings, in addition to their load-lifting capacity and the expenditure of a working liquid are characterized by stiffness, vibrational stability, and sensitivity to the direction of the external load. By the stiffness of the bearing we mean the ratio of the variation in magnitude of external load to the variation in eccentricity. Investigations have shown that stiffness of a hydrostatic bearing is higher than that of a hydrodynamic bearing.

Vibrational stability is determined by the speed of the rotor at which, as a result of vibrations, the completeness of the fluid film in the bearing is disturbed and a contact between shaft and bearing occurs. The higher stiffness of hydrostatic bearings potentially determines their higher resistance to vibration.

With greater revolutions of a rotor installed on hydrostatic bearings (10,000-30,000 rpm), we should consider the influence of dynamic effect (the load-lifting capacity of such a bearing is somewhat higher with rotation taken into account than it is without accounting for rotation) and more strictly define the zone of rotor equilibrium, taking into account vibrational stability.

The sensitivity of hydrostatic bearings to the direction of the external load, as was found, is substantially less than that of hydrodynamic bearings, in which it depends upon both the point of supply of the lubricating liquid and the relative motion of the rubbing surfaces which form the liquid wedge.

The effect of the supersaturation of vapor and its condensation on turbine operations

Along with the difficulties involved in solving purely structural questions in the planning of turbines for extraterrestrial power plants, there is also the difficulty of solving such questions as the supersaturation of vapor expanding on the turbine blades and its condensation inside the turbine.

The essence of supersaturation is the fact that with the rapid expansion the working medium does not manage to be condensed and can be presented in the form of vapor although, according to the condition of thermodynamic equilibrium, partial condensation should occur. This reduces the efficiency of the turbine.

The radial extent of the turbine blades for the oversaturated state of vapor should be less than for equilibrium. Therefore, a turbine cascade designed with partial condensation taken into account passes more of the working medium.



The transition from the oversaturated state of the working medium to equilibrium is accompanied by a reduction in the efficiency of the turbine. Since the size of the heat exchangers which ensure heat transfer into the system increases in inverse proportion to the efficiency of the turbine, the consideration of the supersaturation processes makes it possible to create lighter structures as a whole.

The extraneous particles in the working medium are the condensation nuclei. Therefore, working media used in such a device must have a minimum of such particles. Condensation is the consequence of the equilibrium expansion of any saturated vapor. It gives rise to a reduction in turbine efficiency and causes the erosion of blades and other structural elements. Erosion is caused by the collision of the slowly moving film of condensed fluid and separate drops of it with the rapidly moving parts of the rotor. Experience shows that in order for erosion to occur, the quantity of liquid phase of the working medium in the turbine should not exceed 10-12% and circular velocity of the blades must not exceed 275 m/s [51]. High speeds are permissible only in turbines with the additional heating of vapor between the stages of the turbine. In this case, the vapor remains dry. However, intermediate heating necessitates an increase in dimensions and weight of the steam generator and radiator. The use of even one or two stages of vapor reheating complicates construction and increases turbine weight. Therefore, the superheating of steam can be recommended only as an extreme measure.

#### Some features of electric generators

Electric generators for extraterrestrial power units, as a rule, are mounted on one shaft with the turbine (i.e., without reducing gear) and have high speed - 20,000 r/min and above (speed is limited by the maximum possible speed from the point of view of strength and by the circular velocity on the ends of the working blades).

Approximately 5 to 20% of the power supply to the generator goes into the heating of the parts of the generator (the winding of the rotor and the stator, etc.). To remove heat from the generator

a special system is necessary, whereupon the heat carrier is passed through the channels directly in the generator's stator. In this case, the windings should be well insulated from the heat carrier.

The winding material (copper, silver) can be heated to a temperature of  $\sim 700^{\circ}\text{C}$  and since the windings of the rotor are located in the field of action of centrifugal forces, they will work in the area of plastic deformations.

As an example of a system with a turbodynamo method of converting heat energy into electrical energy, let us examine the diagram in Fig. 3.11 [50]. The working parameters of a cycle are given on this diagram. A nuclear reactor serves as the source of heat energy. With the aid of a liquid-metal heat carrier (potassium and sodium alloy) of the first system, heat from the reactor is transferred to the steam generator.

The heat carrier of the second system in the steam generator is heated, vaporized, and superheated and, in this state, it enters a mercury turbine which brings into rotation the electric generator and the pumps of the first and second systems.

The mercury which has passed through the turbine goes through the condenser and supercooler; then it enters the mercury pump and further - for cooling the generator - and into the bearings.

Figure 3.12 shows a section of a combined rotating unit. In the unit on one shaft a mercury steam turbine, an electric generator, a mercury pump, and the pump for the heat carrier of the first system (Na-K) [50] have been installed.

The turbine of the unit is a two-stage, axial turbine and operates on a Rankine cycle; power generated is 7 hp at 40,000 r/min.

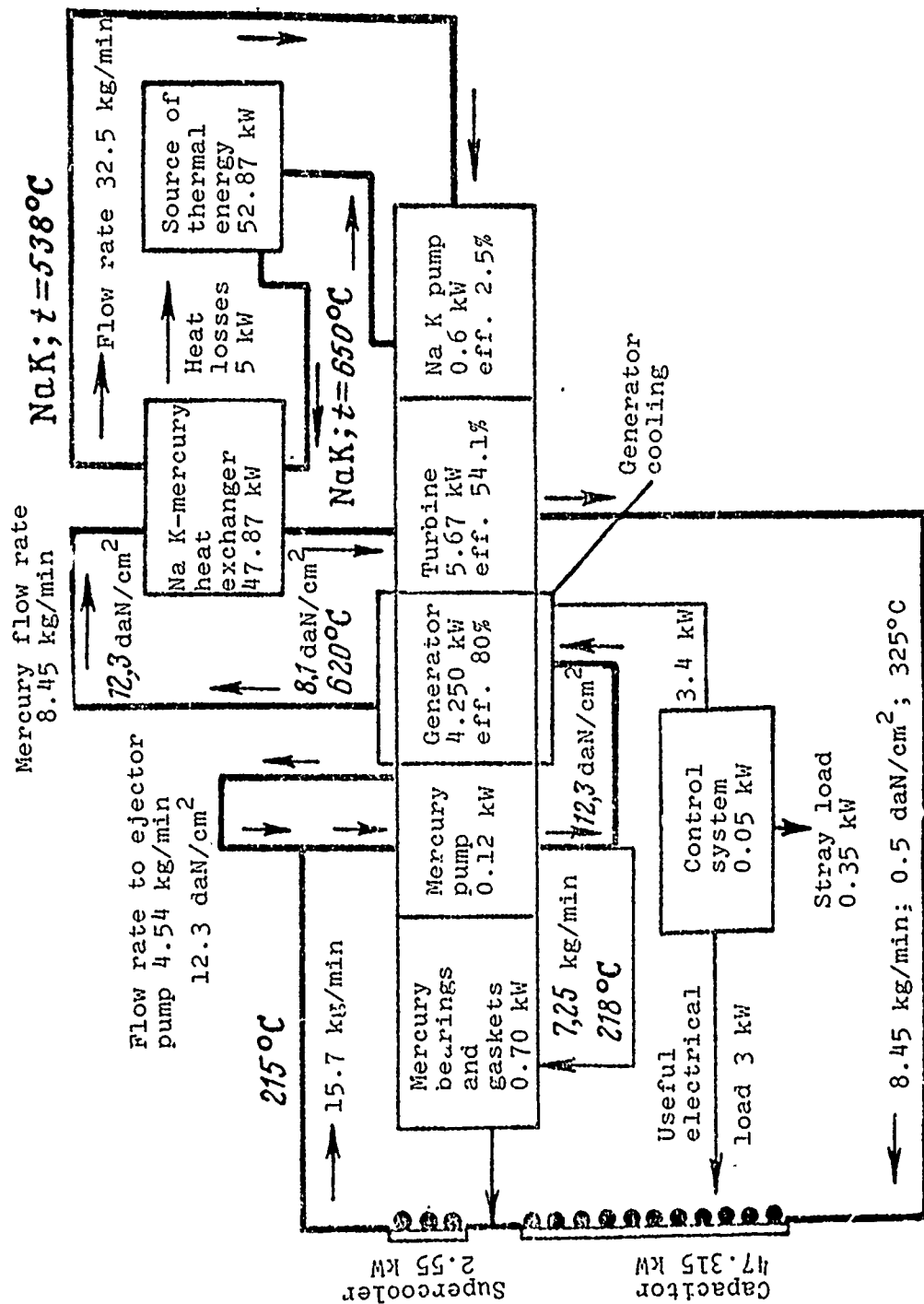


Fig. 3.11. System for converting thermal energy into electrical energy.

The generator consists of a rotor with a six-pole permanent magnet and a stator with a two-phase winding. To prevent the penetration of the mercury, the stator has a seal. To avoid the condensation of mercury in the cavity of the rotor, the generator should operate at a temperature of  $370^{\circ}\text{C}$  or above. With a useful electrical power of 3 kW efficiency of the generator is 80%.

Voltage deviated from nominal by no more than 5% with a power factor on the order of 0.8-1.0. To obtain the assigned frequency (20,000 Hz) with minimum weight the optimum rotor speed of 40,000 r/min was selected. Output frequency is maintained with a control system, with an accuracy of  $\pm 1\%$ , with useful power varying from 0 to 3 kW.

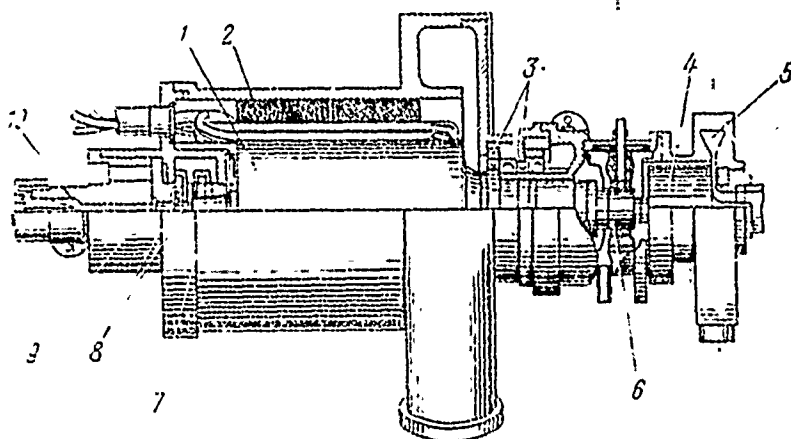


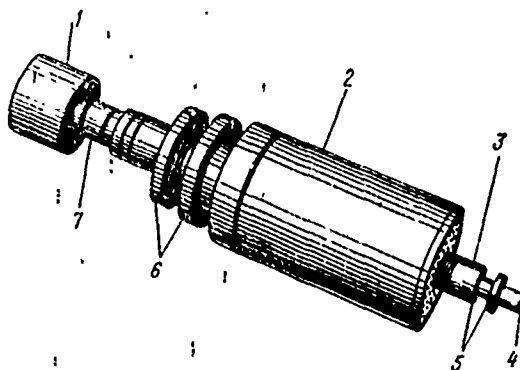
Fig. 3.12. The longitudinal plan of a turbogenerator with pumps of the first and second loops: 1 - generator rotor; 2 - generator stator; 3 - turbine wheel; 4 - Na-K pump rotor; 5 - Na-K diffuser; 6, 7 - mercury radial bearings; 8 - mercury thrust bearing; 9 - mercury centrifugal pump; 10 - mercury jet-edge booster pump.

The mercury pump has a centrifugal-type impeller with a diameter of 8.7 mm. The pump develops a pressure of  $12.3 \text{ daN/cm}^2$  with a flow rate of  $20.24 \text{ kg/min}$  and a total efficiency of 35%.

The pressure at pump input is extremely low -  $0.42 \text{ daN/cm}^2$ . To prevent cavitation, a jet-edge booster pump has been installed before the entry to the centrifugal pump.

The Na-K pump consists of a permanent magnet installed on the end of the shaft of the unit and fixed ring channels such as the channels of the centrifugal pump. The magnet, while rotating, carries the flow of Na-K after it and forces it to be rotated in the ring channels; because of this, the pump works similarly to a centrifugal pump. Despite the fact that pump efficiency is a total of ~2.5%, such a method of providing circulation in the loop is implemented (with minimum construction weight and the minimum resistance along the entire system). At a rated capacity of 32.5 kg/min and a temperature of ~538°C the pressure developed by the pump is 0.133 daN/cm<sup>2</sup>.

Fig. 3.13. One of the variants of a turbogenerator rotor (see Fig. 3.12): 1 - rotor of Na-K pump; 2 - generator rotor; 3 - mercury radial bearing; 4 - mercury pump; 5 - mercury thrust bearings; 6 - mercury steam turbine (blades are covered by a band); 7 - mercury radial bearing.



The rotor of a combined rotating unit is installed on two radial bearings. To absorb the axial forces of the rotor there is a bilateral thrust bearing. Both the radial and thrust bearings operate on mercury according to the principle of hydrodynamic bearings. The bearing capacity of the radial (journal) bearings is 22.7 daN and of the thrust (axial) bearing is 9.1 daN. The flow rate of the mercury on the bearings is 7.25 kg/min at 218°C.

Figure 3.13 shows one of the variants of the rotor of a combined rotating unit.

In finishing the system node-by-node tests of all units are conducted, characteristics are noted, and vibrational tests are

made over a frequency range from 5 to 3000 Hz with maximum loading up to 25 g, simulating the conditions of orbit injection.

Figure 3.14 shows a sketch of a turbogenerator layout.

#### Stress analysis of working blades

The turbine blades are the most stressed and critical parts of a turbine unit. They operate at high temperatures and experience high mechanical loads from centrifugal and gas-dynamic forces. Furthermore, the blades experience secondary stresses from the transiency of operating conditions with rapid time variation in the thermal condition ("thermal shock") and also from the mechanical vibrations of the blade foil (especially in the presence of resonance).

The determination of tensile stresses in the blade foil from centrifugal forces

Under the effect of centrifugal forces in the blade foil there will appear torsional, flexural, and tensile stresses, of which the basic stress is tensile stress.

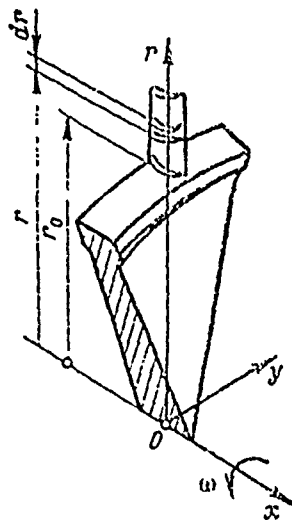


Fig. 3.15. Coordinate system.

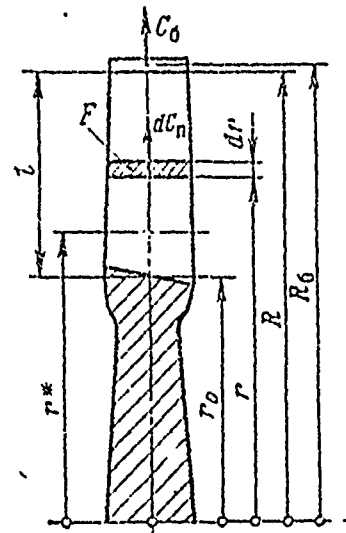


Fig. 3.16. Stress analysis of blade.

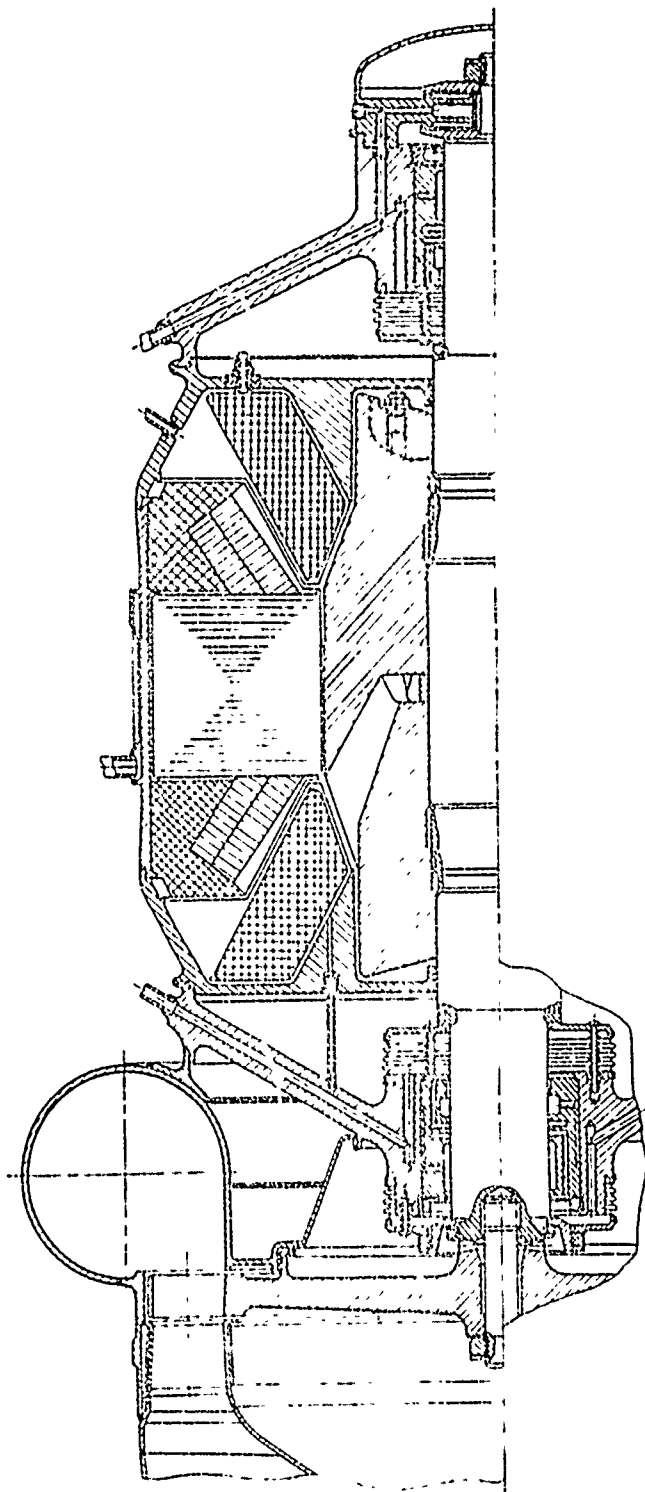


Fig. 3.14. Turbogenerator design.

Flexural stresses from centrifugal forces are used to compensate the flexural stresses from the effect of gas-dynamic forces (see below). Torsional stresses are usually low and in tentative calculations can be disregarded.

The following system of coordinate axes (Fig. 3.15) has been taken in the stress analysis of a blade foil.

The Ox axis agrees with the rotor's axis of rotation and is directed in the direction of the gas flow; the Or axis (or Oz) is perpendicular to the axis of rotation (Ox) and passes through the center of gravity of the root section of the blade; the Oy axis is perpendicular to the Ox and Or axes and is directed so that the smallest angle of turn up to a coincidence with the Or axis is obtained with a turn in the direction of the angular velocity of the rotor.

Let us examine a method of determining stresses in the blade foil from centrifugal forces in the example of a blade with a band web (Fig. 3.16).

For convenience in determining stresses  $\sigma_p$  in an arbitrary cross section (on radius  $r^*$ ) of a blade, let us divide the complete centrifugal force  $C$  acting on this cross section by the centrifugal force of the blade foil strictly  $C_n$  and the centrifugal force of the band web  $C_a$ . Obviously,

$$C = C_n + C_a. \quad (3.3)$$

Let us find these forces, for which we take an element of a blade with radius  $r$  and thickness  $dr$ . Then the centrifugal force created by this blade element is

$$dC_n = \rho \omega^2 F r dr,$$

where  $\rho$  is the density of the blade material in  $\text{kg/m}^3$ ;



$\omega$  is the angular velocity of disk rotation in rad/s;

$F \equiv F(r)$  is the cross-sectional area of the blade on the current radius  $r$  in  $m^2$ .

The complete centrifugal force in section  $r^*$  from the mass of the foil itself is

$$C_n = \omega^2 \int_{r^*}^R F r dr. \quad (3.4)$$

The centrifugal force of the band web is

$$C_6 = \omega^2 V R_6. \quad (3.5)$$

where  $V$  is the volume of the band web in  $m^3$ .

The total centrifugal force acting in section  $r^*$  is

$$C = C_n + C_6 = \omega^2 \left( \int_{r^*}^R F r dr + V R_6 \right). \quad (3.6)$$

Dropping the superscript "\*" with  $r$ , we obtain the following formula for tensile stresses

$$\sigma_p = \omega^2 \left( \frac{\int_0^R F r dr}{F} + \frac{V R_6}{F} \right). \quad (3.7)$$

Formula (3.7) is the basic design formula for determining tensile stresses on an arbitrary radius of a blade with any law of variation for the cross-sectional area.

The character of the variation in tensile stresses from centrifugal forces along the blade radius is shown in Fig. 3.17.

The cross-sectional area of a blade usually varies according to exponential law:

$$F(r) = F(R) + [F(r_0) - F(R)] \left( \frac{R-r}{l} \right)^n \quad (3.8)$$

The value of the exponent  $n = 0$  corresponds to a blade of constant cross section;  $n = 1$  to a blade with a linear law of cross section variation.

For turbine blades we usually assume  $n = 2-4$ ; when  $n \geq 3$  (for ordinary values  $F(R)/F(r_0) = 0.2-0.4$ ) the maximum stresses will be found not in the root section (curve b).

If  $F = \text{const}$ , then

$$\sigma_p = q_{\infty}^2 \left[ \frac{R^2 - r^2}{2} + \frac{V R_0}{F} \right] \quad (3.7a)$$

Maximum stress for such a blade will obviously be in the root section:

$$\sigma_{p \max} = q_{\infty}^2 \left[ \frac{R^2 - r_0^2}{2} + \frac{V R_0}{F} \right] \quad (3.7b)$$

Determining flexural stresses in a blade foil from gas-dynamic forces

Flexural stresses from gas-dynamic forces occupy the second place in value after tensile stresses from centrifugal forces.

Let us first determine the gas-dynamic forces acting on a blade. For this we shall examine the operation of the cascade of the turbine rotor wheel (Fig. 3.18).

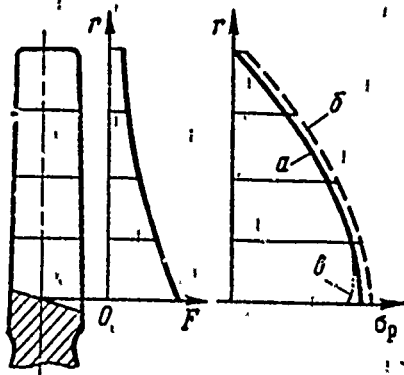


Fig. 3.17. Stresses from centrifugal forces in a blade foil of variable cross section a - without the band web; b - with the band web.

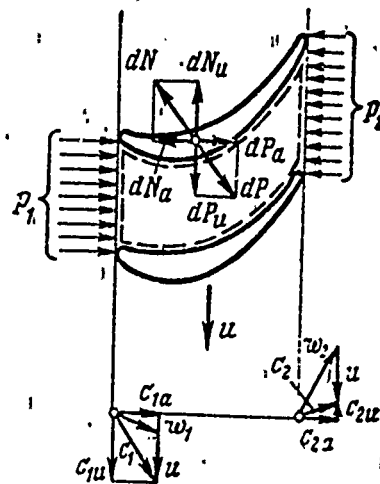


Fig. 3.18. Determining the gas forces acting on the blade foil.

From gas-dynamic analysis of a turbine, the following gas (steam) parameters are known:

the projections of gas velocities onto an axis coinciding with the axis of shaft rotation and onto an axis perpendicular to it,

$c_{1a}$ ;  $c_{1u}$ ;  $c_{2a}$ ;  $c_{2u}$ ;

circular velocities on a given radius  $u$ ; gas density (steam)

$\rho_1$  and  $\rho_2$ ; gas pressure (steam)  $p_1$  and  $p_2$ .

The subscript "1" indicates quantities which characterize the state of the gas at stage input, the subscript "2" at stage output.

We know that the sum of the external forces acting on a certain volume of gas is equal to the vector difference between the momentum of the gas flowing in and the momentum of the gas flowing out through the control surface limiting this volume, (in Fig. 3.18 indicated by dashes).

Assuming that the particles of gas flowing around the blade move along cylindrical surfaces, we shall examine the cylindrical layer on radius  $r$  with thickness  $dr$  (this assumption is equivalent to the fact that the ring-shaped areas at input and output of the rotor wheel are equal). Let us separate a stream of gas flowing around one blade and apply to the interfaces the forces of interaction.

A blade element acts on the gas with force  $dN$ . The force of the gas pressure on the element is  $dP = -dN$ . The components of this gas force are equal, respectively, to  $dP_a$  (in the plane passing through the axis of rotation) and  $dP_u$  (in the plane of rotation).

Obviously,  $dP_a = -dN_a$ ;  $dP_u = -dN_u$ .

Forces per unit length of the blade (intensities of distributed loads), in the corresponding plane are equal to

$$p_x = \frac{dP_a}{dr}; \quad p_y = \frac{dP_u}{dr}. \quad (3.9)$$

Let us find the components of load intensity. The mass of the gas flowing through a surface element in a unit of time (referred to one blade) is

$$dm = \frac{2\pi r dr}{z} Q_1 c_{1a} = \frac{2\pi r dr}{z} Q_2 c_{2a}, \quad (3.10)$$

where  $z$  is the number of working blades.

After examining the change in momentum in an axial direction, we obtain  $dm(c_{2a} - c_{1a}) = (p_2 - p_1)(2\pi r dr)/(z) + dN_a$ , hence

$$dP_a = -dN_a = \frac{2\pi r dr}{z} (p_2 - p_1) - \frac{2\pi r dr}{z} Q_1 c_{1a} (c_{2a} - c_{1a})$$

and, finally,

$$p_x = \frac{dPa}{dr} = \frac{2\pi r}{z} (p_2 - p_1) - \frac{2\pi r}{z} \rho_1 c_{1a} (c_{2a} - c_{1a}). \quad (3.11)$$

The positive direction of  $p_x$  corresponds to the direction of the intensity along the flow (along the direction of the Ox axis).

We now find the intensity of load distribution in the plane of rotation. The change in momentum in the plane of rotation is  $dm(c_{2u} - c_{1u}) = dN_u$ , hence

$$dP_u = -dN_u = -\frac{2\pi r dr}{z} \rho_1 c_{1a} (c_{2u} - c_{1u})$$

and the intensity of the distributed load in the plane of rotation is

$$p_y = -\frac{2\pi r}{z} \rho_1 c_{1a} (c_{2u} - c_{1u}). \quad (3.12)$$

The positive direction of  $p_y$ , which can be determined from this formula, corresponds to the positive direction of the vectors of velocities  $c_{2u}$  and  $c_{1u}$ .

We should note that for axial compressors (pumps)  $p_y$  is directed against rotation, and for blades of axial turbines, it is directed with the rotation.

If we know the intensities of distributed load  $p_x$  and  $p_y$ , we shall now find the bending moments. Let us look for them in a certain fixed section  $r^*$  (see Fig. 3.16):  $M_x$  relative to the Ox axis in the rOy plane and  $M_y$  relative to the Oy axis in the rOx plane:

$$dM_x = p_y dr (r - r^*); \quad dM_y = p_x dr (r - r^*).$$

Integrating these expressions along the length of the blade from  $r^*$  to  $R$ , we obtain bending moments in the section  $r^*$ :

$$\begin{aligned} M_x &= \int_{r^*}^R p_y(r - r^*) dr; \\ M_y &= \int_{r^*}^R p_x(r - r^*) dr. \end{aligned} \quad (3.13)$$

In the root section of the blade bending moments will be maximum:

$$\begin{aligned} M_{x \max} &= \int_{r_0}^R p_y(r - r_0) dr; \\ M_{y \max} &= \int_{r_0}^R p_x(r - r_0) dr. \end{aligned} \quad (3.13a)$$

Bending stresses are determined separately relative to the principal axes of inertia  $\xi$  and  $\eta$ <sup>1</sup> for individual points of the cross section furthest from the axes (Fig. 3.19). Such points in the blade cross section are:  $A(\xi_A; \eta_A)$ ;  $B(\xi_B; \eta_B)$  and  $C(\xi_C; \eta_C)$ .

We shall find the moments from the gas forces relative to the principal axes of inertia (see Fig. 3.19):

$$M_\xi = M_x \cos \beta + M_y \sin \beta; \quad M_\eta = M_x \sin \beta - M_y \cos \beta. \quad (3.14)$$

---

<sup>1</sup>The principal axes of inertia pass through the center of gravity of the cross section; for approximate calculations we can assume that the  $\xi$  axis is parallel to the chord connecting the leading edge of the profile with the trailing edge. The  $\eta$  axis is perpendicular to the  $\xi$  axis. For a stricter definition of the position of the principal axes see reference [39].

The  $\xi$  axis is directed from the leading edge of the profile of the section toward the trailing edge; the  $\eta$  axis is directed from the back to the face of the cross-sectional profile of the blade (see Fig. 3.19).

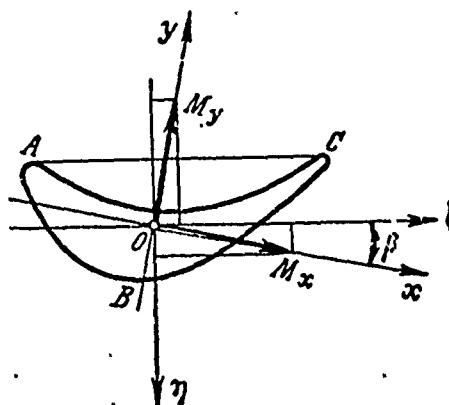
Flexural stresses at any point of the cross section are determined by the relation

$$\sigma_H = \frac{M_\xi}{I_\xi} \eta + \frac{M_\eta}{I_\eta} \xi, \quad (3.15)$$

where  $I_\xi$  and  $I_\eta$  are the principal moments of inertia for the cross section of the blade,  $m^4$ .

The signs of the bending moments in this equation must be considered positive if they cause a bend deformation convex to the side of the positive direction of the corresponding axis. The signs of coordinates  $\xi$  and  $\eta$  correspond to the direction of the axes.

Fig. 3.19. Determining bending moments relative to the principal axes of inertia.



In writing formula (3.15) we assume the following rule of signs for bending moments and stresses: tensile stress is assumed positive and compressive stress negative.

Usually in turbine machines the principal moments of inertia for blade cross sections are connected with the relationship  $I_\eta > (10-15)I_\xi$ , while the values of bending moments are of the same order. Therefore, bending stresses, for example, at point A, can be determined approximately from formula

$$\sigma_{IIA} \approx \frac{M_{\xi}}{I_{\xi}} \eta_A$$

(3.15a)

#### The bend of blades from centrifugal forces

Under the effect of centrifugal forces blades bend when the centers of gravity of separate sections along the length of the blade do not coincide with the Or axis which passes through the center of gravity of the root section.

Let us examine the bending of a blade under the effect of gas forces  $P_x$  and  $P_y$  in the field of centrifugal forces (Fig. 3.20). Let us assume that the axis of the centers of gravity of the unbent blade coincides with the Or axis. Under the effect of forces  $P_x$  and  $P_y$  the blade will bend. Acting on the bent blade will be the centrifugal force creating moments  $M_{xC}$  and  $M_{yC}$ , which attempts to turn the axis of the blade to a neutral position.

Thus, the action of the centrifugal forces makes the total bend of the blade less than it would be under the action of gas forces only (see the dashed line of bend on Fig. 3.20). The bending stresses of the blade will be less. These are used for unloading blades from extremely large bending stresses by gas-dynamic forces. It is possible to so design a blade that in the framing or near it low or even zero bending moment will appear.

There are two design methods for reducing bending stresses in blades or, as they say, two methods of "unloading" the blade.

In the first case, a blade with a rectilinear axis passing through the cross-sectional centers of gravity is installed in framing with an inclination so that the axis is to the side of the action of the gas-dynamic bending forces (relative to the axis passing through the center of gravity of the root section of the blade). Such a method is technologically convenient and frequently used for unloading short turbine blades.



Another means of unloading consists of the fact that the line of the centers of gravity for the blade cross section is a specially selected curve. The fit of the blade in the web is radial in this case, without inclination.

The shortcoming of these methods of bending-moment compensation is their one-mode nature. Actually, bending moments from centrifugal forces depend upon the rotational speed of the rotor, and moments from gas forces on the density of the gas and other parameters of the flow, which are different for various conditions of turbine operations.

Usually turbines are designed so that the bending moment from centrifugal force is a certain fraction of gas-dynamic moment, i.e.,

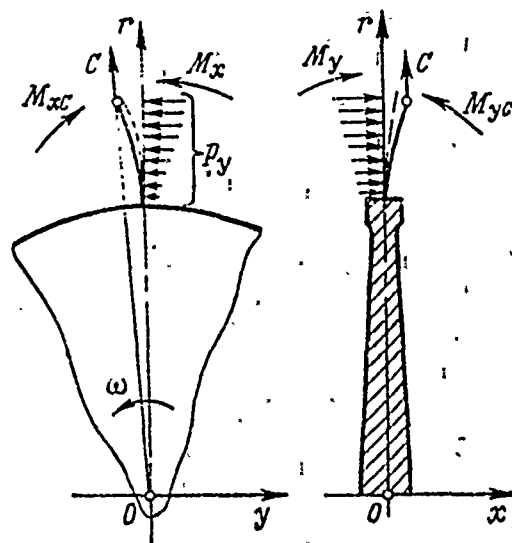
$$M_{xc} = -\gamma M_x; M_{yc} = -\gamma M_y, \quad (3.16)$$

where  $\gamma$  is the coefficient of compensation.

The value of  $\gamma$  is selected with the operation of blades in various modes taken into account and usually comprises 0.3-0.6. A blade with linear stagger makes it possible to perform the assigned compensation only in one cross section, for which the cross section with the greatest bending stresses is naturally taken. The root section is usually such a section.

There is a more effective way of unloading the blade by centrifugal forces - the attachment of a blade in a hinged joint so that the total bending moment in the framing will equal zero on any mode of operation for the turbine wheel. The blade, in this case, can be lighter than with rigid framing. However, due to design complexity, this can only be done for cold blades (long compressor blades) and only for the compensation of bending moments in the plane of rotation of the disk.

Fig. 3.20. Compensation of gas-dynamic bending moments by moments from centrifugal forces.



#### Total stresses and safety factors of blades

In each cross section of a blade the total stress is defined as the sum of tensile and bending stresses:

$$\sigma_{\Sigma} = \sigma_p + \sigma_{II}. \quad (3.17)$$

The safety factor is determined from expression

$$n = \sigma_{B, \tau}^t / \sigma_{\Sigma}, \quad (3.18)$$

where  $\sigma_{B, \tau}^t$  is the rupture strength of the blade material taking into account temperature and time.

Obviously the safety factor of the blade along the radius will not remain constant; it will change depending upon the variation and stresses  $\sigma_{\Sigma}$  along the radius and the quantity  $\sigma_{B, \tau}^t$  due to the variable temperature of the blade (Fig. 3.21). Usually the minimum safety factor is  $n = 1.2-1.5$  and corresponds to the unsafe sections of the blade. For turbine blades the unsafe section, counting from the root, is approximately 20-30% of the length of the blade.

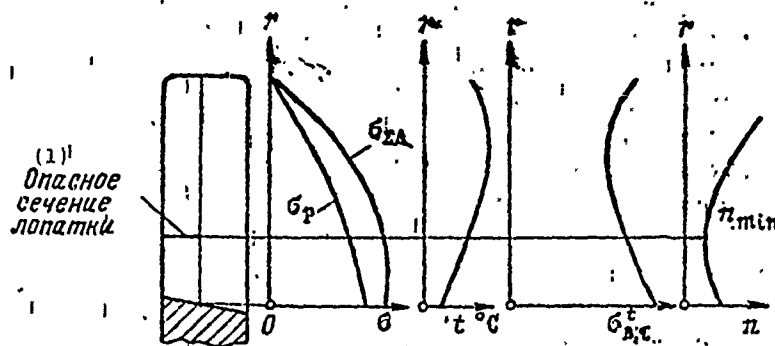


Fig. 3.21. Determining the unsafe cross section of a turbine blade.

KEY: (1) Unsafe cross section of blade.

In short blades where bending is insignificant, stress analysis is limited to the determination of only those stresses from centrifugal forces. In this case,

$$n_p = \frac{\sigma_{H,\tau}^t}{\sigma_p} \quad (3.18a)$$

Usually the value of the safety factor  $n_p$  is somewhat higher than when taking bending stresses into account:  $n_p = 1.5-2.0$ .

#### Vibrational analysis of blades

A frequent defect occurring in working turbines is the breakdown of blades from vibration. The direct cause of vibration breakage is the fatigue of the material during the action of alternating loads which cause stress higher than the endurance limits. The mechanism of failure can be visualized thus.

When vibrations exist, first small cracks appear on the edge of the blade. During vibration, the cracks increase and when the operating cross section of the blade is reduced to a certain value because of a crack, breakoff begins. The fracture (the point

at which the blade obtained the initial crack) has a characteristic flat polished surface. In the cross section where the blade was broken and the crack has not yet developed, the fracture surface is crystalline.

The breakdown of one blade usually leads to the failure of the remaining blades and the turbine as a whole.

To prevent vibration breakage and control it successfully when it does appear, it is necessary to correctly evaluate the possible sources of the onset of the defect. For this purpose it is necessary to determine the natural frequencies of blade vibration; to determine the disturbing forces and to produce their wave analysis; to construct a frequency diagram and reveal the possible resonant frequencies over the range of operating revolutions of the motor and find which are the most dangerous. The various vibrational modes follow: flexural, torsional, flexural-torsional, and edge vibration (when almost the entire surface of the blade is fixed and only individual points on the edge, sometimes the closed areas of the blade, vibrate). Edge vibrations have very high-frequencies and appear in fine blades.

Flexural vibrations are the most dangerous because their frequency can be within the range of the working rpm. The other wave forms of turbine blades have a high frequency and do not always fall within the range of working rpm's.

Edge vibrations have a frequency on the order of 10,000 vibrations per second and can be excited with a certain combination of nozzle and rotor blade quantities during vibrational combustion in the combustion chambers. These vibrations as yet have not been generalized.

Figure 3.22 shows the types of vibration cracks in turbine blades.

Let us examine only the flexural vibrations of blades.

# Determining the frequencies of inherent (free) vibrations of blades

In the vibrational analysis of blades let us use the following assumption.

1. The blade is a rod one end of which is tightly sealed and the other is free. The axis of the unbent blade (in free position) is rectilinear and is directed strictly along the  $z$ -axis (Fig. 3.23).

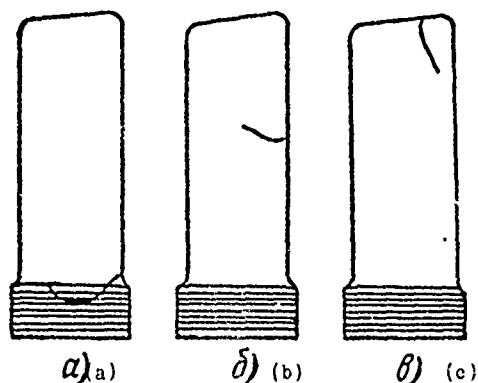


Fig. 3.22. Types of vibration cracks in turbine blades.

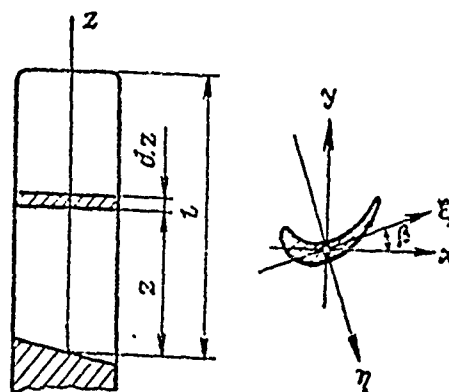


Fig. 3.23. Calculation diagram of a blade (for vibrational analysis).

2. We shall examine blade vibrations only in the smallest rigidity plane, i.e., relative to the principal side axis.

3. We assume the blade is not twisted but is turned a certain angle  $\beta = \text{const}$  (there is no rotational inertia of the section).

4. There is no rotation, i.e., there are no longitudinal forces being caused by centrifugal forces (the effect of centrifugal forces on vibration frequency in a blade will be discussed later).

The natural frequencies of blade vibration will be determined by the method of the direct compilation of a frequency equation using the familiar D'Alembert principle.

External loads during blade vibration are the forces of inertia. The linear load from the force of inertia is expressed by equality

$$q = -\left(F \frac{\partial^2 \eta}{\partial t^2}\right), \quad (a)$$

or

$$q = -\rho F \ddot{\eta}, \quad (a')$$

where  $\rho F$  is the linear mass of the blade (the mass of a unit length of a blade);

$\rho$  is the density of the blade material;

$F$  is the area of the current blade cross section;

$\eta = \eta(z, t)$  is the bending function (the equation of an elastic line) of the blade.

The external force of inertia is balanced by the internal elastic forces.

As we know, the bending moment during bending of a beam is

$$M_{\eta} = E I_{\xi} \frac{d^2 \eta}{dz^2}, \quad (b)$$

or

$$M_{\eta} = E I_{\xi} \eta'', \quad (b')$$

where  $E$  is the elasticity modulus of the first kind;

$I_{\xi}$  is the moment of inertia of the cross sectional area of a blade relative to the  $\xi$  axis;

$\eta''$  is the second derivative with respect to  $z$  of the function of deflection.

Differentiating this equation, we find the expression for shearing force:

$$\frac{d^2 M_{\eta}}{dz^2} = Q = (EI_{\xi} \eta''). \quad (c)$$

After we differentiate equation (c) once more, we obtain an expression for linear load from the internal elastic forces:

$$\frac{d^2 M_{\eta}}{dz^2} = \frac{dQ}{dz} = q = (EI_{\xi} \eta'')'. \quad (d)$$

Let us make the external linear load equal to the linear load from internal forces [equations (a') and (d)]; then the general differential equation for an oscillating blade will be written in the form

$$(EI_{\xi} \eta'')'' + qF \ddot{\eta} = 0. \quad (3.19)$$

To solve differential equation (3.19) let us use Fourier's method - the separation of variables  $z$  and  $t$ . We shall introduce designations:

$$\eta(z, t) = u(z), \quad g(t) = ug, \quad (e)$$

where  $u(z)$  is the function of deflection, depending only on the  $z$  coordinate;

$g(t)$  is the function of deflection depending only on time  $t$ .

If we differentiate equation (e) four times with respect to  $z$  and two times with respect to  $t$  and substitute these derivatives into equation (3.19), we obtain

$$(EI_{\xi} u'')'' g + qF u \ddot{g} = 0, \quad (3.20)$$

hence

$$\frac{(EI_{\xi} u'')''}{\rho F u} = -\frac{\ddot{g}}{g} = \omega_c^2 = \text{const.} \quad (3.21)$$

In the left side of the obtained equality we find the function  $(EI_{\xi} u'')''/\rho F u$  depending only on the  $z$  coordinate, and in the right side the function  $-\ddot{g}/g$  depending only on time  $t$ . Both these functions are equal at any values for  $z$  and  $t$  and this is possible only when each of them is equal to the same constant value. We shall designate this constant as  $\omega_c^2$ .

From equation (3.21) we obtain two differential equations:

$$\ddot{g} + \omega_c^2 g = 0; \quad (3.22)$$

$$(EI_{\xi} u'')'' - \omega_c^2 \rho F u = 0. \quad (3.23)$$

Equation (3.22) is an equation of harmonic blade vibrations. The period of harmonic vibrations is

$$T = \frac{2\pi}{\omega_c}, \quad (3.24)$$

and vibration frequency is

$$f = \frac{1}{T} = \frac{\omega_c}{2\pi}, \quad (3.25)$$

where  $\omega_c$  is the angular velocity of the natural oscillations of the blade (this is also the physical meaning of the constant  $\omega_c$  in equation (3.21)).

The solution of equation (3.22) gives

$$g = A \cos \omega_c t + B \sin \omega_c t. \quad (3.26)$$



Equation (3.23) is a differential equation in the form of an elastic line of a vibrating blade since it contains only geometric and mass characteristics of a blade and the frequency of its free oscillations. This equation is not solved in general form. We can obtain a solution of a uniformly heated (or cold) blade of constant cross section. Let us examine this case when  $F = \text{const}$ ;  $EI_\xi = \text{const}$ .

We introduce relative variable  $\bar{z} = z/l$ . Let us note that:

$$\begin{aligned} \left[ u \left( \frac{z}{l} \right) \right]' &= \frac{1}{l} u' \left( \frac{z}{l} \right); \quad \left[ u \left( \frac{z}{l} \right) \right]'' = \frac{1}{l^2} u'' \left( \frac{z}{l} \right); \\ \left[ u \left( \frac{z}{l} \right) \right]''' &= \frac{1}{l^3} u''' \left( \frac{z}{l} \right); \quad \left[ u \left( \frac{z}{l} \right) \right]^{IV} = \frac{1}{l^4} u^{IV} \left( \frac{z}{l} \right). \end{aligned} \quad (3.27)$$

Then equation (3.23) assumes the form

$$EI_\xi u^{IV} - \omega_c^2 l^4 \rho F u = 0, \quad (3.27')$$

or

$$u^{IV} - \alpha^4 u = 0; \quad (3.28)$$

where

$$\alpha = \frac{\omega_c^2 l^4 \rho F}{EI_\xi} \quad (3.29)$$

is a parameter of differential equation (3.28).

From equality (3.29) we can determine the square of the inherent angular velocity of blade vibrations:

$$\omega_c^2 = \left( \frac{\alpha}{l} \right)^2 \sqrt{\frac{EI_\xi}{\rho F}}, \quad (3.30)$$

where  $\alpha$  is still unknown.

Equation (3.28) is a linear differential equation of the fourth order. A full solution is written in the form

$$u(\bar{z}) = A \cos \alpha \bar{z} + B \sin \alpha \bar{z} + C \operatorname{ch} \alpha \bar{z} + D \operatorname{sh} \alpha \bar{z}. \quad (3.31)$$

Instead of particular solutions  $\cos \alpha \bar{z}$ ;  $\sin \alpha \bar{z}$ ;  $\operatorname{ch} \alpha \bar{z}$  and  $\operatorname{sh} \alpha \bar{z}$ , A. N. Krylov introduced linear combinations of angular and hyperbolic functions which were given the name of Krylov functions [22].

Using these functions, we obtain from equation (3.31)

$$u(\bar{z}) = AS(\alpha \bar{z}) + BT(\alpha \bar{z}) + CU(\alpha \bar{z}) + DV(\alpha \bar{z}), \quad (3.31')$$

where

$$\left. \begin{aligned} S(\alpha \bar{z}) &= \frac{1}{2} (\operatorname{ch} \alpha \bar{z} + \cos \alpha \bar{z}); \\ T(\alpha \bar{z}) &= \frac{1}{2} (\operatorname{sh} \alpha \bar{z} + \sin \alpha \bar{z}); \\ U(\alpha \bar{z}) &= \frac{1}{2} (\operatorname{ch} \alpha \bar{z} - \cos \alpha \bar{z}); \\ V(\alpha \bar{z}) &= \frac{1}{2} (\operatorname{sh} \alpha \bar{z} - \sin \alpha \bar{z}). \end{aligned} \right\} \quad (3.32)$$

---

<sup>1</sup>Remember that the hyperbolic sine and cosine are determined by expressions:

$$\operatorname{sh} x = \frac{e^x - e^{-x}}{2}; \quad \operatorname{ch} x = \frac{e^x + e^{-x}}{2},$$

and their derivatives:

$$(\operatorname{sh} x)' = \operatorname{ch} x; \quad (\operatorname{ch} x)' = \operatorname{sh} x.$$

Functions  $S$ ,  $T$ ,  $U$  and  $V$  during differentiation have the property of circular replacement, i.e.,

$$\left. \begin{aligned} S(\bar{az}); & \quad S'(\bar{az}) = aS'(\bar{az}); \\ S''(\bar{az}) = a^2 U(\bar{az}); & \quad S'''(\bar{az}) = a^3 T(\bar{az}); \\ T(\bar{az}); & \quad T'(\bar{az}) = aS(\bar{az}); \\ T''(\bar{az}) = a^2 V(\bar{az}); & \quad T'''(\bar{az}) = a^3 U(\bar{az}); \\ U(\bar{az}); & \quad U'(\bar{az}) = aT(\bar{az}); \\ U''(\bar{az}) = a^2 S(\bar{az}); & \quad U'''(\bar{az}) = a^3 V(\bar{az}); \\ V(\bar{az}); & \quad V'(\bar{az}) = aU(\bar{az}); \\ V''(\bar{az}) = a^2 T(\bar{az}); & \quad V'''(\bar{az}) = a^3 S(\bar{az}). \end{aligned} \right\} \quad (3.33)$$

The use of these functions makes it possible to immediately obtain a solution to equation (3.28) which satisfies the boundary conditions. We have the following boundary conditions for our problem:

- 1)  $\bar{z} = 0$ ;  $u(0) = 0$  (deflection in the seal is zero);
- 2)  $\bar{z} = 0$ ;  $u'(0) = 0$  (the angle of pitch of the section in the framing is equal to zero);
- 3)  $\bar{z} = 1$ ;  $u''(\alpha) = 0$  (bending moment at the free blade tip is equal to zero);
- 4)  $\bar{z} = 1$ ;  $u'''(\alpha) = 0$  (shearing force at the free blade tip is equal to zero).

If we use the first two boundary conditions, we obtain  $A = 0$ ;  $B = 0$ . Then the solution to (3.31') will be

$$u(\bar{z}) = CU(\bar{az}) + DV(\bar{az}). \quad (3.31'')$$

We shall use the third and fourth boundary conditions (when  $\bar{z} = 1$ ). From formulas (3.33) we obtain:

$$U''(\alpha) = \alpha^2 S(\alpha); \quad V''(\alpha) = \alpha^2 T(\alpha);$$

$$U'''(\alpha) = \alpha^3 V(\alpha); \quad V'''(\alpha) = \alpha^3 S(\alpha).$$

Substituting these expressions into equality (3.31"), accordingly, for the third and fourth boundary condition we obtain

$$Ca^2 S(\alpha) + Da^2 T(\alpha) = 0;$$

$$Ca^3 V(\alpha) + Da^3 S(\alpha) = 0.$$

The solution to this system of uniform algebraic equations relative to C and D will have a nonzero value if its determinant is equal to zero, i.e.,

$$\begin{vmatrix} S(\alpha) & T(\alpha) \\ V(\alpha) & S(\alpha) \end{vmatrix} = 0,$$

or  $S^2(\alpha) - V(\alpha)T(\alpha) = 0$ ; hence, using equalities (3.32), we obtain

$$\operatorname{ch} u \cos \alpha = -1. \quad (3.34)$$

Equation (3.34) has an infinite number of roots. However only the first of them have any value for us:

$$a_1 = 1.875; \quad a_2 = 4.694; \quad a_3 = 7.855;$$

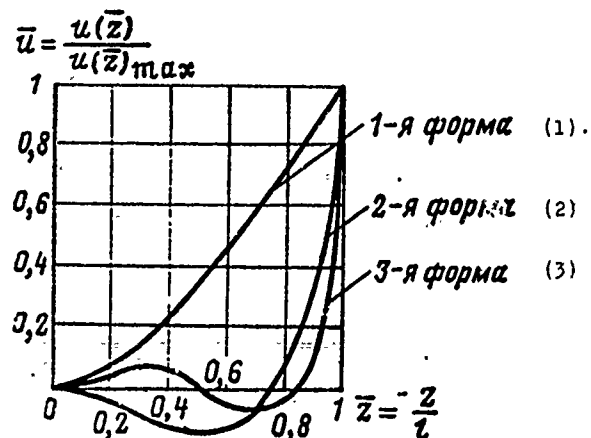
$$a_4 = 10.996; \quad a_5 = 14.137; \quad a_6 = 17.279 \quad \text{etc.}$$

Each value of  $\alpha$  corresponds to its own form of elastic lines (Fig. 3.24), according to the number of nodal points, and its own inherent circular vibration frequency, determined by equality (3.30).

For example, for the 1st form of vibrations the inherent angular velocity of vibrations is

$$\omega_{c1} = \left( \frac{1,875}{l} \right)^2 \sqrt{\frac{EI_{\xi}}{qF}}. \quad (3.30')$$

Fig. 3.24. Forms of flexural blade vibrations.  
KEY: (1) 1st form; (2) 2nd form; (3) 3rd form.



Accordingly, the vibration frequency (in Hz) for this case is

$$f_1 = \frac{\omega_{c1}}{2\pi} = \frac{0,56}{l^2} \sqrt{\frac{EI_{\xi}}{qF}}. \quad (3.25')$$

Integral method of determining the natural frequencies of blade vibrations

This method of determining the natural frequencies of blade vibrations, as indicated, is appropriate for only the simplest case when a blade has a constant temperature along its length and the cross section is constant. However, for the majority of the problems this solution is not appropriate. Therefore, let us examine the general case of a vibrating blade which has  $F \neq \text{const}$ ;  $EI_{\xi} \neq \text{const}$ .

The initial differential equation of natural oscillations was obtained above (3.23):

$$(EI_{\xi} u'')'' = \omega_c^2 q F u.$$

Remember that the left side of this equation is linear load from the internal elastic forces. Let us integrate this equation. We obtain the expression for shearing force

$$(EI_{\xi}u'')' = \omega_c^2 \int_0^z qFudz + C_1.$$

The integration constant  $C_1$  is found from the boundary condition: when  $z = l$  the shearing force is zero, i.e.,

$$(EI_{\xi}u'')'_{z=l} = 0,$$

hence

$$C_1 = -\omega_c^2 \int_0^l qFudz.$$

Substituting the value of  $C_1$  into the expression for shearing force, we obtain

$$(EI_{\xi}u'')' = \omega_c^2 \left( \int_0^z qFudz - \int_0^l qFudz \right) = -\omega_c^2 \int_z^l qFudz.$$

Integrating this expression again, we obtain the equation for bending moment

$$EI_{\xi}u'' = -\omega_c^2 \int_0^z \int_z^l qFudz^2 + C_2.$$

The integration constant  $C_2$  is found from the boundary condition: when  $z = l$  the bending moment is zero, i.e.,

$$(EI_{\xi}u'')_{z=l} = 0,$$

hence

$$C_2 = \omega_c^2 \int_0^l \int_z^l qFudz^2.$$

Then the bending moment is

$$EI_{\xi} u'' = -\omega_c^2 \left( \int_0^z \int_z^l q F u dz^2 - \int_0^l \int_z^l q F u dz^2 \right) = \omega_c^2 \int_z^l \int_z^l q F u dz^2.$$

If we designate  $\int_z^l \int_z^l q F u dz = M_u$  (the integral operator, proportional to bending moment), we obtain

$$EI_{\xi} u'' = \omega_c^2 M_u,$$

or

$$u'' = \omega_c^2 \frac{M_u}{EI_{\xi}}.$$

After we integrate this equation, we find the angle of pitch for the elastic line:

$$u' = \omega_c^2 \int_0^z \frac{M_u}{EI_{\xi}} dz + C_3.$$

The integration constant  $C_3 = 0$ , since  $u'(0) = 0$  when  $z = 0$ .

Let us integrate the last time. We shall obtain the equation for the deflection of a vibrating blade:

$$u = \omega_c^2 \int_0^z \int_0^z \frac{M_u}{EI_{\xi}} dz^2 + C_4.$$

The integration constant  $C_4 = 0$ , since  $u(0) = 0$  when  $z = 0$ .

Finally, the linear integral equation of an elastic line for a vibrating blade is

$$u = \omega_c^2 \int_0^z \int_0^z \frac{dz^2}{EI_{\xi}} \int_z^l \int_z^l q F u dz^2. \quad (3.35)$$

We shall designate

$$\int_0^z \int_0^z \frac{dz^2}{EI_\xi} \int_z^1 \int_z^1 q F u dz^2 = K_{11}. \quad (3.36)$$

Then equation (3.35) can be written as

$$u = \omega_c^2 K_{11}. \quad (3.37)$$

As follows from the theory of integral equations, equation (3.37) leads to a Fredholm linear homogeneous equation of the second kind with parameter  $\lambda$

$$y(z) = \lambda \int_a^b K(zs) y(s) ds, \quad (3.38)$$

which has a number of important properties allowing the use of these equations for the solution of practical problems.

In equation (3.38) function  $y(s)$  is unknown and must be determined so that it is satisfied identically for all values of  $z$  in the range of  $a \leq z \leq b$ .

Function  $K(zs)$  is called the nucleus of this equation or Green's function. The quantity  $\lambda$  is called the parameter of the integral equation, the eigenvalue or the eigenvalue of equation (3.38).

Equation (3.38) besides the trivial solution  $y(z) = 0$ , has untrivial solutions in fully defined cases. The latter solutions are called eigen or fundamental functions of equation (3.38) corresponding to a given eigenvalue of  $\lambda$ .

$K(zs)$  is the nucleus of the integral equation which determines its fundamental properties and has a simple physical sense: this is the function of the effect of an elastic system, i.e., the amplitude value of the deflection of a beam at an arbitrary point  $z$  under the effect of a single source applied at point  $s$ .



The peculiarity of Green's function is its substance and continuity along the beam, i.e., over the range

$$a < z < b; \quad a < s < b.$$

Furthermore, for any elastic system, Green's functions have the property of symmetry or reciprocity, i.e.,  $K(z, s) = K(s, z)$ .

In the theory of integral equations it is proven that:

- a homogeneous integral equation has an infinite set of eigenvalues for  $\lambda$ ;
- all the eigenvalues of  $\lambda$  are real. The physical sense of  $\lambda$  is the square of the natural frequencies of a system:

$$\lambda_n = \omega_{cn}^2;$$

- each eigenvalue of  $\lambda$  corresponds to at least one eigenfunction; the number of linearly independent eigenfunctions which correspond to a given eigenvalue is finite;

- the eigenfunctions of an integral equation with a symmetrical nucleus form complete normal and orthogonal (orthonormalized) sets of functions bound by the relation

$$\int_a^b q_i y_i y_j dz = \begin{cases} 0 & \text{при } i \neq j \\ 1 & \text{при } i = j \end{cases} \quad (3.39)$$

при = when

where  $q_\Sigma$  is the generalized transverse load.

The obtained linear integral equation (3.37) has the following properties:

- it has an infinite number of eigenvalues  $\omega_{c1}^2, \omega_{c2}^2, \omega_{c3}^2, \dots$ , i.e., the vibrating blade has an infinite number of natural frequencies;
- each eigenvalue corresponds to a strictly defined eigenfunction  $u_1, u_2, u_3, \dots$ , i.e., its own form of elastic line;

- all eigenfunctions form an orthogonal set of functions

$$\int_0^l Q F u_i u_j dz = \begin{cases} 0 & \text{при } i \neq j \\ 1 & \text{при } i = j \end{cases} \quad (3.39')$$

при = when

The last property is used in determining the natural frequencies of vibrations and the form function for orders above the first (i.e.,  $\omega_{ck}^2$  and  $u_k$  where  $k = 2, 3, 4 \dots$ ).

Integral equation (3.37) is usually solved by the method of successive approximation (simple iteration). The advantage of this method is the fact that with it it is possible to calculate a system where all parameters are given numerically (tabular). As a result of calculation, along with the frequencies, wave forms are obtained which gives a concrete physical meaning to the solution of the problem.

If a certain function is preset numerically, it is first necessary to normalize this function.<sup>1</sup> This means that each value of the function is divided by its norm (usually the norm is the peak value of the modulus of the function in the assigned range of variation), i.e.,

$$\bar{u}(\bar{z}) = \frac{u(\bar{z})}{u(\bar{z})_{\max}} \quad (3.40)$$

---

<sup>1</sup>To compare two different functions of one class the concept of the function norm exists. The function norm is the numerical value of the important parameter or a set of parameters inherent in all comparable functions, sometimes simply the "scale" of the function. The norm of the function is designated  $||u||$  or  $u|$ .

A function whose norm is equal to one is called normalized. In vibration problems for the function norm we usually use the highest value of the modulus of a function in a given range of variation, which can be designated  $u|_{\max}$ .

Figure 3.25 shows the operation of normalization for a certain function  $u(\bar{z})$ . The curve  $\bar{u}(\bar{z})$  is obtained from the curve  $u(\bar{z})$  by dividing each value of the ordinates of the first curve by its norm  $u(\bar{z})/\max$ . The second curve is normalized since its norm  $\bar{u}(\bar{z})/\max$  is equal to one.

The process of successive information will consist of determining eigenfunction  $\bar{u}_{(i+1)}$  and eigenvalue  $\omega_{c(i+1)}^2$  if there is an initial approximation of function  $\bar{u}_1$ , based on the formula of simple iteration

$$\bar{u}_{(i+1)} = \omega_{c(i+1)}^2 K u_i. \quad (3.41)$$

In this formula there are two unknowns:  $\bar{u}_{(i+1)}$  and  $\omega_{c(i+1)}^2$ . The method of successive approximations enables us to find the unknown. For this we find integral operator  $K u_1$  from the function of the initial approximation  $\bar{u}_1$ . The first approximation will be obtained by normalizing the result:

$$\bar{u}_{i+1} = \omega_{c(i+1)}^2 K u_i \frac{1}{(\omega_{c(i+1)}^2 K u_i)|_{\max}}. \quad (3.42)$$

Since the unknown number  $\omega_{c(i+1)}^2$  is in both the function and the norm as the multiplier, it is shortened, which makes it possible to carry out further calculations without determining it in the intermediate stages.

After determining  $\bar{u}_{(i+1)}$  the operation is repeated and we find the following approximation:

$$\bar{u}_{(i+2)} = \omega_{c(i+2)}^2 K u_{(i+1)} \quad (3.43)$$

etc., until two neighboring approximations give sufficiently good eigenfunction agreement.

The unknown parameter of  $\omega_c^2$  is found from formula (3.43) under the conditions that the values of the functions of the last two approximations are equal:

$$\bar{u}_{(l+2)} \approx \bar{u}_{(l+1)}. \quad (3.44)$$

Then equation (3.43) has the form

$$\bar{u}_{(l+1)} = \omega_c^2 \bar{u}_{(l+2)} K u_{(l+1)}. \quad (3.43')$$

Since the last equality must be valid throughout the range of function variation, it, of course, will also be valid for the maximum values of the function, i.e., the norm. Therefore, we can write equality (3.43') as follows:

$$\bar{u}_{(l+1)}|_{\max} = 1 = (\omega_c^2 \bar{u}_{(l+2)} K u_{(l+1)})|_{\max}, \quad (3.43'')$$

hence

$$\omega_c^2 = \frac{1}{(K u_{(l+1)})_{\max}}. \quad (3.45)$$

The last expression is the calculation for determining the square of the angular velocity of the natural vibrations of the blade. The calculation is reduced to a table; the agreement accuracy of the two successive approximations can be checked conveniently (at a glance) graphically, for which the function  $\bar{u} = \bar{u}(z)$  is plotted for the initial and subsequent approximations (see, for example, analysis 3.1).

As we know, the method of successive approximation always leads to a search for the smallest eigenvalue integral equation (i.e., the lowest frequency of natural vibrations) and the proper form of the elastic line regardless of the originally assigned form function for the elastic line.

For plotting the converging process of successive approximation when seeking the highest values of natural frequencies and the corresponding forms of elastic line, the condition of orthogonality (3.39') is used. The formula for determining the eigenfunction  $u_{k(i+1)}$ , if the function  $u_{k,i}$  is known, will have the following form:

$$u_{k(i+1)}(z) = \omega_{ck(i+1)}^2 K_k u_{k,i} \quad (3.46)$$

where  $\omega_{ck(i+1)}^2$  is an approximation for the square of the frequency of k-th order vibrations.

The integral operator is

$$K_k u_{k,i} = K u_{k,i} + C_1 u_1 + C_2 u_2 + \dots + C_{k-1} u_{k-1} \quad (3.47)$$

where  $K u_{k,i}$  is the integral operator corresponding to the function  $\bar{u}_{k,i}$  for the i-th approximation (determined according to the formula (3.36));

$C_1 u_1; C_2 u_2 \dots$  are the terms which remove the effect of the component form functions of the lowest orders which appear in the process of successive approximation;

$C_1; C_2 \dots$  are the coefficients of orthogonality.

For a more detailed definition of natural frequencies and form functions for higher orders, see reference [10]. This reference also discusses the methodology of vibrational analysis for a blade with a band web taken into account. Let us note only that any addition of weight to a vibrating system (to a blade or any other elastic system) reduces the natural frequency of vibrations for the system.

Example 3.1. Find the lowest frequency of natural vibrations for a turbine blade whose parameters are indicated in Table 3.1. The length of the blade is  $l = 0.142$  m; the material is KhN70VNTYu (EI617) alloy;  $\rho = 8.4 \cdot 10^3$  kg/m<sup>3</sup>. In the analysis we take into

account variation in the modulus of elasticity due to nonuniform heating of the blade longitudinally. The values of  $F$  and  $I_\xi$  are obtained from gas-dynamic analysis.

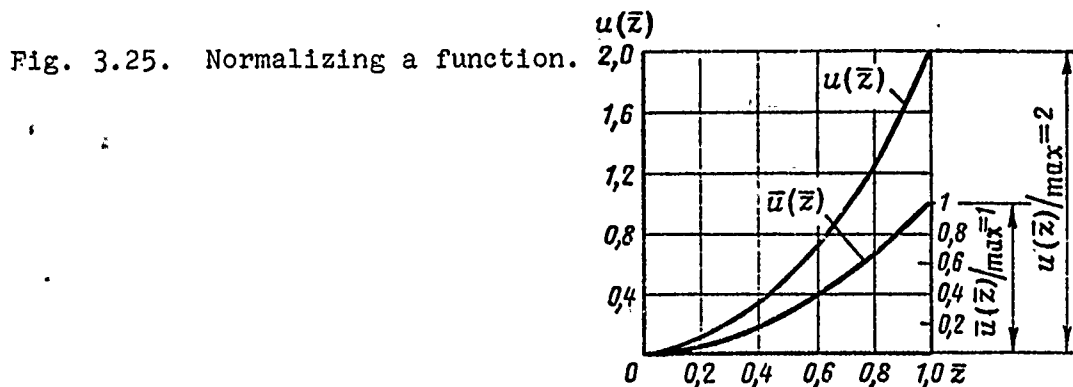
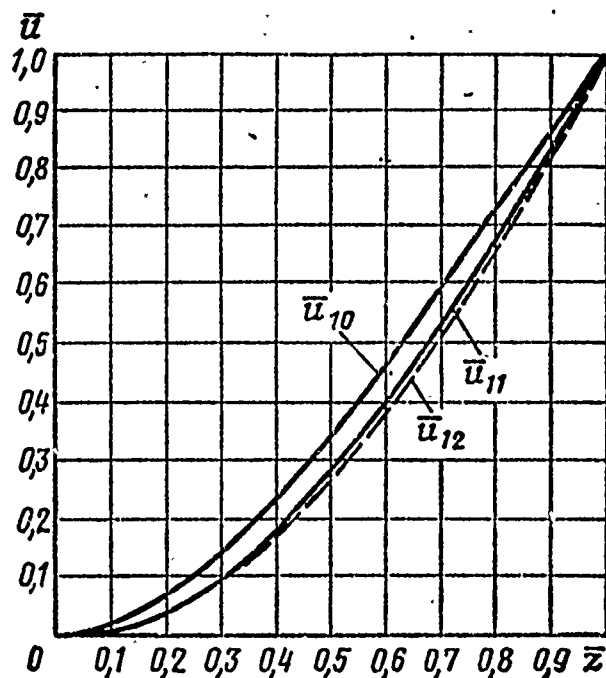


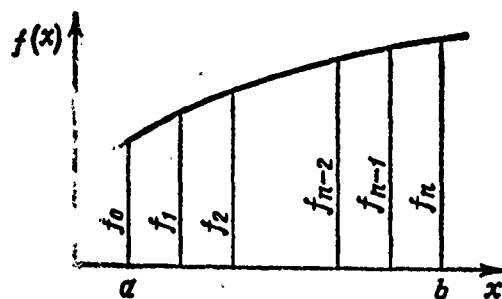
Fig. 3.26. The initial and two subsequent approximations of the first form of the elastic line of a vibrating blade (example of calculation).



For analysis the blade is divided into ten equal sections (generally we can take any number of sections and they do not have to be equal). As the zero approximation we take the elastic line of a cantilever of constant cross section (function  $\bar{u}_{10}$ ), which

satisfies the boundary conditions of the problem (this function is already normalized).

Fig. 3.27. Integration of the  $f(x)$  function by the trapezoid method.



The analysis will use formula (3.25). Integration will be performed according to the trapezoid method.<sup>1</sup>

Integration in lines (8) and (15) begins from the blade tip since according to the boundary conditions when  $\bar{z} = 1$ , the shearing force is equal to zero. Integration in lines (9) and (16) is also performed from the blade tip (when  $\bar{z} = 1$  the bending moment is zero). In lines (11), (18) and (12), (19) we integrate from the beginning of reading (since when  $\bar{z} = 0$  the angle of pitch and the deflection of the blade are equal to zero).

Both the zero and the subsequent approximations of function  $\bar{u}$  are drawn on the graph (Fig. 3.26).

The angular velocity of natural blade vibrations is determined from formula (3.45), taking into account the remote factor:

---

<sup>1</sup>As we know, the formula of trapezoids has the following form (if the number of points of division is equal to  $n$ ) (see Fig. 3.27)

$$\int_a^b f(x) dx \approx \frac{\Delta x}{2} (f_0 + 2f_1 + 2f_2 + \dots + 2f_{n-1} + f_n), \text{ where } \Delta x = \frac{b-a}{n}.$$

The greater  $n$  the more accurate the formula.

$$\omega_{c1}^2 = \frac{1}{\rho \left(\frac{l}{2}\right)^4 \cdot 10^{-7} (K_{u1})_{\max}} = \frac{1}{8,4 \cdot 10^3 \cdot \left(\frac{0,142}{20}\right)^4 \cdot 10^{-7} \cdot 57134} = 8,19 \cdot 10^6,$$

hence

$$\omega_{c1} = 2860 \text{ rad/s}$$

Blade vibration frequency is

$$f_{c1} = \frac{\omega_{c1}}{2\pi} = 456 \text{ vib/s}$$

The effect of revolution on the natural frequency of a blade

In practice the frequency of natural vibrations in a rotating blade is determined according to the frequency of a nonrotating blade with a correction for rotation.

As has already been mentioned in the stress analysis of a blade in a rotating blade under the action of centrifugal forces moment appears which strives to straighten the bent blade during its vibration (see Fig. 3.20). This is equivalent to stiffening a blade, due to which the natural frequency of a rotating blade increases. Particularly strong is the effect of centrifugal forces on the lowest natural frequency (corresponding to the first bending form). The effect on the other frequencies is less substantial. Therefore, it is of interest to calculate this lowest natural frequency with the effect of centrifugal forces taken into account.

Fig. 3.28. The dependence of the natural frequency of a blade on the angular velocity of rotation.  
KEY: (1) rad/s.

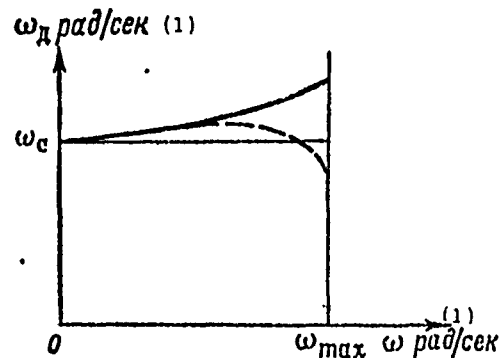




Table 3.1.

(1) № стро- ки	(2) Функция	(3) Множитель	(4) Численные значения функций при величинах $\bar{z}$										
			0	0,1	0,2	0,3	0,4	0,5	0,6	0,7	0,8	0,9	1,0
1	$Q F \text{ кг/м}$	$Q 10^{-4}$	2,7	2,38	2,12	1,82	1,66	1,5	1,3	1,18	1,05	0,98	0,9
2	$t^{\circ}C$	1	570	670	698	704	707	709	710	708	695	670	540
3	$E \text{ н/м}^2$	1000	1,85	1,79	1,76	1,76	1,76	1,76	1,76	1,76	1,77	1,79	1,88
4	$I_{\xi} \text{ м}^4$	$10^{-8}$	0,25	0,19	0,14	0,12	0,09	0,06	0,05	0,04	0,03	0,02	0,02
5	$E I_{\xi} \text{ н} \cdot \text{м}^2$	103	0,462	0,341	0,246	0,211	0,158	0,126	0,088	0,0704	0,0531	0,0358	0,0376
6	$\bar{u}_{10}$	1	0	0,017	0,064	0,132	0,230	0,359	0,461	0,591	0,725	0,862	1,00
7	$(1) \cdot (6)$	$Q 10^{-4}$	0	0,04	0,136	0,24	0,382	0,508	0,599	0,697	0,762	0,845	0,90
8	$\int (7) dz$	$Q \left(\frac{1}{20}\right) 10^{-4}$	9,318	9,278	9,102	8,726	8,104	7,214	6,107	4,811	3,352	1,745	0,0
9	$\int (4) dz$	$Q \left(\frac{1}{20}\right)^2 10^{-4}$	126,196	107,600	39,220	71,392	54,562	39,244	25,923	15,005	6,842	1,745	0
10	$\frac{(9)}{(5)}$	$Q \left(\frac{1}{20}\right)^2 10^{-7}$	273	315	352	338	345	370	295	213	129	48,8	0
11	$\int (10) dz$	$Q \left(\frac{1}{20}\right)^3 10^{-7}$	0	588	1265	1965	2648	3363	4028	4536	4878	5256	5105

KEY: (1) Line No.; (2) Function; (3) Multiplier; (4) Numerical values of functions with quantities  $\bar{z}$ .

Table 3.1. Continued

12	$\int (11) dz = Ku_0$	$q\left(\frac{l}{20}\right)^4 10^{-7}$	0	588	2441	5671	10284	16295	24686	32250	41664	51598	61759
13	$\bar{u}_{11}$	i	0	0,0095	0,0395	0,092	0,167	0,264	0,384	0,522	0,673	0,835	1
14	$(1)-(13)$	$q 10^{-4}$	0	0,0226	0,0837	0,167	0,278	0,396	0,498	0,615	0,707	0,818	0,9
15	$\int (14) dz$	$q\left(\frac{l}{20}\right)^2 10^{-4}$	8,071	8,048	7,942	7,691	7,246	6,572	5,678	4,565	3,243	1,718	0
16	$\int (15) dz$	$q\left(\frac{l}{20}\right)^2 10^{-4}$	113,477	97,358	91,368	65,735	50,798	36,980	24,730	11,497	6,679	1,718	0
17	$\frac{(16)}{(5)}$	$q\left(\frac{l}{20}\right)^2 10^{-7}$	246	285	331	312	322	349	281	206	126	47	0
18	$\int (17) dz$	$q\left(\frac{l}{20}\right)^3 10^{-7}$	0	531	1147	1790	2424	3095	3725	4212	4544	4717	4764
19	$\int (18) dz = Ku_1$	$q\left(\frac{l}{20}\right)^4 10^{-7}$	0	531	2209	5146	9360	14879	21699	29636	38392	47653	57134
20	$\bar{u}_{12}$	1	0	0,009	0,039	0,090	0,164	0,261	0,380	0,518	0,672	0,834	1

The angular velocity  $\omega_d$  of natural vibrations, with rotation taken into account, is determined from formula

$$\omega_d^2 = \omega_c^2 + B\omega^2, \quad (3.48)$$

where  $\omega_c$  is the angular velocity of natural vibrations in a nonrotating blade;

$\omega$  is the angular velocity;

B is the coefficient allowing for the effect of centrifugal forces on the natural frequency of a blade.

Coefficient B depends on the geometric dimensions of the blade and can be determined from formula

$$B = \frac{\int_0^l F(r_0 + z) dz \int_0^l \left(\frac{du}{dz}\right)^2 dz}{\int_0^l F u^2 dz}, \quad (3.49)$$

where F is the current cross-sectional area of the blade.

Figure 3.28 shows the character of variation in  $\omega_d$  as a function of the angular velocity of the rotor.

The effect of blade heating on the frequency of its natural vibrations

During turbine operation from the moment of starting up to the steady run the gas temperature and blade temperature vary.

Due to the increase in blade temperature with a change in  $\omega$  the modulus of elasticity for the material is reduced, which leads to a reduction in the frequency of natural vibration, as shown in Fig. 3.28 (dashes).

If the blade temperature for each mode is known then we can account for the effect of heating from formula

$$\omega_t = \omega_c \sqrt{\frac{E_t}{E}}, \quad (3.50)$$

where  $E_t$  is the modulus of elasticity at the assigned temperature;  
 $\omega_c$  and  $E$  are the natural frequency and the modulus of elasticity  
 for a cold blade, respectively.

#### Forced vibrations of blades. Resonance modes

During the work of a turbine gas flow moves along the circulatory part nonuniformly. This nonuniformity is caused by a change in the direction of the gas in the nonrectilinear circulatory section and also by the effect of various racks, flanges, guiding blades, and other structural elements which are located in the circulatory part. The nonuniformity of the flow which actuates the blades is caused by the partial admission of gas in turbines with velocity stages. The nonuniformity of flow creates alternation in the gas forces which load blades during their operation.

Because of this, forced vibrations appear in the blade.

In the time of one revolution of the turbine wheel the force which acts on the blade will change according to a certain law, whereupon it can be presented as the sum of harmonic components (Fig. 3.29):

$$P(t) = P_0 + P_1 \sin(\omega_1 t + \varepsilon_1) + P_2 \sin(\omega_2 t + \varepsilon_2) + \dots + P_k \sin(\omega_k t + \varepsilon_k) + \dots, \quad (3.51)$$

where  $P_0, P_1, \dots, P_k$  are the amplitude values of each of the harmonic components;

$\varepsilon_1, \varepsilon_2, \dots, \varepsilon_k$  are the angles of phase shift for the corresponding harmonics.

Each of the harmonics of the angular frequency of forced vibrations  $\omega_k$  is a multiple of angular velocity  $\omega$  of the rotor; the order of harmonic  $k$  determines this multiplicity:

$$\omega_k = k\omega = k2\pi n_c, \quad (3.52)$$

where  $k$  is the harmonic number;  $k = 1, 2, 3, \dots$ ;  
 $n_c$  is the number of revolutions of the rotor per second.

Forced vibrations by themselves will be dangerous if the value of the exciting force is high, able to cause significant amplitudes of vibrations. However, in practice, the so-called resonance modes will be dangerous.

As we know, the condition of resonance is the equality of forced frequencies  $\omega_B = \omega_k$  to the frequencies of natural vibrations  $\omega_c$ , i.e.,

$$\omega_B = \omega_c. \quad (3.53)$$

In this case, even small forces are capable of causing significant amplitudes of vibrations and leading to blade breakdown.

In a turbine a large number of different harmonics of excitation can occur. However, not all these harmonics will be dangerous from the point of view of resonance. To establish the degree of danger for any harmonic a frequency (resonance) diagram (Fig. 3.30) has been plotted for each turbine stage. The diagram is a graph of the dependence of the frequencies of free [determined by equation (3.48)] and forced [see equation (3.52)] vibrations of a blade on the angular velocity or the number of revolutions per second.

In view of the difficulty of obtaining curves  $P = P(t)$  when plotting a frequency diagram and a preliminary evaluation of the

danger of any resonance, we must take into account that the amplitude of the force  $P$  and its harmonic components rapidly increase with a decrease in the number of revolutions. Therefore, of practical interest is an examination of forced vibrations in a range of revolutions  $n = (0.8-1.05)n_{\max}$ .

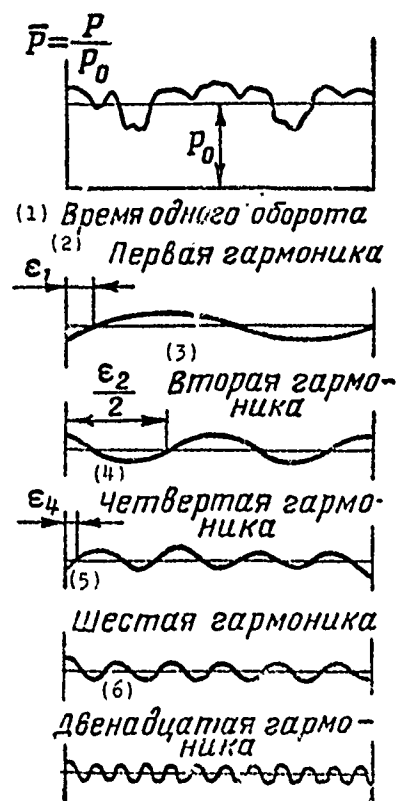


Fig. 3.29. Decomposition of the distributing gas force into harmonics.  
KEY: (1) Time of one revolution; (2) First harmonic; (3) Second harmonic; (4) Fourth harmonic; (5) Sixth harmonic; (6) Twelfth harmonic.

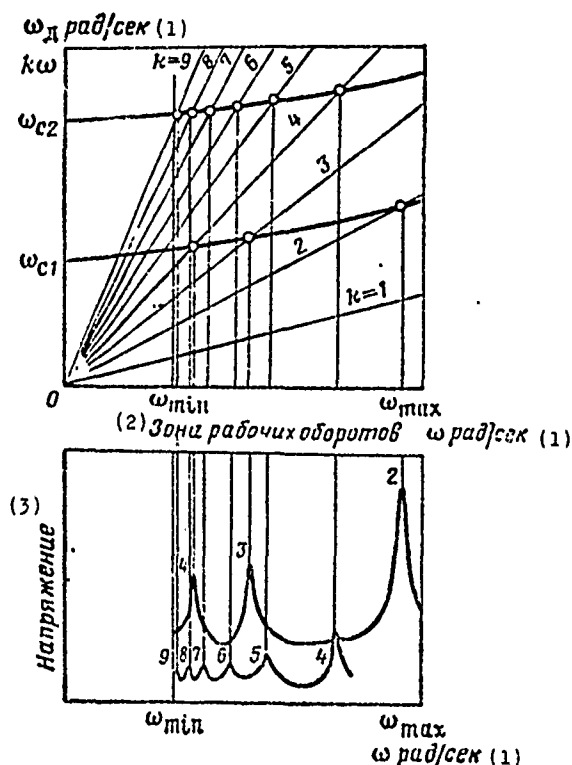


Fig. 3.30. Resonance diagram and resonance modes for the first two tones of blade vibrations.  
KEY: (1) rad/s; (2) Zone of working revolutions; (3) Stress.

With the action of harmonics of one force, the harmonics of the lowest orders are more dangerous. For clarity, along with the frequency diagram, we shall plot a graph showing the dependence of stresses on angular velocity  $\omega$  during forced oscillations of a blade.

At each of the points of intersection by a ray of exciting forces with the graph of natural frequencies resonance will occur. In these modes "bursts" are observed, i.e., sharp increase in amplitudes and an increase in stresses.

An analysis of the frequency characteristic shows which harmonics of forced vibrations will be dangerous and makes it possible to soundly implement the design of a turbine node so as to avoid dangerous resonance modes.

The following practical methods of combatting resonance modes in blades exist.

1. Elimination of the dangerous exciter harmonics. This can sometimes be done by a small structural alteration of the turbine unit. Let us assume that dangerous harmonic  $k = 4$  (based on the number of racks). If we change the number of racks, increasing it, for example, to 5, then the dangerous harmonic disappears.

2. To build the resonance frequency out of the blade, i.e., to change the inherent angular velocity  $\omega_c$ . This can be done by a certain variation in the blade's dimensions, however, so as not to disturb the gas-dynamic characteristics of the turbine and not to make a basic alteration of the turbine stage. It is possible, for example, to use hollow blades, to cut the angle of the blade foil in the periphery near the trailing edge, to use blades with band webs, to combine blades into groups by connectors or to cast blades with band webs in groups.

All these measures allow the redistribution of mass and the rigidity of the blade foil and, consequently, a variation in  $\omega_c$ .

3. The damping of blade vibrations. There are several methods of damping vibrations in elastic systems based on energy dispersion of a vibrating blade. This involves primarily damping in the blade

material (because of the internal friction), mechanical damping in the blade joints. It is possible to damp blades by the installation of two adjacent blades into one slot on the disk. In this case, damping is created by the friction of the vibrating blades about the plane on the joint of two blades. The vibrations of long blades can be damped by passing a wire through the opening in the blades on a free fit. During the rotation of a blade bundle with wire binding where vibrations occur at the contact points, friction, damping the vibrations, will arise. This method of connecting blades by a wire will also increase the rigidity of the blades and  $\omega_c$ .

There is also the so-called aerodynamic damping based on a change in the aerodynamic force during a variation in the angle of attack and the relative flow velocity. Aerodynamic damping is effective only with long blades and small angles of attack.

Experimental checks of natural vibration frequencies have shown a significant deviation in actual frequencies from the frequencies obtained by calculation. Actual frequencies have been lower than those calculated [23].

One of the reasons for this is the fact that the calculation of natural frequencies in a blade is carried out without taking into account deflection caused by the effect of tangent stresses from shearing forces and also without accounting for the inertia of rotation of blade sections during vibrations [see formula (3.25') for blades of constant cross section].

Another practically important reason causing a reduction in natural frequencies of a blade is the effect of the seal. In analyzing blades, we have assumed that the seal was absolutely rigid. In reality during blade vibrations, not only the blade foil itself is deformed but also the neck attached in the disk. This effect is particularly strong in short blades (blades are considered short if  $l/i < 30$  where  $l$  is the length of the blade and  $i$  is the radius of inertia of the blade root).



The actual frequency of natural bending vibrations of the first tone for blades of constant cross section is

$$f_1 = \psi \frac{0,56}{l^2} \sqrt{\frac{EI_x}{\rho F}}, \quad (3.54)$$

where

$$\psi = \frac{f_{\text{эксп}}}{f_{\text{расч}}};$$

$f_{\text{эксп}}$  is the natural frequency of vibrations found experimentally;  
 $f_{\text{расч}}$  is the natural frequency of vibrations found by calculations without taking into account the effect of tangential stresses, the inertia of section rotation, and the seal.

## Stress analysis of turbine disks

Turbine disks are the main load-bearing components of the rotor and enable the development of high circular velocities (up to 300-350 m/s). Turbine disks, just as rotor blades, work under very severe conditions. The following stresses appear in them:

- stress from the centrifugal forces of the disk itself as well as from the centrifugal forces of the blades fixed to the disk;
- assembly stresses (when a disk is fit tightly to a shaft);
- bending stress (from the axial forces of the gas acting on the blades and from the centrifugal forces of the blades with the unsymmetric location of their centers of gravity relative to the middle plane of the disk);
- temperature stresses (during the uneven heating of the disk along the radius and thickness);
- torsional stresses (from the torque on the blades being transferred by the disk to the shaft).

Furthermore, it is necessary to consider that the physical properties of the disk material deteriorate with a temperature increase -  $E$ ,  $\sigma_B$ ,  $\sigma_y$ ,  $\sigma_T$  decrease and the tendency toward plastic flows increases. Thus, the material of the turbine disk must resist creep and fatigue well at elevated temperatures.

Bending stresses and torsion, as a rule, are considerably less than the others and are not usually considered in stress analysis of disks.

Disk analysis is a complicated, statically undefinable problem.

There are three forms of stress analysis for disks.

1. Determining stresses in a disk of known shapes (check calculations).

2. Plotting the disk shapes according to a given law of stress distribution ("disks of constant strength").

3. Determining the safety factor of a disk based on destructive revolutions.

We make the following assumptions in disk analysis:

- the disk is thin and its thickness varies little as compared with the diameter;
- the disk is circular and symmetrical relative to its middle plane;
- external loads (from blades on outer diameter and, when disk is pressed to shaft, on the edge of the internal opening) are distributed uniformly along the thickness of the disk and along the circumference;
- temperatures are distributed uniformly along the thickness and the circumference of the disk, changing only along the radius.

These assumptions enable us to assume that in the disk under the action of centrifugal forces and from nonuniform heating there arise normal stresses: radial and circular, i.e., the disk is located in biaxial stress (longitudinal stresses are absent). There is a fully defined relationship between these stresses, which is caused by the possibility of elastic deformation of the disk at a given point.

Basic for disk analysis are the equation of equilibrium for a rotating disk and the equation of strain compatibility, which make it possible to determine these stresses.

#### Derivation of equations

Let us first examine a cold (more accurately, uniformly heated) disk loaded by centrifugal forces. To derive the equation of equilibrium let us distinguish in the disk an elementary volume and examine the condition of equilibrium of all forces acting on it (Fig. 3.31).

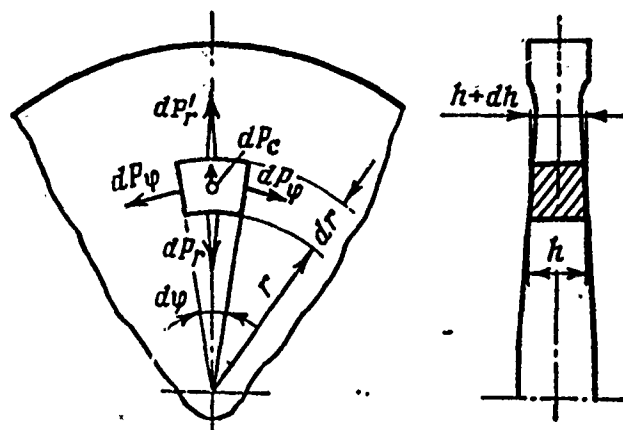


Fig. 3.31. Disk element and forces acting on it during rotation.

In a radial direction three forces act on the element: centrifugal force applied at the element's center of gravity,

$$dP_c = dm r \omega^2 = \rho \omega^2 r^2 h d\varphi dr;$$

the force applied to the internal surface of element (on radius  $r$ ),

$$dP_r = \tau_r h d\varphi;$$

the force applied to the external surface of the element (on radius  $r + dr$ ),

$$\begin{aligned} dP_r' &= dP_r + d(dP_r) = \tau_r h d\varphi + d(\tau_r h d\varphi) \approx \\ &\approx \tau_r h d\varphi + d(\tau_r h) d\varphi. \end{aligned}$$

In a circular direction two forces  $dP_\varphi = \sigma_\varphi h dr$  act on the disk element.

While projecting all forces onto the vertical axis, we obtain

$$dP_c - dP_r' + dP_r - 2dP_\varphi \sin \frac{d\varphi}{2} = 0.$$

(In view of the smallness of angle  $d\varphi$  we can assume  $\left(\frac{d\varphi}{2}\right) \approx \frac{d\varphi}{2}$ ).

Let us substitute into this equality the value of all forces:

$$\frac{d(\sigma_r r h)}{dr} - \sigma_\varphi h + \rho \omega^2 r^2 h = 0. \quad (3.55)$$

Equation (3.55) is called the equation of disk equilibrium. In this equation there are two unknown quantities: stresses  $\sigma_r$  and  $\sigma_\varphi$ . In order to determine them another equation is necessary, which can be obtained from examining the strains of the disk element (Fig. 3.32).

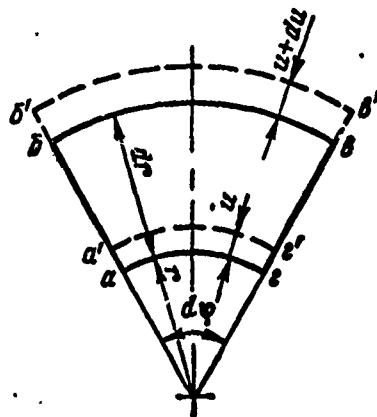


Fig. 3.32. Disk element before and after strain.

We designate the disk element before strain  $a\delta r$  and after strain  $a'\delta'r'$ . We also designate radial displacement on radius  $r$  in terms of  $u$ . Then on radius  $r + dr$  the value of radial strain will be  $u + du$ .

Relative radial strain is

$$\epsilon_r = \frac{a'\delta' - a\delta}{a\delta} = \frac{dr + u + du - u - dr}{dr} = \frac{du}{dr}. \quad (3.56)$$

Relative circular strain is

$$\epsilon_\varphi = \frac{a'z' - az}{az} = \frac{(r + u)d\varphi - rd\varphi}{rd\varphi} = \frac{u}{r}, \quad (3.57)$$

or

$$u = \varepsilon_{\varphi} r. \quad (3.58)$$

Let us differentiate equality (3.58) with respect to  $r$ :

$$\frac{du}{dr} = \frac{d}{dr}(\varepsilon_{\varphi} r) = r \frac{d\varepsilon_{\varphi}}{dr} + \varepsilon_{\varphi}.$$

Substituting the obtained expression from (3.56), we arrive at the condition of strain compatibility:

$$\varepsilon_r = \frac{du}{dr} = r \frac{d\varepsilon_{\varphi}}{dr} + \varepsilon_{\varphi},$$

or

$$r \frac{d\varepsilon_{\varphi}}{dr} + \varepsilon_{\varphi} - \varepsilon_r = 0. \quad (3.59)$$

In order to introduce into equation (3.59) stresses  $\sigma_r$  and  $\sigma_{\varphi}$ , we shall use the dependence of strains on stresses within the limits of elasticity for a biaxial stressed state (generalized Hook's law):

$$\varepsilon_r = \frac{1}{E} (\sigma_r - \mu \sigma_{\varphi}); \quad \varepsilon_{\varphi} = \frac{1}{E} (\sigma_{\varphi} - \mu \sigma_r), \quad (3.60)$$

when  $\mu$  is the Poisson's coefficient.

The equation (3.60) is valid for cold or uniformly heated disks (for the equation for nonuniform heating see below).

Substituting the relationship (3.60) into (3.59), we obtain the condition of strain compatibility expressed through stresses:

$$\frac{d\sigma_r}{dr} - \mu \frac{d\sigma_\varphi}{dr} = \frac{1+\mu}{r} (\sigma_r - \sigma_\varphi). \quad (3.61)$$

Thus, in order to determine the radial and circular stresses in a disk we derived a system of two differential equations (3.55) and (3.61)

System of equations (3.55) and (3.61) can be replaced by one differential equation of the second order relative to displacement  $u$ . For this we solve a system of equations (3.60) relative to  $\sigma_r$  and  $\sigma_\varphi$  with equalities (3.56) and (3.57) taken into account:

$$\sigma_r = \frac{E}{1-\mu^2} \left( \frac{du}{dr} + \mu \frac{u}{r} \right); \quad \sigma_\varphi = \frac{E}{1-\mu^2} \left( \frac{u}{r} + \mu \frac{du}{dr} \right). \quad (3.62)$$

If we substitute equalities (3.62) into (3.55) we obtain a differential equation of the second order relative to  $u$ :

$$\frac{d^2u}{dr^2} + \left( \frac{1}{h} \frac{dh}{dr} + \frac{1}{r} \right) \frac{du}{dr} + \left( \frac{\mu}{h} \frac{dh}{dr} - \frac{1}{r} \right) \frac{u}{r} = -\frac{1-\mu^2}{E} Cr, \quad (3.63)$$

where

$$C = \zeta \omega^2. \quad (3.64)$$

If we can obtain a solution to equation (3.63) relative to the radial displacement of  $u$  for a disk of any shape (defined by function  $h = h(r)$ ), then stresses  $\sigma_r$  and  $\sigma_\varphi$  are determined from expressions (3.62).

Thus, stresses in a rotating disk can be obtained either directly from equations (3.55) and (3.61) or from expressions (3.62) after determining  $u$  from equation (3.63).

From the theory of differential equations we know that the solution to equation (3.63) for a disk of arbitrary shape can be written in the form

$$u = A\varphi_1(r) + B\varphi_2(r) + C\varphi_3(r), \quad (3.65)$$

where  $\varphi_1(r)$  and  $\varphi_2(r)$  are particular solutions of a homogeneous equation corresponding to equation (3.63) [i.e., equation (3.63) without the right side];

$\varphi_3(r)$  is a particular solution to equation (3.63) (i.e., equation with the right side);

A and B are integration constants determined from the boundary conditions.

Coefficient C is taken from expression (3.64).

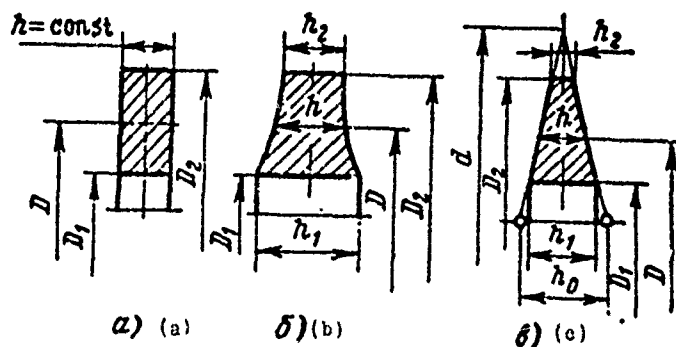


Fig. 3.33. Shapes of the radial cross section of disks:  
 a - disk of constant thickness; b - hyperbolic disk;  
 c - conical disk.

However, equation (3.63) can be integrated in the elementary functions only for certain particular cases, for example, for a disk of constant thickness ( $h = \text{const}$ ), for hyperbolic disks, and certain others.



For conical disks equation (3.63) is integrated in hypergeometric functions (in the form of infinite converging series). Turbine disks virtually always consist of separate sections with different shapes. With sufficient accuracy, the separate sections of disks can be reduced to shapes of the following types.

1. Disks of constant thickness (Fig. 3.33a)  $h = \text{const.}$

2. Hyperbolic disks; the cross section of the disk is bounded by hyperbolas of any order (Fig. 3.33b). The thickness of such a disk changes according to the following law

$$h = \frac{a}{\left(\frac{D}{2}\right)^m},$$

where  $a$  is a constant;  $m$  is the exponent;  $D$  is the current diameter.

The values of coefficient  $a$  and exponent  $m$  can be determined for a curvilinear disk shape from the condition that the curve pass through any two points on the profile with known dimensions. Thus, if  $D_1$ ,  $h_1$ , and  $D_2$ ,  $h_2$  are given, then

$$h_1 = \frac{a}{\left(\frac{D_1}{2}\right)^m}; \quad h_2 = \frac{a}{\left(\frac{D_2}{2}\right)^m},$$

hence, taking the logarithm of this expression, we find

$$m = \frac{\ln\left(\frac{h_1}{h_2}\right)}{\ln\left(\frac{D_2}{D_1}\right)} \quad \text{и} \quad a = h_1 \left(\frac{D_1}{2}\right)^m = h_2 \left(\frac{D_2}{2}\right)^m.$$

It is obvious that a disk of constant thickness can be considered a particular case of hyperbolic disk when  $m = 0$ .

3. Conical disks: the cross section of such a disk is a trapezoid (Fig. 3.33c). The thickness of the disk varies according to law

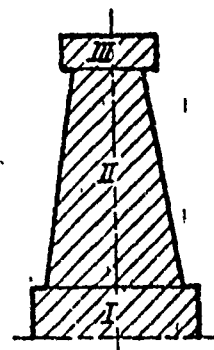
$$h = h_0 \left( 1 - \frac{D}{d} \right),$$

where  $d$  is the diameter of the "complete" cone;

$$d = D_1 + \frac{h_1}{h_1 - h_2} (D_2 - D_1).$$

As an example, Fig. 3.34 presents a schematic representation of a typical disk for a turbine rotor. The disk can be broken down into three sections: Section I is of constant thickness; Section II is conical; Section III is of constant thickness.

Fig. 3.34. Schematic representation of the cross section of a turbine disk.



In similar disks consisting of several sections, stresses are determined separately in each section; during the transition from section to section their coupling conditions are used.

Let us examine the method of determining stresses in rotating disks of arbitrary shape individually for each of three basic types: constant thickness, hyperbolic, and conical.

Disks of constant thickness can be considered a particular case of a hyperbolic disk (when  $m = 0$ ); therefore, we shall not pause especially on them.

Hyperbolic disks. If the thickness of such a disk  $h = a/(D/2)^m$  is substituted into equation (3.63), the solution for  $u$  is obtained in the form (3.65), whereupon, in this case, particular solutions  $\varphi_1$ ,  $\varphi_2$ , and  $\varphi_3$  are elementary functions.

The equations for stresses  $\sigma_r$  and  $\sigma_\varphi$  can be obtained from formulas (3.62) after substituting in them the solutions for  $u$ :

$$\sigma_r = p_A A + p_B B + p_C T''; \quad \sigma_\varphi = q_A A + q_B B + q_C T''. \quad (3.66)$$

where  $p$  and  $q$  are coefficients depending on the geometric dimensions of the disk cross section (including exponent  $m$ ), on the characteristics of the disk material ( $E$ ;  $\mu$ ;  $\rho$ ), on the angular velocity of disk rotation and the present functions of the diameter (or radius), on which stresses are being defined;

$A$  and  $B$  are the integration constants;

$$T' = C \frac{D}{2}.$$

During practical analyses of disks consisting of several sections, the stresses  $\sigma_r$  and  $\sigma_\varphi$  on the current diameter  $D$  are expressed in terms of the known stresses  $\sigma_{r1}$  and  $\sigma_{\varphi1}$  on the initial diameter  $D_1$ . Such formulas can be obtained from formulas (3.66) if we determine the constants  $A$  and  $B$  from the following conditions: when  $D = D_1$   $\sigma_r = \sigma_{r1}$ ;  $\sigma_\varphi = \sigma_{\varphi1}$ , and then again substitute them into formulas (3.66). The results are written in the following form:

$$\left. \begin{aligned} \sigma_r &= \alpha_r \sigma_{r1} + \alpha_\varphi \sigma_{\varphi1} + \alpha_C T; \\ \sigma_\varphi &= \beta_r \sigma_{r1} + \beta_\varphi \sigma_{\varphi1} + \beta_C T, \end{aligned} \right\} \quad (3.67)$$

where  $\alpha_r$ ;  $\alpha_\varphi$ ;  $\alpha_C$ ;  $\beta_r$ ;  $\beta_\varphi$ ;  $\beta_C$  are the coefficients which for hyperbolic disks represent lengthy algebraic expressions.

These coefficients are conveniently determined according to special nomograms depending upon the arguments  $x = D_1/D$  and  $z = h/h_1$  (see Fig. 3.33b).

We should note that coefficients  $\alpha_C$  and  $\beta_C$  have a linear dependence on the density of disk material. Graphs for  $\alpha_C$  and  $\beta_C$  are plotted for steel disks. In analyzing disks of other material the coefficient  $\alpha_C$  and  $\beta_C$ , determined from the graphs, must be multiplied by the ratio  $\rho/\rho_{CT}$  where  $\rho$  is the density of the disk material and  $\rho_{CT}$  is the density of the steel.

Coefficient T in formulas (3.67) is equal to

$$T = \left( \frac{Dn}{10^6} \right)^2,$$

where D is the diameter on which stresses are determined, mm;  
n is the disk rpm.

If  $n = 0$ , the third terms on the right side of formula (3.67) disappear and we obtain expressions for stresses in a nonrotating disk loaded on the boundaries by external forces.

Graphs for determining the coefficients  $\alpha$  and  $\beta$  for hyperbolic disks are given in Figs. 3.35-3.40.

For disks of constant thickness ( $m = 0$ ;  $z = 1$ ) the graph of coefficients  $\alpha$  and  $\beta$  are given separately as a function of one argument  $x = D_1/D$  (Fig. 3.41).

Conical disks. The equation (3.63) for conical disks is transformed into a hypergeometric differential equation whose solution is given in the form of infinite series and, for practical use, can be represented only in the form of a nomogram or numerical tables.

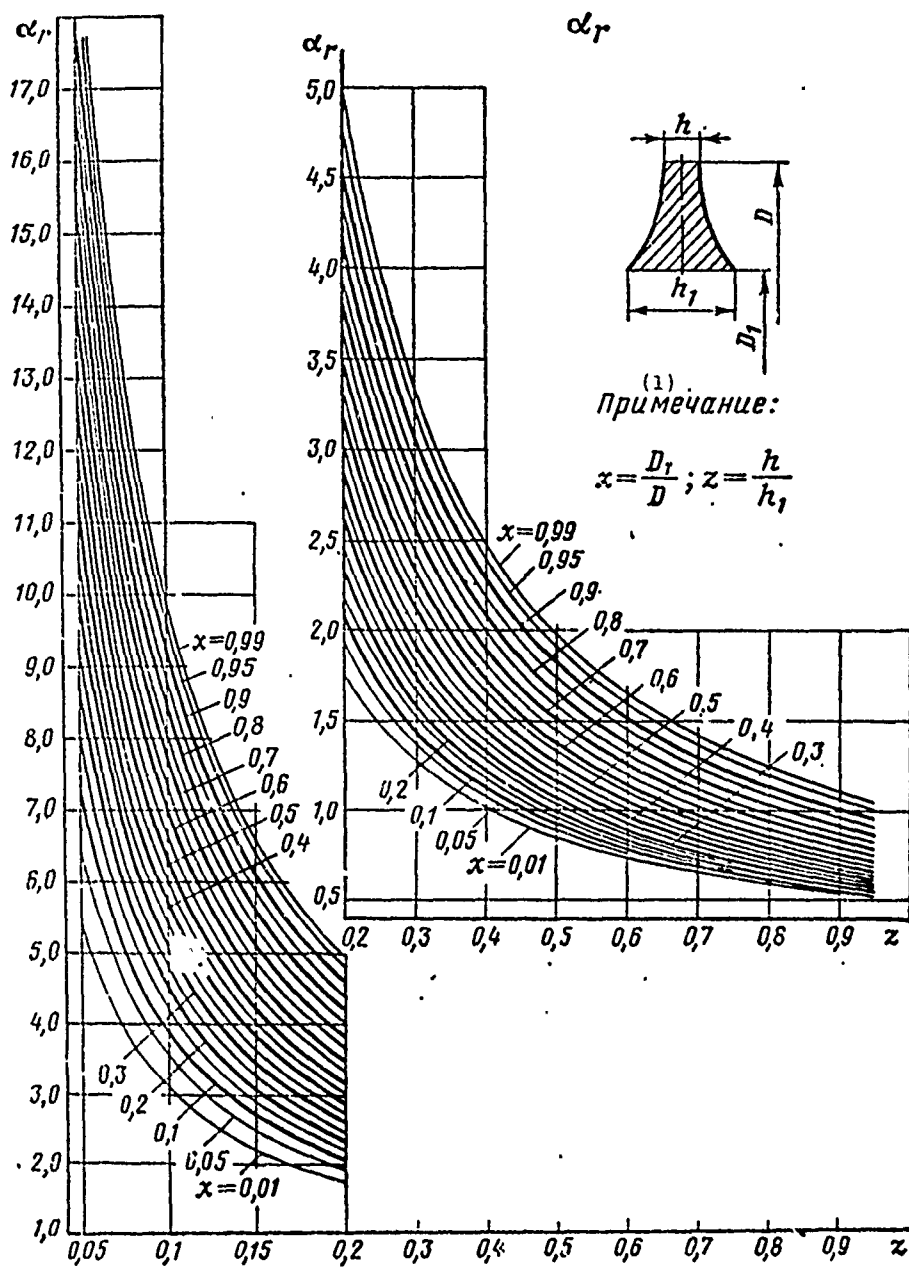


Fig. 3.35. Nomogram for determining the coefficient in designing hyperbolic disks.  
KEY: (1) Note.

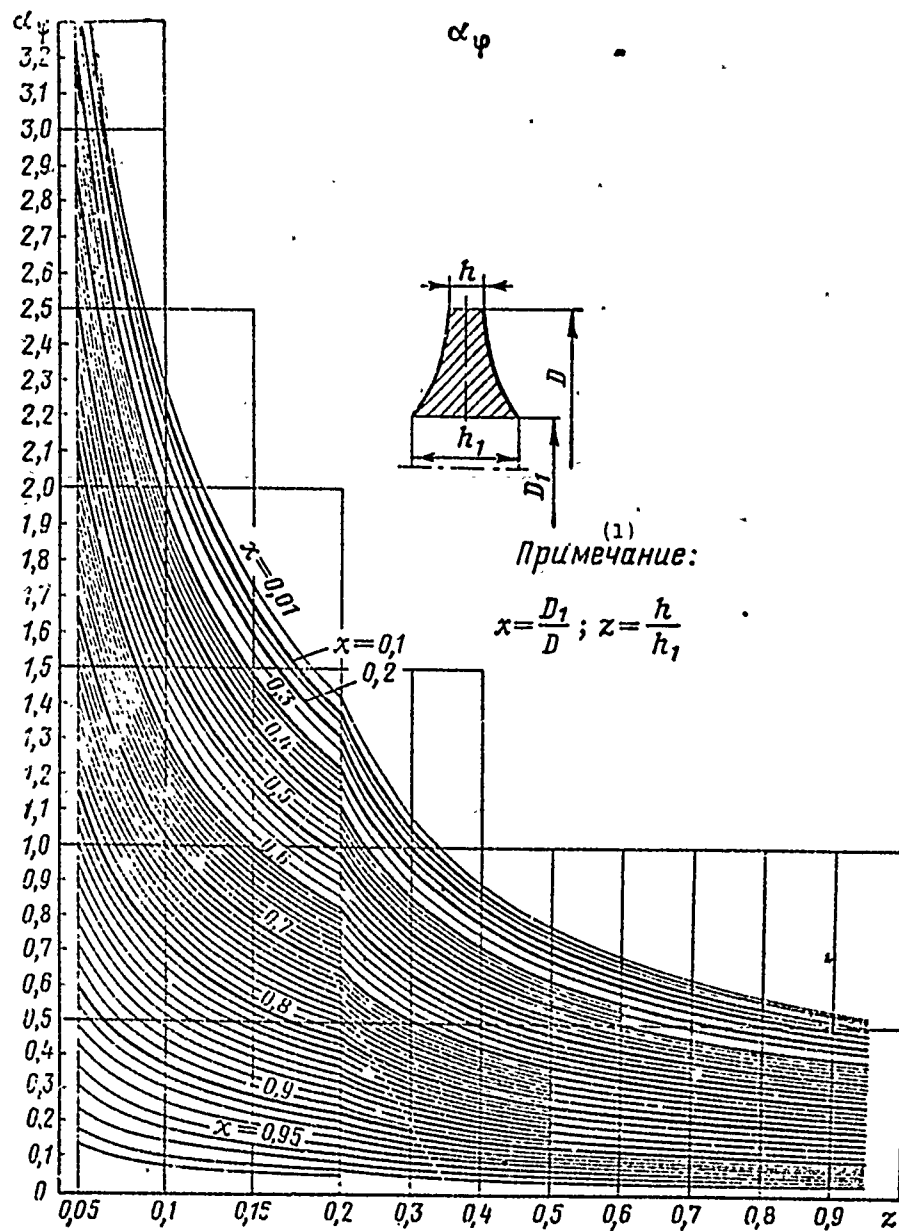


Fig. 3.36. Nomogram for determining the coefficient in designing hyperbolic disks.  
KEY: (1) Note.

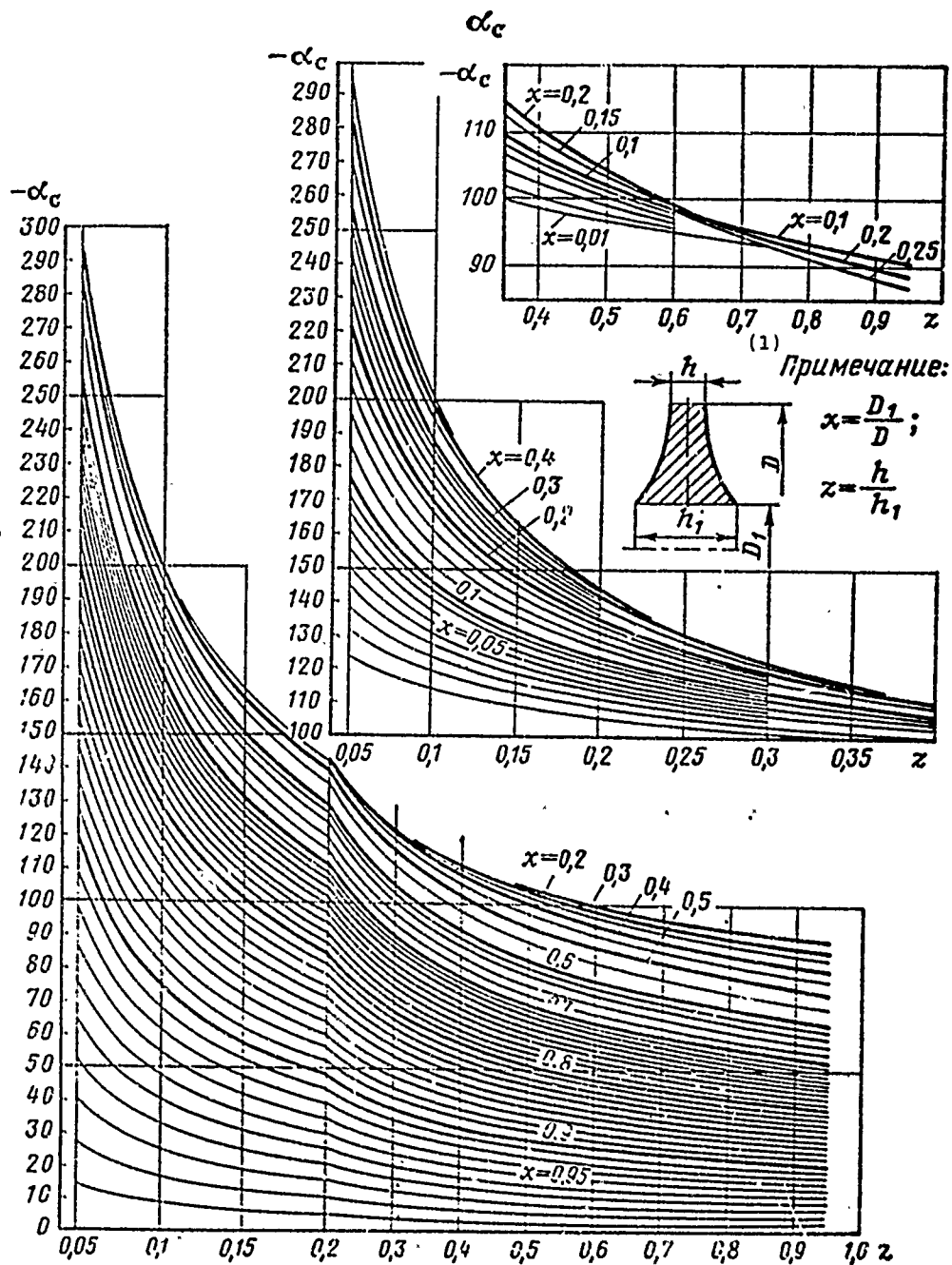


Fig. 3.37. Nomogram for determining the coefficient in designing hyperbolic disks.  
KEY: (1) Note.

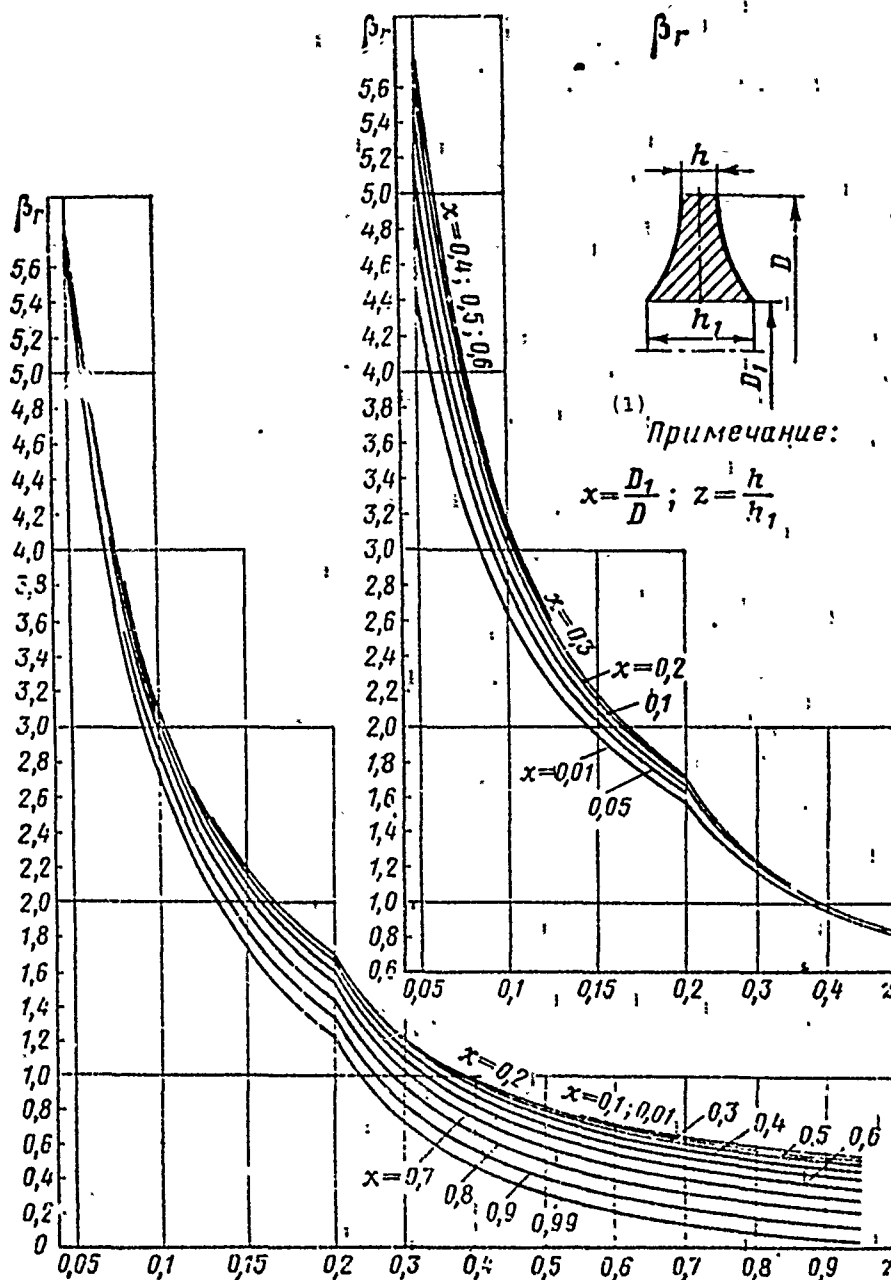


Fig. 3.38. Nomogram for determining the coefficient in designing hyperbolic disks.  
 KEY: (1) Note.



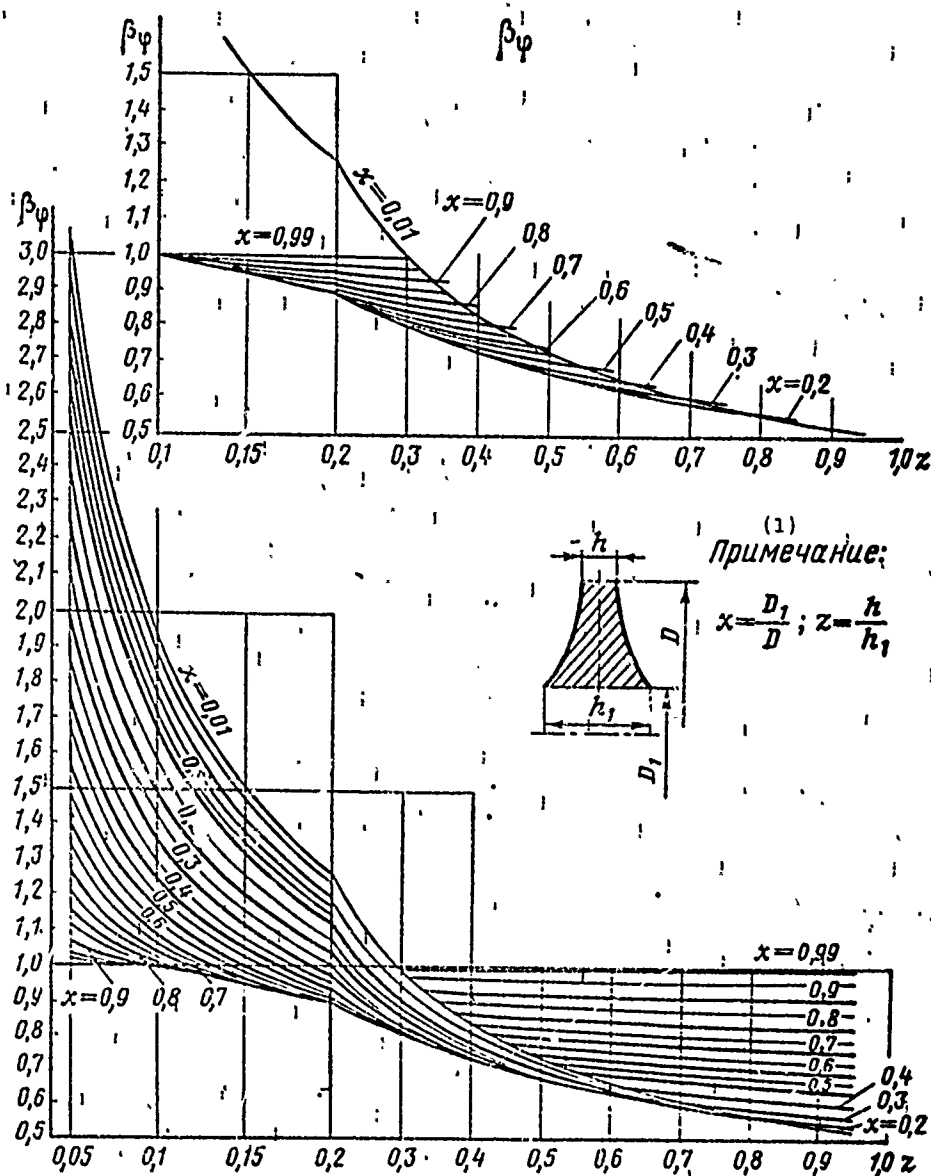


Fig. 3.39. Nomogram for determining the coefficient in designing hyperbolic disks.  
 KEY: (1) Note.

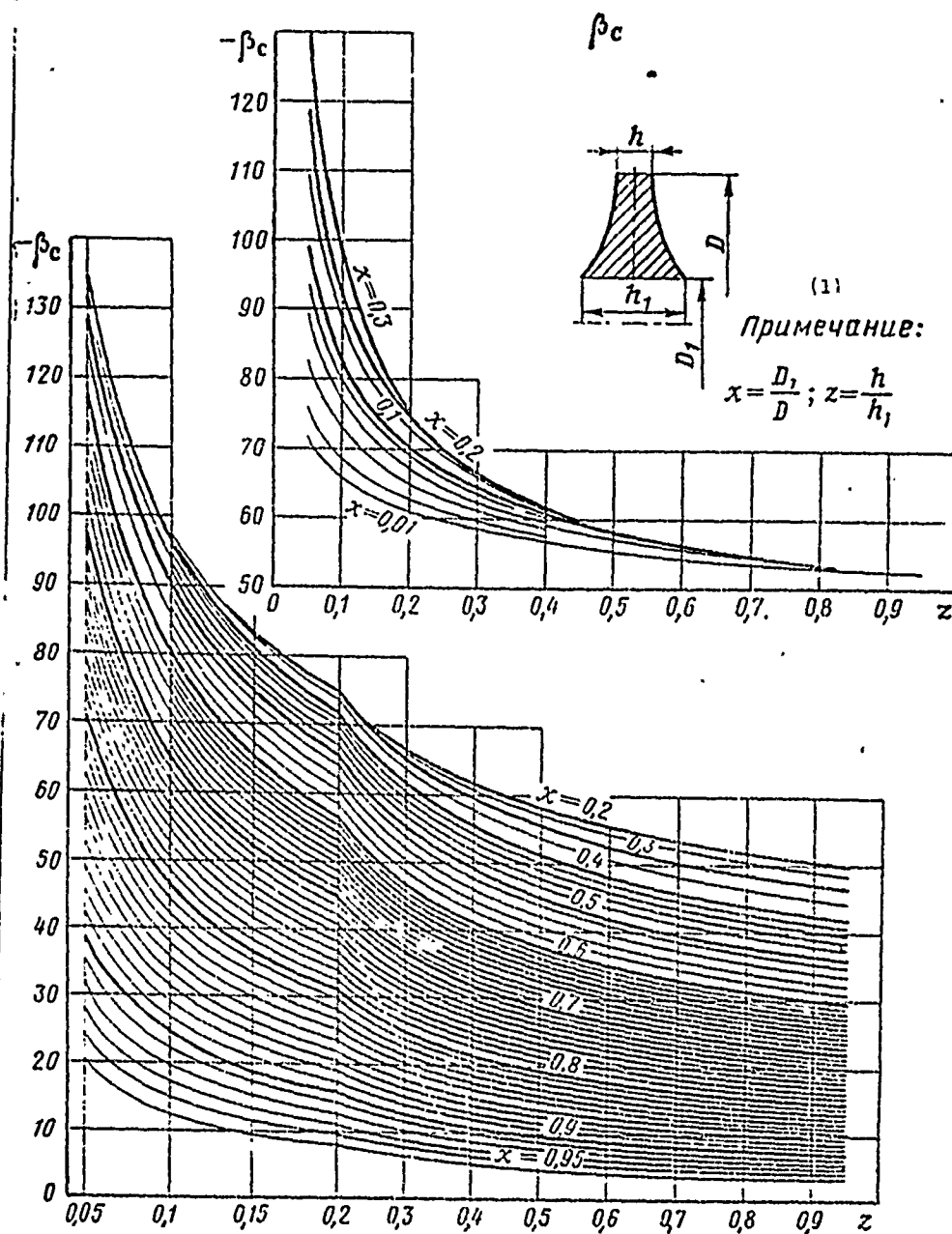


Fig. 3.40. Nomogram for determining the coefficient in designing hyperbolic disks.  
 KEY: (1) Note.

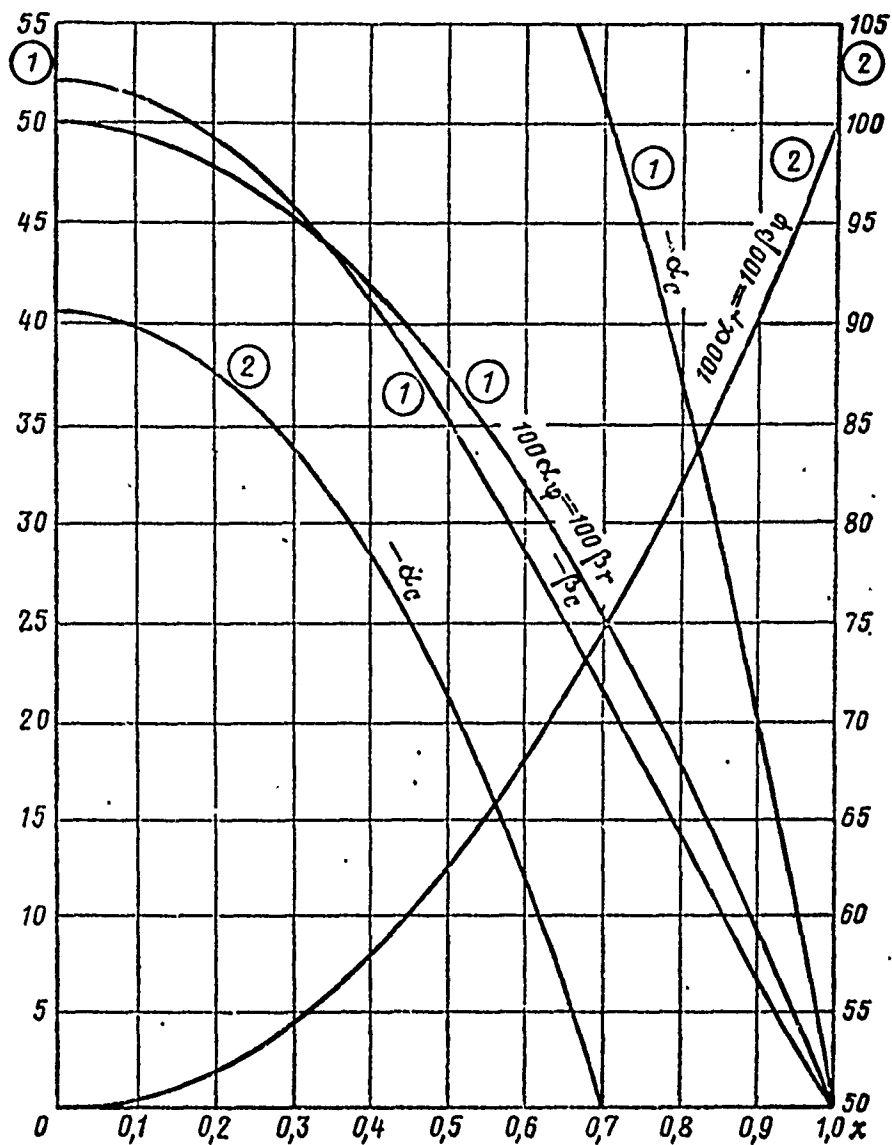


Fig. 3.41. Nomogram for determining coefficients in designing disks of constant thickness.

The solution can be written in the form (3.66) or with transformation it can be similar for hyperbolic disks, in the form of (3.67):

$$\left. \begin{aligned} \sigma_r &= \alpha_r \sigma_{r1} + \alpha_\varphi \sigma_{\varphi1} + \alpha'_C T_d \\ \sigma_\varphi &= \beta_r \sigma_{r1} + \beta_\varphi \sigma_{\varphi1} + \beta'_C T_d \end{aligned} \right\} \quad (3.67'')$$

Coefficients  $\alpha$  and  $\beta$ , as for hyperbolic disks, depend on the geometric form, the disk material, and diameters  $D$  and  $D_1$ . Numerical values of the coefficients are given in the form of nomograms where they are determined as a function of two arguments:

$$t_1 = \frac{D_1}{d} \quad \text{and} \quad t = \frac{D}{d} \quad (\text{see Fig. 3.33c}).$$

Graphs for determining coefficients  $\alpha$  and  $\beta$  for conical disks are illustrated in Figs. 3.42-3.47. If the disks are not made of steel, coefficients  $\alpha'_C$  and  $\beta'_C$ , as for hyperbolic disks, must be multiplied by the ratio  $\rho/\rho_{CT}$ . In formulas (3.67')  $T_d = (dn/10^6)^2$ , where  $d$  is the diameter of the complete cone in mm.

In analyzing disks of hyperbolic and conic shapes we must assume that in the center of a disk without openings up to a certain diameter  $D \leq D_a$  the thickness of the disk is constant (which usually is the case). Coefficients  $\alpha$  and  $\beta$  for hyperbolic and conic disks are given for the arguments  $x = (D_1)/(D) \geq 0.01$  and  $t_1 = (D_1)/(d) \geq 0.01$ .

#### *Boundary conditions*

For disk analysis differential equations of the second order were obtained. Therefore, in order to compute stresses we must have at least two boundary conditions.

Let us examine two cases: a disk without a central opening (solid disk) and a disk with a central opening.

Solid disk. 1. The first boundary condition will be the equality of the radial and circular stresses in the center of the disk because of the symmetry of the load, i.e., when  $r = 0$   $\sigma_{r0} = \sigma_{\varphi 0}$ .

2. The second boundary condition will be that stress is known on the outer radius of the disk, i.e., when  $r = R_g$ :

- a)  $\sigma_{rB} = 0$  if the disk does not have a blade and is loaded only with forces of inertia of the mass itself;
- b)  $\sigma_{rB} = \sigma_{rA}$  if on the crown of the disk blades are attached.

Uniformly distributed load from centrifugal forces of blades  $\sigma_{rA}$  acting on the cylindrical surface on radius  $R_g$  (Fig. 3.48) can be determined from formula

$$\sigma_{rA} = \frac{P_{jz}}{2\pi R_g h_g} = \frac{z_k F_k z + 2\pi Q r_1^2 F_1 \omega^2 + 2\pi Q r_2^2 F_2 \omega^2}{2\pi R_g h_g}, \quad (3.68)$$

where  $\sigma_k$  is the stress in the blade root from centrifugal forces;

$F_k$  is the area of the blade root cross section;

$z$  is the number of blades;

$F_2$  is the cross-sectional area of the disk crown joint in a plane passing through the axis of rotation;

$F_1$  is the cross-sectional area of the transitional part of the blade from the foil to the joint also in a plane passing through the axis of rotation;

$r_1$  and  $r_2$  are the radii of the centers of gravity of areas  $F_1$  and  $F_2$ , respectively.

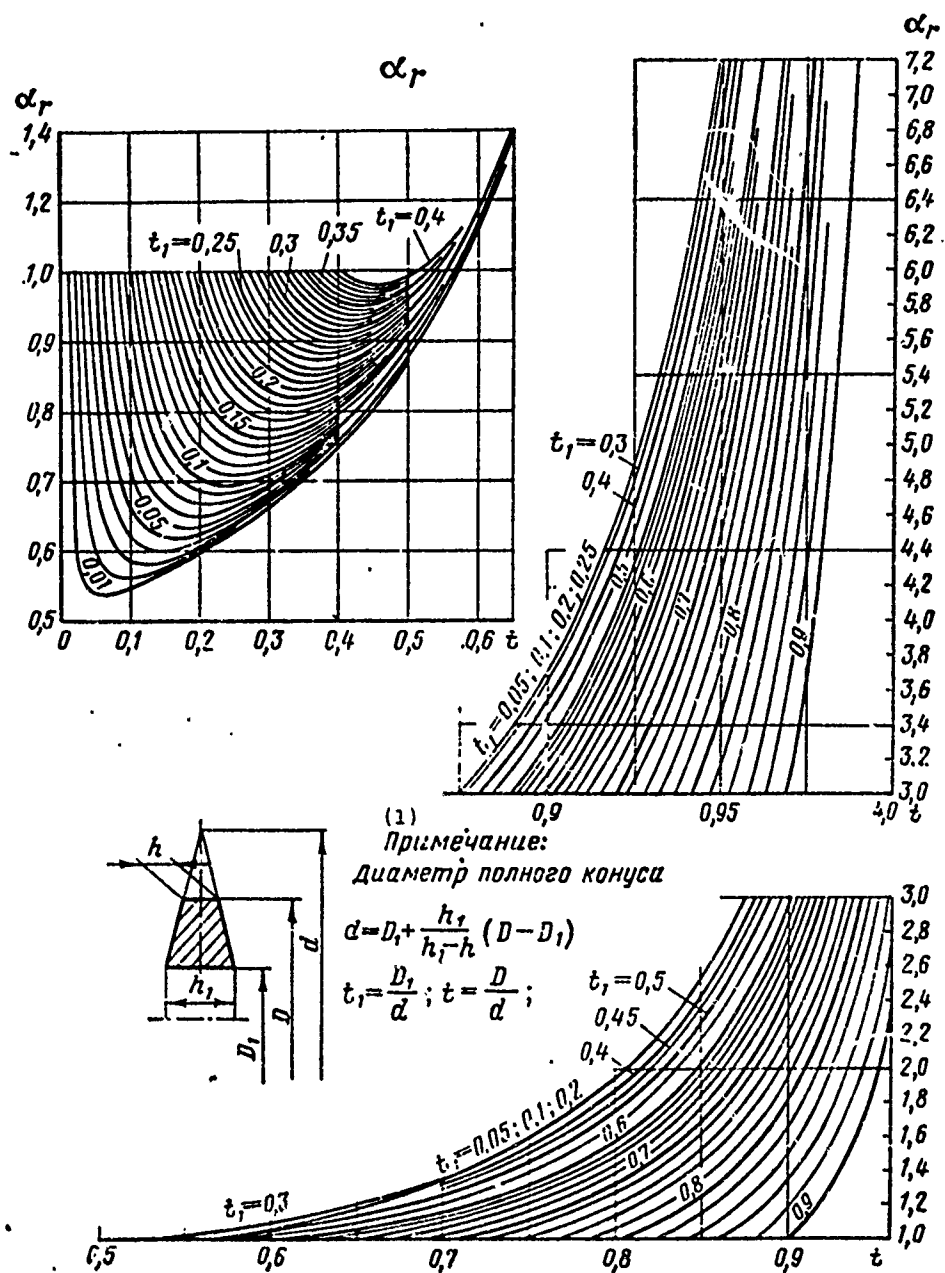


Fig. 3.42. Nomogram for determining coefficient in designing conical disks.

KEY: (1) Note: diameter of full cone.

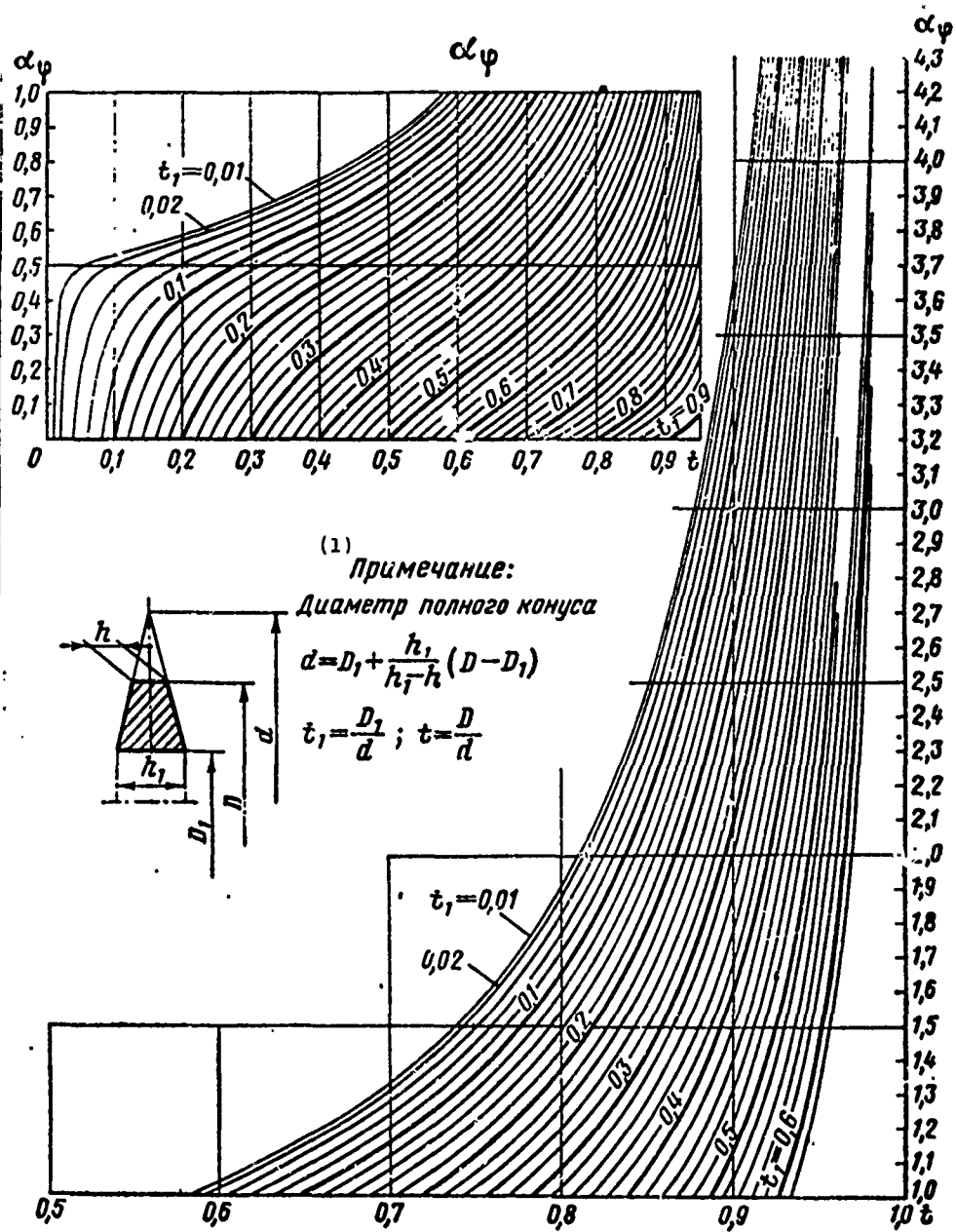


Fig. 3.43. Nomogram for determining coefficient in designing conical disks.

KEY: (1) Note: diameter of full cone.

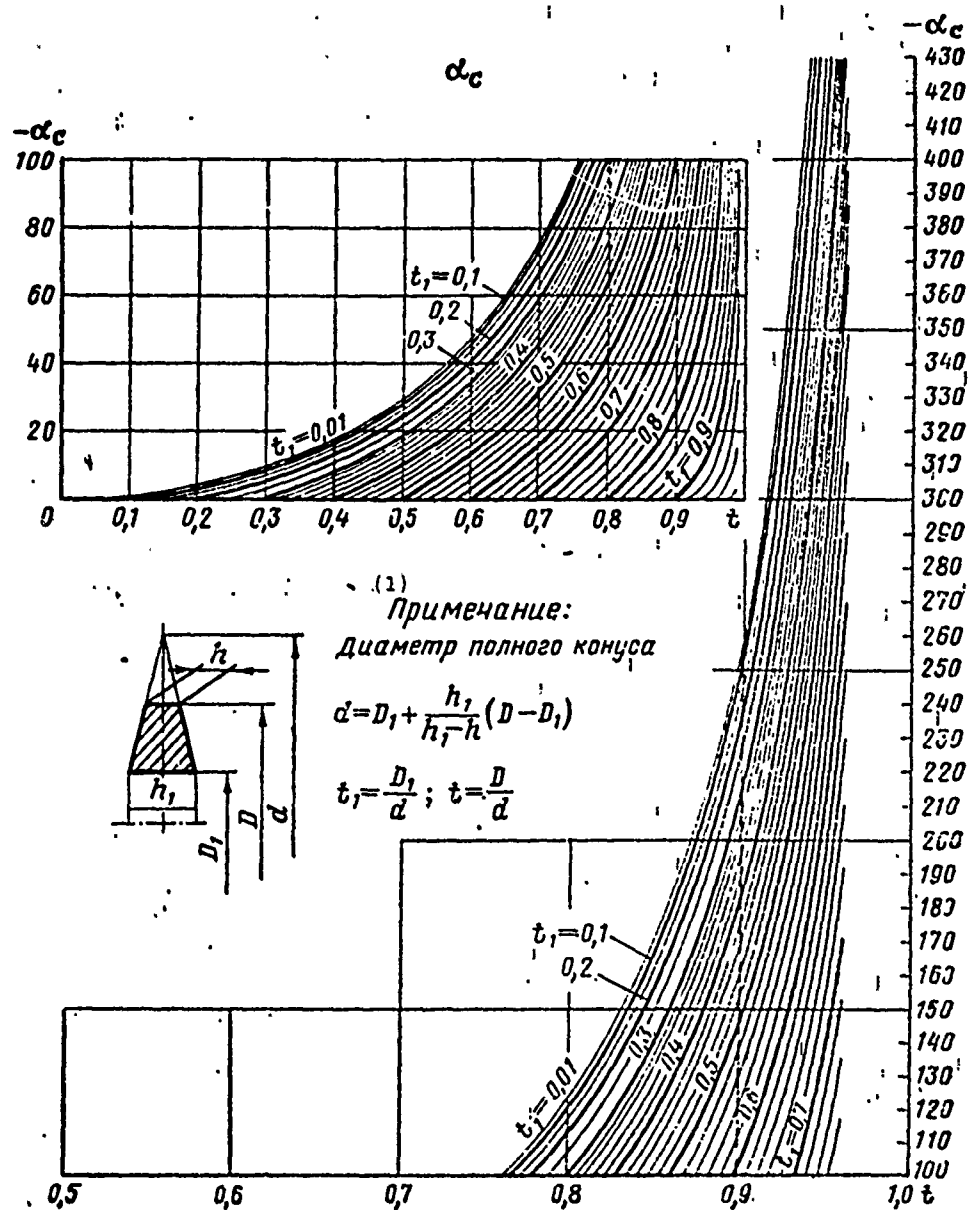


Fig. 3.44. Nomogram for determining coefficient in designing conical disks.  
KEY: (1) Note: diameter of full cone.



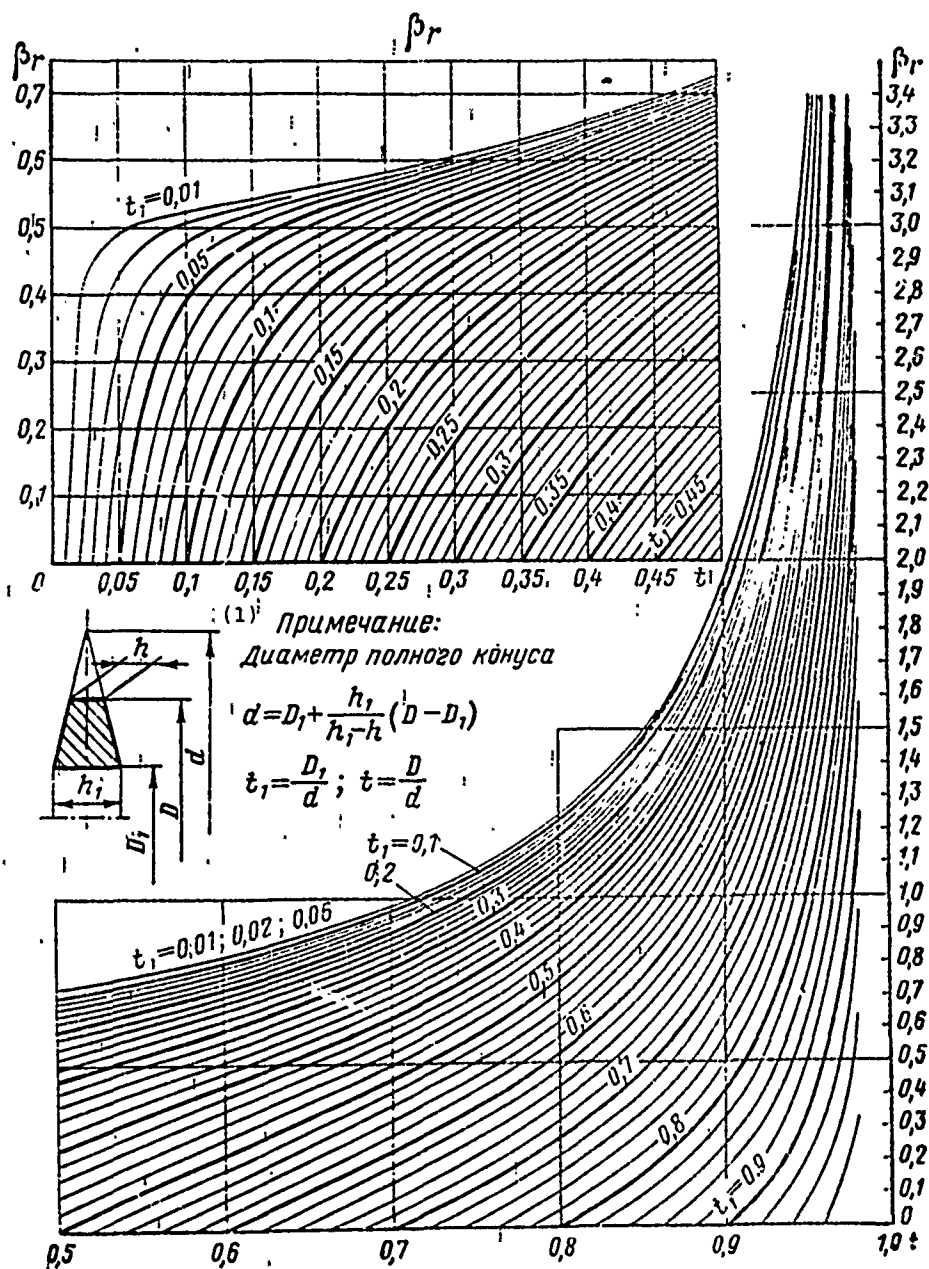


Fig. 3.45. Nomogram for determining coefficient in designing conical disks.

KEY: (1) Note: diameter of full cone.

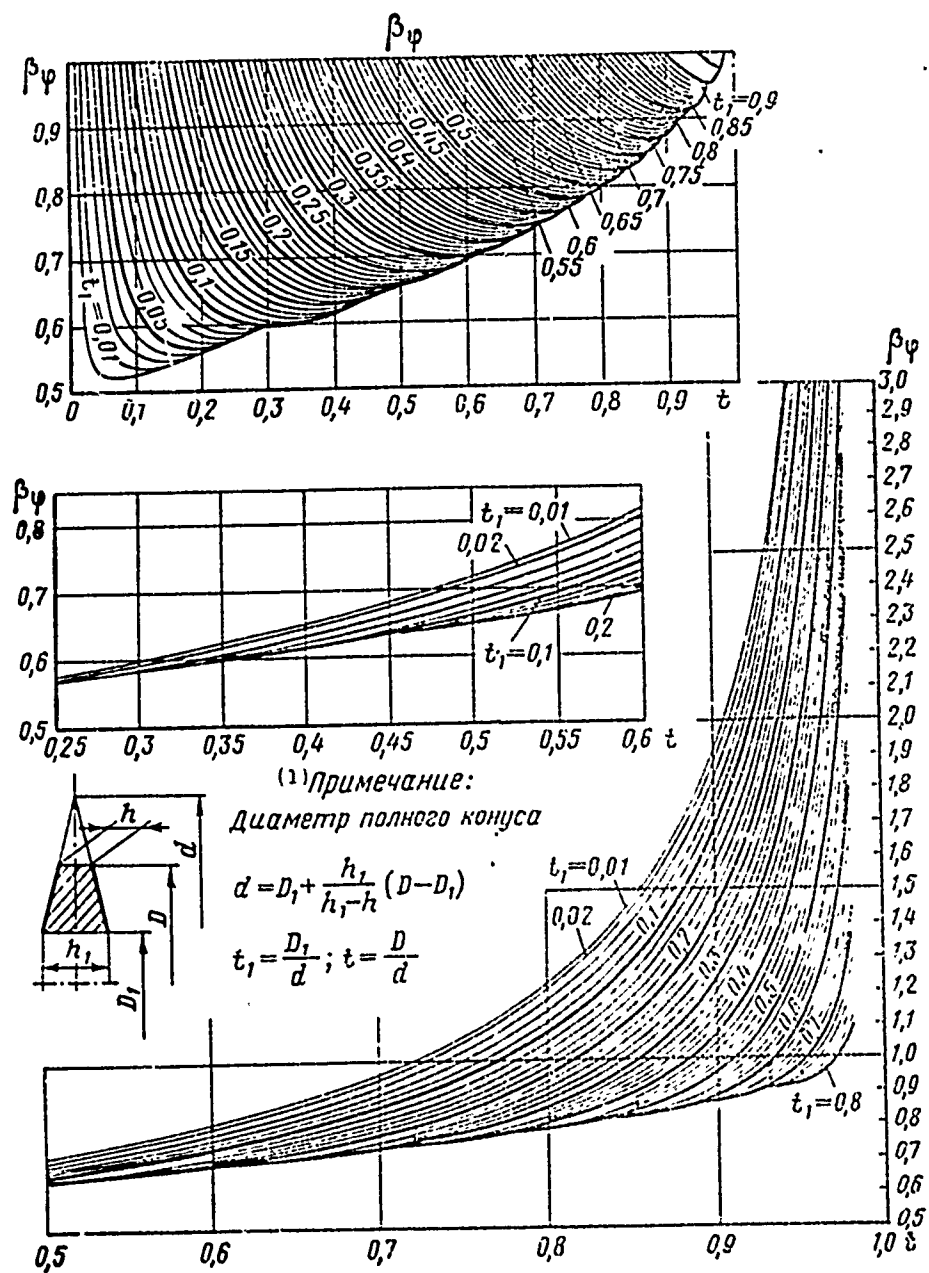


Fig. 3.46. Nomogram for determining coefficient in designing conical disks.

KEY: (1) Note: diameter of full cone.

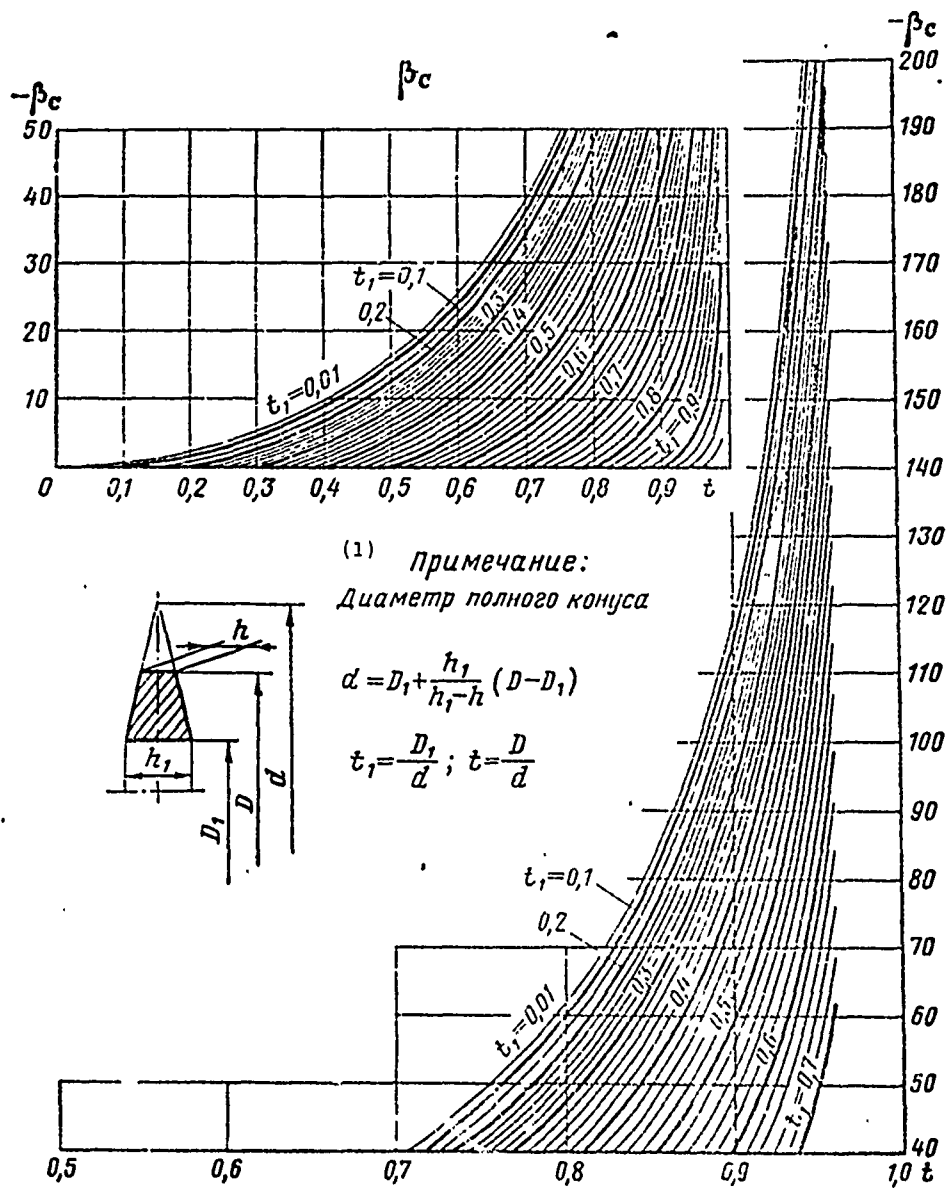


Fig. 3.47. Nomogram for determining coefficient in designing conical disks.

KEY: (1) Note: diameter of full cone.

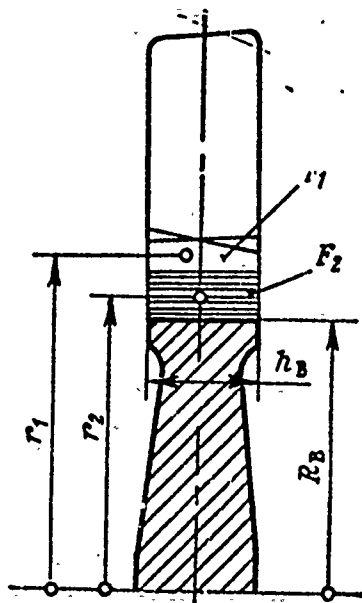


Fig. 3.48. Determining the intensity of centrifugal forces on the outer radius.

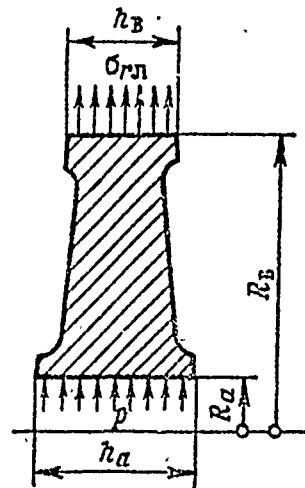


Fig. 3.49. Boundary conditions for a disk with a central opening.

If the blades are made together with the disk or are soldered (welded), the last two terms and expression (3.68) will be absent and radius  $R_b$  can be taken as the radius of the blade root. The load from the blades is applied conditionally to the cylindrical surface on a radius corresponding to the point of intersection of the middle plane of the disk with the internal loop of the circulatory part.

A disk with a central opening (Fig. 3.49). 1. The first boundary condition when  $r = R_a$ :

- a)  $\sigma_{ra} = 0$  if the disk has a free opening;
- b)  $\sigma_{ra} = -p$  if the disk is fitted to the shaft with tension.

External load  $p$  is taken with a minus sign since it causes compressive stresses at the spot where the disk is fitted.

2. The second boundary condition, as in a disk with a central opening, when  $r = R_b$ :

- a)  $\sigma_{rB} = 0$  if the disk does not bear a load on the external radius;
- b)  $\sigma_{rB} = \sigma_{rA}$  if blades are attached on the disk crown.

Allowing for nonuniform disk heating  
(determining thermal stresses)

In turbine operation heat flux is propagated from blades through the joints to the disk, and in the disk from the crown to the hub. Thus, disk temperature rises along the radius from the center to the crown. Due to this, thermal stresses appear in the disk, which can be of the same order of magnitude as the stresses from centrifugal forces, and they must be taken into account.

Thermal stresses can be determined separately for nonrotating disks and then algebraically added with the stresses from centrifugal forces.

In order to avoid high thermal stresses, the disk material must have the smallest possible coefficient of linear expansion (thermal strain will be less) and considerable heat conductivity (temperature gradient along the disk radius will be less). The disk material must have the appropriate mechanical properties with allowance for their reduction at high temperatures.

In our analysis we shall assume that the temperature in the disk changes only along the radius (on a given radius we shall assume the temperature is constant throughout the thickness).

The modulus of elasticity  $E$  and the coefficient of linear expansion  $\alpha$  will be considered constant within each of the sections in which the disk is divided during analysis.

The equation of equilibrium for a nonrotating disk is obtained from equation (3.55) if we assume  $C = \rho\omega^2 = 0$ :

$$\frac{d(\sigma_r r h)}{dr} - \sigma_z h = 0. \quad (3.69)$$

The generalized Hook's law (for elastic strength) with allowance for thermal deformation will have the form

$$\varepsilon_r = \frac{1}{E}(\sigma_r - \mu \sigma_\varphi) + \alpha t; \quad \varepsilon_\varphi = \frac{1}{E}(\sigma_\varphi - \mu \sigma_r) + \alpha t, \quad (3.70)$$

where  $\alpha$  is the coefficient of linear expansion for the disk material;  
 $t$  is the temperature.

On the other hand, according to equalities (3.56) and (3.57) relative strains  $\varepsilon_r = du/dr$ ;  $\varepsilon_\varphi = u/r$ . Allowing for this, we shall express in formulas (3.70) stresses  $\sigma_r$  and  $\sigma_\varphi$  in terms of displacement of  $u$  [analogously to formulas (3.62)]:

$$\left. \begin{aligned} \sigma_r &= \frac{E}{1-\mu^2} \left[ \frac{du}{dr} + \mu \frac{u}{r} - \alpha t (1+\mu) \right]; \\ \sigma_\varphi &= \frac{E}{1-\mu^2} \left[ \frac{u}{r} + \mu \frac{du}{dr} - \alpha t (1+\mu) \right]. \end{aligned} \right\} \quad (3.71)$$

The substitution of these expressions into the equation of equilibrium (3.69) gives a differential equation of the second order relative to the radial displacement of  $u$  (analogously to equation (3.63):

$$\begin{aligned} \frac{d^2 u}{dr^2} + \left( \frac{1}{h} \frac{dh}{dr} + \frac{1}{r} \right) \frac{du}{dr} + \left( \frac{u}{h} \frac{dh}{dr} - \frac{1}{r} \right) \frac{u}{r} = \\ = \alpha t (1+\mu) \left( \frac{1}{h} \frac{dh}{dr} + \frac{1}{t} \frac{dt}{dr} \right). \end{aligned} \quad (3.72)$$

Equation (3.72) differs from equation (3.63) only in the right side. Consequently, its solution will be similar to (3.65):

$$u = A\varphi_1(r) + B\varphi_2(r) + f(t, r). \quad (3.73)$$

Substituting this solution into equation (3.71), we can find  $\sigma_r$  and  $\sigma_\varphi$ .

In order to determine thermal stresses the disk is divided into sections with simple shape. Analysis is carried out through the known stresses  $\sigma_{r1}$  and  $\sigma_{\varphi1}$  on initial diameter  $D_1$  from formulas similar to formulas (3.67) and (3.67'):

$$\left. \begin{aligned} \sigma_r &= \alpha_r \sigma_{r1} + \alpha_\varphi \sigma_{\varphi1} + \alpha_t (E\alpha)_{cp} \Delta t; \\ \sigma_\varphi &= \beta_r \sigma_{r1} + \beta_\varphi \sigma_{\varphi1} + \beta_t (E\alpha)_{cp} \Delta t. \end{aligned} \right\} \quad (3.74)$$

Here coefficients  $\alpha_r$ ,  $\alpha_\varphi$ ,  $\beta_r$ , and  $\beta_\varphi$  are the same as in formulas (3.67) and (3.67') and are determined from the corresponding nomograms for disks of the three above types (constant thickness, hyperbolic, and conical).

Coefficients  $\alpha_t$  and  $\beta_t$  are determined from nomograms as a function of arguments:  $x = (D_1)/(D)$  and  $z = (h)/(h_1)$  for hyperbolic disks (Figs. 3.50, 3.51) and  $t_1 = (D_1)/(d)$  and  $t = (D)/(d)$  for conical disks (Figs. 3.52, 3.53). For disks of constant thickness coefficients  $\alpha_t$  and  $\beta_t$  are determined from nomograms for hyperbolic disks (when  $z = 1$ ).

In order to calculate thermal stresses it is necessary to assign the law of temperature variation along the radius (graphically or analytically). In the rough calculations the law of temperature variation along the radius can be expressed by dependence

$$t = t_0 + (t_n - t_0) \left( \frac{r}{R_n} \right)^{m_1}, \quad (3.75)$$

where  $t_0$  and  $t_n$  are the temperatures in the center and on the outer radius  $R_n$  of the disk;

$r$  is the current radius;

$m_1$  is the exponent;  $m_1 = 2-3$ .

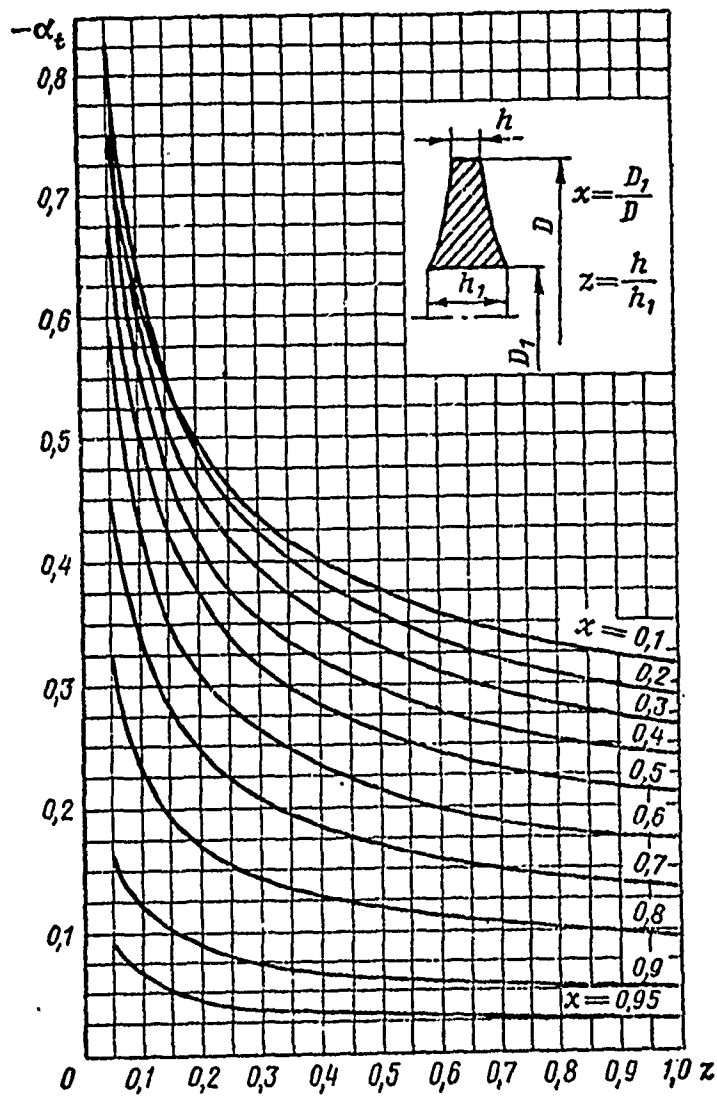


Fig. 3.50. Nomogram for determining coefficient in designing hyperbolic disks.



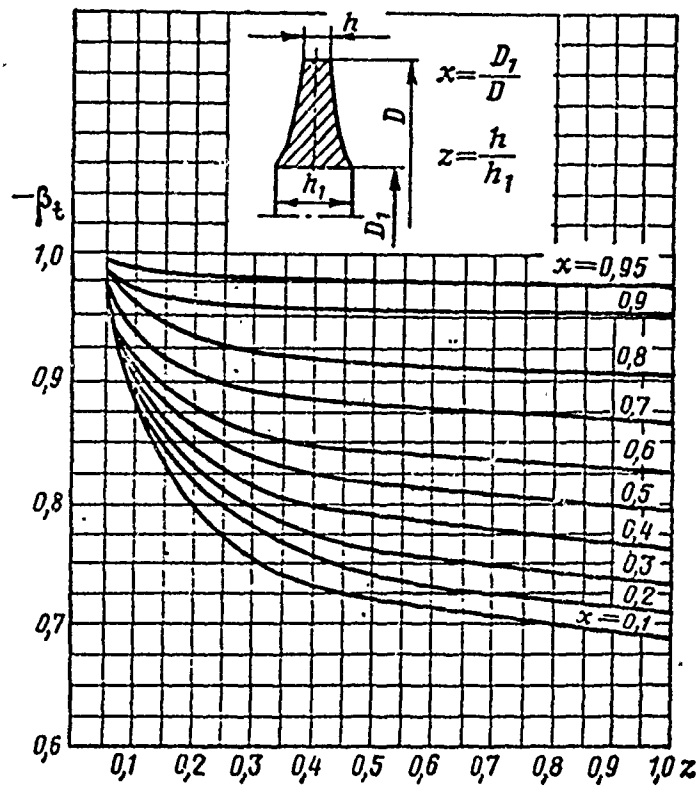


Fig. 3.51. Nomogram for determining coefficient in designing hyperbolic disks.

The values of  $E$  and  $\alpha$  are taken as average on a given section of the disk or corresponding to the averaged temperature on the given section.

#### Boundary conditions

Disk without a central opening:

- when  $r = 0$   $\sigma_{r0} = \sigma_{\phi 0}$ ;
- when  $r = R_B$   $\sigma_{rB} = 0$  (since the disk is not rotating).

A disk with a central opening:

- when  $r = R_a$   $\sigma_{ra} = 0$  or  $\sigma_{ra} = -p$ ;
- when  $r = R_B$   $\sigma_{rB} = 0$  (since the disk is not rotating).

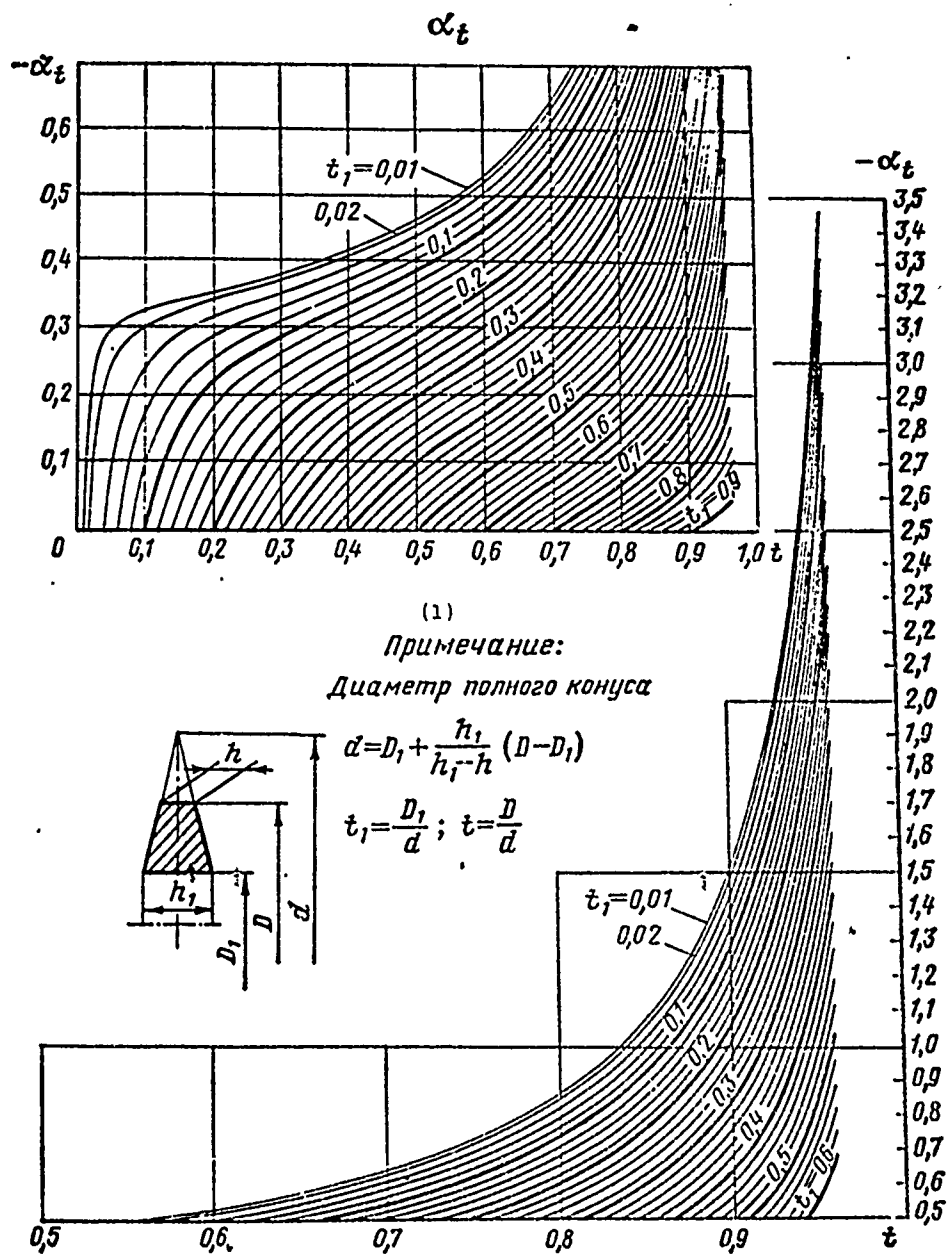


Fig. 3.52. Nomogram for determining coefficient in designing conical disks.

KEY: (1) Note: diameter of full cone.

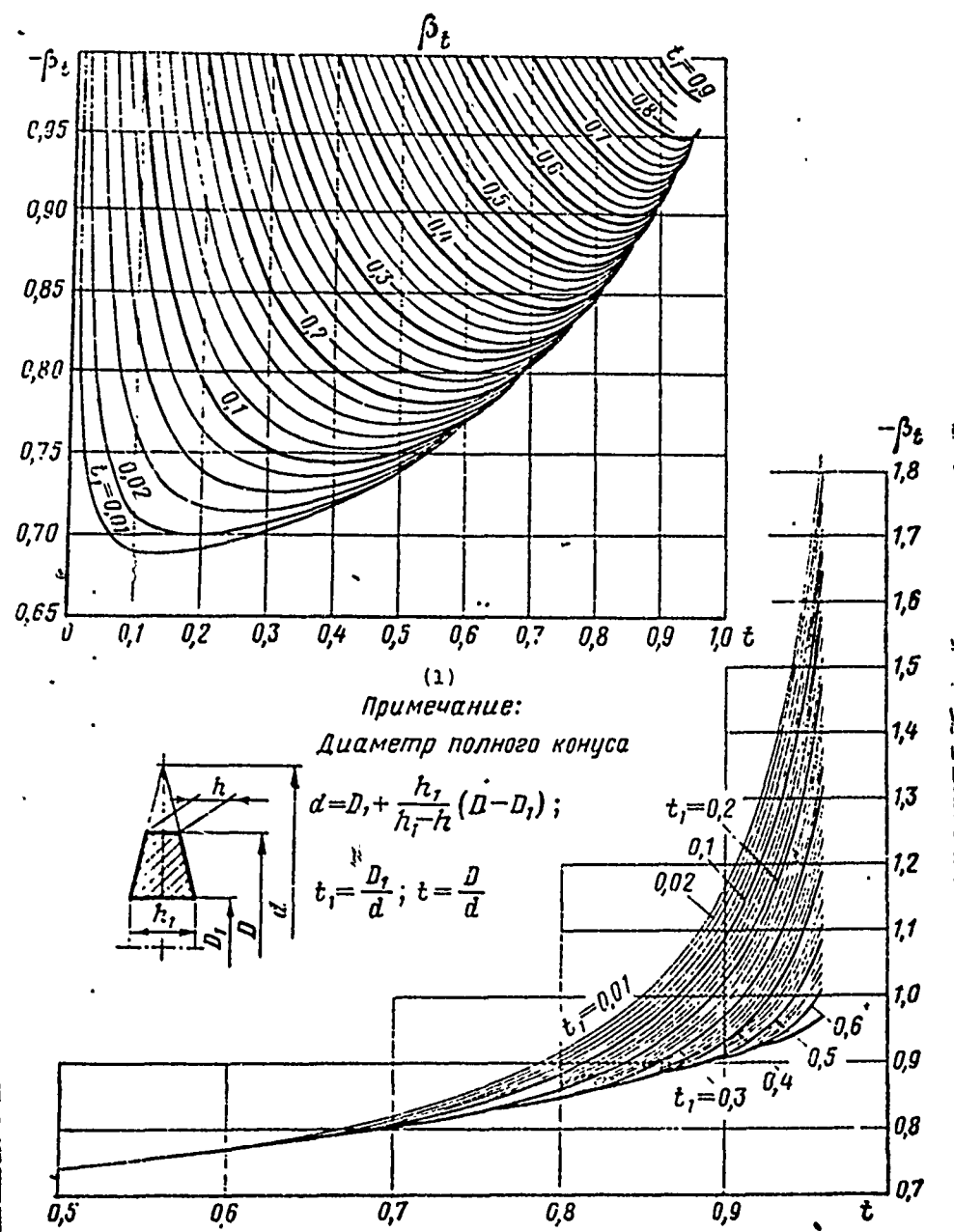


Fig. 3.53. Nomogram for determining coefficient in designing conical disks.  
KEY: (1) Note: diameter of full cone.

### Determining stresses with sharp variation in disk thickness

In a number of cases the thickness of the disks changes sharply with a small change in the radius (transition from the strip of the disk to the hub or the crown). Let us find the ratio of stresses  $\sigma_r$  and  $\sigma_\varphi$  at the site of the abrupt variation in thickness (Fig. 3.54).

Let the stresses be equal to  $\sigma_{r1}$  and  $\sigma_{\varphi1}$  on the diameter  $D_1$  for the part of the disk with thickness  $h_1$ . Average temperature of this part of the disk is  $t_{lcp}$  and, corresponding to this temperature, the modulus of elasticity and the coefficient of linear expansion are  $E_{lcp}$  and  $\alpha_{lcp}$ . Accordingly, for a disk with thickness  $h_1^*$  on this same diameter the stresses will be  $\sigma_{r1}^*$  and  $\sigma_{\varphi1}^*$ , the average temperature of the section of the disk with a diameter greater than  $D_1$  will be  $t_{lcp}^*$ , and the modulus of elasticity and coefficient of linear expansion will be  $E_{lcp}^*$  and  $\alpha_{lcp}^*$ .

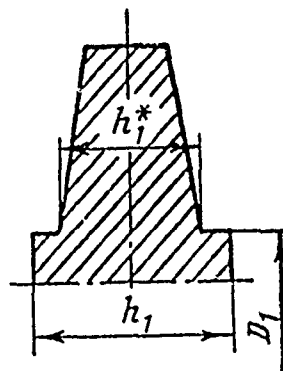
From the condition of the equality of radial internal forces on diameter  $D_1$  we obtain

$$\sigma_{r1} h_1 = \sigma_{r1}^* h_1^*,$$

hence

$$\sigma_{r1}^* = \sigma_{r1} \frac{h_1}{h_1^*}. \quad (3.76)$$

Fig. 3.54. Determining stresses in a disk with an abrupt change in thickness.



The expression for  $\sigma_{\phi}^*$  is obtained from the condition of equality of radial displacements of  $u$  on diameter  $D_1$  for both sections of the disk; according to formulas (3.57) and (3.70)

$$\varepsilon_r = \frac{u}{r}; \quad \varepsilon_z = \frac{1}{E} (\sigma_z - \mu \sigma_r) + \alpha t;$$

on the basis of these formulas we can write

$$u_1 = r_1 \varepsilon_{r1} = \frac{r_1}{E_{1cp}} (\sigma_{z1} - \mu \sigma_{r1}) + \alpha_{1cp} t_{1cp} = \frac{r_1}{E_{1cp}^*} (\sigma_{z1}^* - [\mu \sigma_{r1}^*] + \alpha_{1cp}^* t_{1cp}^*.$$

Hence we find, allowing for equality (3.76),

$$\sigma_{z1}^* = \frac{E_{1cp}^*}{E_{1cp}} \sigma_{z1} + \mu \sigma_{r1} \left( \frac{h_1}{h_1^*} - \frac{E_{1cp}^*}{E_{1cp}} \right) + E_{1cp}^* \Delta(\alpha t)_{cp}, \quad (3.77)$$

where

$$\Delta(\alpha t)_{cp} = \alpha_{1cp} t_{1cp} - \alpha_{1cp}^* t_{1cp}^*.$$

For a cold or uniformly heated disk formula (3.77) assumes the form

$$\sigma_{z1}^* = \sigma_{z1} + \mu \sigma_{r1} \left( \frac{h_1}{h_1^*} - 1 \right). \quad (3.77')$$

## Methods of calculating stresses in a disk

### *Method of two analyses*

Stresses for a disk of arbitrary shape can be computed [see system of equations (3.62)] according to formulas obtained for the appropriate section shape. For each section we have two boundary conditions: On the internal and external radii of the disk section and the adjoint conditions at the junction site of the two neighboring sections. In view of the fact that it can be very

difficult to solve the systems of equations necessary for determining the arbitrary constants by this method, the stresses in the disk will be calculated by the method of two analyses.

In the first analysis stresses in a rotating disk are calculated. Calculation can follow two paths - from the inner radius to the outer (from bushing to crown) or the reverse. Let us consider the first path.

If the disk is solid (without a central hole), then they are assigned arbitrarily by the stress in the center of the disk. According to the first boundary condition  $\sigma'_{r0} = \sigma'_{\phi 0}$  (one prime means that the stresses belong to the first analysis).

If the disk has a central opening, then they are assigned arbitrarily by the circular stress on the edge of the opening, i.e.,  $\sigma'_{\phi a}$ . The radial stress from the edge of the opening is known from the boundary conditions.

With the aid of formulas (3.67), (3.67'), (3.76), and (3.77), stresses in a disk up to the stresses on its outer radius  $\sigma'_{rB}$  and  $\sigma'_{\phi B}$  are determined successfully according to sections. Obviously, stresses on the outer radius will not satisfy the second boundary condition, i.e.,  $\sigma'_{rB} \neq \sigma_{rB} = \sigma_{rH}$ , since stresses in the center of the disk (or on the edge of the opening) will be arbitrary.

The second analysis is performed for a nonrotating disk ( $n = 0$ ). Similarly to the first analysis they are assigned arbitrarily by the stresses in the center of the disk  $\sigma''_{r0} = \sigma''_{\phi 0}$  (or  $\sigma''_{\phi a}$  for a disk with an opening). Since  $n = 0$ , the last terms in equations (3.67) and (3.67') will be equal to zero (two primes indicate that the stresses belong to the second analysis).

In this analysis stresses on the boundaries of all sections up to the outer radius of the disk are determined. The obtained stresses  $\sigma''_{rB}$  and  $\sigma''_{\phi B}$  will also not satisfy the second boundary condition.

The actual stresses on the boundaries of all sections can be found from formulas

$$\sigma_r = \sigma'_r + k\sigma''_r; \quad \sigma_\varphi = \sigma'_\varphi + k\sigma''_\varphi. \quad (3.78)$$

The constant coefficient  $k$  in formula (3.78) is determined from the conditions that radial stress  $\sigma_{rB} = \sigma_{rA}$  on the outer diameter is known (second boundary condition). Actually, radial stress inequalities (3.78), corresponding to the external radius of the disk, is

$$\sigma_{rB} = \sigma_{rA} = \sigma'_{rA} + k\sigma''_{rA},$$

hence:

$$k = \frac{\sigma'_{rA} - \sigma'_{rB}}{\sigma''_{rA}}. \quad (3.79)$$

After determining coefficient  $k$  from formulas (3.78) we find the actual stresses on the boundaries of all sections.

The method of two analyses is based on the property of linear differential equations according to which after adding to the solution of a nonhomogeneous equation any solution to a corresponding homogeneous equation (or a quantity which is a multiple of this solution), we obtain the new solution to the nonhomogeneous equation.

In order to determine stresses in a disk by the method of two analyses, it is advisable to use a table (see example 3.2).

To determine thermal stresses the disk is analyzed according to the method of two analyses just as in the determination of stresses from centrifugal forces. However, in the second analysis we should assume the particular solution to the equation (3.72) is equal to zero.

In practice this indicates that  $\Delta t$  in equations (3.74) will be zero.

In the second analysis, if the thickness of the disk changes abruptly, stresses at the transition spot should be calculated from formulas (3.76) and (3.77). To determine stresses only from centrifugal forces at the site of the abrupt thickness change, instead of formula (3.77), we should use formula (3.77').

Total stresses are found as the algebraic sum of stresses from centrifugal forces and from nonuniform heating on the boundaries of each section.

The stressed state of a disk is evaluated from the equivalent stresses  $\sigma_{\text{эKB}}$ . According to the third strength theory (the theory of the highest deformation energy), equivalent stress is defined as the criterion for the beginning of viscosity. For the biaxial stressed state

$$\sigma_{\text{эKB}} = \sqrt{\sigma_r^2 + \sigma_z^2 - \sigma_r \sigma_z}. \quad (3.80)$$

**Example 3.2.** Determined stresses in a disk of 4Kh12N8G8MFB (EI481) steel. Dimensions of the disk are given in Table 3.2.

Given:  $n = 11,200$  r/min ( $\omega = 1,170$  rad/s);  $\rho = 7.87 \cdot 10^3$  kg/m<sup>3</sup>;  $\sigma_{rn} = 1,400$  daN/cm<sup>2</sup>;  $\mu = 0.3$ .

The disk is broken down into four sections. Using Figures 3.41-3.47, 3.50, 3.51, we find coefficients  $\alpha$  and  $\beta$  and enter them in Table 3.2. We determine the values of  $T$  and  $T_d$ .

The temperature of the disk is taken from Fig. 3.55 and we find its average value for each section. The values of  $E$  and  $\alpha$  correspond to the average temperatures in each section.



Table 3.2.

№ section	Basic data for analysis.					Coefficients for calculating centrifugal stresses.										Coefficients for calculating thermal stresses.				
	$D$ или $d$ мм	$h$ , мм	$t_{нач}$ , °C	$E_{cp}$ , $\text{дан/см}^2$	$\alpha_{cp}$ , $1/^\circ\text{C}$	$x = \frac{D_1}{D_2}$ или $t_2 = \frac{D_1}{D_2}$	$z = \frac{h_1}{h_2}$ или $t_2 = \frac{D_1}{D_2}$	$\alpha_1$	$\alpha_2$	$\alpha_{cp}$ или $\alpha_c$	$\beta_1$	$\beta_2$	$\beta_{cp}$ или $\beta_c$	$T$ или $T_p$	$\alpha_c T$ или $\alpha_{cp} T_p$	$\beta_c T$ или $\beta_{cp} T_p$	$\Delta t$	$\beta_1 E_{cp} \alpha_{cp} \Delta t$	$\beta_2 E_{cp} \alpha_{cp} \Delta t$	
I	$D_0 = 0$	64	250			0	1	0,5	0,5	-90,8	0,5	0,5	-52,3	1,25	-113,6	-65,4	24	-0,333	-0,667	-574
	$D_1 = 100$		274																	-287
II	$D_1^* = 100$	64	274			0,22	0,44	0,865	0,475	-16,05	0,5	0,665	-8,03	26	-417	-209	71	-0,24	-0,804	-2191
	$d = 455$	46	348																	-654
III	$D_2^* = 200$	46	348			0,44	0,66	1,18	0,38	-31,1	0,49	0,765	-14,05	26	-809	-366	82	-0,165	-0,866	-2570
	$d = 455$	28	470																	-548
IV	$D_2^* = 300$	43	470			0,857	1	0,866	0,136	-28,5	0,136	0,866	-10,13	15,35	-438	-155,7	80	-0,0682	-0,932	-202
	$D_3^* = 350$	550																		-2760

Designations: или = or; нач = initial; конеч = final;  $\alpha_{cp}$  = average;  $\text{дан/см}^2 = \text{dan/cm}^2$ .

Analysis of the disk using the two calculation method is presented in Table 3.3. In the first calculation stresses in the center of the disk are given as  $\sigma'_{r0} = \sigma'_{\phi 0} = 2000 \text{ daN/cm}^2$  and in the second calculation  $\sigma''_{r0} = \sigma''_{\phi 0} = 100 \text{ daN/cm}^2$ . Figure 3.55 gives graphs showing the variation in stresses  $\sigma_r$  and  $\sigma_\phi$  along the radius of the disk.

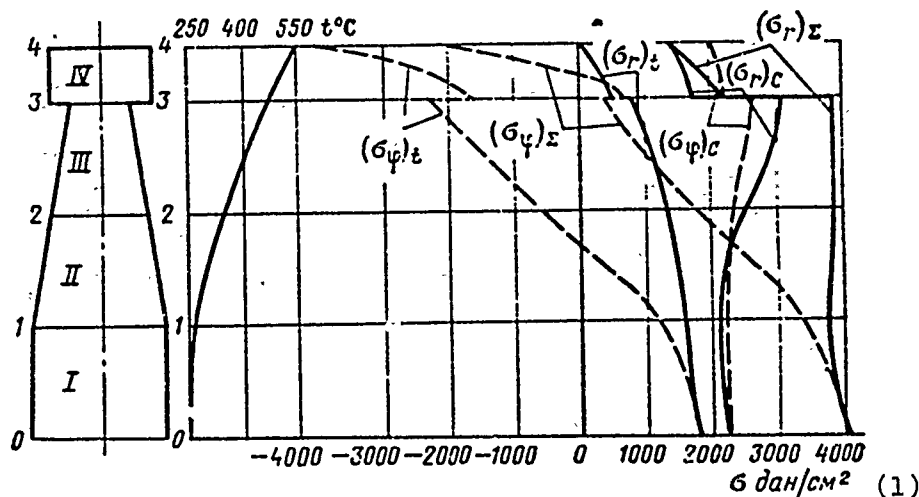


Fig. 3.55. Shape of turbine disk, stresses and temperature distribution in it along the radius (example of calculation).

KEY: (1)  $\text{daN/cm}^2$ .

#### Stress analysis of disks by the integral method

The earlier examined method of analyzing disks is the most accurate. However, nomograms for determining coefficients  $\alpha$  and  $\beta$  are plotted only for one value of the Poisson coefficient  $\mu = 0.3$  while its value in the temperature range of the turbine disk can vary from 0.3 to 0.4 (maximum possible value of the Poisson coefficient with plastic flow is  $\mu_{\max} = 0.5$ ).

Although the effect of  $\mu$  on the value of stresses is not very great, nevertheless sometimes it is necessary to calculate for the values of  $\mu \neq 0.3$ , for example, when analyzing a disk with allowance for plastic flows (see below).

Table 3.3 Analysis of stresses in turbine disks (daN/cm<sup>2</sup>)

Analysis of centrifugal stresses, $\sigma_C$			
	1st analysis	2nd analysis	Actual stresses
$D_{MM}$	$\sigma_r(n+1) = \alpha_r \sigma_{rn} + \alpha_c \sigma_{cn} + \alpha_C T$ $\sigma_\varphi(n+1) = \beta_r \sigma_{rn} + \beta_\varphi \sigma_{\varphi n} + \beta_C T$ $\sigma_r^* = \sigma_r \frac{h}{R^*}$ $\sigma_\varphi^* = \sigma_\varphi + \mu \sigma_r \left( \frac{h}{R^*} - 1 \right)$	$\sigma_r(n+1) = \alpha_r \sigma_{rn} + \alpha_c \sigma_{cn}$ $\sigma_\varphi(n+1) = \beta_r \sigma_{rn} + \beta_\varphi \sigma_{\varphi n}$ $\sigma_r^* = \sigma_r \frac{h}{R^*}$ $\sigma_\varphi^* = \sigma_\varphi + \mu \sigma_r \left( \frac{h}{R^*} - 1 \right)$	$\sigma_C = \sigma' + \varphi \sigma''$ $\varphi = \frac{\sigma_{r,1} - \sigma'_{r,1}}{\sigma'_{r,1}}$
$D_0=0$	$\sigma'_{r0} = 2000$ $\sigma'_{\varphi 0} = 2000$	$\sigma'_{r0} = 100$ $\sigma'_{\varphi 0} = 100$	$\sigma_{r0} = 2000 + 2,7 \cdot 100 = 2270$ $\sigma_{\varphi 0} = 2000 + 2,7 \cdot 100 = 2270$
$D_1=100$	$\sigma'_{r1} = 0,5 \cdot 2000 + 0,5 \cdot 2000 - 113,5 = 1886,5$ $\sigma'_{\varphi 1} = 0,5 \cdot 2000 + 0,5 \cdot 2000 - 5,4 = 1934,6$	$\sigma'_{r1} = 0,5 \cdot 100 + 0,5 \cdot 100 = 100$ $\sigma'_{\varphi 1} = 0,5 \cdot 100 + 0,5 \cdot 100 = 100$	$\sigma_{r1} = 1886,5 + 2,7 \cdot 100 = 2153,5$ $\sigma_{\varphi 1} = 1934,6 + 2,7 \cdot 100 = 2204,6$
$D_2=200$	$\sigma'_{r2} = 0,865 \cdot 1886,5 + 0,475 \cdot 1934,6 - 417 = 2134$ $\sigma'_{\varphi 2} = 0,5 \cdot 1886,5 + 0,665 \cdot 1934,6 - 209 = 2021$	$\sigma'_{r2} = 0,865 \cdot 100 + 0,475 \cdot 100 = 134$ $\sigma'_{\varphi 2} = 0,5 \cdot 100 + 0,665 \cdot 100 = 116,5$	$\sigma_{r2} = 2134 + 2,7 \cdot 134 = 2496$ $\sigma_{\varphi 2} = 2021 + 2,7 \cdot 116,5 = 2335$

Analysis of centrifugal stresses, $\sigma_c$			
	1st analysis	2nd analysis	Actual stresses
$D_3=200$	$\sigma_{r3}'=1,18 \cdot 2134 + 0,38 \cdot 2021 - 809 = 2479$ $\sigma_{\varphi 3}'=0,49 \cdot 2134 + 0,765 \cdot 2021 - 366 = 2224$	$\sigma_{r3}''=1,18 \cdot 134 + 0,38 \cdot 115,5 = 202,5$ $\sigma_{\varphi 3}''=0,49 \cdot 134 + 0,765 \cdot 115,5 = 155$	$\sigma_{r3}=2479+2,7 \cdot 202,5=3026$ $\sigma_{\varphi 3}=2224+2,7 \cdot 155=2642$
$D_3=300$	$\sigma_{r3}''=2479 \frac{28}{48}=1445$ $\sigma_{\varphi 3}''=2224 + 0,3 \cdot 2479 \left( \frac{28}{48} - 1 \right) = 1914$	$\sigma_{r3}''=202,5 \frac{28}{48}=118$ $\sigma_{\varphi 3}''=155 + 0,3 \cdot 202,5 \left( \frac{28}{48} - 1 \right) = 130$	$\sigma_{r3}''=1445+2,7 \cdot 118=1764$ $\sigma_{\varphi 3}''=1914+2,7 \cdot 130=2265$
$D_4=250$	$\sigma_{r4}'=0,835 \cdot 1445 + 0,136 \cdot 1914 - 438 = 1072$ $\sigma_{\varphi 4}'=0,136 \cdot 1445 + 0,866 \cdot 1914 - 155,7 = 1396,3$	$\sigma_{r4}''=0,866 \cdot 118 + 0,136 \cdot 130 = 121,7$ $\sigma_{\varphi 4}''=0,136 \cdot 118 + 0,866 \cdot 130 = 128,4$	$\sigma_{r4}=1072+2,7 \cdot 121,7=1400$ $\sigma_{\varphi 4}=1696,3+2,7 \cdot 128,4=2043$
		$\varphi_1 = \frac{1400-1072}{121,7} = 2,7$	

Analysis of thermal stresses, $\sigma_t$			
	1st analysis	2nd analysis	Actual stresses
	$\sigma_{r(n+1)} = \alpha_r \sigma_{rn} + \alpha_{\varphi} \sigma_{\varphi n} + \alpha_t \times$ $\times (E \alpha)_{cp} \Delta t$ $\sigma_{\varphi(n+1)} = \beta_r \sigma_{rn} + \beta_{\varphi} \sigma_{\varphi n} + \beta_t \times$ $\times (E \alpha)_{cp} \Delta t$ $\sigma_r'' = \sigma_r' \frac{h}{h^*}$ $\sigma_{\varphi}'' = \sigma_{\varphi}' \frac{h}{h^*} + \frac{E_{cp}^*}{E_{cp}} \left( \frac{h}{h^*} - \frac{E_{cp}^*}{E_{cp}} \right) + E_{cp}^* \Delta (a')_{cp}$	$\sigma_{r(n+1)} = \alpha_r \sigma_{rn} + \alpha_{\varphi} \sigma_{\varphi n}$ $\sigma_{\varphi(n+1)} = \beta_r \sigma_{rn} + \beta_{\varphi} \sigma_{\varphi n}$ $\sigma_r'' = \sigma_r' \frac{h}{h^*}$ $\sigma_{\varphi}'' = \sigma_{\varphi}' \frac{h}{h^*} + \frac{E_{cp}^*}{E_{cp}} \left( \frac{h}{h^*} - \frac{E_{cp}^*}{E_{cp}} \right) + E_{cp}^* \Delta (a')_{cp}$	$\sigma_r'' = \sigma_r' + \varphi \sigma_r''$ $\sigma_{\varphi}'' = \sigma_{\varphi}' + \varphi \sigma_{\varphi}''$
$D_{MM}$			

	Analysis of thermal stresses, $\sigma_t$			Total stresses, $\sigma_t$
	1st analysis	2nd analysis	Actual stresses	
$D_0=0$	$\sigma'_{r0}=2000$ $\sigma'_{\phi 0}=2000$	$\sigma'_{r0}=100$ $\sigma'_{\phi 0}=100$	$\sigma_{r0}=2000+(-1,138)100=$ $=1866$ $\sigma_{\phi 0}=2000+(-1,138)100=$ $=1866$	$\sigma_{r0}=2270+1866=4136$ $\sigma_{\phi 0}=2270+1866=4136$
$D_1=100$	$\sigma'_{r1}=0,5 \cdot 2000+0,5 \cdot 2000-$ $-287=1713$ $\sigma'_{\phi 1}=0,5 \cdot 2000+0,5 \cdot 2000-$ $-574=1426$	$\sigma'_{r1}=100$ $\sigma'_{\phi 1}=100$	$\sigma_{r1}=1713+(-1,138)100=$ $=1599$ $\sigma_{\phi 1}=1426+(-1,138)100=$ $=1312$	$\sigma_{r1}=2156,5+1599=3756$ $\sigma_{\phi 1}=2204,6+1312=3517$
$D_2=200$	$\sigma'_{r2}=0,865 \cdot 1713+0,475 \times$ $\times 1426=654=1505$ $\sigma'_{\phi 2}=0,5 \cdot 1713+0,665 \times$ $\times 1426=2190=-385$	$\sigma'_{r2}=134$ $\sigma'_{\phi 2}=116,5$	$\sigma_{r2}=1505+(-1,138)134=$ $=1353$ $\sigma_{\phi 2}=-385+(-1,138) \times$ $\times 116,5=-517$	$\sigma_{r2}=2496+1353=3848$ $\sigma_{\phi 2}=2235+(-517)=1718$
$D_3=300$	$\sigma'_{r3}=1,18 \cdot 1505+0,38 \times$ $\times (-385)=548=1030$ $\sigma'_{\phi 3}=0,49 \cdot 1505+0,765 \times$ $\times (-385)=2570=-2127$	$\sigma'_{r3}=202,5$ $\sigma'_{\phi 3}=155$	$\sigma_{r3}=1030+(-1,138) \times$ $\times 202,5=850$ $\sigma_{\phi 3}=-2127+(-1,138) \times$ $\times 155=-230$	$\sigma_{r3}=3026+850=3876$ $\sigma_{\phi 3}=2642+(-2303)=339$

	Analysis of thermal stresses, $\sigma_t$			Total stresses, $\sigma_\Sigma$
	1st analysis	2nd analysis	Actual stresses	
$D_3=300$	$\sigma_{r3}' = 1080 \cdot \frac{28}{48} = 632$ $\sigma_{\varphi 3}' = \frac{1,61}{1,71} (-2127) + 0,3 \times$ $\times 1080 \cdot \left( \frac{28}{48} - \frac{1,61}{1,71} \right) + 1,61 \times$ $\times 106 \cdot (21,1 \cdot 10^{-6} \cdot 409 - 23 \times$ $\times 106 \cdot 510) = -7087$	$\sigma_{r3}'' = 202,5 \cdot \frac{28}{48} = 118$ $\sigma_{\varphi 3}'' = \frac{1,61}{1,71} 155 + 0,3 \cdot 202,5 \times$ $\times \left( \frac{28}{48} - \frac{1,61}{1,71} \right) + 1,61 \cdot 106 \times$ $\times (21,1 \cdot 10^{-6} \cdot 409 - 23 \cdot 10^{-6} \times$ $\times 510) = -4846$	$\sigma_{r3}^* = 632 + (-1,138) 118 =$ $= 498$ $\sigma_{\varphi 3}^* = -7087 + (-1,138) \times$ $\times (-4846) = -1574$	$\sigma_{r3} = 1764 + 498 = 2262$ $\sigma_{\varphi 3} = 2265 + (-1577) = 688$
$D_4=350$	$\sigma_{r4}' = 0,866 \cdot 632 + 0,135 \times$ $\times (-7087) - 202 = -619$ $\sigma_{\varphi 4}' = 0,136 \cdot 632 + 0,866 \times$ $\times (-7087) - 2760 = -8804$	$\sigma_{r4}'' = 0,866 \cdot 118 + 0,136 \times$ $\times (-4846) = -544$ $\sigma_{\varphi 4}'' = 0,136 \cdot 118 + 0,866 \times$ $\times (-4846) = -4162$	$\sigma_{r4} = -619 + (-1,138) \times$ $\times (-544) = 0$ $\sigma_{\varphi 4} = -8804 + (-1,138) \times$ $\times (-4162) = -4074$	$\sigma_{r4} = 1400 + 0 = 1400$ $\sigma_{\varphi 4} = 2043 + (-4074) =$ $= -2031$
		$\eta_2 = \frac{0 - (-619)}{(-544)} = -1,138$		

Widely used methods are those based on the solution of integral equations of equilibrium and strain compatibility. Let us examine one of these methods developed by R. S. Kanasochvili [17].

Boundary conditions for disks are assumed the same, i.e., when  $r = R_B$   $\sigma_{rB} = \sigma_{rH}$ ; when  $r = 0$  (disks without a central opening)  $\sigma_{r0} = \sigma_{\varphi 0}$ , when  $r = R_a$  (disk with a central opening)  $\sigma_{ra} = 0$  (opening is free of load) or  $\sigma_{ra} = -P$  (disk is fit into shaft with tension). Using equality

$$d(\tau, h r d\varphi) \approx d(\sigma, h) r d\varphi + \sigma, h dr d\varphi,$$

we shall transform the equation of equilibrium (3.55):

$$\frac{r}{h} \frac{d}{dr}(\sigma, h) + \sigma_r - \sigma_\varphi + \rho \omega^2 r^2 = 0. \quad (3.81)$$

For the equation (3.81) relative to  $\sigma_r$  with boundary conditions taken into account we obtain the equation of equilibrium in the form

$$\sigma_r = \frac{1}{h} \left[ \int_{R_a}^r \frac{h}{r} (\sigma_\varphi - \sigma_r) dr - \int_{R_a}^r \rho \omega^2 r h dr + \sigma_{ra} h_a \right]. \quad (3.82)$$

The equation of strain compatibility is obtained in the following manner. Let us examine the sum  $\mu \varepsilon_\varphi + \varepsilon_r$ . Allowing for equalities (3.56) and (3.58),

$$\mu \varepsilon_\varphi + \varepsilon_r = \mu \varepsilon_\varphi + \frac{d}{dr}(\varepsilon_\varphi r).$$

Substituting the value of  $\varepsilon_\varphi$  from equalities (3.70), we obtain

$$\mu \varepsilon_\varphi + \varepsilon_r = \frac{\mu(\sigma_\varphi - \mu \sigma_r + E \alpha t)}{E} + \frac{d}{dr} \left( \frac{r(\sigma_\varphi - \mu \sigma_r + E \alpha t)}{E} \right).$$

On the other hand, substituting the values of  $\varepsilon_r$  and  $\varepsilon_\varphi$  from equalities (3.70), we obtain

$$\begin{aligned} \mu \varepsilon_\varphi + \varepsilon_r &= \frac{\mu}{E} (\tau_\varphi - \mu \tau_r + E \alpha t) + \frac{1}{E} (\tau_r - \mu \tau_\varphi + E \alpha t) = \\ &= \frac{(1 + \mu) [(1 - \mu) \tau_r + E \alpha t]}{E}. \end{aligned}$$

Thus

$$\frac{\mu (\tau_\varphi - \mu \tau_r + E \alpha t)}{E} + \frac{d}{dr} \left( \frac{r (\tau_\varphi - \mu \tau_r + E \alpha t)}{E} \right) = \frac{(1 + \mu) [(1 - \mu) \tau_r + E \alpha t]}{E}.$$

Let us multiply all terms of the obtained expression by  $r^\mu$ :

$$\begin{aligned} \frac{d}{dr} \left( r^\mu \frac{\tau_\varphi - \mu \tau_r + E \alpha t}{E} \right) r^\mu + \frac{\mu}{E} r^\mu (\tau_\varphi - \mu \tau_r + E \alpha t) &= \\ &= \frac{1 + \mu}{E} r^\mu [(1 - \mu) \tau_r + E \alpha t], \end{aligned}$$

or

$$\frac{d}{dr} \left[ \frac{r^{1+\mu}}{E} (\tau_\varphi - \mu \tau_r + E \alpha t) \right] - \frac{1 + \mu}{E} r^\mu [(1 - \mu) \tau_r + E \alpha t] = 0.$$

Integrating this expression, we obtain

$$\frac{r^{1+\mu}}{E} (\tau_\varphi - \mu \tau_r + E \alpha t) \Big|_{R_a}^r - \int_{R_a}^r \frac{r^\mu}{E} (1 + \mu) [(1 - \mu) \tau_r + E \alpha t] = 0,$$

or

$$\begin{aligned} \frac{r^{1+\mu}}{E} (\tau_\varphi - \mu \tau_r + E \alpha t) - \frac{R_a^{1+\mu}}{E_a} (\tau_{\varphi a} - \mu \tau_{ra} + E_a \alpha_a t_a) - \\ - \int_{R_a}^r \frac{r^\mu}{E} (1 + \mu) [(1 - \mu) \tau_r + E \alpha t] = 0. \end{aligned} \quad (3.83)$$



Solving the last equation relative to  $\sigma_\varphi$ , we obtain the equation of strain compatibility

$$\begin{aligned} \varepsilon_\varphi = \varepsilon_r - (1-\mu)\varepsilon_r - Eat + \frac{(1-\mu^2)E}{r^{1+\mu}} \int_{R_a}^r \frac{r^\mu \sigma_r dr}{E} + \\ + \frac{(1+\mu)E}{r^{1+\mu}} \int_{R_a}^r r^\mu a dr + A \frac{E}{r^{1+\mu}}. \end{aligned} \quad (3.84)$$

Here

$$A = \frac{R_a^{1+\mu}}{E_a} (\varepsilon_{ra} - \mu \varepsilon_{ra} + E_a a_a t_a). \quad (3.85)$$

From a system of two integral equations (3.82) and (3.84) stresses  $\sigma_r$  and  $\sigma_\varphi$  are determined by the method of successive approximations. Let us show the procedure for these calculations.

To determine the first approximation of  $\sigma_r$  we assume in equation (3.84)  $(\sigma_r)/(E) = \text{const.}$  Then the equation (3.84) is easily integrated and becomes

$$\varepsilon_\varphi \approx \varepsilon_r + \frac{(1+\mu)E}{r^{1+\mu}} \int_{R_a}^r r^\mu a dr - Eat + B \frac{E}{r^{1+\mu}}, \quad (3.86)$$

where B is the new integration constant.

After we substitute from equation (3.86) the approximate value of difference  $(\sigma_\varphi - \sigma_r)$  into the equation of equilibrium (3.82), we find the first approximation for  $\sigma_r$ :

$$\sigma_{r1} = \frac{1}{h} \left\{ \int_{R_a}^r \left[ \frac{(1+\mu)E}{r^{1+\mu}} \int_{R_a}^r r^\mu a dr - Eat \right] \frac{h}{r} dr - \varrho \omega^2 \int_{R_a}^r r h dr + \right.$$

$$\left. \frac{1}{r} B \int_{R_2}^r \frac{Eh}{r^{2+\mu}} dr + h_a \sigma_{ra} \right\}. \quad (3.87)$$

For a disk with a central opening  $\sigma_{ra}$  is known. Constant B is determined from the known load on the outer loop (when  $r = R_B$   $\sigma_{rB} = \sigma_{rH}$ ).

For a solid disk, in order not to pass to the limit when  $r = 0$ , we assume that up to a certain small value of  $r = R_a$  the equality  $\sigma_{ra} = \sigma_{\varphi a}$  is preserved (usually, in this case, we assume  $R_a = 0.1R_B$ ). Then from equation (3.86) we obtain

$$B = R_a^{1+\mu} \sigma_a t_a. \quad (3.88)$$

In equation (3.86) there remains one unknown quantity  $\sigma_{ra}$ , which is determined from the known load on the outer loop.

Usually no less than two approximations are made for  $\sigma_r$  in order to assure the accuracy of the obtained results, especially as the determination of  $\sigma_{r2}$  does not require a large amount of computation.

Without making the first approximation of  $\sigma_{\varphi 1}$ , we immediately determine  $\sigma_{r2}$ . From equality (3.84) we find the difference  $(\sigma_{\varphi 1} - \sigma_{r1})$  after the substitution into this equality of the value of  $\sigma_{r1}$ :

$$\begin{aligned} \sigma_{\varphi 1} - \sigma_{r1} = & \frac{(1+\mu)E}{r^{1+\mu}} \int_{R_a}^r r^\mu t dr - E t - (1-\mu) \sigma_{r1} + \\ & + \frac{(1-\mu^2)E}{r^{1+\mu}} \int_{R_a}^r \frac{r^\mu \sigma_{r1}}{E} dr + A \frac{E}{r^{1+\mu}}. \end{aligned} \quad (3.89)$$

Substituting the difference  $(\sigma_{\varphi 1} - \sigma_{r1})$  into equation (3.82), we obtain the second approximation for  $\sigma_r$ :

$$\begin{aligned} \sigma_{r2} = \frac{1}{h} \left\{ \int_{R_a}^r \left[ \frac{(1+\mu)E}{r^{1+\mu}} \int_{R_a}^r r^2 a t dr - E a t \right] \frac{h}{r} dr - \rho \omega^2 \int_{R_a}^r r h dr + \right. \\ \left. - \int_{R_a}^r \left[ \frac{(1-\mu^2)E}{r^{1+\mu}} \int_{R_a}^r \frac{r^2 \sigma_{r1}}{E} dr - (1-\mu) \sigma_{r1} \right] \frac{h}{r} dr + h_a \sigma_{ra} + A \int_{R_a}^r \frac{E h}{r^{2+\mu}} dr \right\}. \quad (3.90) \end{aligned}$$

The constant A for a disk with an opening is determined from the equation (3.90) with a known load on the outer loop. For a disk with a central opening when  $r = R_a$   $\sigma_{ra} = \sigma_{\varphi a}$  and according to formula (3.85)

$$A = \frac{R_a^{1+\mu}}{E_a} [(1-\mu) \sigma_{ra} + E_a a_a t_a]. \quad (3.91)$$

Substituting this value of A into equation (3.90), we determine  $\sigma_{ra}$  and then all the other values of  $\sigma_{r2}$ . After determining  $\sigma_{r2}$  (and if this approximation is sufficient) we find the values of  $\sigma_{\varphi 2}$  from equation (3.89):

$$\begin{aligned} \sigma_{\varphi 2} = \sigma_{r2} + \frac{(1+\mu)E}{r^{1+\mu}} \int_{R_a}^r r^2 a t dr - E a t - (1-\mu) \sigma_{r1} + \\ + \frac{(1-\mu^2)E}{r^{1+\mu}} \int_{R_a}^r \frac{r^2 \sigma_{r1}}{E} dr + A \frac{E}{r^{1+\mu}}. \quad (3.92) \end{aligned}$$

For a solid disk the determination of  $\sigma_{\varphi 2}$  should begin with  $r = R_a$  and instead of the constant A, we should substitute its value from formula (3.91).

For greater accuracy in determining  $\sigma_{\phi 2}$  the values of  $\sigma_{r2}$  should also be substituted instead of  $\sigma_{r1}$  in all terms of equation (3.92). However, while only slightly affecting the result, this somewhat increases the computational work and is expedient only in exceptional cases when  $\sigma_{r2}$  differs considerably from  $\sigma_{r1}$ .

Total stresses are determined from the cited equations. If we must calculate the stresses only from forces of inertia (the disk is cold or uniformly heated), then all terms containing  $t$  and  $E$  disappear. In determining thermal stresses we should assume  $\omega = 0$ .

#### Stresses in disks of constant thickness:

Disks of constant thickness are used in some designs in spite of the loss in weight as compared with disks of conical and hyperbolic shapes with identical safety factors.

The differential stress equations for disks of constant thickness can be solved completely for the given disk parameters (dimensions, material, temperature radial distribution, and boundary conditions). It is simplest to analyze the effect of individual factors on stress using an example of such disks.

Figures 3.56 and 3.57 present graphs showing the distribution of radial and circular stresses along the radius of a disk of constant thickness: a) rotating, uniformly heated without a loop load (Fig. 3.56); b) nonrotating, but nonuniformly heated (Fig. 3.57).

An analysis of the curves (see Fig. 3.56) leads to the following conclusions:

- circular stresses  $\sigma_{\phi}$  are always greater than radial stresses  $\sigma_r$ ;
- in a disk having an opening of "zero" radius (puncture), stresses  $\sigma_{\phi}$  double while stresses  $\sigma_r$  reduce to zero. In this case,  $\sigma_{\text{ЭНБ}}$  is twice as long as it is for a disk without an opening. Hence the conclusion concerning the more rational shape of a disk without an opening.

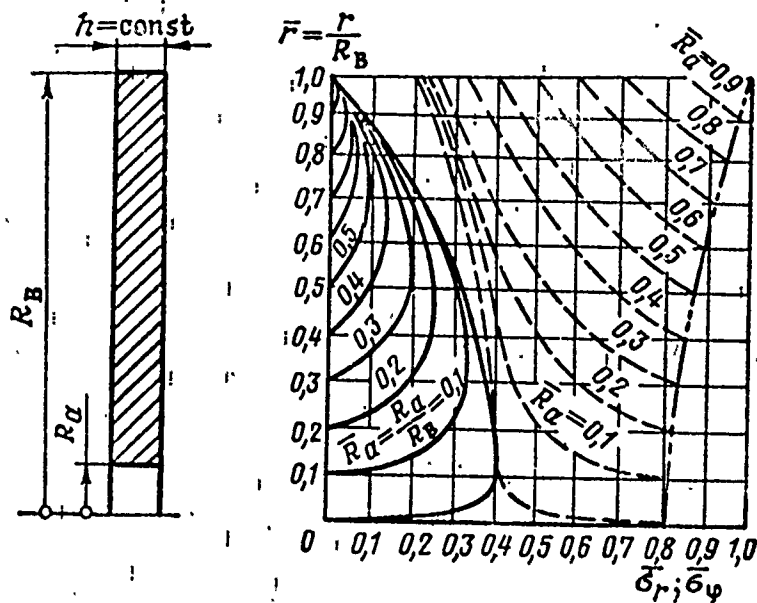


Fig. 3.56. Distribution of stresses  $\bar{\sigma}_r$  and  $\bar{\sigma}_\phi$  from centrifugal forces along the radius of a disk of constant thickness: solid line  $-\bar{\sigma}_r$ ; dashes  $-\bar{\sigma}_\phi$ .

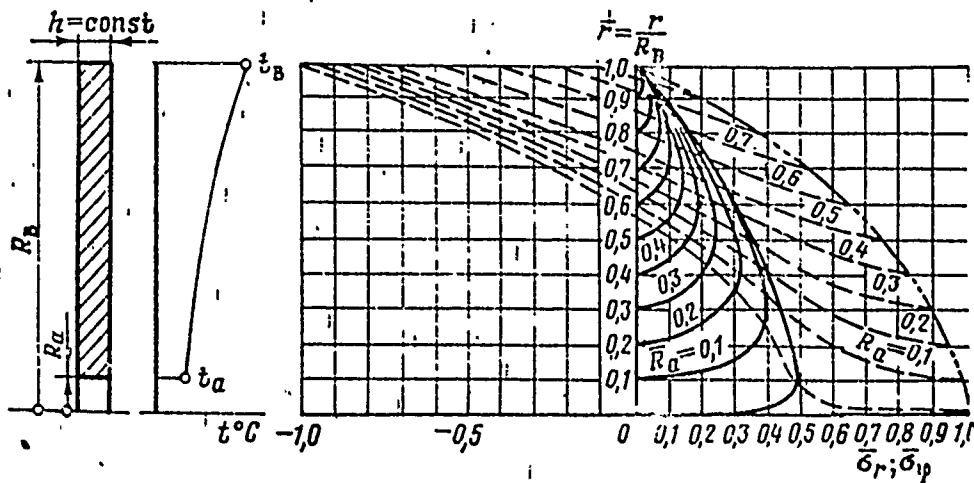


Fig. 3.57. Distribution of the stresses  $\bar{\sigma}_r$  and  $\bar{\sigma}_\phi$  for a nonrotating disk of constant thickness with nonuniform heating along the radius: solid line  $-\bar{\sigma}_r$ ; dashes  $-\bar{\sigma}_\phi$ .

When  $\bar{r}_a \rightarrow 1$  radial stresses approach zero while circular stresses approach maximum.

In examining thermal stresses (see Fig. 3.57) we can make the following conclusions.

- Thermal stresses are due to nonuniform heating of the disk. With uniform heating there will be no thermal stresses.

- Thermal stresses substantially distort the pattern of stresses obtained only from the rotation of the disk, particularly the pattern of stresses  $\sigma_\varphi$ . On the periphery of the disk with the examined character of temperature variation negative (compressive) stresses appear.

We should note that the strength of the disk will be different depending upon whether it is heated or not, even if in the heated disk there is no temperature gradient. If the degree of heating determines the strength of the disk material, nonuniform heating determines its thermal stresses.

#### Analyzing disk with allowance for plastic flow

An attempt to obtain higher criteria for a turbine and reduce its weight has lead to an increase in the angular velocities of rotors and stresses in the disk up to their operation in the elastic-plastic region. In individual sections of the disk stresses reach the yield point  $\sigma_T$ . Meanwhile, other less loaded sections are loaded with additional forces. All this leads to a redistribution of stresses in the disk and is particularly apparent at high temperatures, since with an increase in temperature the yield point drops continuously.

We should mention one more effect connected with plastic flow. As a consequence of the plastic flow of material under elevated temperatures, a continuous decrease in thermal stresses (stress

relaxation) occurs and with steady creep the thermal stresses completely disappear.

Let us examine one of the methods of analyzing disks with allowance for plasticity - the method of variable elasticity parameters [7].

Figure 3.58 is a tensile strain diagram. Below the stress equal to yield point (point a) for most metals there is a linear dependence between stress  $\sigma$  and relative strain  $\epsilon$

$$\sigma = E\epsilon, \quad (3.93)$$

where  $E = \operatorname{tg} \alpha$  is the modulus of elasticity of the first kind.

Beyond the yield point (point b) where plastic flow occurs, stresses can be written by analogy in the form

$$\sigma = D\epsilon, \quad (3.94)$$

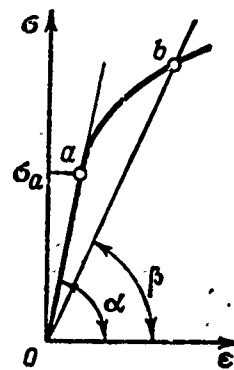
where  $D = \operatorname{tg} \beta$  is the modulus of plasticity.

The principal difference between relationships (3.93) and (3.94) lies in the fact that the modulus of elasticity  $E$  remains the same for all points of an elastic body and does not depend on the amount of strain. The value, however, of the modulus of plasticity  $D$  depends on the degree of deformation and, therefore, is different at each point of the zone of the  $\sigma$ - $\epsilon$  diagram, where plastic flow occurs.

In the general case of the three-dimensional stress in an elastic body the following dependence also occurs, analogous to (3.93):

$$\sigma_i = E\epsilon_i, \quad (3.95)$$

Fig. 3.58. Strain diagram for steel.



In this formula

$$\sigma_1 = \frac{1}{\sqrt{2}} \sqrt{(\sigma_1 - \sigma_2)^2 + (\sigma_2 - \sigma_3)^2 + (\sigma_3 - \sigma_1)^2}; \quad (3.96)$$

$$\epsilon_1 = \frac{\sqrt{2}}{3} \sqrt{(\epsilon_1 - \epsilon_2)^2 + (\epsilon_2 - \epsilon_3)^2 + (\epsilon_3 - \epsilon_1)^2}, \quad (3.97)$$

where  $\sigma_1$  is the generalized intensity of stresses;

$\epsilon_1$  is the strain intensity;

$\sigma_1, \sigma_2, \sigma_3$  are the principal stresses;

$\epsilon_1, \epsilon_2, \epsilon_3$  are the principal relative elongations.

As shown, for the case of plastic flow with any three-dimensional stress a dependence similar to (3.94) occurs:

$$\sigma_1 = D \epsilon_1, \quad (3.98)$$

where  $D$  is the modulus of plasticity as in formula (3.94).

The relationship (3.98) also occurs in the case of simple stress. This makes it possible when analyzing any three-dimensional stress (elastic or elastic-plastic), to use the  $\sigma$ - $\epsilon$  diagrams obtained during tensile tests.



In the examined theory during plastic flow the material is assumed incompressible; hence it follows that the Poisson coefficient  $\mu = 0.3$  and  $\mu = 0.5$ . Therefore, the dependence of the strain components on the stress components for a biaxial stressed state of a disk [see formula (3.70)] can be written in the form

$$\epsilon_r = \frac{1}{D} (\sigma_r - 0.5\sigma_\varphi) + \alpha t; \quad \epsilon_\varphi = \frac{1}{D} (\sigma_\varphi - 0.5\sigma_r) + \alpha t. \quad (3.99)$$

Research has established that stresses in an elastic disk when  $\mu = 0.3$  and  $\mu = 0.5$  are virtually identical. Consequently, when analyzing disks we can use formulas (3.99) for strains both in plastic and in elastic regions and, therefore, equations of equilibrium and strain compatibility are also real for disks which have regions of plastic flow.

Thus, an analogy has been established between the main equation necessary for analyzing disks in elastic and elastic-plastic regions. The principal difference is that when analyzing an elastic disk the modulus of elasticity  $E$  is known on each radius of the disk and depends only on temperature while the modulus  $D$  depends, in addition, on the value of strain on a given radius, which is not known beforehand.

Elastic-plastic flow should be analyzed by the method of successive approximations. For analysis we must have strain curves similar to the curves in Fig. 3.59 for a given disk material.

Fig. 3.59. Strain diagram for 23Kh2NVFA (EI-659) steel.

KEY: (1)  $\text{daN/mm}^2$ .

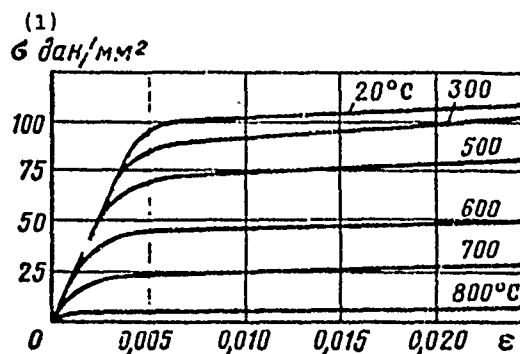
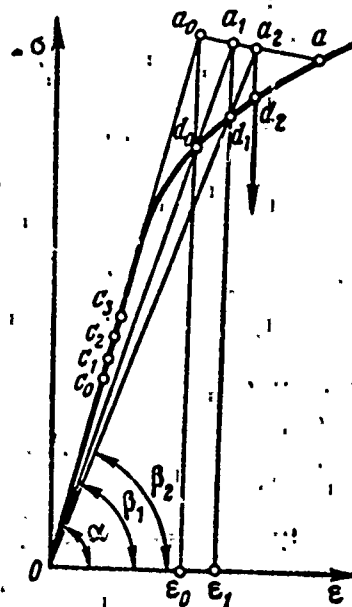


Fig. 3.60. Plotting of successive approximations (disk analysis with allowance for plastic flow).



We shall divide a disk into sections and calculate these stresses, assuming that the disk operates entirely in the elastic region ( $\mu = 0.5$ ). The stresses obtained are used for the zero approximation.

Based on the values of  $\sigma_r$  and  $\sigma_\varphi$  on the middle radius of each section,  $\sigma_1$  is calculated. For disks the stress intensity is computed from a formula obtained from formula (3.96) with  $\sigma_1 = \sigma_r$ ;  $\sigma_2 = \sigma_\varphi$ ;  $\sigma_3 = 0$  [see formula (3.80)]:

$$\sigma_i = \sqrt{\sigma_r^2 + \sigma_\varphi^2 - \sigma_r \sigma_\varphi}.$$

<sup>1</sup>As the zero approximation we can also use stresses corresponding to the elastic state of the disk, calculated when  $\mu = 0.3$ . However, the calculation of the first and following approximations is performed with  $\mu = 0.5$ .

Let us proceed with the successive approximations. Let  $\sigma_1$  for any section of the disk correspond to point  $a_0$ , which lies on an extension of the initial linear segment of the strain diagram (Fig. 3.60). Strain  $\epsilon_0$  corresponding to point  $a_0$  satisfies stress  $\sigma_{d0}$  which is characterized by point  $d_0$ . If we draw ray  $Od_0$ , then  $D_1 = \operatorname{tg} \beta_1 = (\sigma_{d0})/(\epsilon_0)$ .

Similar calculations are performed for each section of the disk. The values of  $D_1$  obtained are used for the new values of the modulus of elasticity on each section.

After this we perform a new analysis of the disk as elastic (with modulus of elasticity  $D_1$ ). As a result, we obtain stresses  $\sigma_r$  and  $\sigma_\phi$  in the first approximation. According to them we calculate the values of  $\sigma_1$  for the average radius of each section. Let these stresses in the examined section satisfy point  $a_1$ , lying on the extension of ray  $Od_0$ . Based on strain  $\epsilon_1$  and stress  $\sigma_{d1}$ , corresponding to point  $d_1$  we determine the new value of the modulus of plasticity for a given section:

$$D_2 = \operatorname{tg} \beta_2 = \frac{\sigma_{d1}}{\epsilon_1}.$$

Based on the values thus obtained for each section, we analyze the disk as elastic in the second approximation, etc.

The process of successive approximations for the examined section is illustrated by the line  $a_0; a_1; a_2; \dots; a$ . The intersection point  $a$  of this line with the strain diagram corresponds to stress  $\sigma_a$  and deformation  $\epsilon_a$  which occur in the middle of a given section of an elastic-plastic disk.

The curves illustrating the process of successive approximations for two sections differ in form from the curve  $a_0; a_1; a_2; \dots; a$ ; even the very curve corresponding to the averaged temperature of this section will be different.

It should be noted that if stresses do not exceed the yield point, this process is illustrated by a set of points  $c_0; c_1; c_2; \dots; c$ , lying on the linear section of the strain diagram.

Usually, two or three approximations are sufficient for analysis. After the results converge, radial elongations in the disk on radius  $r_a$  can be found from formula

$$\Delta r = \frac{r_a}{E_a} (\sigma_{\varphi a} - 0.5 \sigma_{ra}) + \alpha_a t_a r_a. \quad (3.100)$$

After all the calculations we can find the boundary between the elastic and plastic regions of the disk.

#### Stress analysis of disks based on breaking revolutions

The reliability of the studied disk is determined by comparing the stresses arising in it with the stresses at which the disk breaks, i.e., the safety factor is evaluated:

$$n_{\Delta r} = \frac{\sigma_{\text{в,т}}^t}{\sigma_{\text{экр max}}} = \frac{\omega_{\Delta r}}{\omega_{\text{рaб max}}},$$

where  $\sigma_{\text{в,т}}^t$  is the stress-rupture strength of the material with allowance for its operating temperature and operating time under load;

$\omega_{\Delta r}$  is the angular velocity of the disk at which breaking stresses  $\sigma_{\text{в,т}}^t$  arise in all sections;

$\omega_{\text{рaб max}}$  is the maximum angular velocity of the disk.

If  $n_{\Delta r} < 1$  on a certain section  $\Delta r$ , this still does not mean that the disk is broken since plastic flow occurs only in this section, while in the remaining (elastic) part of the disk the stresses are redistributed, increasing over those calculated.

Rupture sets in only when plastic flow is propagated in the entire diametric cross section of the disk. This is also the basis for analyzing disks based on breaking revolutions.

Thus, the safety factor of the disk can be evaluated not according to the stress-rupture strength  $\sigma_{B,T}^t$  but according to the yield point  $\sigma_T$ :

$$n_T = \frac{\sigma_T}{\sigma_{\text{экр max}}} = \frac{\omega_T}{\omega_{\text{пак max}}},$$

where  $\omega_T$  is the velocity of disk rotation at which stresses corresponding to yield point occur in all sections.

Analysis is formed on the assumption that with the breaking number of revolutions (or the corresponding angular velocity  $\omega_T$ ) centrifugal force of half the disk  $P_c$  and the loop load  $P(\sigma_{r,n})$  are equalized by internal forces  $P(\sigma_T)$  acting in the diametric cross section (Fig. 3.61). This condition can be written in the form of a sum of the projections of all forces onto the vertical axis:

$$P(\sigma_{r,n})_{\omega_T} + P_{c\omega_T} = P(\sigma_T). \quad (3.101)$$

The subscript  $\omega_T$  indicates that the condition is written for angular velocity  $\omega_T$  when the disk breaks.

Let us find the values of components in equality (3.101) (see Fig. 3.61):

$$P(\sigma_{r,n}) = 2 \int_0^{\frac{\pi}{2}} R_n d\varphi h_n \sigma_{r,n}(\omega_T) \cos \varphi = 2\sigma_{r,n}(\omega_T) R_n h_n,$$

where

$$\int_0^{\pi/2} \cos \varphi d\varphi = 1.$$

10

4

2

1

• 1994

2004

$$n_r = \frac{\omega_r}{\omega} = \sqrt{\frac{\int_0^{R_n} \sigma_r h dr}{\sigma_{r,1}(\omega) R_n h_n + q \omega^2 \int_0^{R_n} h r^2 dr}} \quad (3.102)$$

Usually,  $n_r = 1.2-1.5$  and the safety factor is  $n_{gn} = 1.4-1.8$ .

## Analysis of critical shaft speed

With the use of turbines of rapidly revolving shafts a phenomenon called "critical rpm" was detected.

It was noticed that during the slow rotation of a rotor no noticeable vibrations are observed. The rotor rotates smoothly. With the achievement of a certain number of revolutions the rotor begins, without visible cause, to vibrate sharply, which can lead to the breakdown of a clearly strong shaft. With a further increase in revolutions the rotor again begins to rotate quietly.

The rpm at which a shaft loses stability and begins to vibrate is called critical.

Stress analysis of shafts is studied in courses on the strength of materials and machine parts. Therefore, in this section we shall examine only the questions of transient stability of shafts.

Let us consider a shaft arranged vertically (for the elimination of the effect of its weight) in the middle cross section of which is attached a disk with mass  $m$ . Let us assume that the mass of the shaft is low as compared with the mass of the disk; however, the shaft possesses elastic properties. Let us also assume that the center of gravity of the disk  $c$  is displaced relative to the geometric center  $O_1$  by quantity  $e$  (Fig. 3.62). We further assume that supports allowing the shaft to rotate freely are absolutely rigid.

When the rotor only begins to rotate and the elastic axis of the shaft is still a straight line (Fig. 3.62a), then, as a result of the displacement of the disk's center of gravity with respect to the axis of rotation, there appears centrifugal force  $m\omega^2 e$ . Under the effect of this force the shaft begins to be deflected, which, in turn, leads to an increase in the centrifugal force (Fig. 3.62b):  $P_c = m(y + e)\omega^2$ .



Since the shaft is elastic, then, as deflection increases, force  $P_y$  of internal strength (the elastic force), counteracting the centrifugal force of the disk, will also increase. Assuming the deflections are small, we can consider that the elastic force will be proportional to the shaft deflection:  $P_y = Cy$  ( $C$  is the proportionality factor;  $y$  is the shaft deflection at the disk attachment point).

The physical meaning of coefficient  $C$  has been explained in the following example. It is known that the deflection of a beam under the effect of force  $P$ , applied in the middle between supports, is

$$y = \frac{Pl^3}{48EI},$$

hence

$$C = \frac{P}{y} = \frac{48EI}{l^3}.$$

Thus, the quantity  $C$  is a force which causes a unit deflection of the beam in the direction of its action. This quantity is called the stiffness coefficient; its dimensionality is

$$[C] = \frac{\text{unit force}}{\text{unit length}}$$

At each given moment the centrifugal force of the disk and the internal forces of elasticity must compensate each other, i.e.,

$$m(y + e)\omega^2 = Cy.$$

From this equality we find the expression for the deflection of a shaft:

$$y = \frac{m e \omega^2}{C - m \omega^2} = \frac{e}{\frac{C}{m \omega^2} - 1} \quad (3.103)$$

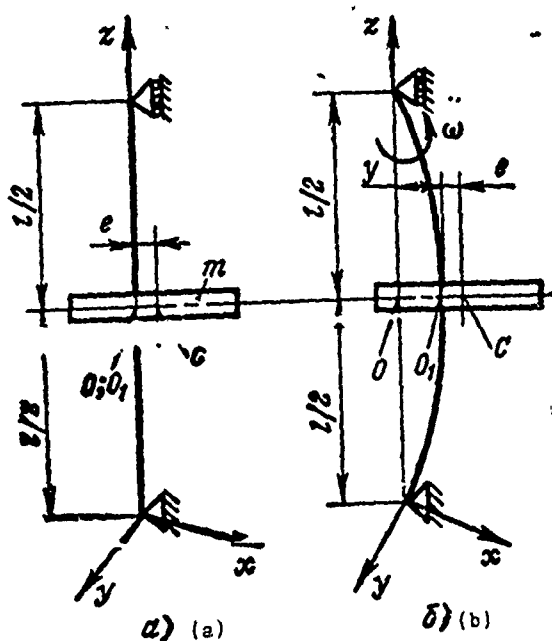


Fig. 3.62. A shaft with an unbalanced disk.

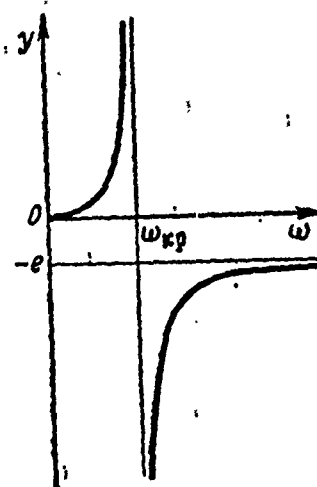


Fig. 3.63. Deflection of a shaft with an unbalanced disk versus the angular velocity of its rotation.  
Designation:  $\omega_{kp}$  = critical

Figure 3.63 presents the dependence of shaft deflection on the speed of its rotation. On the graph it is apparent that when the shaft is not rotating, the centrifugal force of the disk is equal to zero and shaft deflection is zero. With an increase in angular velocity the shaft deflection also begins to increase. At a certain angular velocity the deflection becomes infinite. Let us find this value of angular velocity. From equation (3.103) it is apparent that deflection  $y$  is equal to infinity if the denominator of the fraction in the second term of the equality is equal to zero, i.e.,

$$\frac{C}{m\omega^2} - 1 = 0,$$

hence

$$\omega_{kp} = \sqrt{\frac{C}{m}} \text{ rad/s} \quad (3.104)$$

designation  $\omega_{kp}$  = critical

The value of  $\omega_{kp}$  in formula (3.104) has been called critical angular velocity. The corresponding critical rpm is

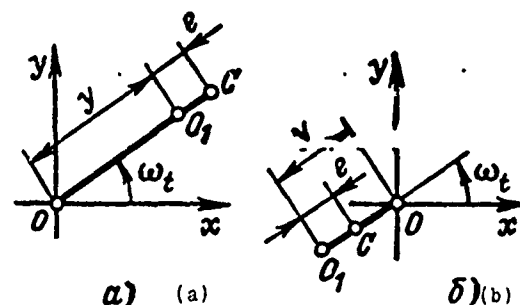
$$n_{kp} = \frac{30\omega_{kp}}{\pi} = 9,55 \sqrt{\frac{C}{m}} \text{ r/min}$$

With a further increase in angular velocity (when  $\omega > \omega_{kp}$ ) the shaft deflection becomes negative, while in absolute value it begins to drop; with infinitely high rpm the deflection becomes equal to  $-e$ .

The minus sign indicates that when  $\omega > \omega_{kp}$  the shaft is deflected in a direction opposite the eccentricity. When  $\omega = \infty$  the disk will rotate around its own center of gravity. Thus, at extremely high angular velocity, self-centering occurs.

Let us observe the location of the center of gravity of the disk at various angular velocities. Figure 3.64 illustrates the mutual arrangement of points O, O<sub>1</sub>, and C with angular velocities less than (Fig. 3.64a) and greater than (Fig. 3.64b) critical.

Fig. 3.64. Mutual arrangement of the  $O$  axis of bearings, the  $O_1$  axis of the shaft at the disk attachment point, and the center of gravity of the disk at various angular velocities: a -  $\omega < \omega_{кр}$ ; b -  $\omega > \omega_{кр}$ .



As experimental and theoretical studies have shown, at angular velocities less than and greater than critical, the shaft is dynamically stable. At critical angular velocity the shaft is dynamically unstable.

It is conditionally accepted to call shafts operating in the subcritical region rigid and in the supercritical region flexible (Fig. 3.65).

As seen from formula (3.103) and the graph in Fig. 3.63, when  $\omega = \omega_{кр}$  the shaft obtains an infinite deflection. Actually, at an angular velocity near critical the shaft deflections increase but remain finite (see Fig. 3.65). This is caused by the fact that with great deflection the centrifugal force of the disk is balanced not only by the transverse force of elasticity but also by the force directed along the axis of the deflected shaft.

Turbine operation at rpm near critical is not permissible. In practice we assume that the operating angular velocity must be  $\omega \leq 0.7\omega_{кр}$  or  $\omega \geq 1.3\omega_{кр}$ .

The effect of gyroscopic moment on critical angular velocity. The concept of shaft precession

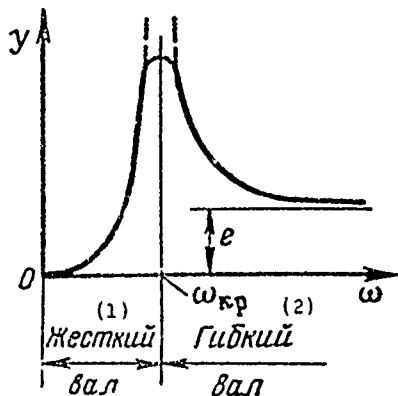


Fig. 3.65. The concepts of "rigid shaft" and "flexible shaft".  
KEY: (1) Rigid shaft, (2) Flexible shaft.

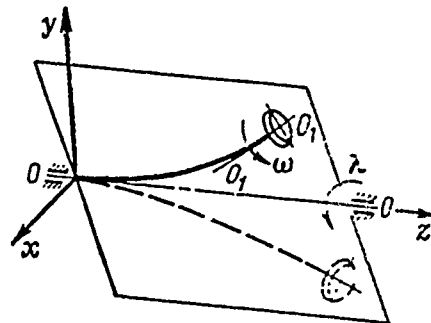


Fig. 3.66. The precession of a shaft with a disk.

Formula (3.104) for critical angular velocity is valid only for the case when a disk is located precisely in the middle between supports and during rotation the shaft is displaced in a parallel manner without rotation relative to the diameter.

In the overwhelming number of cases a disk is located asymmetrically on the shaft and, simultaneously with the revolution around its own axis with angular velocity  $\omega$ , it rotates along with the elastic line relative to the axis of the bearings with angular velocity  $\lambda$ . This can be represented as the vibrations of a shaft rotating along with the disk with angular velocity  $\omega$  relative to axis  $O_1 - O_1$  in a plane rotating with angular velocity  $\lambda$  relative to axis  $O - O$  (Fig. 3.66). The projection of the disk onto a thick plane will complete the oscillating motions (to rotate around its own diameter).

Such complex motion of bodies in mechanics is called precession while angular velocity  $\lambda$  of the elastic line with the disk is called the angular velocity of precession or the angular frequency of natural (free) vibrations of the rotating shaft. Two cases of precessive motion are:

*forward precession* - if the disk and the elastic line of the shaft rotate in the same direction;

*reverse precession* - if the disk and the elastic line of the shaft rotate in opposite directions.

Particular cases of precession are: *forward synchronous precession* when  $\lambda$  and  $\omega$  are equal not only in sign but in absolute value, and *reverse synchronous precession* when  $\lambda$  and  $\omega$  are opposite in sign but equal in absolute value.

Precessive motion of a disk is connected with the summation of two rotary motions, which leads to the appearance of gyroscopic moment.

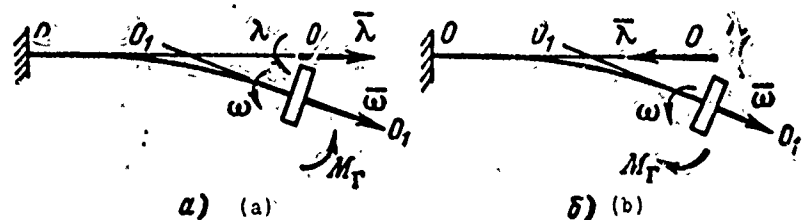


Fig. 3.67. The effect of gyroscopic moment on a shaft-disk system: a - forward precession; b - with reverse precession.

Let us examine the effect of gyroscopic moment on a disk-shaft system (Fig. 3.67). With forward precession (Fig. 3.67a) gyroscopic moment tends to decrease the deflection and turn the deflected shaft to a neutral position, i.e., increases system rigidity. Therefore, in accordance with formula (3.104), we should expect an increase in critical angular velocity.

With reverse precession (Fig. 3.67b) gyroscopic moment tends even more to deflect the shaft, i.e., to reduce system rigidity, which leads to a reduction in the critical angular velocity.

### Critical angular velocities of a single-disk rotor with allowance for gyroscopic moment

Let the disk in a shaft-disk system be attached to the shaft asymmetrically (Fig. 3.68); therefore, during precession gyroscopic moment will act on the shaft in addition to centrifugal force. Let us make the following assumptions.

1) The shaft is weightless but it has elastic properties (the mass of the shaft is negligible as compared with the mass of the disk). To reduce calculation error the weight of the shaft can be reduced to the weight of the disk.

2) The shaft supports are absolutely rigid.

3) The forces of resistance to the motion of the disk and the shaft are negligible.

During the precession of the disk its instantaneous position in space can be determined by coordinates  $x$ ,  $y$ , and  $z$  and projections  $\phi$  and  $\psi$  on the  $xOz$  and  $yOz$  planes of the angle between the tangent to the elastic line at the disk attachment point and the  $z$ -axis.

To obtain equations of motion for the studied system we shall use a Lagrange equation of the 2nd kind:

$$\frac{d}{dt} \left( \frac{\partial T}{\partial \dot{q}} \right) - \frac{\partial T}{\partial q} + \frac{\partial \Pi}{\partial q} = 0, \quad (3.105)$$

where  $q$  are the generalized coordinates (in our case,  $x$ ,  $y$ ,  $\phi$  and  $\psi$ );

$\dot{q} = dq/dt$  is the generalized velocity;

$T$  is the kinetic energy of the precessing disk;

$\Pi$  is the potential energy of the system.

Fig. 3.68. Determining critical angular velocities of a rotating shaft with one disk, allowing for gyroscopic moment.

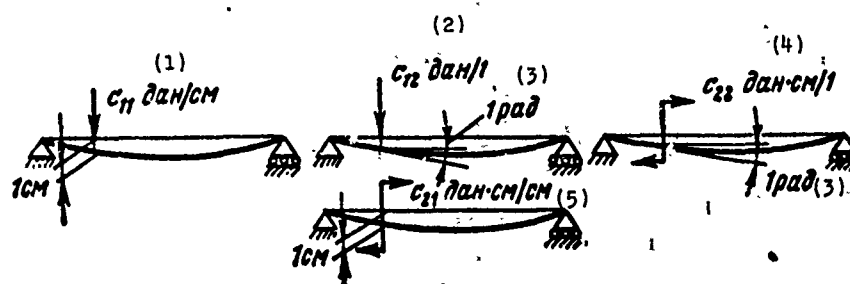
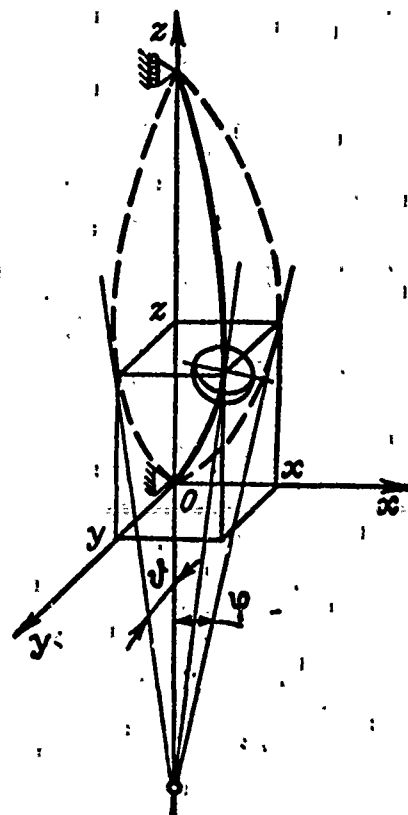


Fig. 3.69. Explanation of the physical meaning of rigidity coefficients.

KEY: (1)  $\text{daN/cm}$ ; (2)  $\text{daN/l}$ ; (3)  $\text{rad}$ ; (4)  $\text{daN}\cdot\text{cm/l}$ ; (5)  $\text{daN}\cdot\text{cm/cm}$ .



We assume that the disk and shaft accomplish small vibrations; therefore, we shall not allow for variation in the  $z$  coordinate, the sines of the angles  $\varphi$  and  $\theta$  will be replaced by the angles themselves and the cosines by one. Then the expressions for kinetics and potential energy obtain the form:

$$T = \frac{1}{2} [m(\dot{x}^2 + \dot{y}^2) + J_A(\dot{\varphi}^2 + \dot{\theta}^2) + J_n \omega^2 + J_n \omega(\dot{\varphi} - \dot{\theta})]; \quad (3.106)$$

$$\Pi = \frac{1}{2} [c_{11}(x^2 + y^2) + 2c_{12}(x\varphi + y\theta) + c_{22}(\varphi^2 + \theta^2)], \quad (3.107)$$

where  $m$  is the mass of the disk;

$J_A$  and  $J_n$  are the equatorial (diametric) and polar moments of inertia for the disk, respectively;

$c_{11}$ ,  $c_{12}$ ,  $c_{21}$ ,  $c_{22}$  are the shaft rigidity coefficients.

Based on the reciprocity theorem for displacement  $c_{12} = c_{21}$ . The physical meaning of the rigidity coefficient is explained in Fig. 3.69.

Differentiating equations (3.106) and (3.107) with respect to each of the coordinates and substituting the obtained expressions into equation (3.105), we obtain four differential equations for system motion:

$$\left. \begin{aligned} m\ddot{x} + c_{11}x + c_{12}\varphi &= 0; \\ m\ddot{y} + c_{11}y + c_{12}\theta &= 0; \\ J_A\ddot{\varphi} + J_n\omega\dot{\theta} + c_{21}x + c_{22}\varphi &= 0; \\ J_A\ddot{\theta} - J_n\omega\dot{\varphi} + c_{21}y + c_{22}\theta &= 0. \end{aligned} \right\} \quad (3.108)$$

We multiply the second and fourth equations of (3.108) by  $i = \sqrt{-1}$  and add, in pairs, the first to the second and the third to the fourth. The following substitution is used:

$$\bar{w} = x + iy; \bar{\psi} = \varphi + i\theta. \quad (3.109)$$

Then, instead of four equations of motion, we have only two:

$$\left. \begin{aligned} m\ddot{\bar{w}} + c_{11}\bar{w} + c_{12}\bar{\psi} &= 0; \\ J_A\ddot{\bar{\psi}} - iJ_n\omega\dot{\bar{\psi}} + c_{21}\bar{w} + c_{22}\bar{\psi} &= 0. \end{aligned} \right\} \quad (3.110)$$

The solution to the obtained system of two differential equations can be written in the form

$$\bar{w} = W e^{i\lambda t}; \quad \bar{\psi} = \Psi e^{i\lambda t}, \quad (3.111)$$

where  $\lambda$  is the natural angular velocity of this system in rad/s;

$W$  and  $\Psi$  are the amplitude values of complex coordinates  $w$  and  $\psi$ .

If we substitute solution (3.111) into the equation of motion (3.110), we obtain a system of homogeneous linear algebraic equations relative to  $W$  and  $\Psi$ :

$$\left. \begin{aligned} (c_{11} - m\lambda^2)W + c_{12}\Psi &= 0; \\ c_{21}W + (c_{22} - J_A\lambda^2 + J_n\omega\lambda)\Psi &= 0. \end{aligned} \right\} \quad (3.112)$$

The system of equations (3.112) has a nonzero solution if the determinant of this system is zero, i.e.,

$$\Delta(\lambda) = \begin{vmatrix} c_{11} - m\lambda^2 & c_{12} \\ c_{21} & c_{22} - J_A\lambda^2 + J_n\omega\lambda \end{vmatrix} = 0. \quad (3.113)$$

Expanding the determinant of (3.113) a complete equation of the 4th power relative to  $\lambda$  is obtained. However, it is extremely difficult to solve such an equation.

Let us make some transformations for which we shall use the substitution

$$\omega = s\lambda, \quad (3.114)$$

where  $s = \omega/\lambda$  is a constant.

The geometric sense of this constant will be examined when we analyze the graph of the system's frequency characteristic.

Allowing for the substitution of (3.114), the determinant (3.113) assumes the form

$$\Delta(\lambda^2) = \begin{vmatrix} c_{11} - m\lambda^2 & c_{12} \\ c_{21} & c_{22} - [J_A - J_n s] \lambda^2 \end{vmatrix} \equiv 0. \quad (3.115)$$

If we expand the determinant (3.115), we obtain not a complete but a biquadratic equation relative to  $\lambda$ :

$$m(J_A - J_n s)\lambda^4 - [mc_{22} + c_{11}(J_A - J_n s)]\lambda^2 + (c_{11}c_{22} - c_{12}^2) = 0. \quad (3.116)$$

Equation (3.116) is called the frequency equation. It defines the dependence of natural angular frequencies (velocities) of a shaft with one disk for assigned parameters of a system.

It is possible to use this equation; however, it is more convenient to use in computations an equation which has, instead of the rigidity coefficients, coefficients of unit load or, as they are called, coefficients of compliance.

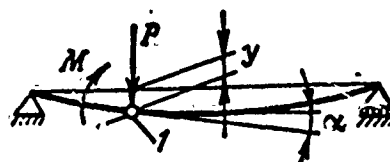
In order to find the relationship between the coefficient of rigidity and unit load, let us examine a beam on two supports loaded by force  $P$  and moment  $M$  (Fig. 3.70). Under the effect of the force and the moment the beam at point 1 will be deflected by quantity  $y$  and turned by angle  $\alpha$ .

If we use a "method of deformation," we can express the force and the moment in terms of deformations:

$$P = c_{11}y + c_{12}\alpha; \quad M = c_{21}y + c_{22}\alpha, \quad (3.117)$$

where  $c_{11}$ ,  $c_{12}$ ,  $c_{21}$ , and  $c_{22}$  are the rigidity coefficients.

Fig. 3.70. Determining the relationship between the coefficients of rigidity and unit load.



From the system of equations (3.117) we find the value of deflection  $y$  and the angle of turn  $\alpha$ :

$$\left. \begin{aligned} y &= \frac{\begin{vmatrix} P & c_{12} \\ M & c_{22} \end{vmatrix}}{\begin{vmatrix} c_{11} & c_{12} \\ c_{21} & c_{22} \end{vmatrix}} = \frac{c_{22}}{c_{11}c_{22} - c_{12}^2} P - \frac{c_{21}}{c_{11}c_{22} - c_{12}^2} M; \\ \alpha &= \frac{\begin{vmatrix} c_{11} & P \\ c_{21} & M \end{vmatrix}}{\begin{vmatrix} c_{11} & c_{12} \\ c_{21} & c_{22} \end{vmatrix}} = -\frac{c_{21}}{c_{11}c_{22} - c_{12}^2} P + \frac{c_{11}}{c_{11}c_{22} - c_{12}^2} M. \end{aligned} \right\} \quad (3.118)$$

On the other hand, if we use the "method of forces," we can express the deflection  $y$  and angle turn  $\alpha$  in terms of force  $P$  and moment  $M$ :

$$y = a_{11}P + a_{12}M; \quad \alpha = a_{21}P + a_{22}M, \quad (3.119)$$

where  $a_{11}$ ,  $a_{12}$ ,  $a_{21}$ ,  $a_{22}$  are the coefficients of the unit load.

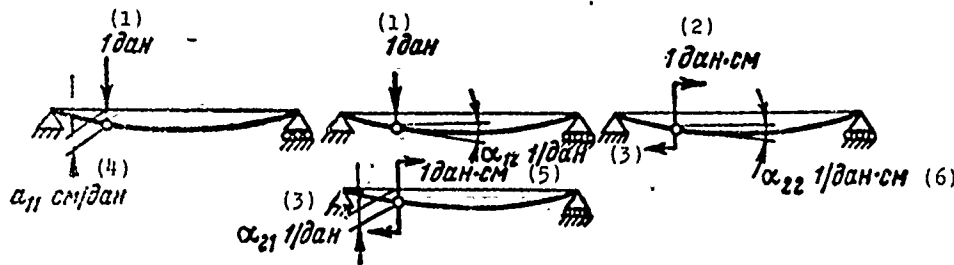


Fig. 3.71. Explanation of the physical sense of the coefficients of unit load.

KEY: (1) daN; (2) daN·cm; (3) 1/daN; (4) cm/daN; (5) daN·cm; (6) 1/daN·cm.

The physical sense of these coefficients is clear from Fig. 3.71. From the reciprocity theorem of displacements it also follows that  $a_{12} = a_{21}$ . Coefficients of unit load can be found by structural mechanics methods, for example, the Vereshchagin method with the aid of the Mohr integral (integral of unit moment) or according to the Castigliano theorem.

Comparing the coefficients with  $P$  and  $M$  in equalities (3.118) and (3.119), we find expressions for the relationship between the coefficients of rigidity and unit load:

$$\left. \begin{aligned} \frac{c_{22}}{c_{11}c_{22} - c_{12}^2} &= a_{11}; \\ \frac{-c_{12}}{c_{11}c_{22} - c_{12}^2} &= a_{12}; \\ \frac{-c_{21}}{c_{11}c_{22} - c_{12}^2} &= a_{21}; \end{aligned} \right\}$$

(3.120)

$$\left. \begin{aligned} \frac{c_{11}}{c_{11}c_{22} - c_{12}^2} &= a_{22}; \\ \frac{1}{c_{11}c_{22} - c_{12}^2} &= a_{11}a_{22} - a_{12}^2. \end{aligned} \right\}$$

If we divide all terms of equation (3.116) by  $(c_{11}c_{22} - c_{12}^2)$ , with allowance for equalities (3.120), we obtain a frequency equation written in terms of the coefficients of unit load:

$$m(a_{11}a_{22} - a_{12}^2)(J_n - J_n s)\lambda^4 - [a_{11}m + a_{22}(J_n - J_n s)]\lambda^2 + 1 = 0. \quad (3.121)$$

Studying equation (3.121) (or equation 3.116), we can find the horizontal asymptotes with the ordinates:

$$\lambda_{1,2} = 0; \quad \lambda_{3,4} = \pm \sqrt{\frac{a_{22}}{m(a_{11}a_{22} - a_{12}^2)}} = \pm \sqrt{\frac{c_{11}}{m}},$$

and also one inclined asymptote  $\lambda = (J_n)/(J_n)\omega$ .

Let us assign various values for the coefficient  $s = \omega/\lambda = \text{const.}$  Then equation (3.121) is solved as a biquadratic equation relative to  $\lambda$  for each given value of  $s$  and the roots of this equation give the ordinates of the graph of the equation (3.121)  $\lambda = \lambda(\omega)$ , the frequency characteristic. The corresponding abscissas are found from expressions  $\omega = s\lambda$ .

Figure 3.72 shows a graph of the frequency characteristic. Assigning any value to  $s$ , we cut, as it were, the frequency characteristic with ray  $s = (\omega)/(\lambda) = \text{ctg } \alpha_1$  and find the intersection points of this ray with the frequency characteristic. This is the geometric sense of the coefficient  $s$ . Obviously,  $s$  can change within the range  $-\infty \leq s \leq \infty$ .

Fig. 3.72. Complete frequency characteristics of a single-disk system.

KEY: (1) Region of reverse precession; (2) Region of forward precession; (3) Asymptote.

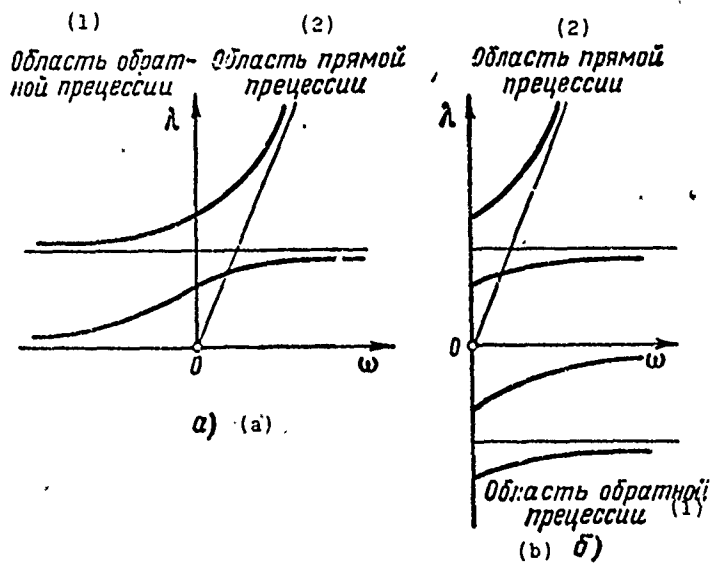
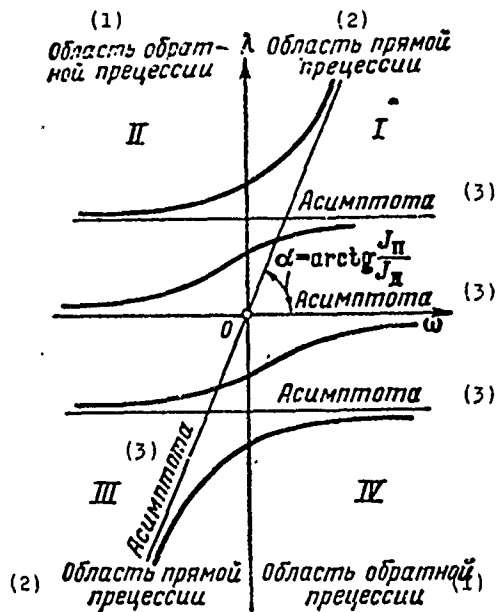


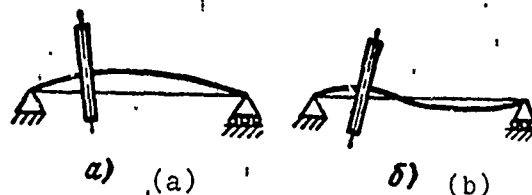
Fig. 3.73. Frequency characteristic of a single-disk system.

KEY: (1) Region of reverse precession; (2) Region of forward precession.

The frequency characteristic is symmetric relative to the origin of coordinates. This means that the curves coincide exactly in the I and III and in the II and IV quadrants. Therefore, they are bounded by its representation only in the two neighboring quadrants: in I and II (Fig. 3.73a) or in I and IV (Fig. 3.73b). The latter representation more accurately expresses the physical essence: for a given direction of shaft rotation (we assume it is positive) both forward (positive values of  $\lambda$ ), and reverse precession (negative values of  $\lambda$ ) occur. However, from the mathematical point of view, it is more convenient to deal with continuous curves, i.e., with the representation of characteristics as shown in Fig. 3.73a.

Analysis of the frequency characteristic shows that in the examined single-disk system each value of angular velocity corresponds to two natural angular frequencies (velocities) in the region of forward precession and two in the region of reverse precession. For the entire set of angular shaft velocities there is an infinite number of natural angular frequencies.

Fig. 3.74. Shapes of the elastic line during the vibration of a rotating shaft with one disk.



When  $\omega = 0$  there are two frequencies of bending vibrations for forward and two for reverse precession. Since the shaft is not turning there is no gyroscopic moment and the frequencies in the regions of forward and reverse precession, by pairs, are equal (in absolute value).

When  $\omega > 0$  in the region of forward precession, the numerical values of  $\lambda$  are greater than when  $\omega = 0$ , and in the region of reverse precession are less. This is explained by the effect of the gyroscopic moment which, during forward precession, increases shaft rigidity and during reverse decreases it.



When  $\lambda = \omega$ , forward synchronous precession occurs, and when  $\lambda = -\omega$ , reverse synchronous precession occurs.

The frequency characteristic has two branches. Branches with the lowest frequencies correspond to the first shape of elastic line (Fig. 3.74a), while branches with the highest frequencies correspond to the second shape of the elastic line (Fig. 3.74b).

In many practical cases disks can be assumed thin. Then  $J_{\Pi}/J_A \approx 2$  or  $J_{\Pi} \approx 2J_A$ .

In addition, for forward synchronous precession  $\lambda = \omega$ ,  $s = 1$  and equation (3.121) assumes the form

$$m(a_{11}a_{22} - a_{12}^2)J_A\lambda^4 + (a_{11}m - a_{22}J_A)\lambda^2 - 1 = 0, \quad (3.122)$$

hence

$$\lambda = \omega_p = \omega_{kp} = \sqrt{-\frac{1}{2} \frac{a_{11}m - a_{22}J_A}{m(a_{11}a_{22} - a_{12}^2)J_A} \pm \sqrt{\frac{1}{4} \left[ \frac{a_{11}m - a_{22}J_A}{m(a_{11}a_{22} - a_{12}^2)J_A} \right]^2 + \frac{1}{m(a_{11}a_{22} - a_{12}^2)J_A}}}. \quad (3.123)$$

In this case, the resonance rotational velocity  $\omega_p$  is equal to critical  $\omega_{kp}$ .

For reverse synchronous precession  $\lambda = -\omega$ ,  $s = -1$  and the equation (3.121) assumes the form

$$3m(a_{11}a_{22} - a_{12}^2)J_A\lambda^4 - [a_{11}m + 3a_{22}J_A]\lambda^2 + 1 = 0, \quad (3.124)$$

hence

$$\lambda = -\omega_p = -\sqrt{\frac{1}{2} \frac{a_{11}m + 3a_{22}J_A}{3m(a_{11}a_{22} - a_{12}^2)J_A} \pm \frac{1}{2}}$$

$$r = \sqrt{\frac{1}{4} \left[ \frac{a_{11}m + 3a_{22}l_1}{3m(a_{11}a_{22} - a_{12}^2)J_A} \right]^2 - \frac{1}{3m(a_{11}a_{22} - a_{12}^2)J_A}} \quad (3.125)$$

Example 3.3. Determine the angular velocities of a shaft on two supports with a cantilevered disk for forward and reverse synchronous precessions. The dimensions are clear from the sketch (Fig. 3.75). The weight of the shaft is disregarded. The disk will be considered thin ( $J_{\Pi}/J_A = 2$ ). The mass of the disk is  $m = 0.158 \text{ daN} \cdot \text{s}^2/\text{cm}$ . The diametric moment of inertia for the disk is  $J_A = 42.5 \text{ daN} \cdot \text{s}^2 \cdot \text{cm}$ . The shaft material is steel,  $E = 2.1 \cdot 10^6 \text{ daN/cm}^2$ .

Let us determine the coefficients of unit load with the aid of the Mohr integral:

$$a_{11} = \frac{1}{EI_1} \int_0^{l_1} \frac{(l_3 - l_2)^2}{l_2^2} x^2 dx + \frac{1}{EI_2} \int_{l_1}^{l_3} \frac{(l_3 - l_2)^2}{l_2^2} x^2 dx +$$

$$+ \frac{1}{EI_2} \int_{l_1}^{l_3} (l_3 - x)^2 dx = 4.57 \cdot 10^{-6} \text{ cm/daN}$$

$$a_{22} = \frac{1}{EI_1} \int_0^{l_1} \left( \frac{x}{l_2} \right)^2 dx + \frac{1}{EI_2} \int_{l_1}^{l_3} \left( \frac{x}{l_2} \right)^2 dx + \frac{1}{EI_2} \int_{l_1}^{l_3} dx = 0.0279 \cdot 10^{-6} \text{ l/daN} \cdot \text{cm};$$

$$a_{12} = a_{21} = - \left[ \frac{1}{EI_1} \int_0^{l_1} \frac{l_3 - l_2}{l_2^2} x dx + \frac{1}{EI_2} \int_{l_1}^{l_3} \frac{l_3 - l_2}{l_2^2} x^2 dx + \right.$$

$$\left. + \frac{1}{EI_2} \int_{l_1}^{l_3} (l_3 - x) dx \right] = -0.337 \cdot 10^{-6} \text{ l/daN}$$

$$a_{11}a_{22} - a_{12}^2 = 4.57 \cdot 10^{-6} \cdot 0.0279 \cdot 10^{-6} - (-0.337 \cdot 10^{-6})^2 = 0.014 \cdot 10^{-12} \text{ l/daN}^2.$$

For forward synchronous precession, based on equation (3.123), we find

$$\begin{aligned}\omega_{sp} &= \sqrt{-\frac{1}{2} \frac{4,57 \cdot 10^{-6} \cdot 0,158 - 0,0279 \cdot 10^{-6} \cdot 42,5}{0,158 \cdot 42,5 \cdot 0,014 \cdot 10^{-12}} +} \\ &+ \sqrt{\frac{1}{4} \left[ \frac{4,57 \cdot 10^{-6} \cdot 0,158 - 0,0279 \cdot 10^{-6} \cdot 42,5}{0,158 \cdot 42,5 \cdot 0,014 \cdot 10^{-12}} \right]^2 + \frac{1}{0,158 \cdot 42,5 \cdot 0,014 \cdot 10^{-12}}} = \\ &= \sqrt{2,46 \cdot 10^6} + \sqrt{6,06 \cdot 10^{12} + 10,6 \cdot 10^{12}} = 2560 \text{ rad/s.}\end{aligned}$$

For reverse synchronous precession, based on equation (3.125), we obtain

$$\begin{aligned}\omega_{p1,2} &= \sqrt{\frac{1}{2} \frac{4,57 \cdot 10^{-6} \cdot 0,158 + 3 \cdot 0,0279 \cdot 10^{-6} \cdot 42,5}{3 \cdot 0,158 \cdot 42,5 \cdot 0,014 \cdot 10^{-12}} \pm} \\ &\pm \sqrt{\frac{1}{4} \left[ \frac{4,57 \cdot 10^{-6} \cdot 0,158 + 3 \cdot 0,0279 \cdot 10^{-6} \cdot 42,5}{3 \cdot 0,158 \cdot 42,5 \cdot 0,014 \cdot 10^{-12}} \right]^2 - \frac{1}{3 \cdot 0,158 \cdot 42,5 \cdot 0,014 \cdot 10^{-12}}} = \\ &= \sqrt{7,575 \cdot 10^6} \pm \sqrt{57,2 \cdot 10^{12} - 3,54 \cdot 10^{12}}; \\ \omega_{p1} &= \sqrt{7,575 \cdot 10^6} - 7,33 \cdot 10^6 = 495 \text{ rad/s} \\ \omega_{p2} &= \sqrt{7,575 \cdot 10^6} + 7,33 \cdot 10^6 = 2860 \text{ rad/s}\end{aligned}$$

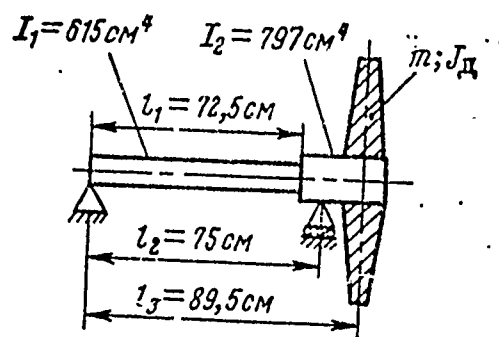


Fig. 3.75. Calculation diagram of a turbine rotor (for the calculation example).

Natural frequencies of vibrations in a rotating shaft with allowance for distributed mass

Let us examine a straight shaft with hinged supports on the ends.

We assume that the linear mass of the shaft is  $m_1$ , the moment of inertia of its cross-sectional area is  $I$ , the modulus of elasticity for the material is  $E$ . The shaft rotates with angular velocity  $\omega$

(Fig. 3.76). At distance  $x$  from the left support let there be deflection  $y$  with dynamic equilibrium.

The equation for dynamic equilibrium of the shaft is

$$EI \frac{d^4 y}{dx^4} = m_1 \omega^2 y. \quad (3.126)$$

We introduce dimensionless coordinate  $\bar{x} = (x)/(l)$ .

After designating

$$\alpha^4 = m_1 \frac{\omega^2 l^4}{EI}, \quad (3.127)$$

from equation (3.126) we obtain

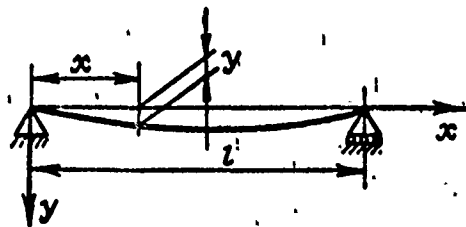
$$y^{IV} - \alpha^4 y = 0. \quad (3.126')$$

The common integral of the equation (3.126')

$$y = A \cos \alpha \bar{x} + B \sin \alpha \bar{x} + C \operatorname{ch} \alpha \bar{x} + D \operatorname{sh} \alpha \bar{x}, \quad (3.128)$$

where  $A$ ,  $B$ ,  $C$ , and  $D$  are arbitrary constants determined by the boundary conditions.

Fig. 3.76. Determining the critical rpm of a shaft, allowing for distributed mass.



For the assumed design of a shaft on two supports the boundary conditions will be:

$$\left. \begin{array}{l} \text{when } \bar{x}=0 \quad y(0)=0; \quad y''(0)=0; \\ \text{when } \bar{x}=1 \quad y(1)=0; \quad y''(1)=0; \end{array} \right\} \quad (3.129)$$

substituting the boundary conditions into equation (3.128) we obtain four equalities which define the constants A, B, C, and D:

$$\left. \begin{aligned} A + C &= 0; \\ -A + C &= 0; \\ A \cosh \alpha + B \sinh \alpha + C \cosh \alpha + D \sinh \alpha &= 0; \\ -A \cosh \alpha - B \sinh \alpha + C \cosh \alpha + D \sinh \alpha &= 0, \end{aligned} \right\} \quad (3.130)$$

hence it follows that  $A = C = 0$  and equalities (3.130) assume the form:

$$\left. \begin{aligned} B \sinh \alpha + D \cosh \alpha &= 0; \\ -B \sinh \alpha + D \cosh \alpha &= 0. \end{aligned} \right\} \quad (3.130')$$

The determinant of this system of equations is

$$\Delta(\alpha) = 2 \sinh \alpha \cosh \alpha. \quad (3.131)$$

We are interested in a zero solution, which means that the shaft preserves its rectilinear shape. Therefore, the determinant (3.131) of system (3.130') must be equal to zero:

$$\sinh \alpha \cosh \alpha = 0. \quad (3.131')$$

We need only the real roots, and equality (3.131') assumes the form

$$\sinh \alpha = 0. \quad (3.132)$$

This means that  $D = 0$ ; quantity B, however, remains arbitrary. The roots of equation (3.132) are other than zero and equal

$$\alpha_1 = \pi; \alpha_2 = 2\pi; \alpha_3 = 3\pi; \dots; \alpha_n = n\pi. \quad (3.133)$$

The corresponding equilibrium forms of the elastic line (Fig. 3.77)

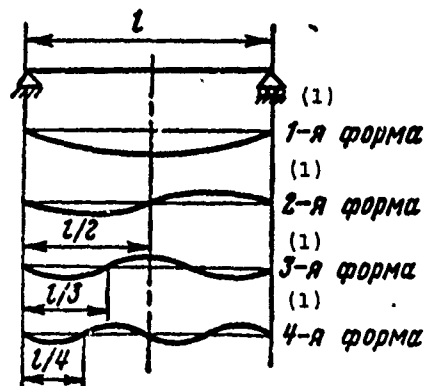
$$\left. \begin{aligned} y_1 &= B \sin \pi \bar{x} = B \sin \frac{\pi x}{l}; \\ y_2 &= B \sin 2\pi \bar{x} = B \sin \frac{2\pi x}{l}; \\ &\dots \dots \dots \end{aligned} \right\} \quad (3.134)$$

Each value of  $\alpha$  corresponds to its own value of angular velocity (at which the shaft will vibrate), determined from formula (3.127):

$$\left. \begin{aligned} \omega_1 &= \pi^2 \sqrt{\frac{EI}{m_1 l^4}}; \\ \omega_2 &= 4\pi^2 \sqrt{\frac{EI}{m_1 l^4}}; \\ &\dots \dots \dots \end{aligned} \right\} \quad (3.135)$$

Thus, the rotating shaft with distributing mass theoretically has an infinite number of natural frequencies of vibration.

Fig. 3.77. Forms of the shaft's elastic line during vibrations.  
KEY: (1) form.



When analyzing the natural frequency (or natural angular velocities) of rotors with distributed mass, the mass of the shaft can be taken into account by reducing it to the mass of the disk.

A simple adding of the mass of the shaft to the mass of the disk is too rough an approach. The best approach is the method of reducing the mass of the shaft to the mass of the disk based on the assumption that the kinetic energy of a rotating shaft is equal to the kinetic energy of a certain reduced mass concentrated at the spot where the disk is attached to the shaft. With this we assume that the elastic line of the vibrating shaft has the same form as during static deflection under the effect of a uniformly distributed load. This method of presentation does not take into account shaft rotation.

A stricter accounting for the mass of the shaft at certain critical velocities, proposed in reference [20], requires a very large amount of computation.

As studies have shown, the critical velocity of a system without taking the mass of the shaft into account will be higher than the first natural angular frequency of the system with mass taken into account. Disregarding the mass of a shaft can lead to particularly large errors (up to 50%) in systems with long shafts.

The mass of short rigid shafts with a low frequency of vibrations can be disregarded and this, of course, appreciably simplifies the problem of determining critical velocities.

#### Critical angular velocities of complex systems

The frequency equation (3.121) makes it possible to calculate critical angular velocities and vibration frequencies for a shaft of a single-disk system with allowance for gyroscopic moment. An equation of the 4th power relative to  $\lambda$  is obtained.

If the number of disks in the rotor is more than one, the frequency equation is made considerably more complicated. Thus, for a two-disk system the determinant (3.115) will have the form

$$\Delta(\lambda^2) =$$

$$= \begin{vmatrix} c_{11} - m_1 \lambda^2 & c_{12} & c_{13} & c_{14} \\ c_{21} & c_{22} - (J_{s1} - J_{n1} s) \lambda^2 & c_{23} & c_{24} \\ c_{31} & c_{32} & c_{33} - m_2 \lambda^2 & c_{34} \\ c_{41} & c_{42} & c_{43} & c_{44} - (J_{s2} - J_{n2} s) \lambda^2 \end{vmatrix} = 0, \quad (3.136)$$

and the frequency equation will be of the 8th power relative to  $\lambda$  (or of the 4th power relative to  $\lambda^2$ ).

For a three-disk system the frequency equation will be of the 12th power relative to  $\lambda$ , etc. These equations become difficult to solve by ordinary methods.

It should be noted that high speed computers, however, can solve this problem. There are other methods also which, if we use some approximation, enable us to determine the critical angular velocities of complex systems. Among these methods is the solution to integral equations of free vibrations using the method of successive approximations.

The integral equation for free flexural vibrations in a rotating rotor on two supports, having an arbitrary law of variation for the cross-sectional area of the shaft along the length and a load-carrying row of disks located arbitrarily along the length (Fig. 3.78) has the form

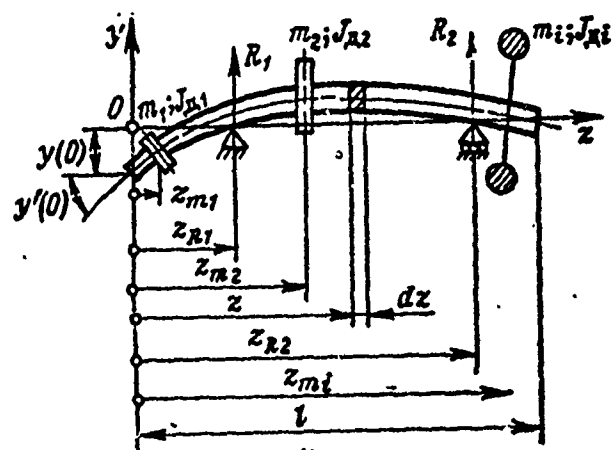


$$y(z) = \omega_c^2 \left[ \int_0^z \int_0^z \frac{M_y}{EI} dz^2 + \frac{z}{z_{R2} - z_{R1}} (K_{R1} - K_{R2}) - \frac{1}{z_{R2} - z_{R1}} (z_{R2} K_{R1} - z_{R1} K_{R2}) \right], \quad (3.137)$$

where  $M_y$  is the linear integral operator, proportional to bending moment ( $M(z) = \omega_c^2 M_y$ );

$$M_y = \int_0^z dz \left( \int_0^z Q F y dz + \sum_1^i m_i y_i z_i \right) + \\ - \sum_1^i J_{x_i} y_i' z_i - \frac{z - z_{R1}}{z_{R2} - z_{R1}} \varepsilon_{R1} [M(l)_0 - (l - z_{R2}) Q(l)_0] + \\ + \frac{z - z_{R2}}{z_{R2} - z_{R1}} \varepsilon_{R2} [M(l)_0 - (l - z_{R1}) Q(l)_0]. \quad (3.138)$$

Fig. 3.7c. Diagram of a two-support rotating shaft.



Here the linear integral operators are

$$K_{R1} = \int_0^{z_{R1}} \int_0^z \frac{M_y}{EI} dz^2; \quad K_{R2} = \int_0^{z_{R2}} \int_0^z \frac{M_y}{EI} dz^2; \quad (3.139)$$

$\rho$  is the mass density of the shaft material;

$I$  is the moment of inertia of the cross-sectional area;

$E$  is the modulus of elasticity of the shaft material;

$F$  is the cross-sectional area of the shaft;

$m_i$  is the mass of the  $i$ -th disk;

$J_{di}$  is the diametric mass moment of inertia of the disk;

$\varepsilon_i$ ;  $\varepsilon_{R1}$ ;  $\varepsilon_{R2}$  are unit functions;

$$\varepsilon_i = \begin{cases} 0 & \text{при } z < z_{mi} \text{ или } z < z_{R1} \\ 1 & \text{при } z > z_{mi} \text{ или } z > z_{R1} \end{cases}$$

при = when, или = or

$Q(z)_0$  is the total shearing force on the shaft end only from inertial load;

$M(z)_0$  is the total bending moment on the shaft end only from inertial loads.

Formula (3.137) enables us to find the critical angular velocity of a shaft on two supports, taking into account the gyroscopic effect of the disks and the mass of the shaft.

If the first support corresponds to the origin of coordinates, then in formulas (3.137) and (3.138) we should assume  $z_{R1} = 0$ . If the rotor does not have cantilevers, then  $z_{R1} = 0$  and  $z_{R2} = 0$ . If a nonrotating shaft is studied, in formula (3.138) the term

$\sum_{i=1}^n J_{di} y_i' \varepsilon_i$  is equal to zero.

See reference [10] for a more detailed application of integral equations for determining critical velocities.

The concept of forced vibrations. Factors causing the vibration of rotating shafts

If a periodically changing external load acts on a system, the system will accomplish forced vibrations. The amplitudes of these vibrations depend on the value of the exciting force, its frequency, and the elastic-mass characteristics of the turbine elements. Usually in working turbines the frequency spectrum of exciting forces is rather wide. Therefore, all turbine elements continually oscillate as a result of which dynamic stresses develop in them and determine, to a considerable degree, the reliability of the turbine as a whole.

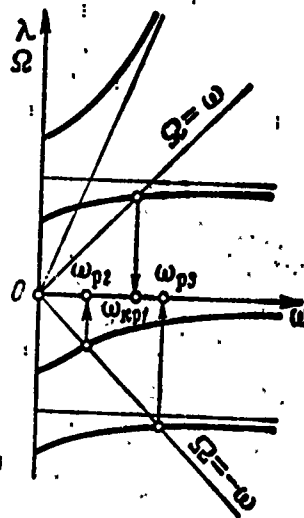
Frequencies  $\Omega$  of an exciting force can be very different. Usually they are connected with the angular velocity  $\omega$  of the rotor by relationship

$$\Omega = k\omega, \quad (3.140)$$

when  $k = 1, 2, 3, \dots, n$  is the harmonic number of the frequency of the exciting force or a multiple number of the frequency of this force.

Exciters of forced vibrations can be gas-dynamic forces acting on the working blades and being transmitted through the disks to the shafts, as well as various alternating shearing forces which arise as a result of inaccuracies in the manufacture of parts of the rotor, gears connected with the rotor, etc., misalignment of the rotor couplings, nonuniform tightening of bolts along the flanges of rotor components, different shaft rigidity in two directions, etc. The most dangerous exciting force is the shearing force from rotor unbalance, always present to some extent. With unbalance the vector of the exciting force will rotate with the same angular velocity as the rotor and, consequently, the angular frequency of this force will be equal to the velocity of the shaft rotation (in this case, the multiple number  $k = 1$ ).

Fig. 3.79. Resonance modes for a single-disk rotor:  $\omega_{kp1}$  with forward synchronous precession;  $\omega_{p2}$  and  $\omega_{p3}$  with reverse synchronous precession.



Forced vibrations are most dangerous when the frequency of the exciting force becomes equal or near the frequency of natural vibrations. The amplitudes of the vibrations can become very high even with a low value for the driving force. The resonance condition for a rotating rotor is

$$\Omega = \lambda(\omega), \quad (3.141)$$

i.e., resonance sets in when the frequency  $\Omega$  of the driving force is equal to the frequency  $\lambda$  of natural vibrations of the rotor for a given angular velocity  $\omega$ .

As has been discussed, the most dangerous frequency of exciting force is the frequency from the vector of the inherent unbalance of the rotor ( $k = 1$ ); in the case of resonance ( $\Omega = \lambda = \omega_{kp}$ ), forward synchronous precession occurs. Angular velocity  $\omega_{kp}$  is called critical angular velocity.

If forward synchronous precession can arise in any rotor (because of inherent unbalance), reverse synchronous precession ( $\Omega = \lambda = -\omega$ ), as all other resonance modes, will appear only in the presence of an exciting force of corresponding frequency in the system.

Resonance modes can be shown on the frequency characteristic of a single-disk system (Fig. 3.79). For this, along with the angular frequency of natural vibrations, the frequency of the exciting force will be plotted on the axis of the ordinates. The intersection points of the "excitation rays" with the curves of the frequency characteristic give the values of the resonance frequencies for the natural vibrations of the system and the corresponding angular velocities of the rotor.

#### Methods of combating critical modes

When designing, it is necessary to adopt measures for non-resonance turbine operation throughout the range of working rpms. Sometimes resonance cannot be avoided. Then damping is used to decrease the amplitudes of vibration. Let us examine measures which are designed for this.

1. A shift of critical modes to the region of high rpms. An increase in critical rpms is possible by increasing the rigidity of the rotor during bending, which is achieved either by enlarging the shaft's cross section or by introducing additional supports.

2. A shift of critical modes to rpms below working rpms. As is known, rotors whose critical rpm is less than the working rpm are called flexible. Such a shift of critical modes can be achieved by reducing shaft rigidity during bending. However, an excessive decrease in rigidity can lead to inadmissible deflections of the shaft and make it difficult to maintain clearances in the circulatory part. In addition, since, in this case, the working rpms are higher than critical, it is necessary to ensure passage through critical velocity during acceleration and stopping of the rotor. Rotor operation in the supercritical region is tempting because, in this region of velocities  $\omega_{pa6} \gg \omega_{kp}$  [ $pa6$  = operating;  $kp$  = critical], the rotor is self-centering and this leads to a decrease in the load on the supports. Therefore, in spite of the above difficulties, the use of flexible rotors is advisable. For a safe transition

through the critical mode during acceleration and stopping of such a rotor, special devices which limit the deflections of the shaft are used.

A shift of the critical modes to lower rpms can be accomplished by introducing into the design of the supports special devices which restrict the rigidity of the support while preserving sufficient rigidity and strength of the shaft itself

Usually, "elastic" supports are not purely elastic since they are also the location of vibration dampers. In order to show the effect of an elastic support, let us examine the diagram in Fig. 3.80.

Critical velocity of a rotor with an elastic support can be determined from the equality (without allowing for gyroscopic moment)

$$\omega_{kp} = \sqrt{\frac{c_{np}}{m}}, \quad (3.142)$$

where  $c_{np}$  is the cited coefficient of rotor rigidity at the point of disk attachment (with allowance for the pliability of the support). The coefficient of rigidity

$$c_{np} = \frac{P}{y_{np}}, \quad (3.143)$$

where  $y_{np} = y_B + y_{on,np}$  is the displacement of the shaft at the point of disk attachment under the effect of the force  $P$ ;

$y_B$  and  $y_{on,np}$  are the displacement of this point because of the deflection of the shaft and the deformation of the elastic support, respectively.

We shall express displacement  $y_{on,np}$  in terms of the deformation of the support itself (Fig. 3.80a):  $y_{on}(l_1/l)$ . On the other hand,  $y_{on} = P_{on}/c_{on}$ , where  $P_{on} = P(l_1/l)$  is the reaction of the elastic support. Consequently,

$$y_{on np} = \frac{P}{c_{cn}} \frac{l_1^2}{l^2},$$

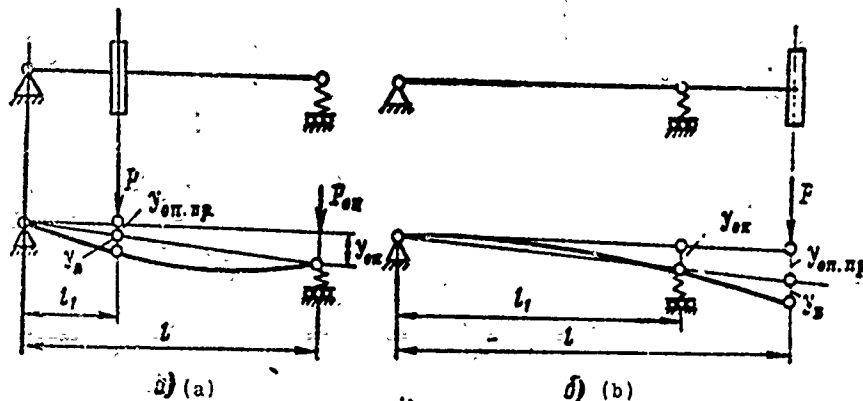


Fig. 3.80. The effect of support pliability on the critical rpms of a rotor: a - with a disk located between supports; b - with a cantilevered disk.

Hence

$$c_{np} = \frac{P}{y_{np}} = \frac{P}{y_n + \frac{P}{c_r} \frac{l_1^2}{l^2}},$$

or

$$\frac{1}{c_{np}} = \frac{1}{\frac{P}{y_n}} + \frac{1}{c_{on} \frac{l_1^2}{l^2}} = \frac{1}{c_n} + \frac{1}{c_{on np}}, \quad (3.144)$$

where  $c_n$  is the rigidity coefficient of the shaft during bending at the disk attachment point;

$c_{on np}$  is the rigidity coefficient of the elastic support reduced to the disk attachment point.

For the rotor diagram presented in Fig. 3.80a,

$$c_s = \frac{3EI}{l_1^2(l-l_1)^2}.$$

Similarly, for the rotor diagram in Fig. 3.80b

$$\frac{1}{c_{np}} = \frac{1}{c_n} + \frac{1}{c_{on np}},$$

where

$$c_s = \frac{3EI}{l(l-l_1)^2}; \quad c_{on np} = c_{on} \frac{l_1^2}{l^2}.$$

This diagram amounts to a rotor without special elastic elements in the supports if the latter are not absolutely rigid. Therefore, when the elasticity of the supports is commensurate with the elasticity of the rotor, the critical rpm must be determined with support pliability taken into account, i.e., it is necessary to examine the single "rotor-housing" elastic system.

#### Damping critical rotor modes

In the revolution of a turbine rotor various forces of resistance act on it. They include forces of friction in the bearings, the forces of friction between the rotor elements and the medium in which it is rotating, the forces of internal friction in the shaft material, etc. These forces create moment of resistance to rotation which is overcome by the external torque but does not affect the amount of shaft deflection although it prevents the precessive motion of the shaft and reduces its deflection.

These forces of resistance are used for damping the vibrations if the resonance modes are in the working range or must be passed through in the process of starting.



Existing methods of damping are reduced either to the introduction of additional resistance, which prevents precessive motion, into the "rotor-support" system or to a change in the dynamic properties of the system during the buildup of deflection.

Figure 3.81 shows an elastic-damping support with a linear characteristic, made in the form of a thin ring installed between the rim of the bearing and the housing of the turbine. The necessary pliability of the ring is ensured by selecting its thickness and fitting a combination of projections formed by grinding the faces on the outside of the ring and rounding it off on the inside. The second ring is solid and unshaped. It intensifies the damping ability of the first ring because of the gap between it and the outer rim of the bearing.

Figure 3.82 illustrates the design of an elastic-damping support with a nonlinear characteristic. After the gap  $h$  is eliminated and a rigid shaft sleeve is included, the support changes its characteristics; now its rigidity becomes greater. Since the gap  $h$  is small, the working fluid in it dampens the vibrations,

Figure 3.83 is the diagram of a shaft with a rigid support 1 and a dampened support 2. Upon the displacement of the support a piston moves in a cylinder filled with a viscous liquid which flows through special openings in the pistons and absorbs the energy of the vibrations.

Fig. 3.81. Diagram of an elastic-dampened support with a linear characteristic.  
KEY: (1) Projections.

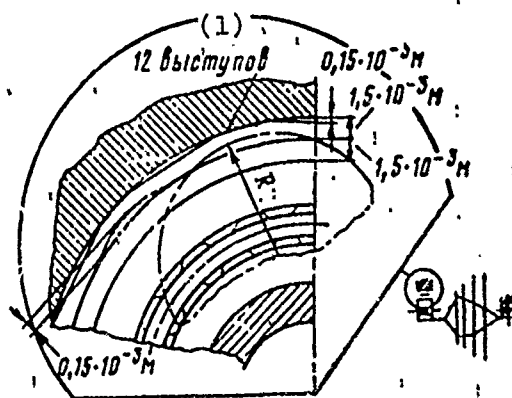


Fig. 3.82. Diagram of an elastic-dampened support with variable elasticity.

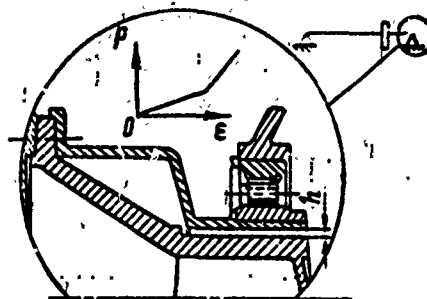


Figure 3.84 shows one of the wide used designs for a dampened support. Here between the insert of the bearing and the housing is located a packet of several thin steel tapes with a certain clearance. The gaps between the plates are filled with a lubricant. Because of the very low rigidity of the tapes the support has insignificant elasticity. However, the elasticity of the support can change widely, increasing the thickness of the plates and the number of them.

Such a support has a nonlinear characteristic, i.e., the dependence of the force acting on the support on the displacement of support has a nonlinear character.

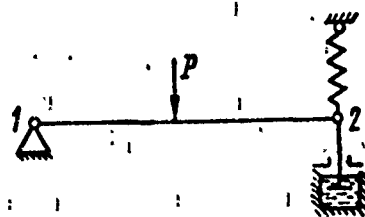


Fig. 3.83. Diagram of damping device.

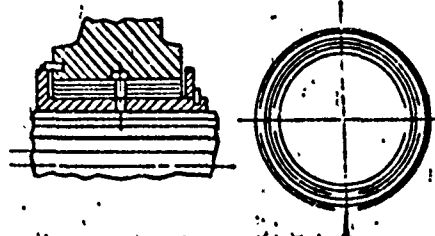


Fig. 3.84. Diagram of damped support with nonlinear characteristic.

## Vibrations in rotors on hydrostatic bearings

Vibrations of the rotor on hydrostatic bearings has the following peculiarities. With a given drop in the pressures of the working fluid on the bearing (difference in feed and discharge pressures), the rotor below a certain rpm accomplishes only forced vibrations with a frequency equal to the velocity of its rotation. When the frequency of free rotor vibrations agrees with the angular velocity, undesirable critical velocities and resonance vibrations are possible.

With a further increase in the rpm simultaneously with the forced vibrations there arises rotor vibrations with a frequency unlike the velocity of rotor rotation. Such vibrations, not connected with external excitation, are called auto-oscillations. A rotating rotor on hydrostatic bearings has the property of self-excitation; therefore, it is an auto-oscillatory system. Self-excitation and auto-oscillation of a system can lead in certain modes to a vigorous growth in vibration amplitudes. Externally they are similar to resonance modes of rotor operation; however, in essence, they differ severely from them since they do not bring about rotor unbalance. Frequently these modes are called modes of shaft stability loss.

Before proceeding to a calculation of rotor vibrations, let us examine the forces which arise in a hydrostatic bearing.

### Forces acting on the rotor pivot

Let us assume that the rotor axis is displaced relative to the bearing axis by a quantity  $r$ , the rotor rotates with velocity  $\omega$ , and the center of the pivot has a forward velocity  $v$  relative to the center of the bearing (Fig. 3.85). This velocity can be due to the precession of the shaft in the bearings or the vibrational motion of the shaft which appears from the action of external forces on the rotor.

In the calculation of forces, we make the following assumption. We shall assume that the flow of the working fluid in all elements of the bearing is turbulent. This assumption is valid since lubrication is accomplished by a liquid-metal heat carrier with low viscosity. In addition, the high angular velocity contributes to the turbulent flow of the lubricant. We shall assume that the motion of the fluid in the bearing is quasi-stationary, i.e., the calculation of nonstationary forces in bearings is performed according to formulas of stationary flow. This is valid if the ratio of the Reynolds numbers for the stationary and pulsating components of the flow is  $Re_{\text{пульс}}/Re_{\text{стан}} = 0-1.0$  [пульс = pulsation; стан = stationary]. Usually this relationship is maintained in the designs being studied.

It is further assumed that the working fluid is incompressible, the viscosity of the fluid is constant, and there are no breaks in the lubricating layer.

With these assumptions we shall set up an equation of the flow rate for the  $i$ -th chamber of an  $N$ -chamber hydrostatic bearing with diaphragm or capillary compensation (Fig. 3.85):

$$Q_{\text{н}i} - 2Q_{\text{т}i} + Q_{i, i+1} + Q_{i, i-1} + Q_{\text{в}i} = 0, \quad (3.145)$$

where  $Q_{\text{н}i}$  is the flow rate through the nozzle,  $\text{cm}^3/\text{s}$ ;

$Q_{\text{т}i}$  is the flow rate through the end connector of the chamber;

$Q_{i, i+1}$ ;  $Q_{i, i-1}$  are the flow rates along the connectors with  $i + 1$  and  $i - 1$  chambers;

$Q_{\text{в}i}$  is the flow rate of the liquid displaced from the  $i$ -th chamber, caused by the forward speed of the pivot.

The first three terms in equation (3.145) can be represented in the following form:

$$\left. \begin{aligned} Q_{*i} &= \mu_{*} f_{*} \sqrt{\frac{2}{\rho} (\rho_s - p_i)}; \\ Q_{\tau i} &= f_{\tau i} \left[ \sqrt{(0.0625 V_i)^2 + \mu_{\tau i}^2 \frac{2}{\rho} (p_i - p_c)} - 0.0625 V_i \right]; \\ Q_{i,i+1} &= \varphi [l_k, \delta_{i,i+1}; \delta_{i,i+1}^2; (p_{i+1} - p_i), \rho, V_{i,i+1} \cdot \bar{u}]; \end{aligned} \right\} (3.146)$$

$Q_{i, i-1}$  is written similarly to  $Q_{i, i+1}$ ;

$$V_i = \frac{\omega D}{2} - v \cos(\varphi_i - \psi).$$

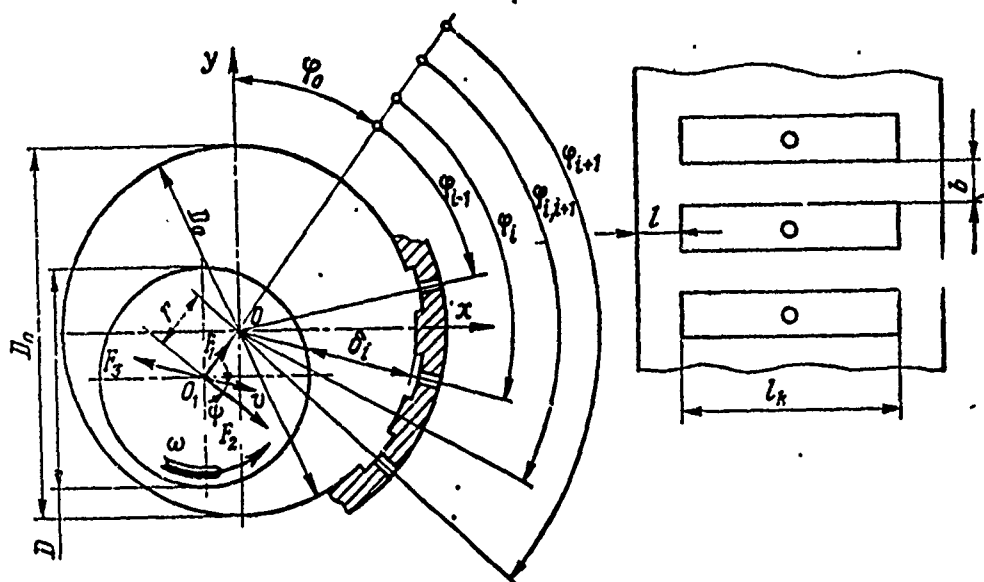


Fig. 3.85. Diagram of forces acting on rotor pivot.

In expressions (3.146) we have used the following designations:

$\mu_{*}, \mu_{\tau i}$  are the coefficients of flow rate through the nozzle and the end of the chamber;

$f_{*}, f_{\tau i}$  are the areas of the nozzle and the end slot of the  $i$ -th chamber,  $\text{cm}^2$ ;

$p_B, p_C$  are the pressures at input and output of the bearing, daN/cm<sup>2</sup>;

$p_i$  is the pressure in the  $i$ -th chamber of the bearing, daN/cm<sup>2</sup>;

$\omega$  is the angular velocity of the rotor, 1/s;

$v$  is the forward speed of the pivot, cm/s;

$\bar{u}$  is the ratio of the average velocity of the velocity profile in the slot to the maximum. For sufficiently high Reynold's numbers ( $Re > 1000$ ) this quantity varies from 0.8-0.9;

$\rho$  is the density of the working fluid, kg/cm<sup>3</sup>;

$\delta_{i, i+1}$  is the radial gap between the pivot and the bearing along the middle of the connector between the  $i$ -th and the  $(i + 1)$ -th chambers;

$l_H$  is the length of the bearing chamber.

The change in the gap between the pivot and the bearing with respect to the angle of turn is described by formula

$$\delta = \delta_0(1 + \varepsilon \cos \varphi), \text{ where } \delta_0 = (D_0 - D)/(2), \varepsilon = (l)/(\delta_0).$$

The system of reading angles is such that the position of the  $i$ -th chamber is determined by angle

$$\varphi_i = \frac{2\pi}{N} \left( i - \frac{1}{2} \right),$$

while the angular positions of the middles of the connectors between the  $i$ -th and the  $i + 1, (i - 1)$ -th chambers are

$$\varphi_{i, i-1} = \frac{2\pi}{N}(i-1); \varphi_{i, i+1} = \frac{2\pi}{N}i \quad (i=1, 2, \dots, N),$$

where  $N$  is the number of bearing chambers;

$\psi$  is the angle between the direction of the forward speed of the pivot and the direction perpendicular to the center-to-center distance (see Fig. 3.85).

During the forward speed of the pivot  $v$ , the pivot displaces liquid in the direction of motion and frees a place for the working liquid. In order to write the flow rate of the displaced liquid, we assume that on the half of the pivot towards the direction of motion sources of working fluid are located and on the other side are drains. The flow rate of the sources must be equal to the flow rate of the drains and the total flow rate of the displaced liquid:

$$Q = vD(L+l),$$

where  $l$  is the width of the end connector, and  $L = l_H + l$ .

We assume that the intensity of the sources and the drains along the angular coordinate changes according to sinusoidal law:  $q(\varphi) = q_0 \times \sin(\varphi - \psi)$ .

From the condition  $VD(L+l) = \int_{\psi}^{\psi+\pi} q(\varphi) d\varphi$  we obtain

$$q_0 = v \frac{D(L+l)}{2}$$

Then for the  $i$ -th chamber

$$Q_{s,i} = \int_{\varphi_{i,l-1}}^{\varphi_{i,l+1}} q(\varphi) d\varphi = \frac{vD}{2} (L+l) [\cos(\varphi_{i,l+1} - \psi) - \cos(\varphi_{i,l-1} - \psi)]. \quad (3.147)$$

We shall introduce designations:

$$h_i = \frac{p_i - p_c}{p_n - p_c}; \quad V_i^2 = \frac{2}{\rho} \Delta p; \quad V_0 = \frac{\omega D}{2V_*}; \quad v_0 = \frac{v}{V_*},$$

where  $\Delta p = p_B - p_C$ .

The quantity  $h_i$  is the relative pressure in the  $i$ -th chamber counted from the pressure of the drain and referred to the difference in the input and drain pressures. This difference is called the pressure differential in the bearing  $\Delta p$ .

The quantity  $V_*$  has the measurement cm/s and is a characteristic velocity which depends on the pressure differential in the bearing.  $V_0$  and  $v_0$  are the relative values of circular and forward velocities of the pivot (related to velocity  $V_*$ ).

With allowance for these designations and equations (3.146) and (3.147), from equation (3.145) we obtain

$$A_l \cdot h_{l-1} + B_l h_l + C_l \sqrt{D_l + h_l} + \sqrt{1 - h_l} + E_l h_{l+1} + G_l = 0. \quad (3.148)$$

The coefficients of this equation are:

$$\begin{aligned} A_l &= \frac{1}{\mu_{\kappa} f_{\kappa}} \frac{2lk \delta_{l,l-1}^2}{b \lambda_{l,l-1} \bar{u} [V_0 - v_0 \cos(\varphi_{l,l-1} - \psi)]}; \\ B_l &= -\frac{1}{\mu_{\kappa} f_{\kappa}} \frac{2l_k}{l \bar{u}} \left\{ \frac{\delta_{l,l+1}^2}{\lambda_{l,l+1} [V_0 - v_0 \cos(\varphi_{l,l+1} - \psi)]} + \right. \\ &\quad \left. + \frac{\delta_{l,l-1}^2}{\lambda_{l,l-1} [V_0 - v_0 \cos(\varphi_{l,l-1} - \psi)]} \right\}; \\ C_l &= -\frac{2\mu_{\tau} l f_{\tau l}}{\mu_{\kappa} f_{\kappa}}; \quad D_l = \frac{\{0,0625 [V_0 - v_0 \cos(\varphi_l - \psi)]\}^2}{\mu_{\tau l}^2}; \\ E_l &= \frac{1}{\mu_{\kappa} f_{\kappa}} \frac{2lk \delta_{l,l+1}^2}{b \lambda_{l,l+1} \bar{V} [V_0 - v_0 \cos(\varphi_{l,l+1} - \psi)]}; \\ G_l &= \frac{1}{\mu_{\kappa} f_{\kappa}} \left\{ V_0 \left( 2f_{\tau l} \cdot 0,0625 + \frac{l_k \delta_{l,l-1}}{2} - \frac{l_k \delta_{l,l+1}}{2} \right) - \right. \\ &\quad - v_0 \left[ 2f_{\tau l} \cdot 0,0625 \cos(\varphi_l - \psi) + \frac{l_k \delta_{l,l-1}}{2} \cos(\varphi_{l,l-1} - \psi) - \right. \\ &\quad \left. \left. - \frac{l_k \delta_{l,l+1}}{2} \cos(\varphi_{l,l+1} - \psi) + \frac{v_0 D}{2} (L + l) [\cos(\varphi_{l,l+1} - \psi) - \cos(\varphi_{l,l-1} - \psi)] \right] \right\}. \end{aligned}$$



The coefficients of hydraulic friction in the slots along the connectors between the chambers has been determined from formula

$$\lambda_{i,i-1} = \frac{4}{\left(2,6 + 5,1 \lg \frac{\delta_{i,i-1}}{2\Delta}\right)^2},$$

where  $\Delta$  is the height of the projections on the surface of the bearing;

$\lambda_{1, i-1}$  is calculated similarly to  $\lambda_{1, i+1}$ .

The coefficients of flow rate through the end slots have been calculated from formula

$$\mu_{r,i} = \frac{1}{\sqrt{2,3 + \xi_i}},$$

where

$$\xi_i = \lambda_i \frac{l}{2\delta_i}; \quad \lambda_i = \frac{4}{\left(2,6 + 5,1 \lg \frac{\delta_i}{2\Delta}\right)^2}.$$

The problem of finding the forces in a hydrostatic bearing will be solved if we find the relative pressures in the bearing chambers  $h_i$ . To find  $N$  of unknown  $h_i$  we can set up for each chamber an equation in the form of (3.148) and obtain a system of  $N$  equations:

$$\left. \begin{aligned} A_i h_{i-1} + B_i h_i + C_i \sqrt{D_i + h_i} + \sqrt{1 - h_i} + E_i h_i + G_i = 0 \\ (i=1, 2, \dots, N). \end{aligned} \right\} \quad (3.149)$$

The radicals signs in the system of equations (3.149) are determined by the signs of the radicands. For unknown  $h_i$  the relationship  $h_{i+N} = h_i$ , i.e.,  $h_0 = h_N$ ,  $h_{N+1} = h_1$ , is valid.

The system of equations (3.149) should be solved by the method of successive approximations (Newton's method). In the zero

approximation we assume  $h_{i0} = 0.5$  ( $i = 1, 2, \dots, N$ ). Calculation continues until the error for all roots is less than 1%.

Based on the calculated values of  $h_i$ , we calculate the dimensionless radial  $\bar{F}_r$  and tangential  $\bar{F}_t$  components of the force acting on the rotor pivot in a hydrostatic bearing. The radial force is directed along the line of the pivot and bearing centers, while the tangential force is perpendicular to the line of the centers.

The quantities  $\bar{F}_r$  and  $\bar{F}_t$  are determined from formulas:

$$\bar{F}_r = \sin \frac{\pi}{N} \sum_{i=1}^N h_i \cos \varphi_i; \quad \bar{F}_t = \sin \frac{\pi}{N} \sum_{i=1}^N h_i \sin \varphi_i. \quad (3.150)$$

If we introduce the quantity of relative flow rate through the bearing

$$Q_0 = \frac{Q}{\mu_* f_* V_*}, \quad (3.151)$$

its expression in terms of  $h_i$  will be

$$Q_0 = \sum_{i=1}^N \sqrt{1 - h_i}. \quad (3.152)$$

With assigned geometric dimensions for the bearing the values of coefficients with unknowns and equations (3.149) depend only on the relative eccentricity  $\epsilon$ , the relative rotational velocity of the pivot  $V_0$ , the relative forward speed of the pivot  $v_0$  and the angle  $\psi$  which determines the direction of the forward speed of the pivot. Consequently, the values of relative pressures in the chambers  $h_i$  and the values of dimensionless forces  $\bar{F}_r$ ,  $\bar{F}_t$  and flow rate  $Q_0$  will depend only on the indicated parameters  $\epsilon$ ,  $V_0$ ,  $\delta_0$ , and  $\psi$ .

The values of dimensionless forces  $\bar{F}_r$  and  $\bar{F}_t$  with forward pivot velocity  $v = 0$ , which correspond to the stationary values

of forces in the absence of pivot vibrations and depend only on  $\varepsilon$  and  $V_0$ , we designate  $\bar{F}_{r0}$  and  $\bar{F}_{t0}$ :

$$\bar{F}_{r0} = F_r(\varepsilon, V_0, v_0=0); \bar{F}_{t0} = F_t(\varepsilon, V_0, v_0=0).$$

Then the components of the forces in the bearings which arise during the forward displacement of the pivot can be written in the form  $\bar{F}_{r1} = \bar{F}_r - \bar{F}_{r0}$ ;  $\bar{F}_{t1} = \bar{F}_t - \bar{F}_{t0}$ .

The projection of these components onto the direction of the forward velocity of the pivot is designated  $\bar{F}_c$ , while the projection onto the perpendicular direction is  $\bar{F}_{c1}$ :

$$\bar{F}_c = \bar{F}_{t1} \cos \psi - \bar{F}_{r1} \sin \psi; \bar{F}_{c1} = \bar{F}_{t1} \sin \psi + \bar{F}_{r1} \cos \psi.$$

The characteristics are calculated on a computer. The values of  $N$ ,  $D$ ,  $D_0$ ,  $L$ ,  $\mu_m$ ,  $f_m$ ,  $l_m$ ,  $b$ ,  $l$ ,  $\Delta$ ,  $\bar{u}$  and the values of the parameters  $\varepsilon$ ,  $v_0$ ,  $V_0$ , and  $\psi$  are given as the initial data. For each of the parameters a series of values is given, and for all combinations of parameter value the quantities  $\bar{F}_r$  and  $\bar{F}_t$  are computed.

Usually the direction of the projection of force  $\bar{F}_c$  onto the vector of forward pivot velocity  $V$  is opposite to this vector and does not depend upon angle  $\psi$ . The projection of this same force onto the direction perpendicular to the forward pivot velocity  $\bar{F}_{c1}$  is also independent of angle  $\psi$ , but, in magnitude, is less by one order than the component  $\bar{F}_c$  and is commensurate with calculation error. Therefore, the quantity  $\bar{F}_{c1}$  can be disregarded.

The force  $\bar{F}_{r0}$  acting along the center line is directed from the center of the pivot to the center of the bearing, while the force  $\bar{F}_{t0}$  acting perpendicularly to the center line is directed from the center of the pivot in the direction of rotor rotation, as indicated in Fig. 3.85.

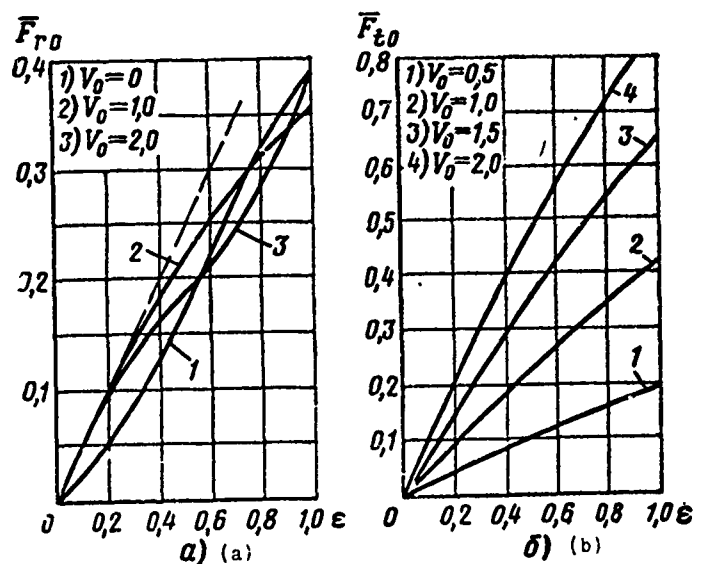


Fig. 3.86. Dependence of dimensionless forces  $\bar{F}_{r0}$ ,  $\bar{F}_{t0}$  on eccentricity  $\epsilon$ .

The third equation of the initial system of equations (3.146) is valid only for the range  $V l_H \delta / 2Q = 0.2-18$ , i.e., cannot be used for the case  $V_0 = 0$ . When  $V_0 = 0$ , instead of the third equation of the system (3.146), the following equation is used:

$$Q_{i,i+1} = \mu_{i,i+1} \cdot f_{i,i+1} \sqrt{p_{i+1} - p_i} \quad (3.153)$$

Then the same solution method is used as in case  $V_0 \neq 0$ .

The typical dependence of dimensionless forces  $\bar{F}_{r0}$ ,  $\bar{F}_{t0}$  on relative eccentricity  $\epsilon$  and relative rotational velocity  $V_0$  is presented in Fig. 3.86. Figure 3.87 illustrates the dependence of dimensionless force  $\bar{F}_c$  on relative forward pivot velocity  $v_0$  and parameters  $\epsilon$ ,  $V_0$ .

These dependences are obtained in analysis of the bearing with the following data:  $N = 8$ ,  $L = 4.7$  cm,  $b = 1.09$  cm,  $\Delta = 1.5 \cdot 10^{-4}$  cm,  $D = 3.785$  cm,  $\mu_{\text{ж}} f_{\text{ж}} = 2.06 \cdot 10^{-2}$  cm<sup>2</sup>,  $l = 0.3$  cm,  $\bar{u} = 0.88$ ,  $D_0 = 3.8$  cm,  $l_H = 4.4$  cm.

To solve the problem of the vibration of a rotor on hydrostatic bearings we need the analytical dependence of forces on displacements and rates of displacements of the rotor pivot relative to the bearing.

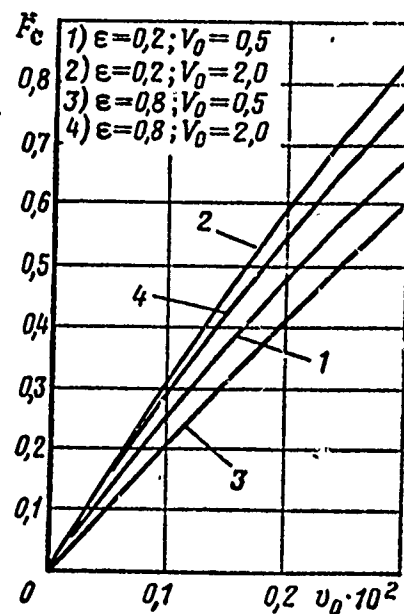
In hydraulic bearings the dependences of dimensionless forces on relative parameter  $\epsilon$ ,  $V_0$  and  $v_0$  are continuous functions and can be approximated sufficiently well by power polynomials.

Thus, function  $\bar{F}_{r0}(\epsilon)$  can be, for a certain range of relative velocity  $V_0$ , approximated by an analytical dependence of the form

$$\bar{F}_{r0} = \alpha_1 \epsilon (1 + \beta_1 \epsilon^2 + \gamma_1 \epsilon^4),$$

where  $\alpha_1$ ,  $\beta_1$ ,  $\gamma_1$  are coefficients which depend on the geometric dimensions of the bearing and the relative rotational velocity  $V_0$ .

Fig. 3.87. Dependence of dimensionless force  $\bar{F}_c$  on pivot velocity  $v_0$ .



For practical analyses  $\bar{F}_{r0}(\epsilon)$  can be expressed by a simpler linear dependence

$$\bar{F}_{r0} = \alpha_1 \epsilon. \quad (3.154)$$

The selection of any form of approximating dependence depends on what kind of problem is being solved. For example, in solving the problem of small vibrations in an unloaded rotor we can limit ourselves to a linear dependence of the form (3.154). If, however, we are examining the effect of forced vibrations on modes of auto-vibration of currents or we are examining vibrations whose amplitudes are commensurate with the value of the radial gap in the bearings, we must take into account the nonlinearity of the characteristics  $\bar{F}_{r0}(\epsilon)$ .

Dependences  $\bar{F}_{t0}$  and  $\bar{F}_c$  can be approximated by the linear relationships:

$$\bar{F}_{t0} = a_2 \epsilon V_0; \bar{F}_c = a_3 v_0. \quad (3.155)$$

A transition from dimensionless quantities  $\bar{F}$ ,  $\epsilon$ ,  $V_0$  and  $v_0$  to dimensioned quantities  $F$ ,  $r$ ,  $\omega$ ,  $\delta$  is effected with the aid of the following relationships:

$$F = \bar{F} \Delta p D L; \quad r = \epsilon \delta_0; \quad \omega = \frac{2V_0}{D} \sqrt{\frac{2}{\epsilon} \Delta p}; \quad v = v_0 \sqrt{\frac{2}{\epsilon} \Delta p}; \\ \Delta p = p_s - p_c.$$

By themselves the dimensioned forces can be written in linear form:  $F_1 = k_1 r$ ;  $F_2 = k_2 \omega r$ ;  $F_3 = k_3 v$ , where subscripts 1, 2, 3 correspond to the former subscripts r, t, c, respectively.

Coefficients  $k_1$ ,  $k_2$ ,  $k_3$  are connected with coefficients  $a_1$ ,  $a_2$ ,  $a_3$  by relationships:

$$k_1 = a_1 \frac{DL}{\delta_0} \Delta p; \quad k_2 = a_2 \frac{D^2 L}{2 \sqrt{2} \delta_0} \sqrt{\epsilon \Delta p}; \quad k_3 = a_3 \frac{DL}{\sqrt{2}} \sqrt{\epsilon \Delta p}.$$

If the projections of displacement  $r$  and forward pivot velocity  $v$  onto the axes of a rectangular system of coordinates are designated  $x$ ,  $y$ , and  $\dot{x}$ ,  $\dot{y}$ , then the projections of forces  $F_1$ ,  $F_2$  and  $F_3$  onto the same axes, with allowance for the directions of the forces, are

$$\left. \begin{aligned} F_{1x} &= -k_1 x; & F_{2x} &= -k_2 \omega y; & F_{3x} &= -k_3 \dot{x}; \\ F_{1y} &= -k_1 y; & F_{2y} &= -k_2 \omega x; & F_{3y} &= -k_3 \dot{y}. \end{aligned} \right\} \quad (3.156)$$

### Vibrations of a symmetric rotor.

Let us study a rotor as a weightless shaft with an unbalanced disk in the center of the span. A diagram of such a rotor and the system of coordinates used are shown in Fig. 3.88.

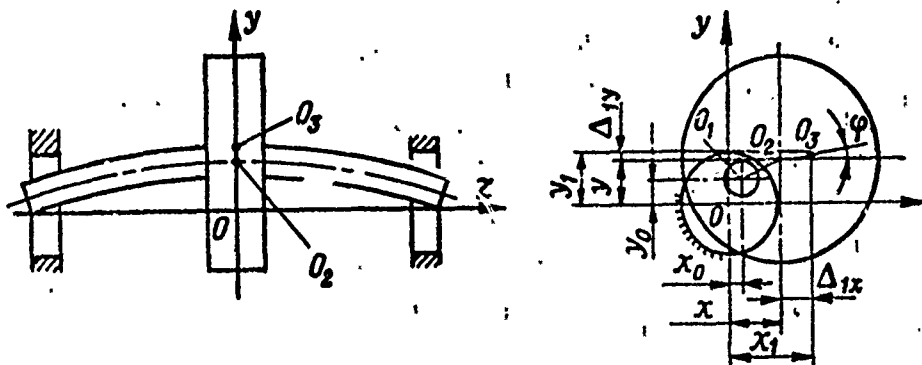


Fig. 3.88. Diagram of a symmetric rotor installed on hydrostatic bearings.

We introduce the following designations:  $O$  is the center of the bearing;  $O_1$  is the center of the rotor pivot;  $O_2$  is the geometric center of the disk;  $O_3$  is the center of mass of the disk;  $m$  is the mass of the disk (kg);  $c$  is the flexural rigidity of the shaft (daN/cm);  $\Delta_1$  is the distance between the geometric center and the center of the mass of the disk (cm);  $x_0$ ,  $y_0$  are the projections of the displacement of the pivot center relative to the bearing center (cm);  $x$ ,  $y$  are the projections of the displacements of the geometric center of the disk relative to the center of the bearing (cm);

$x_1, y_1$  are the projections of the displacements of the center of mass of the disk relative to the center of the bearing (cm);  $\omega$  is the angular velocity of shaft rotation (1/s).

Coordinates  $x, y$ , and  $x_1$  and  $y_1$  are connected by relationships:

$$x_1 = x + \Delta_1 \cos(\omega t + \varphi_0); \quad y_1 = y + \Delta_1 \sin(\omega t + \varphi_0). \quad (3.157)$$

Equations of motion for the studied rotor can be obtained if in accordance with d'Alembert's principle, we equate the disk's forces of inertia to the shaft's forces of elasticity and the shaft's forces of elasticity are equated to the forces in the hydrostatic bearings. Finally we obtain the system of equations

$$\left. \begin{aligned} m\ddot{x}_1 + c(x - x_0) &= 0; \\ m\ddot{y}_1 + c(y - y_0) &= 0; \\ c(x - x_0) &= 2k_1 x_0 + 2k_2 \omega y_0 + 2k_3 \dot{x}_0; \\ c(y - y_0) &= 2k_1 y_0 - 2k_2 \omega x_0 + 2k_3 \dot{y}_0. \end{aligned} \right\} \quad (3.158)$$

Let us introduce further designations:

$$\begin{aligned} \frac{2k_1}{m} &= \omega_1^2; \quad \frac{c}{m} = \omega_2^2; \quad \omega_0^2 = \frac{\omega_1^2 \omega_2^2}{\omega_1^2 + \omega_2^2}; \\ \frac{2k_3}{m} &= n, \quad \frac{2k_2}{m} = n_1, \quad r = x + iy; \quad i = \sqrt{-1}. \end{aligned} \quad (3.159)$$

Taking into account these designations and expressions (3.157) system (3.158) can be reduced to a nonhomogeneous equation

$$\begin{aligned} \frac{\omega_1^2 + \omega_2^2}{\omega_2^2} \ddot{r}_0 + i\omega \frac{n_1}{\omega_2^2} \ddot{r}_0 + \frac{n}{\omega_2^2} \ddot{r}_0 + \omega_1^2 r_0 - i\omega n_1 \dot{r}_0 + \\ + n \dot{r}_0 = \Delta_1 \omega^2 e^{i(\omega t + \varphi_0)}. \end{aligned} \quad (3.160)$$



The general solution to (3.160) consists of a particular solution to the nonhomogeneous equation and a general solution to the corresponding homogeneous equation. The particular solution of the nonhomogeneous equation describing forced vibrations is

$$r_0 = A_0 e^{i(\omega t + \varphi_0 + \varphi_1)}. \quad (3.161)$$

If we substitute (3.161) into (3.160), we obtain

$$\left. \begin{aligned} A_0 &= \frac{\Delta_1}{\sqrt{\left(\frac{\omega_1}{\omega}\right)^4 \left(1 - \frac{\omega^2}{\omega_0^2}\right)^2 + \left(\frac{n - n_1}{\omega}\right)^2 \left(1 - \frac{\omega^2}{\omega_2^2}\right)}}; \\ \operatorname{tg} \varphi_1 &= \frac{\omega(n - n_1) \left(1 - \frac{\omega^2}{\omega_2^2}\right)}{\omega_1^2 \left(1 - \frac{\omega^2}{\omega_0^2}\right)}. \end{aligned} \right\} \quad (3.162)$$

The general solution to the homogeneous equation corresponding to equation (3.160) is

$$r = a_0 e^{st}. \quad (3.163)$$

If we substitute (3.163) into equation (3.160), we obtain the characteristic equation

$$s^2(\omega_1^2 + \omega_2^2) - \omega_1^2 \omega_2^2 + i[s^3 n - s^2 \omega n_1 - s \omega_2^2 n + \omega \omega_2^2 n_1] = 0. \quad (3.164)$$

The quantity  $s$  is, in the general case, a complex quantity:  
 $s = v + i\eta$ .

If among the roots of the characteristic equation (3.164) there is even one root with a negative imaginary part, the system described by equation (3.160) will be dynamically unstable, i.e., vibrations with increasing amplitude will occur in it.

The question of system stability can be solved using the Routh-Hurwitz criterion. For system stability it is necessary and sufficient that a matrix made up of the coefficients of the frequency equation and the even-order diagonal minors of this matrix be positive. The Routh-Hurwitz matrix, in this case, has the form

$$\begin{vmatrix} n & -\omega n_1 & -\omega_2^2 n & \omega n_1 \omega_2^2 & 0 & 0 \\ 0 & \omega_1^2 + \omega_2^2 & 0 & -\omega_1^2 \omega_2^2 & 0 & 0 \\ 0 & n & -\omega n_1 & \omega_2^2 n & \omega n_1 \omega_2^2 & 0 \\ 0 & 0 & \omega_1^2 + \omega_2^2 & 0 & -\omega_1^2 \omega_2^2 & 0 \\ 0 & 0 & n & -\omega n_1 & -\omega^2 n & \omega n_1 \omega_2^2 \\ 0 & 0 & 0 & \omega_1^2 + \omega_2^2 & 0 & -\omega_1^2 \omega_2^2 \end{vmatrix} = \nabla$$

For system stability the following conditions are necessary and sufficient:

$$\begin{aligned} n(\omega_1^2 + \omega_2^2) &> 0; \quad n^2 \omega_2^4 (\omega_1^2 + \omega_2^2) > 0; \\ -\omega^2 n_1^2 \omega_2^8 (\omega_1^2 + \omega_2^2) + n^2 \omega_2^{10} \omega_1^2 &> 0, \end{aligned}$$

then the system is stable when

$$n > 0, \quad \omega < \frac{n}{n_1} \omega_0. \quad (3.165)$$

For the self-excitation rate  $\omega_c^* = (n)/(n_1)\omega_0$ , in all roots  $s$  of the characteristic equation  $\eta > 0$ , the vibrations described by expression (3.163) will be attenuating and only forced vibrations will exist in the system. When  $\omega > \omega_c^*$  in the system, along with forced vibrations there will also be autovibrations described by expression (3.163).

The quantity  $s$  on the boundary of the autovibrations can be found from equation (3.164) with allowance for the fact that on the boundary  $\omega n_1 = \omega_0 n$ :

$$S = v = \omega_0. \quad (3.166)$$

Thus, near the boundary of stability the general solution to equation (3.160) has the form

$$r_0 = A_0 e^{i(\omega t + \tau_0 + \tau_1)} + a_1(t) e^{i\omega_0 t},$$

where

$$a_1(t) = a_0 e^{-\gamma t},$$

when  $\omega > \omega_c^*$  function  $a(t)$  will be increasing and when  $\omega < \omega_c^*$  decreasing.

From the cited expressions it follows that in the rotor studied on hydrostatic bearings it is possible for self-exciting vibrations to arise. Near the boundary of autovibrations the autovibration frequency is equal to the natural frequency of vibrations corresponding to the conservative system

$$\gamma^2 = \omega_0^2 = \frac{\omega_1^2 \omega_2^2}{\omega_1^2 + \omega_2^2},$$

which is defined as both rigidity of the rotor  $c$  and the rigidity of the bearings  $k_1$ . The rotational velocity of the rotor at which autovibrations arise is proportional to the natural frequency of rotor vibrations:

$$\omega_c^* = \frac{n}{n_1} \omega_0.$$

Autovibrations occur in modes in which the work of nonconservative force  $F_2$  becomes greater than the work of the force of resistance

$F_3$ . The value of the work of nonconservative forces in the system when  $\omega > \omega_c^*$  is positive, and this means that work is supplied to the system. This work is expended on increasing the amplitude of vibrations.

Since positive work is performed only by hydrodynamic force  $F_2$  which depends on the angular velocity of the rotor, the energy of rotation, i.e., the power of the drive, is spent on vibration.

From this analysis we can obtain a few more results if we examine the effect of the pressure drop on the characteristics of the bearing.

Earlier it was shown that coefficient  $k_1$  is proportional to the pressure drop in the bearing  $\Delta p$ , while coefficients  $k_2$  and  $k_3$  are proportional to

$$\omega_1 = \omega_{1x} \sqrt{\Delta p}; \quad n = n_x \sqrt{\Delta p}; \quad n_1 = n_{1x} \sqrt{\Delta p},$$

where  $\omega_{1x}$ ,  $n_x$ ,  $n_{1x}$  are the corresponding quantities during pressure drop  $\Delta p = 1.0 \text{ daN/cm}^2$ .

Then the natural frequency of rotor vibration depends on the pressure drop in the bearings:

$$\omega_0^2 = \frac{\omega_2^2 \cdot \omega_{1x}^2 \Delta p}{\omega_2^2 + \omega_{1x}^2 \Delta p}.$$

When  $\Delta p \rightarrow 0$   $\omega_0 \rightarrow 0$ , while when  $\Delta p \rightarrow \infty$   $\omega_0 \rightarrow \omega_2$ .

For rotors of pumps and turbogenerators in an extraterrestrial engine with high rigidity and a high frequency of natural vibrations on the rigid supports, in order to reduce the expenditure of power on the vibration of the working medium through the bearing, we attempt to reduce the pressure drop in the bearings, i.e., in order that

$$\omega_2^2 \gg \omega_{1x}^2 \Delta p, \quad \text{or} \quad \frac{\omega_{1x}^2 \Delta p}{\omega_2^2} \ll 1.$$

In this case,

$$\omega_0^2 = \frac{\omega_{1x}^2 \Delta p}{\frac{\omega_{1x}^2 \Delta p}{\omega_2^2} + 1} \approx \omega_{1x}^2 \Delta p; \quad \omega_0 = \omega_{1x} \sqrt{\Delta p}.$$

If the rigidity of the rotor is greater by one order than the rigidity of the bearing ( $k_1 = 0.1c$ ), the rotor can be considered absolutely rigid. Error in determining the natural angular frequency, in this case, does not exceed 5% and we can assume that the natural frequency of vibrations is proportional to  $\sqrt{\Delta p}$ . Since the ratio  $\omega_c/\omega_0 = n/n_1 = n_x/n_{1x}$  does not depend on pressure drop in the bearing, the revolutions of autovibration appearance are also proportional to  $\sqrt{\Delta p}$ :

$$\omega_c^* = \frac{n_x}{n_{1x}} \omega_{1x} \sqrt{\Delta p}.$$

In hydrostatic bearings the role of the damping coefficient is played by expression  $n - n_1 = (n_x - n_{1x})\sqrt{\Delta p}$ , i.e., with forced vibrations the value of damping in hydrostatic bearings is proportional to  $\sqrt{\Delta p}$ .

For a rigid rotor the formulas for amplitude and phase of forced vibrations (3.164) assume the form

$$A_0 = \frac{\Delta_1}{\sqrt{\left(\frac{\omega_{1x}^2 \Delta p}{\omega^2}\right)^2 \left(1 - \frac{\omega^2}{\omega_{1x}^2 \Delta p}\right)^2 + \left(\frac{n_x - n_{1x}}{\omega}\right)^2 \Delta p}},$$

$$\operatorname{tg} \varphi_1 = \frac{\omega (n_x - n_{1x}) \sqrt{\Delta p}}{\omega_{1x}^2 \Delta p \left(1 - \frac{\omega^2}{\omega_{1x}^2 \Delta p}\right)}.$$

In the mode  $\omega^2 = \omega_{1x}^2 \Delta p$  we have

$$A_0 = \frac{\Delta_1 \omega_{1x}}{n_x - n_{1x}}; \quad \varphi_1 = \frac{\pi}{2},$$

i.e., in a rigid rotor on hydrostatic bearings in the mode  $\omega = \omega_{1x} \sqrt{\Delta p}$ , the amplitude of forced vibrations does not depend on pressure drop in the bearings. With a change in the pressure drop in the bearings the resonance frequency of the rotor also changes.

### 3.2. THERMOEMISSION ENERGY CONVERTER

Converters in which the electrical current is obtained as a result of the emission of electrons from a heated cathode to an anode are called thermoemission converters. If the gap between the anode and the cathode is a pure vacuum and does not contain vapors of any element, such converters are called thermoelectronic.

A thermoemission converter is formed with a hot cathode and a cold anode arranged opposite each other with a small gap. With an increase in cathode temperature the kinetic energy of the electrons also increases. They overcome the forces of attraction of the atomic nuclei, escape from the surface, and form an electron cloud around the cathode. This process is called thermoemission.

After flying through interelectron gap and hitting the cold anode, the electrons create negative potential on it, while the cathode is charged positively. By closing the circuit electric current is obtained.

If the gap between electrodes is filled with vapors, for example, cesium vapors, such a converter is called a thermionic converter.

These converters have the following advantages.

Comparatively high efficiency. In present developments it is determined on a level of  $\eta = 10-15\%$  and in the future can reach higher value (this efficiency is half that found in a turbogenerator).

Systems with thermionic converters are appreciably simpler than mechanical converters. They are simpler in design and lighter, since they do not contain rotating elements, turbines, or complex devices.

---

<sup>1</sup>Since thermionic converters are used widely, they are frequently called simply emission converters.

However, the use of thermionic converters still involves many difficulties including the following.

Certain problems of the operating process of converters have been poorly studied.

Cathodes of the converters operate at temperatures above  $1400^{\circ}\text{C}$  in contact with cesium vapor whose corrosiveness is well known. Under these conditions, to select material which will operate for a long period of time is difficult.

The anodes of converters must have an insulation which, on the one hand, will not break at high temperatures and, on the other hand, has high heat conductivity for cooling the anode. Such insulating material is difficult to find.

A converter is more effective the less the gap between the anode and the cathode. The gap is 0.01 mm and reaches 0.5 mm or more.

With such a comparatively small gap thermal strains in the converter are commensurate with the gap, which fact complicates design.

And, finally, in the manufacture of thermionic converters many unresolved technological problems arise which determine the functionality of the design (for example, to solder or weld multilayer construction of different types of materials).

All thermionic converters can be broken down into three large groups based on design:

- converters combined with reactor fuel element;
- converters combined with a radiator;
- converters combined with a heat exchanger.



## STRUCTURAL DIAGRAMS AND DESIGN OF CONVERTERS

### A thermionic converter combined with a reactor fuel element

Figure 3.89 shows the design of such a converter. The fuel element combined with this converter is called the electrogenerating element. As is seen from the figure, this element consists of elements of the fuel element itself and elements of the converter.

The fuel element consists of the fuel pellets (for example, UC) 1, the fuel shell 2, the neutron moderator 3, placed into a pressurized cavity of two shells 4 and 5 and a reflector 6. The radial reflector is not shown here but is made as an ordinary reflector of the reactor. Between the fuel shell and the reflector is the converter which consists of cathode 7 and its insulation 8, anode 9 and its insulation 10.

The heat flow from the substance being divided heats the cathode to 1300-2000°C. The gaseous fission products of the fuel during reactor operation are carried through the openings in the pellets 1, the shell 2, and the commutation busbar 11 through the nozzle 12 to the outside. The liquid metal (sodium, lithium) washing the shell 4 of the fuel element maintains the temperature of the anode within 600-800°C.

The anode and cathode, connected in series, have openings for the passage of cesium vapors, which ensures the neutralization of the space charge. Waste cesium through the opening in the reflectors 6 and the discharging jet 13 is carried from the housing.

Current from the extreme anode, by the commutation busbar 14 and rod 11; enters the commutation plate 15 installed in the reactor tank on insulator 16.

The anode can be made from stainless steel, niobium; the cathode from molybdenum, niobium; the commutation elements from beryllium

copper; the retarder from metal hydride; the reflector from beryllium oxide.

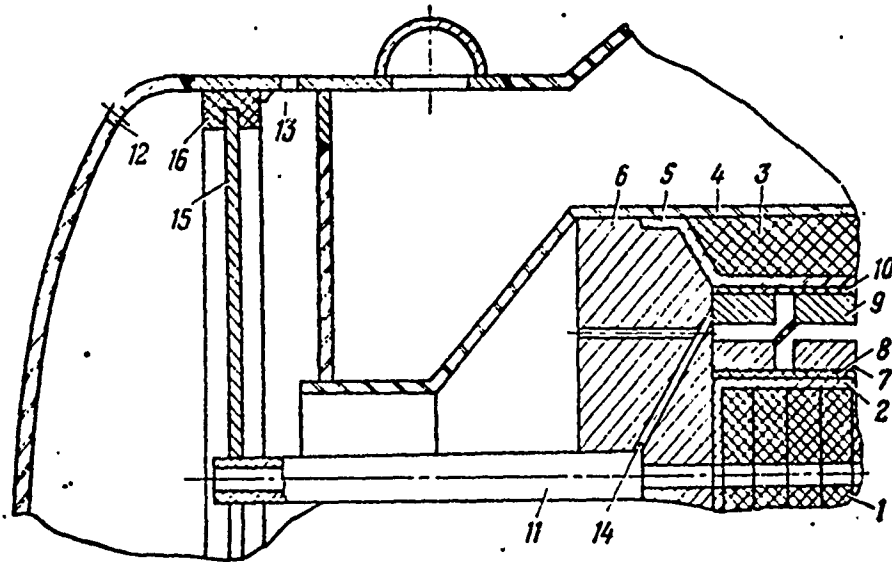


Fig. 3.89. Diagram of a thermionic converter combined with a reactor fuel element.

The combination of a thermionic converter with a reactor fuel element has irrefutable advantages. Among them is the very lightweight construction. The transmission of heat to the thermionic cathode is accomplished by the shortest path, which allows us to use a low-temperature anode and moderator during high cathode temperature.

The design allows the use of reactors of different types - high-speed and thermal. The development of a system with a large range of power is possible.

The design also has shortcomings: the reactor fuel element and the converter are a permanent all-welded structure, organically involved in the total structure of the reactor. This complicates its finishing and testing.

In the creation of the design serious technological difficulties appear because it is necessary to connect a large number of heterogeneous materials, on which high strength and tight-seal requirements are imposed.

For instance, the anode package is a complex structural element. In it the shells which cover the substitute, the layer of insulation, and the anode itself have been assembled and should operate jointly. If we heat these shells to the same temperature, then the shells made, for example, from stainless steel will so expand that the layer of insulation, for example, beryllium oxide which has a coefficient of linear expansion half as low, will be extended. And since beryllium oxide has low tensile strength, it can crack and the entire unit go out of operation. In order to overcome this disadvantage, contraction stresses should be created in the beryllium oxide before installation of the anode package in the reactor.

#### A thermionic converter combined with a radiator

Figure 3.90 shows a diagram of a thermionic converter combined with a radiator. The converter consists of the cathode 1 installed by means of a layer of beryllium oxide 2 on the external wall 3 of the heat trap of the solar concentrator. For uniform heating of all anodes the converter of wall 3 is heated by liquid metal 4, for example, aluminum, sodium. Anode 5-6, which is also the radiator, is installed by the central part 6 on three spherical insulators 7 of aluminum oxide ( $\text{Al}_2\text{O}_3$ ). These insulators ensure the proper clearance between anode and cathode.

The anode has been split in order to guarantee the soldering of the corrugated membrane 8 to the insulator 9 which serves simultaneously as the bracing spot of the cathode to the housing of the heat trap.

The membrane 8 insulates the discharge gap from outer space. The gap is filled with cesium vapor which enters during cathode

warm-up from the accumulator 10. The accumulator is porous metal, for example, nickel impregnated with liquid cesium and placed in a sealed ampoule welded to the anode. This ensures the precise metering of cesium in the gap and convenient installation.

The anode is braced to the housing of the heat trap by means of an elastic element 11, which is a thin-wall sealed box filled with argon.

The anode is made from molybdenum, the cathode from tungsten, the shell of the heat trap from molybdenum, the others from stainless steel, the insulators from aluminum and beryllium oxide.

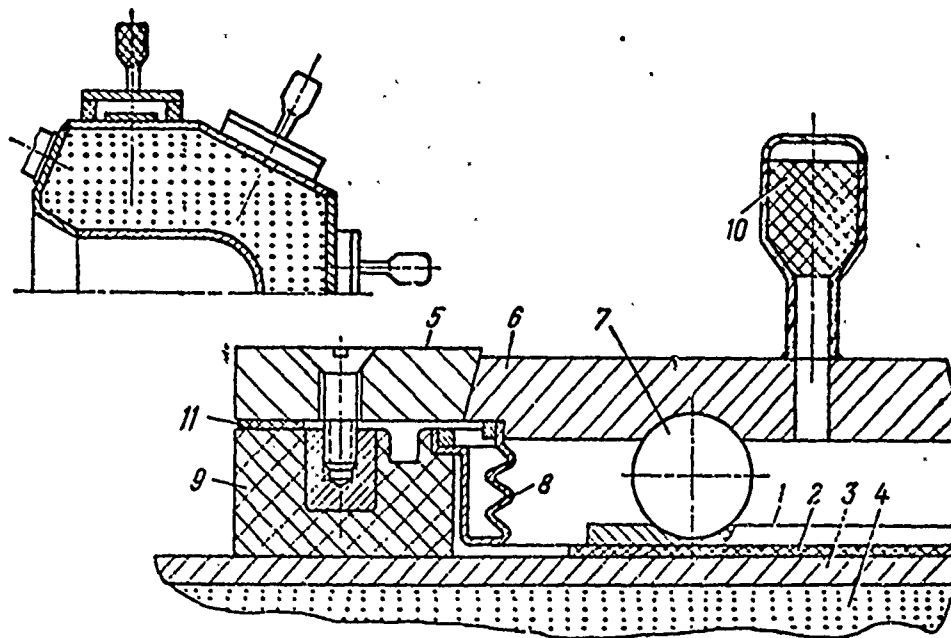


Fig. 3.90. Diagram of a thermionic converter combined with a radiator.

Such a thermionic converter design has certain advantages. It is simple; it allows the finishing of the converter itself independent of the energy source.

The shortcoming in this design is the impossibility of obtaining the optimum dimensions of the converter. The dimensions of the anode and the radiating surface are close. It is known that the maximum power which can be taken from the radiating surface at anode temperatures does not exceed  $3 \text{ W/cm}^2$ . Thus, the radiating capacity of the anode surface will limit the structural parameters.

The use of a nuclear reactor in the form of a power source in this diagram leads to the necessity for increasing the temperature of the liquid metal with identical converter parameters in order to compensate the heat dissipation during the flow of the working medium along the pipes. An increase in the temperature of the liquid metal in the reactor is undesirable since this complicates the design of the most important unit - the power plant of the engine.

A thermionic converter combined with a heat exchanger

Such a converter consists of a housing (Fig. 3.91), two tube boards, and a set of electrogenerating elements.

These elements consist of an internal hot shell 1, insulator 2, cathode 3, anode 4, insulator 5, and outer cylindrical shell 6.

The electrogenerating element is attached to a two-layer pipe board 7, 8; in the gap between the layers cesium vapors pass.

The heating of the converter is accomplished by lithium which, flowing along the internal cavity of the shell 1, releases heat to the converter cathode. The anode can be cooled by sodium which enters two collectors 9 of the heat exchanger housing. Since niobium and stainless steel weld badly, an intermediate ring 10 is provided in the design. The electrical current from all cathodes is collected on the commutation plate 11.

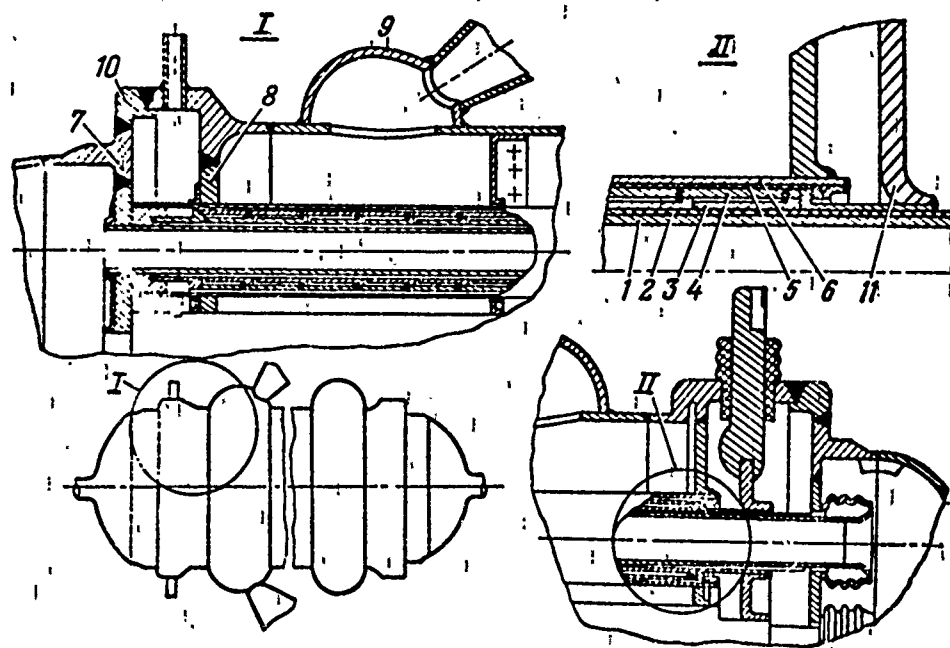


Fig. 3.91. Diagram of a thermionic generator combined with a heat exchanger.

Advantages of this design lie in the ease of finishing and operation. Optimum dimensions of the converter can be selected both for the anode and cathode, because the radiator does not determine the amount of heat released; the heat capacity of the reactor is not connected with the overall size of the anode unit.

The shortcomings are the increased thermal mode of the reactor and the large mass of the entire structure as compared with the earlier examined diagram.

One of the installations described [41], with a power of 27 kW, has cathodes from thoriated tungsten and anodes of tungsten. The neutralization of the space charge is accomplished by introducing cesium plasma into the clearances. The diameter of the fuel element of uranium carbide is  $d = 2.5$  mm. The combined area of the electrodes is  $S = 2000$  cm<sup>2</sup>. Cathode temperature  $t_k = 1727^\circ\text{C}$  and anode temperature  $t_a = 727^\circ\text{C}$ . The value of specific power  $W = 10$  W/cm<sup>2</sup> and installation efficiency  $\eta = 9.7\%$ , mass  $G = 640$  kg.

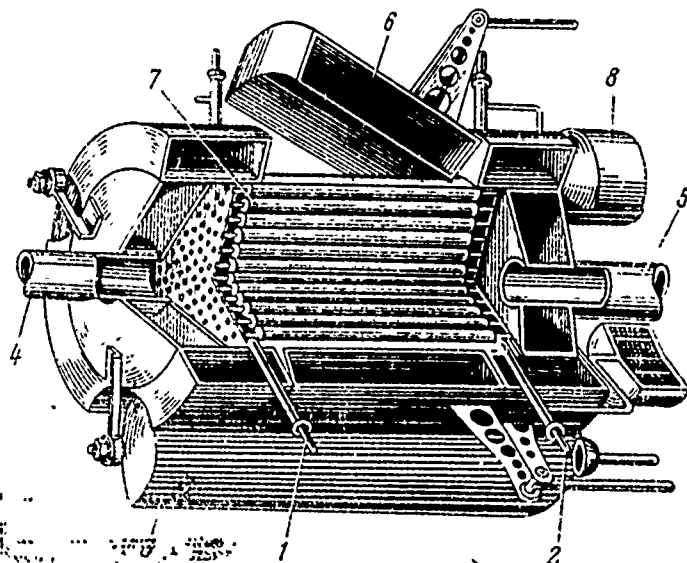


Fig. 3.92. Overall view of reactor-generator: 1, 2 - current leads; 3 - regulating rods; 4, 5 - metal input and output fittings; 6 - emergency rod; 7 - fuel elements; 8 - cesium tank.

Another installation has a power of  $N = 300$  kW. The size of the active zone is  $D \times l = 32 \times 28$  cm. The number of fuel elements is 546, reactor mass is 264 kg. The overall efficiency of the installation is 12%; the efficiency of the thermoemission elements is 14%. Specific power  $W = 11-12$  W/cm<sup>2</sup> with a current density  $i = 8$  A/cm<sup>2</sup>. Cathode temperature  $t_k = 1815^\circ\text{C}$  and cathode material is UC-ZrC. Anode temperature  $t_a = 982-1094^\circ\text{C}$ ; specific mass  $\gamma = 1.91$  kg/kw. The overall view of the installation is shown in Fig. 3.92.

There is information on a thermoemission installation where the motive power is a radioisotope of curium  $\text{Cm}^{242}$  with a half life of 162 days and a heat-liberation value of  $q = 15$  W/g. This installation with a power of  $N = 100$  W has a cathode area of

$S = 80 \text{ cm}^2$ ; cathode temperature  $t_K = 927^\circ\text{C}$  and anode temperature  $t_a = 427^\circ\text{C}$ . The mass is  $G = 10 \text{ kg}$  and operating life one year.

There has been described in literature [41] an installation with a power of 40 kW and pore dimensions of  $D \times L = 49.5 \times 120 \text{ cm}$  without a heat carrier.

The heat passes to the cathode through the walls and from the anode is released into space by radiation. Temperatures  $t_K = 2027^\circ\text{C}$ ,  $t_a = 1427^\circ\text{C}$ ,  $t_{\text{излучат}} = 1227^\circ\text{C}$  [излучат = radiation]. Voltage is  $V = 24\text{--}28 \text{ V}$ .

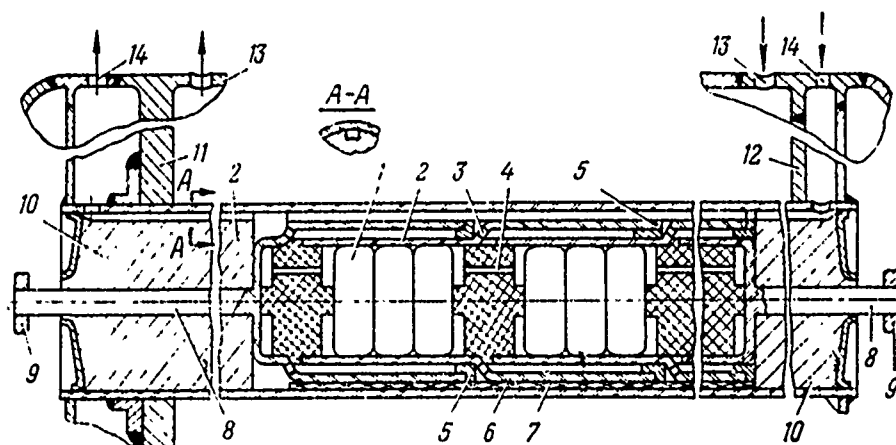


Fig. 3.93. Structural diagram of an electrogenerating element.

The thermoemission converter combined with a heat trap, whose structural diagram is shown in Fig. 3.90, has the following basic parameters: cathode diameter  $d = 3.8 \text{ cm}$  radiator  $10.2 \text{ cm}^2$ ,  $t_K = 1827^\circ\text{C}$ , power of one element  $N = 85 \text{ W}$ , current  $I = 64 \text{ A}$  when  $V = 1.3 \text{ V}$ ; efficiency  $\eta = 15\%$ , specific mass  $\gamma = 3.4 \text{ kg/kw}$ . The interelectron gap is  $0.13 \text{ mm}$  and the anode is nickel. Specific power of the element is  $W = 8 \text{ V/cm}^2$ .



Figure 3.93 is a diagram of an electric generating element of a reactor [52]. The fuel pellets 1 of uranium carbide UC have been set into the cathode shell of converter 2, made as one with the tungsten anode. Thermal separation of the cathode and the anode is provided by a large number of openings 3, which also serve to feed cesium vapor into the gaps of the converter. Alignment of converters is accomplished by washers 4 and rings 5 of aluminum oxide  $Al_2O_3$ . These elements are good thermal and electrical insulators.

Anodes are installed in cylindrical shell 6 on insulators 7 of BeO. Commutation current is ensured by rod 8 and plate 9 of bronze. The material of the end reflectors 10 is beryllium oxide BeO. The electric generating element is fastened to load-bearing plate 11 by welding; diaphragm 12 serves as the support of the end of the element; sodium is fed and bled through openings 13, cesium through openings 14. Cross section A-A shows the channel in the end reflector for the passage of cesium vapor.

Figure 3.94 is another diagram for an electric generating element of a reactor.

The fuel pellets 1 are installed in the shell of cathode 3 which is made as one with anode 5. The shell of the cathode rests with one end on insulating disk 4. Anodes 5, by means of insulator 6, are placed in pipes 7 and 9, which limit the moderator 8. End reflector 2 is also placed along the edges in pipe 9.

One end of the electric generator is attached to load-bearing plates 11 by welding, the other rests on diaphragm 14. The current is switched by rods 10 and plates 12 insulated from the reactor by disks 13.

#### Stress analysis of converter parts

Many converter parts are similar to reactor parts; therefore, they should be studied according to the methodology presented in

Chapter II. A new element is the anode unit which experiences thermal stresses.

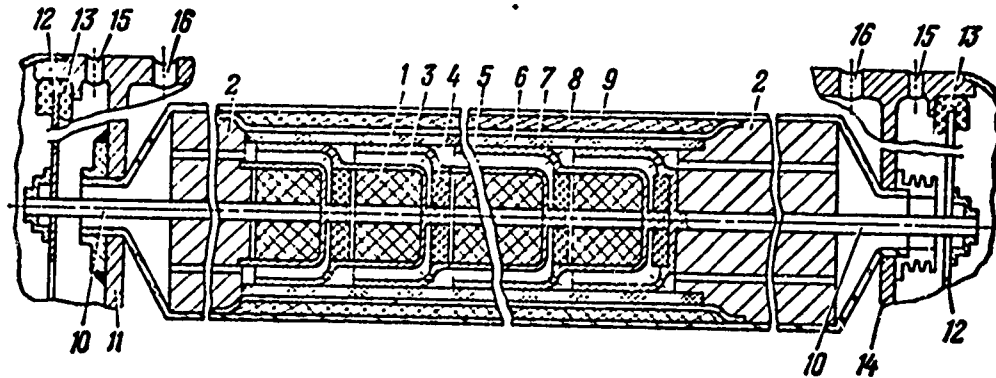


Fig. 3.94. Structural diagram of an electric generating element: 1 - fuel; 2 - end reflector; 3 - cathode-anode; 4 - insulating disk; 5 - molybdenum disk; 6 - insulating layers; 7-9 - steel shells; 8 - moderator; 10, 12 - switching rod and plate; 11 - support plate of reactor; 13 - insulator; 14 - support plate of reactor; 15 - cesium input and output; 16 - lithium input and output.

#### Analysis of thermal stresses in the anode package

The anode package is a multilayer cylindrical shell which experiences thermal stresses during warmup and operation.

Let us analyze the thermal stresses of a three-layer shell shown in Fig. 3.95a. The initial data are given: geometric dimensions, material, temperature gradient throughout the thickness of the package. We should find the stresses  $\sigma_{\phi 1}$ ,  $\sigma_{\phi 2}$ ,  $\sigma_{\phi 3}$ . Our analysis is based on the assumption that the shells are tightly soldered to each other. We shall disregard stresses arising in the axial direction, i.e.,  $\sigma_{x1} = 0$ . This assumption is permissible in the first rough calculation which we shall study. Also we shall disregard the differences in the shell radii, assuming  $R_1 = R_2 = R_3 = R$ .

We shall set up one of the shell sections arbitrarily (Fig. 3.95b) and examine strain in the package relative to this section. Obviously common deformation of the rings can be simply represented, as shown in Fig. 3.95b. From the figure it is apparent that thermal stress of the package leads to an increase in radius  $R$ . On the other hand, common deformation leads to the appearance of different reactive forces  $P$  of the layers (Fig. 3.95c). It is known that with thermal strain the full strain is

$$\varepsilon_{\varphi n} = \varepsilon_{\varphi y} + \varepsilon_t,$$

where  $\varepsilon_t = \alpha \Delta t$ ;  $\Delta t = t_1 - t_0$ .

Since  $\varepsilon_{\varphi y} = \sigma_{\varphi} / E$ , then

$$\left. \begin{aligned} \varepsilon_{\varphi n1} &= \frac{\sigma_{\varphi1}}{E_1} + \alpha_1 \Delta t_1; \\ \varepsilon_{\varphi n2} &= \frac{\sigma_{\varphi2}}{E_2} + \alpha_2 \Delta t_2; \\ \varepsilon_{\varphi n3} &= \frac{\sigma_{\varphi3}}{E_3} + \alpha_3 \Delta t_3. \end{aligned} \right\} \quad (3.167)$$

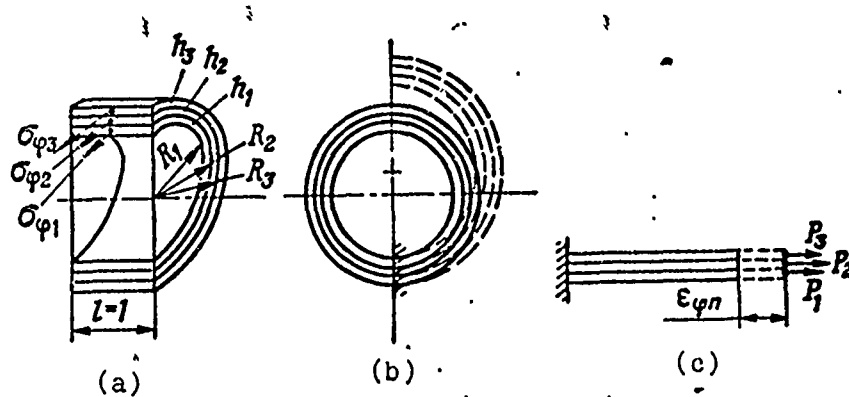


Fig. 3.95. Calculation of the anode package.

Conditions of strain compatibility in the circular direction are

$$\left. \begin{aligned} \varepsilon_{\varphi n1} &= \varepsilon_{\varphi n2} = \varepsilon_{\varphi n3} = \varepsilon_{\varphi n k}; \\ \sum_{k=1}^l P_l &= 0, \end{aligned} \right\}$$

(3.168)

or  $\sum_{k=1}^l \varepsilon_{\varphi k} h_k = 0$ , if we assume that

$$\sigma_{\varphi l} = \frac{P_l}{h_l l},$$

where  $k$  is any  $k$ -th layer (number of layers  $l$ ;  $1 \leq k \leq l$ ). Obviously, these two conditions make it possible to solve the problem posed.

If we substitute the equation (3.167) into (3.168), we obtain

$$\left. \begin{aligned} \frac{\sigma_{\varphi 1}}{E_1} + \alpha_1 \Delta t_1 &= \frac{\sigma_{\varphi 2}}{E_2} + \alpha_2 \Delta t_2; \\ \frac{\sigma_{\varphi 1}}{E_1} + \alpha_1 \Delta t_1 &= \frac{\sigma_{\varphi 3}}{E_3} + \alpha_3 \Delta t_3; \\ \sigma_{\varphi 1} h_1 + \sigma_{\varphi 2} h_2 + \sigma_{\varphi 3} h_3 &= 0. \end{aligned} \right\} \quad (3.169)$$

Let us represent this system in the form

$$\left. \begin{aligned} E_2 \varepsilon_{\varphi 1} - E_1 \varepsilon_{\varphi 2} &= E_1 E_2 (\alpha_2 \Delta t_2 - \alpha_1 \Delta t_1); \\ E_3 \varepsilon_{\varphi 1} - E_1 \varepsilon_{\varphi 3} &= E_1 E_3 (\alpha_3 \Delta t_3 - \alpha_1 \Delta t_1); \\ \sigma_{\varphi 1} h_1 + \sigma_{\varphi 2} h_2 + \sigma_{\varphi 3} h_3 &= 0. \end{aligned} \right\} \quad (3.170)$$

If we solve the system relative to the unknown stresses  $\sigma_{\varphi 1}$ ,  $\sigma_{\varphi 2}$ ,  $\sigma_{\varphi 3}$ , we obtain

$$\sigma_{\varphi 1} = \frac{\Delta_1}{\Delta}; \quad \sigma_{\varphi 2} = \frac{\Delta_2}{\Delta}; \quad \sigma_{\varphi 3} = \frac{\Delta_3}{\Delta},$$

where

$$\Delta = \begin{vmatrix} E_2 & -E_1 & 0 \\ E_3 & 0 & -E_1 \\ h_1 & h_2 & h_3 \end{vmatrix} = E_1(E_1h_1 + E_2h_2 + E_3h_3);$$

$$\Delta_1 = E_1^2[E_2h_2(a_2\Delta t_2 - a_1\Delta t_1) + E_3h_3(a_3\Delta t_3 - a_1\Delta t_1)];$$

$$\Delta_2 = E_1E_2[E_1h_1(a_1\Delta t_1 - a_2\Delta t_2) + E_3h_3(a_3\Delta t_3 - a_2\Delta t_2)];$$

$$\Delta_3 = E_1E_3[E_1h_1(a_1\Delta t_1 - a_3\Delta t_3) + E_2h_2(a_2\Delta t_2 - a_3\Delta t_3)].$$

Hence

$$\sigma_{\varphi 1} = E_1 \frac{E_2h_2(a_2\Delta t_2 - a_1\Delta t_1) + E_3h_3(a_3\Delta t_3 - a_1\Delta t_1)}{E_1h_1 + E_2h_2 + E_3h_3};$$

$$\sigma_{\varphi 2} = E_2 \frac{E_1h_1(a_1\Delta t_1 - a_2\Delta t_2) + E_3h_3(a_3\Delta t_3 - a_2\Delta t_2)}{E_1h_1 + E_2h_2 + E_3h_3};$$

$$\sigma_{\varphi 3} = E_3 \frac{E_1h_1(a_1\Delta t_1 - a_3\Delta t_3) + E_2h_2(a_2\Delta t_2 - a_3\Delta t_3)}{E_1h_1 + E_2h_2 + E_3h_3}.$$

The stress in the k-th layer of an i-layer shell is

$$\sigma_{\varphi k} = E_k \frac{\sum_{i=1}^i E_i h_i (a_i \Delta t_i - a_k \Delta t_k)}{\sum_{i=1}^i E_i h_i}, \quad (3.171)$$

where the subscripts k, i are the numbers 1, 2, ..., k, ..., i, which is the solution to the problem.

The first evaluation of shell strength can be the general formula for the safety factor

$$n = \frac{\sigma_{n,\tau}^f}{\sigma_{\varphi \max}},$$

where  $n \geq 1.1$ .

### 3.3. THERMOELECTRIC AND PHOTOELECTRIC CONVERTERS

The operation of a thermoelectric converter is based on the thermoelectric effect. If in a closed circuit, for example, of two different semiconductors, we heat one junction and cool the other, a potential difference arises between them.

Thermoelectric converters have a number of advantages. They are comparatively simple in design since they do not contain rotating unbalanced parts, as, for example, mechanical converters, and the operating process is performed at low temperature, which simplifies their use.

Disadvantages are as follows.

Low efficiency. In present power plants it is 2-4%. This is very low efficiency for power plants used in an extraterrestrial engine.

All semiconductor materials of the converters sublime in outer space; therefore, they must be protected.

They have high specific weight, regardless of the capacity of the power plant.

Since the mass of the power plant is proportional to its power, these converters are used for generators of low and medium powers (up to 5 kW).

We present a table of the main semiconductors used in extraterrestrial electric rocket engines (Table 3.4) [41], [46].

As is apparent from the table, the germanium-silicon element operates at comparatively high temperatures of the cold and hot junction, is the most stable of all others in vacuum, but has the

worst efficiency. In the table the products of the quality factor  $z$  times the temperature of the hot junction ( $t_r$  °C), which characterize the efficiency of the element, are presented.

Table 3.4.

(2) Наименование полупроводника	(3) Формула	(1) Температуры °C		Доброт- ность $z\bar{t}$ (6)
		холодно- го спая (4)	горячего спая (5)	
(7) Германиекремниевый	GeSi	280	850	0,6
(8) Свинцовотеллури- вый	PbTe	175	800	0,4
			400	1,0
(9) Германиекремниевый, свинцо- теллури- вый	GeSiPbTe	247	820	0,8
			800	0,8
(10) Свинцовословотеллури- вый	PbSnTe	200	650	1,0
			650	0,9

KEY: (1) Temperature °C; (2) Semiconductors; (3) Formula; (4) cold junction; (5) hot junction; (6) Quality factor  $z\bar{t}$ ; (7) Germanium-silicon; (8) Lead telluride; (9) Germanium-silicon, lead telluride; (10) Lead-tin telluride.

A lead telluride element has high efficiency but is not stable in vacuum; the temperature of the cold junction is low, which makes the radiator heavy. Two other elements have average properties as compared with the first two.

Let us examine the classification of thermoelectric converters. Based on the structural diagram, they are made on converters which are combined with a nuclear reactor or an isotopic source of heat, converters combined with a radiator, and converters combined with a heat exchanger.

## STRUCTURAL DIAGRAMS AND DESIGN OF CONVERTERS

### Thermoelectric converter combined with an isotopic source and a radiator

As is seen from Fig. 3.96, the heat source in this design is a radioactive isotope 1 located in ampoule 2 and transmitting heat to the hot junction of the converter through the heat-conductive packing 3 and the heat-conductive shell 4. Semiconductor elements 5 are installed on insulators 6 and are contained in hermetically sealed shell 7, which is also the radiator of the device.

The materials in this design include the following: shells, stainless steel or molybdenum; insulators, beryllium oxide; heat-conductive material, beryllium. Since the housing is sealed, it is possible to use the highly effective lead telluride element.

The advantages of such a design are its simple and lightweight nature; the disadvantage lies in the fact that it is difficult to combine in one structure optimal cold-junction temperature, which is determined by the size of the radiating surface, and optimal hot-junction temperature, which is determined by the power of the source and the heat-conducting capacity of many materials. We should keep in mind that the radiating ability of the converter's surface is not high. Obviously, it is difficult to introduce the necessary parameters into this design since it is not easy to separate into separate elements.

### Solar thermoelectric converter combined with radiator

A design using solar energy to heat the hot junction of the heat generator is shown in Fig. 3.97.

Sun rays passing through the transparent cover 1 of silicon oxide heat the heat-conductive plate 2 of molybdenum or aluminum and the hot junction p-n of element 3.



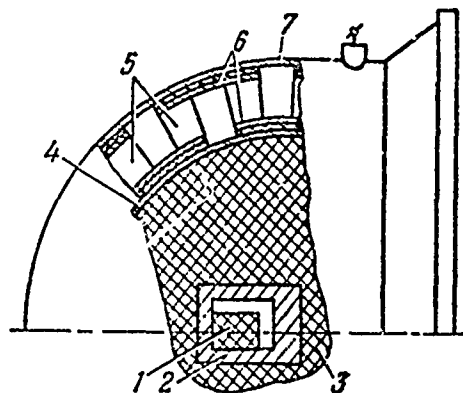


Fig. 3.96. Diagram of a thermoelectric converter combined with an energy source and a radiator.

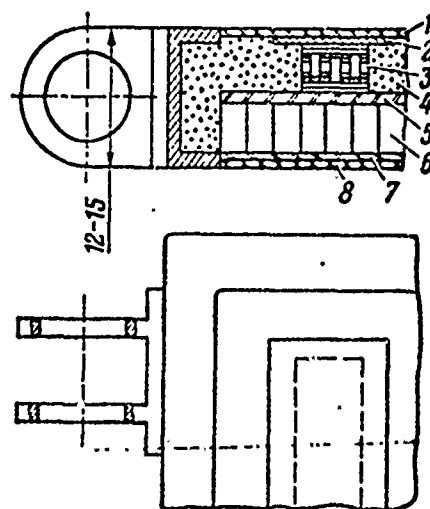


Fig. 3.97. Diagram of a thermoelectric converter combined with a radiator.

The heat passing through the p-n element proceeds toward its cold junction. To avoid dissipation, all p-n elements are placed in insulation 4, usually fiber glass. From the cold junction the heat is removed by plate 5, which has good heat conductivity, and then by the brass honeycomb 6, which creates a stiff housing for the entire structure and is filled with heat-conductive materials for withdrawing heat from the radiating surface of the converter 7. The radiator 7 is also covered with a thin layer of silicon oxide 8 to protect the surface from damage. As seen from the figure, this device is not very thick, which ensures its successful use in auxiliary power plants.

#### Thermoelectric converter combined with heat exchange

A thermoelectric converter (Fig. 3.98) consists of shells 1 and 3, connected by corrugated spacer 2, insulator 4, and a unit of p-n elements.

In the figure we see internal commutation 5 of the stubs of semiconductors and layer 6 which ensures the connection between the different materials. The plates 5 are made of molybdenum; the unit of p-n elements has the properties of ceramic materials. The space between the stubs is filled with insulation 7.

The shell material is stainless steel or niobium depending upon the working medium. The insulator is made from beryllium oxide, the internal commutation from molybdenum, the external from beryllium bronze, and the insulation from glass wool.

The advantage of this design is the optimal temperatures of the cold and hot junction, the possibility of finishing the converter in a "pure" form without other parts of the installation, the possibility of giving a transformer unit any applicable shape - flat, axisymmetric, etc.

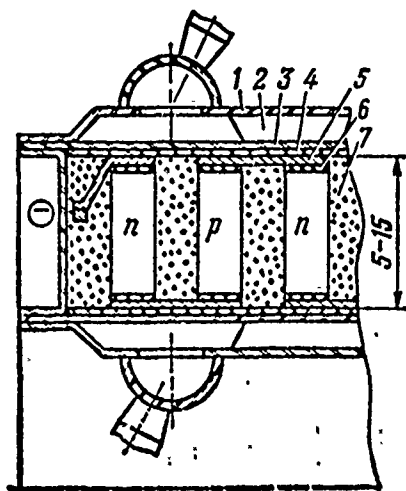


Fig. 3.98. A thermoelectric converter combined with a heat exchanger.

We know of a design [41] of thermoelectric generator which is mounted on a reactor without a liquid heat-transfer agent. The reactor has a cylindrical core consisting of fuel elements in the form of plates of uranium dicarbide  $UC_2$  with 90%  $U^{235}$  enrichment and graphite. The charge of  $U^{235}$  is 49 kg. The core with maximum temperature in the center of  $1770^\circ C$  is circled by a radial reflector of beryllium with four control rods located in the reflector.

A thermoelectric converter consists of several thousand semi-conductors filled with germanium-silicon alloy, arranged on the outer surface of the reactor housing, having a temperature of  $1000^{\circ}\text{C}$ . The thermoelectric generator has four groups, each of which includes four parallel circuits of thermoelements. The power of the converter is  $N = 500 \text{ W}$  with a current intensity of  $I = 88 \text{ A}$ . Heat removal is effected by cooling fins. The operating time of the installation is 4000 hours. The design of separate elements of the installation is shown in Fig. 3.99.

Soldering (surfaces  $\Gamma$ ,  $X$ ) is a possible method of connecting the semiconductor elements 1 with the hot 2 and cold 3 units.

The purpose of the sylphon 4 in this design is to hermetically seal the cavity of the semiconductors. The main disadvantage of this unit is the difficulty involved in soldering a large number of unlike elements.

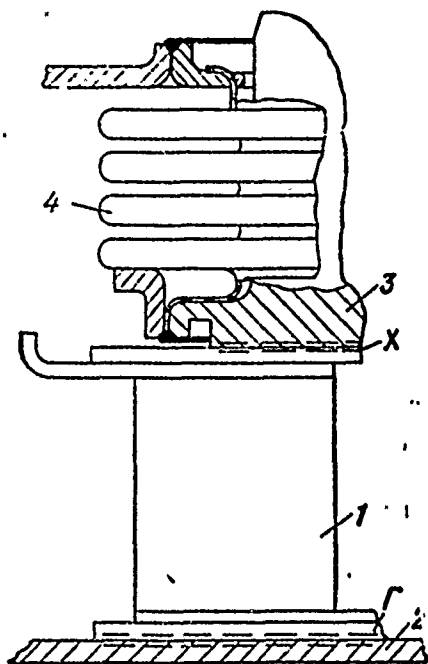


Fig. 3.99. Design of thermoelectric converter elements.

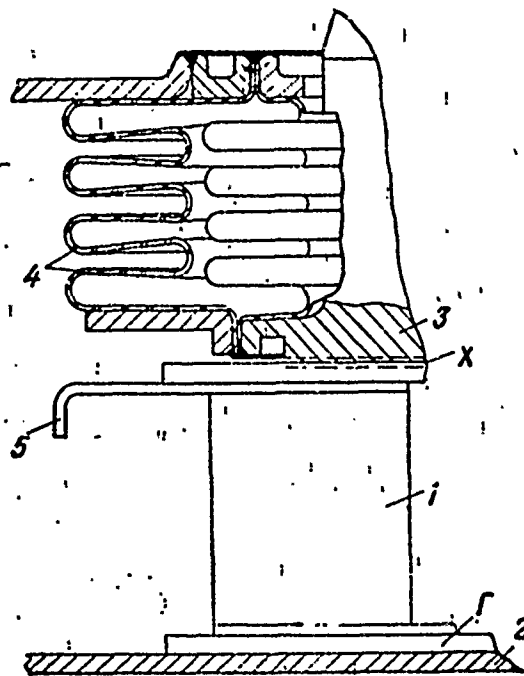


Fig. 3.100. Design of a dismantable thermoelectric converter.

Figure 3.100 shows a simpler design for the unit connecting the converters with the housing parts. The hot surface of the converter 1 and the hot surface of the housing 2 are not soldered. A parting of the design along the hot joint, while simplifying construction, leads to considerably higher heat losses than would occur in the previous case. The construction of a double sylphon 4 provides a seal for the cavity of the semiconductor elements and sufficient reinforcement of converter unit clamping during warmup.

Figure 3.101 shows another method of joining the converter with the housing parts. Semiconductors 1 are tightly soldered to the hot 2 and cold 3 shells of the housing.

Shell 2 is heated by liquid sodium, which is located in cavity 5. Corrugated element 4 compensates for the thermal strains of the unit.

Variation in the volume of sodium during warmup is compensated by the corrugated element 5. This same element, by moving wall 6 during warmup, with folds 7 provides thermal power control. The reverse motion of wall 6 is accomplished by pneumatic spring 8.

From literary sources [41] the following data on thermoelectric generators are known: operating temperatures  $T_r = 582-593^\circ\text{C}$ ;  $T_x = 177-209^\circ\text{C}$ ; useful power  $N = 3-5$  W; heat source power  $N_T = 96$  W, efficiency  $\eta = 4-5\%$ . The battery consists of 27 thermoelements of lead solenoid and provides voltage  $V = 2.5-2.8$  V.

Another installation has a useful power of  $N = 250$  W. Thermoelectric elements are made of PbTe (n-type) - GeBiTe (p-type); they are installed on the outer surface of a reactor housing (32 groups of elements, 24 pieces in each group). All 768 elements provide a voltage of 28 V;  $T_r = 614^\circ\text{C}$ ;  $T_x = 344^\circ\text{C}$ .

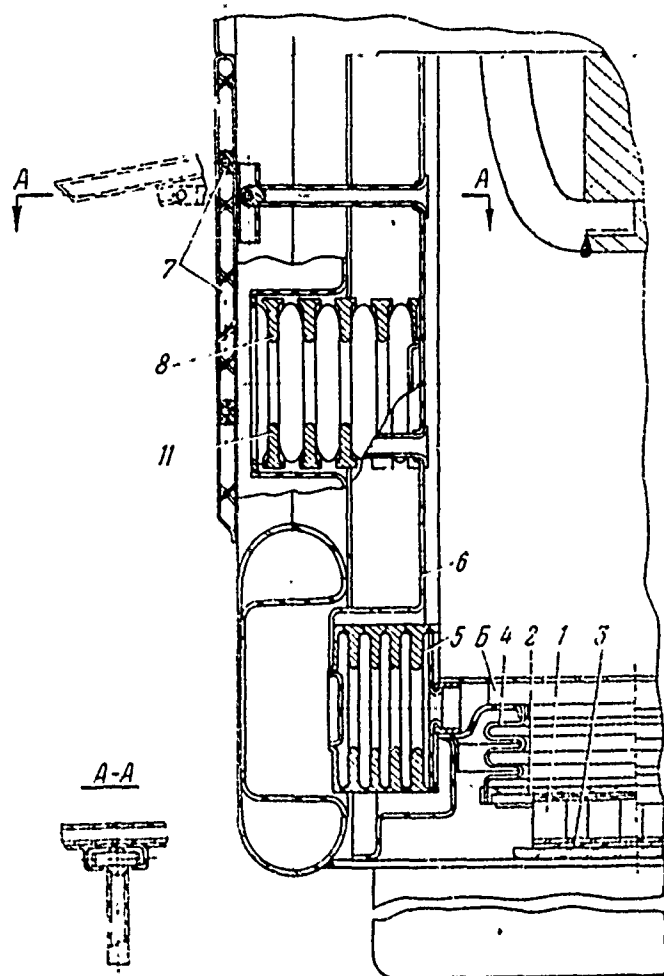


Fig. 3.101. Controllable thermoelectric converter.

The following data pertains to a thermoelectric generator combined with a radiator (Fig. 3.102): thermal power of the reactor 35 Kw, electrical power 500 W with a voltage of 28.5 V. Converters are made of GeSi; temperature drop is from 468 to 310°C. The generator consists of 14,400 elements which provide a power of 0.37 W and a voltage of 0.1 V each. The operating time of the installation is 1 year.

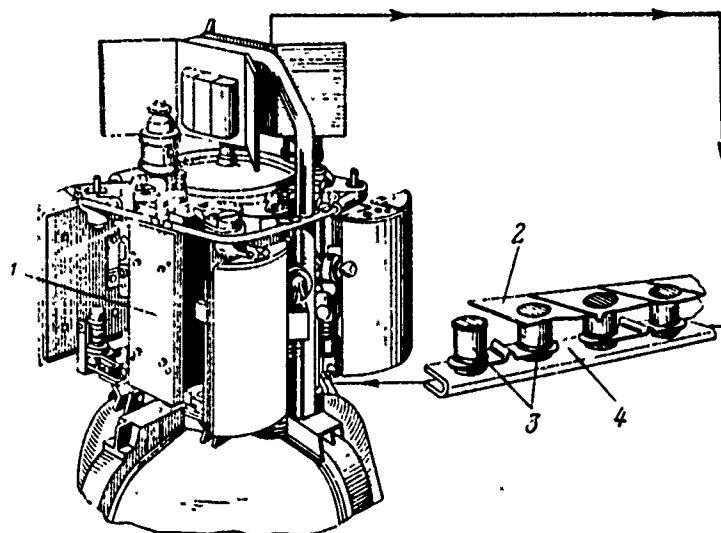


Fig. 3.102. Thermoelectric generator combined with a radiator: 1 - reactor; 2 - radiator; 3 - thermoemission power converters; 4 - piping.

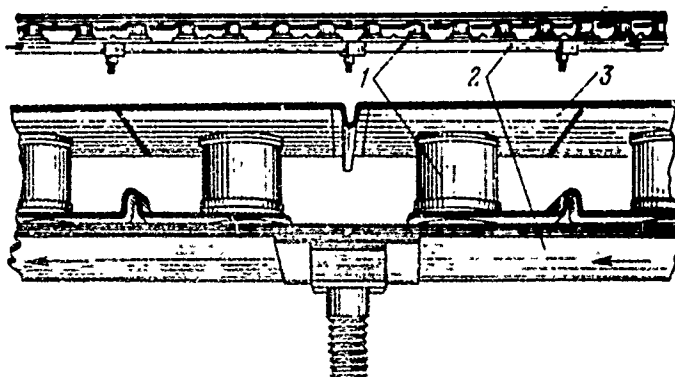


Fig. 3.103. Generating element.

A unit of each generating element (Fig. 3.103) consists of its own converter 1, piping with liquid hot metal 2, radiator 3. The shape of the piping 2 is cylindrical to reduce the heat loss and evaporation; a compensator for thermal strain in the form of corrugation is welded to the radiator 3.

## Photoelectric Converters

In a photoelectric converter, frequently called a solar battery, potential difference between positive and negative parts of the semiconductor arises under the effect of light quanta. This is caused by photons knocking out a certain number of free electrons.

Photoelectric converters are a widely known type of converter for low electrical powers. They are widely used in various space vehicles. Their advantages are the following: they are simple in design and operation, provide "free" solar energy, and, therefore, in some cases are irreplaceable.

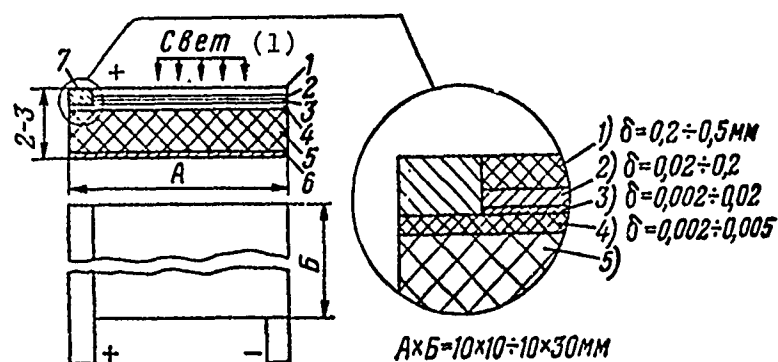


Fig. 3.104. Design of a photoelement.  
KEY: (1) Light.

The disadvantages are the drop in efficiency of these elements as a result of their irradiation in space by flows of charged particles and the change in the composition and properties of a semiconductor, as well as the degrading of the photoelectric properties of elements upon an increase in their temperature. It is known that heating an element by  $80^\circ\text{C}$  leads to a triple drop in its power.

A photoelectric converter is made of selenium, germanium, or silicon semiconducting elements. The most widespread are silicon elements because of their good spectral sensitivity to solar radiation and also the highest specific power.

Photoelement energy, by which we mean the ratio of useful power to the power of the incident light, is determined by a number of factors:

- the spectrum of the incident light,
- the optical properties of the surface,
- the technological factors and the quality of the semi-conductors.

Photoelement efficiency is 7-10% [46]; the efficiency of a power plant on photoelements reaches 4%. The voltage in these elements is  $V = 0.4$  V; current density is  $i = 1.8 \cdot 10^{-2} - 5 \cdot 10^{-2}$  a/cm<sup>2</sup>; specific power is  $W = 0.72 \cdot 10^{-2} - 2.0 \times 10^{-2}$  W/cm<sup>2</sup>.

Figure 3.104 shows a single photoelement. As is apparent from the figure, the photoelement is a multilayer ceramic plate. On top on the working side, it is covered with a glass-like optically transparent composition 1, which strengthens and protects the element from the effect of outer space. Also provided are an interference filter 2, a binding substance 3, a semiconductor of the 4p-type, a semiconductor of the 5n-type, and commutation plates 6 and 7.

The base of the element is a silicon plate 5 with a large number of n-type impurities. On the top is a thin layer 4 of p-type material. Layer thickness is several microns. Electrodes are soldered: at the bottom, plates 6 to the entire width of the element; at the top, only strip 7 to the p-element. Welding is performed after the application of the nickel coating to connect the ceramics with the metal.

An external load is connected to these contacts. During the illumination of the photoelectric converter a positive current proceeds from the upper contact through the load to the lower contact.

The battery of the photoelements, with an area of 1 m<sup>2</sup> and a useful area of 0.7 m<sup>2</sup>, located in a flow of solar radiation with density  $S = 1000$  W/m<sup>2</sup>, makes it possible to obtain electrical power



of 40 W with allowance for all losses. The mass of the battery is 10 kg. The operating time is one and a half years.

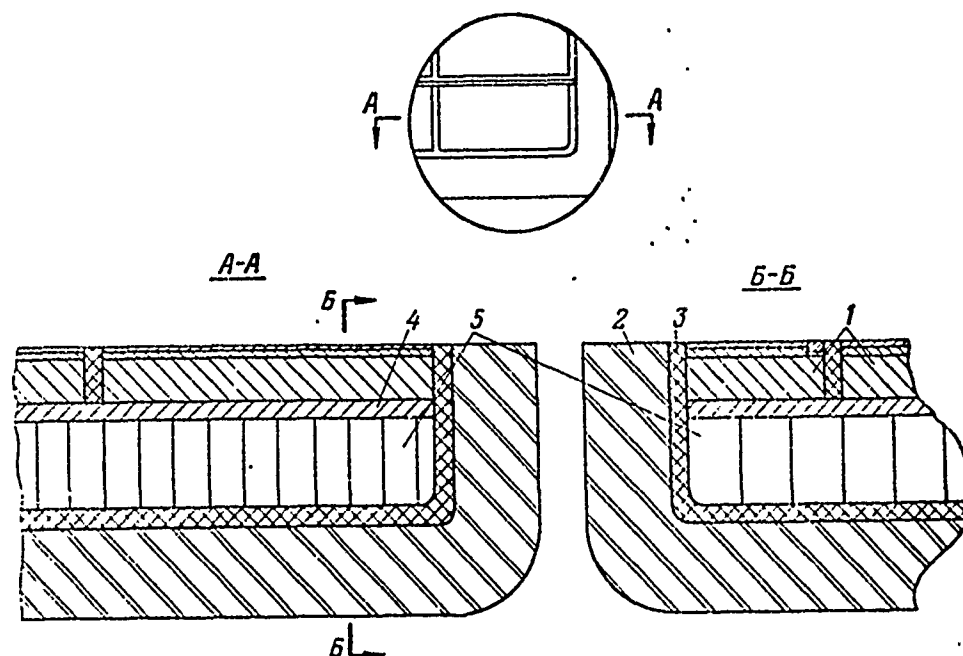


Fig. 3.105. Battery of a photoelectric generator.

Figure 3.105 is a possible version of the design of such a battery. The photoelements 1 are placed in housing 2 of a lightweight alloy by insulating layers 3 and 4. Layer 5 of a lightweight corrugated foil provides the necessary panel stiffness.

We know [41] the parameters of batteries being developed or being used on various earth satellites. The battery for a space vehicle has the following data: area  $2.76 \text{ m}^2$ , power 150 W, mass 34 kg. Other photobatteries have an area of  $21 \text{ m}^2$ , electrical power up to 1 kW, and a mass of 130 kg.

In conclusion we should mention that it is advisable to use photoelectric converters at comparatively low power (up to 1 kW) and an operating period up to 2 years.

## CHAPTER IV

### HEAT EXCHANGERS

#### 4.1. RADIATOR-COOLERS

The purpose of a radiator cooler is to release heat into outer space.

The radiator is an integral part of a space power plant since heat radiation is the only method of heat exchange in outer space.

The radiator in size and weight occupies a considerable space in the power plant. Radiator designs frequently determine the effectiveness of the power plant as a whole and should be based on the following considerations.

Radiator dimensions are inversely proportional to the fourth power of its surface temperature. Therefore, the temperature of the radiator must be the highest possible in order to reduce its weight and size.

Under launching conditions the radiator must have the smallest dimensions possible for installation in the carrier rocket. It must satisfy conditions of vibrational stability and pressurization. In outer space the radiator must occupy a position which is shaded by the reactor shield. Devices are provided which shut off a certain section of the cooler when the pressurization has been impaired due to meteorite punctures or other factors.

Radiator coolers are divided into several groups based on their structural diagram. With respect to the physical state of the heat-transfer agent, coolers are broken down into coolers with liquid and coolers with gas heat-transfer agent. Extraterrestrial rocket engines usually use liquid-metal coolers in which the heat carriers are metals. There are coolers with heat transfer by solid walls with no liquid heat carrier in the system.

Based on the component diagram, all coolers can be divided into folding and unfolding.

Each of these designs can be made independent of the other design elements, but can be combined with various units of the power plant or power converters.

Finally, liquid-metal radiators can have a single-phase or multi-phase working medium, for example, two-phase when the radiator-cooler is combined with a condenser and liquid metal is in the liquid and vapor state. Let us examine several typical structural diagrams for radiator-coolers.

## STRUCTURAL DIAGRAMS OF RADIATOR-COOLERS

### Conical rigid unfolding radiators

Figure 4.1 presents the diagram of such a radiator. It consists of two collectors 1 to which liquid metal flowing along the pipes 2 is fed and drained. Pipes 2 are welded with radiating membrane 3 and, for rigidity, are fixed by frame 4. Shield 5 is installed on the inside of the radiator to protect the elements within.

The advantages of this radiator are the design simplicity and the possibility of using automatic welding for the units and elements.

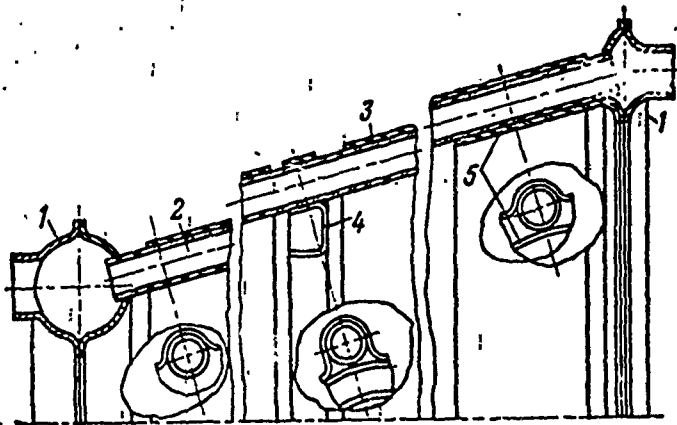


Fig. 4.1. Conical rigid unfolding radiator.

The disadvantages are the comparatively heavy construction and the ineffective use of the surface of radiation - heat exchange is performed on one side. The large space inside the radiator is virtually unused. Sometimes, in this space, starting pumps and heat compensation tanks are installed; however, the completely empty space is not used. Such a design is applicable for low-power extraterrestrial rocket engines [ERE]. Radiator dimensions are outlined in the fairing of the launching carrier rockets.

There are considerable temperature gradients and, consequently, stresses in the radiator in working mode. We should consider this factor when the radiator is switched to the power circuit of the power unit; analysis should also include launching conditions if the radiator is receiving launching loads.

#### Conical flexible unfolding radiators

In this diagram (Fig. 4.2) the pipes 2 carrying the heat-transfer agent and collectors 1 are welded into one unit, which bears no load during launch except the load of its own mass. In the operating state the pipes experience thermal stresses which must be calculated.

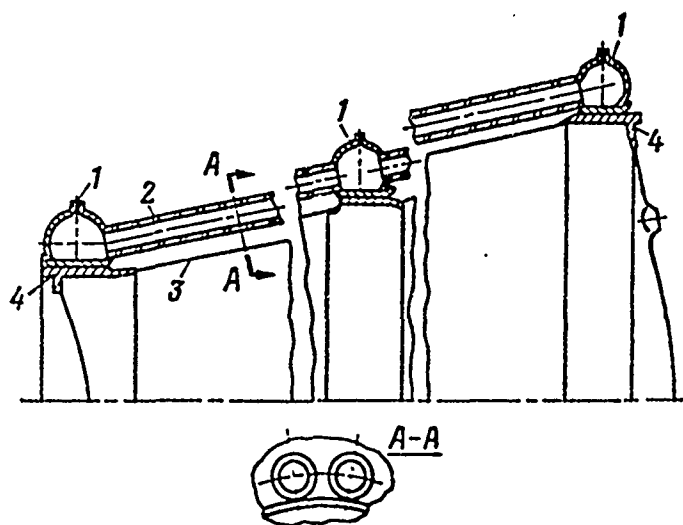


Fig. 4.2. A conical flexible unfolding radiator.

The stressed frame which connects the radiator with other elements is a closed thin-wall conical shell 3, which, in order to increase rigidity, is under the pressure of neutral gas. The shell has rigid flanges 4. The side surface of the shell is a supplementary radiating surface. The shell is welded to one of the collectors.

The advantages of this system is the low weight of the radiator and the possibility of reducing thermal strains as compared with the preceding diagram. The disadvantage is the one-sided use of the radiation surface. This diagram, as the preceding can be used in a low-power ERE.

#### Flat unfolding radiators

These radiators (Fig. 4.3) consist of two collectors 1 to which the coolant is fed and drained, cooling pipes 2 to which the radiating surfaces 3 are soldered. Each plane of the radiator consists of several (four on the diagram) panel sections connected by hinge 4

The hinge 4 and its gasket 5, 6 provides for the hermetic seal of the radiator in launch conditions, the folding of the radiator and the hermetic seal and attachment of the sections in working folded conditions. Usually there are valves in the hinge unit which cut off the output of liquid metal when a radiator pipe is punctured.

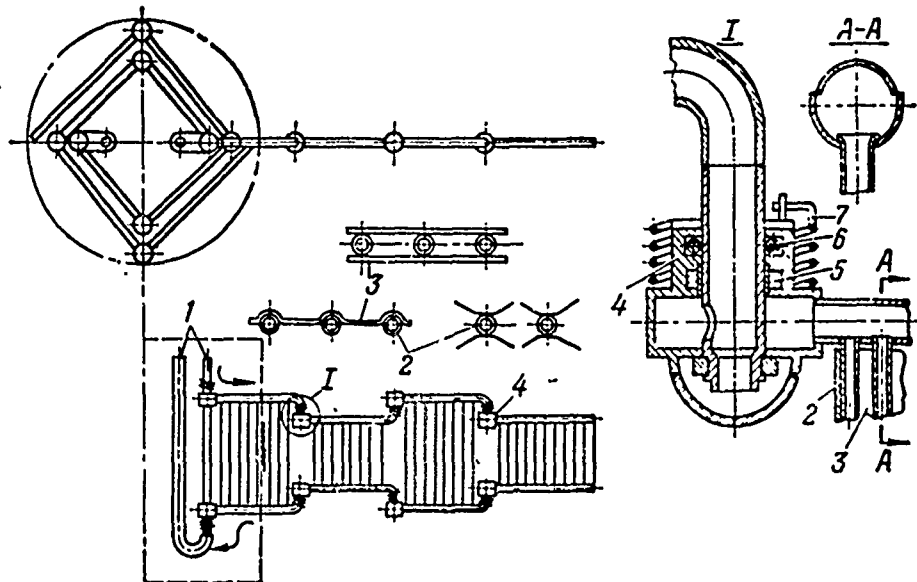


Fig. 4.3. A flat unfolding radiator.

The two planes of the radiator in launch position are folded along the axis of symmetry and are kept from unfolding by a light shell which is ejected in space.

The advantage of this design is the possibility of obtaining an effective radiator of practically any size. The two-dimensional shape of the radiator is convenient for the best use of the radiating surfaces and for protecting the reactor from radiation.

A disadvantage of this design is its great complexity as compared with the previous design discussed. Metal losses are inevitable when unfolding to operating mode in space.

### Folding conical radiators.

As seen from Fig. 4.4, these radiators consist of a toroidal frame combined with collectors 1 and 2, radiator panels 3, hinges 4, and flexible elements 5.

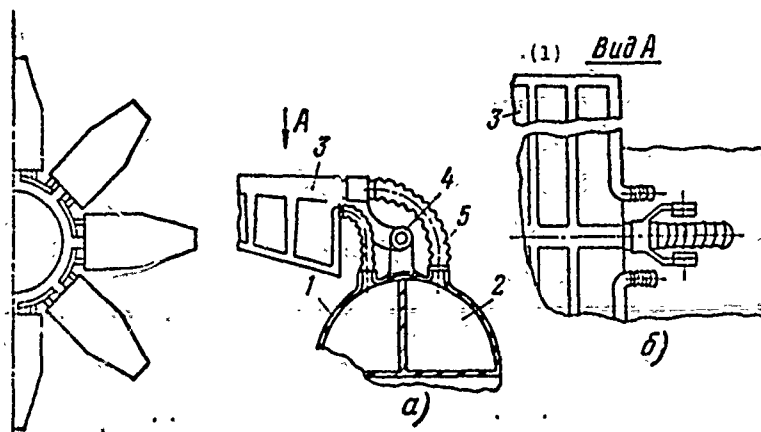


Fig. 4.4. Folding conical radiator.  
KEY: (1) View.

In the launch state (Fig. 4.4a and b) radiator panels 3 have the same contours as the carrier rocket fairing. In operating state the panels unfold at hinge 4 of "dry" design, without being washed by liquid metal, which is an advantage. The seal of the panels and collectors 1 and 2 is effected by corrugated element 5. The pipes and the membranes of panel 3 are made as in the earlier discussed diagram.

The advantage of this radiator is the comparatively simple design. The entire surface is used for radiation. There is no metal loss in the unfolding mode.

The disadvantage is the difficulty in protecting the radiator from reactor radiation; therefore, its use is limited to power plants where the irradiation is permissible. The comparatively large mass is also a disadvantage. This radiator is used in low-power installations.

## High-power unfolding conical radiators

A conical radiator (Fig. 4.5) folds along collector 1 located perpendicularly to the axis of symmetry of the radiator. The diagram shows the flow of the working medium along pipes 2 connected by connecting pieces 3.

The advantages of this radiator are the small launching size, the almost complete use of the surface for radiation, and the good positioning of the radiator relative to the shade screen of the reactor. We should note only the somewhat complex design of the radiator as a whole.

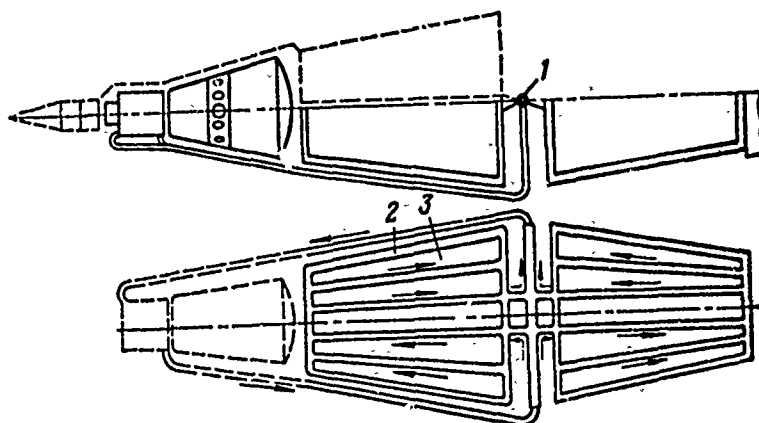


Fig. 4.5. High-power unfolding conical radiator.

## Radiators combined with thermoelectric power converters

The diagram (Fig. 4.6) gives an example of such a radiator. Heat removal is accomplished by fin 1, made of aluminum and protected from sublimation in vacuum by a special coating. Heat passes to the radiator along a brass stub 2, soldered to the cold end of the thermoelectric generator 3.

Such a design is applicable for radioactive isotopic sources.



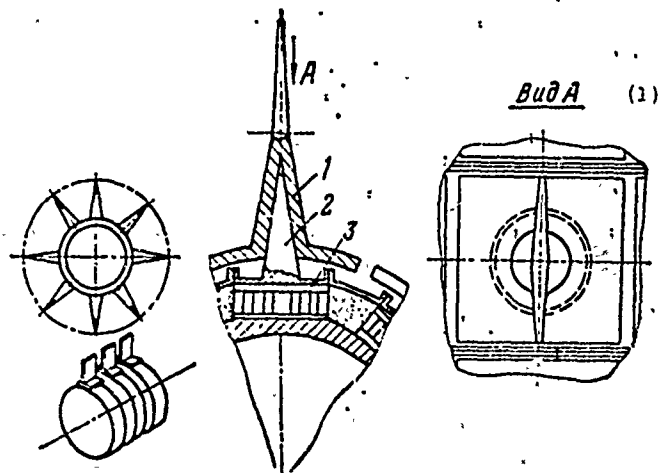


Fig. 4.6. Diagram of radiator combined with a thermoelectric energy converter.  
KEY: (1) View.

#### Radiator element design

Figure 4.7a and b shows the typical design of assembled radiator collectors. The shape of the collectors is determined by the method of assembly and inspection. Obviously, a seam can be welded and checked reliably when the structure enables inspection from two sides. This is particularly important for the seam holding pipes 1. This is why the pipes are welded to half of the collector 2 first and then the collectors 2 and 3 are welded. For this both halves of the collectors have special crimps.

The shape of the radiating surface is shown in Fig. 4.7b. A thin aluminum or steel shell is welded or soldered to stainless steel, niobium, or molybdenum pipes.

The critical element of the radiator is the hinge, joint which provides for the unfolding of the radiator sections in space.

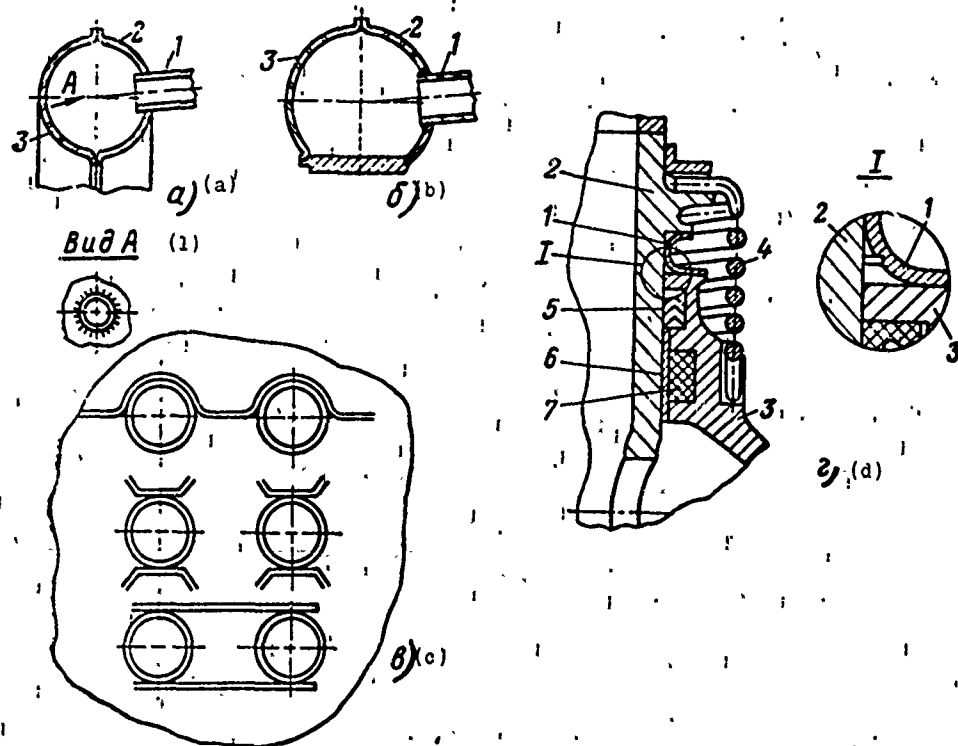


Fig. 4.7. Design of radiator elements.  
 KEY: (1) View.

In Fig. 4.7d this joint is shown in the power plant starting stage. The vacuum of the radiator and the hermetic seal of the units are ensured by a thin membrane 1, welded to two of its sections 2 and 3. This membrane does not interfere with the unfolding of the radiator after launch. By intensifying spring 4 the sections are unfolded in space. In order to facilitate breakaway, the membrane is notched.

The clearances in the hinge after unfolding are sealed by baffle 5. This seal is not completely airtight. It is designed to operate only during warmup and launch. The hermetic seal of the hinge unit in working position is provided by liquid-metal seal 6, 7. The seal consists of a thin shell 6 and a low-melting metal 7. The shell 6 after welding to pin 3 of the section is finished cleanly and precisely. Metal 7 is selected so that its melting

point does not exceed the temperature of the heat carrier in launching conditions. If this temperature is 150-250°C, the metal of the seal can be lead (melting point approximately 300°C).

During warmup of the radiator in space the metal melts. The increase in its volume during melting and warmup leads to tight clamping and to the subsequent welding of shell 6 to pin 2. Thus, the hinge unit becomes completely airtight during the operation of the insulation.

### Stress analysis of radiator elements

In radiators the thermal loads causing thermal stresses are basic. In studying thermal stresses in radiators, we shall, as before, assume that a steady flow of heat is passing through a part. Thus, the temperature gradient along a section of a part will also be steady.

We shall further assume that radiator elements are operating in the elastic stage, i.e., plastic deformation will not be studied.

The stresses obtained are compared with the characteristics of the stress-rupture strength of the material, i.e., we shall determine the strength of radiator elements with allowance for their temperature and operating time.

Radiator pipes are heated nonuniformly, which is the reason for the occurrence of stresses. For their first approximate evaluation the radiator diagram can be presented as shown in Fig. 4.8a. A certain number of pipes having different temperatures are joined with the collectors. Let us assume that the cross sections of pipes  $F$  and the coefficients of linear expansion  $\alpha$  are identical. During power plant operation the average pipe temperatures are different, which causes axial loading on individual pipes and can lead to stability loss in the compressed pipes. There is a substantial nonuniformity of temperatures along the axis of separate pipes, a

nonuniformity of temperature distribution along the cross section, which leads to additional stresses.

For the first evaluation of radiator pipe strength the following calculation should be made. Tensile and compressive stresses for the most heavily loaded pipes, which appear as a result of nonidentical averaged temperature, should be evaluated. Based on the forces of compression, their stability should be evaluated. Then we should evaluate the stresses which appear as a result of the presence of temperature gradients along the axis of symmetry of a pipe and its cross section. And, finally, the stresses occurring in the pipe where it is braced to the collector are evaluated. The last calculation will not be studied in this section. Similar problems will be examined in Chapter V.

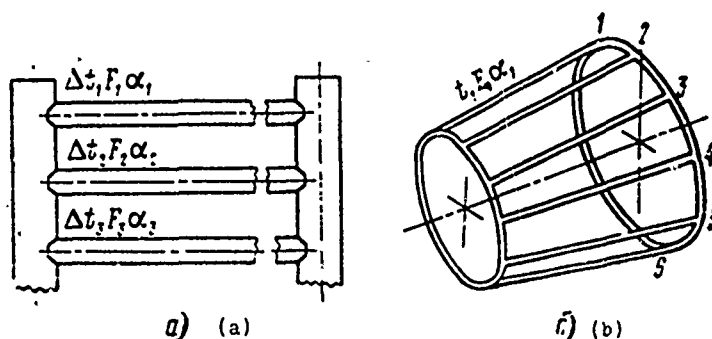


Fig. 4.8. Radiator diagram.

#### Thermal stresses in radiator pipes with nonuniform heating

The ends of the pipes are rigidly attached. This case is of interest from the point of view of the appearance of stresses in a pipe under the worst possible conditions. The following are given  $E$ ,  $\alpha$ ,  $F$  and  $\Delta t$ , where  $\Delta t = t - t_0$ .

Temperature  $\Delta t$  is averaged. This temperature along the axis of the pipe is a variable quantity,

$$\Delta t_{cp} = \frac{1}{e} \int_0^e \Delta t dx.$$

The subscript "cp" [cp = average] with t will be omitted below.  
We know that relative strain in heated parts is

$$\varepsilon = \varepsilon_t + \varepsilon_y,$$

where  $\varepsilon_t$  is the thermal strain of a free part due to heating;

$\varepsilon_y$  is the elastic strain of a heated part, which appears as a result of constraint and overlapping of connections.

The separation of these strains is one of the problems of analysis since the stressed state of the element is determined only by component  $\varepsilon_y$ . The value of strain  $\varepsilon_t$  is known.

In the studied case the rigid attachment of the part results in  $\varepsilon = 0$ ; then  $\varepsilon = -\varepsilon_t = -\alpha \Delta t$  and stress in the pipe is

$$\sigma = -E\alpha\Delta t. \quad (4.1)$$

Thus, with a rigid attachment the pipes thermal elongation leads to the appearance in the attachment of compressive forces of reaction (Fig. 4.9).

Example 4.1. Find the stress in a steel pipe rigidly attached on the edges during its heating to 100°C. It is known that  $E = 2 \cdot 10^6$  daN/cm<sup>2</sup>,  $\alpha = 10 \cdot 10^{-6}$  1/°C. Obviously,  $\sigma = -10 \cdot 2 \cdot 100 = -2000$  daN/cm<sup>2</sup>.

As is apparent from the example, thermal stresses can be considerable even at such low pipe heating temperatures. In practice considerably higher temperatures are encountered; the preservation of design functionality is explained by the fact that under actual

conditions there are no absolutely rigid pipe fastenings and also the plastic deformations which occur lead to a redistribution of stress.

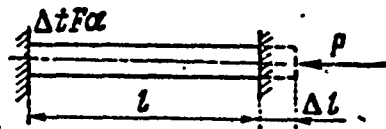


Fig. 4.9. Determining thermal stresses.

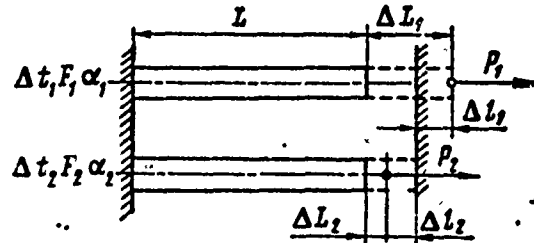


Fig. 4.10. Determining thermal stresses.

Let us examine stresses in pipes which have a movable attachment (Fig. 4.10).

The stresses are in two pipes connected by collectors. The following are given:  $\alpha_1, \Delta t_1, E_1, F_1$ . Find  $\sigma_1, \sigma_2, P_1, P_2, \alpha_2, \Delta t_2, E_2, F_2$ . Initial conditions will be:

$$\epsilon_1 = \epsilon_2; \quad \Sigma P_i = 0. \quad (4.2)$$

Generalized strains  $\epsilon$  are made up of thermal and elastic strains. Thermal strains in the pipes will be

$$\Delta L_1 = L \alpha_1 \Delta t_1; \quad \Delta L_2 = L \alpha_2 \Delta t_2.$$

Elastic strains in the pipes, caused by forces  $P$ , will be

$$\Delta l_1 = \frac{P_1 L}{E_1 F_1}; \quad \Delta l_2 = \frac{P_2 L}{E_2 F_2}.$$

We allow for  $P_1 + P_2 = 0$  or  $P_2 = -P_1$ , as well as  $P = \sigma F$ . From the first condition

$$L\alpha_1\Delta t_1 + \frac{P_1 L}{E_1 F_1} = L\alpha_2\Delta t_2 + \frac{P_2 L}{E_2 F_2};$$

$$P_1 = - \frac{\alpha_1\Delta t_1 - \alpha_2\Delta t_2}{\frac{1}{E_1 F_1} + \frac{1}{E_2 F_2}}.$$

Finally,

$$\sigma_1 = - \frac{\alpha_1\Delta t_1 - \alpha_2\Delta t_2}{F_1 \left( \frac{1}{E_1 F_1} + \frac{1}{E_2 F_2} \right)}; \quad \sigma_2 = - \frac{\alpha_1\Delta t_1 - \alpha_2\Delta t_2}{F_2 \left( \frac{1}{E_1 F_1} + \frac{1}{E_2 F_2} \right)}. \quad (4.3)$$

Thus we obtain the unknown forces and stresses in the pipes. With a larger number of pipes the problem is still solved similarly. Mobility of the attachment appreciably reduces stresses in the pipes, which is apparent from the following example.

Example 4.2. Find the stress in pipes which have the same parameters and operate under the conditions in the preceding example (example 4.1).

Since  $\alpha_1 = \alpha_2$ ;  $E_1 = E_2$ ;  $F_1 = F_2$ , formula (4.3) will have the form

$$\sigma_1 = - \frac{\alpha(\Delta t_1 - \Delta t_2)}{2/E} = -0.5E\alpha(t_1 - t_2),$$

where  $\Delta t_1 - \Delta t_2 = t_1 - t_0 - (t_2 - t_0) = t_1 - t_2$ .

Thus, the free attachment of two pipes reduces the stresses in them by half.

The stress and forces in pipes in the general case. Let us examine three pipes.

The following are given:  $\alpha_1 F_1 \Delta t_1$ ;  $\alpha_2 F_2 \Delta t_2$ ;  $\alpha_3 F_3 \Delta t_3$ . Find  $\sigma_1$ ,  $\sigma_2$ ,  $\sigma_3$ .

The basic initial conditions for setting up a system of equations reduces to the two equations:

$$\left. \begin{array}{l} \Delta L_i + \Delta l_i = \text{const.} \\ \sum P_i = 0, \end{array} \right\} \quad (4.4)$$

or, in simpler form,

$$\varepsilon_{ti} + \varepsilon_{yi} = \text{const}; \quad \sum_1^i P_i = 0.$$

Let us write expressions for thermal  $\varepsilon_{ti}$  and elastic  $\varepsilon_{yi}$  strains in the pipes. All strains and elastic forces are considered positive, i.e., oriented on the x-axis (Fig. 4.11). The actual sign of the forces and strains will be apparent after solving the system of equations.

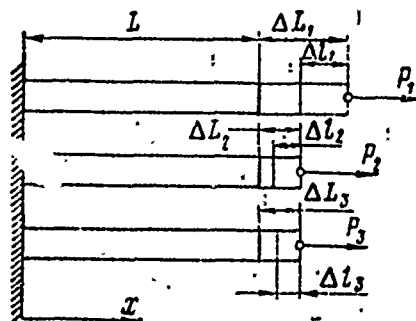
Thermal and elastic strains are

$$\begin{aligned} \varepsilon_{t1} &= \alpha_1 (t_1 - t_0) = \alpha_1 \Delta t_1; & \varepsilon_{y1} &= \frac{P_1}{F_1 E_1} = \frac{P_1}{A_1}; \\ \varepsilon_{t2} &= \alpha_2 \Delta t_2; & \varepsilon_{y2} &= \frac{P_2}{A_2}; \\ \varepsilon_{t3} &= \alpha_3 \Delta t_3; & \varepsilon_{y3} &= \frac{P_3}{A_3}. \end{aligned}$$

where  $A_1 = F_1 E_1$ ;  $A_2 = F_2 E_2$ ;  $A_3 = F_3 E_3$ .



Fig. 4.11. Determining thermal stresses in the general case.



In accordance with condition (4.4), we set up the following system of equations:

$$\frac{P_1}{A_1} + \alpha_1 \Delta t_1 = \frac{P_2}{A_2} + \alpha_2 \Delta t_2;$$

$$\frac{P_1}{A_1} + \alpha_1 \Delta t_1 = \frac{P_3}{A_3} + \alpha_3 \Delta t_3;$$

$$P_1 + P_2 + P_3 = 0.$$

Or, in more detail,

$$P_1 A_2 - P_2 A_1 = A_1 A_2 (\alpha_2 \Delta t_2 - \alpha_1 \Delta t_1);$$

$$P_1 A_3 - P_3 A_1 = A_1 A_3 (\alpha_3 \Delta t_3 - \alpha_1 \Delta t_1);$$

$$P_1 + P_2 + P_3 = 0.$$

Hence

$$P_1 = \frac{\Delta_1}{\Delta}; \quad P_2 = \frac{\Delta_2}{\Delta}; \quad P_3 = \frac{\Delta_3}{\Delta},$$

where

$$\Delta = \begin{vmatrix} A_2 & -A_1 & 0 \\ A_3 & 0 & -A_1 \\ 1 & 1 & 1 \end{vmatrix} = A_1 (A_1 + A_2 + A_3);$$

$$\Delta_1 = A_1^2 [A_2 (\alpha_2 \Delta t_2 - \alpha_1 \Delta t_1) + A_3 (\alpha_3 \Delta t_3 - \alpha_1 \Delta t_1)];$$

$$\Delta_2 = A_1 A_2 [A_1 (\alpha_1 \Delta t_1 - \alpha_2 \Delta t_2) + A_3 (\alpha_3 \Delta t_3 - \alpha_2 \Delta t_2)];$$

$$\Delta_3 = A_1 A_3 [A_1 (\alpha_1 \Delta t_1 - \alpha_3 \Delta t_3) + A_2 (\alpha_2 \Delta t_2 - \alpha_3 \Delta t_3)].$$

Hence

$$P_1 = A_1 \frac{A_2(a_2\Delta t_2 - a_1\Delta t_1) + A_3(a_3\Delta t_3 - a_1\Delta t_1)}{A_1 + A_2 + A_3},$$

$$P_2 = A_2 \frac{A_1(a_1\Delta t_1 - a_2\Delta t_2) + A_3(a_3\Delta t_3 - a_2\Delta t_2)}{A_1 + A_2 + A_3},$$

$$P_3 = A_3 \frac{A_1(a_1\Delta t_1 - a_3\Delta t_3) + A_2(a_2\Delta t_2 - a_3\Delta t_3)}{A_1 + A_2 + A_3}.$$

The condition in the k-th pipe in the presence of i pipes

$$P_k = A_k \frac{\sum_1 A_n (a_n \Delta t_n - a_k \Delta t_k)}{\sum_1 A_n},$$

where subscripts n, k, i are the numbers; n = 1, 2, 3, ..., k, ..., i.

The value and sign of stresses are thus:

$$\sigma_1 = \frac{P_1}{F_1}; \quad \sigma_2 = \frac{P_2}{F_2}; \quad \sigma_3 = \frac{P_3}{F_3}; \quad \dots \quad \sigma_k = \frac{P_k}{F_k}.$$

For extended pipes the safety factor is determined from formula

$$n = \frac{\sigma_{n,\tau}}{\sigma_{\max}}; \quad n \geq 1.1 \div 1.2.$$

Thermal stresses in radiator pipes with a temperature gradient in the cross section.

In the cross section of pipes and radiator elements a certain temperature gradient is established which leads to the appearance of thermal stresses.

The following is an approach to solving this problem.

We shall fix the element rigidly in the axial direction. Then elastic and thermal strains will equal each other, i.e.,  $\Delta L = \Delta l$ . Let us find the stresses in the element in this position.

The application of bonds leads to a disruption of the boundary conditions of a free system. We restore the boundary conditions by applying to the system a force equal to the reaction arising in the attachment, but opposite in direction. Let us find the stresses from this force. They will only be elastic.

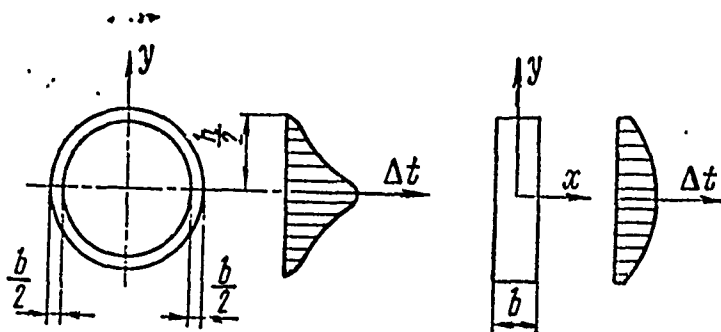


Fig. 4.12. Symmetrical temperature gradient.

It is completely obviously that the sum of the stresses of the first and second calculations gives us the real thermal stresses in the element.

Examples of gradients can be very different. Let us examine the first case when the temperature gradient is symmetric (Fig. 4.12) relative to the axis.

In the presence of such a temperature gradient throughout the cross section in a free, unattached element, thermal stresses arise. We shall evaluate these stresses.

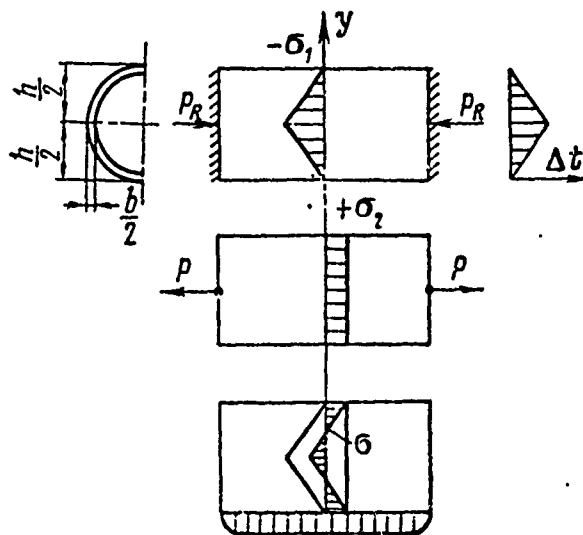


Fig. 4.13. Determining the stresses with a symmetric temperature gradient.

Let us assume that this cross-sectional temperature gradient will be preserved for the entire length of the element (Fig. 4.13).

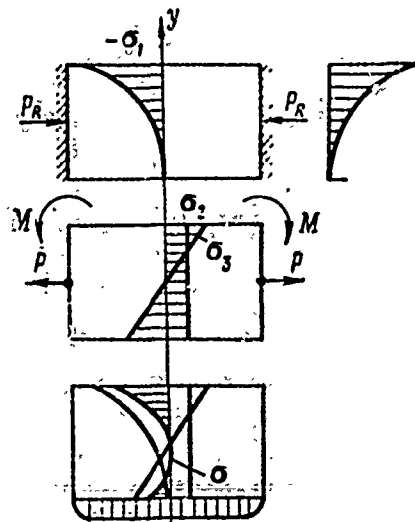
The following are known:  $E$ ,  $\alpha$ ,  $\Delta t$ ; find stress  $\sigma$ .

If we represent such an element in the free state, its elongation as a result of heating will be proportional to the temperature gradient;  $\epsilon = \alpha \Delta t$ , where  $\Delta t = t - t_0$  is the temperature variation with heating. If attachment is effected, compressive stresses  $\sigma_1 = -E\alpha\Delta t$  arise.

The diagram of compressive stresses will accurately trace the temperature gradient and will be identical in any section of the fixed element.

Let us find the stresses arising in the element if we free it from attachment. For this we apply tensile stresses to the ends of the rod, which ensure zero stresses on the ends.

Fig. 4.14. Stress diagrams during an asymmetric temperature gradient.



These stresses can be created by force

$$P = \int_{-h/2}^{h/2} E\alpha\Delta t b dy, \quad (4.5)$$

which at a sufficient distance from the end cause uniformly distributed stresses

$$\sigma_2 = \frac{P}{F} = \frac{1}{F} \int_{-h/2}^{h/2} E\alpha\Delta t b dy, \quad (4.6)$$

Thus, nonuniform symmetric heating of a free element along its cross section leads to the appearance of stresses which are determined from formula

$$\sigma = -E\alpha\Delta t + \frac{1}{F} \int_{-h/2}^{h/2} E\alpha\Delta t b dy. \quad (4.7)$$

Figure 4.13 shows a diagram of stresses along the cross section and along the axis of the sample.

If cross-sectional temperature distribution is not symmetric, we first proceed as before. After implementing a rigid attachment for the element (Fig. 4.14), we obtain, as earlier, stresses in the cross section  $\sigma_1 = -E\alpha\Delta t$ .

Now we free the element from its attachment; in order to preserve the boundary conditions we apply to its ends tension  $P$ . We obtain

$$\sigma_2 = \frac{P}{F} = \frac{1}{F} \int_{-h/2}^{h/2} E\alpha\Delta t b dy.$$

Bending moment  $M$ , which arises due to the asymmetry of the stresses on the ends, is

$$M = \int_{-h/2}^{h/2} E\alpha\Delta t b y dy,$$

and bending stress, as a result of this moment, is

$$\sigma_3 = \frac{M y}{J} = \frac{y}{J} \int_{-h/2}^{h/2} E\alpha\Delta t b y dy.$$

Thus, full stress in the section is

$$\sigma = -E\alpha\Delta t + \frac{1}{F} \int_{-h/2}^{h/2} E\alpha\Delta t b dy + \frac{y}{J} \int_{-h/2}^{h/2} E\alpha\Delta t b y dy. \quad (4.8)$$

The stress diagram is presented in Fig. 4.14.

## Thermal stresses in a flat radiator panel

The purpose of calculation is to find  $\sigma$  based on known  $E$ ,  $\alpha$ ,  $\Delta t$ .

a) Pure bend. We shall derive the equation for the forces of elasticity in a rectangular plate.

We know that if we heat a free quadratic rectangular plate so that the temperature through the thickness will vary according to linear law, and in the plane parallel to the plate's surface the temperature will be constant; deformation of the layers relative to the middle surface will be symmetric and the middle surface will have the shape of a sphere.

A similar character of plate deformation is obtained when distributed bending moments are applied along the edges of a free plate.

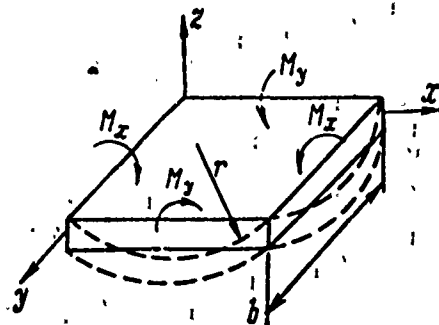
In those cases the bend of the plate in two mutually perpendicular directions will be a pure bend similar to the bend of a prismatic rod in accordance with the hypothesis of the preservation of a two-dimensional shape for the cross sections and their rotation relative to the neutral axis and their normality to the elastic curve during bend. This case is well known; therefore, we shall begin with it.

Let us examine the bend of a plate by distributed bending moments applied along the contour:

Let the  $xy$  plane be combined with the middle surface of the plate until its deformation. The  $x$ - and  $y$ -axes will be directed, as shown in Fig. 4.15, along its edges. The upward direction is taken as the positive direction of the  $z$ -axis. Through  $\bar{M}_x$  we designate the bending moment per unit length acting along the edges parallel to the  $y$ -axis. Moments will be positive if they are directed, as shown in drawing, i.e., compression occurs on the upper surface of the plate and extension on the lower. The thickness of the plate,

is designated  $h$ ; we shall assume it to have a low value as compared with the other dimensions.

Fig. 4.15. Coordinate axes.



We shall examine an element taken from the plate, as shown in Fig. 4.16a, with two pairs of surfaces parallel to the  $xz$  and  $yz$  planes. Since distributed moments act on the plate contour (Fig. 4.15), only these moments will act at any point.

Let us assume that during bend the lateral faces of the element remain flat and turn relative to the neutral axes in such a manner that they remain normal to the curved middle surface of the plate. This means that the middle surface will not be subjected to stretching during the bend and that, consequently, the middle surface will be the neutral surface of the plate at the same time.

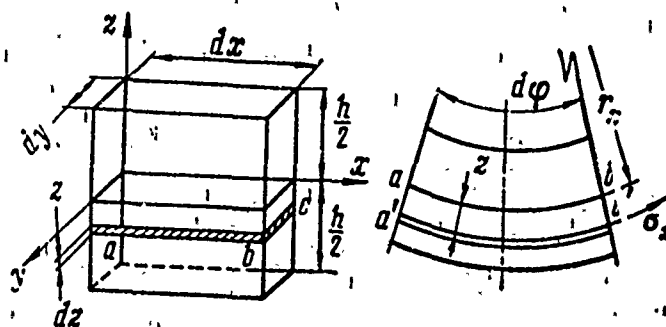


Fig. 4.16. Plate element.



We shall use Hooke's law for a two-dimensional stressed state:

$$\varepsilon_x = \frac{1}{E}(\sigma_x - \mu\sigma_y); \quad \varepsilon_y = \frac{1}{E}(\sigma_y - \mu\sigma_x),$$

or

$$\sigma_x = \frac{E}{1-\mu^2}(\varepsilon_x + \mu\varepsilon_y); \quad \sigma_y = \frac{E}{1-\mu^2}(\varepsilon_y + \mu\varepsilon_x).$$

Let  $1/r_x$  and  $1/r_y$  designate the curvature of the neutral surface in sections parallel, respectively, to planes  $xz$  and  $yz$ .

Let us find the relative elongations in directions  $x$  and  $y$  for elementary layer  $abcd$ , which is distance  $z$  from the neutral layer (Fig. 4.16b):

$$\varepsilon_x = \frac{\widetilde{a'b'} - \widetilde{ab}}{\widetilde{ab}} = \frac{(r_x + z)d\varphi - r_x d\varphi}{r_x d\varphi} = \frac{z}{r_x};$$

similarly  $\varepsilon_y = (z)/(r_y)$ .

We obtain stresses in the layer:

$$\left. \begin{aligned} \sigma_x &= \frac{Ez}{1-\mu^2} \left( \frac{1}{r_x} + \mu \frac{1}{r_y} \right); \\ \sigma_y &= \frac{Ez}{1-\mu^2} \left( \frac{1}{r_y} + \mu \frac{1}{r_x} \right). \end{aligned} \right\} \quad (4.9)$$

Thus, stresses  $\sigma_x$  and  $\sigma_y$  are proportional to the distance  $z$  of the  $abcd$  layer from the neutral surface and depend on the curvature of the curved plate. Stresses (4.9) caused bending moments  $M_x$  and  $M_y$ , which are applied to the plate (Fig. 4.16c):

$$M_x = \int_{-h/2}^{h/2} \sigma_x z dy dz; \quad M_y = \int_{-h/2}^{h/2} \sigma_y z dx dz.$$

We substitute the value of  $\sigma_x$  and  $\sigma_y$  and allow for the fact that  $\bar{M}_x = (M_x)/(d_y)$ ,  $\bar{M}_y = (M_y)/(d_x)$ . Then

$$\left. \begin{aligned} \bar{M}_x &= \frac{E}{1-\mu^2} \left( \frac{1}{r_x} + \mu \frac{1}{r_y} \right) \int_{-h/2}^{h/2} z^2 dz = \\ &= \frac{Eh^3}{12(1-\mu^2)} \left( \frac{1}{r_x} + \mu \frac{1}{r_y} \right); \\ \bar{M}_x &= D \left( \frac{1}{r_x} + \mu \frac{1}{r_y} \right) = D (w_x'' + \mu w_y''), \end{aligned} \right\} \quad (4.10)$$

similarly

$$\bar{M}_y = D \left( \frac{1}{r_y} + \mu \frac{1}{r_x} \right) = D (w_y'' + \mu w_x''),$$

where D is the cylindrical rigidity;  $D = \frac{Eh^3}{12(1-\mu^2)}$ ;

w is the deflection of the plate in the direction of the z-axis;

$$w_x'' = \frac{1}{r_x}; \quad w_y'' = \frac{1}{r_y}.$$

The expressions obtained enable us to conclude that the maximum stresses are obtained on the surface of the plate with the substitution of  $z = h/2$  into equation (4.9):

$$(\sigma_x)_{\max} = \frac{6\bar{M}_x}{h^2}; \quad (\sigma_y)_{\max} = \frac{6\bar{M}_y}{h^2}.$$

In the problem which we are studying,  $\bar{M}_x = \bar{M}_y = \bar{M}$ ; then

$$\begin{aligned} \varepsilon_x = \varepsilon_y = \varepsilon &= \frac{z}{r}; \quad \bar{M} = D \left( \frac{1}{r_x} + \mu \frac{1}{r_x} \right) = \\ &= \frac{D}{r} (1 + \mu) = \frac{Eh^3}{12r(1-\mu)}, \end{aligned}$$

i.e., the plate bends along a spherical surface whose curvature is defined by the quantity  $1/r_x = 1/r_y = 1/r$ . The stress  $\sigma_x = \sigma_y = \sigma = 6\bar{M}/h^2$ .

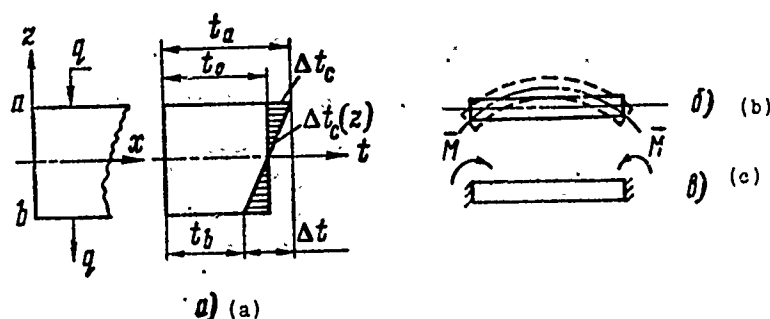


Fig. 4.17. Determining the temperature gradient.

Let us examine the deformation of a plate during thermal loading.

If we read the temperature from the middle surface of the plate, assuming that on one side it is heated and on the other cooled, it is natural to conclude that the thermal deformations of expansion and contraction will be proportional to the distance from the middle surface. Consequently, we arrive at the same deformation law as in the pure bend of a plate by bending moments.

If heat is supplied to and drawn from a plate which is uniformly heated to temperature  $t_0$ , as was shown in Fig. 4.17a, it can be established that in the steady thermal mode the temperature variation along the thickness will be linear, while the temperature of the plate's neutral surface will remain constant, i.e., be equal to  $t_0$ .

Such a temperature variation in a section causes analogous thermal deformation. These deformations in an unattached plate will be proportional to the distance from the middle surface; thus, the law of variation for thermal deformation is completely identical to the law of deformation with a pure bend by bending moments. Figure 4.17a shows the temperatures of a plate element during such heating.

In the calculation the following temperature gradient will be encountered:  $\Delta t_c(z)$ ,  $\Delta t$  and  $\Delta t_c$ , determined according to the formulas

$$\left. \begin{aligned} \Delta t_c(z) &= t - t_0; \\ \Delta t_c &= t_a - t_0; \quad \Delta t_c = t_b - t_0; \\ \Delta t &= t_a - t_b = 2\Delta t_c, \end{aligned} \right\} \quad (4.11)$$

where  $\Delta t_c(z)$  is the current value of the temperature gradient along a panel cross section;

$\Delta t_c$  is the limiting value of the temperature gradient along a panel cross section which, for the problem studied, is identical on both surfaces (a and b) and differs only in sign;

$\Delta t$  is the total temperature gradient - the difference in temperatures of surfaces a and b of the panel.

This gradient is easily determined experimentally. The strained and stressed state of such a panel, free from support or attachment, is easy to find.

The thermal deformation of a section is

$$\Delta t(z) = \frac{\Delta t}{2} z \frac{1}{h/2} = \frac{\Delta t z}{h};$$

$$\epsilon_t = \alpha \Delta t(z) = \frac{\alpha \Delta t z}{h}.$$

Such a panel will be zero since there is no containment by these deformations (Fig. 4.17b). Obviously, thermal stresses arise when thermal deformations are contained. Let us examine the extreme case when a panel is rigidly attached along the perimeter. In the attachment reactive moment arises (Fig. 4.17c)  $\epsilon = 0$ ;  $\epsilon = -\epsilon_t$ ; if we equate the known values of  $\epsilon$  and  $\epsilon_t$ , we obtain

$$\frac{z}{r} = -\frac{\alpha \Delta t z}{h}, \quad \text{hence} \quad \frac{1}{r} = -\frac{\alpha \Delta t}{h};$$

then

$$\bar{M} = -\frac{D(1+\mu)}{r} = -\frac{Eh^3(1+\mu)}{12(1-\mu^2)} \frac{\alpha \Delta t}{h} = -\frac{Eh^2 \alpha \Delta t}{12(1-\mu)},$$

hence

$$\sigma = \frac{6\bar{M}}{h^2} = -\frac{E\alpha \Delta t}{2(1-\mu)} = -\frac{E\alpha \Delta t_c}{1-\mu}. \quad (4.12)$$

As is apparent from the formula, the stresses are identical to stresses occurring in rod elements. The factor  $1/(1-\mu)$  shows that our element is a plate.

Let us examine what kind of stress and strain state there will be in a panel if the temperature along its cross section changes according to a more common but linear law.

The law of temperature variation shown in Fig. 4.18a differs from the earlier examined law in that the neutral surface of the plate is heated.

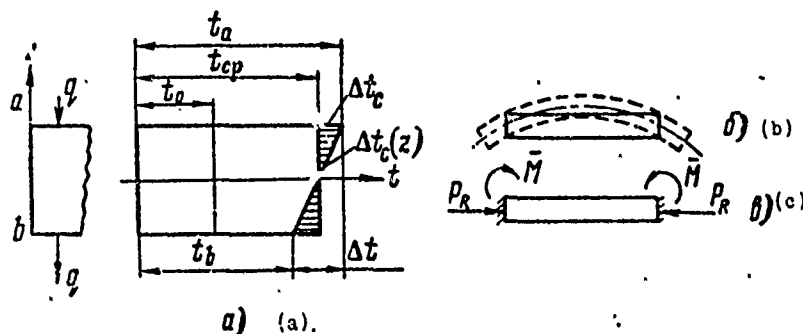


Fig. 4.18. Determining stresses in a plate.

Let us examine the stresses and strain of surface a when the panel is free from attachment. The temperature gradient will be equal to the sum of the two values.

$$\Delta t = t_a - t_0 = t_{cp} + \Delta t_c - t_0 = \Delta t_{cp} + \Delta t_c,$$

where  $\Delta t_{cp}$  is the gradient occurring on the neutral surface of the panel as a result of its heating. Thermal strain is

$$\varepsilon_t = \alpha \Delta t = \alpha \Delta t_{cp} + \alpha \Delta t_c.$$

Stresses in the panel  $\sigma_0 = 0$ , since  $\varepsilon = \varepsilon_t + \varepsilon_y = \varepsilon_t$ . The shape of the panel after warmup is shown in Fig. 4.18b by dashes.

The limiting value of thermal stresses is found if the panel is rigidly fixed. Then if we examine surface a,

$$\varepsilon_x = 0; \quad \varepsilon_y = -\varepsilon_t; \quad \varepsilon_y = -\alpha \Delta t_{cp} - \alpha \Delta t_c.$$

Stress

$$\sigma = -\frac{E\alpha\Delta t_{cp}}{1-\mu} - \frac{E\alpha\Delta t_c}{(1-\mu)}. \quad (4.13)$$

For surface b

$$\sigma = -\frac{E\alpha\Delta t_{cp}}{1-\mu} + \frac{E\alpha\Delta t_c}{(1-\mu)}.$$

b) The bend of a free plate with an arbitrary law of temperature variation for the cross section (Fig. 4.19). The strained state of the plate depends on the temperature gradient on its surface and through its cross section. With a complex nonlinear law of temperature variation in the cross section, thermal stresses in a free plate will not be zero. The temperature gradient in the cross section  $\Delta t(z) = t - t_0$ .

Then instead of  $\Delta t(z)$  we shall write  $\Delta t$ . In order to find the stresses nearer the edge of the plate, we proceed in accordance with the general rules examined above.

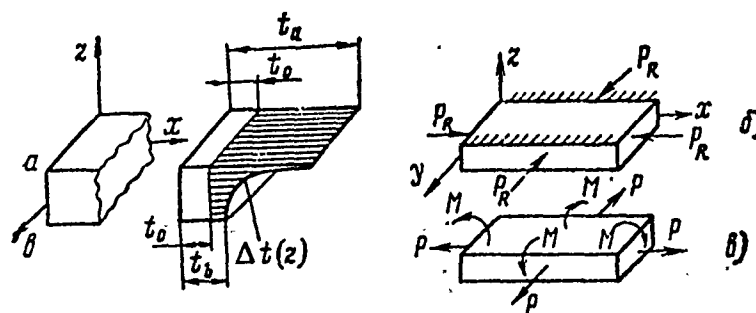


Fig. 4.19. Determining stresses in a plate.

After attaching a cold plate rigidly along the edges (Fig. 4.19b), we heat it. Compressive stresses will arise:

$$\sigma_{x1} = \sigma_{y1} = \sigma_1 = -\frac{Ea\Delta t}{1-\mu},$$

and in the attachment there will be the forces and moments of free action  $P_x$ ,  $P_y$ ,  $M_x$ ,  $M_y$ . In order to ensure the boundary conditions of a free plate, we apply the forces  $P_x$  and  $P_y$  to its edges; we obtain near its attachment the tensile stress

$$\sigma_{x2} = \frac{P}{F} = \frac{1}{(1-\mu)F} \int_{-h/2}^{h/2} Ea\Delta t b dz,$$

where  $F = bh$ .

The formula for  $\sigma_{y2}$  will be similar.

Let us note that for a rectangular plate  $\sigma_{x2}$  can be unequal to  $\sigma_{y2}$ . After applying bending moments  $M_x$  and  $M_y$  which compensate the asymmetry of the temperature field, we obtain the stress

$$\sigma_{x3} = \frac{M_z}{J} = \frac{z}{(1-\mu)J} \int_{-h/2}^{h/2} E\alpha\Delta t b z dz.$$

The value of  $\sigma_{y3}$  is written similarly; thus, finally,

$$\sigma_{x1} = -\frac{E\alpha\Delta t}{1-\mu} + \frac{1}{(1-\mu)F} \int_{-h/2}^{h/2} E\alpha\Delta t b dz \cdot \frac{z}{(1-\mu)J} \int_{-h/2}^{h/2} E\alpha\Delta t b z dz. \quad (4.14)$$

The safety factor of the plate is

$$n = \frac{\sigma_{n.t.}}{\sigma_{l \max}}, \text{ where } \sigma_l = \sqrt{\sigma_x^2 + \sigma_y^2 - \sigma_x \sigma_y}.$$

#### 4.2. HEAT EXCHANGE EQUIPMENT

As was shown in Chapter III, the thermal energy obtained in any energy source (for example, in a nuclear reactor) goes into heating the working medium and obtaining vapor which drives the steam turbine and the electrical generator connected with it. Such a power cycle of converting thermal energy until electrical is not possible without a continuous heat supply from the energy source to the receiver. Energy transfer can be effected directly by the working medium (heat transfer agent), but more frequently it is performed in heat exchange equipment with the aid of a heating and a heated transfer agent.

Based on the type of thermal process, heat exchange equipment can be divided into the following three groups.



Heat exchangers in which the heat transfer agents do not undergo a change in aggregate state (regenerators, coolers of gas turbines).

Condensers and evaporators in which one of the heat transfer agents changes aggregate state. In the first case, the heating transfer agent is condensed and in the second the heated agent is evaporated (condensers of steam turbines, regenerative preheaters, various evaporators).

Condensers-evaporators in which both heat transfer agents undergo a change in aggregate state; condensation of the heating agent and evaporation of the heated agent occur.

As heat transfer agents in space power plants, as a rule, liquid metals are used (mercury, sodium, potassium, sodium and potassium alloy, lithium, bismuth, lead, lead and bismuth alloy, etc.).

Liquid-metal heat transfer agents have relatively high boiling temperatures, which makes it possible to maintain low pressures in the power plant loops. This is particularly important for space power plants where heat removal is possible only at high temperatures. Moreover, the extremely high intensity of heat exchange in liquid metals provides high power output from a unit volume of the reactor core. Liquid metals, as simple substances, are not subject to decomposition and allow a virtually unlimited increase in the temperature and intensity of irradiation in the installation.

On the other hand, the high necessary temperatures of the liquid-metal heat carriers and the requirement to provide high reliability for heat exchangers intended for extraterrestrial power units (because of their operation without servicing for a long period of time) leads to strict requirements on the design of heat exchanging equipment.

This equipment should ensure the most effective process of heat transfer with the minimum design weight and acceptable hydraulic

resistance in the channels, as well as high reliability during prolonged operation.

Operational reliability is achieved by an absolute seal to prevent the mixing of the heat transfer agents in the first and second loops. This is connected with the induced  $\gamma$ -activity acquired by the heat carrier of the first loop in transit through the reactor as a result of the action of neutron flows. Furthermore, with a breakdown in the coating density of the nuclear reactor fuel elements, the heat carrier of the first loop can be loaded by nuclear fuel fission fragments.

Through the active reactor core, along with the heat carrier, pass the products of the corrosion and erosion of the structural elements of the first loop. The radioactive isotopes formed in this case can settle on the walls of the piping and the heat exchanger, raising the radioactivity of the loop (to control this phenomenon in the first loop a special purification system for the heat transfer agent is usually provided).

Strict requirements for the seal of heat exchange equipment are also dictated by the danger of the contamination of the heat carrier in the first loop by foreign matter from the power loop, which can cause a breakdown in reactor operation.

To provide a seal for the heat exchange equipment during prolonged operation it is recommended to weld all connections. Seal is ensured by the selection of appropriate manufacturing procedures and quality inspection methods (operational control) for the welded joints. To check the seal vacuum tests are made on the item as a whole and the welds are inspected with a helium leak detector or by other means.

Most frequently damage appears at the location of welds on pipes as a result of thermal stress occurring during operation. Therefore, in addition to quality welding technique, it is necessary to provide structural measures reducing these stresses to a minimum

which is done by introducing into the design various compensators for thermal strains.

It goes without saying that the materials of heat exchange equipment should satisfy the requirements of compatibility with heat carriers and possess good weldability, high thermal conductivity, and sufficient strength.

#### Structural diagrams of heat exchange equipment

In nuclear space installations recuperative (surface) heat exchange equipment is used, as a rule.

There are various structural diagrams for heat exchangers. The simplest is the pipe-in-pipe (Fig. 4.20, 4.21, 4.22). Such heat exchangers have only one channel for passage of the heating and the heated transfer agents. Equipment of this type with straight pipes can be rigid (Fig. 4.20a), with compensation by flexible elements (Fig. 4.20b) for the difference in lengths and with the use of a reverse heat exchange pipe (Fig. 4.21).

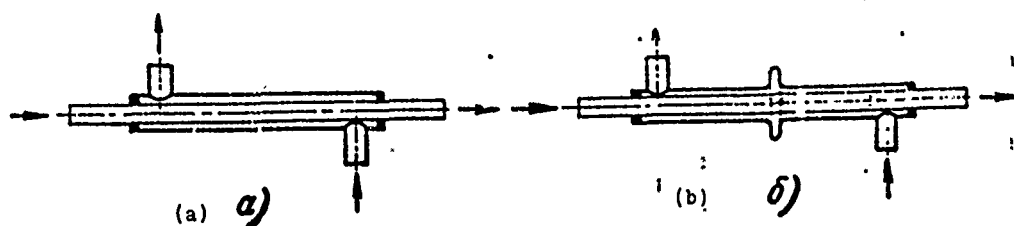


Fig. 4.20. Straight pipe-in-pipe heat exchanger:  
a - without compensator; b - with compensator.

Equipment with bent pipes can be of different designs. The simplest is the U-shaped design (Fig. 4.22a) and the design in the form of flat (Fig. 4.22b) and spiral coils.

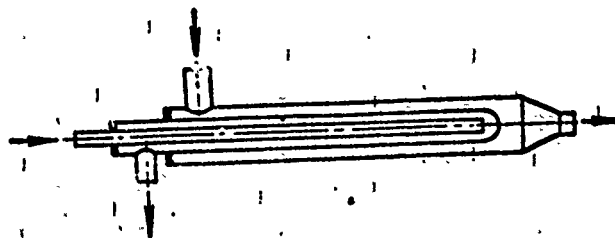


Fig. 4.21. Heat exchanger with single reverse heat exchange pipe.

Jacket-and-pipe heat exchange equipment is a development of the pipe-in-pipe equipment. Taking into account the increase in the pipe cross section, the flow rate of the heat transfer agent and the power are also increased. Just as the pipe-in-pipe equipment, the jacket-and-pipe heat exchanger with straight tubes can be rigid (Fig. 4.23) with compensation for the thermal elongation by flexible elements (Fig. 4.24a), with a floating head (Fig. 4.24b) and with reverse heat exchange tubes (Fig. 4.24c).

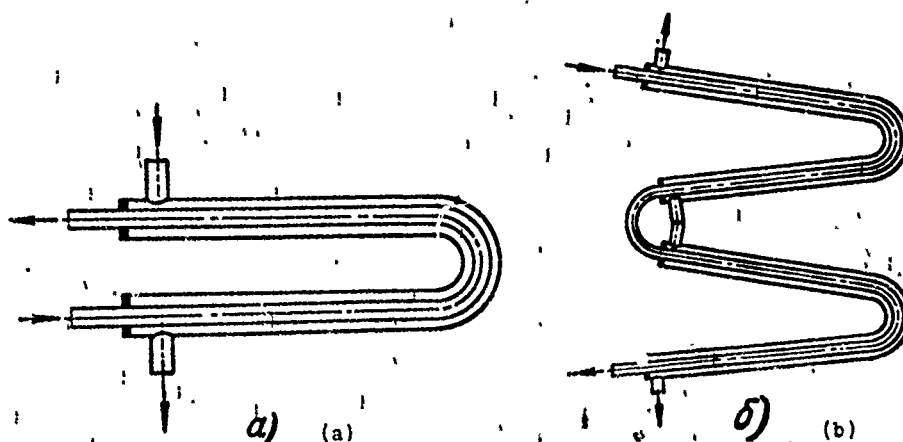


Fig. 4.22. Pipe-in-pipe heat exchanger: a - U-shaped; b - in the form of a flat coil.

Equipment with bent pipes must have U-shaped pipes, a common pipe panel and cylindrical jacket (Fig. 4.25a); U-shaped pipes and

a U-shaped jacket (Fig. 4.25b);  $\Pi$ -shaped pipes (Fig. 4.25c); pipes arranged between the parallel pipe panels in a cylindrical jacket and having a sinusoidal bend (Fig. 4.25d); flat coils (Fig. 4.26a) and spiral coils (Fig. 4.26b).

Fig. 4.23. Jacket-and-pipe heat exchanger with straight pipes of rigid construction.

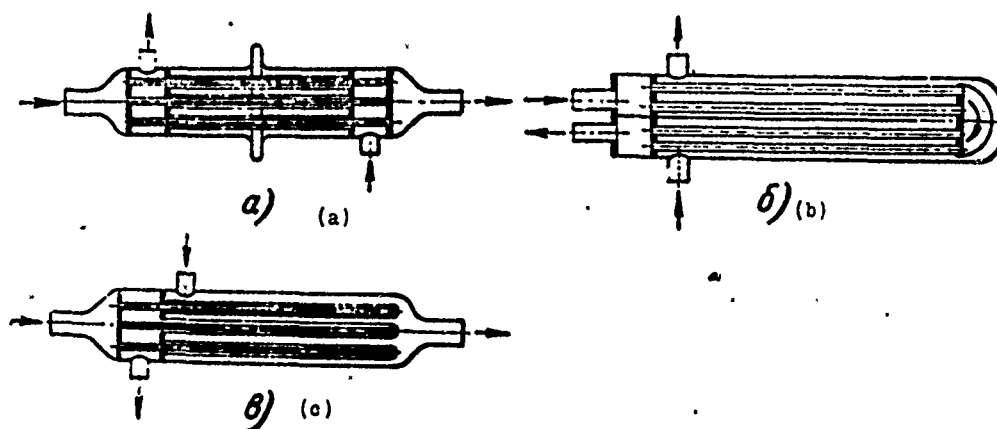
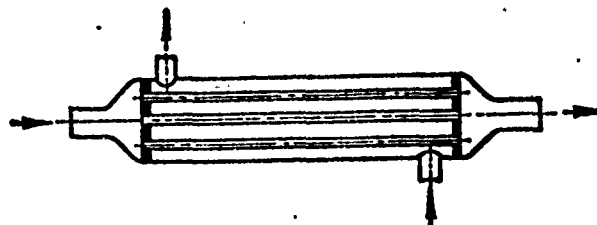


Fig. 4.24. Jacket-and-pipe heat exchangers with compensation for thermal elongations: a - with pipe covers and compensator on jacket; b - with floating head; c - with reverse heat exchange pipes.

To increase heat removal and heat exchange effectiveness we can develop the heat exchange surface by increasing the perimeter and length of the channels separating one heat exchange agent from the other or by changing the shape of the channels (Fig. 4.27) and increasing their number or yet by forming an additional surface with ribs, pins, coils, etc., (Fig. 4.28). The effectiveness of

the additional surface depends on its geometric shape, the heat conductivity of the material, and the method of joining elements to the main surface.

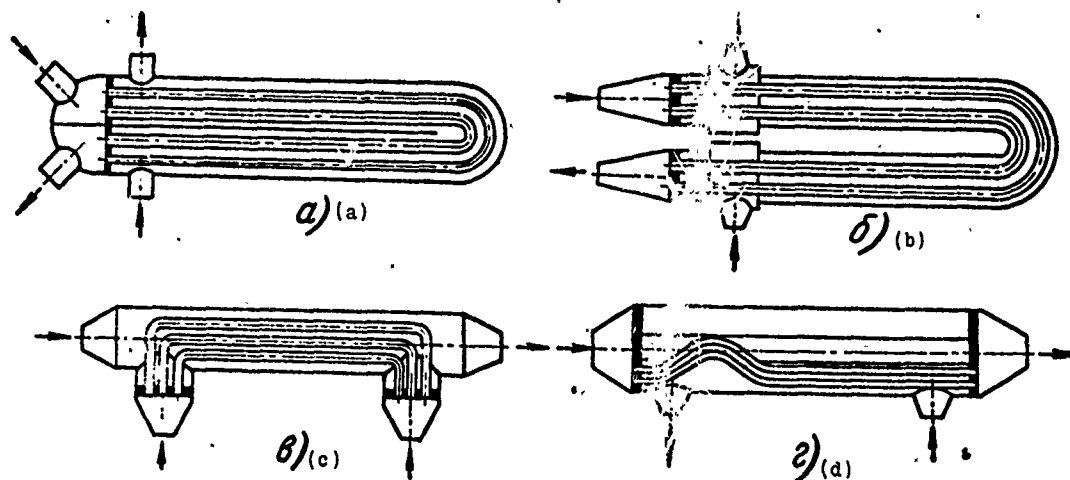


Fig. 4.25. Jacket-and-pipe heat exchangers with bent pipes: a - with U-shaped pipes and a common pipe panel; b - with U-shaped pipes and a U-shaped jacker; c - with Π-shaped pipes; d - with sinusoidal bend.

For this purpose there are installed longitudinal and lateral fins of various shapes (Fig. 4.24b, 4.29) or pipe covers which increase the path of the heat exchange agent in the interpipe space (in the first case) or increase the rate of flow of the pipes with the heat carrier of another loop.

In order to ensure the normal operation of a heat exchanger under weightless conditions during space flight, devices for twisting the heat carrier are found in each tube.

All these measures increase the heat transfer coefficient and reduce the size and weight of the heat exchanger.

The mechanical strength of heat exchanger design is affected by thermal elongations of the parts, thermal shocks and vibrations, particularly during alternating modes and emergency jettisoning of load, (the heat carrier temperature variation occurs much more rapidly in nuclear installations, in some cases, than in ordinary power systems). Therefore, in the design of the nodes, compensation for thermal elongation must be provided. This can be done in various ways:

- installing a compensator on the housing (see Fig. 4.24a);
- connecting the pipe panels to the housing through flexible elements (Fig. 4.30);
- using a "floating" pipe panel (see Fig. 4.21b);
- using reverse heat exchange pipes (see Fig. 4.21, 4.24c);
- using U-shaped pipes in cylindrical (see Fig. 4.25a) or in U-shaped (see Fig. 4.25b) housings;
- by giving the pipes a bent shape for self-compensation in operating conditions (see Fig. 4.25c, 4.25d).

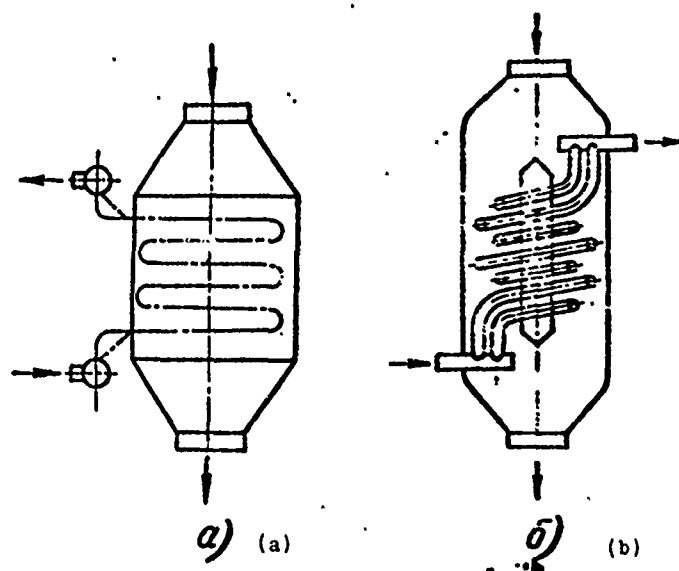


Fig. 4.26. Jacket-and-pipe heat exchangers: a - with flat coils; b - with spiral coils.

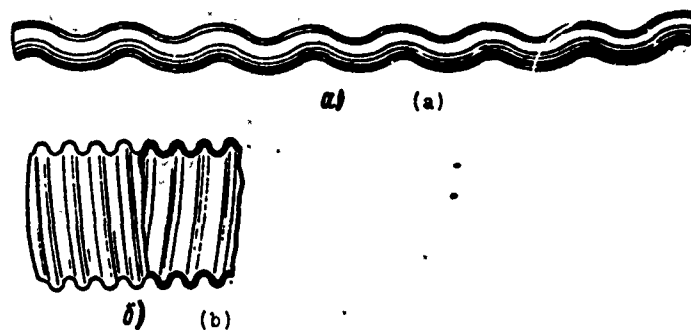


Fig. 4.27. Increasing the surface of the channels:  
a - by distorting the channel axis; b - by radial  
corrugation.

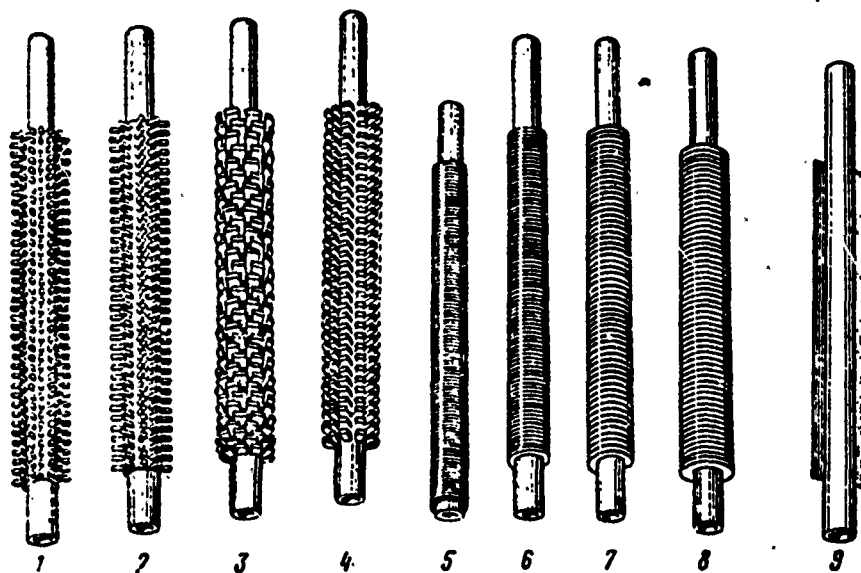


Fig. 4.28. Different methods of increasing pipe surface:  
1 - circular pins with a staggered arrangement; 2 - circular  
pins with a corridor arrangement; 3 - elliptical pins with  
a staggered arrangement; 4 - elliptical pins with a corridor  
arrangement; 5 - short disk ribs; 6 - high disk ribs; 7 -  
short spiral ribs; 8 - high spiral ribs; 9 - smooth pipe  
with two longitudinal ribs.



All the welding seams on the pipes must be butt-welded for the convenience of quality check using x-ray and gammagraph equivalent.

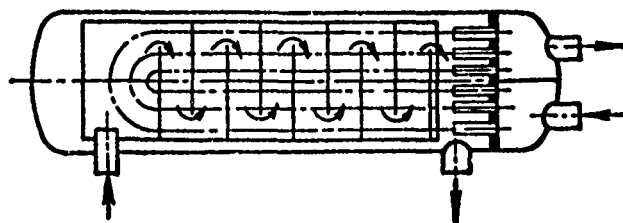
Thermal shocks occurring during the emergency jettisoning of the load are usually a threat to the pipe and housing joints of the heat exchanger. Therefore, branching should be done by extending a short branch from the main tube, to which the drain is butt-welded (Fig. 4.31). Drain pockets can also be made in a similar manner. Branch pipes with jackets are used as a protective measure (Fig. 4.32).

Welding elements which differ considerably in thickness adds to the complexity of the manufacture of heat exchange equipment. With a thickness ratio greater than 4:1 for the welded elements, there is a danger of burning up the thin wall and insufficiently burning the solid section.

Such a connection is the welding of the pipes to the pipe panels. Figure 4.33 shows some methods of welding. The best is joint II. With a pipe wall thickness less than 2-3 mm argon-arc welding is performed with a tungsten electrode using method III.

Method I gives the highest quality welding, but it requires tedious mechanical processing of the pipe panel under the weld. Moreover, such a joint is suitable only for flat pipe panels.

Fig. 4.29. Jacket-and-pipe heat exchanger with lateral partitions for ensuring the movement of the medium and the inter-pipe space.



Joint IV can be recommended during the repair of equipment when the earlier applied seam must be completely removed.

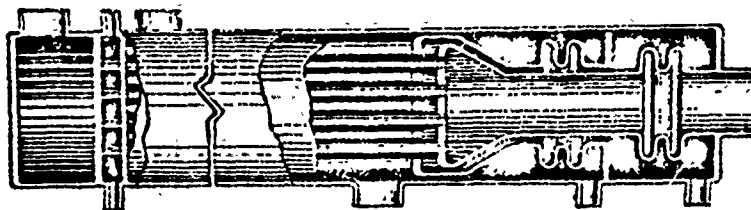


Fig. 4.30. Heat exchanger with the connection of the pipe panels to the housing through flexible elements.

After welding, the pipes are expanded to the full depth of the pipe panel to ensure good thermal contact and prevent the formation of slot corrosion.

To protect the reactor core from soil the internal surface of the heat exchangers must be made with a high degree of purity. For this purpose, in the design of heat exchange equipment only those materials can be used which have, in addition to acceptable strength properties, resistance to corrosion under the long use of heat transfer agents. The composition of the inert gas (argon) used during welding must be monitored since the degree of argon purity determines the quality of the welding of a seam.

After preparing all internal surfaces the equipment must be carefully screened of welding traces, dirt, and grease by mechanical cleaning, degreasing (dichloroethane or other solvent), rinsing, and drying.

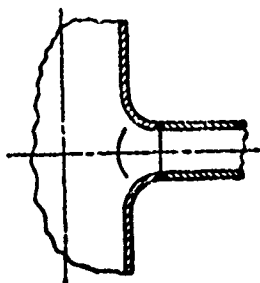


Fig. 4.31. Welding pipe drains to the main pipe.

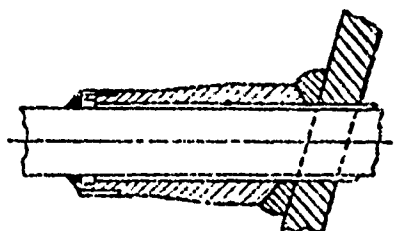


Fig. 4.32. Branch pipe with jacket.

In the design of a heat exchanger there must be provided special lines for rinsing all cavities. Drainage and filler tubes must be arranged so as to eliminate the formation of gas pockets during the filling of the heat exchanger with the heat carrier.

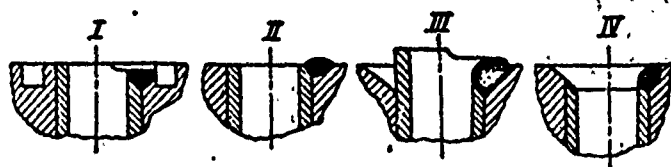


Fig. 4.33. Welding pipes to pipe panels.

As an example of the heat exchange equipment made for space power plants, let us examine the steam generator of an energy conversion system [50]. The mercury steam generator (Fig. 4.34) with a thermal capacity of approximately 50 kW is designed to heat, evaporate, and superheat 0.141 kg of mercury per second. The steam generator is made in a single-flow design and serves to obtain dry superheated vapor both in earth's gravity and in weightless condition. This steam generator is a jacket-and-pipe design; seven pipes through which mercury flows are enclosed in a pipe (jacket) 51 mm in diameter, filled with a sodium and potassium alloy. To improve heat exchange under weightless conditions the steam generator is made in the form of a spiral. In addition, devices are installed for twisting the mercury.

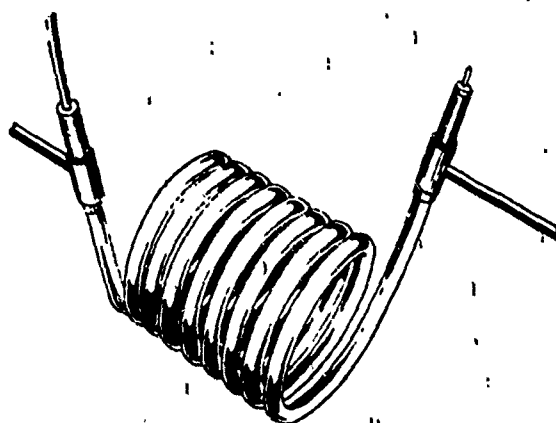


Fig. 4.34. Pipe-in-pipe steam generator in the form of a spiral coil.

In one version of steam generator an average heat flux of  $31.4 \text{ kW/m}^2$  was obtained during the boiling of the mercury.

### Materials for heat exchange equipment

Materials acceptable for heat exchange equipment in nuclear power plants must satisfy the following conditions:

- be corrosion- and erosion-resistant in the medium of the heat transfer agent;
- have high mechanical properties at a given thermal mode;
- possess high oxidation-resistance and stability under operating conditions at high temperature;
- weld well and undergo mechanical processing well;
- have satisfactory thermophysical characteristics, particularly a high heat conductivity factor;
- be sufficiently inexpensive.

These requirements are less strict than the requirements on the materials of reactors which operate at higher temperatures; however, they are more strict than the requirements on materials of heat exchange equipment for common power purposes.

If the heat exchange equipment is located in the reactor housing or within its shield, there is also a requirement for radiation resistance.

At temperatures below  $500^\circ\text{C}$  most of the acceptable liquid-metal heat carriers have an insignificant effect on the structural materials. At higher temperature the question of material selection is much more complex to solve.

The strength of materials in a liquid-metal medium is strongly affected by various impurities in the heat transfer agent (particularly oxygen and nitrogen) and also by the considerable temperature drop in the circulatory loop of the heat carrier, which causes intensified mass transfer in the system.

The following types of corrosion are distinguished:

- solution, which usually is accompanied by the precipitation of solutes on the colder section of the system (thermal mass transfer);
- the transfer of the components of one structural material to another through the heat-exchange fluid in systems of heterogeneous materials (isothermal mass transfer);
- the penetration of liquid metal inside the material.

In systems from austenitic stainless steel on alkaline liquid-metal heat carriers the thermal mass transfer becomes noticeable at 500-600°C with the temperature contrast in the system on the order of several tens of degrees. In this case corrosion damage is localized at points with maximum temperature and the rate of material solution is proportional to approximately  $v^{0.8}$  where  $v$  is the velocity of heat carrier motion. In systems with boiling liquid metal, solution and mass transfer develop to an even greater degree.

Thermal and isothermal mass transfer is intensified when oxygen exists in the liquid metal. In this case, in the system are formed both oxides of the liquid-metal heat carrier and complex oxides of the components of the structural material.

Many high-melting and heat-resistant metals (Nb, Mo etc.) are subject to strong oxidation. Therefore, in a liquid-metal heat carrier which is in contact with these metals oxygen content should not be above 0.0005%.

Let us introduce some of the most important recommendations concerning the main liquid metal heat carriers recently in use.

As compared with other heat carriers, alkaline metals are more aggressive with respect to structural materials; the corrosion resistance of materials in sodium, potassium, and their alloys differs little. Potassium facilitates a certain speed gain of mass transfer in loops of steel and alloys containing nickel. The most widespread materials in these media are stainless chrome-

nickel steel of the austenitic class, which can be used for continuous operation at temperatures up to 600°C. No more than 0.01% oxygen content is allowed in the heat carrier. These steels weld well and have other satisfactory technological properties.

At temperatures higher than 700°C it is possible to use oxidation-resistant and heat-resistant metals and alloys.

At temperatures of 800°C and above the use of refractory metals (tantalum, molybdenum, niobium, tungsten, vanadium) and alloys based on them is promising. It is necessary to watch that the oxygen content in the medium of the heat carrier is no more than 0.01%.

The presence of nitrogen in liquid metal impairs the anti-corrosion properties of high-melting structural materials.

At temperatures of 800-1000°C, for operation in a medium of alkali metals cermet materials based on tungsten carbides, tantalum, and titanium, can be used.

Lithium with respect to structural materials behaves more aggressively than sodium and potassium. The corrosion resistance of materials adversely affects the impurities, especially nitrogen and oxygen. The oxygen impurity begins to show when its content in the lithium is 0.5% and in the material is 0.02-0.05%. The nitrogen impurity is even more dangerous.

For operation in a lithium medium it is not recommended to use steel and alloys with a large nickel content. Stainless steels with a content of 15-18% Cr and 10-15% Ni, as well as austenitic alloys based on Cobalt and nickel, can be used at temperatures not higher than 500-600°C. At such temperatures and above (700-800°C) stainless ferrite and chrome steels (0Kh13, 1Kh13, 2Kh13, 1Kh12M2BF, Kh25T) without nickel are preferable. Steel 1Kh12MV<sup>4</sup>B has satisfactory durability at 800°C.

To clean lithium of the oxygen and nitrogen impurities hot traps with zirconium as an absorber are used, facilitating the deceleration of the structural material corrosion. Thus, for chrome steel with the use of traps the rate of corrosion is reduced by a factor of approximately 10.

To operate in a lithium medium the following high-melting alloys can be used; 99% Nb + 1% Zr; 99% Mo + 0.5% Ti; 74% W + 26% Re; 90% V + 8% Ti + 2% Hf.

#### Stress analysis of the elements of heat exchange equipment

For most elements of heat exchange equipment the main load is uniform internal or external pressure.

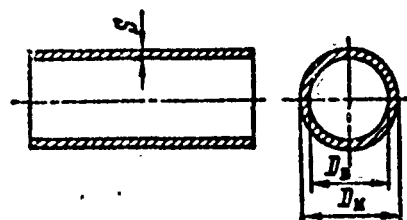
In addition, the vehicle is subject to the effect of additional loads - inertial loads connected with the injection of the vehicle into orbit, as well as forces and moments arising because of different thermal expansions in various parts of the vehicle. Stresses caused by the additional loads can sometimes exceed the stresses from the main load. To reduce the effect of these loads it is possible, for example, to install additional supports and compensators on the conduits, but sometimes it is necessary to increase the thickness of the element.

Loads can be constant, cyclic, or short-term. Therefore, during structural design the form of loading and the ability of the structural material to deform must be taken into account. The main elements of the heat exchange equipment operate, as a rule, under conditions of steady loads and are made from plastic materials. In this case, structural efficiency is more properly estimated according to maximum loads (the evaluation of strength under maximum stresses gives somewhat higher results).

However, if the loading is cyclic or the appearance of plastic zones in the metal is inadmissible (for example, because of corrosion

considerations) and also if deformations of any element are determined, the method of maximum loads can not be used. In this case, calculation is performed using the method of "elastic calculation" (i.e., on the assumption that the parts work in the elastic region) with the determination of maximum stresses.

Fig. 4.35. Circular cylindrical element.



For structural design it is necessary to know the service conditions of the equipment - its structural diagram, form, character, and value of loads (main and additional), as well as working temperatures (selected on the basis of thermal and gas-dynamics calculations), the structural material and its strength characteristics, taking into account operating temperatures and time under load.

Let us analyze the main structural elements in heat exchanging equipment.

1. A circular cylindrical element with internal pressure [29]. Wall thickness (in mm) is determined from formula (Fig. 4.35)

$$S = \frac{pD_s}{230\sigma_{\text{дог}} - p} + c, \quad (4.15)$$

or

$$S = \frac{pD_n}{230\sigma_{\text{дог}} + p} + c,$$



where  $p$  is the permissible working pressure,  $\text{daN/cm}^2$ ;

$\varphi$  is the strength factor of the cylindrical element (taking into account the weakening of the structure due to welding and also due to the perforations in both the circular and longitudinal directions);

$c$  is the wall thickness allowance (for corrosion, minus tolerance, etc.);

$\sigma_{\text{доп}}$  is the permissible stress of the structural material taking into account the operating conditions of the element;  $\sigma_{\text{доп}} = \eta \sigma_{\text{доп}}^*$ , here  $\sigma_{\text{доп}}^*$  is the nominal allowable stress for a given structural material,  $\text{daN/mm}^2$ , ( $1 \text{ daN/mm}^2 = 100 \text{ kN/m}^2$ );  $\eta$  is the correction factor, taking into account structural and operational peculiarities of the element and the method of stress analysis (in this analysis  $\eta = 1$ ).

The calculated strength factor  $\varphi$  of a cylindrical element is used for solid (not perforated) cylindrical elements equal to  $\varphi_{\text{св}}$  (strength factor of weld seam). The value of  $\varphi_{\text{св}}$  depends on the type of welding: with one-way hand welding  $\varphi_{\text{св}} = 0.7$ , one-way automatic welding 0.8, one-way hand welding with packing ring 0.9, hand welding with auxiliary welding from the top of the seam 0.95, automatic welding with bilateral penetration, 1.0. For the perforated cylindrical element there is also considered the weakening of the element in the longitudinal ( $\varphi_1$ ) and circular ( $\varphi_2$ ) directions.

Table 4.1.

(1) Допуск на толщину стенки, мм	А	
	(2) для камер	(3) для труб
-0,015	0,18	0,20
-0,010	0,11	0,15
-0,005	0,05	0,10

KEY: (1) Wall thickness tolerance, mm; (2) for chamber; (3) for pipe.

Allowance  $c$  for housing is usually 1 mm when  $S - c$  is no more than 20 mm. When  $(S - c) > 20$  mm  $c = 0$ . Allowance for chambers and pipes is determined from formula  $c = A(S - c)$ , where  $A$  is a numerical coefficient (see Table 4.1).

The permissible working pressure is determined from formula

$$p = \frac{230 (S - c) \varphi \sigma_{\text{nom}}}{D_n + (S - c)}$$

or

$$p = \frac{230 (S - c) \varphi \sigma_{\text{nom}}}{D_n - (S - c)}$$

Reduced stress is

$$\sigma_{np} = \frac{p [D_n + (S - c)]}{230 (S - c) \varphi}$$

or

$$\sigma_{np} = \frac{p [D_n - (S - c)]}{230 (S - c) \varphi}$$

Maximum permissible pressure of hydro tests is

$$p_{\text{max}} = 125 \varphi \sigma_s \frac{S - c}{D_n} \left( 1 - \frac{S - c}{D_n} \right),$$

where  $\sigma_s$  is the ultimate strength of the structural material.

Formulas presented of the above are valid under the condition:  
for housing and chambers  $1 + 2 (S - c) / (D_n) \leq 1.5$ ;  
for pipes  $(D_n) / (D_n - 2)(S - c) \leq 1.6$ .

Additional tensile (compressive) stress is

$$\sigma_p = \frac{Q}{100F},$$

where  $Q$  is the stretching (compressive) force on one element, daN;  
 $F$  is the cross-sectional area of the element,  $\text{cm}^2$ .

Secondary bending stress is

$$\sigma_n = \frac{M_n}{100W_n},$$

where  $M_n$  is the bending moment, daN·cm;  
 $W_n$  is the moment of bend resistance,  $\text{cm}^3$ .

Secondary stress from torque is

$$\tau = \frac{M_k}{100F_p},$$

where  $M_k$  is the torque, daN·cm;  
 $W_p$  is the resistance to torque,  $\text{cm}^3$ .

For a round section  $W_p = 2W_n$ .

The condition of strength in the presence of secondary loads is

$$(\sigma_p + 0,8\sigma_n)^2 + 3\tau^2 \leq (1,2\sigma_{\text{don}}^2 - \sigma_{np}^2).$$

2. A convex elliptical bottom under internal pressure [29].  
 Wall thickness is determined from formula (Fig. 4.36)

$$S = \frac{pD_n}{400 \sigma_{\text{don}} - p} \frac{D_n}{2h_n} + c, \quad (4.16)$$

where  $z = 1 - (d/D_n)$  is the coefficient allowing for the weakening of the bottom due to the opening.

In planning we must bear in mind that the distance from the edge of the opening to the edge of the bottom (measured according to projection) should not be less than  $0.1D_B + S$ . If there are several openings in the bottom, the distance between the edges of two neighboring openings (also measured according to projection) must not be less than the diameter of the smallest opening.

Allowance  $c$  is 3 mm when  $(S - c) \leq 10$  mm; 2 mm when  $(S - c) \leq 20$  mm; 1 mm when  $(S - c) \leq 30$  mm; when  $(S - c) > 30$  mm  $c = 0$ .

Permissible pressure is

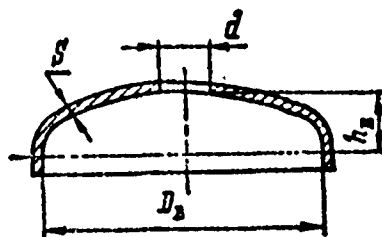
$$p = \frac{800(S - c) z \sigma_{\text{дон}}}{D_n + 2 \frac{h_n}{D_n} (S - c)} \frac{h_n}{D_n}.$$

Here  $\sigma_{\text{дон}} = \eta \sigma_{\text{дон}}^*$ ;  $\eta = 1.05$ .

Reduced stress is

$$\sigma_{np} = \frac{p [D_n + 2(S - c)] \frac{h_n}{D_n}}{800(S - c) z} \frac{D_n}{h_n}.$$

Fig. 4.36. Convex elliptical bottom.



Maximum permissible pressure of hydro test is

$$p_{\text{max}}^r = \frac{300(S - c) z \sigma_n}{D_n + 2 \frac{h_n}{D_n} (S - c)} \frac{h_n}{D_n}.$$

Calculation formulas are valid under the condition:

- a) for bottoms without openings  $0.2 \leq (h_B)/(D_B) \leq 0.3$ ;
- b) for bottoms with openings  $0.2 \leq (h_B)/(D_B) \leq (0.3)/(z) \leq 0.5$ .

If  $(h_B/D_B) > 0.3$ , the wall thickness of the bottom is determined according to the strength conditions of the bottom's rim.

3. Round pipe grid (panel) [32]. Reduced thickness of pipe grid is

$$S_{np} = S \sqrt[3]{\varphi}, \quad (4.17)$$

where  $\varphi = 0.9(1 - 0.905(d^2)/(t^2))$  with triangular division (Fig. 4.37a);

$\varphi = 0.9(1 - 0.785(d^2)/(t^2))$  with squared division (Fig. 4.37b);  
 S is the minimum actual thickness of the grid.

a) Pipe grid with U-shaped bundle of pipes (see Fig. 4.25a).  
 Maximum stress in center of pipe wall is

$$\sigma_{max} = 3.1 \cdot 10^{-3} p \left( \frac{D}{S_p} \right)^2.$$

Minimum actual wall thickness is

$$S = \frac{D}{\sqrt[3]{\varphi}} \sqrt{\frac{3.1 \cdot 10^{-3} p}{\sigma_{don}}}.$$

b) Fixed pipe grid (wall) - straight pipe bundle - floating pipe wall (see Fig. 4.24b). Maximum stress

$$\sigma_{max} = \frac{6M_{max}}{S^2 \varphi^{2/3}},$$

where  $M_{\max}$  is the maximum bending moment which can be determined from Table 4.2 as the function of the parameter of system compliance  $\epsilon$ .

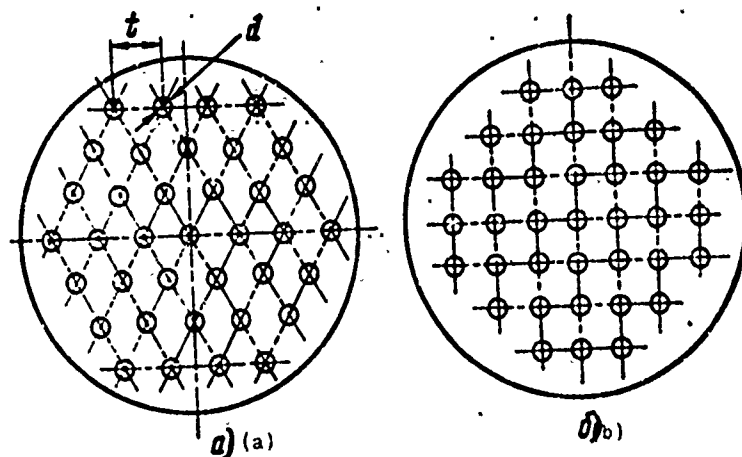


Fig. 4.37. Arrangement of openings in pipe grid (panel):  
a - triangular division; b - squared division.

Table 4.2.

$\epsilon$	(1) Трубная решетка (доска)		$\epsilon$	(1) Трубная решетка (доска)	
	фиксированная	плавающая		фиксированная	плавающая
	(2)	(3)		(2)	(3)
	$4M_{\max}' p D^2$			$4M_{\max}' p D^2$	
0,5	0,128	0,207	6	0,0280	0,0456
1	0,127	0,206	7	0,0208	0,0388
2	0,112	0,178	8	0,0156	0,0322
3	0,0853	0,112	9	0,0153	0,0291
4	0,0570	0,0726	10	0,0146	0,0258
5	0,0386	0,0556			

KEY: (1) Pipe grid (panel); (2) Fixed; (3) Floating.

The compliance parameter is determined from formula

$$\varepsilon = 1,28 \frac{D}{S_{np}} \sqrt[4]{\frac{d_{cp}}{l_r} \frac{S_r}{D} \frac{S_{rp}}{D} \frac{n}{\varphi} \frac{E_r}{E_p} (1 + \psi)},$$

where  $d_{cp}$  is the average diameter of the pipes;

$l_r$  is pipe length;

$D$  is the average diameter of the housing;

$n$  is the safety factor;

$E_r$  and  $E_p$  are the moduli of elasticity for the material of the pipes and the panel, respectively, daN/cm<sup>2</sup>;

$$\psi = \left( \frac{S_{max}}{S_{\phi m c}} \right)^3.$$

Minimum effective panel thickness is

$$S = \sqrt[3]{\frac{6M_{max}}{\sigma_{\phi m c}^{2/3}}}.$$

c) Two fixed pipe grids of one thickness (see Fig. 4.23).

Maximum stress is

$$\sigma_{max} = \frac{6M_{max}}{S^2 \varphi^{2/3}}.$$

Maximum bending moment is

$$M_{max} = \frac{D^2 p}{400} \left[ 1 - \frac{d^2 n}{D^2} - 4 \frac{d_{cp} S_r n E_r}{D^2 p} (\alpha_r t_r - \alpha_k t_k) + \frac{\varepsilon^4}{2} \right] f(\varepsilon),$$

where

$$\varepsilon = 1,52 \frac{D}{S_{rp}} \sqrt[4]{\frac{d_{cp}}{l_r} \frac{S_r}{D} \frac{S_{rp}}{D} \frac{n}{\varphi} \frac{E_r}{E_p}};$$

$$\varphi = 0,37 \varphi \frac{l}{D} \frac{S_{np}}{S_k} \frac{S_{np}^2}{DS};$$

$E_T$  and  $E_p$  are the moduli of elasticity for the material of the pipes and the pipe grid;

$S_H$  is the housing wall thickness;

$\alpha_T$  and  $\alpha_H$  are the coefficients of linear expansion for the pipes and the housing, respectively.

Function  $f(\epsilon)$  is determined from Table 4.3 as a function of  $\epsilon$  and  $\beta$ .

Minimum effective panel thickness is

$$S = \sqrt{\frac{6M_{\max}}{\sigma_{\lambda 0} \varphi^{2/3}}}$$

Table 4.3.

$\epsilon$	$f(\epsilon)$		$\epsilon$	$f(\epsilon)$	
	$\beta=0$	$\beta=0,015$		$\beta=0$	$\beta=0,015$
0	0,205	0,204	4	0,020	0,012
1	0,200	0,190	5	0,015	0,005
2	0,140	0,120	6	0,010	0,001
3	0,040	0,030	7	0,007	0

Stability analysis of thin-wall cylindrical shells under the effect of compressive loads

Critical lengths can be determined from formula [12]

$$L_{kp} = 1,642 \sqrt{1 - \mu^2} D \sqrt{\frac{D}{S}} \quad (4.18)$$

or from the graph in Fig. 4.38.

Case 1. The shell is loaded with external force (Fig. 4.39).



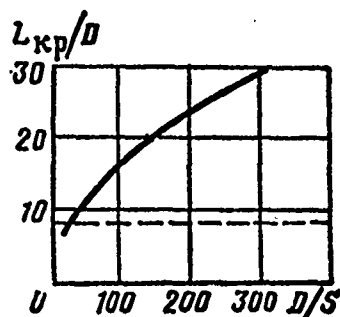


Fig. 4.38. Graph for determining critical lengths of cylindrical shells.

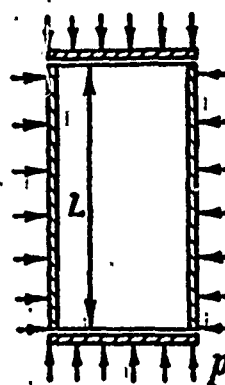


Fig. 4.39. Thin-wall circular cylindrical shell under the effect of compressive loads.

a) Critical external shearing pressure (theoretical) for a long shell ( $L > L_{kp}$ ) can be determined from Bresse's formula [36]:

$$p_{kp}^r = \frac{E^t}{4(1-\mu^2)} \left( \frac{S}{r} \right)^3, \quad (4.19)$$

where  $r$  is the radius of the shell.

b) Critical comprehensive external pressure (theoretical) for a short shell  $L < L_{kp}$  can be determined from Mises' formula [36]:

$$p_{kp}^r = \frac{E^t S}{r} \frac{1}{\left( n^2 + \frac{1}{2} \frac{r^2 r^2}{L^2} \right)} \times \left[ \frac{1}{\left( \frac{n^2 L^2}{\pi^2 r^2} + 1 \right)} + \frac{S^2}{12(1-\mu^2)r^2} \left( n^2 + \frac{r^2 r^2}{L^2} \right)^2 \right]. \quad (4.20)$$

The positive integer  $n$  is selected so that  $p_{kp}^r$  has the lowest value. The approximate value of  $n$  can be determined from the graph (Fig. 4.40) or from approximate formula [12]

$$n^2 = \frac{\pi \cdot D}{L} \sqrt{\frac{0.75 D \sqrt{1-\mu}}{S}}$$

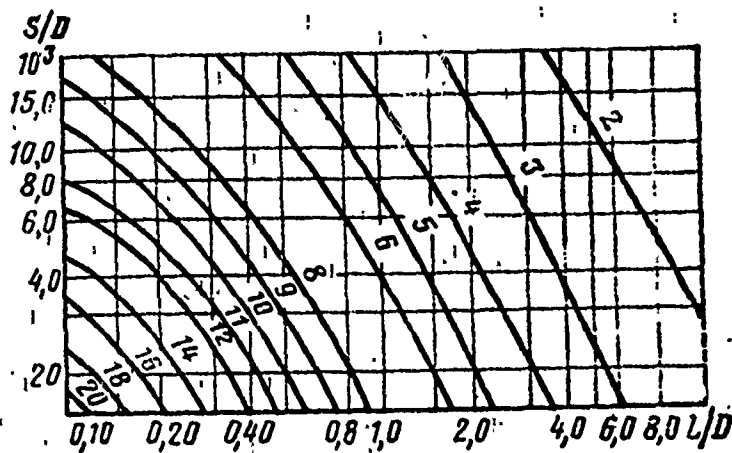


Fig. 4.40. Graph for determining value of  $n$ .

Case 2. The shell is loaded with an axial load (Fig. 4.41).

a) The critical axial force (according to Euler) for a very long shell ( $L_1 > 40D$ ) is

$$P_{np} = \frac{\pi^3 (D_n^4 - D_n^4) E'}{64 L_{np}^2}$$

where  $L_{np}$  is the reduced length;  $L_{np} = L$  with free support on the ends;  $L_{np} = L/2$  with restrained ends.

b) Critical stress with axial compression for a short shell can be determined from Alekseyev's formula [33]:

$$\sigma_{np} = 2.35 E' \left( \frac{S}{r} \right)^{3.2} \quad (4.21)$$

Case 3. The shell is loaded simultaneously by axial compressive stress  $\sigma$  and lateral pressure  $p$  (Fig. 4.42).

The stability condition for this case [33]

$$\frac{\sigma}{\sigma_{kp}} + \frac{p}{p_{kp}^T} \leq 1,$$

where  $\sigma_{kp}$  is determined from formula (4.21),  $p_{kp}^T$  from formula (4.19) or formula (4.20).

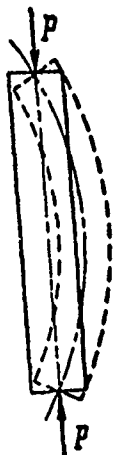


Fig. 4.41. Stability losses in a long shell over the action of axial force.

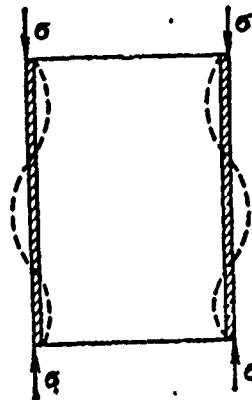
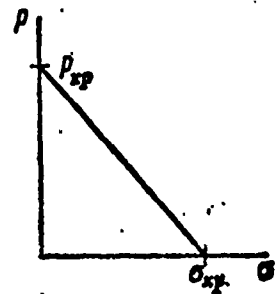


Fig. 4.42. Stability losses in a cylindrical shell with the joint action of lateral pressure and axial compressive stresses.



Case 4. The shell is loaded along the ends by bending moment (pure bend) only, as shown in Fig. 4.43.

Critical stress [11] is

$$\sigma_u = 0,22E' \left( \frac{S}{r} \right).$$

Stability of cylindrical shells reinforced  
by closely arranged circular stiffening  
ribs (Fig. 4.44)

Critical comprehensive external pressure is determined from  
formula [36]

$$p_{kp}^r = \frac{E' S}{r} \frac{1}{\left(n^2 - 1 + \frac{a_1^2}{2}\right)} \left[ \frac{S^2}{12(1-\mu^2)r^2} (a_1^2 + n^2 - 1)^2 + \right. \\ \left. + \frac{a_1^4}{(a_1^2 + n^2)^2} - \frac{I(n^2 - 1)^2}{S l r^2} \right], \quad (4.22)$$

where.

$$a_1 = \frac{\pi r}{l} \quad [28];$$

$I$  is the moment of inertia for the cross section of an elastic  
rib together with the connected band,  $\text{mm}^4$ ;

$l$  is the distance between neighboring reinforcing ribs.



Fig. 4.43. Stability losses  
in a cylindrical shell with pure  
bend.

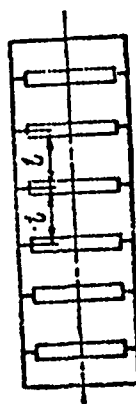


Fig. 4.44. A circular cylindrical  
shell reinforced by circular ribs.

The value of  $n$  for thin cylindrical shells can be determined approximately from formula [36]

$$n = \sqrt[3]{\frac{3M}{k}},$$

where

$$k = \frac{E' I}{r^3 l} + \frac{E' S^3}{12(1-\mu^2)}; \quad M = \frac{E' S}{r} \alpha_1^4.$$

For all cases studied the actual critical pressure is determined from formula [36]

$$p_{kp}^A = \eta_1 \eta_2 p_{kp}^T,$$

where  $\eta_1$  is the correction factor characterizing the imperfection of the geometric shape of the shell;  $\eta_1 = 0.65-1.0$ ;

$\eta_2$  is the correction factor characterizing the deviation of shell material properties from Hooke's law at the moment of stability loss.

The value of coefficient  $\eta_2$  can be determined from the graph (Fig. 4.45) where the solid line is plotted for the case  $\sigma_{kp}^T / \sigma_T \leq 2$  and the dashes for the case  $\sigma_{kp}^T / \sigma_T \geq 2$ ; critical yield limit is

$$\sigma_{kp}^T = \eta_1 \frac{r}{S} p_{kp}^T.$$

The stability reserve of a shell is determined by coefficient  $N$ , which is equal to the ratio of the actual critical pressure  $p_{kp}^A$  to the working pressure  $p_{pa6}$ . The numerical value of coefficient  $N$  is recommended as no less than 3.0. During hydraulic tests it can be  $N = 2.5$ .

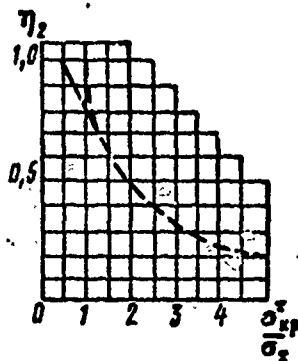


Fig. 4.45. Graphs for determining correction factor.

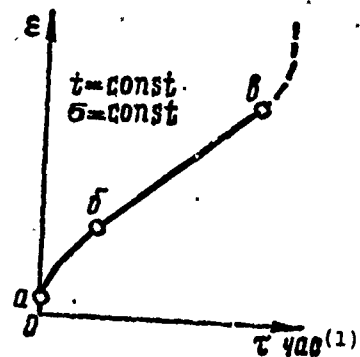


Fig. 4.46. Primary creep curve.  
KEY: (1) hour.

Stability of thin-walls cylindrical elements during omnidirectional compression under creep conditions

The stress corresponding to working pressure (below the yield limit  $\sigma_T$ ) is determined from formula

$$\sigma_p = \frac{pD}{2S} \quad (4.23)$$

Critical stress with elastic stability loss is

$$\sigma_{kp} = \frac{p_{kp}^* D}{2S},$$

where  $p_{kp}^*$  is the actual critical pressure with elastic stability loss.

Critical strain with elastic stability loss is

$$\epsilon_{kp} = \frac{3 p_{kp}^* D}{8ES}.$$

In the general case, critical time is determined on the basis of the primary creep curves (Fig. 4.46), which are plotted for the steels selected, the prescribed temperature, and constant stress  $\sigma_p$  (assuming that the creep properties for uniaxial extension and compression are identical). On the axis of ordinates the creep flow  $\epsilon$ , equal to  $\epsilon_{kp}$ , is plotted. Critical time  $\tau_{kp}$  is the abscissas. Section *ab* is the first (transition) period of creep, characterized by a decrease in creep rate. Section *bc* is the second period of creep (creep rate constant). Specifically, for this developed section of uniform creep the critical time (in hours) during stability loss can be determined from formula

$$\tau_{kp} = \left( \frac{4}{3} \right)^{n-1} \frac{\sigma_p \left( 1 - \frac{p}{p_{kp}^2} \right)}{EB_1 \sigma_p^n},$$

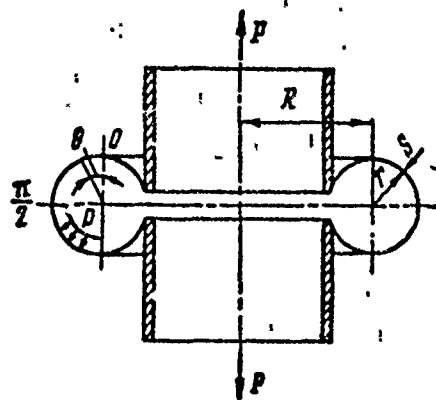
where  $n$  is the creep index with uniaxial tension;

$B_1$  is the creep factor with uniaxial tension,  $1/h \text{ (daN/cm}^2\text{)}^n$ .

Prolonged creep occurs generally in the second period and is characterized by comparatively low stresses at low temperatures.

The formula for critical time is derived on the assumption that stability losses occur under conditions of prolonged creep when creep flows, accumulated in the first period, can be disregarded since they are small as compared with the total strain of the element.

Fig. 4.47. Diagram of a torr compensator.



## Analysis of compensators

1. Torr compensator (Fig. 4.47). Analysis is performed in the presence of axial force  $P$  and pressure  $p$ . The following parameters are introduced:

$$\alpha_0 = \frac{r}{R}; \quad \beta_0 = \frac{r}{S}; \quad \lambda = \sqrt{12(1-\mu^2)} \alpha_0 \beta_0,$$

where  $\mu$  is the Poisson coefficient; when  $\mu = 0.3$   $\lambda = 3.3 \alpha_0 \beta_0$ .

a) The action of axial force  $P$ .

Axial displacement of the compensator  $\Delta$  (in cm):

$$\text{when } \lambda > 4 \quad \Delta = \frac{\lambda}{\alpha_0 S E} P;$$

$$\text{when } \lambda < 4 \quad \Delta = \frac{\lambda^2 c_1}{2 \alpha_0 S E} P,$$

where  $c_1$  is the coefficient depending upon parameter  $\lambda$  (see below).

Maximum circular stresses (at points  $\theta = 0$ ):

$$\text{when } \lambda > 4 \quad \sigma_{\varphi, P}^{\max} = \frac{0.518}{\lambda^{1/3}} \sigma_0; \quad \text{when } \lambda < 4 \quad \sigma_{\varphi, P}^{\max} = 0.550 \frac{k_0}{\lambda} \sigma_0,$$

where  $k_0$  is the coefficient depending upon parameter  $\lambda$  (see below);

$$\sigma_0 = \frac{3 \alpha_0}{\pi S^2} P.$$

Maximum meridional stresses are:

$$\text{when } \lambda > 4 \quad \sigma_{M, P}^{\max} = \frac{0.754}{\lambda^{1/3}} \sigma_0 \quad (\text{at points } \theta = \pm \frac{1.225}{\lambda^{1/3}});$$



when  $\lambda < 2,3$   $\sigma_{M,p}^{\max} = (c_1 - c_3) \sigma_0$  (at points  $\theta = \pm \frac{\pi}{2}$ );

when  $2,3 < \lambda < 4$   $\sigma_{M,p}^{\max} = c_3 \left(1 + \frac{c_1}{3c_3}\right)^{3,2} \sigma_0$  (at points

$$\theta = \pm \arcsin \frac{1}{2} \sqrt{1 + \frac{c_1}{3c_3}}.$$

Here coefficients  $c_1$  and  $c_3$  are functions of parameter  $\lambda$ .

In the cited formulas the following designations were used:

$$k_0 = \frac{N_0}{D_0}; \quad c_1 = \frac{N_1}{D_0}; \quad c_3 = \frac{N_3}{D_0},$$

where

$$D_0 = (1,74 + 0,126\lambda^2) 10^{11}; \quad N_0 = (4,36 + 0,0273\lambda^2) 10^{10}\lambda^2;$$

$$N_1 = (1,74 + 0,0170\lambda^2) 10^{11}; \quad N_3 = (3,64 + 0,0038\lambda^2) 10^9\lambda^2.$$

b) The action of pressure  $p$ .

Maximum meridional stresses:

$$\sigma_{M,p}^{\max} = \frac{1}{2} \frac{2 + \alpha_0}{1 + \alpha_0} \sigma_p.$$

Maximum circular stresses

$$\sigma_{\varphi,p}^{\max} = \frac{1}{2} \sigma_p,$$

where  $\sigma_p = (pr)/(S)$ .

The graphs in Fig. 4.48 present the dependences

$$-\frac{\sigma_{M,p}^{\max}}{\sigma_0} \text{ and } \frac{\sigma_{M,p}^{\max}}{\Delta} \cdot \frac{R}{E}$$

on parameter  $\lambda$ . The character of the variation in these quantities indicates that it is not advisable to design torr compensators with parameter  $\lambda < 4$  since, in this case, meridional stresses rise sharply.

Total maximum stresses must satisfy the following conditions:

$$\left. \begin{aligned} \frac{\sigma_{M,p}^{\max}}{1,4} + \sigma_{M,p}^{\max} &\leq \sigma_{\text{дон}}^* \\ \sigma_{\varphi,p}^{\max} + \sigma_{\varphi,p}^{\max} &\leq \sigma_{\text{дон}}^* \end{aligned} \right\}$$

where  $\sigma_{\text{дон}}^*$  is the nominal permissible stress for a given structural material,  $\text{daN/cm}^2$ .

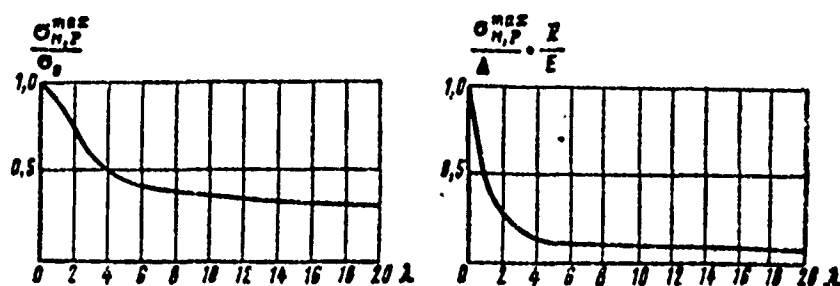


Fig. 4.48. Graphs showing the dependence of  $\frac{\sigma_{M,p}^{\max}}{\sigma_0}$  and  $\frac{\sigma_{M,p}^{\max}}{\Delta} \cdot \frac{R}{E}$  on parameter  $\lambda$ .

2. Lens compensator (Fig. 4.49). As for the torr compensator, analysis is performed for axial force  $P$  and pressure  $p$ .

a) Action of axial force  $P$  in the elastic region.

Axial displacement of compensator:

$$\Delta = 2k_1^y \frac{R_n^2}{S^3 E} P,$$

where

$$k_1^y = 0,290 \frac{(z-1)^3}{z^2(1+z)}; \quad z = \frac{R_n}{R_{nn}}.$$

Maximum meridional stresses:

$$\sigma_{M,P}^{\max} = k_2^y \frac{P}{S^2},$$

where

$$k_2^y = 0,48 \frac{R'_n - R'_n}{R_n}.$$

When

$$\frac{r}{R_n} < 0,01 \quad k_2^y \approx 0,48(z-1).$$

b) Action of pressure p in the elastic region.

Maximum meridional stresses:

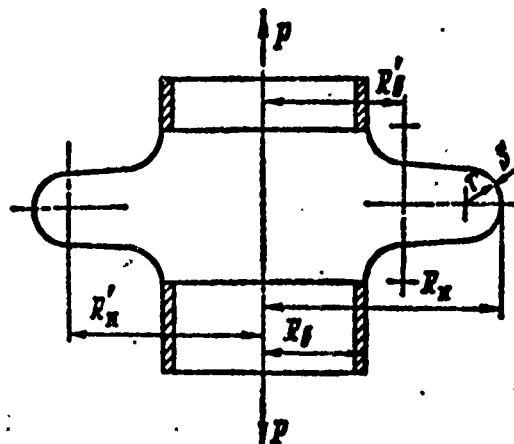
$$\sigma_{M,p}^{\max} = k_p^y \frac{p R_n^2}{S^2},$$

where

$$k_p^y = 0,5 \left(1 - \frac{1}{z}\right)^2.$$

Analysis of a lens compensator with allowance for elastic-plastic deformations.

Fig. 4.49. Diagram of a lens compensator.



Displacement of the compensator from the action of axial force P:

$$\Delta = 2k_1^n \frac{R_n^2}{S^3 E} P,$$

where

$$k_1^n = 0,264 \left( \frac{z^2 - 1}{z^2} - \frac{4 \ln^2 z}{z^2 - 1} \right).$$

Maximum meridional stresses from pressure p:

$$\sigma_{M,p}^{\max} = k_p^n \frac{p R_n^2}{S^2},$$

where

$$k_p^n = 0,5 \left( 1 - \frac{1}{z} \right) \frac{1+z}{1+3z}.$$

Total maximum stresses must satisfy the following condition:

$$\sigma_{M,p}^{\max} + \sigma_{M,p}^{\max} \leq 1,4 \sigma_{\text{don}}.$$

## CHAPTER V

### MOTORS

#### 5.1. PLASMA MOTORS

In plasma motors thrust is created during the outflow of the plasma of the working medium. Plasma obtains acceleration upon interaction with its own or an external magnetic field.

Plasma motors have a high specific impulse  $I_{\text{sp}} = 20-100 \text{ km/s}$ , exceeding the specific impulse of liquid and solid propellant rocket engines.

In the creation of plasma motors there are substantial difficulties; the problems of the continuous operation of individual thermally stressed elements, electrode erosion, etc., have not been solved. Materials which could resist high thermal loading for a long period of time remain to be developed.

Let us examine briefly the classification of plasma motors. They can be divided into three groups: *pulsed motors*, *ac motors*, and *dc motors*.

In pulsed motors the generation and acceleration of plasma is accomplished by the energy of capacitor discharge. The advantage of such motors is the possibility of obtaining a comparatively less stressed anode-cathode unit with respect to thermal and power stresses. In pulsed motors it is easier to guarantee the protection

of the anode-cathode system from overheating by spreading the discharge contact spot on the surface. The problems of cooling, repeated switching of the motor, and frequent use are simpler to solve. The disadvantage is the comparatively heavy weight of the capacitors.

These motors are generally used for correction. High-thrust motors can be used for individual cosmonaut use.

In dc motors the generation and acceleration of the plasma is accomplished by direct current. The motors can be electromagnetic or electrothermal. They can be both sustainer motors for inter-orbital flights and correction motors. A characteristic of these motors is the high-temperature operating mode of the anode-cathode system.

Ac motors are electromagnetic motors in which the generation and acceleration of plasma is accomplished by alternating current. They include motors with a progressive magnetic field, high-frequency, superhigh-frequency, and electrothermal motors. They can be designed for various purposes.

The high temperatures of the plasma require particular attention be given to the coolant system and the selection of the materials, which in turn requires the solution of a large number of complex structural and technological problems.

The type of working medium (solid, liquid, or gas) determines the structural shape of the power supply system and the plasma generator.

Based on the arrangement of the cathode-anode system, these motors are divided into *coaxial*, *face* and *track*.

## STRUCTURAL DIAGRAMS AND DESIGNS OF THE MOTORS

## Pulsed pinch plasma motor

This motor (Fig. 5.1) consists of a plasma generator unit, accelerator, and system for feed, cooling and electric power.

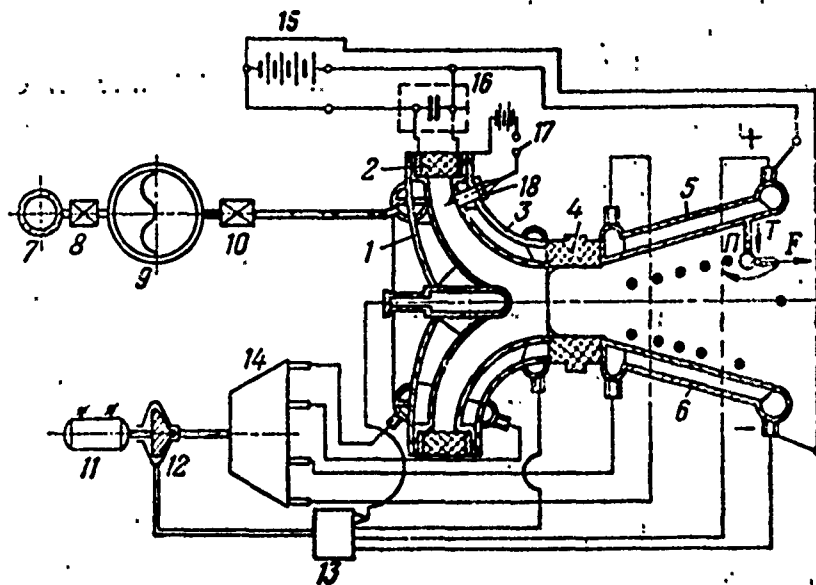


Fig. 5.1. Diagram of a pulsed pinch plasma motor.

The plasma generator unit is the pinch type and consists of cathode 1, insulating spacer 2, anode 3, and elements for supplying the coolant and current.

The cathode and anode are made in the form of connected two-layer shells with a toroidal surface. The anode gradually becomes a cylindrical nozzle.

The accelerator unit is the track type and consists of insulating plate 4, anode 5, and cathode 6. Electrodes, as in the plasma generator, are two-layer for the supply and removal of the liquid coolant.

The feed system unit consists of a gas cylinder with the controlling gas 7, the pressure divider 8, the container 9, with the working medium (argon) equipped with a barrier diaphragm, and the dosing device 10.

The cooling system unit consists of a pump with an electric drive 11, 12, dosing device 13, and cooler 14.

The electric power system consists of the current supply 15, condensers 16, discharger-modulator 17, and the ignition device 18.

To the terminals of the anode and cathode and to the discharger-modulator voltage is fed. Then the reducing valve 8 of the controlling gas cylinder 7 is opened; the working gas from container 9 through the dosing device 10 moves to the discharge gap of the generator.

The arc is ignited by device 18. The purpose of the discharger-modulator 17 is to ensure a certain cyclic discharge of the capacitor; thus, the operating mode of the motor and its thrust is controlled within a wide range.

Ionization of gas in the discharge gap, with the aid of devices 17 and 18, leads to the discharge of the capacitor of the plasma generator over the entire gap between the anode and the cathode and displacement of the plasmoid along the generator channel; during the plasmoid's displacement it is pinched, i.e., formed into a torus or ring, and the ejection from the nozzle portion of the anode into the accelerating system of the motor occurs. In the accelerating system there is a synchronous discharge of the accelerator capacitor, which leads to the deformation of a magnetic field in the accelerator, acceleration, and ejection of plasma into space.

Then overcharging of the capacitor leads to a repetition of this process.

#### axial plasma dc motor

This motor consists (Fig. 5.2) of a plasma generator unit, accelerator unit, and systems for feeding the working medium, cooling, and electric power supply.



In the plasma generator unit the evaporator 1 is welded to cathode 6 and comprises with it the main force part. The plasma generator itself includes part 2 and nozzle 3, which is also the insulation spacer between the plasma generator and its accelerator.

The accelerator unit consists of anode 4, cathode 6, and the winding of the electromagnet 5. The cathode 6 is common for the plasma generator and the accelerator. It is a multilayer all-welded shell construction of heat resistant material and has a preheater 7 of tungsten. In the feed system is the container 8 for liquid metal, electromagnetic pump 9, and dose device 10.

The cooling system consists of container 11, electromagnetic pump 12, metal distributor 13, and cooler-radiator 14, 15.

The electric supply system consists of a dc source 16, control system, current distribution and commutation.

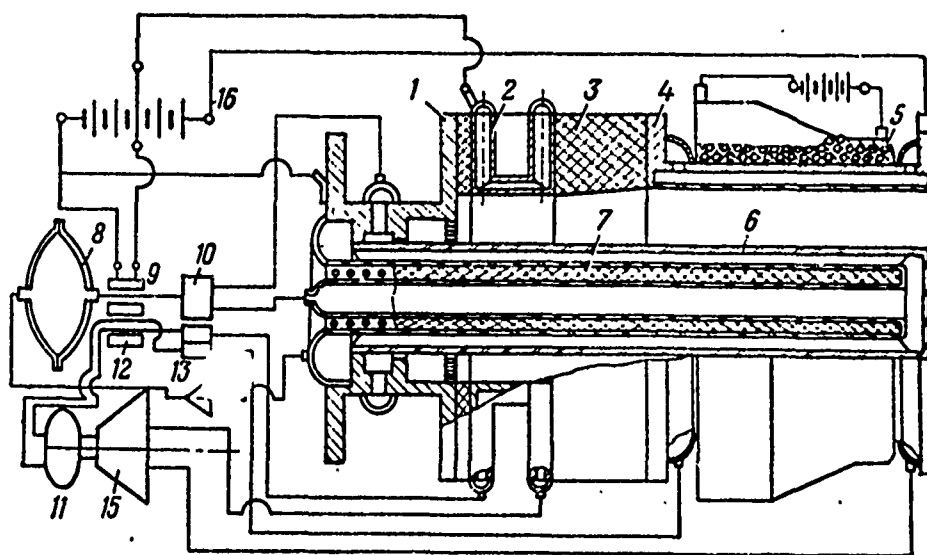


Fig. 5.2. Diagram of a coaxial plasma motor.

The working medium of the electromagnetic pump is fed to the distributor, then to the collector of the evaporator housing of the motor and to the cooling system. The vaporous working medium

enters through the injector into the plasma generator where it is ionized in the interelectrode space. From the plasma generator it enters the thermal nozzle and then into the coaxial accelerator.

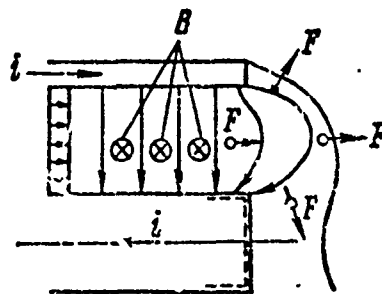
The electrode system is cooled by the working medium in radiators insulated from each other. For insulating the cathode and anode unit separators of thorium oxide or aluminum are used.

On the anode is placed a profiled solenoid with a winding of copper wire insulated from the anode by the application of a layer of aluminum oxide. The purpose of the solenoid is to create a magnetic field for plasma acceleration. Along with this there is an improvement in the temperature mode of the plasma and an increase in motor efficiency.

In the first design of coaxial motors important characteristics were noted: the length of electrodes, particularly the cathode, after a certain value affects somewhat the effectiveness of motor operation. The cathode is subject to strong heating and erosion. The face of the electrodes has considerable significance in obtaining thrust.

Figure 5.3 is a simplified diagram of the equipotential surfaces of plasma on the face of a coaxial motor. If there is no external magnetic field, the plasma is heated by the heating effect of the current which increases in the walls of the cathode. Its own magnetic field presses the plasma to the surface of the cathode and before the cathode. On the face of the cathode the form of the plasma bunch is similar to the form of the electrode; the temperature effect on the face of the cathode, leading to its erosion, is the greatest.

Fig. 5.3. Simplified diagram of the vectors of current, field, and forces in a coaxial motor.



If an external magnetic field is created by the solenoid, then, apart from plasma acceleration, it leads to the stabilization of the processes of heating and plasma displacement. The appearing axial solenoid magnetic field leads to the appearance of a circular component of force acting on the plasma element and to the stabilization of plasma particle rotation. The Hall effect on the face and the more uniform plasma temperature distribution along the radius of the interelectrode gap improve motor operation, increase its efficiency, and decrease cathode erosion and temperature.

The characteristic bunching of the plasma behind the cathode, as it were, extending the cathode, makes it possible to shorten it somewhat without substantial losses.

#### Coaxial plasma dc motor with shortened cathode

This motor consists of a plasma generation unit, an accelerator, a fuel feed system, and systems for cooling and electric power (Fig. 5.4).

The plasma generator unit consists of superhigh-frequency current inductor 1, discharge chamber 2, and heat nozzle. The discharge chamber is formed by two coaxial cylindrical shells of quartz glass welded on the faces to the collectors of the liquid coolant supply. Usually this is an organosilicon liquid.

The discharge chamber is covered with a copper inductor connected with the high-frequency current supply. The inductor is cooled by the same organosilicon liquid. The discharge chamber is connected with the accelerator by an insulator having the form of the heat nozzle.

The anode of accelerator 3 consists of two molybdenum shells connected with a fluted adaptor and cathode 4 of the coaxial type, which can be cooled and is protected from erosion in the radial part by its own magnetic field and by the aluminum oxide applied to the surface.

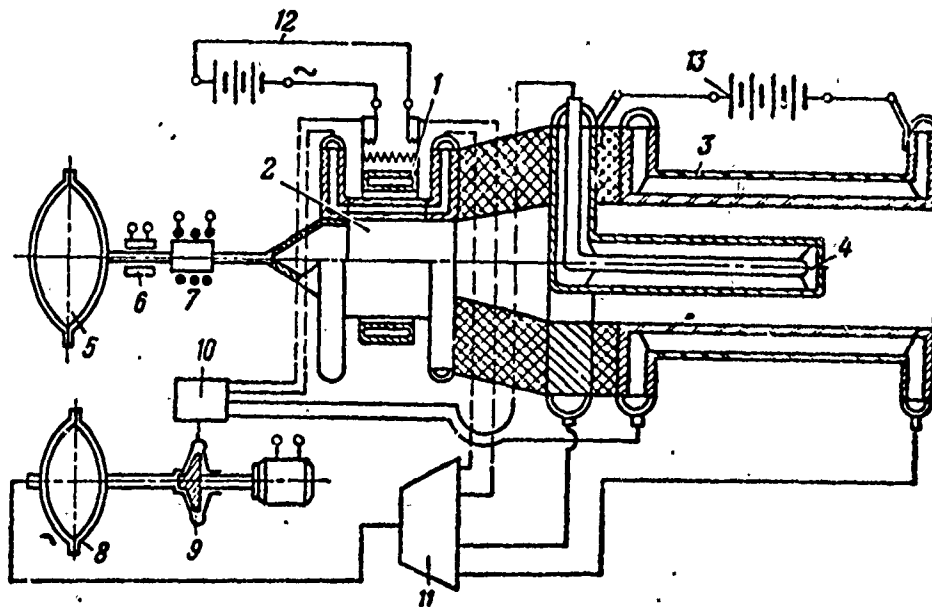


Fig. 5.4. Diagram of a plasma coaxial motor with shortened cathode.

The feed system consists of a tank with working medium 5, electromagnetic pump 6, evaporator and doser of the working medium 7.

The coolant system consists of a tank with organosilicon liquid, electric pump 9, distributor 10, and cooler-radiator 11.

The electric power supply system consists of a superhigh-frequency generator 12 and a dc generator 13.

The working medium is fed by the electromagnetic pump into the evaporator-doser and then in vapor state to the plasma generator. In the generator under the effect of high-frequency currents the vapors of the working medium are ionized. From the generator the plasma proceeds to the heat nozzle and then to the accelerator.

Fig. 5.5. Simplified diagram of forces acting on a plasma particle.

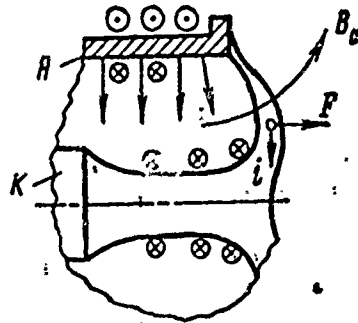


Figure 5.5 is a simplified diagram of forces acting on an elementary plasma particle. The forces illustrated compress the plasma into a band in the center and reduce the effect of the thrust on the face of the anode.

Some shortening of the anode does not affect appreciably the forces acting on the flow of plasma in the accelerator.

#### Face-type dc plasma motor

Figure 5.6 shows a diagram of a plasma motor with a face-type layout of the anode-cathode system and a liquid working medium. The main advantage of this design is the rational form of the cathode which presents the contact of structural materials with the central part of the plasma bunch having the maximum temperatures.

This motor consists of the following main units: an accelerator-generator, working medium feed, cooling system, and power supply.

The accelerator-generator unit consists of a ring-shaped molybdenum cathode 1 which can be cooled by the organosilicon liquid, heat-resistant insulator 2, and tungsten anode 3.

The working medium supply unit consists of tank 4 with compressed gas, tank 5 with the working medium and the heater, dosing device 6, and injector 7.

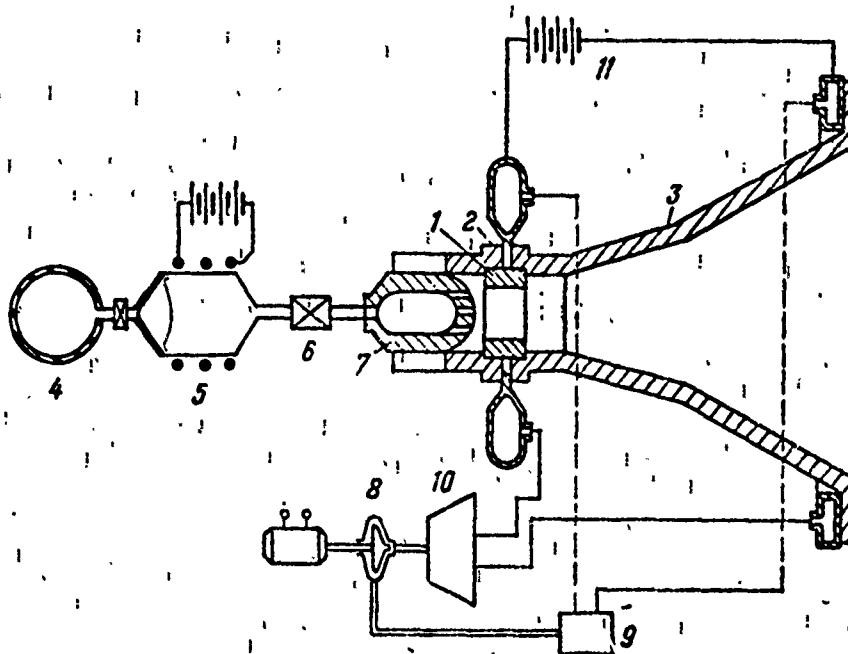


Fig. 5.6. Diagram of a face-type plasma motor.

The cooling unit consists of electric pump 8, distributor 9, and cooler-radiator, 10.

The power supply unit consists of a current source 11 and wiring from it to the anode-cathode system and the heater.

After voltage is fed to the terminals of the anode and cathode and to the starting spark gap (not shown on diagram) under the pressure of the controlling gas on the membrane of tank 5, the working medium, passing the dosing device 6, enters through injectors 7 into the spark gap of the motor. Directly by the injector the working medium vapors are ionized and the plasma is further accelerated.

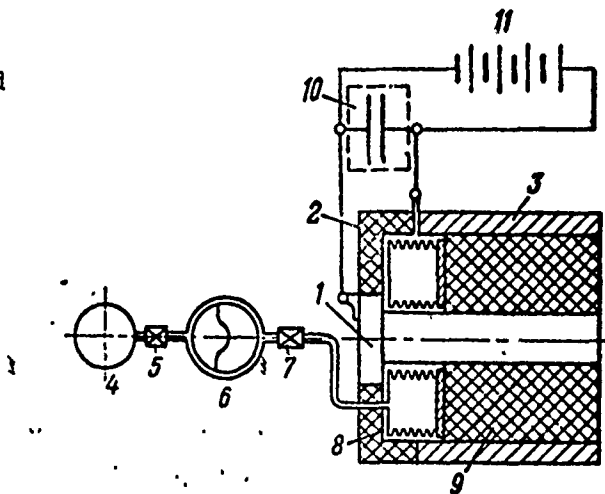
Heat discharge from the anode walls is accomplished by radiation, cooling of the cathode walls by the organosilicon liquid; this same liquid cools the current supplies to the anode and the cathode.

### Pulsed plasma face-type motor with a solid working medium

Pulsed motors can also be made with a solid working medium. This motor (Fig. 5.7) consists of an accelerator-generator unit, a feed unit, and a power supply system.

The plasma accelerator-generator unit includes cathode 1, insulating element 2, and anode 3. The feed unit includes gas cylinder 4 with the controlling gas, reducing valve 5, container with controlling fluid 6, dosing device 7, drive 8 for moving the working medium, and working medium 9 (teflon). The power supply system consists of capacitor 10 and power source 11.

Fig. 5.7. Diagram of a pulsed plasma motor with a solid working medium.



When operating voltage is fed to the cathode and the anode, on the surface of the face of the teflon ring there occurs a surface discharge, evaporation, and ionization of the teflon evaporation products. Forces of the emerging electromagnetic field act on the forming plasma, accelerate it, and, as a result, create the thrust of the motor.

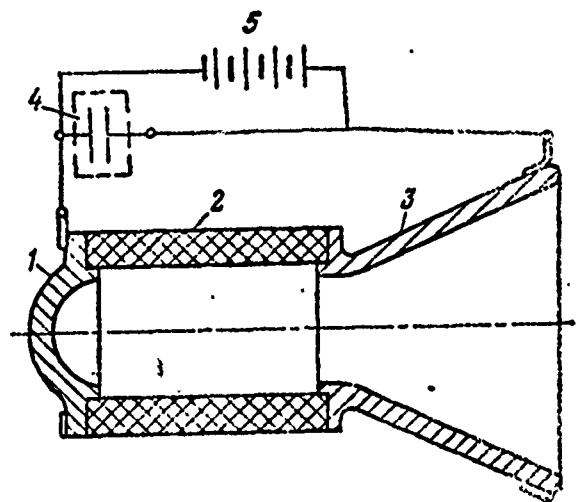
To compensate for the expenditure of teflon from the face there is a working medium feed system. Compressed gas through the reducing valve 5 presses the working liquid out of tank 6 into sealed, freely expanding chamber 8, thus ensuring the displacement of the grain in the discharge gap.

### Pulsed plasma motor with combustion chamber

In the motor shown in Fig. 5.8 the grain of solid fuel 2 of teflon forms a discharge chamber between the cathode 1 and anode 3. Surface discharge in the chamber leads to evaporation of the teflon, ionization of its vapor, and ejection of it from the nozzle, which is the anode of the motor.

Figure 5.9 shows the design of a plasma pulsed motor for the orientation of an artificial satellite in outer space [9].

Fig. 5.8. Diagram of a pulsed plasma motor with ablating chamber.



The motor has a thrust of 10 sn, specific impulse 50,000 m/s, pulsed frequency 10 Hz, working medium flow rate 0.002 g/s. The working medium is teflon, 10-hour lifetime, capacitance of the capacitor battery 0.005 F.

The motor consists of a plasma accelerator-generator unit, working medium feed system, and power supply system.

The accelerator-generator consists of two copper electrodes 1, 2, in which the grain of the solid working medium 3 is placed; ignition device 4 is on one of the electrodes.



The grain of the working medium is moved by rod 5, controlled by the pneumatic-hydraulic cylinder of the feed system. The electrode bracing panel is the wall of the motor housing, in which are located capacitors 6 and discharge initiator unit 7. The motor housing is made of argon to improve capacitor operation.

Figure 5.10 shows the design of a plasma pulsed motor operating on a liquid working medium. It consists of cathode 1, anode 2, on which initiator 3 is located, a tank with the working medium 4 and a porous rod 5, and capacitors 6. The working medium, heated in tanks 4, through the porous rod 5 is drawn into the interelectrode space of the motor. The high-voltage discharge between the cathode and the initiators 3 generates a plasmoid which is then accelerated in the interelectrode gap of the motor.

#### Stress analysis of motor elements

The stress analysis of a motor reduces mainly to finding the coefficients of safety for parts operating for a long period of time in conditions of high temperatures and high temperature gradients. A peculiarity of this analysis is the study of parts from high-melting materials - tungsten, molybdenum, ceramics, etc.

There are a large number of cylindrical shells in the motor. Let us analyze the shells.

#### Steady-state equation of the elastic forces in a cylindrical shell

The geometric dimensions of a shell,  $r$ ,  $h$ , modulus of elasticity  $E$ , are given; it is necessary to find the stresses  $\sigma_x$ ,  $\sigma_\phi$  and bend in the direction of the  $z$ -axis,  $w$ .

Let us assume that the forces of internal pressure  $p$  act on a shell element. We apply to it forces which compensate the element interaction forces (Fig. 5.11).

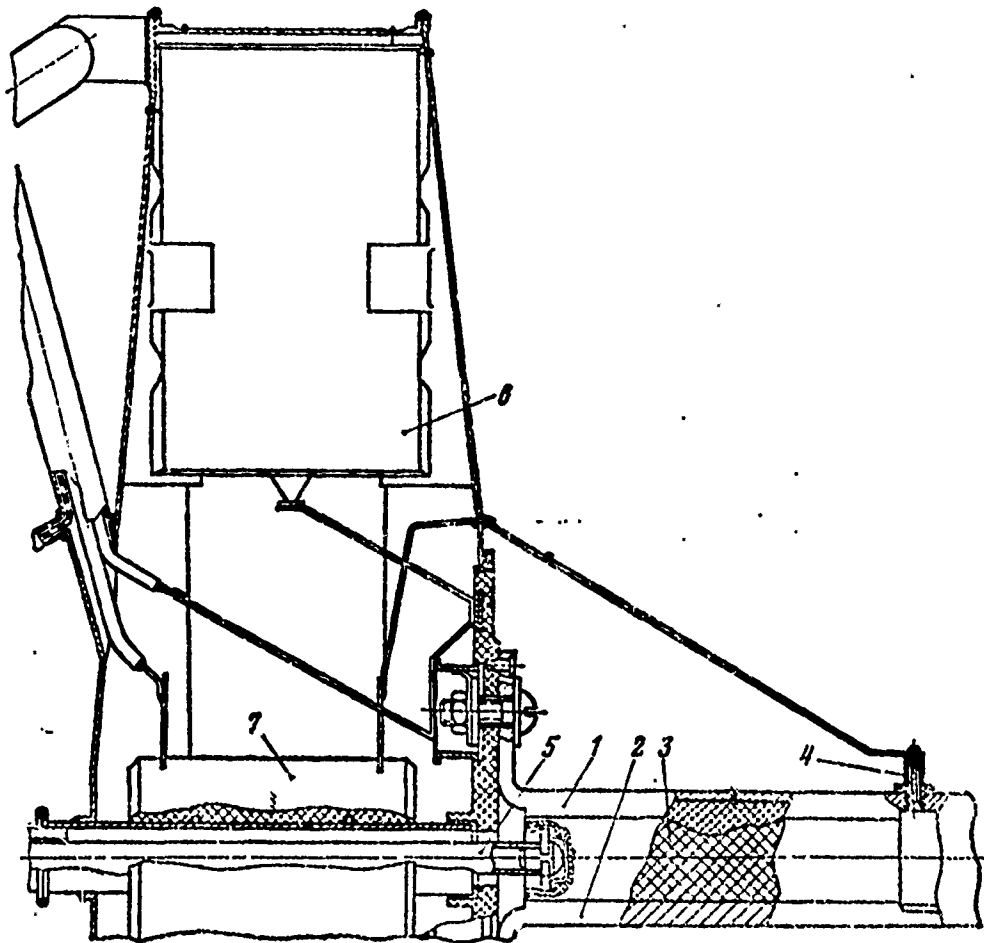
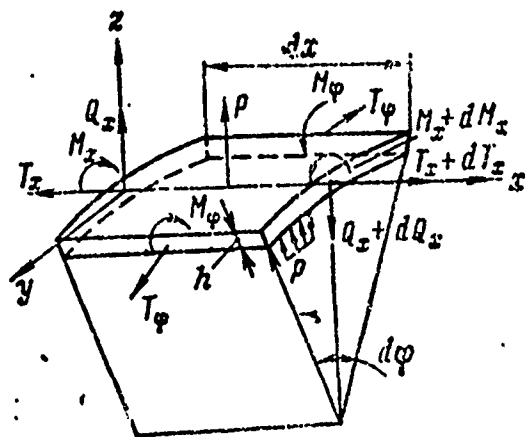


Fig. 5.9. Design of a plasma motor.

Fig. 5.11. Element of a cylindrical shell.



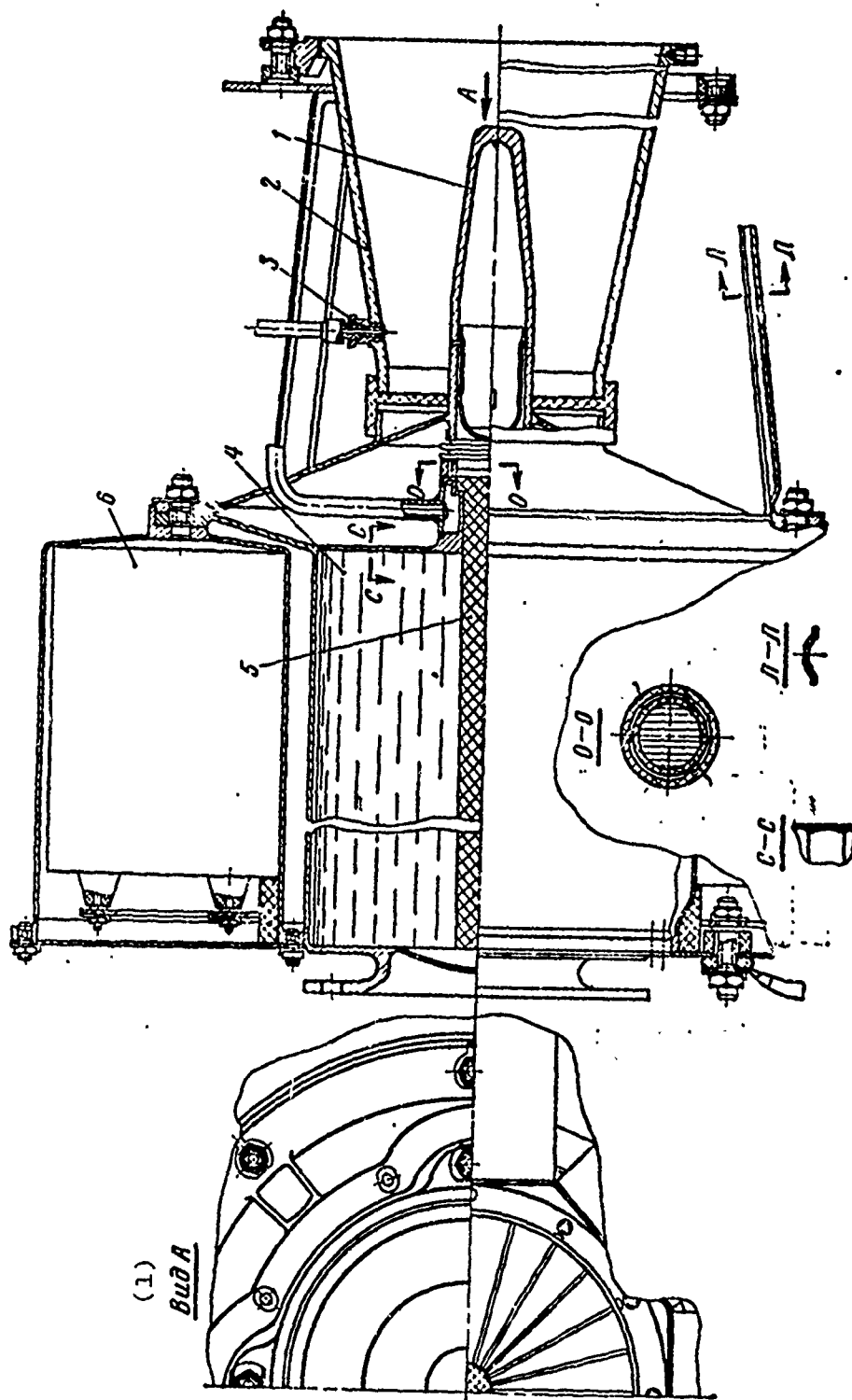


Fig. 5.10. Design of a plasma motor.  
KEY: (1) View.

Along the faces of the element forces  $T_\varphi$  and moments  $M_\varphi$  will act in a circular direction. They are equal to each other along both faces due to the axial symmetry of the shell.

In the axial direction forces  $T_x$ ,  $Q_x$  and moment  $M_x$  will change along the selected element since, in this direction, there can be no loading symmetry. Usually forces and moments applied to the faces are examined as loads distributed along the length. We shall designate them with a bar. Obviously,

$$\begin{aligned} T_x &= \bar{T}_x r d\varphi; & T_x + dT_x &= \bar{T}_x r d\varphi + d(\bar{T}_x r d\varphi); \\ M_x &= \bar{M}_x r d\varphi; & M_x + dM_x &= \bar{M}_x r d\varphi + d(\bar{M}_x r d\varphi); \\ Q_x &= \bar{Q}_x r d\varphi; & Q_x + dQ_x &= \bar{Q}_x r d\varphi + d(\bar{Q}_x r d\varphi); \\ T_\varphi &= \bar{T}_\varphi dx; & M_\varphi &= \bar{M}_\varphi dx; & P &= pr d\varphi dr. \end{aligned}$$

Let us project all forces onto the x- and z-axes and find the sum of the moments relative to the axes parallel to y and coinciding with the right face of the element. We obtain

$$\left. \begin{aligned} d(\bar{T}_x r d\varphi) &= 0; \\ -d(\bar{Q}_x \cdot r d\varphi) - 2\bar{T}_\varphi dx \frac{\sin d\varphi}{2} + pr d\varphi dx &= 0; \\ -d(\bar{M}_x r d\varphi) + \bar{Q}_x r d\varphi dx &= 0. \end{aligned} \right\} \quad (5.1)$$

The first equation of system (5.1) indicates that forces  $T_x$  are constant. Let us consider them equal to zero. If they are other than zero, strain and stresses from them are easily computed and can be summed with those which are obtained from the solution of the remaining two equations:

$$\bar{Q}_x + \frac{1}{r} \bar{T}_\varphi = p; \quad \bar{M}_x - \bar{Q}_x = 0. \quad (5.2)$$

These two equations contain three unknown quantities:  $\bar{T}_\varphi$ ,  $\bar{Q}_x$  and  $\bar{M}_x$ . Let us examine the strain of the middle surface of the shell under the action of forces  $\bar{T}_\varphi$ .

Forces  $\bar{T}_\varphi$ , while acting normally to the cross section of the shell in a circular direction, create circular "membrane" (momentless) stresses  $\sigma_\varphi = \bar{T}_\varphi/h$ .

We must determine  $\bar{T}_\varphi$  as a function of deformation  $w$ . For this we should find stresses  $\sigma_\varphi$  as a function of deformation  $w$ .

Let us calculate the relative strain of the element  $\varepsilon_\varphi$  (Fig. 5.12a):

$$\varepsilon_\varphi = \frac{\overbrace{a'b'} - \underbrace{ab}}{\underbrace{ab}} = \frac{(r+w)d\varphi - r d\varphi}{r d\varphi} = \frac{w}{r}.$$

Hence

$$\sigma_\varphi = E\varepsilon_\varphi = \frac{Ew}{r}; \quad \bar{T}_\varphi = \frac{Ehw}{r}. \quad (5.3)$$

We find moment loads and stresses of shells from these loads. While examining the shells under the action of bending moment  $M_x$ , we reach the conclusion, based on symmetry consideration, that the curvature along the circumference remains constant; the curvature however, in the  $x$  direction will be  $d^2w/dx^2$ .

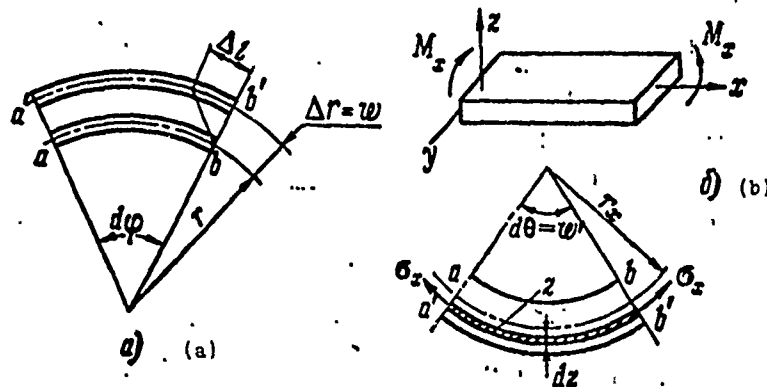


Fig. 5.12. Obtaining relative strains of the shell.

This is obtained as a result of the deformation of the plate by bending moment distributed along the edge (Fig. 5.12b). The edge of the shell can be represented as an element of this plate. The curvature of the plate as a result of the effect of bending moment is

$$k = \frac{1}{r_x} = \frac{d^2 w}{dx^2},$$

which agrees with the formula for rod curvature.

Stresses will be determined from the familiar Hooke relationship for a plate:

$$\left. \begin{aligned} \sigma_x(M) &= \frac{E}{1-\mu^2} (\varepsilon_x + \mu \varepsilon_y); \\ \sigma_y(M) &= \frac{E}{1-\mu^2} (\varepsilon_y + \mu \varepsilon_x). \end{aligned} \right\} \quad (5.4)$$

Relative strain,  $\varepsilon_x$  is found from Fig. 5.12:

$$\varepsilon_x = \frac{\overbrace{a'b'}^{\text{deformed}} - \overbrace{ab}^{\text{undeformed}}}{ab} = \frac{\overbrace{ab}^{\text{deformed}} + z d\theta - \overbrace{ab}^{\text{undeformed}}}{r_x d\theta} = \frac{z}{r_x} = z \frac{d^2 w}{dx^2}; \quad \varepsilon_y = 0.$$

Since the deformation of a plate in this direction from bending moment  $M_x$  does not occur,

$$\sigma_x(M) = \frac{Ez}{1-\mu^2} \frac{d^2 w}{dx^2}; \quad \sigma_y(M) = \mu \sigma_x \quad (5.5)$$

and bending moment is

$$\left. \begin{aligned} \overline{M}_x &= - \int_{-h/2}^{h/2} \sigma_x z dz = - \frac{E w''}{1-\mu^2} \int_{-h/2}^{h/2} z^2 dz = \\ &= - \frac{E h^3}{12(1-\mu^2)} w'' = + D w''; \\ \overline{M}_y &= \mu \overline{M}_x, \end{aligned} \right\} \quad (5.6)$$

where  $D = \frac{Eh^3}{12(1-\mu^2)}$ . Let us return to equation (5.2). Dropping  $\bar{Q}_x$ , we obtain

$$\bar{Q}_x = \bar{M}_x' \text{ and then } \bar{M}_x' + \frac{1}{r} \bar{T}_\varphi = p,$$

hence, with the aid of equations (5.3) and (5.6), we find

$$\frac{d^2}{dx^2} \left( D \frac{d^2 w}{dr^2} \right) + \frac{Ehw}{r^2} = p. \quad (5.7)$$

This equation enables us to solve the problem of cylindrical shell deformation.

Analysis of a cylindrical shell with constant parameters

In the majority of cases, the thickness of a shell  $h$ , cylindrical rigidity  $D$ , and modulus of elasticity  $E$  are constant quantities. Only pressure  $p$  is variable. Equation (5.7) will have the following form

$$w^{IV} + \frac{Eh}{r^2 D} w = p/D, \quad (5.8)$$

or, if we designate  $\beta^4 = \frac{Eh}{4r^2 D} = \frac{3(1-\mu^2)}{r^2 h^2}$ ,

$$w^{IV} + 4\beta^4 w = \frac{p}{D}. \quad (5.9)$$

This is a linear nonhomogeneous differential equation of the fourth order. Its integral contains the sum of the solutions of the equations without the right side and the particular solution:

$$w = e^{-\beta x} (C_1 \sin \beta x + C_2 \cos \beta x) + e^{\beta x} (C_3 \sin \beta x + C_4 \cos \beta x) + w_q, \quad (5.10)$$

where  $w_p$  is the particular solution to equation (5.9);

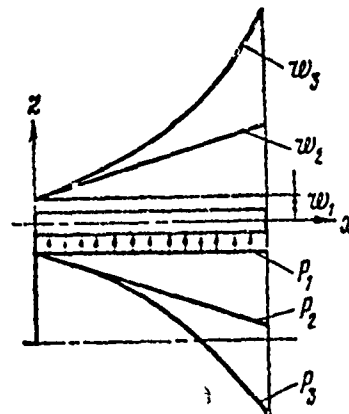
$C_1, C_2, C_3, C_4$  are the integration constants which are determined from the conditions on the ends of the shell.

Let us examine the particular cases of solution for this equation.

Case 1. Stress and strain of a free shell loaded by pressure.

Let us consider a shell without supports, loaded by pressure (Fig. 5.13). We know  $p, h, r, E$ . Find  $\sigma_\varphi, w, n$ .

Fig. 5.13. Shell loaded with pressure.



Strains and stresses in the shell from surface loading are determined by the particular integral of equation (5.9). For the types of surface loading encountered in practice  $w^{IV} = 0$  which is valid for a load whose action is expressed by the law  $p = Bx^n$ , where  $B$  is a constant and  $n \leq 3$ .

This condition is satisfied by a uniformly distributed load, for example, gas pressure, hydrostatic liquid pressure, a load arising during the thermal loading of a shell. Then equation (5.9) will have the form  $(Eh)/(r^2)w = p$  and the bend of the shell under the effect of this pressure is  $\frac{Eh}{r^2}w = p$

$$w = w_p = \frac{r^2}{Eh} p. \quad (5.11)$$



It is significant also that when  $n < 1$  the particular integral describes the stressed and strained state of a momentless shell since quantity  $w''$  which characterizes the moment stress of the shell is zero. If pressure  $p = \text{const}$ , then bend, slope angle, and the second derivative will be equal:

$$w = w_q = \frac{r^2}{Eh} p; \quad w' = 0; \quad w'' = 0;$$

also equal to zero are derivatives of higher orders:  $w^{\text{III}} = w^{\text{IV}} = 0$ . The expression obtained shows that radial strain of the shell will be constant for all its sections. There will be no sag or bend, which also follows from the fact that the slope angle of the tangent to the elastic line of the strained shell is equal to zero (on Fig. 5.13  $w_1 = 0$ ). Stress is found from dependence (5.3):

$$\sigma_r = E \frac{w}{r} = \frac{pr}{h}.$$

We easily find the bend of a shell from external pressure when it changes as a function of  $x$  according to law  $p = B_0 + B_1 x$ . Then

$$w = w_q = \frac{r^2}{Eh} (B_0 + B_1 x); \quad w' = \frac{r^2 B_1}{Eh}; \quad w'' = w''' = w^{\text{IV}} = 0.$$

The form of the strained shell is shown in Fig. 5.13.

In these examples stress does not create moment loading on the shell, which is easy to establish from the fact that the second derivative of bend  $w$  is equal to zero, i.e., stresses will only be membrane stresses. They are determined from formula

$$\sigma_r = E \frac{w}{r} = \frac{r}{h} (B_0 + B_1 x).$$

Variation in pressure on the shell can be described by a more complex law. For example,  $p = B_0 + B_1x + B_2x^2$ . We find the value of the bend from this pressure in the form

$$w_q = A_0 + A_1x + A_2x^2. \quad (5.12)$$

The values of coefficients:

$$A_0 = \frac{r^2}{Eh} B_0; \quad A_1 = \frac{r^2}{Eh} B_1; \quad A_2 = \frac{r^2}{Eh} B_2.$$

Bend is

$$w = w_q = \frac{r^2}{Eh} B_0 + \frac{r^2}{Eh} B_1x + \frac{r^2}{Eh} B_2x^2.$$

Such loading will not be momentless since the second derivative  $w$ , characterizing precisely such loading, will not be equal to zero.

Membrane stresses  $\sigma_\varphi$  are usually basic, determining the strength of the shell. In approximate calculation we are frequently limited to finding these stresses. Strength evaluation will reduce to a comparison of the obtained stresses  $\sigma_\varphi$  with the ultimate strength of the material, obtained on samples with allowance for the time of their operation and temperature:  $n = \sigma_{BT}^t / \sigma_\varphi$ . Condition  $n \geq 1$  should be fulfilled.

Case 2. Temperature stresses and strain in a free shell.

The quantities  $h$ ,  $r$ ,  $E$ ,  $\Delta t$  are given. Find  $\sigma_\varphi$ ,  $w$ ,  $n$ .

Let us assume that the shell has constant parameters  $h$ ,  $r$ ,  $E$ . The modulus of elasticity  $E$  is considered equal to its average value. Temperature gradient  $\Delta t$  is a variable quantity and depends upon coordinate  $x$  of the shell. In general form,

$$\Delta t = t - t_0 = Bx^n,$$

where B is a coefficient;

n is the exponent equal to 0, 1, 2, with uniform heating, linear and quadratic variation in the temperature gradient, respectively.

We further assume that the temperature of the shell is constant throughout its thickness.

As indicated, the relative strain of an element during heating is determined by formula

$$\varepsilon = \varepsilon_t + \varepsilon_y,$$

where  $\varepsilon_t$  is the thermal strain of a free element;

$\varepsilon_y$  is the elastic strain of an element due to the constriction of its deformation.

For a cylindrical shell relative strains in the circular direction  $\varepsilon_\varphi = \varepsilon_{\varphi t} + \varepsilon_{\varphi y}$ , are substantial and are easily converted to radial strain w with formula  $w = r\varepsilon_\varphi$ . Finally

$$w = w_t + w_y.$$

Free thermal strain  $w_t$  is known (Fig. 5.14a):

$$w_t = r\varepsilon_{\varphi t} = r\alpha\Delta t.$$

It is also known that the stress in the shell creates the elastic component of total thermal strain in the element  $w_y$ . Finding it involves considerable difficulties.

Elastic component of shell strain is found by common procedures for a temperature problem.

a) We impose on a cold shell rigid bonds in the form of a rigid housing and then heat it to temperature t. Thermal expansion of the shell does not occur, compressive stress arises in it, and on the surface a reaction from the rigid walls in the form of pressure  $p_{Rt}$ . The same effect can be obtained if we compress a shell expanding to  $w_t = r\alpha\Delta t$  by external pressure up to the initial parameter.

It is known that such a rigid attachment of the shell corresponds to the conditions when elastic and thermal strains are equal but opposite in sign:

$$w^* = 0; w_y^* = -w_z^* = -ra\Delta t; \quad (5.13)$$

The asterisks indicate that bends are obtained during the rigid attachment of the shell. Let us find the wall reaction  $p_{Rt}$ , which holds the shell in a compressed undeformed state. Shell deformation from pressure  $p_{Rt}$ , in general form, is

$$w^* = A\Delta t = ABx^n,$$

where  $A$  is a coefficient.

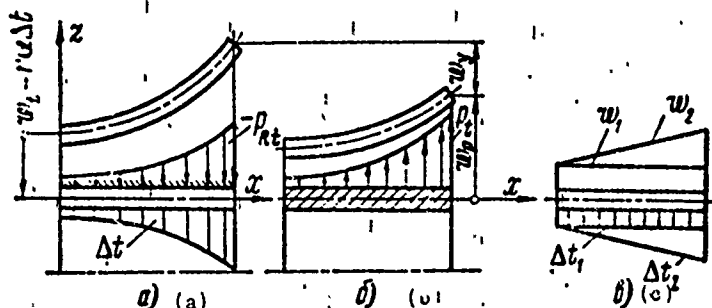


Fig. 5.14.

For the studied case  $w^{*IV} = 0$ ; then bend  $w^*$  can be determined from equation:

$$w^{*IV} + \frac{Eh}{r^2 D} w^* = \frac{p_{Rt}}{D},$$

assuming  $w^{*IV} = 0$ :

$$w^* = w_0 + w_1 + w_2, \text{ since } w_0 = 0, \text{ and } w_0 = 0, \text{ и } \frac{Eh}{r^2 D} w^* = \frac{p_{Rt}}{D},$$

hence

$$w^* = \frac{r^2}{Eh} p_{Rt}.$$

Bend  $w$  is an elastic bend of the shell as a result of pressure  $p_{Rt}$ . This bend is known from relationship (5.13):  $w^* = -r\alpha\Delta t$ . Equating those values of  $w^*$ , we obtain the pressure  $p_{Rt}$ , which holds the shell in a compressed state as a result of the application of a rigid bond:

$$\frac{r^2}{Eh} p_{Rt} = -r\alpha\Delta t$$

and

$$p_{Rt} = -\frac{Eh}{r} \alpha\Delta t.$$

The obtained shell deformation  $w_y^* = -w_t^* = -r\alpha\Delta t$  and reaction forces  $-p_{Rt}$  differ from the actual since actually there is no rigid attachment. The shell is free.

b) In order to obtain the pure deformation of the shell, we should apply the load arising in the shell during its attachment but with opposite sign. We find the bend of the shell from the reaction  $p_t = -p_{Rt}$  from equation

$$w^{IV} + \frac{Eh}{r^2D} w = \frac{p_t}{D} = \frac{Eh\alpha\Delta t}{rD}. \quad (5.14)$$

c) The sum of the two deformations obtained from equations (5.13) and (5.14), which we shall designate  $w_p$ , gives us the elastic component of total shell deformation during its thermal loading:

$$w_y = -r\alpha\Delta t + w_p.$$

Hence we find the stresses arising in the shell from thermal loads:

$$\sigma_\varphi = E\varepsilon_\varphi = E \frac{w_y}{r} = -E\alpha\Delta t + E \frac{w_p}{r}. \quad (5.15)$$

d) The numerical value of total thermal deformation by heating a free shell is found from relationship

$$w = w_t + w_y = r\alpha\Delta t - r\alpha\Delta t + w = w_p. \quad (5.16)$$

Thus, the bend obtained from equation (5.14) is the total bend of the shell as the result of its thermal loading.

The procedure for determining  $w_y$  and  $w_p$  is shown in Fig. 5.14.

Let us examine the stress and strain of the shell as a result of a given temperature gradient  $\Delta t$ .

If the temperature gradient is a constant value, i.e.,  $\Delta t = \text{const}$ , then from equation (5.14) it is apparent that  $w^{IV} = 0$ . Then  $w = w_0 + w_q = w_q$ ;  $w_0 = 0$ . Furthermore,

$$\frac{Eh}{r^3 D} w = \frac{Eh \alpha \Delta t}{r D};$$

hence

$$\begin{aligned} w &= w_q = r \alpha \Delta t; & w' &= w'' = w''' = w^{IV} = 0; \\ w_y &= -r \alpha \Delta t + w_p = 0; & \sigma_\varphi &= 0; \\ w &= w_t + w_y = w_t = r \alpha \Delta t. \end{aligned}$$

Thus, uniform heating of a free shell does not cause thermal stresses in it; shell deformation is equal to unconstricted thermal deformation.

If the temperature gradient varies according to linear law, i.e.,  $\Delta t = B_0 + B_1 x$ , it is apparent from equation (5.14) that

$$\begin{aligned} w^{IV} &= 0; & w &= w_0 + w_q = w_q; & w_0 &= 0; \\ w &= w_q = r \alpha \Delta t = r \alpha (B_0 + B_1 x); \\ w' &= r \alpha B_1; & w'' &= w''' = w^{IV} = 0; \\ w_y &= -r \alpha \Delta t + w_p = 0; & \sigma_\varphi &= 0; \\ w &= w_t + w_y = w_t = r \alpha \Delta t = r \alpha (B_0 + B_1 x). \end{aligned}$$

Thus, a linear law of temperature gradient variation along the axis of the free shell does not cause thermal stresses. Its strain is equal to unconstrained thermal strain.

Let us examine the case when the temperature gradient varies according to parabolic law  $\Delta t = B_0 + B_1 x + B_2 x^2$ .

Since  $w = A\Delta t$ , then  $w^{IV} = 0$ ; further

$$\begin{aligned} w &= w_0 + w_q = w_q; \quad w_0 = 0; \\ w &= w_q = r\alpha\Delta t = r\alpha(B_0 + B_1 x + B_2 x^2). \end{aligned}$$

However,

$$w' = r\alpha(B_1 + 2B_2 x); \quad w'' = 2r\alpha B_2,$$

i.e., with a quadratic law of temperature gradient variation the shell will not be in a momentless membrane state. Thermal stresses will arise in it. Deformations of a free shell are shown in Fig. 5.14c.

Case 3. A shell is loaded on the edge by distributed moment and shearing force.

The quantities  $E, h, r, \bar{Q}_0, \bar{M}_0$  are given. Determine  $\sigma_\varphi, \sigma_x, w, n$ .

Let us examine a long cylindrical shell (Fig. 5.15) to the edge of which are applied bending moments  $\bar{M}_0$  and shearing forces  $\bar{Q}_0$ ; these forces and others are uniformly distributed along the edge of the shell, i.e., when  $x = 0$ . For the sake of simplicity, the bars over  $Q$  and  $M$  are eliminated.

Pressure  $p = 0$ ; therefore, in the general solution (5.10) we should assume  $w_q = 0$  and seek the general integral of the homogeneous differential equation (5.9), i.e., solution to the equation without the right side.

It is known that, in this case, the integral (5.9) expresses the edge effect, i.e., the effect of radial distributed forces and moments acting on the edges of the shell. Since the applied forces produce local bend, rapidly diminishing to zero as the distance from the end increases, we conclude that the second term in the right side of equation (5.10) must be zero. Therefore,  $C_3 - C_4 = 0$ ,

$$w = e^{-\beta x} (C_1 \sin \beta x + C_2 \cos \beta x). \quad (5.17)$$

Constants  $C_1$  and  $C_2$  are determined from the boundary conditions: when  $x = 0$   $M_x = M_0 = Dw''$ ;  $Q_x = Q_0 = Dw'''$ . If we differentiate equation (5.17) three times, we obtain

$$\begin{aligned} w' &= \beta e^{-\beta x} [C_1 (\cos \beta x - \sin \beta x) - C_2 (\cos \beta x + \sin \beta x)]; \\ w'' &= 2\beta^2 e^{-\beta x} [-C_1 \cos \beta x + C_2 \sin \beta x]; \\ w''' &= 2\beta^3 e^{-\beta x} [C_1 (\cos \beta x + \sin \beta x) + C_2 (\cos \beta x - \sin \beta x)]. \end{aligned}$$

We substitute into these equations the following boundary conditions:

$$C_1 = -\frac{M_0}{2\beta^2 D}; \quad C_2 = \frac{1}{2\beta^3 D} (Q_0 + \beta M_0).$$

Finally,

$$w = \frac{e^{-\beta x}}{2\beta^3 D} [\beta M_0 (\cos \beta x - \sin \beta x) + Q_0 \cos \beta x]. \quad (5.18)$$

Maximum bend on the loaded end is

$$w(0) = \frac{1}{2\beta^3 D} (\beta M_0 + Q_0). \quad (5.19)$$

The slope angle of the tangent to the elastic line on the loaded end of the shell is found by differentiating expression (5.13):



$$w' = -\frac{e^{-\beta x}}{2\beta^2 D} (2\beta M_0 \cos \beta x + Q_0 (\cos \beta x + \sin \beta x)) \quad (5.20)$$

and, finally, when  $x = 0$

$$w'(0) = -\frac{1}{2\beta^2 D} (2\beta M_0 + Q_0). \quad (5.21)$$

If we introduce the following designations:

$$\begin{aligned} \varphi &= e^{-\beta x} (\cos \beta x + \sin \beta x); \quad \psi = e^{-\beta x} (\cos \beta x - \sin \beta x); \\ \theta &= e^{-\beta x} \cos \beta x; \quad \zeta = e^{-\beta x} \sin \beta x, \end{aligned}$$

the expressions for bend and its derivative can be represented in the following form:

$$\left. \begin{aligned} w &= \frac{1}{2\beta^2 D} (-\beta M_0 \varphi + Q_0 \psi); \\ w' &= -\frac{1}{2\beta^2 D} (2\beta M_0 \theta + Q_0 \zeta); \\ w'' &= \frac{1}{\beta D} (\beta M_0 \varphi + Q_0 \zeta); \\ w''' &= -\frac{1}{D} (2\beta M_0 \theta - Q_0 \psi). \end{aligned} \right\} \quad (5.22)$$

The numerical values of functions  $\varphi$ ,  $\psi$ ,  $\theta$  and  $\zeta$  are presented in Table 5.1 [38].

Functions  $\varphi$  and  $\psi$  are presented in Fig. 5.16, function  $\zeta$  in Fig. 5.17.

From the curves and the table it is apparent that the functions determining shell bend, with an increase in quantity  $\beta x$ , approach zero. Consequently, bend has only a local character, as suggested initially, in the calculation of integration constants.

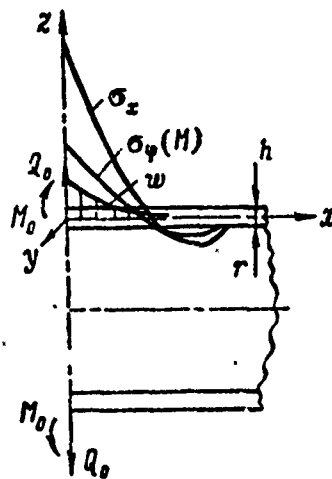


Fig. 5.15.

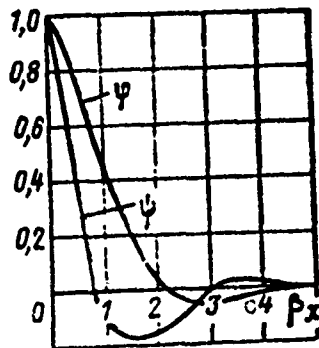


Fig. 5.16. Graph of functions  $\varphi$  and  $\psi$ .

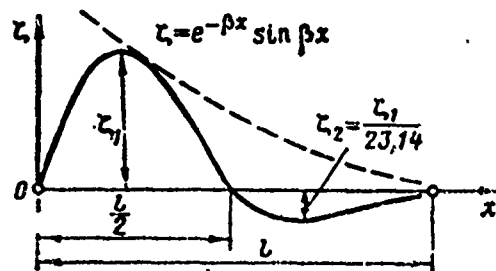


Fig. 5.17. Graph of function  $\zeta$ .

The curves presented make it possible to establish boundaries which distinguish a long shell from a short one. From formula (5.17) it is apparent that shell bend  $w$  and its derivatives are attenuating curves. Wave length is

$$l = \frac{2\pi}{\beta} = \frac{2\pi}{\sqrt[4]{3(1-\nu^2)/rh}} = 4.8 \sqrt{rh}.$$

Table 5.1.

$3x$	$\varphi$	$\psi$	$\theta$	$\delta$
0	1,0000	1,0000	1,0000	0
0,1	0,9907	0,8100	0,9003	0,0903
0,2	0,9651	0,6398	0,8024	0,1627
0,3	0,9267	0,4888	0,7077	0,2189
0,4	0,8784	0,3564	0,6174	0,2610
0,5	0,8231	0,2415	0,5323	0,2908
0,6	0,7628	0,1431	0,4539	0,3099
0,7	0,6997	0,0599	0,3798	0,3199
0,8	0,6354	0,0093	0,3131	0,3223
0,9	0,5712	0,0657	0,2527	0,3185
1,0	0,5083	0,1108	0,1988	0,3096
1,1	0,4476	0,1457	0,1510	0,2957
1,2	0,3899	0,1716	0,1091	0,2807
1,3	0,3355	0,1897	0,0729	0,2626
1,4	0,2849	0,2011	0,0419	0,2430
1,5	0,2334	0,2068	0,0158	0,2226
1,6	0,1959	0,2077	0,0059	0,2018
1,7	0,1576	0,2047	0,0235	0,1812
1,8	0,1234	0,1985	0,0376	0,1610
1,9	0,0932	0,1899	0,0484	0,1415
2,0	0,0667	0,1794	0,0563	0,1230
2,1	0,0439	0,1675	0,0618	0,1057
2,2	0,0244	0,1548	0,0652	0,0895
2,3	0,0080	0,1416	0,0668	0,0748
2,4	0,0056	0,1282	0,0669	0,0613
2,5	0,0165	0,1199	0,0658	0,0493
2,6	0,0254	0,1019	0,0636	0,0383
2,7	0,0320	0,0895	0,0608	0,0287
2,8	0,0369	0,0777	0,0573	0,0204
2,9	0,0403	0,0666	0,0534	0,0132
3,0	0,0423	0,0563	0,0493	0,0071
3,1	0,0431	0,0469	0,0450	0,0019
3,2	0,0431	0,0383	0,0407	0,0024

Table 5.1. (Continued)

$\beta x$	$\varphi$	$\psi$	$\theta$	$\zeta$
3,3	0,0122	0,0306	0,0334	0,0058
3,4	0,0408	0,0237	0,0323	0,0085
3,5	0,0389	0,0177	0,0283	0,0103
3,6	0,0366	0,0124	0,0245	0,0121
3,7	0,0341	0,0079	0,0210	0,0131
3,8	0,0314	0,0040	0,0177	0,0137
3,9	0,0285	0,0008	0,0147	0,0140
4,0	0,0258	0,0019	0,0120	0,0139

With each half-wave (for example, sinusoid in Fig. 5.17) the amplitude of the function changes sign and decreases in absolute magnitude by a factor of 23.14. If the maximum of all functions agreed with the origin of coordinates  $x = 0$ , we could conclude that with a cylindrical shell length of  $l_d = l/2 = 2.4\sqrt{rh}$ , its calculation as a "long" shell, without allowing for the mutual effect of both edges, leads to error not exceeding 5%. However, since the maximum amplitudes of these functions do not always agree with the edge of the shell, for ordinary calculations a cylindrical shell can be assumed "long" if  $l_d \geq 3\sqrt{rh}$ .

After finding moment  $\bar{M}_x$  and bend  $w$ , we find from expression (5.16) moment  $\bar{M}$  and the value of force  $\bar{T}$  from equation (5.3).

It is obvious that the outer cross section will also be the most stressed. On it are the following bending moments and forces; moment  $M_x = Dw''M_0$ ; moment  $M_\varphi = \mu M_x$ ; tension

$$\bar{T}_\varphi = \frac{Ehw}{r} = \frac{Eh}{r2^{3/2}D} (3M_0 + Q_0).$$

According to these loads, stresses are

$$\tau_\varphi = \frac{\bar{T}_\varphi}{h} = \frac{Ew}{r}; \quad \sigma_x = \frac{6M_x}{h^2}; \quad \sigma_\varphi(M) = \frac{6M_\varphi}{h^2} = \mu \sigma_x. \quad (5.23)$$

Hence generalized stress is

$$\sigma_1 = \sqrt{\sigma_x^2 + [\tau_\varphi(M) + \sigma_\varphi]^2 - \tau_x(\tau_\varphi(M) + \sigma_\varphi)}.$$

The coefficient of safety is  $n = \frac{\sigma_{n,\tau}}{\sigma_{1 \max}}$ ;  $n \geq 1$ .

As seen from Fig. 5.15 and 5.18, the most stressed spot of the shell is the circumference passing through point A.

Case 4. Stresses in a supported shell loaded with pressure.

The edge of the shell has a hinged support (Fig. 5.19). The quantities  $r$ ,  $h$ ,  $E$ ,  $p$  are given. Find  $\sigma_\varphi$ ,  $\sigma_x$ ,  $\sigma_\varphi(M)$ ,  $w$ . The initial equation is

$$w = e^{-\beta x} (C_1 \sin \beta x + C_2 \cos \beta x) + w_q. \quad (5.24)$$

The following solution sequence is selected. We determine the deformation of a free, unsupported shell under the action of pressure  $p$ . Then we apply to the end of the shell force  $Q_0$  so that total shell deformation at the support point is zero. This procedure makes it possible to use the results of the preceding calculations.

Deformation of a free shell is determined by the particular integral

$$w_q = \frac{pr^2}{Eh} = \delta,$$

where  $\delta$  is the bend of the free shell under the action of pressure  $p$ .

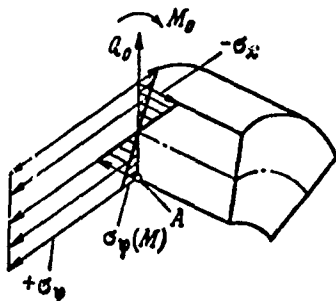


Fig. 5.18. Diagram of shell stresses.

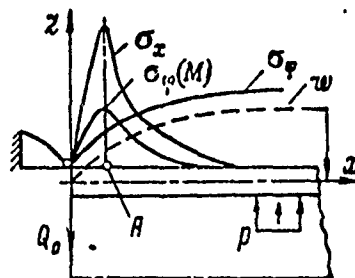


Fig. 5.19. Stresses in a shell with a hinged support.

The bend of the shell as a result of force  $Q_0$  is found from the general solution to equation (5.17) obtained during the solution of equation (5.9). Integration constants  $C_1, C_2$  of the general solution are determined from conditions:

$$\text{when } x = 0 \quad w_0(0) = -\delta; \quad w_0''(0) = 0, \text{ since } M_x = M(0) = 0.$$

Then from equation (5.19) we find the necessary reaction  $Q_0$  for fulfilling these conditions:

$$w(0) = \frac{1}{2\beta^3 D} Q_0 = -\delta; \quad Q_0 = -2\beta^3 D \delta.$$

Now we find

$$\begin{aligned} w &= \frac{e^{-\beta x}}{2\beta^3 D} Q_0 \cos \beta x + \frac{nr^2}{Eh}; \\ w' &= -\frac{e^{-\beta x}}{2\beta^2 D} Q_0 (\sin \beta x + \cos \beta x); \\ w'' &= \frac{e^{-\beta x}}{\beta D} Q_0 \sin \beta x. \end{aligned}$$

According to formulas (5.23) we can find

$$\begin{aligned} \sigma_r &= E \frac{w}{r} \quad (\text{при } x=0 \quad \sigma_r=0); \\ \sigma_x &= \frac{6Dw''}{h^2}; \quad \sigma_x(M) = \mu \sigma_r. \end{aligned}$$

(при = when)

The stress diagram is shown in Fig. 5.19.

The edge of the shell has a rigid attachment (Fig. 5.20). Solution is found from formula (5.24). The deformation of a free shell from pressure  $p$  is

$$w_q = \frac{pr^2}{Eh} = \delta.$$

We find the necessary values of  $M_0$  and  $Q_0$  to satisfy these conditions from equations (5.19) and (5.21):

$$M_0 = 2\beta^2 D\delta; \quad Q_0 = -4\beta^3 D\delta.$$

$$\begin{aligned} w &= \frac{e^{-\beta x}}{2\beta^3 D} [3M_0 (\cos \beta x - \sin \beta x) + Q_0 \cos \beta x] + \frac{pr^2}{Eh}; \\ w' &= -\frac{e^{-\beta x}}{2\beta^2 D} [2\beta M_0 \cos \beta x + Q_0 (\cos \beta x + \sin \beta x)]; \\ w'' &= \frac{e^{-\beta x}}{\beta D} [\beta M_0 (\cos \beta x + \sin \beta x) + Q_0 \sin \beta x]. \end{aligned} \quad (5.25)$$

## Stresses

$$\tau_{\varphi} = E \frac{w}{r}; \quad \sigma_x = \frac{6Dw''}{h^2}; \quad \tau_r(M) = \mu \sigma_x.$$

The stress diagram is shown in Fig. 5.20.

**Case 5.** Stresses and strains of a shell having supports, as a result of thermal loading.

The edge has a hinged support (Fig. 5.21). The quantities  $r$ ,  $h$ ,  $E$ ,  $\Delta t$  are given. Find  $\sigma_{\varphi}$ ,  $\sigma_x$ ,  $w$ .

a) Shell deformation with thermal loading is

$$w = w_t + w_y, \text{ where } w_t = ra\Delta t.$$

b) Elastic deformation in the shell with the application of rigid bonds is

$$w = 0; \quad w_y = -w_t = -ra\Delta t.$$

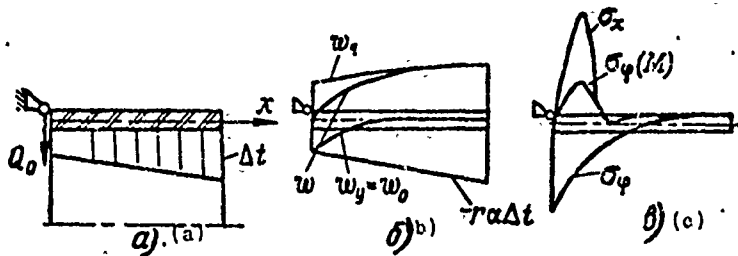


Fig. 5.21. Analysis of a cylindrical shell.

c) Elastic deformation of the shell from pressure arising as a result of the application of bonds is determined from formulas (5.8) and (5.14):

$$w_p^{IV} + \frac{Eh}{r^2D} w_p = \frac{Eha\Delta t}{rD}.$$



Solution is sought from formula

$$w_p = w_0 + w_q = e^{-\beta x} (C_1 \sin \beta x + C_2 \cos \beta x) - w_q.$$

We assume that  $\Delta t = Bx^n$ , where  $n \leq 3$ , then

$$w^{IV} = 0 \quad \text{and} \quad w_q = r\alpha \Delta t = \delta.$$

We have obtained the deformation of a shell for a case in which there are no supporting devices. We designate this deformation  $\delta$ . But the fact is, at the support point reaction  $Q_0$  arises, which does not allow the edge section to be moved. We shall find the value of the general solution to the equation for  $w_0$ :

$$w_0 = e^{-\beta x} (C_1 \sin \beta x + C_2 \cos \beta x).$$

Integration constants  $C_1$  and  $C_2$  are found from conditions:

$$\text{when } x=0 \quad w_0(0) = -\delta(0); \quad w_0'(0) = 0.$$

Here  $\delta(0)$  is the value of the particular integral  $w_q$  on the edge of the shell  $\delta(0) = r\alpha \Delta t(0)$ , where  $\Delta t(0)$  is the temperature gradient on the edge of the shell.

From equation (5.19) we find the reaction of the support

$$Q_0 = -2\beta^3 D \delta(0)$$

and the unknown deformation

$$w_p = \frac{e^{-\beta x}}{2\beta^3 D} Q_0 \cos \beta x + r\alpha \Delta t = w_0 + w_q.$$

d) Let us find the elastic deformation and its derivative for determining stresses in the shell:

$$w_y = -ra\Delta t + w_p = w_0 = \frac{e^{-\beta x}}{2\beta^3 D} Q_0 \cos 3x;$$

$$w'_y = -\frac{e^{-\beta x}}{2\beta^2 D} Q_0 (\sin \beta x + \cos 3x); \quad w''_y = \frac{e^{-\beta x}}{\beta D} Q_0 \sin \beta x.$$

The curve of  $w_y$  variation is shown in Fig. 5.21b. Circular stresses in the shell are

$$\sigma_\varphi = E \frac{w_y}{r}.$$

Let us note that they will be the greatest when  $x = 0$ .

Stresses in the shell from bending are

$$\sigma_x = \frac{6M_x}{h^2} = \frac{6Dw''}{h^2}; \quad \sigma_z(M) = \mu \sigma_x.$$

The stress curve is shown in Fig. 5.21c.

e) Total shell deformation is

$$w = w_t + w_y = ra\Delta t + w_0 = w_p.$$

As in other cases, total deformation is the result of the solution to equation (5.14). The character of the total deformation curves is seen in Fig. 5.21d.

The edge has a rigid attachment. Let us introduce formulas for calculating strains and stresses.

The strain of the shell during thermal loading is

$$w_t = w_t + w_y = ra\Delta t + w_y.$$

Elastic deformation of the shell is

$$w_y = -ra\Delta t + w_p.$$

The value of  $w_p$  is found from formulas (5.14):

$$w_p = w_0 + w_y = e^{-\beta x} (C_1 \sin \beta x + C_2 \cos \beta x) + w_y,$$

where  $w_y = \alpha \Delta t$ .

The integration constants  $C_1, C_2$  are determined from the conditions:

$$x=0; w_0(0) = -\delta(0); w_0'(0) = 0, \text{ where } \delta(0) = \alpha \Delta t(0).$$

We find  $M_0 = 2\beta^2 D \delta(0)$ ;  $Q_0 = -4\beta^3 D \delta(0)$ . Then we calculate  $w, w', w'', \sigma_\varphi, \sigma_x, \sigma_\varphi (M)$  according to formulas similar to the formulas in Case 4 and the total deformation of the shell is  $w = w_t + w_y = w_p$ .

Let us examine an example of the calculation.

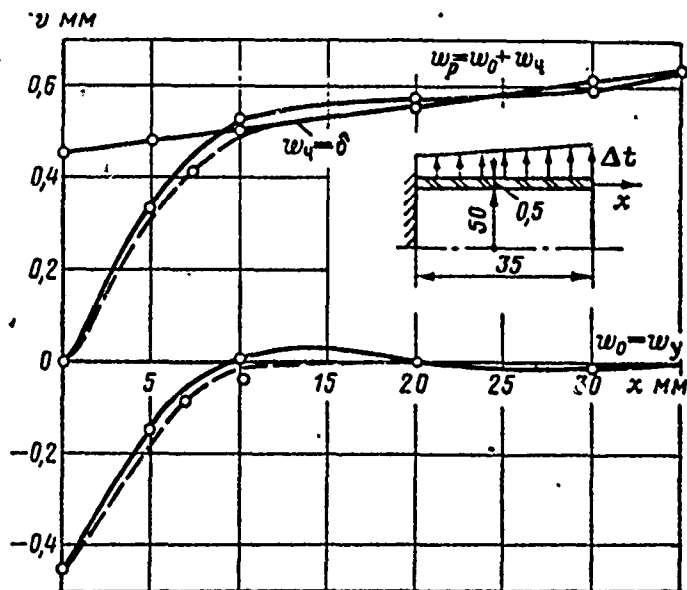


Fig. 5.22. Analysis of a cylindrical anode.

Example 5.1. Find the stress and the coefficient of safety for a cylindrical anode whose dimensions are shown in Fig. 5.22 if the following is given: material is Kh18N9T steel;  $E = 1.45 \cdot 10^4$  daN/mm<sup>2</sup>;  $\alpha = (21.2-22.2)10^{-6}$  1/°C. The left end of the anode is rigidly attached. The temperature along the length of the anode is distributed linearly.

1. Law of temperature variation along the anode is  $\Delta t = B_0 + B_1 x$ .

From the condition when  $x = 0$   $\Delta t = 430^\circ\text{C}$ ; when  $x = l$   $\Delta t = 580^\circ\text{C}$  we obtain  $B_0 = 430$ ;  $B_1 = 4.3$ .

2. Let us evaluate the length of a shell:

$$l_s \geq 3 \sqrt{r h} = 3 \sqrt{50 \cdot 0.5} = 15 \text{ mm},$$

i.e., the shell is long;  $l = 35$ .

3. We find the reaction  $Q_0$  and  $M_0$ . If the shell did not have an attachment, its deformation would be equal to the deformation of a free shell, i.e.,  $\delta = \alpha \Delta t$ ; at the attachment point  $\delta_0 = \alpha \Delta t_0 = 50 \cdot 21.2 \cdot 10^{-6} \cdot 430 = 0.455$  mm.

Since the shell is attached, we deform its end by quantity  $\delta_0 = -0.455$  and find what force  $Q_0$  and moment  $M_0$  should be applied for this. We solve the system of equations (5.19) with boundary conditions:

$$\begin{aligned} x=0; \quad w(0) &= -\delta_0; \quad w'(0) = 0; \\ w(0) &= \frac{1}{23^3 D} (3M_0 + Q_0) = -\delta_0; \quad w'(0) = \frac{1}{23^2 D} (3M_0 + Q_0) = 0. \end{aligned}$$

hence

$$\begin{aligned} M_0 &= 23^3 D \delta_0 = 2 \cdot 0.2572 \cdot 166,3 \cdot 0.455 = 10,02 \text{ daN mm/mm}; \\ Q_0 &= -13^3 D \delta_0 = -1 \cdot 0.2573 \cdot 166,3 \cdot 0.455 = -5,14 \text{ daN/mm}. \end{aligned}$$

We determine

$$\beta = \frac{1,29}{\sqrt{rh}} = \frac{1,29}{\sqrt{50 \cdot 0,5}} = 0,275 \text{ 1/mm};$$

$$D = \frac{Eh^3}{12(1-\mu^2)} = \frac{1,45 \cdot 10^4 \cdot 0,5^3}{12(1-0,32)} = 166,3 \text{ daN} \cdot \text{mm}.$$

4. We find

$$w_p = \frac{e^{-\beta x}}{2\beta^3 D} [\beta M_0 (\cos \beta x - \sin \beta x) + Q_0 \cos \beta x] + \delta = w_0 + \delta;$$

$$\sigma_r = E \frac{w_y}{r}, \text{ where } w_y = w_p - r\alpha \Delta t.$$

Calculation is reduced in Table 5.2. Let us determine the coefficients:

$$2\beta^3 D = 2 \cdot 0,257^3 \cdot 166,3 = 5,65 \text{ daN/mm}^2;$$

$$\beta M_0 = 0,257 \cdot 10,02 = 2,58 \text{ daN/mm};$$

$$\frac{E}{r} = \frac{1,45 \cdot 10^4}{50} = 290 \text{ daN/mm}^3.$$

The bend determining the stress in a cylindrical shell is found in line 10. Actually,

$$w_y = w_p - r\alpha \Delta t; \text{ since } w_p = w_0 + \delta \text{ and } \delta = r\alpha \Delta t, \text{ then } w_y = w_0.$$

Figure 5.22 presents curves of  $w_0$ ,  $w_y$ ,  $\delta$  and the total anode bend  $w_\Sigma$  as a result of its heating.

5. We find

$$w'' = \frac{e^{-\beta x}}{\beta D} [\beta M_0 (\cos \beta x + \sin \beta x) + Q_0 \sin \beta x];$$

$$\sigma_x = \frac{6Dw''}{h^2}; \quad \sigma_\varphi(M) = \mu \sigma_x.$$

The calculation is presented in lines 16-23 of Table 5.2.

Let us determine the coefficients:

$$\beta D = 0,257 \cdot 166,3 = 42,6 \text{ daN/mm};$$

$$\frac{6D}{h^2} = \frac{6 \cdot 166,3}{0,5^2} = 3980 \text{ daN/mm}^2.$$

Stress distribution along the anode is indicated in Fig. 5.23.

Case 6. Thermal stresses in a free shell. The quantities  $h$ ,  $r$ ,  $\Delta t$  are given. Find  $\sigma_\varphi$ ,  $\sigma_x$ ,  $\sigma_\varphi(M)$ ,  $w$ .

It is known that thermal stresses in a free shell occur if the law of temperature variation along the length is nonlinear, i.e., if  $\Delta t = Bx^n$  when  $n \geq 2$ . We assume  $\Delta t = B_0 + B_1 x^2$ .

Deformation of the shell is

$$w = w_t + w_y, \text{ where } w_t = r\alpha\Delta t.$$

We find the elastic component of the deformation.

With the application of rigid bonds

$$w = 0; w_y = -w_t = -r\alpha\Delta t.$$

Deformation of the shell from the stress arising as a result of the application of bonds is determined from equation (5.14):

$$w_p^{IV} + \frac{Eh}{r^2 D} w_p = \frac{Eh\alpha\Delta t}{rD}.$$

We obtain

$$w_p = w_0 + w_r = e^{-\beta x} (C_1 \sin \beta x + C_2 \cos \beta x) + e^{\beta x} (C_3 \sin \beta x + C_4 \cos \beta x) + w_q.$$

Table 5.2.

(1) № ст- ро- ки	(2) Функция	(3) Мно- жи- тель	$x = 0$	5	10	20	30	$x = 35$
1	$\beta x$	1	0	1,285	2,57	5,14	7,71	8,99
2	$e^{-\beta x}$	1	1	0,275	0,0765	0,0059	0,00045	0,000123
3	$e^{-\beta x/233D}$	1	0,177	0,0486	0,0135	0,0005	0,000079	0,0000218
4	$\sin \beta x$	1	0	0,958	0,5403	-0,909	0,9901	0,4169
5	$\cos \beta x$	1	1	0,2837	-0,8415	0,4169	0,1433	-0,909
6	(5) - (4)	1	1	-0,6713	-1,3818	1,3259	-0,8498	-1,3259
7	$\beta M_0(6)$	1	2,58	-1,73	-3,55	3,42	-2,19	-3,42
8	$Q_0(5)$	1	-5,14	-1,48	4,33	-2,14	-0,721	4,68
9	(7) + (8)	1	-2,56	-3,21	0,77	1,28	-2,91	1,25
10	(3)(9) = $w_0$	1	-0,455	-0,156	0,0104	0,00134	-0,0003	0,0000
11	$\Delta t$	1	430	451,5	473	516	559	580
12	$a$	10-6	21,2	21,5	21,6	21,8	22,1	22,2
13	$w_q = r a \Delta t$	1	0,455	0,485	0,511	0,562	0,617	0,643
14	$w_p = (10) + (13)$	1	0	0,329	0,511	0,563	0,617	0,643
15	$\sigma_p = \frac{E}{r} (10)$	1	-132	-45,3	30,2	0,39	-0,057	0
16	$e^{-\beta x/3D}$	1	0,0235	0,00645	0,0018	0,00014	0,0000	0,0000
17	(4) + (5)	1	1	1,2447	-0,3012	-0,4921	1,1304	-0,4921
18	$\beta M_0(7)$	1	2,58	3,21	-0,776	-1,27	2,92	-1,27
19	$Q_0(4)$	1	0	-4,93	-2,78	4,67	-5,09	-2,14
20	(18) + (19)	1	2,58	-1,72	-3,56	3,40	-2,17	-3,41
21	$W'' = (16)(21)$	1	0,0514	-0,0113	-0,00546	0,00018	0,00002	-0,00001
22	$\sigma_x$	1	245	-45,1	-25,8	1,9	-0,09	-0,04
23	$\sigma_p(M)$	1	73,5	-13,5	-7,75	0,57	-0,03	-0,01

KEY: (1) No.; (2) Function; (3) Factor.

Let us find  $w_q$ . Assuming that  $w^{IV} = 0$ , we obtain

$$w_q = r a \Delta t = r a (B_0 + B_1 x^2) = A_0 + A_1 x^2.$$

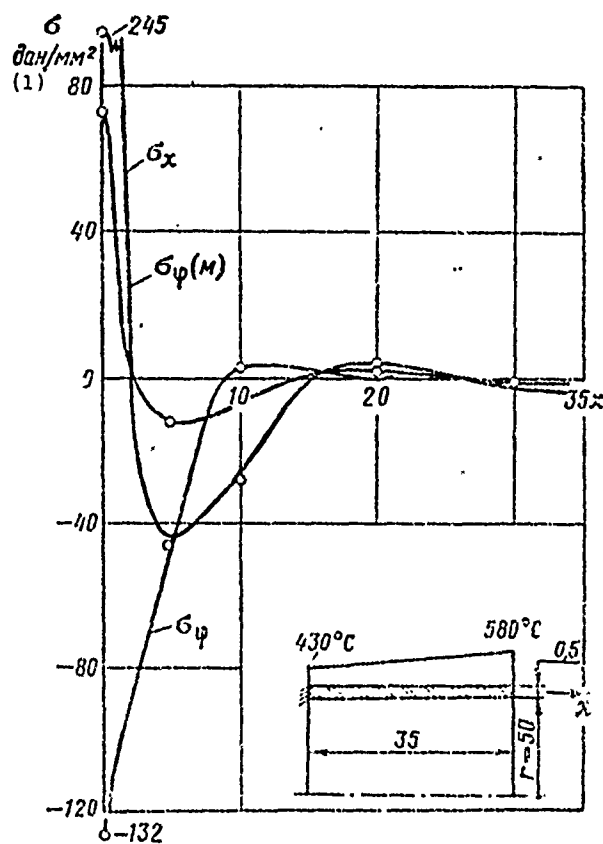
We find the general integral  $w_0$ .

Integration constants  $C_1, C_2, C_3, C_4$  are determined from boundary conditions:

$$\text{when } x=0 \quad \dot{w}_p(0) = \ddot{w}_p(0) = 0;$$

$$\text{when } x=l \quad \dot{w}_p(l) = \ddot{w}_p(l) = 0.$$

Fig. 5.23. Stresses in a cylindrical anode.  
KEY: (1)  $\text{daN/mm}^2$ .



If we differentiate the general solution for  $w_p$  three times, we obtain

$$\begin{aligned} w_p' &= e^{-\beta x} \sin \beta x (-\beta C_1 - \beta C_2) + e^{-\beta x} \cos \beta x (\beta C_1 - \beta C_2) + \\ &\quad + e^{\beta x} \sin \beta x (\beta C_3 - \beta C_4) + e^{\beta x} \cos \beta x (\beta C_3 - \beta C_4) + 2A_1 x; \\ w_p'' &= e^{-\beta x} \sin \beta x (2\beta^2 C_2) + e^{-\beta x} \cos \beta x (-2\beta^2 C_1) + \end{aligned}$$



$$\begin{aligned}
 & + e^{\beta x} \sin \beta x (-2\beta^2 C_4) + e^{\beta x} \cos \beta x (2\beta^2 C_3) + 2A_1; \\
 w_p'' = & e^{-\beta x} \sin \beta x (2\beta^3 C_1 - 2\beta^3 C_2) + e^{-\beta x} \cos \beta x (2\beta^3 C_1 + 2\beta^3 C_2) + \\
 & + e^{\beta x} \sin \beta x (-2\beta^3 C_3 - 2\beta^3 C_4) + e^{\beta x} \cos \beta x \times \\
 & \times (2\beta^3 C_3 - 2\beta^3 C_4). \quad (5.26)
 \end{aligned}$$

After substituting the boundary conditions into these equations, we find integration constants C. The problem is simplified by the fact that for a long shell we can determine them independently.

When  $x = 0$  we find  $C_1, C_2$ , if we assume  $C_3 = C_4 = 0$ . Then

$$w_p'(0) = e^{-\beta x} \sin \beta x (2\beta^2 C_2) - e^{-\beta x} \cos \beta x (2\beta^2 C_1) + 2A_1 = 0,$$

or

$$-2\beta^2 C_1 + 2A_1 = 0;$$

$$w_p''(0) = e^{-\beta x} \sin \beta x (2\beta^3 C_1 - 2\beta^3 C_2) + e^{-\beta x} \cos \beta x (2\beta^3 C_1 + 2\beta^3 C_2) = 0,$$

or  $C_1 + C_2 = 0$ .

When  $x = l$  we seek  $C_3, C_4$ , after assuming  $C_1 = C_2 = 0$ :

$$w_p'(l) = e^{\beta l} \sin \beta l (-2\beta^2 C_4) + e^{\beta l} \cos \beta l (2\beta^2 C_3) + 2A_1 = 0;$$

$$w_p''(l) = e^{\beta l} \sin \beta l (-2\beta^3 C_3 - 2\beta^3 C_4) + e^{\beta l} \cos \beta l (2\beta^3 C_3 - 2\beta^3 C_4) = 0.$$

Thus, integration constants  $C_1, C_2, C_3, C_4$  are defined. From equation (5.26) we find the values of  $w_p$  and  $w_p''$ , and then the elastic deformation and stresses in the shell:

$$w_y = r\alpha\Delta t + w_0 + r\alpha\Delta t = w_0;$$

$$\sigma_r = E \frac{w_y}{r}; \quad \sigma_x = \frac{6M_x}{h^2} = \frac{6Dw_y''}{h^2}; \quad \sigma_r(M) = \mu\sigma_x.$$

Total deformation of the shell is

$$w = r\alpha\Delta t + w_y = r\alpha\Delta t + w_0.$$

Let us plot the curve for the shell's coefficient of safety  $n = \frac{\sigma_{\theta, \tau}^t}{\sigma_l}$ .

The quantity  $\sigma_{\theta, \tau}^t$  will be variable since the temperature along the axis of the shell is variable. A variable quantity also is generalized stress

$$\sigma_l = \sqrt{\sigma_x^2 + [\sigma_\psi + \sigma_\varphi(M)]^2 - \sigma_x [\sigma_\psi + \sigma_\varphi(M)]}.$$

If we plot both of these curves and their ratio, we obtain the curve for the coefficient of safety  $n = f(x)$ .

Example 5.2. Find thermal stresses in a free cylindrical shell (Fig. 5.24) if the following is given:  $\alpha = 6.5 \cdot 10^{-6} \text{ deg}^{-1}$ ;  $E = 2.83 \cdot 10^6 \text{ daN/cm}^2$ ;  $\mu = 0.3$ ;  $\Delta t = 2160 + 1.73x^2$ .

Elastic deformation of the shell is  $w_y = r\alpha\Delta t + w_p$ .

Let us find deformation  $w_p$  from equation (5.14):

$$w_p = w_0 + w_u = e^{-\beta x} (C_1 \sin \beta x + C_2 \cos \beta x) + e^{\beta x} (C_3 \sin \beta x + C_4 \cos \beta x) + w_u.$$

Particular solution of  $w_u$ :

$$w_u = r\alpha\Delta t = 126 \cdot 6.5 \cdot 10^{-6} (2160 + 1.73x^2) = 1770 \cdot 10^{-4} + 1.417 \cdot 10^{-4} x^2 = A_0 + A_1 x^2.$$

Let us find the general solution to equation (5.14) without the right side.

We find the quantities  $\beta$ ,  $L$ , and then the coefficients  $C_1$ ,  $C_2$ ,  $C_3$ ,  $C_4$  from boundary conditions:

$$\text{when } x = 0 \quad w_p'(0) = w_p''(0) = 0; \quad \text{when } x = l \quad w_p'(l) = w_p''(l) = 0.$$

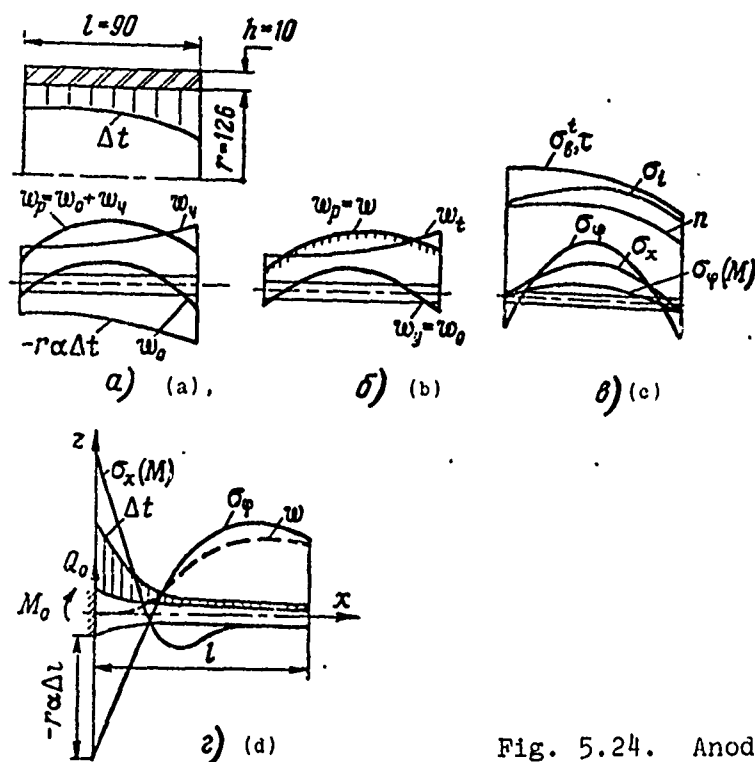


Fig. 5.24. Anode analysis.

On the left end when  $x = 0$  we find  $C_1, C_2$ , if we assume  $C_3 = C_4 = 0$ . On the right end when  $x = l$  we find  $C_3, C_4$  if we assume  $C_1 = C_2 = 0$ .

Thus, when  $x = 0$   $-23^2 C_1 + 28.34 \cdot 10^{-5} = 0$ ;  $C_1 + C_2 = 0$ ; hence

$$C_1 = 10.8 \cdot 10^{-4} \text{ c.u.}; \quad C_2 = -10.8 \cdot 10^{-4} \text{ c.u.}$$

When

$$x = l \quad -3.12(-23^2 C_4) - 25.8(23^2 C_3) + 28.31 \cdot 10^{-5} = 0;$$

$$-3.12(-C_3 - C_4) - 25.8(C_3 - C_4) = 0;$$

hence

$$C_3 = 0.46 \cdot 10^{-4} \text{ c.u.}; \quad C_4 = 0.33 \cdot 10^{-4} \text{ c.u.}$$

and bend is

$$\begin{aligned} w_0 &= C_1 e^{-\beta x} \sin \beta x + C_2 e^{-\beta x} \cos \beta x + C_3 e^{\beta x} \sin \beta x + C_4 e^{\beta x} \cos \beta x = \\ &= 10,8 \cdot 10^{-4} e^{-\beta x} \sin \beta x - 10,8 \cdot 10^{-4} e^{-\beta x} \cos \beta x + \\ &+ 0,46 \cdot 10^{-4} e^{\beta x} \sin \beta x + 0,33 \cdot 10^{-4} e^{\beta x} \cos \beta x. \end{aligned}$$

Calculation is reduced in Table 5.3. After computing  $w_0$  in line 14 and  $w_1$  in line 15 we find total deformation of the shell in line 17 according to formula

$$w = w_1 + w_0 = r \Delta t + w_0$$

and tensile strength in the circular direction according to formula

$$\sigma_\varphi = E \frac{w_0}{r} = -\frac{2,83 \cdot 10^6}{12,6} w_0 = 22,5 \cdot 10^4 \cdot w_0.$$

We determine  $w_p''$  according to formulas (5.26):

$$\begin{aligned} w_p'' &= (2\beta^2 C_2) e^{-\beta x} \sin \beta x - (2\beta^2 C_1) e^{-\beta x} \cos \beta x - (2\beta^2 C_1) e^{\beta x} \sin \beta x + \\ &+ (2\beta^2 C_3) e^{\beta x} \cos \beta x + 2A = -28,3 \cdot 10^{-5} e^{-\beta x} \sin \beta x - 28,3 \cdot 10^{-5} e^{-\beta x} \cos \beta x - \\ &- 0,865 \cdot 10^{-5} e^{\beta x} \sin \beta x + 1,2 \cdot 10^{-5} e^{\beta x} \cos \beta x + 2,11 \cdot 10^{-5}. \end{aligned}$$

Computation of  $w_p''$  is presented in lines 19-23 of Table 5.3. In lines 24-26 we find the stresses  $\sigma_x$ ,  $\sigma_\varphi(M)$ ,  $\sigma_{\varphi\Sigma}$ , calculated according to formulas

$$\sigma_x = \frac{6M_x}{h^2}, \text{ где } M_x = D w'' = 2,59 \cdot 10^5 \cdot w'';$$

$$\sigma_\varphi(M) = \mu \sigma_x(M) = 0,3 \sigma_x(M);$$

$$\sigma_{\varphi\Sigma} = \sigma_\varphi + \sigma_\varphi(M);$$

$$\begin{aligned} w_p''' &= (2\beta^3 C_1 - 2\beta^3 C_2) e^{-\beta x} \sin \beta x + (2\beta^3 C_1 + 2\beta^3 C_2) e^{-\beta x} \cos \beta x - \\ &- (2\beta^3 C_3 + 2\beta^3 C_4) e^{\beta x} \sin \beta x + (2\beta^3 C_3 - 2\beta^3 C_4) e^{\beta x} \cos \beta x = \\ &= 20,5 e^{-\beta x} \sin \beta x - 7,5 e^{\beta x} \sin \beta x + 1,21 e^{\beta x} \cos \beta x. \end{aligned}$$

Computation of  $w''$  is made in lines 27-30 of Table 5.3.

We find the stresses  $\tau_x(Q)$  in line 31 of Table 5.3 computed according to formula

$$\tau_x(Q) = \frac{2}{3} \frac{Q_x}{h}; \quad Q_x = Dw''' = 2,59 \cdot 10^5 w'';$$

$$\tau_x(Q) = 0,173 \cdot 10^6 w''.$$

As is apparent from the table, the value of shearing stress is not high. In the future we shall disregard it. Generalized stress in the shell is

$$\sigma_l = \sqrt{\sigma_x^2 + \sigma_{\varphi}^2 - \sigma_x \sigma_{\varphi}},$$

and the coefficient of safety  $n = \frac{\sigma_{n,r}^l}{\sigma_{l \max}}$ .

Figure 5.24c shows the obtained coefficients of safety and stress curves in the shell.

#### Analysis of a cylindrical shell with variable parameters

Let us solve equation (5.7) for a shell whose parameters are arbitrary.

The quantities  $E$ ,  $h$ ,  $\alpha$ ,  $\Delta t$  are given. All these quantities can be variable. Find  $\sigma_\varphi$ ,  $\sigma_x$ ,  $\sigma_\varphi(M)$ ,  $w$ .

We shall examine a case when the left end of the shell has a rigid attachment and the right is free (Fig. 5.24d). Let us assume that the shell is long. It is possible by direct integration of differential equation (5.7), with allowance for boundary conditions, to obtain a nonhomogeneous linear integral equation and to solve it by the method of successive approximation. Since equation (5.7)

belongs to the class of differential equations containing a large parameter, the process of successive approximation will be slowly convergent, which is not convenient in approximate calculation when calculation is performed on ordinary digital computers.

It is advisable to return to the calculation method already used: to represent the stressed state of the shell as the sum of the momentless stressed state and the stressed state as a result of local loads causing a moment stressed state rapidly attenuating as the distance from the loading zone becomes greater. Thus, the solution to equation (5.7) will be composed of its particular solution and its general solution without the right side,

$$w_p = w_0 + w_q.$$

The initial differential equation (5.7) for the case of thermal loading assumes the form

$$(Dw_p)'' + \frac{Eh}{r^2} w_p = \frac{hEa\Delta t}{r}. \quad (5.27)$$

Let us free the shell from attachment and find its deformation from heating by temperature  $\Delta t$ , i.e., the particular solution. If we assume that  $\Delta t = f(x^n)$ , where  $n \leq 3$ , i.e., quantity  $(Dw_p)'' = 0$ ; then

$$\frac{Eh}{r^2} w_q = \frac{hEa\Delta t}{r},$$

hence

$$w_q = ra\Delta t. \quad (5.28)$$

We shall find the common solution to equation (5.27) without the right side:

$$(Dw_0)'' + \frac{Eh}{r^2} w_0 = 0.$$

Table 5.3.

(1) № стро- ки	(2) Функция	(3) Мно- жи- тель	$x=0$	3'	6	$x=9$
1	$\beta x$	1	0	1,087	2,473	3,26
2	$\sin \beta x$	1	0	0,8853	0,8233	-0,1199
3	$\cos \beta x$	1	1	0,4651	-0,5676	-0,9927
4	$e^{-\beta x}$	1	1	0,337	0,114	0,039
5	$e^{\beta x}$	1	1	2,964	8,8	26,0
6	$e^{-\beta x} \sin \beta x$	1	0	0,2986	0,0936	-0,0046
7	$e^{-\beta x} \cos \beta x$	1	1	0,1572	-0,0646	-0,0382
8	$e^{\beta x} \sin \beta x$	1	0	2,625	7,25	-3,12
9	$e^{\beta x} \cos \beta x$	1	1	1,381	-4,99	-25,8
10	10,8·(5)	10 <sup>-4</sup>	0	3,22	1,01	-0,0496
11	-10,8·(7)	10 <sup>-4</sup>	-10,8	-1,7	0,696	0,412
12	0,46 (8)	10 <sup>-4</sup>	0	1,21	3,34	-1,435
13	0,33 (9)	10 <sup>-4</sup>	0,33	0,455	-1,35	-8,25
14	$w_0$	10 <sup>-4</sup>	-10,4	3,18	3,39	-0,59
15	1,417, $x^2$	10 <sup>-4</sup>	0	2,8	51	115
16	$W_4(15)=1770$	10 <sup>-4</sup>	1770	1782,9	1821	1885
17	$w_p = w_4 + w_0$	10 <sup>-4</sup>	1760	1783	1824	1875
18	$\sigma_{\varphi} = E \frac{(20)}{r}$	1	-235	71,5	76,3	-216
19	-28,3·(6)	10 <sup>-5</sup>	0	-8,45	-2,64	0,13
20	-28,3·(7)	10 <sup>-5</sup>	-28,3	-4,45	+1,82	+1,05
21	-0,805·(8)	10 <sup>-5</sup>	0	-2,27	-6,26	2,7
22	1,2 (9)	10 <sup>-5</sup>	1,2	1,66	-5,99	-34,0
23	$w'' = 28,34 + (19) +$ $+ (20) + (21) + (22)$	10 <sup>-5</sup>	1,24	14,83	15,27	1,22
24	$\sigma_x$	1	+20	+240	+246	+19,7
25	$\sigma_{\varphi}(M)$	1	+6	+72	+74	+5,9
26	$\sigma_{\varphi \Sigma}$	1	-229	142	150	-210
27	206·(6)	10 <sup>-6</sup>	0	61,5	19,2	-0,95
28	-7,5·(8)	10 <sup>-6</sup>	0	19,6	-54,5	23,4
29	1,24·(9)	10 <sup>-6</sup>	1,24	1,71	-6,2	-32
30	$w_p''' = (27) + (28) +$ $+ (29)$	10 <sup>-6</sup>	1,24	43,6	-41,5	-9,5
31	$\tau_x(Q)$	1	0,21	+7,53	-7,13	-1,63

KEY: (1) No.; (2) Function; (3) Factor.

Let us designate

$$\frac{Eh}{r^2} = A. \quad (5.29)$$

We shall integrate this equation four times.

The first integral

$$(Dw_0)' = - \int_0^x Aw_0 dx + C_1.$$

From the condition when  $x = 0$   $(Dw_0)' = Q_0$  we find  $C_1 = Q_0$ ;  
from the condition when  $x = l$   $(Dw_0)' = 0$  we obtain

$$Q_0 = \int_0^l Aw_0 dx,$$

and finally,

$$\begin{aligned} (Dw_0)' &= - \int_0^x Aw_0 dx + \int_0^l Aw_0 dx = \\ &= - \left( \int_0^x Aw_0 dx - \int_0^l Aw_0 dx \right) = -Q_x. \end{aligned} \quad (5.30)$$

The second integral

$$Dw_0 = - \int_0^x Q_x dx + C_2.$$

From the condition  $x = 0$   $(Dw_0) = M_0$ , we find  $C_2 = M_0$ . From  
the condition when  $x = l$   $(Dw_0) = 0$  we obtain

$$M_0 = \int_0^l Q_x dx,$$

and, finally

$$Dw'' = - \int_0^x Q_x dx + \int_0^l Q_x dx = - \left( \int_0^x Q_x dx - \int_0^l Q_x dx \right) = -M_x. \quad (5.31)$$



We integrate this equation once more:

$$w'_0 = - \int_0^x \frac{M_x}{D} dx + C_3.$$

For long shells, if it is necessary to find the bend of the shell  $w$  and stress  $\sigma_\varphi$ , it is advisable to use the condition when  $x = l$

$w'_0(l) = 0$ ; we obtain  $C_3 = \int_0^l \frac{M_x}{D} dx$  and, finally,

$$\begin{aligned} w'_0 &= - \int_0^x \frac{M_x}{D} dx + \int_0^l \frac{M_x}{D} dx = \\ &= - \left( \int_0^x \frac{M_x}{D} dx - \int_0^l \frac{M_x}{D} dx \right) = -w'_x. \end{aligned} \quad (5.32)$$

The next integration leads to the result

$$w_0 = - \int_0^x w'_x dx + C_4.$$

For a long shell it is advisable to find  $C_4$  from the condition when

$x = l$   $w(l) = 0$ . Then  $C_4 = \int_0^l w'_x dx$  and

$$w_0 = - \int_0^x w'_x dx + \int_0^l w'_x dx = - \left( \int_0^x w'_x dx - \int_0^l w'_x dx \right). \quad (5.33)$$

The solution to equation (5.33) should be reached by the method of successive approximation. For the initial equation we can take any function which satisfies the boundary condition when  $x = 0$   $w_0 = -\delta$ ; when  $x = l$   $w = 0$ . Usually a rectilinear function is used. After two or three approximations a sufficiently accurate value for deflection  $w_0$  is usually obtained.

Full deflection of shell  $w_p = w_0 + w_q$ . Stresses in the shell are determined by the elastic component of the bend

$$w_y = w_p - r\alpha\Delta t = w_0 + w_q - r\alpha\Delta t.$$

Since  $w_q = r\alpha\Delta t$ , the function  $w_0$  will be the elastic bend. The usual form of bend and stress diagram is shown in Fig. 5.24d.

Example 5.3. Find the circular stresses of a cylindrical anode by the integral method. The conditions for the problem are the same as in example 5.1. Calculation is presented in Table 5.4.

Let us find the bend of the shell  $w_0$  from formula (5.33). The initial function  $w_0$  is a straight line with a bend at the attachment spot  $\delta_0 = r\alpha\Delta t_0 = 0.455$  mm. This quantity is found in the "factor" column.

We obtain the bend  $w_{01}$  in the first approximation in line 10 and in the second approximation in line 19. This bend determines stresses  $\sigma_\varphi$  in the shell (line 21):

$$\sigma_\varphi = \frac{E}{r} w.$$

Full bend of the shell we find in line 22:  $w = w_0 + w_q = w_0 + r\alpha\Delta t$ .

Bends  $w$  are shown in Fig. 5.22 by the dashes.

Stress in a shell in the presence of temperature gradient through the thickness

Let us assume that temperature gradient  $\Delta t$  through the thickness of the shell changes according to linear law (Fig. 5.25) and is identical on its entire length. At points located at a considerable distance from the ends of the shell there is no bend. The shell element is in the same stressed state as a plate with nonuniform heating.

Table 5.4.

№ стро- (1) ки	Функция (2)	Множит- (3) тель	$x_0=0$	7	14	21	28	$x_l=35$
1	$w_0$	$\delta_0$	-1	-0,8	-0,6	-0,4	-0,2	0
2	$\int A w_0 dx$	$-A \delta_0 (l/10)$	0	-1,8	-3,2	-4,2	-4,8	-5,0
3	$Q_x$	$-A \delta_0 (l/10)$	5,0	3,2	1,8	0,8	0,2	0
4	$\int Q_x dx$	$-A \delta_0 (l/10)^2$	0	8,2	13,2	15,8	16,8	17,0
5	$M_x$	$-A \delta_0 (l/10)^2$	-17,0	-8,8	-3,8	-1,2	-0,2	0
6	$w'$	$-A \delta_0 / D (l/10)^3$	0	-25,8	-38,4	-43,4	-44,6	-45
7	$w'_x$	$-A \delta_0 / D (l/10)^3$	45	19,2	6,6	1,6	0,2	0
8	$w$	$-A \delta_0 / D (l/10)^4$	0	64,2	90,0	98,2	100	100,2
9	$w_x$	$-A \delta_0 / D (l/10)^4$	-100,2	-36	-10,2	-2,0	-0,2	0
10	$\overline{w}_{01}$	1	-1	-0,36	-0,1	-0,02	-0,0	0
11	$\int A w_{01} dx$	$-A \delta_0 (l/10)$	0	-1,36	-1,82	-1,94	-1,95	-1,96
12	$Q_x$	$-A \delta_0 (l/10)$	1,96	0,60	0,14	0,02	0	0
13	$\int Q_x dx$	$-A \delta_0 (l/10)^2$	0	2,56	3,3	3,46	3,48	3,48
14	$M_x$	$-A \delta_0 (l/10)^2$	-3,48	-0,92	-0,18	-0,02	0	0
15	$w'$	$-A \delta_0 / D (l/10)^3$	0	-4,4	-5,5	-5,7	-5,72	-5,72
16	$w'_x$	$-A \delta_0 / D (l/10)^3$	5,72	1,32	0,22	0,02	0	0
17	$w$	$-A \delta_0 / D (l/10)^4$	0	7,04	8,58	8,82	8,84	8,84
18	$w_x$	$-A \delta_0 / D (l/10)^4$	-8,84	-1,80	-0,26	-0,02	0	0
19	$\overline{w}_{02}$	1	-1	-0,205	-0,029	-0,002	0	0
20	$w_{02}=w$	1	-0,455	-0,093	-0,0013	0,000	0	0
21	$\sigma_\varphi$	1	-132	-27	-0,3	0	0	0
22	$w$	1	0	0,382	0,51	0,562	0,617	0,643

KEY: (1) No.; (2) Function; (3) Factor.

Stress on the outer surface of the shell at points removed from the ends, by analogy with a plate, is

$$\sigma_x = \frac{E \alpha \Delta t}{2(1-\mu)}; \quad \sigma_p = \frac{E \alpha \Delta t}{2(1-\mu)}, \quad (5.34)$$

if

$$\Delta t = t - t_0 \text{ and } t > t_0.$$

Near the faces of a shell there will occur a certain bend as a result of the effect of its attachment.

Let us examine the stresses in a shell if its ends have no support. In this case, stresses  $\sigma_x$  on the end will be equal to zero. Since the stresses (5.34) can be obtained as a result of applying bending moment to the face of the shell, we shall apply moment  $M_0 = M_x$ , which is attained by a rigid attachment of the shell end. With allowance for the sign,

$$M_0 = -\frac{\sigma_x h^2}{6}; \quad M_0 = -\frac{E\alpha\Delta t h^2}{12(1-\mu)} \quad (5.35)$$

In order to create the same conditions as exist without attachment of the face ( $\sigma_x = 0$ ), it is necessary to apply distributed moment of the same magnitude but of the opposite sign. Stresses in a free end will be defined as the sum of stresses determined by formula (5.34) and stresses caused by moment  $M_0$  (Fig. 5.25).

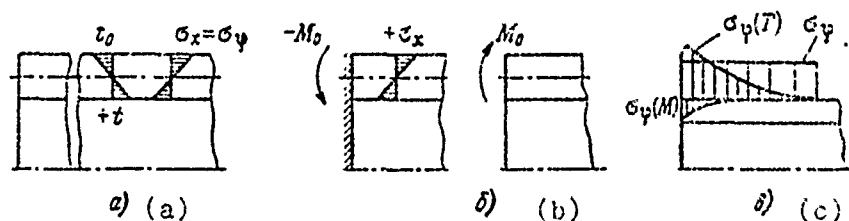


Fig. 5.25. Determining stresses in the presence of a temperature gradient through the thickness.

Loads in a free shell caused by moment  $M_0$  applied to the end are known:

$$\left. \begin{aligned} M_0 &= \frac{E\alpha\Delta t h^2}{12(1-\mu)}; \quad \sigma_x(M) = \frac{6M_0}{h^2}; \\ M_\varphi(0) &= \nu M_0 = \frac{E\alpha\Delta t h^2 \mu}{12(1-\mu)}; \quad \sigma_\varphi(M) = \mu \sigma_x(M); \\ T_\varphi(0) &= \frac{Eh}{r} [w(0)] = \frac{Eh}{r} \frac{M_0}{2\beta^2 D} = \\ &= \frac{Eh\alpha\Delta t}{2\sqrt{3}(1-\mu)} \sqrt{1-\mu^2}; \quad \sigma_\varphi(T) = \frac{T_\varphi(0)}{h}. \end{aligned} \right\} \quad (5.36)$$

These formulas show that on the free face maximum thermal stress acts in a circular direction. If we add stresses  $\sigma_\varphi$  from formula (5.34) with stresses  $\sigma_\varphi$  caused by moments  $M_\varphi$  and force  $T_\varphi$  [formula (5.36)], we obtain

$$(\varepsilon_r)_{\max} = \frac{E\alpha\Delta t}{2(1-\mu)} \left( 1 - \mu + \frac{\sqrt{1-\mu^2}}{\sqrt{3}} \right). \quad (5.37)$$

When  $\mu = 0.3$  this stress is 25% greater than the stress (5.34) calculated for points at a great distance from the faces.

In brittle material we should, thus, fear cracks from the ends of the shell and not in the middle. Figure 5.25c and 5.26 show stress diagrams for the end and the center part of the shell having a temperature gradient through the thickness.

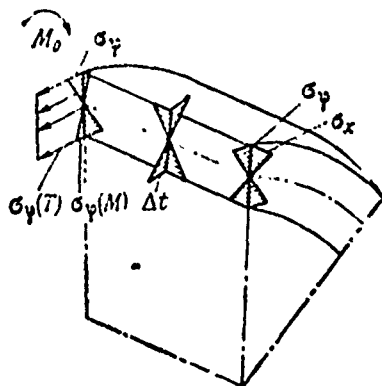


Fig. 5.26. Thermal stresses in a cylindrical shell.

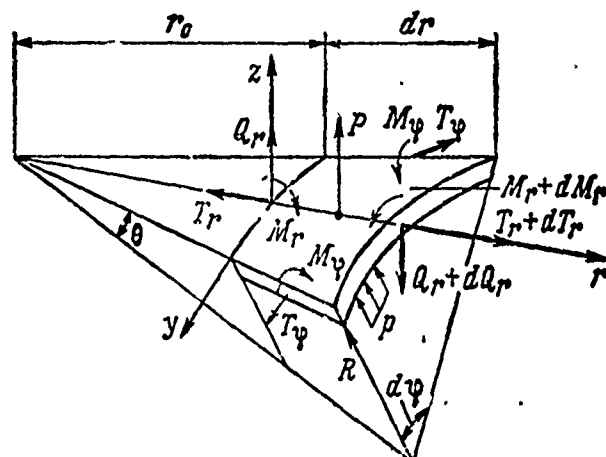


Fig. 5.27. Moments acting on an element of a "conical shell."

### Analysis of conical shells

A conical shell experiences internal pressure and thermal loadings. Let us consider an axisymmetric problem. Therefore, the unknown stresses and strains of the elements are functions only of coordinate

$x$  or  $r$  (distance along the generatrices of the shell from the summit of the cone to the examined section).

Figure 5.27 shows the positive internal loads applied to an element cut out of a conical shell. Let us find the membrane stresses  $\sigma_r$  and  $\sigma_\varphi$  and strains of the shell.

If we assume, for example, that the internal pressure on the shell is constant and acts on the entire internal surface of an uncut shell (Fig. 5.28), the axial force in an arbitrary section is determined by radius  $r$ :

$$N_x = p\pi r^2 \sin^2 \theta, \quad (5.38)$$

where  $\theta$  is the angle of the generatrix of the shell with the  $x$ -axis.

Axial force  $N_x$  causes normal stresses constant along the perimeter:

$$\sigma_r = \frac{N_x}{\pi r h \sin 2\theta},$$

where  $h$  is the thickness of the shell and generally variable.

Particularly, when  $N_x$  is determined from formula (5.38),

$$\sigma_r = \frac{pr}{2h} \operatorname{tg} \theta.$$

Let us find circular stresses  $\sigma_\varphi$ . We shall examine the equilibrium of the shell element (Fig. 5.29) separated into spherical or conical section.

Projecting the external and internal forces onto the normal to the surface of the shell, we obtain  $pRd\varphi dr = \sigma_\varphi h dr d\varphi$ ,

$$\sigma_{\varphi} = \frac{pR}{h} = \frac{pr \operatorname{tg} \theta}{h}, \quad (5.39)$$

where  $R$  is the shell's radius of curvature.

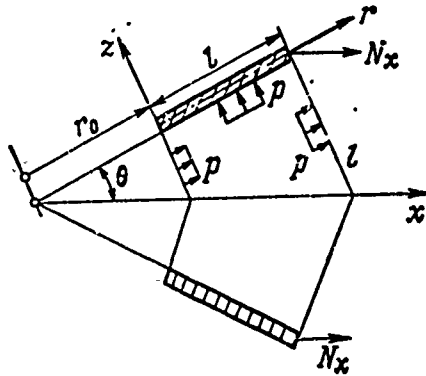


Fig. 5.28. Determining the axial force of a "conical shell."

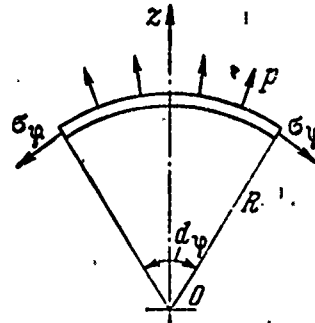


Fig. 5.29. Equilibrium of a shell element.

Membrane stresses  $\sigma_r$  and  $\sigma_{\varphi}$  are the reason for the appearance of deformation. The greatest stresses  $\sigma$  lead to shell deformation in a radial direction:

$$w = \frac{\sigma_{\varphi} R}{E} = \frac{pr^2}{Eh} \operatorname{tg}^2 \theta. \quad (5.40)$$

Radial displacements toward an increase in the shell's radius of curvature  $R$  are assumed positive. Pressure  $p$  acting on the internal surface of the shell from the center to the periphery is also assumed positive.

As in a cylindrical shell, we express all strains and internal forces in terms of full radial displacements of  $w$ .

Thus, the relative deformation in a circular direction is

$$\varepsilon_{\varphi} = \frac{w}{R} = \frac{w}{r \operatorname{tg} \theta}.$$

Curvature variation along the generatrices is

$$k_r = \frac{d^2 w}{dr^2}.$$

Curvature variation in a circular direction, connected with the variation in the shell's radius of curvature  $R$  because of a turn of the elements by angle  $dw/dr$ ,

$$k_\varphi = -\frac{1}{r} \frac{dw}{dr}.$$

The last expression is derived in the following manner. The initial curvature of the shell in a circular direction is  $1/R = 1/r \operatorname{tg} \theta$ . Due to the turn of the generatrix by angle  $dw/dr$ , the radius of curvature acquires a new value:

$$R_{\text{нов}} = \frac{r \sin \theta}{\cos \left( \theta + \frac{dw}{dr} \right)} \approx \frac{r \sin \theta}{\cos \theta - \frac{dw}{dr} \sin \theta},$$

hence the variation in curvature is

$$k_\varphi = \frac{1}{R_{\text{нов}}} - \frac{1}{R} = -\frac{1}{r} \frac{dw}{dr}.$$

We shall disregard the curvature variation because of displacement of  $w$ .

Full circular normal stresses are

$$\sigma_\varphi = E \varepsilon_\varphi = E \frac{w}{r \operatorname{tg} \theta}.$$

Linear bending moments are

$$\left. \begin{aligned} \overline{M}_r &= D(k_r + \mu k_\varphi) = D \left[ w'' + \frac{\mu}{r} w' \right], \\ \overline{M}_\varphi &= D(k_\varphi + \mu k_r) = D \left[ \frac{1}{r} w' + \mu w'' \right]. \end{aligned} \right\}$$

(5.4<sub>2</sub>)



Linear shearing forces, obtained from the condition that the moments acting on the shell's element are equal to zero, are

$$\overline{M}_r r d\theta - \left( \overline{M}_r + \frac{d\overline{M}_r}{dr} dr \right) (r + dr) + \overline{M}_\varphi dr d\theta + \overline{Q}_r r d\theta dr = 0;$$

$$Q_r = \frac{d\overline{M}_r}{dr} + \frac{\overline{M}_r}{r} - \frac{\overline{M}_\varphi}{r} = \frac{1}{r} \frac{d}{dr} (r \overline{M}_r) - \frac{1}{r} \overline{M}_\varphi.$$

Finally, the solving differential equation will have the form

$$\frac{d^2}{dr^2} \left[ r D \frac{d^2 w}{dr^2} \right] + \mu \frac{d}{dr} \left[ \frac{dD}{dr} \frac{dw}{dr} \right] + \frac{Eh}{r \operatorname{tg}^2 \theta} w = r p. \quad (5.42)$$

This is a linear differential equation of the fourth order with variable coefficients. Let us consider how it can be simplified.

If the shell thickness along the length is constant, i.e.,  $h = \text{const}$  and  $D = \text{const}$ , equation (5.42) assumes the form

$$(r w'')'' - \left( \frac{1}{r} w' \right)' + \frac{Eh w}{Dr \operatorname{tg}^2 \theta} = \frac{r}{D} p, \quad (5.43)$$

or in transformed form

$$\left\{ r \left[ \frac{1}{r} (r w')' \right]' \right\}' + \frac{Eh w}{Dr \operatorname{tg}^2 \theta} = \frac{r}{D} p. \quad (5.44)$$

When  $\theta = \pi/2$ , equations (5.42) and (5.44) are transformed into differential equation for an elastic surface of a circular plate loaded by an axisymmetric load.

To integrate equation (5.44) we expand it [16]:

$$r w^{(4)} + 2 w''' - \frac{1}{r} w'' + \frac{1}{r^2} w' + 4 \frac{w}{r^2} = 4 \frac{\operatorname{tg}^2 \theta}{E h r^2} r p, \quad (5.45)$$

where

$$\beta = \frac{\sqrt[4]{12(1-\mu^2)}}{\sqrt{2 \frac{h}{r_0} \operatorname{tg} \theta}} = \frac{\sqrt[4]{3(1-\mu^2)}}{\sqrt{\frac{h}{r_0} \operatorname{tg}^2 \theta}};$$

$r_0, R_0$  are the initial radii of a truncated shell.

The obtained equations (5.44) and (5.45) are basic for the stress analysis of a shell under the action of applied pressure.

Let us examine the case of the thermal loading of a shell if there is an axisymmetric temperature field, variable along the length, with a constant temperature along the thickness of the wall (Fig. 5.30).

The stressed and strained state of conical shells can be determined according to the same procedure as for cylindrical shells. We assume the system is axisymmetric. The unknown stresses and strains are functions only of one coordinate,  $x$  or  $z$ .

The general, total strain of a shell with thermal loading is

$$w = w_t + w_y,$$

where  $w_t = R\alpha\Delta t$  is the thermal deformation of an unrestrained shell;

$w_y$  is the elastic deformation of a shell due to the constraint of its deformation.

Elastic deformation is found as the sum of deformations - the deformation of a rigidly fixed shell  $w_y$  and its elastic deformation as a result of the application of reactive forces occurring during the rigid attachment. From condition  $w = 0$

$$w_y^* = -w_t = -R\alpha\Delta t.$$

This deformation corresponds to the pressure fixing the shell.  
Let us find it. Assuming that  $\Delta t = Rr^n$ , where  $n = 0, 1, 2$  we obtain

$$w = Ar^n \text{ и } \left\{ r \left[ \frac{1}{r} (rw')' \right] \right\}' = 0;$$

then

$$\frac{Ehw}{Dr \lg^2 \theta} = \frac{r p_{Rt}}{D};$$

hence

$$w = \frac{r^2 \lg^2 \theta p_{Rt}}{Eh}. \quad (B)$$

Equating the expressions (A) and (B)

$$-R\alpha\Delta t = \frac{r^2 \lg^2 \theta p_{Rt}}{Eh},$$

we obtain the pressure arising during the rigid fixation of a shell,

$$p_{Rt} = -\frac{Eh\alpha\Delta t}{r \lg \theta} = -\frac{Eh\alpha\Delta t}{R}.$$

If we apply this pressure  $P_t = -P_{Rt}$  to the shell, we obtain the deformation  $w_p$  which restores the given boundary conditions, from equation

$$\left\{ r \left[ \frac{1}{r} (rw')' \right] \right\}' + \frac{Ehw}{Dr \lg^2 \theta} = \frac{r}{D} \frac{Eh\alpha\Delta t}{R} \quad (5.46)$$

or

$$rw^{IV} + 2w''' - \frac{1}{r}w'' + \frac{1}{r}w' + 4\beta^4 \frac{w}{r_0^2} = 4\beta^4 \frac{\alpha \lg \theta}{r_0^2} \Delta t. \quad (5.47)$$

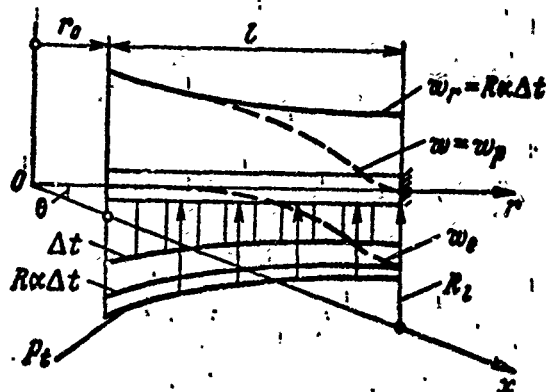


Fig. 5.30.

The elastic deformation of the shell, causing the stresses, is  $w_y = -Ra\Delta t + w_p$ .

Circular stresses caused by these deformations are

$$\sigma_\varphi = -Ea\Delta t + E \frac{w_p}{R}. \quad (5.48)$$

Total deformation of the shell

$$w = w_1 + w_y = ra\Delta t - ra\Delta t + w_p = w_p.$$

Thus, the problem reduces to solving equation (5.47); determining the precise integral of this equation, in the general case, is difficult. This is a linear nonhomogeneous equation of the fourth order with variable coefficients. Let us examine two methods of solving it.

The general procedure for solving equation (5.47) will be similar to that for solving equation (5.7) of a cylindrical shell.

The solution to equation (5.47) will be

$$w_p = w_0 + w_1,$$

where  $w_0$  is the general solution to equation (5.47) without the right side;

$w_1$  is the particular solution to equation (5.47).

We shall find the particular solution.

Usually temperature variation along the anode can be described by law  $\Delta t = B_0 + B_1 r^2$ . If we represent the bend as  $w_1 = A_0 + A_1 r^2$ , we find from equation (5.47)

$$\left\{ r \left[ \frac{1}{r} (rw') \right]' \right\}' = 0 \quad \text{and} \quad \frac{Eh}{Dr \operatorname{tg}^2 \theta} = \frac{r}{D} \frac{Eh a \Delta t}{r \operatorname{tg} \theta},$$

hence

$$w_1 = r \operatorname{tg} \theta a \Delta t = Ra \Delta t.$$

The assumed law of  $\Delta t$  enables us to obtain the particular solution characterizing the momentless state of the shell.

With a more complex law of temperature variation the value of coefficients  $A_0, A_1, A_2$  should be found by the method of undetermined coefficients. Let us assume that the law of variation for  $\Delta t$  is described by formula

$$\Delta t = B_0 + B_1 r + B_2 r^2,$$

and the particular integral by equation

$$w_q = A_0 + A_1 r + A_2 r^2.$$

Substituting the expressions into equation (5.47), we obtain

$$w_q' = A_1 + 2A_2 r; \quad w_q'' = 2A_2; \quad w_q''' = w_q^{IV} = 0.$$

Consequently,

$$\begin{aligned} -\frac{1}{r}(2A_2 r) + \frac{1}{r^2}(A_1 + 2A_2 r) + 4\beta^4 \frac{1}{r_0^2} (A_0 + A_1 r + A_2 r^2) = \\ = 4\beta^4 \frac{\alpha \operatorname{tg} \theta}{r_0^2} (B_0 + B_1 r + B_2 r^2), \end{aligned}$$

hence

$$A_0 = 0; \quad A_1 = \alpha \operatorname{tg} \theta B_0; \quad A_2 = \alpha \operatorname{tg} \theta B_1.$$

Finally,

$$w_q = \alpha \operatorname{tg} \theta \cdot B_0 r + \alpha \operatorname{tg} \theta B_1 r^2.$$

Let us find  $w_0$ . According to the method of asymptotic integration [16], we shall seek solution to a homogeneous equation [equation (5.47) without the right side] in the form of  $w_0 = \psi e^{kp}$ , where

$$k = \pm (1 \pm i)\beta; \quad (5.49)$$

here  $\rho$  is a variable quantity;

$\psi$  is the function  $r$ .

Function  $\psi$  is represented by an asymptotic theory

$$\psi = \psi_0 + \frac{\psi_1}{k} + \dots + \frac{\psi_n}{k^n}.$$

The integration of the homogeneous equation is performed on the assumption that  $\beta$  is a sufficiently large quantity ( $\beta \geq 1$ ), i.e., solution is intended for shells with a small cone angle ( $\theta \leq 60^\circ$ ) and little relative wall thickness ( $h/R_0$  or  $h/r_0$ ), which usually corresponds to anode design.

We substitute equation (5.49) and its derivatives into the homogeneous equation corresponding to equation (5.47) and equate to zero the terms with identical powers of  $k$ , assuming that  $k$  and  $\beta$  are of the same order.

From the condition that terms of the order of  $k^4$  are equal to zero, assuming that  $k^4 = -4\beta^4$ , we obtain the equation:

$$rk^4(q')^4\psi_0 + 4\beta^4 \frac{1}{r^2} \psi_0 = 0,$$

hence

$$q = r_0^{-0.5} \int_{r_0}^r \frac{dr}{\sqrt{r}}. \quad (5.50)$$

From the condition that terms on the order of  $k^3$  are equal to zero, we obtain the equation

$$r[4(q')^3\psi_0' + 6(q')^2q''\psi_0 + 2(q')^3\psi_0] = 0.$$

Hence, using equation (5.50), we determine

$$\psi_0 = \left(\frac{r}{r_0}\right)^{0.25} = \left(\frac{R}{R_0}\right)^{0.25}.$$

Thus, the solution to the nonhomogeneous equation (5.47) in the first approximation, which is sufficiently accurate for practical calculations, i.e., when the asymptotic series  $\psi$  is replaced by the first term, function  $\psi_0$ , assumes the form

$$w_0 = \psi_0 [e^{-\rho}(C_1 \sin \rho + C_2 \cos \rho) + e^{\rho}(C_3 \sin \rho + C_4 \cos \rho)],$$

where, unlike expression (5.50),

$$\rho = \beta r_0^{-0.5} \int_{r_0}^r \frac{dr}{\sqrt{r}} = 2\beta \left[ \left( \frac{r}{r_0} \right)^{0.5} - 1 \right]. \quad (5.51)$$

Analysis of dependence (5.51) shows that the terms  $\psi_0 e^{-\rho}(C_1 \sin \rho + C_2 \cos \rho)$  represent radial displacements, which are maximum near the edge  $r = r_0$  and rapidly decrease with an increase in  $r$ . The terms  $\psi_0 e^{\rho}(C_3 \sin \rho + C_4 \cos \rho)$  describe the radial displacements which are maximum near the edge  $r = r_1$  and rapidly decreasing with a decrease in  $r$  as compared with  $r_1$ .

Thus, if the shell is long, we can determine constants  $C_1, C_2$  assuming  $C_3 = C_4 = 0$ , and, on the other hand, determine constants  $C_3, C_4$ , assuming  $C_1 = C_2 = 0$ , which considerably simplifies calculation without introducing appreciable errors in the obtained results.

The length of a conical shell will be evaluated in a manner similar to the length of a cylindrical shell. Let us examine the function

$$\rho = \frac{2\beta}{\sqrt{r_0}} (\sqrt{r} - \sqrt{r_0}) = \frac{2\sqrt{12(1-\mu^2)}}{\sqrt{r_0} \sqrt{2 \frac{h}{r_0} \epsilon}} (\sqrt{r} - \sqrt{r_0}). \quad (5.52)$$

We multiply the numerator and denominator of this expression by  $(\sqrt{r} + \sqrt{r_0})$  and introduce the substitutions  $r \operatorname{tg} \theta = R$ ,  $r_0 \operatorname{tg} \theta_0 = R_0$ ,  $r - r_0 = l$ ; we obtain

$$\rho = \frac{2.56l}{\sqrt{Rh} + \sqrt{R_0h}}.$$

Hence the length on which a full cycle occurs in the variation of functions  $\sin \rho$  or  $\cos \rho$  is

$$l = \frac{2\pi}{2.56} (\sqrt{Rh} + \sqrt{R_0 h}) = 2.45 (\sqrt{Rh} + \sqrt{R_0 h}).$$

The shell can be considered long if the following condition is fulfilled

$$l_x \geq 1.5 (\sqrt{Rh} + \sqrt{R_0 h});$$

or if verification is made along radius  $R = R_0$

$$l_x \geq 3\sqrt{R_0 h}, \quad (5.55)$$

i.e., the formula fully agrees with the formula determining the length of a cylindrical shell.

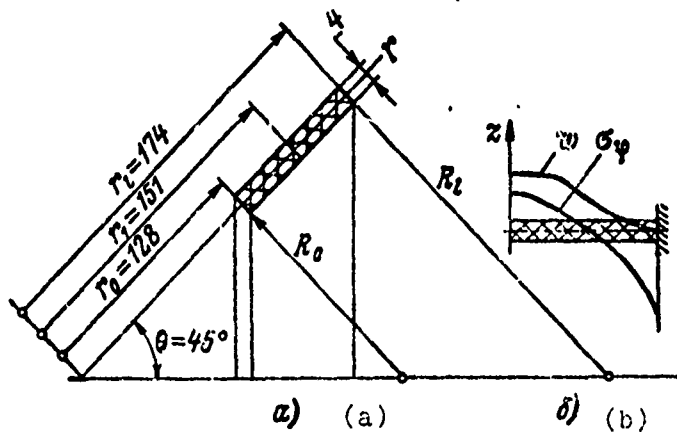


Fig. 5.31. Analysis of a "conical shell."

Example 5.4. Find the circular thermal stresses  $\sigma_\phi$  in an anode of a motor by the asymptotic integration method if the following is given: material - graphite,  $E = 8 \cdot 10^4$  daN/cm<sup>2</sup>;  $\alpha = 3.15 \cdot 10^{-6}$  1/°C;  $\mu = 0.34$ ; anode temperature is  $t_{r0} = 1433.5^\circ\text{C}$ ;  $t_{r1} = 1365^\circ\text{C}$ ;  $t_{r2} = 1226.3^\circ\text{C}$ .



The diagram of the shell is shown in Fig. 5.31. Calculation is performed along the sections  $r_0, r_1, r_2$ :

$$r_0=12,8 \text{ cm}; r_1=15,1 \text{ cm}, r_2=17,4 \text{ cm}; l=4,6 \text{ cm}; \theta=45^\circ; h=0,4 \text{ cm}.$$

1. We shall find the law of variation in the temperature field along the length of the anode:

$$\Delta t = B_0 + B_1 r + B_2 r^2.$$

Let us determine  $B_0, B_1, B_2$  from the conditions:

$$\text{when } r = r_0 \quad t = t_0 = 1433,5; \text{ when } r = r_1 \quad t = t_1 = 1365;$$

$$\text{when } r = r_2 \quad t = t_2 = 1226,3.$$

We shall set up system of equations:

$$B_0 + B_1 r_0 + B_2 r_0^2 = 1433,5;$$

$$B_0 + B_1 r_1 + B_2 r_1^2 = 1365;$$

$$B_0 + B_1 r_2 + B_2 r_2^2 = 1226,5,$$

hence we find

$$B_0 = \frac{\begin{vmatrix} t_0 & r_0 & r_0^2 \\ t_1 & r_1 & r_1^2 \\ t_2 & r_2 & r_2^2 \end{vmatrix}}{\begin{vmatrix} 1 & r_0 & r_0^2 \\ 1 & r_1 & r_1^2 \\ 1 & r_2 & r_2^2 \end{vmatrix}} = 528,5; \quad B_1 = 151; \quad B_2 = -6,64$$

and the temperature field

$$\Delta t = 528,5 + 151r - 6,64r^2.$$

2. Let us find the particular solution  $w_4$  to equation (5.46).

We assume  $w_q = A_0 + A_1 r + A_2 r^2 + A_3 r^3$ ; substituting this value into equation (5.46), we obtain

$$w_q' = A_1 + 2A_2 r + 3A_3 r^2; \quad w_q'' = 2A_2 + 6A_3 r; \quad w_q''' = 6A_3; \quad w_q^{IV} = 0.$$

Substituting the values of  $w_q$ ;  $w_q'$ ;  $w_q''$ ;  $w_q'''$ ;  $w_q^{IV}$  into equation (5.46) and equating the terms with identical functions relative to  $r$ , we obtain

$$A_0 = 0; \quad A_1 = a \operatorname{tg} \theta B_0; \quad A_2 = a \operatorname{tg} \theta B_1; \quad A_3 = a \operatorname{tg} \theta B_2.$$

Finally,

$$w_q = 523,5 a \operatorname{tg} \theta \cdot r + 151 a \operatorname{tg} \theta r^2 - 6,61 a \operatorname{tg} \theta r^3.$$

3. Let us find the general solution to equation (5.46):

$$w_p = \psi_0 [e^{-\varrho} (C_1 \sin \varrho + C_2 \cos \varrho) + e^{\varrho} (C_3 \sin \varrho + C_4 \cos \varrho)] + w_q.$$

Here

$$\psi_0 = \left( \frac{r}{r_0} \right)^{0,25};$$

$$\varrho = \frac{23}{\sqrt{r_0}} (\sqrt{r} - \sqrt{r_0}); \quad \beta = \frac{\sqrt[4]{12(1-\mu^2)}}{\sqrt{2 \frac{h}{r_0} \operatorname{tg} \theta}}.$$

Let us establish the length of the shell from formula

$$l_n > 3 \sqrt{R_0 h}.$$

Usually, in the problems which we are examining the shells are long. In our example, the shell is short since

$$l_n > 3 \sqrt{0,4 \cdot 12,8} = 6,78 \text{ cm}.$$

The shell dimension, in our problem, is  $l = 4.6$  cm. However, for the first evaluation of stresses we shall consider it long. Maximum stresses arise in the right, rigidly attached end of the shell. Then the conditions for finding unknowns  $C_3$  and  $C_4$  will be

$$r = r_l; \quad w_p(l) = 0; \quad w'_p(l) = 0.$$

Unknowns  $C_3$  and  $C_4$  are obtained from equations:

$$\begin{aligned} w_p &= \psi_0 e^q (C_3 \sin q + C_4 \cos q) + A_1 r + A_2 r^2 + A_3 r^3; \\ \psi_0 &= \left( \frac{r}{r_0} \right)^{0.25}; \quad q = \frac{23}{\sqrt{r_0}} (\sqrt{r} - \sqrt{r_0}); \\ w'_p &= e^q C_3 [\sin q (\psi'_0 + \psi_0 q) + \psi_0 q' \cos q] + e^q C_4 [\cos q (\psi'_0 + \psi_0 q') + \\ &\quad + A_1 + 2A_2 r + 3A_3 r^2]; \\ \psi'_0 &= \frac{0.25}{r_0^{0.25}} r^{-0.75}; \quad q' = \frac{3}{\sqrt{r_0}} r^{-0.5}. \end{aligned}$$

These equations for  $w_p$  and  $w'_p$  are sufficient for determining  $C_3$  and  $C_4$ .

Let us introduce the values of  $w''_p$  for determining  $C_3$  and  $C_4$  if the shell has hinged supports:

$$\begin{aligned} w''_p &= e^q C_3 \sin q (\psi''_0 + 2\psi'_0 q' + \psi_0 q'') + e^q C_4 \cos q [\psi''_0 + 2\psi'_0 q' + 2\psi_0 (q')^2] - \\ &\quad - e^q C_4 \sin q [\psi_0 q'' + 2\psi'_0 q' + 2\psi_0 (q')^2] + \\ &\quad + e^q C_4 \cos q (\psi''_0 + 2\psi'_0 q' + \psi_0 q'') + 2A_2 + 6A_3 r; \\ \psi''_0 &= -\frac{0.1875}{r_0^{0.25}} r^{-1.75}; \quad q'' = -\frac{0.53}{\sqrt{r_0}} r^{-1.5}. \end{aligned}$$

We shall find  $C_3$  and  $C_4$  for conditions:

$$\begin{aligned} r &= r_l; \quad w(r_l) = 0; \quad w'(r_l) = 0; \\ z &= \frac{\sqrt[4]{12(1-\mu^2)}}{\sqrt{2 \frac{\pi}{r_0} \operatorname{tg} b}} = \frac{\sqrt[4]{12(1-0.3^2)}}{\sqrt{2 \frac{0.4}{12.8} \cdot 1}} = 7.12; \end{aligned}$$

$$\psi_0 = \left(\frac{r}{r_0}\right)^{0.25} = 0.53 r^{0.25}; \quad \psi_0(r_1) = 1.08;$$

$$q = \frac{25}{\sqrt{r_0}} (\sqrt{r} - \sqrt{r_0}) = 3.98 (\sqrt{r} - 3.58); \quad q(r_1) = 2.265;$$

$$A_1 = \alpha \lg \theta B_0 = 3.15 \cdot 10^{-6} \cdot 1.528,5 = 1,83 \cdot 10^{-3};$$

$$A_2 = \alpha \lg \theta B_1 = 3.15 \cdot 10^{-6} \cdot 1.151 = 0,546 \cdot 10^{-3};$$

$$A_3 = \alpha \lg \theta B_2 = -3.15 \cdot 10^{-6} \cdot 1.6,61 = -2 \cdot 10^{-6};$$

$$r_1 = 17,4; \quad r_1^2 = 302,8; \quad r_1^3 = 526;$$

$$\begin{aligned} w_p(l) &= 1,08 [e^{2,265} (C_3 \sin 2,265 + C_4 \cos 2,265)] + \\ &+ 1,83 \cdot 10^{-3} r_1 + 0,546 \cdot 10^{-3} r_1^2 - 2 \cdot 10^{-5} r_1^3 = \\ &= 1,08 \cdot 9,58 (-C_3 \cdot 0,64 - C_4 \cdot 0,77) + 1,83 \cdot 10^{-3} 17,4 + \\ &+ 0,546 \cdot 10^{-3} \cdot 302,8 - 2 \cdot 10^{-5} \cdot 526 = 0, \end{aligned}$$

hence

$$6,62C_3 + 7,96C_4 = 0,2108;$$

$$\psi_0 = \frac{0,25}{r_0^{0,25}} r^{-0,75} = 0,53 \cdot 0,25 r^{-0,75}; \quad \psi_0'(r_1) = 0,0154;$$

$$q' = \frac{3}{\sqrt{r_0}} r^{-0,5} = 3,98 \cdot 0,5 r^{-0,5}; \quad q'(r_1) = 4,55;$$

$$\begin{aligned} w_p'(r_1) &= 9,58C_3(-0,64)[0,0154 + 1,08(1 + 4,55)] + \\ &+ 9,58C_4(-0,77)[0,0154 + 1,08(4,55 - 1)] + \\ &+ 1,83 \cdot 10^{-3} + 2 \cdot 0,546 \cdot 10^{-3} \cdot 17,4 - 3 \cdot 2 \cdot 10^{-5} \cdot 17,42. \end{aligned}$$

We obtain  $36,8C_3 + 28,4C_4 = 0,02068$ . Solving this system, we find  $C_3 = -0,0558$ ,  $C_4 = 0,073$ . Finally,

$$\begin{aligned} w_p &= \left(\frac{r}{r_0}\right)^{0,25} e^q (-55,8 \cdot 10^{-3} \sin q + 73 \cdot 10^{-3} \cos q) + 1,83 \cdot 10^{-3} r + \\ &+ 0,546 \cdot 10^{-3} r^2 - 2 \cdot 10^{-5} r^3. \end{aligned}$$

Substituting the values of  $r_0$ ,  $r_1$ ,  $r_2$ , we obtain  $w(r_0) = 0.138$  cm,  $w(r_1) = 0.1104$  cm,  $w(r_2) = 0$ .

Stresses in a circular direction or

$$\begin{aligned}\sigma_{\varphi}(r_0) &= E \left( -\alpha \Delta t + \frac{w}{R} \right) = \\ &= 80 \cdot 10^3 \left( -3,5 \cdot 10^{-6} \cdot 1433,5 + \frac{0,138}{12,8} \right) = 4,02 \text{ daN/mm}^2; \\ \sigma_c(r_1) &= 1,77 \text{ daN/mm}^2; \quad \sigma_{\varphi}(r_1) = -3,44 \text{ daN/mm}^2.\end{aligned}$$

Figure 5.31 shows the bends and stresses of an anode.

#### Integral method of solving the equation of a conical shell

As is apparent from the example of shell analysis, the asymptotic method is rather cumbersome. In many cases, calculations should be performed according to the integral method.

Let us examine a case when the anode parameters  $h$ ,  $E$ ,  $D$  are constant and the only variable is  $\Delta t$ .

The initial equation will have the form

$$(rw'')' - \left( \frac{1}{r} w' \right)' + \frac{Ehw}{Dr \operatorname{tg}^2 \theta} = \frac{hE\alpha \Delta t}{D \operatorname{tg} \theta}. \quad (5.54)$$

The procedure for solving the problem remains the same. We shall seek a general solution to equation (5.54) as the sum of its particular solution and a general solution without the right side:

$$w_p = w_0 + w_r.$$

Let us find the particular solution. We assume that the temperature gradient is given by formula  $\Delta t = B_0 + B_1 r + B_2 r^2$ .

We also assume  $w_r = A_0 + A_1 r + A_2 r^2 + A_3 r^3$ . Let us substitute this expression into (5.54), equate the terms with identical functions relative to  $r$ , and obtain the values for  $A_0$ ;  $A_1$ ;  $A_2$ ;  $A_3$  and, consequently,  $w_r$ :

$$A_0=0; \quad A_1=\alpha \operatorname{tg} \theta B_0; \quad A_2=\alpha \operatorname{tg} \theta B_1; \quad A_3=\alpha \operatorname{tg} \theta B_2;$$

$$w_4=\alpha \operatorname{tg} \theta B_0 r+\alpha \operatorname{tg} \theta B_1 r^2+\alpha \operatorname{tg} \theta B_2 r^3. \quad (5.55)$$

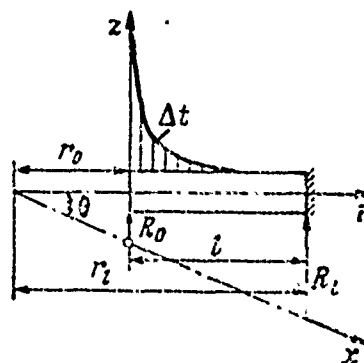
Let us find the general solution. We shall consider equation (5.54) without the right side:

$$(rw'')' - \left(\frac{1}{r} w'\right)' + \frac{Ehw}{Dr \operatorname{tg}^2 \theta} = 0; \quad (5.56)$$

designating  $Eh/D \operatorname{tg}^2 \theta = A$ , we integrate the equation (5.56) once:

$$(rw'')' - \left(\frac{1}{r} w'\right)' \Big|_{r_0}^r = - \int_{r_0}^r \frac{Aw}{r} dr + C_1. \quad (5.57)$$

Fig. 5.32. The integral method of shell analysis.



We find the arbitrary integration of  $C_1$  from the boundary condition. We shall examine a shell with a rigid attachment on the right end (Fig. 5.32). The boundary conditions for such a shell, in order to determine  $C_1$  and then  $C_2$ , will be

$$\text{when } r = r_0 \quad Dw'' = 0, \text{ or } w'' = 0; \quad Dw'' = 0, \text{ or } w'' = 0. \quad (5.58)$$

Substituting into equation (5.57) boundary conditions (5.53) and assuming that  $(rw'')' = rw''' + w''$ , we find  $(rw'')'|_{r=r_0} = 0$  and  $C_1 = 0$ . Let us turn our attention to the following dependence:

$$\left(\frac{1}{r}w'\right)\Big|_{r_0}^r = \frac{1}{r}w' - \frac{1}{r_0}w'(0); \quad w'' - \frac{1}{r}w' = r \left(\frac{1}{r}w'\right)';$$

if we substitute this dependence into (5.57), we obtain

$$rw'' + r\left(\frac{1}{r}w'\right)' + \frac{1}{r_0}w'(0) = -\int_{r_0}^r \frac{Aw dr}{r},$$

or

$$w'' + \left(\frac{1}{r}w'\right)' + \frac{w'(0)}{r_0} \frac{1}{r} = -\frac{1}{r} \int_{r_0}^r \frac{Aw dr}{r}. \quad (5.59)$$

We integrate this equation once more:

$$w'' + \left(\frac{1}{r}w'\right)' \Big|_{r_0}^r = -\frac{w'(0)}{r_0} \int_{r_0}^r \frac{dr}{r} - \int_{r_0}^r \frac{1}{r} \int_{r_0}^r \frac{Aw dr^2}{r} + C_2. \quad (5.60)$$

Using condition (5.58), we determine  $C_2 = 0$ . Allowance is made for

$$\begin{aligned} \left(\frac{1}{r}w'\right)\Big|_{r_0}^r &= \frac{1}{r}w' - \frac{w'(0)}{r_0}; \\ w'' + \frac{1}{r}w' &= \frac{1}{r}(rw'' + w') = \frac{1}{r}(rw')'. \end{aligned}$$

Substituting these dependences into (5.60), we obtain

$$\frac{1}{r}(rw')' - \frac{w'(0)}{r_0} = -\frac{w'(0)}{r_0} \int_{r_0}^r \frac{dr}{r} - \int_{r_0}^r \frac{1}{r} \int_{r_0}^r \frac{Aw dr^2}{r},$$

or

$$(rw')' = \frac{w'(0)r}{r_0} \left(1 - \int_{r_0}^r \frac{dr}{r}\right) - r \int_{r_0}^r \frac{1}{r} \int_{r_0}^r \frac{Aw dr^2}{r}. \quad (5.61)$$

We integrate this equation once again:

$$rw' = \frac{w'(0)}{r_0} \int_{r_0}^r r \left( 1 - \int_{r_0}^r \frac{dr}{r} \right) dr - \int_{r_0}^r r \int_{r_0}^r \frac{1}{r} \int_{r_0}^r \frac{Aw}{r} dr^3 + C_3,$$

or

$$w' = \frac{w'(0)}{r_0 \cdot r} \int_{r_0}^r r \left( 1 - \int_{r_0}^r \frac{dr}{r} \right) dr - \frac{1}{r} \int_{r_0}^r r \int_{r_0}^r \frac{1}{r} \int_{r_0}^r \frac{Aw}{r} dr^3 + \frac{C_3}{r}. \quad (5.62)$$

Boundary conditions for finding  $C_3$  and then  $C_4$  will be:

$$\text{when } r=r_l \quad w'(l)=0; \quad w(l)=0. \quad (5.63)$$

It is advisable to also allow for the fact that when  $r = r_0$

$$w'(0) = \frac{C_3}{r_0},$$

or

$$C_3 = w'(0) r_0,$$

where  $w'(0)$  is the slope angle of the tangent to the elastic line of the shell at the origin of coordinates.

Equation (5.62) will assume the form

$$w' = \frac{w''(0)}{r_0} n' - w'_a + \frac{r_0}{r} w'(0) = w'(0) \left( \frac{n'}{r_0} + \frac{r_0}{r} \right) - w'_a,$$

where

$$\begin{aligned} n' &= \frac{1}{r} \int_{r_0}^r r \left( 1 - \int_{r_0}^r \frac{dr}{r} \right) dr; \\ w'_a &= \frac{1}{r} \int_{r_0}^r r \int_{r_0}^r \frac{1}{r} \int_{r_0}^r \frac{Aw}{r} dr^3. \end{aligned} \quad (5.64)$$



Substituting conditions (5.63) into (5.62), we obtain

$$\frac{w'(0)}{r_0 r_l} \int_{r_0}^{r_l} r \left( 1 - \int_{r_0}^r \frac{dr}{r'} \right) dr - \frac{1}{r_l} \int_{r_0}^{r_l} r \int_{r_0}^r \frac{1}{r'} \int_{r_0}^r \frac{Aw dr^3}{r} + \frac{r_0}{r_l} w'(0) = 0,$$

or

$$\frac{w'(0)}{r_0} n_l' - w_{al}' + \frac{r_0}{r_l} w'(0) = 0,$$

where

$$\left. \begin{aligned} n_l' &= \frac{1}{r_l} \int_{r_0}^{r_l} r \left( 1 - \int_{r_0}^r \frac{dr}{r'} \right) dr; \\ w_{al}' &= \frac{1}{r_l} \int_{r_0}^{r_l} r \int_{r_0}^r \frac{1}{r'} \int_{r_0}^r \frac{Aw dr^3}{r}. \end{aligned} \right\} \quad (5.65)$$

Hence

$$w'(0) = \frac{w_{al}'}{\frac{n_l'}{r_0} + \frac{r_0}{r_l}}. \quad (5.66)$$

Let us integrate equation (5.62) for the last time. We allow for the fact that the quantity  $w'(0)$  has been determined by us and is known:

$$w = w'(0) \int_{r_0}^r \left( \frac{n'}{r_0} + \frac{r_0}{r} \right) dr - \int_{r_0}^r w_a' dr + C_4. \quad (5.67)$$

The value of the constant  $C_4$  is found from conditions (5.63). The physical meaning of the constant  $C_4$  is the bend of the shell at the origin of coordinates. We shall designate it  $w(0)$ . (This is apparent if we substitute into equation (5.67) the value of  $r = r_0$ ). Thus,  $C_4 = w(0)$ .

Briefly equation (5.67) can be written as

$$w = w'(0) n + w_a + w(0), \quad (5.68)$$

where

$$\left. \begin{aligned} n &= \int_{r_0}^r \left[ \frac{1}{r_0} \frac{1}{r} \int_{r_0}^r r \left( 1 - \int_{r_0}^r \frac{dr}{r} \right) dr + \frac{r_0}{r} \right] dr; \\ w_a &= \int_{r_0}^r \frac{1}{r} \int_{r_0}^r r \int_{r_0}^r \frac{1}{r} \int_{r_0}^r \frac{A w}{r} dr^4; \end{aligned} \right\} \quad (5.69)$$

If we substitute into equation (5.68) conditions (5.63), we obtain

$$w'(0) \int_{r_0}^{r_1} \left( \frac{n'}{r_0} + \frac{r_0}{r} \right) dr - \int_{r_0}^{r_1} w_a' dr + w(0) = 0,$$

hence

$$w(0) = -w'(0) n_1 + w_{a1}, \quad (5.70)$$

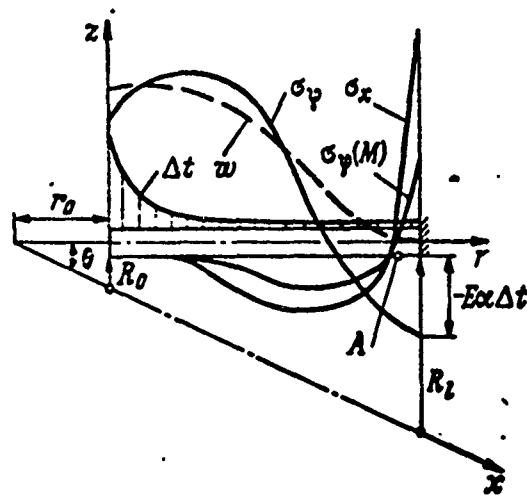
where

$$\left. \begin{aligned} n_1 &= \int_{r_0}^{r_1} \left[ \frac{1}{r_0 r} \int_{r_0}^r r \left( 1 - \int_{r_0}^r \frac{dr}{r} \right) dr + \frac{r_0}{r} \right] dr; \\ w_{a1} &= \int_{r_0}^{r_1} \frac{1}{r} \int_{r_0}^r r \int_{r_0}^r \frac{1}{r} \int_{r_0}^r \frac{A w}{r} dr^4. \end{aligned} \right\} \quad (5.71)$$

Equation (5.68) makes it possible to finally obtain shell deflection. Briefly it can be written as  $w = Kw$ . Similarly, we can obtain an equation for other type of shell attachments.

The obtained equation is a homogeneous linear integral equation. It is solved by the method of successive approximations. Methods of solving integral equations are examined in reference [7].

Fig. 5.33. Thermal stresses in a "conical shell."



The typical distribution of thermal stresses in a conical shell is shown in Fig. 5.33. The most stressed point is point A.

## 5.2. ION MOTORS

In ion motors the thrust is created as a result of the ejection into space of positively charged particles of the working medium with their subsequent neutralization by electrons.

Ion motors have a maximum specific impulse of 50-250 km/s. They possess high efficiency. However, ion motors have comparatively low thrust from the midsection.

We shall briefly examine the classification of ion motors.

Based on the method of working medium ionization the motors are divided into two groups: motors with *surface ionization* and motors with *volume ionization* of the working medium. The first group is subdivided into two subgroups: motors with high ionization on *porous tungsten* and with ionization on *smooth tungsten*. The second group is subdivided into motors in which working medium ionization is accomplished in an *arc discharge*, motors with ionization by *superhigh-frequency currents* and with ionization by *oscillating discharge*.

Based on the design of the ion-optical system, the motors are divided into *grid*, *plate*, *ring*.

Based on the method of working medium feed, ion motors can be classified into several groups: with *forced feed of the working medium by inert gas*, with a *wick feed system*, with *dosing of the working medium on the basis of the electrolytic principle*, with *working medium fed by the inherent pressure of saturated vapors*.

In view of the small expenditure of working medium, the feed system provides fine regulation of flow rate, which is accomplished by various methods - capillary, valve, etc.

## PRINCIPAL AND STRUCTURAL DIAGRAMS OF MOTORS

### Ion grid motor with surface ionization and forced feed of the working medium

This motor (Fig. 5.34) consists of an ion emitter-ionizer unit, the ion beam shaping grid unit, the feed system unit, and the power supply.

The ionizing unit consists of a sealed niobium chamber 1, heater 2, ionizer 3, which is a plate of porous tungsten shaped in the form of cylindrical surfaces - bands 3 - between which are soldered plates 4 to protect the extraction grid from ion bombardment. In the ionizer unit there are also screens 5 which reduce heat losses.

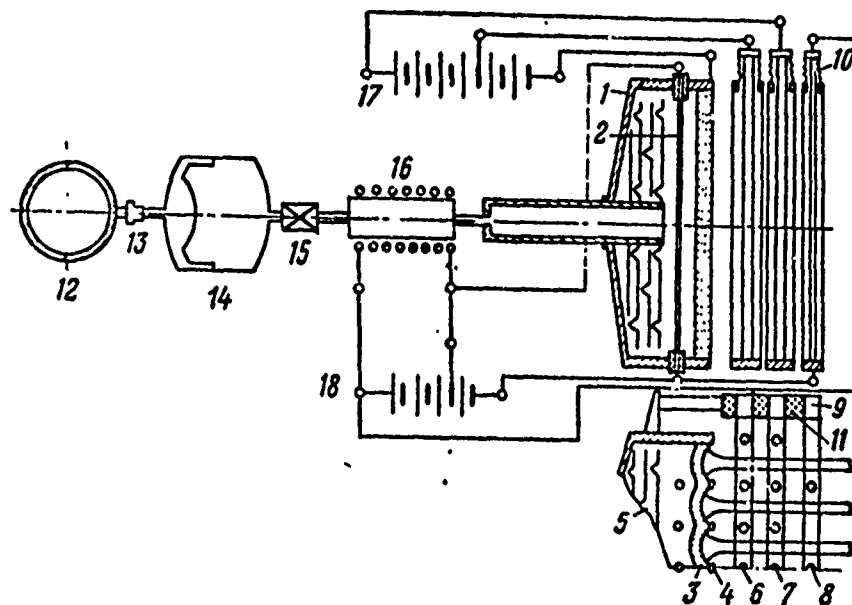


Fig. 5.34. Diagram of ion grid motor.

The ion beam shaping unit consists of an accelerating (extracting) grid 6, retarding (shaping) grids 7 and beam neutralization grids 8.

Each grid is a tungsten filament tightened to the frame 9 by means of fluted adapter 10. The frames are braced to each other and to the motor housing through insulating plates 11.

The working medium feed unit is designed on the principle of working medium displacement by the pressure of inert gas. It consists of tank 12 with neutral gas compressed to a high pressure, transforming valve 13, working medium container 14, dosing device 15, and evaporator 16.

The electric power supply system consists of current supply 17, 18, to provide the energy of the electrodes in the ion-optical system and motor heating.

After feeding voltage to the terminals of the ion-optical system the motor is ready for operation. Then the transforming valve 13 of the gas cylinder 12 with the controlling gas is open. To the membrane of tank 14 liquid cesium is drawn through the proportioning valve into evaporator 16 and chamber 1 of the motor ionizer by gas pressure. The porous tungsten plate of the ionizer, heated to 1200°K by radiation of the tungsten grid of heater 2, ionizes the cesium vapor, positive particles of which are extracted through the pores of the porous tungsten into the ion-optical system where they are accelerated up to the necessary velocity.

The beam of positive particles is neutralized by electrons emitted by the heated tungsten grid 8.

The advantage of this system is its simplicity. The disadvantage of the motor is grid erosion, as well as the high heat loss through the porous tungsten plate.

Motor with a plate-type ion-optical system  
and surface ionization of the working medium

The motor (Fig. 4.35) consists of the ionizer unit, the ion-optical system, the feed system, the feed switching system, and the electrical power system.

The ionizer unit consists of the ionizer housing 1, ionizer heater 2, ion emitter 3, plate 4 which is soldered to the ion emitter to protect the extracting plate from erosion. In the ionizer housing are installed screen 5 to reduce heat losses of the housing.

The ion-optical system unit consists of an accelerating electrode 6, shaping electrode 7, neutralizing electrode 8. Each electrode is a plate with openings, connected to the ionizer housing through insulator 9.

The motor feed unit is designed on the basis of the electrolytic principle of dosing. The working medium (cesium) is inclosed in a ceramic capsule 10 with heater 13 protected by screen 12. When the capsule is heated to 700°K, the ceramics takes on the properties of an ion emitter. At this temperature the cesium begins to evaporate from the ceramics and under the pressure of the saturated vapor is directed to the ionizer housing. When a potential difference is created between the working medium and the electrode capsule 11, the cesium flow rate can be controlled very accurately.

Repeated on-and-off switching of the motor is accomplished by cutoff valve 17 controlled by inert gas and located in gas cylinder 14 equipped with a pressure reducer 15 and cock 16.

Power is fed to the motor electrodes and the working medium tank of the neutralizer is heated by electrical power system 18, 19, 20, 21.

The motor operates in a manner similar to the preceding.

The main disadvantage of these two motors is the high average temperature, which leads to high heat losses and design complication in order to ensure long operation. The temperatures of the ion emitter, heater, and housing can reach  $t_g = 1200-1250^\circ\text{C}$ ,  $t_H = 1700-1750^\circ\text{C}$ ,  $t_n = 1000^\circ\text{C}$ .

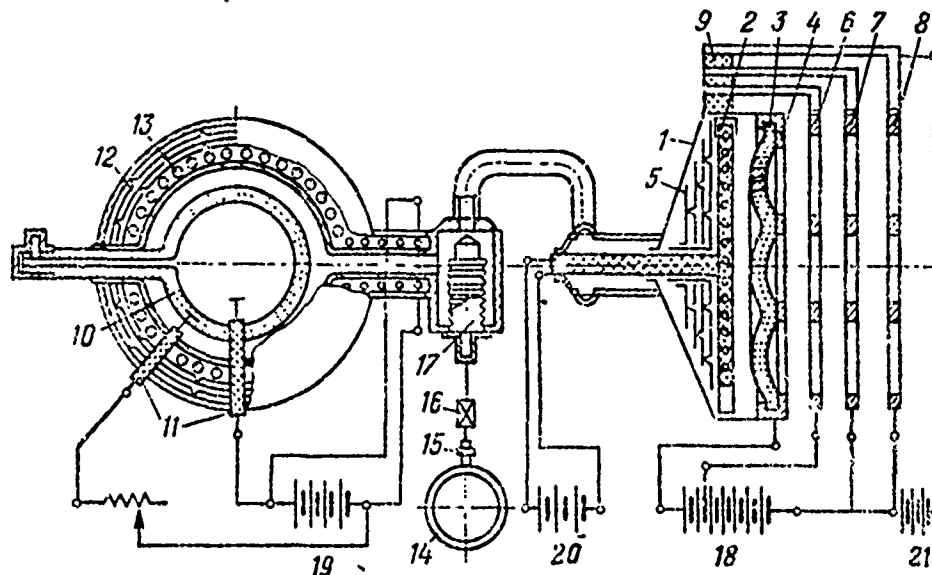


Fig. 5.35. Diagram of ion motor with surface ionization of working medium.

#### Ion motor with surface ionization on smooth tungsten

This motor (Fig. 5.36) consists of an ionizer unit, a beam shaping grid unit, a feed system, and a motor power supply system.

The ionizing unit consists of feed electrode 1, tubes with slotted openings; ionizer 2, a stainless steel plate covered with tungsten; and heater 3. Unlike the previous ionization diagrams, in this one bombardment by molecular particles of the working medium (cesium) of the heated smooth surface of tungsten is achieved.

The accelerating system consists of an acceleration electrode 1, the form of a grid with tungsten segments 4 soldered on it and neutralization grid 5 also of tungsten. Both grids are mounted on frames connected with the housing by insulators.

The cesium feed system is force-fed by the pressure of the saturated vapor of the working medium. It consists of a tank with the working



medium 6 and heater 7. The working medium is fed to the ionizers by system 8, 9, 10, 11, similar to that shown in Fig. 5.35. The power system and electric heating is shown by positions 12, 13, 14.

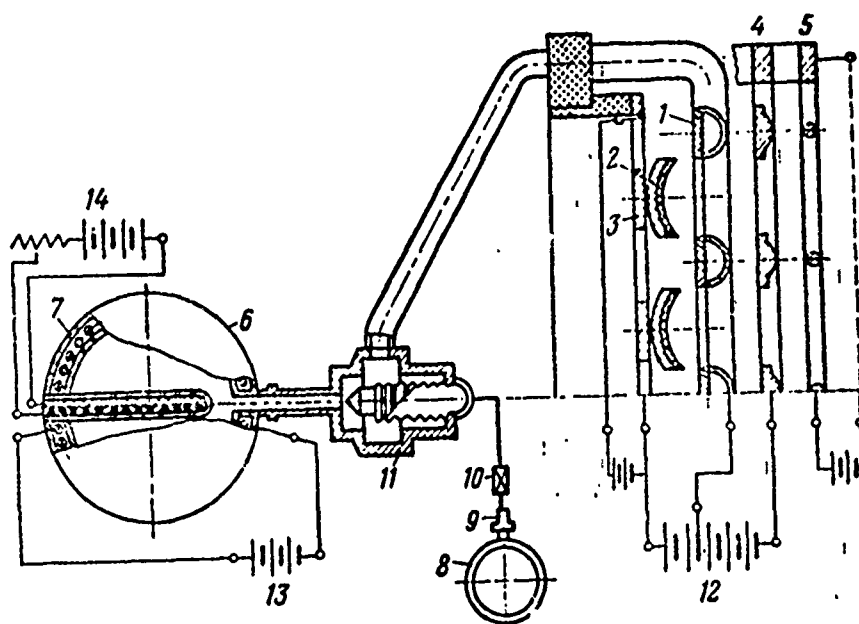


Fig. 5.36. Diagram of an ion motor with counterflow working medium feed.

This motor has advantages over the preceding. It is structurally simpler. There is no ionizer unit of porous tungsten. The surface of the tungsten is polished, as a result of which its self-radiation as compared with porous tungsten is reduced by a factor of approximately three. There are no heaters having higher temperature than the emitting surface. In this design the heater is combined with an emitter and, therefore, the tungsten and the heater temperatures are near.

However, this design is not as widely used because of a number of disadvantages. The motor has comparatively low efficiency since losses from particle acceleration are greater than in the design with porous tungsten. The working medium has a low usage factor.

There are difficulties in providing the feed of the molecular beam from the slot on the emitter surface. Nonuniformity of flow and nonuniformity of mirror heating are possible and can lead to overheating of the ionizer. Secondary processes are complex. Since the ion beam passes through the molecular beam, collision and overcharging of particles are unavoidable and lead to losses. The problem of protecting electrodes from erosion is more complex than in the design with porous tungsten.

#### Ion motor with volume ionization of the working medium by an oscillating discharge

This motor (Fig. 5.37) consists of an ionizing unit, an ion-optical system electrode unit, a working medium feed system, and a power supply system.

The ionizing unit consists of housing 1 made in the form of a cylindrical chamber with openings on the end wall, cathode 2 of tantalum plate, cathode heater 3, anode 4, stabilization winding 5.

The ion-optical system consists of electrodes: accelerating 6, shaping 7, and neutralizing 8.

The feed system is forced by the pressure of the saturated cesium vapor. The cesium tank 9 has heater 10 which ensures cesium evaporation. Precise control of the feed is accomplished by a capillary 11. The power supply system consists of power sources 12 which provide power to the heater of the service tank 9, sources 13, 14 supplying power to the main electrodes 2, 4, 6, and heaters 15 of the cathode, neutralizer, and solenoid 5.

With the heating of the tantalum plate of the motor cathode, the electron cloud which arises oscillates in the chamber between the cathode and the anode, ionizing the working medium, which can be cesium vapor, mercury, or gases - argon, etc.

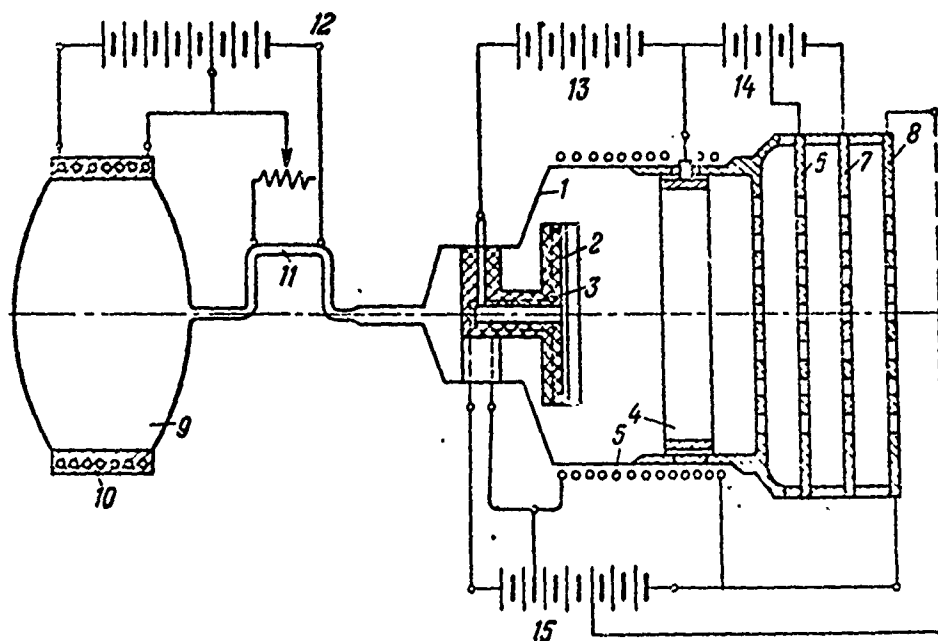


Fig. 5.37.

The positive ions are extracted through the openings of the ion-optical system as in the other ion motors examined above.

This motor has two appreciable advantages. First, it is low-temperature. The hottest element of the ionizer, the cathode, heats to 700-750°C if the working medium is cesium or mercury and to 550-560°C if the working medium is argon. The provisional temperature of the motor housing does not exceed 250°C in the first case, and 100°C in the second. Thus, thermal losses in this motor are minimum.

Second, the motor has the property of automatic control. With an increase in the temperature of the cathode, ionization decreases, and with a decrease in the temperature it increases (the cathode operates on the decaying side of the characteristic in accordance with the Langmuir curve).

An advantage of this motor is also the possibility of a broader choice of working mediums.

The disadvantage is its large size as compared with similar motors based on the principle of surface ionization.

#### MOTOR ELEMENT DESIGN

##### Ion emitter and ionizer unit

The bracing and the shape of the porous tungsten plate are shown in Fig. 5.38.

For versions a, b, and c of the figure it is characteristic that the ionizer itself is made from one piece of porous tungsten having rectangular, square, hexahedral, or circular shape. Along the perimeter the ionizer is joined by welding or soldering with a steel, molybdenum, or niobium shell. To shape the ion beam molybdenum or niobium plates are soldered to the outer shaped surface of porous tungsten.

The advantage of this bracing design lies in the fact that the length of the connecting surface of the ionizer housing and the porous plate is the smallest.

As is known, porous tungsten is very brittle, while the steel, molybdenum, or niobium shell is plastic and pliable. The joining of such a pair is complicated. Even electron-beam welding does not ensure the absence of cracks and burning of material at the joint. Welding by the electron-beam method is performed automatically, maintaining a constant rate of seam formation. On the angular section of the weld seam a programmed automatic device is necessary to keep the welding rate constant. This is why angles in a porous plate are rounded off.

Soldering the porous plate with the housing is more desirable since cracking of the emitter is less likely. In soldering, the housing and the emitter are heated simultaneously.

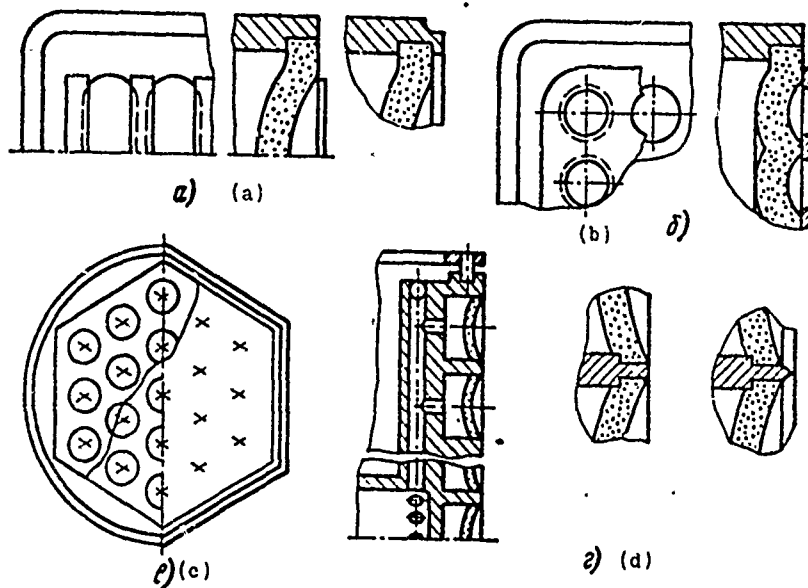


Fig. 5.38. Ion emitter design.

The shape of emitter plates, illustrated in Fig. 5.38a, b, c, has disadvantages. The high temperature of the plate ( $1200^{\circ}\text{C}$ ) requires an even higher temperature for the heater (up to  $1700^{\circ}\text{C}$ ) and, consequently, the work of the motor is accompanied by large heat losses since the porous plate is comparatively large.

The emitters shown in Fig. 5.38a are also bad because of the fact that their uniform heating cannot be ensured. The drum-cover plates, installed for beam shaping, have temperatures, unlike porous tungsten temperatures, which correspond to the appearance of cracks in the unit.

A more perfected design is presented in Fig. 5.38d. The radiation surface is reduced to a minimum. Some increase in the length of the soldered surface as compared with the preceding designs is compensated

by the perfected circular shape of the emitters, convenient for electron-beam welding and soldering.

#### Ion-optical system unit

Figure 5.39 shows elements of the ion-optical system of grid design. Grid 1 of tungsten, molybdenum, or tantalum is mounted on frame 2 of stainless steel. One end of the grid filament is welded to the frame; the other, in order to compensate for thermal elongations and the creation of tension, is attached to bellows 3. The bellows must be two-layer as shown in the figure, if it is to compensate for the tension of one filament, and one-layer if two filaments are compensated. The frames are attached to each other by bushing 4 of aluminum oxide. The bellows are not required for grids whose design is shown in Fig. 5.40. The electrodes here are made in the form of rigid hollow tubes. Such shape allows the use of the internal cavity of the accelerating electrode pipe as a beam neutralizer. For this, it is covered with tungsten and has an additional heater.

An example of a plate electrode design is shown in Fig. 5.41a. A plate with openings 1 is attached to the motor housing 4 by means of a thin rigid stamped shell 2 and three insulators 3 of aluminum oxide. Metal elements are soldered to it to provide reliable centering and insulator bracing.

Frequently the openings of the plate electrode are the tracing spot of the neutralizer; Fig. 5.41b shows various versions of neutralizers.

#### Heater unit

The simplest possible heater design is shown in Fig. 5.42a. On a ceramic plate 1 are installed tungsten filaments 2, fixed in their seats by an open plate of beryllium oxide. The disadvantage of the heater is the high heat loss.

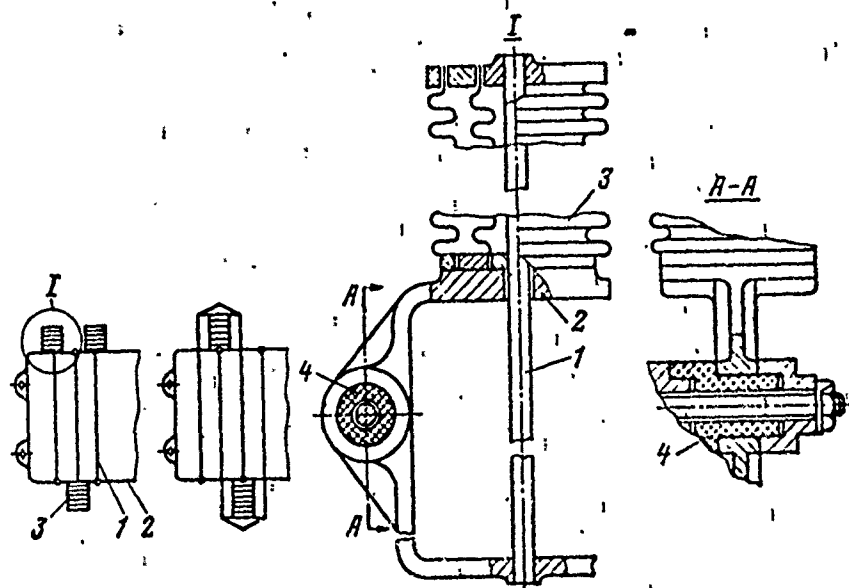


Fig. 5.39. Design of ion-optical system elements.

The heater in Fig. 5.42b is made directly on the ionizer housing. The tungsten wire is insulated from the housing by ceramic washers.

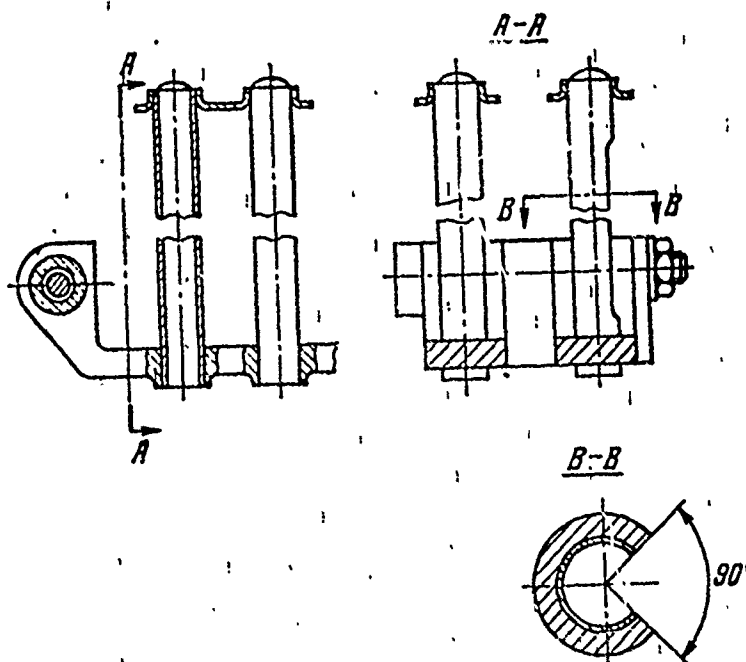


Fig. 5.40. Electrode design.

Figure 5.42c shows the design of a plate heater. The construction of the tank and the servicing equipment for the working medium is shown in Fig. 5.43. The diagram illustrates the servicing device 1, the tank with the working medium 2, a porous diaphragm 3, and a porous membrane 4.

Figure 5.44 presents an ion motor designed for the orientation of earth satellites. Cesium vapor is ionized on the surface of the ion emitter 4 of porous tungsten, heated to  $1230^{\circ}\text{C}$ , and extracted by accelerating electrode 6, heated to  $1130^{\circ}\text{C}$ . Beam shaping is accomplished by decelerating electrode 7 solderings 8 for ion neutralization.

The Cesium is fed from tank 10 under the pressure of the saturated vapor, for which it is heated to  $100\text{--}150^{\circ}\text{C}$ . Dosage is accomplished by the porous diaphragm 12 of ceramic, with the use of the electrostatic effect of the diaphragm. On the outer wall of the diaphragm a thin film of copper is deposited. Fine control of working medium flowrate is accomplished by changing the voltage of the "copper layer-plate." Figure 5.45 presents the overall view of the motor [9], developing thrust  $R = 7 \cdot 10^{-3} \text{ N}$ ; current in the ion beam is 12 mA; potential of the accelerating electrode is 8 V, of the decelerating electrode 4 kV. Figure 5.46 shows the overall view of a motor with volume ionization. The cesium in vapor state through opening 1 passes through distributor 2 into the discharge chamber. Cathode 3, anode 4, and anticathode 5 create the conditions for ionizing the cesium, whose ions are extracted by the accelerating electrode grid 6. Stabilization of the ion beam is effected by the electromagnet coil 6.

Figure 5.47a and c shows the design of ion motor units with volume ionization of cesium vapor. Cesium vapor is ionized in chamber 1 as a result of the oscillating discharge between cathode 2, a flat tungsten spiral, and tungsten anode 3 in the form of a ring. The cathode and the anode are insulated from the chamber walls by insulators 4.



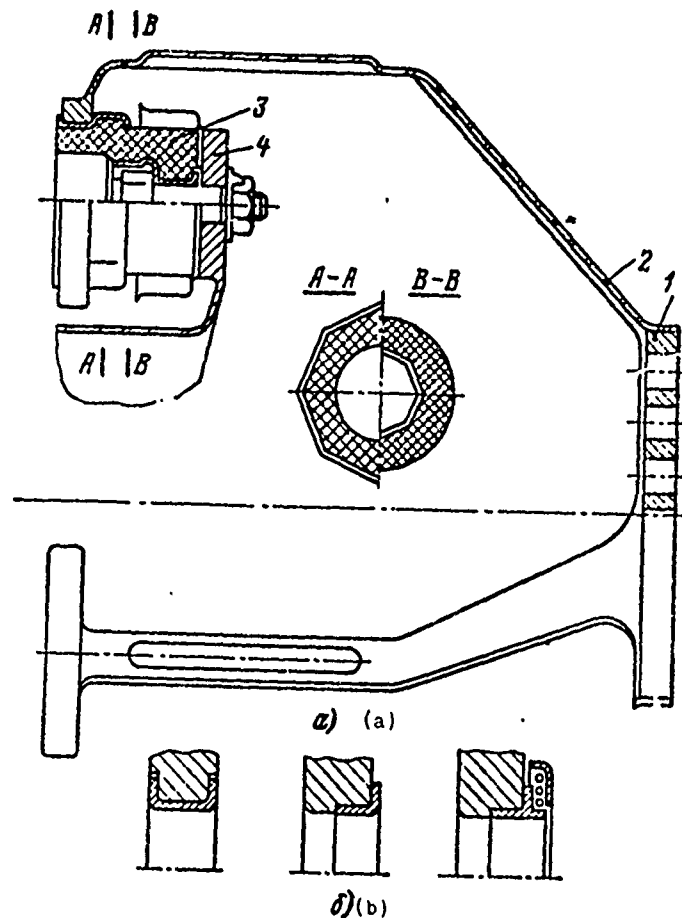


Fig. 5.41. Plate electrode design.

Positive particles of ionized plasma are extracted, accelerated, and neutralized by the ion-optical system of the motor 5, 6.

Liquid cesium is fed by forcing it from the tank under the pressure of compressed argon in the gas cylinder. The compressed argon through the transforming valve acts on the deformable diaphragm, feeding cesium to the dosing valve.

The peculiarity of the valve design is the fine control of the flow rate, using bimetallic plate 8. This plate, if its temperature is changed by the heater 9, bends and opens a path into the ionization chamber 1.

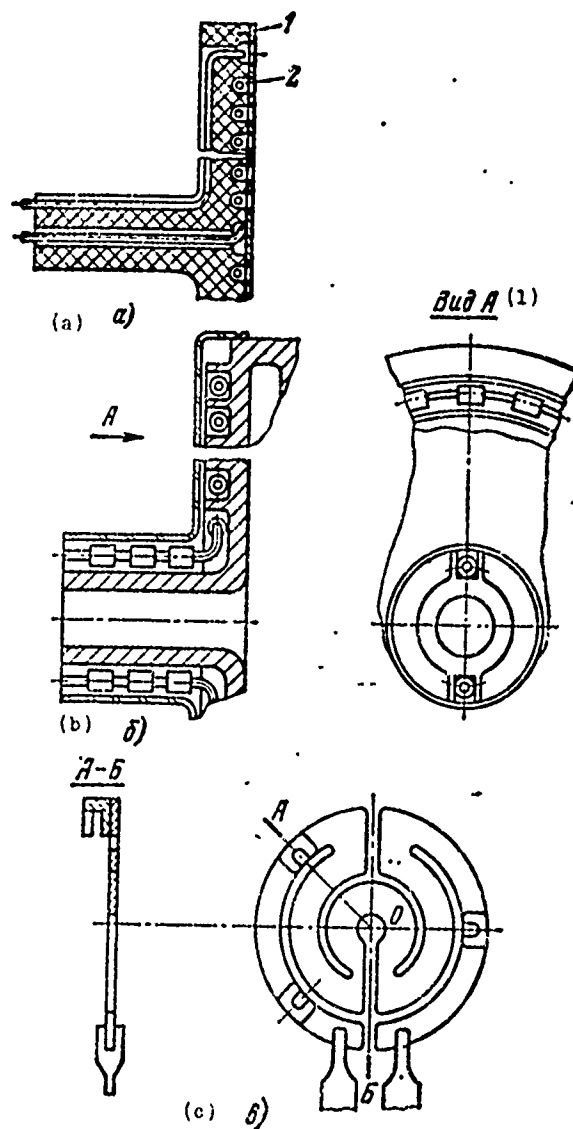


Fig. 5.42. Heater design.  
KEY: (1) View.

Figure 5.48 shows a version of ion motor design with volume ionization.

The motor consists of a hollow cathode 1, cylindrical anode 2, extracting electrode 3, neutralizer 4, and bracing element 5. The heated working medium, leaving the cathode opening 2, is ionized by

electrons from the cathode and then is extracted, accelerated, and neutralized by the electrode system 3, 4.

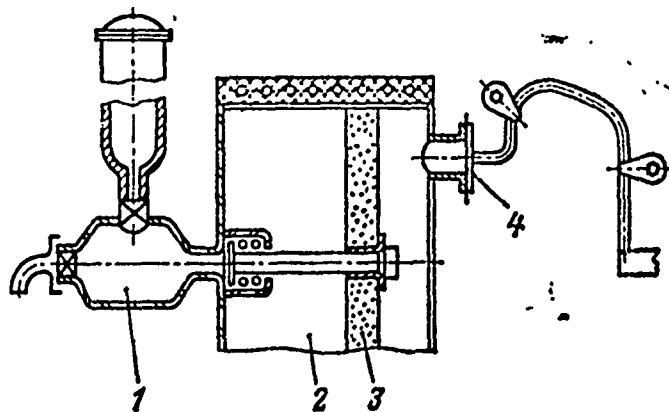


Fig. 5.43. Structural diagram of tank with working medium.

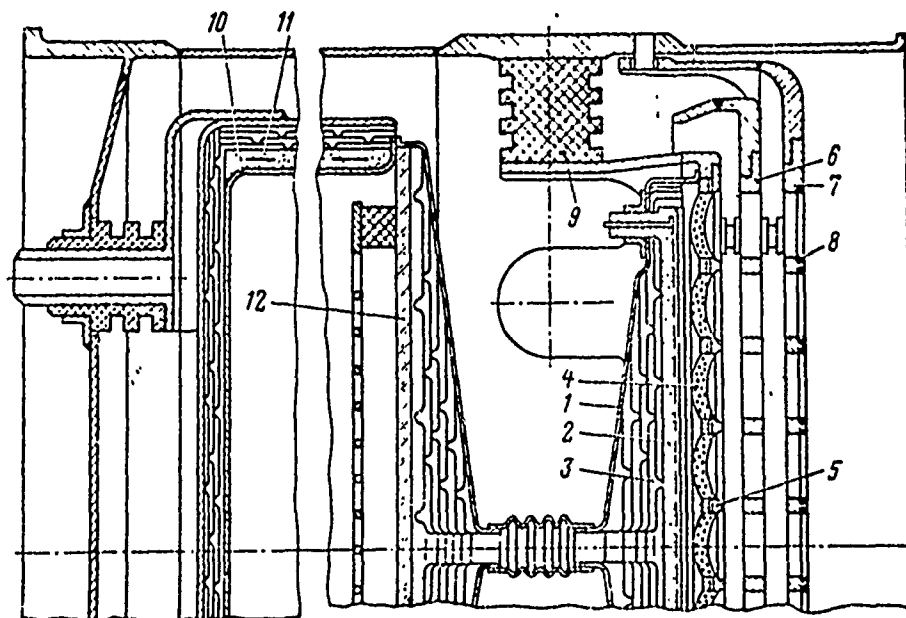


Fig. 5.44. Ion motor design: 1 - housing; 2 - heater; 3 - screen; 4 - porous plate; 5 - cover plate; 6, 7 - electrodes; 8 - neutralizer; 9 - insulator; 10 - tank wall; 11 - heater; 12 - porous plate.

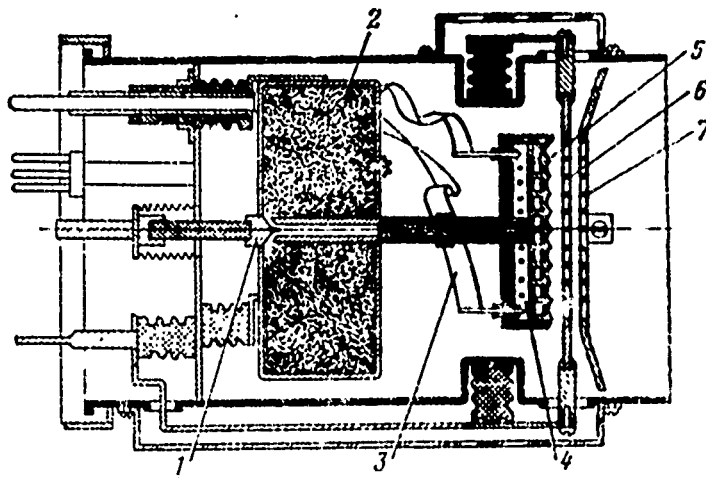


Fig. 5.45. Overall view of ion motor: 1 - cesium flow valve; 2 - tank with working medium; 3 - switching tape; 4 - heater; 5 - ionizer; 6 - accelerating electrode; 7 - decelerating and neutralizing electrode.

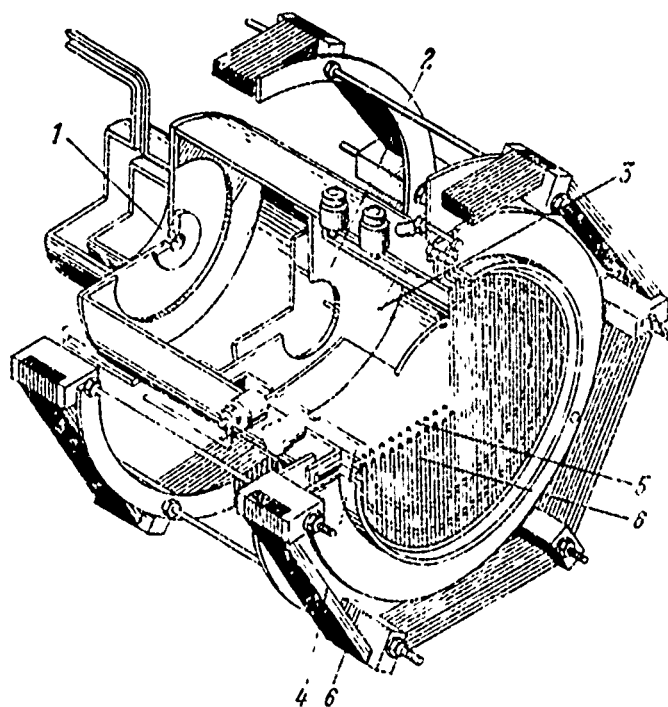


Fig. 5.46. Motor with volume ionization of working medium.

## Stress analysis of motor elements

Axisymmetric shells of complex form are encountered in motors. Let us analyze them.

We separate from the shell, by two meridional and two circular cross sections, an element with dimension  $dx dy$  (Fig. 5.49). Internal forces and moments are applied to the faces of this element.

Through  $\bar{T}_x$  and  $\bar{T}_y$  we designate the tensile stresses per unit length of the corresponding section;  $\bar{Q}_x$  and  $\bar{Q}_y$  are lateral forces;  $\bar{S}$  is shearing force. These force factors are given in  $\text{daN/mm}$ .

The same designations are introduced for relative bending moments  $\bar{M}_x$  and  $\bar{M}_y$  and torque  $\bar{H}$ . They are given in  $\text{daN}\cdot\text{mm/mm}$ ;  $p$  is internal pressure, in  $\text{daN/mm}^2$ .

Positive directions for forces and moments are indicated in Fig. 5.50. These forces and moments, expressed through relative values, will be:

$$\begin{aligned}
 P &= p \, dx \, dy; \\
 T_x &= \bar{T}_x \, dy; & T_x + dT_x &= \left( \bar{T}_x + \frac{\partial \bar{T}_x}{\partial x} dx \right) dy'; \\
 T_y &= \bar{T}_y \, dx; & T_y + dT_y &= \left( \bar{T}_y + \frac{\partial \bar{T}_y}{\partial y} dy \right) dx; \\
 Q_x &= \bar{Q}_x \, dy; & Q_x + dQ_x &= \left( \bar{Q}_x + \frac{\partial \bar{Q}_x}{\partial x} dx \right) dy'; \\
 Q_y &= \bar{Q}_y \, dx; & Q_y + dQ_y &= \left( \bar{Q}_y + \frac{\partial \bar{Q}_y}{\partial y} dy \right) dx; \\
 S &= \bar{S} \, dy; & S + dS &= \left( \bar{S} + \frac{\partial \bar{S}}{\partial x} dx \right) dy'; \\
 M_x &= \bar{M}_x \, dy; & M_x + dM_x &= \left( \bar{M}_x + \frac{\partial \bar{M}_x}{\partial x} dx \right) dy';
 \end{aligned}$$

$$\left. \begin{aligned} M_y &= \bar{M}_y dx; & M_y + dM_y &= \left( \bar{M}_y + \frac{\partial \bar{M}_y}{\partial y} dy \right) dx; \\ H &= \bar{H} dy; & H + dH &= \left( \bar{H} + \frac{\partial \bar{H}}{\partial x} dx \right) dy'. \end{aligned} \right\} \quad (5.72)$$

It is characteristic that in the expressions for forces and moments in the form of deformation axial symmetry, the values of  $d$  in the front and back parts of the element are equal to each other. Segments  $dy$  to the right and left are different since their deformation in the direction of the axis can be substantial.

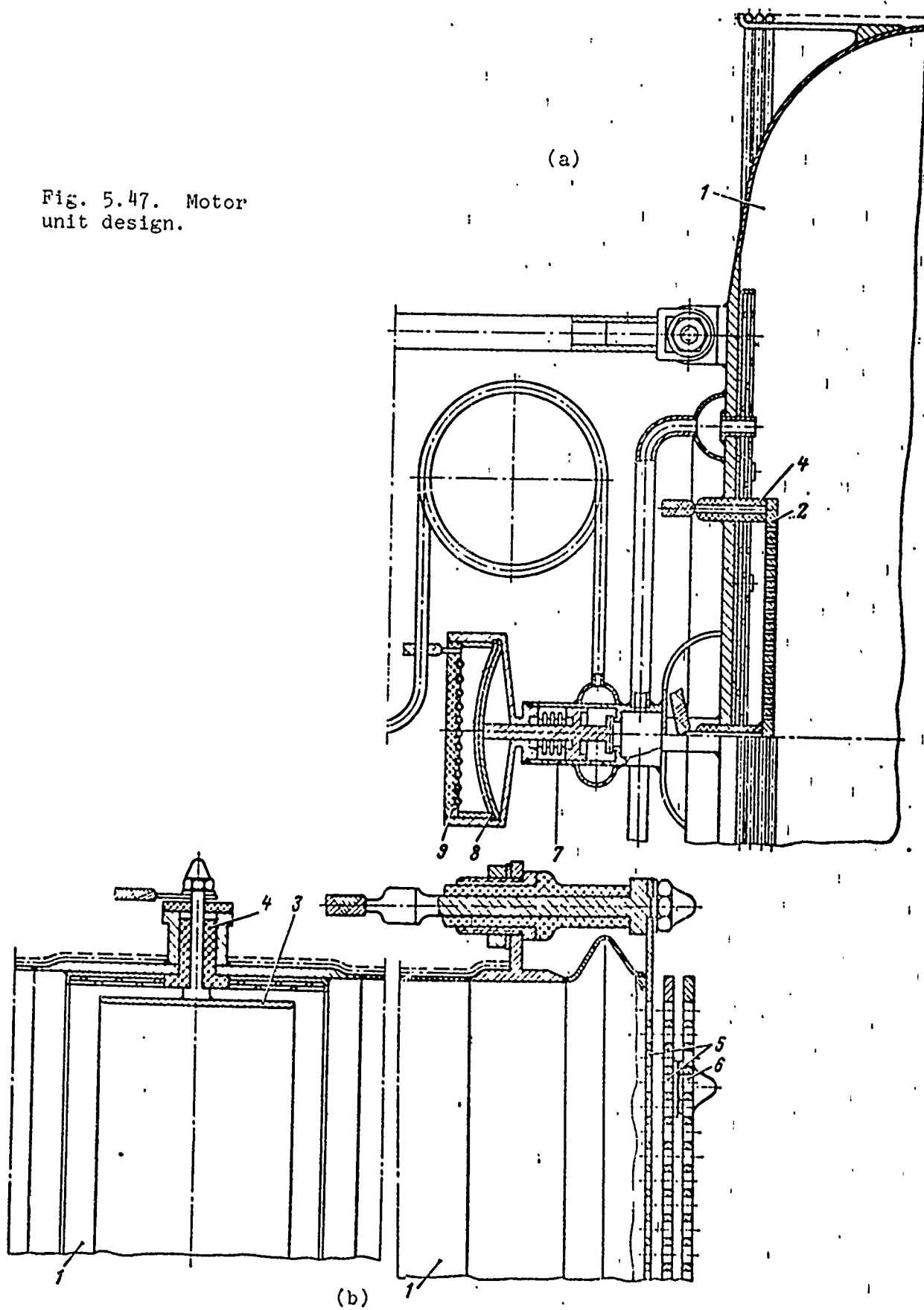
It is easy to show that

$$dy' = dy \left( 1 + \frac{dx}{R_2 \operatorname{tg} \theta} \right).$$

External forces acting on the shell are assumed to be asymmetric; therefore internal forces do not have the properties of axial symmetry. If the loads are symmetric, the internal force factors will not depend upon  $y$ .

Steady-state equations are composed for a deformed shell, i.e., we shall assume that due to the rather large local displacement in  $w$ , the radii of curvature for the middle surface have changed noticeably and acquired the values of  $R_1'$  and  $R_2'$ .

Fig. 5.47. Motor  
unit design.







Let us project all forces acting on the element onto the normal to the middle surface. If we disregard quantities of the highest order of smallness, we obtain

$$\begin{aligned}
 & p \, dx \, dy - \bar{T}_y \, dx \frac{dy}{R_2} - \bar{T}_x \, dy \frac{dx}{R_1} + \bar{S} \, dy \frac{\partial}{\partial x} \left( \frac{\partial w}{\partial y} \right) dx + \\
 & + \bar{S} \, dx \frac{\partial}{\partial y} \left( \frac{\partial w}{\partial x} \right) dy + \bar{Q}_x \, dy - \left( \bar{Q}_x + \frac{\partial \bar{Q}_x}{\partial x} dx \right) dy + \\
 & + \bar{Q}_y \, dx - \left( \bar{Q}_y + \frac{\partial \bar{Q}_y}{\partial y} dy \right) dx = 0,
 \end{aligned}$$

hence, after substitution of  $dy'$  and transformations, we find

$$p - \frac{\bar{T}_y}{R_2} - \frac{\bar{T}_x}{R_1} + 2\bar{S} \frac{\partial^2 w}{\partial x \partial y} - \frac{\bar{Q}_x}{R_2 \lg \theta} - \frac{\partial \bar{Q}_x}{\partial x} - \frac{\partial \bar{Q}_y}{\partial y} = 0. \quad (5.73)$$

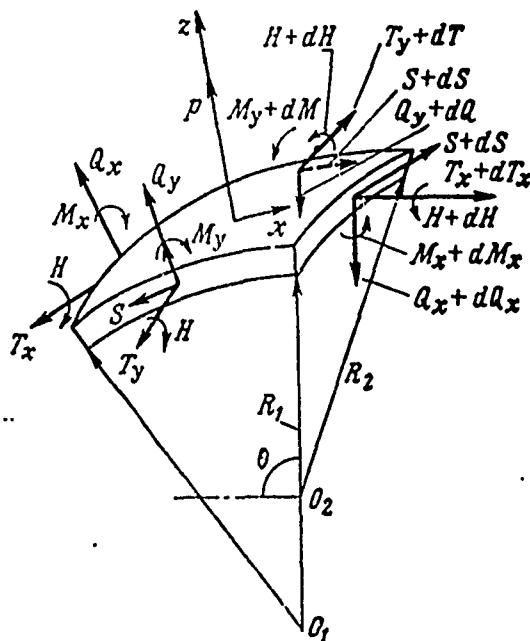
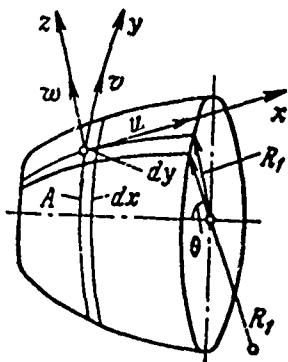


Fig. 5.49. Axes of coordinates. Fig. 5.50. Loads acting on a shell element.

This equation enables us to allow for the noticeable change in shell shape during loading. Its distortion leads to a twist of the middle surface, and the forces  $S$  give components along the normal. However, usually the fourth and fifth terms are disregarded and steady-state equations have the form

$$p - \frac{\bar{T}_y}{R_2} - \frac{\bar{T}_x}{R_1} - \frac{\partial \bar{Q}_x}{\partial x} - \frac{\partial \bar{Q}_y}{\partial y} = 0. \quad (5.74)$$

Let us find other equations. We shall project all forces in the direction of the tangents to the arc of the meridian and the arc of the circle. This gives

$$\begin{aligned} & \left( \bar{T}_x + \frac{\partial \bar{T}_x}{\partial x} dx \right) dy' - \bar{T}_x dy - \bar{T}_y dx \frac{dy}{R_2 \lg \theta} - \bar{S} dx + \\ & + \left( \bar{S} + \frac{\partial \bar{S}}{\partial y} dy \right) dx - Q_x dy \frac{dx}{R_1} + Q_y dx \frac{\partial}{\partial y} \left( \frac{\partial w}{\partial x} \right) dy = 0; \\ & \left( \bar{T}_y + \frac{\partial \bar{T}_y}{\partial y} dy \right) dx - \bar{T}_y dx + \left( \bar{S} + \frac{\partial \bar{S}}{\partial x} dx \right) dy' - \bar{S} dy + \\ & + \bar{S} dx \frac{dy}{R_2 \lg \theta} - \bar{Q}_y dy \frac{dy}{R_2} + \bar{Q}_x dy \frac{\partial}{\partial x} \left( \frac{\partial w}{\partial y} \right) dx = 0. \end{aligned}$$

Hence

$$\left. \begin{aligned} \frac{\bar{T}_x}{R_2 \lg \theta} + \frac{\partial \bar{T}_x}{\partial x} - \frac{\bar{T}_y}{R_2 \lg \theta} + \frac{\partial \bar{S}}{\partial y} - \frac{Q_x}{R_1} + Q_y \frac{\partial^2 w}{\partial x \partial y} &= 0; \\ \frac{\partial \bar{T}_y}{\partial y} + \frac{2\bar{S}}{R_2 \lg \theta} + \frac{\partial \bar{S}}{\partial x} - \frac{Q_y}{R_2} + Q_x \frac{\partial^2 w}{\partial x \partial y} &= 0. \end{aligned} \right\} \quad (5.75)$$

Let us take, finally, the sum of the moments of all forces relative to the tangent to the arc of the meridian and the tangent to the arc of the circle:

$$\left( \bar{M}_y + \frac{\partial \bar{M}_y}{\partial y} dy \right) dx - \bar{M}_y dx - \bar{Q}_y dx dy - \bar{H} dy +$$

$$\begin{aligned}
& + \left( \bar{H} + \frac{\partial \bar{H}}{\partial x} dx \right) dy' - \bar{H} dx \frac{\partial y}{R_2' \operatorname{tg} \theta} = 0; \\
& \left( \bar{M}_x + \frac{\partial \bar{M}_x}{\partial x} dx \right) dy' - \bar{M}_x dy - \bar{Q}_x dx dy - \bar{M}_y dx \frac{dy}{R_2' \operatorname{tg} \theta} + \\
& + \left( \bar{H} + \frac{\partial \bar{H}}{\partial y} dy \right) dx - \bar{H} dx = 0,
\end{aligned}$$

hence

$$\bar{Q}_y = \frac{\partial \bar{M}_y}{\partial y} + \frac{\partial \bar{H}}{\partial x} + \frac{2\bar{H}}{R_2' \operatorname{tg} \theta}; \quad \bar{Q}_x = \frac{\partial \bar{M}_x}{\partial x} + \frac{\partial \bar{H}}{\partial y} + \frac{\bar{M}_x - \bar{M}_y}{R_2' \operatorname{tg} \theta}.$$

We shall disregard, as above, the quantities

$$2\bar{H}/R_2' \operatorname{tg} \theta \quad \text{and} \quad (\bar{M}_x - \bar{M}_y)/R_2' \operatorname{tg} \theta.$$

Then

$$\bar{Q}_y = \frac{\partial \bar{M}_y}{\partial y} + \frac{\partial \bar{H}}{\partial x}; \quad \bar{Q}_x = \frac{\partial \bar{M}_x}{\partial x} + \frac{\partial \bar{H}}{\partial y}.$$

Substituting  $\bar{Q}_y$  and  $\bar{Q}_x$  into equation (5.74), we obtain

$$p - \frac{\bar{T}_y}{R_2'} - \frac{\bar{T}_x}{R_1'} - \frac{\partial^2 \bar{M}_x}{\partial x^2} - 2 \frac{\partial^2 \bar{H}}{\partial x \partial y} - \frac{\partial^2 \bar{M}_y}{\partial y^2} = 0.$$

Curvatures  $1/R_1'$  and  $1/R_2'$  differ from  $1/R_1$  and  $1/R_2$ , respectively, by quantities  $\partial^2 w / \partial x^2$  and  $\partial^2 w / \partial y^2$ . Thus

$$\frac{1}{R_1'} = \frac{1}{R_1} - \frac{\partial^2 w}{\partial x^2}; \quad \frac{1}{R_2'} = \frac{1}{R_2} - \frac{\partial^2 w}{\partial y^2}.$$

Finally, we obtain

$$\begin{aligned}
p - \bar{T}_x \left( \frac{1}{R_1} - \frac{\partial^2 w}{\partial x^2} \right) - \bar{T}_y \left( \frac{1}{R_2} - \frac{\partial^2 w}{\partial y^2} \right) - \\
- \frac{\partial^2 \bar{M}_x}{\partial x^2} - 2 \frac{\partial^2 \bar{H}}{\partial x \partial y} - \frac{\partial^2 \bar{M}_y}{\partial y^2} = 0.
\end{aligned} \tag{5.76}$$

Equations (5.74), (5.75), (5.76) should be fulfilled by the equations of shell deformations.

Let us examine shell deformation. As already indicated, the geometry of a shell is wholly determined by the radius of curvature of the arc of the meridian  $R_1$ , by the second principal radius  $R_2$ , and by angle  $\theta$  between the normal to the middle surface and the axis of symmetry. The shape of the middle surface after deformation is called the elastic surface of the shell. It can be characterized by three projections of the full displacement of point A onto the x-, y-, and z-axes. Let us designate these projections  $u$ ,  $v$ , and  $w$ , respectively (see Fig. 5.49).

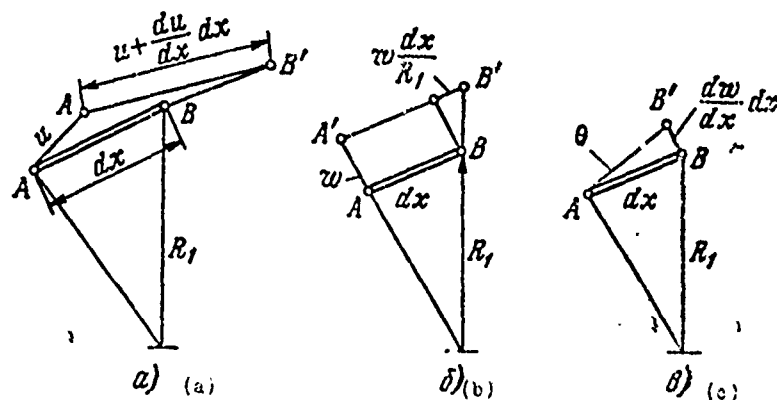


Fig. 5.51. Finding the radial deformation of an element.

The x-axis and the displacement of  $u$  are directed along the tangent to the arc of the meridian,  $y$  and  $z$  along the tangent to the arc of the circle, and  $z$  and  $w$  along the normal. If shell deformation is axisymmetric, displacement of  $v$  vanishes.

We shall express the deformation arising in the shell in terms of displacements of  $u$ ,  $v$ , and  $w$ . We find the components of deformation  $\epsilon_x$ ,  $\epsilon_y$ , and  $\gamma_{xy}$  in the middle surface and designate them  $\epsilon_{cx}$ ,  $\epsilon_{cy}$ ,  $\epsilon_{cxy}$ .

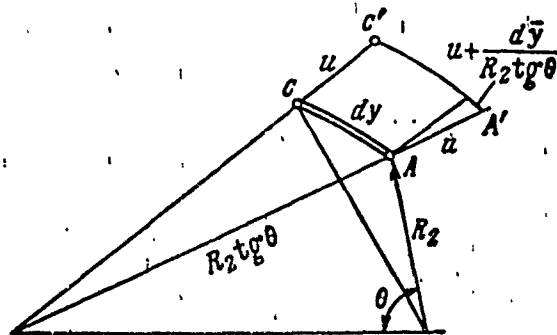
The quantity  $\epsilon_{cx}$  consists of three terms. The first term is conditioned by displacement  $u$ . The left end of the element  $dx$  (Fig. 5.51a) obtains displacement  $u$ , and the right end  $-u + \frac{dy}{dx}dx$ . Displacement  $w$  is considered, for the present, equal to zero. The length increment of the element will be  $(\partial u / \partial x)dx$  and the corresponding elongation per unit length  $\partial u / \partial x$ .

The second term is conditioned by displacement  $w$  (Fig. 5.51b). If before deformation the length was  $dx$ , after deformation it will be  $dx + (wdx/R_1)$ . The length increment is  $wdx/R_1$  and the corresponding elongation will be  $w/R_1$ .

Finally, the third term is conditioned by the turn of the element  $dx$  in the plane of the arc of the meridian (Fig. 5.51c) in the absence of displacement  $u$ . Segment  $AB'$  is larger than segment  $AB$  by the quantity  $(dx/\cos \theta) - dx$ . Corresponding elongation is  $(1 - \cos \theta)/\cos \theta \approx \theta^2/2$ . Since angle  $\theta = \partial w / \partial x$ , elongation is  $\frac{1}{2} \left( \frac{\partial w}{\partial x} \right)^2$ .

This quantity is a quadratic function of bend. With small bends it can be disregarded.

Fig. 5.52. Finding the circular deformation of an element.



Summing the obtained expressions, we find

$$\epsilon_{cx} = \frac{\partial u}{\partial x} + \frac{w}{R_1} + \frac{1}{2} \left( \frac{\partial w}{\partial x} \right)^2. \quad (5.77)$$

Similarly, we can set up an expression for  $\epsilon_{cy}$ . Here we should, however, add one more term.

Let us examine the element  $dy$  (Fig. 5.52). If both ends of this element achieve displacement  $u$ , segment  $AC$  is extended by  $u(du/R_2 \operatorname{tg} \theta)$ . Relative elongation will be  $u/(R_2 \operatorname{tg} \theta)$ . The first three terms are written similarly to  $\epsilon_{cx}$ . We shall obtain

$$\epsilon_{cy} = \frac{\partial v}{\partial x} + \frac{w}{R_2} + \frac{1}{2} \left( \frac{\partial w}{\partial y} \right)^2 + \frac{u}{R_2 \operatorname{tg} \theta}. \quad (5.78)$$

In order to find the angle of shift  $\gamma_{cxy}$ , we shall examine element  $dxdy$  in the plan (Fig. 5.53a). During deformation, three points  $ABC$  occupied the position  $A'B'C'$ .

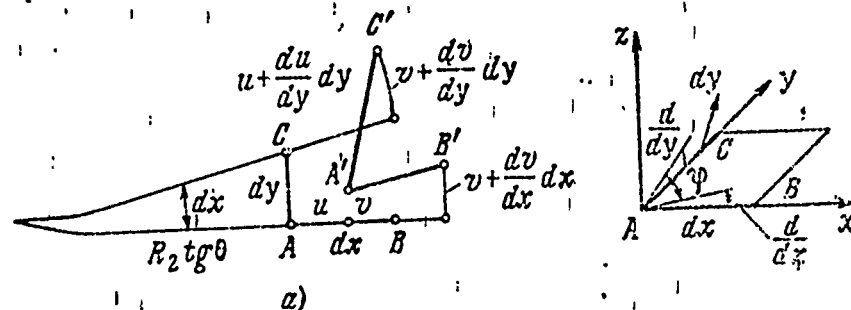


Fig. 5.53.

The angle between the segments  $A'B'$  and  $AB$   $\gamma_1 = \partial v / \partial x$ . The angle between the segments  $A'C'$  and  $AC$  is

$$\gamma_2 = \frac{1}{dy} \left[ \frac{\partial u}{\partial y} dy - \left( u + \frac{\partial u}{\partial y} dy \right) \right] du.$$

Disregarding quantities of the highest order, we find

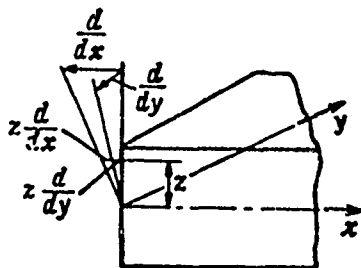
$$\gamma_2 = \frac{\partial u}{\partial y} - v \frac{\partial u}{\partial y} = \frac{\partial u}{\partial y} - \frac{v}{R_2 \operatorname{tg} \theta}.$$

The angle of shift is the variation in the angle BAC and is equal to the sum of the obtained angle:

$$\gamma_1 + \gamma_2 = \frac{\partial v}{\partial x} + \frac{\partial u}{\partial y} - \frac{v}{R_2 \operatorname{tg} \theta}.$$

To this quantity there must be added one more term, caused by bend  $w$ . Let us examine Fig. 5.53b. Due to the fact that the segments  $dx = AB$  and  $dy = AC$  are rotated, respectively, by angles  $\partial w / \partial x$  and  $\partial w / \partial y$ , the angle between them does not remain a right angle. It changes exactly by the quantity of the unknown term.

Fig. 5.54. Finding the components of deformation.



As we know, the cosine of the angle between the two straight lines  $\cos \varphi = l_1 l_2 + m_1 m_2 + n_1 n_2$ , where  $l_1, l_2, m_1, m_2, n_1, n_2$  are the direction cosines of the lines forming angle  $\varphi$ .

In our case

$$\varphi = 90^\circ - \gamma_g;$$

$$l_1 = 1; \quad m_1 = 0; \quad n_1 = \partial w / \partial x;$$

$$l_2 = 0; \quad m_2 = 1; \quad n_2 = \partial w / \partial y.$$

Consequently,  $\cos (90^\circ - \gamma_g) \approx \gamma_g = \frac{\partial w}{\partial x} \frac{\partial w}{\partial y}$ .

Thus, in the middle surface the angle of shift is

$$\gamma_{cxy} = \frac{\partial v}{\partial x} + \frac{\partial u}{\partial y} - \frac{v}{R_2 \operatorname{tg} \theta} + \frac{\partial w}{\partial x} \frac{\partial w}{\partial y}. \quad (5.79)$$

We find here deformation  $\epsilon_x$ ,  $\epsilon_y$ ,  $\gamma_{xy}$  in layers which are distance  $z$  from the middle surface. Let us assume the hypothesis of the invariability of the normal, assuming that the points on the normal to the middle surface remain on the same normal after deformation. Then the displacement of the point which is distance  $z$  from the middle surface will differ from  $u$  and  $v$  by quantities  $z(\partial w / \partial x)$  and  $z(\partial w / \partial y)$  (Fig. 5.54).

Thus,

$$u_z = u - z \frac{\partial w}{\partial x}; \quad v_z = v - z \frac{\partial w}{\partial y}; \quad w_z = w,$$

where  $u_z$ ,  $v_z$ ,  $w_z$  are the displacements of the point which is distance  $z$  from the middle surface.

In addition, at this point we should assume, instead of  $R_1$  and  $R_2$ , the quantities  $R_1 + z$  and  $R_2 + z$  and, accordingly,

$$\frac{1}{R_1 + z} \approx \frac{1}{R_1} \left(1 - \frac{z}{R_1}\right); \quad \frac{1}{R_2 + z} \approx \frac{1}{R_2} \left(1 - \frac{z}{R_2}\right).$$

Here from expressions (5.77), (5.78), (5.79), we easily find the components of deformation in all layers of the shell. For this we substitute, instead of  $u$ ,  $v$ , and  $w$ , the quantities  $u_z$ ,  $v_z$ , and  $w_z$ . Finally, keeping the first powers of  $z$ , we obtain

$$\begin{aligned} \epsilon_x &= \frac{\partial u}{\partial x} + \frac{u}{R_1} + \frac{1}{2} \left( \frac{\partial w}{\partial x} \right)^2 - z \left( \frac{\partial^2 u}{\partial x^2} + \frac{u}{R_1^2} \right); \\ \epsilon_y &= \frac{\partial v}{\partial y} + \frac{v}{R_2} + \frac{1}{2} \left( \frac{\partial w}{\partial y} \right)^2 + \frac{u}{R_2 \operatorname{tg} \theta} - \\ &\quad - z \left( \frac{\partial^2 v}{\partial y^2} + \frac{v}{R_2^2} + \frac{u}{R_2^2 \operatorname{tg} \theta} + \frac{1}{R_2 \operatorname{tg} \theta} \frac{\partial w}{\partial x} \right); \end{aligned}$$



$$\gamma_{xy} = \frac{\partial v}{\partial x} + \frac{\partial u}{\partial y} - \frac{v}{R_2 \operatorname{tg} \theta} + \frac{\partial w}{\partial x} \frac{\partial w}{\partial y} - z \left( 2 \frac{\partial^2 w}{\partial x \partial y} + \frac{v}{R_2^2 \operatorname{tg} \theta} + \frac{1}{R_2 \operatorname{tg} \theta} \frac{\partial w}{\partial y} \right).$$

Terms with the factor  $z$  are deformation caused by the bend and twist of the shell.

In practical calculations, in expressions for flexural deformation the terms  $w/R_1^2$ ,  $w/R_2^2$  do not have a high value; the terms  $u/R_2 \operatorname{tg} \theta$  and  $v/R_2 \operatorname{tg} \theta$  are also very low. With allowance for simplifications, we finally obtain

$$\left. \begin{aligned} \epsilon_x &= \frac{\partial u}{\partial x} + \frac{w}{R_1} + \frac{1}{2} \left( \frac{\partial w}{\partial x} \right)^2 - z \frac{\partial^2 w}{\partial x^2}; \\ \epsilon_y &= \frac{\partial v}{\partial y} + \frac{w}{R_2} + \frac{1}{2} \left( \frac{\partial w}{\partial y} \right)^2 - z \frac{\partial^2 w}{\partial y^2}; \\ \gamma_{xy} &= \frac{\partial v}{\partial x} + \frac{\partial u}{\partial y} + \frac{\partial w}{\partial x} \frac{\partial w}{\partial y} - 2z \frac{\partial^2 w}{\partial x \partial y}. \end{aligned} \right\} \quad (5.80)$$

Error connected with simplifications, does not exceed 2-3%.

Thus, there are six equations for finding the six unknown equations of elasticity. It remains to be found what the stresses  $\sigma_x$ ,  $\sigma_y$ , and  $\tau_{xy}$  are equal to.

Let us examine the side face of the element  $dx dy$  (Fig. 5.55). At distance  $z$  from the middle surface, we distinguish on these faces elementary bands with a width of  $dz$ . Stresses  $\sigma_x$ ,  $\sigma_y$ , and  $\tau_{xy}$  within each band remain unchanged.

Force

$$\bar{T}_x dy = \int_{-h/2}^{h/2} \sigma_x dy dz;$$

since  $dy$  within the face remains a constant quantity, then

$$\bar{T}_x = \int_{-h/2}^{h/2} \sigma_x dz;$$

similarly,

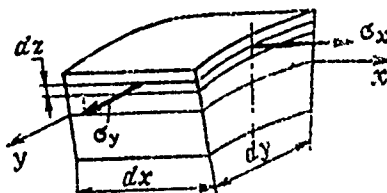
$$\bar{T}_y = \int_{-h/2}^{h/2} \sigma_y dz; \quad \bar{S} = \int_{-h/2}^{h/2} \tau_{xy} dz.$$

Moment

$$\bar{M}_x dy = - \int_{-h/2}^{h/2} \sigma_x z dy dz.$$

The minus sign indicates that positive stress with positive  $c_z$  gives a moment which is opposite in sign to that which was examined when we were setting up steady-state equations (see Fig. 5.50).

Fig. 5.55. Finding stresses.



Thus,

$$\bar{M}_x = - \int_{-h/2}^{h/2} \sigma_x z dz.$$

Precisely thus we find  $\bar{M}_y$  and  $\bar{H}$ . Finally, we obtain

$$\bar{T}_x = \int_{-h/2}^{h/2} \sigma_x dz; \quad \bar{M}_x = - \int_{-h/2}^{h/2} \sigma_x z dz; \quad \left| \right.$$

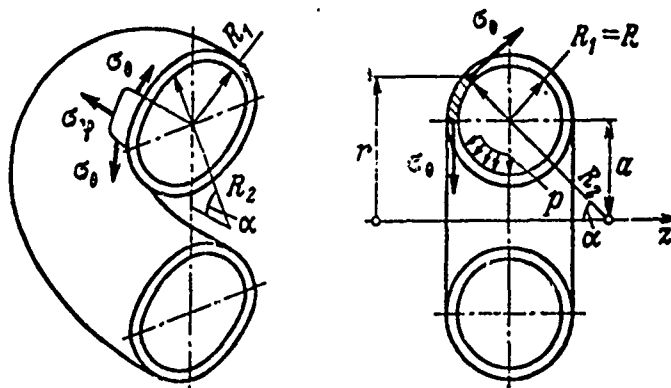
$$\left. \begin{aligned} \bar{T}_y &= \int_{-h/2}^{h/2} \tau_{yz} dz; \quad \bar{M}_y = - \int_{-h/2}^{h/2} \tau_{yz} z dz; \\ \bar{S} &= \int_{-h/2}^{h/2} \tau_{xy} dz; \quad \bar{H} = - \int_{-h/2}^{h/2} \tau_{xy} z dz. \end{aligned} \right\} \quad (5.81)$$

Let us proceed to an examination of specific particular cases of shell analysis.

#### Analysis of a torus-shaped shell

Torus-shaped shells are used in feed systems and motor control systems. The peculiarities of the shell is the variable value of the second principal radius of curvature  $R_2$  (Fig. 5.56).

Fig. 5.56. Torus-shaped shell.



The angle of slope for the principal radius of curvature is

$$\begin{aligned} \alpha = 0; \quad R_2 = \infty; \quad \alpha = \frac{\pi}{2}, \quad R_2 = a + R; \\ \alpha = -\frac{\pi}{2}; \quad R_2 = a - R; \quad R_1 = R = \text{const.} \end{aligned}$$

Let us set up the steady-state equation of an element cut by two planes normal to the surface. For this we find the values of radii

$$R_2 = \frac{a}{\sin \alpha} + R; \quad R_1 = R; \quad r = R_2 \sin \alpha = a + R \sin \alpha.$$

Projecting all forces onto the z-axis, we obtain

$$N_t \sin \alpha 2\pi r - p\pi(r^2 - a^2) = 0,$$

or, substituting the value of r,

$$N_t \sin \alpha 2\pi (a + R \sin \alpha) = p\pi [(a + R \sin \alpha)^2 - a^2]$$

and

$$N_t = \frac{pR(2a + R \sin \alpha)}{2(a + R \sin \alpha)}; \quad \sigma_t = \frac{pR}{2h} \frac{2a + 2 \sin \alpha}{a + R \sin \alpha}. \quad (5.82)$$

From the main equation (2.30) we obtain

$$N_r = \frac{pR}{2}; \quad \sigma_r = \frac{pR}{2h}. \quad (5.83)$$

As is apparent from expressions (5.82) and (5.83), the greatest stress  $\sigma_\theta$  arises at the internal points of the torus-shaped shell when  $\varphi = -\pi/2$ ; in a particular case when  $a = R$ , stress is  $\sigma_\theta = \sigma$ .

#### Thermal stresses of a spherical shell

Stresses in a spherical shell are determined from formulas [4]:

$$\sigma_r = \frac{2Ea}{1-\mu} \left[ \frac{r^3 - a^3}{(1^3 - a^2)r^3} \int_a^b \Delta t r^2 dr - \right. \\ \left. - \frac{1}{r^3} \int_a^r \Delta t r^2 dr \right];$$

$$\sigma_r = \frac{2Ea}{1-\mu} \left[ \frac{2r^3 + a^3}{2(l^3 - a^3)r^3} \int_a^b \Delta t r^2 dr - \frac{1}{2r^3} \int_a^r \Delta t r^2 dr - \frac{1}{2} \Delta t \right] \quad (5.84)$$

Let us examine stresses in the steady flow of heat going from the center to the outer surface of a sphere. We shall designate the temperature on the inner surface  $\Delta t_a$  and the temperature on the outer surface will be zero.

Let us assume that the temperature changes according to linear law:

$$\Delta t = \frac{a}{b-a} t_a \left( \frac{b}{r} - 1 \right).$$

If we substitute this value into formula (5.84), we obtain

$$\left. \begin{aligned} \sigma_r &= \frac{E a t_a}{1-\mu} \frac{a b}{b^3 - a^3} \left[ a + b - \frac{1}{r} (a^2 + a b + b^2) + \frac{a^2 b^2}{r^3} \right]; \\ \sigma_\varphi &= \frac{E a t_a}{1-\mu} \frac{a b}{b^3 - a^3} \left[ a + b - \frac{1}{2r} (a^2 + a b + b^2) - \frac{a^2 b^2}{2r^3} \right]. \end{aligned} \right\} \quad (5.85)$$

As seen from the formulas, stress  $\sigma_r$  is zero when  $r = a$  and  $r = b$ . It becomes maximum or minimum when

$$r^2 = \frac{3a^2 b^2}{a^3 + a b + b^2}.$$

Stress  $\sigma_\varphi$  when  $t_a > 0$  increases with an increase in distance  $r$ .

When  $r = a$

$$\sigma_r = - \frac{E a t_a}{2(1-\mu)} \frac{b(b-a)(a+2b)}{b^3 - a^3};$$

$$\text{when } r = b \quad \sigma_r = \frac{E a t_a}{2(1-\mu)} \frac{a(b-a)(2a+b)}{b^3 - a^3}.$$

If the shell has little thickness, we assume  $b = (1 + m)a$ , where  $m$  is a small quantity. Substituting this value into formulas  $\sigma$  and  $\sigma_\phi$  and disregarding the highest orders of quantity  $m$ , we find

$$\text{when } r = a \quad \sigma_r = -\frac{E a t_a}{2(1-\mu)} \left(1 + \frac{2m}{3}\right);$$

$$\text{when } r = b \quad \sigma_r = \frac{E a t_a}{2(1-\mu)} \left(1 - \frac{2m}{3}\right).$$

If we disregard quantity  $2m/3$ , we shall arrive at the same values for circular stresses as were obtained for a cylindrical shell and for a thin plate with attached edges.

#### Analysis of flexible plates

By flexible we mean those plates which are free and under the action of external forces noticeably change their shape without disrupting the elastic properties of the material. Usually, such plates have a value for parameter  $w/h \geq 1$ .

The difference between such plates and those examined above lies in the fact that to the bending stresses are added tensile or compressive stresses of the middle surface, due to large deflection (Fig. 5.57a).

In deriving the basic equations examined below, we retain the hypothesis of the invariability of the normal to the middle surface and the problem is solved within the limits of elasticity.

Let us set up steady-state equations for a plate element to which we shall give two meridional and two conic sections, with

dimension  $r$ ,  $dr$ . We apply to the element external loading  $P$  and the forces and moments which act along its edges (Fig. 5.57b). The diagram of force action is similar to that presented in Fig. 2.50, only distributed normal forces  $T_r$  and  $T_\varphi$  are added. The element is presented in strained state.

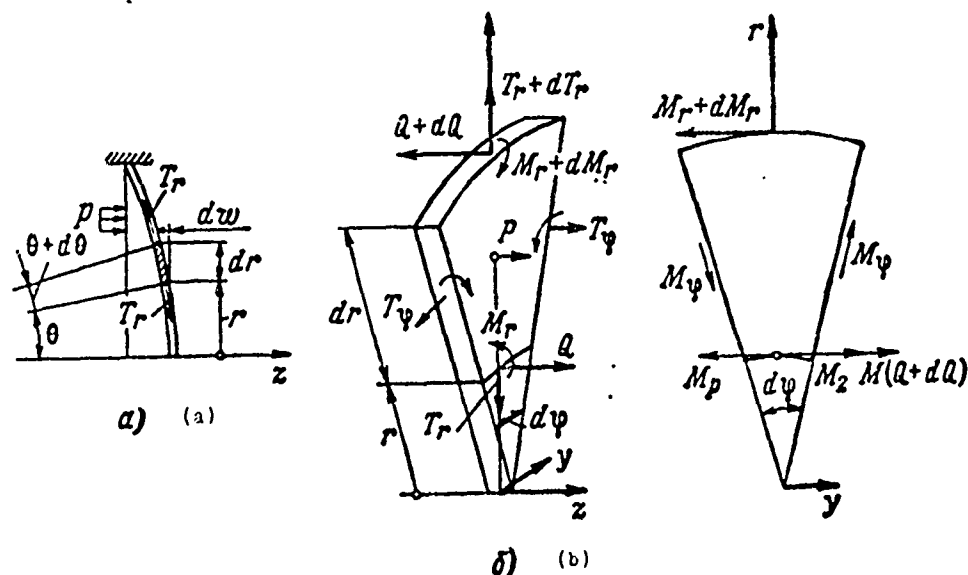


Fig. 5.57. Loads acting on an element of a flexible plate.

The values of the force factors are

$$\begin{aligned} Q &= \bar{Q} r d\varphi; \quad (Q + dQ) = (\bar{Q} + d\bar{Q})(r + dr) d\varphi; \\ T_r &= \bar{T}_r r d\varphi; \quad T_r + dT_r = (\bar{T}_r + d\bar{T}_r)(r + dr) d\varphi; \\ T_\varphi &= \bar{T}_\varphi dr; \\ M_r &= \bar{M}_r r d\varphi; \quad M_r + dM_r = (\bar{M}_r + d\bar{M}_r)(r + dr) d\varphi; \\ M_\varphi &= \bar{M}_\varphi dr; \quad P = pr d\varphi dr; \\ M(P) &= \frac{1}{2} pr d\varphi dr dr; \quad M(Q + dQ) = (\bar{Q} + d\bar{Q})(r + dr) d\varphi dr. \end{aligned}$$

Let us project all forces onto the  $z$ -axis:

$$\begin{aligned} \bar{Q} r d\varphi - (\bar{Q} + d\bar{Q})(r + dr) d\varphi + pr d\varphi dr + \bar{T}_r r d\varphi \cdot \theta - \\ - (\bar{T}_r + d\bar{T}_r)(r + dr) d\varphi (\bar{\theta} + d\theta) = 0; \end{aligned}$$

here, instead of the sines and cosines of the small angles, are substituted angles or units, respectively. After transforming this equation, disregarding small quantities of the second order, we have

$$[r(\bar{T}_r\theta + \bar{Q})]' = pr, \quad (5.86)$$

or

$$r(\bar{T}_r\theta + \bar{Q}) = F(r), \text{ where } F(r) = C + \int pr dr.$$

Let us project all moments onto the y-axis:

$$\begin{aligned} \bar{M}_r d\varphi - (\bar{M}_r + d\bar{M}_r)(r + dr) d\varphi + 2\bar{M}_r dr \frac{d\varphi}{2} \theta - \\ - \frac{1}{2} pr d\varphi dr dr + (\bar{Q} + d\bar{Q})(r + dr) d\varphi dr = 0. \end{aligned}$$

After simplifications similar to those of the first equation, we obtain

$$\bar{M}_r - (\bar{M}_r r)' = -\bar{Q}r. \quad (5.87)$$

The equations obtained do not enable us to determine force T; therefore, we shall set up one more equation, projecting all forces onto the normal to the middle surface of the plate:

$$\begin{aligned} \bar{Q}r d\varphi - (\bar{Q} + d\bar{Q})(r + dr) d\varphi + pr d\varphi dr - \bar{T}_r d\varphi \frac{dh}{2} - \\ - (\bar{T}_r + d\bar{T}_r)(r + dr) d\varphi \frac{dh}{2} - \bar{T}_r dr d\varphi = 0, \end{aligned}$$

hence

$$pr - \bar{T}_r \theta' - (Qr)' - \bar{T}_r \theta = 0. \quad (5.88)$$



We drop  $\bar{Q}$  from equations (5.86) - (5.88). For this, we substitute the expression  $\bar{Q}r = F(r) - \bar{T}_r r \theta$  obtained from equation (5.86) into equation (5.88). Since

$$\left. \begin{aligned} F'(r) &= pr; \\ \bar{T}_r &= (\bar{T}_r)', \end{aligned} \right\} \quad (5.89)$$

equation (5.87) assumes the form

$$(\bar{M}_r)' - \bar{M}_r = F(r) - \bar{T}_r r \theta. \quad (5.90)$$

We have obtained two equations (5.89) and (5.90) of equilibrium for the forces acting on the element and there are five unknown quantities:  $\bar{M}_r$ ,  $\bar{M}_\varphi$ ,  $\bar{T}_r$ ,  $\bar{T}_\varphi$ ,  $\theta$ . To find the equations we lack, we shall examine plate deformation.

Fig. 5.58. Deformation of an element of a flexible plate.

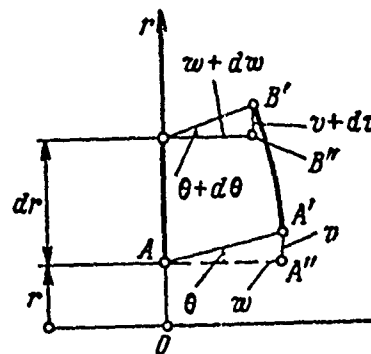


Figure 5.58 shows an element of an arc of the meridian before and after deformation. Full displacement of any point of the arc of the meridian can be decomposed into two components - with respect to the direction of the axis of symmetry  $w$  and with respect to radius  $v$ . The third component, due to symmetry, is zero.

The length of the arc after deformation is  $A'B'' = dr(1 + \epsilon_{rT})$ , where  $\epsilon_{rT}$  is the relative elongation of the middle surface with respect to the direction of the arc of the meridian.

We shall project the closed hexagon BB"B'A'A"A onto the direction of the radius  $r$  and onto the axis of symmetry:

$$v \cdot \frac{1}{r} dr (1 + \varepsilon_{r\tau}) dr \cos \theta - (v \cdot dv) - dr = 0;$$

substituting  $\cos \theta = 1 - (\theta^2/2)$ , we obtain

$$\varepsilon_{r\tau} = v' + \frac{\theta^2}{2}. \quad (5.91)$$

The projection of the hexagon onto the axis of symmetry gives

$$\omega' = -\theta. \quad (5.92)$$

Calculation of relative elongation in a circular direction leads to the results

$$\varepsilon_{\tau} = v/r \quad (5.93)$$

and

$$\varepsilon_{r\tau} - (\varepsilon_{\tau} r)' = \theta^2/2. \quad (5.94)$$

We find here relative elongations  $\varepsilon_{rz}$  and  $\varepsilon_{\phi z}$  at points on the plate which are distance  $z$  from the middle surface, as a result of a deformation relative to the neutral plane. Earlier (Section 2.1) these deformations were determined. They are:

$$\varepsilon_{rz} = z\theta'; \quad \varepsilon_{\phi z} = z \frac{\theta}{r}.$$

Hence total relative deformations are

$$\varepsilon_r = \varepsilon_{r\tau} + z\theta'; \quad \varepsilon_{\tau} = \varepsilon_{\tau r} + z \frac{\theta}{r} \quad (5.95)$$

and, thus, total stresses are

$$\left. \begin{aligned} \varepsilon_r &= \frac{E}{1-\mu^2} \left[ (\varepsilon_{r\tau} + \mu \varepsilon_{\tau\tau}) + z \left( \theta' + \mu \frac{\theta}{r} \right) \right]; \\ \varepsilon_{\tau} &= \frac{E}{1-\mu^2} \left[ (\varepsilon_{\tau\tau} + \mu \varepsilon_{r\tau}) + z \left( \frac{\theta}{r} + \mu \theta' \right) \right]. \end{aligned} \right\} \quad (5.96)$$

If we express, as before, forces  $\bar{T}_r$  and  $\bar{T}_{\tau}$  and moments  $\bar{M}_r$  and  $\bar{M}_{\tau}$  in terms of stresses  $\sigma_r$  and  $\sigma_{\tau}$ , then

$$\begin{aligned} \bar{T}_r &= \int_{-h/2}^{h/2} \sigma_r dz = \frac{Eh}{1-\mu^2} (\varepsilon_{r\tau} + \mu \varepsilon_{\tau\tau}); \\ \bar{T}_{\tau} &= \int_{-h/2}^{h/2} \sigma_{\tau} dz = \frac{Eh}{1-\mu^2} (\varepsilon_{\tau\tau} + \mu \varepsilon_{r\tau}), \end{aligned}$$

hence

$$\varepsilon_{r\tau} = \frac{1}{Eh} (\bar{T}_r - \mu \bar{T}_{\tau}); \quad \varepsilon_{\tau\tau} = \frac{1}{Eh} (\bar{T}_{\tau} - \mu \bar{T}_r). \quad (5.97)$$

Then,

$$\begin{aligned} \bar{M}_r &= \int_{-h/2}^{h/2} \sigma_r z dz = D \left( \theta' + \mu \frac{\theta}{r} \right); \\ \bar{M}_{\tau} &= \int_{-h/2}^{h/2} \sigma_{\tau} z dz = D \left( \frac{\theta}{r} + \mu \theta' \right), \end{aligned} \quad (5.98)$$

where  $D = \frac{Ek^3}{12(1-\mu^2)}$ .

Assuming thickness  $h$  is constant, we replace in expression (5.94)  $\varepsilon_r$  and  $\varepsilon_{\tau}$  by dependences (5.97). Then

$$\bar{T}_r - \mu \bar{T}_{\tau} - (\bar{T}_r r)' + \mu (\bar{T}_{\tau} r)' = Eh \frac{\theta^2}{2}.$$

Let us substitute here  $\bar{T}_\varphi$  from equation (5.89):

$$\bar{T}_r - \mu(\bar{T}_r)' - [(\bar{T}_r)' r]' + \mu(\bar{T}_r)' = Eh \frac{\theta^2}{2};$$

hence

$$-r(\bar{T}_r)'' - (\bar{T}_r)' + \frac{\bar{T}_r r}{r} = Eh \frac{\theta^2}{2}. \quad (5.99)$$

We return to equation (5.90) and drop from it  $\bar{M}_r$  and  $\bar{M}_\varphi$ , taken from formulas (5.98). Then

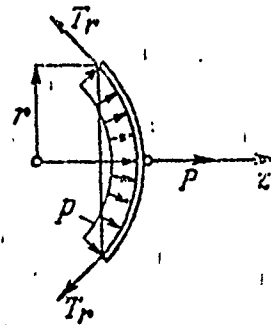
$$D \left[ r \left( \theta' + \mu \frac{\theta}{2} \right) \right]' - D \left( \frac{\theta}{r} + \mu \theta' \right) = F(r) - \bar{T}_r r \theta$$

and after transformation

$$r\theta'' + \theta' - \frac{\theta}{r} = \frac{F(r)}{D} - \frac{T_r r}{D} \theta. \quad (5.100)$$

Thus, we finally obtain two equations (5.99) and (5.100) with two unknowns  $\bar{T}_r$  and  $\theta$ . These equations are nonlinear since the first equation includes the square of an unknown function  $\theta$  and the second equation includes the derivative of unknown  $\theta$ .

Fig. 5.59. Finding force P.



Function  $F(r)$  can be found from the condition of equilibrium for the central part of the shell. Thus, for example (Fig. 5.59), when it is loaded by hydrostatic pressure  $p$ , under the condition of equilibrium for the central part, it follows that:

$$\begin{aligned} -\bar{Q}2\pi r - \bar{T}_r 2\pi r + p\pi r^2 &= 0; \\ r(\bar{T}_r \theta + \bar{Q}) &= F(r) = \frac{pr^2}{2}. \end{aligned}$$

When the plate is loaded by concentrated load  $P$ , we obtain

$$-\bar{Q}2\pi r - \bar{T}_r 2\pi r \theta + P = 0; \quad 2\pi r(\bar{\theta} + \bar{T}_r \theta) = P.$$

Equation (5.100), if pressure  $p$  is acting on the plate, will have the form

$$r\theta'' + \theta - \frac{\theta}{r} = \frac{pr^2}{2D} - \frac{\bar{T}_r r}{D} \theta. \quad (5.101)$$

Finally, in shortened form, the obtained system of equations is:

$$\left. \begin{aligned} r \left[ \frac{1}{r} (r\tilde{T}_r)' \right]' &= -Eh \frac{\theta^2}{2}; \\ r \left[ \frac{1}{r} (r\theta)' \right]' &= \frac{pr^2}{2D} - \frac{\tilde{T}_r}{D}, \end{aligned} \right\} \quad (5.102)$$

where  $\tilde{T} = \bar{T}_r r$ .

Equations (5.102) are equations of a plate in large displacements. They are nonlinear. The first of them includes the square of function  $\theta$  and the second the derivative of functions  $\tilde{T}$  and  $\theta$ .

#### Bends and stresses in a flexible plate

One of the widely known methods of finding the deflection of a flexible plate is the following. It is assumed that the surface

of the plate during large bends is similar to the surface of a rigid plate; the character of the bends is the same but the dependence on external pressure  $p$  is more complex than for rigid plates whereas the bend is proportional to the pressure. Such a method provides satisfactory accuracy if  $w/h \leq 4$ .

Let us find the bend of a plate, assuming it is rigid. Then  $\tilde{T} = 0$  and the first equation of the system (5.102) is dropped while the second assumes the form

$$\left[ \frac{1}{r} (r\theta)' \right]' = \frac{pr}{2D}.$$

We integrate this equation twice. Two integration constants are sought from conditions: when  $r = 0$   $\theta \neq \infty$ ; when  $r = b$   $\theta = 0$ ; i.e., we shall examine the case when the edges of the plate have a rigid attachment. We obtain

$$\theta = \frac{p}{16D} (r^3 - b^2 r) = \frac{pl^3}{16D} (\bar{r}^3 - \bar{r}),$$

where  $\bar{r} = r/b$ .

This value for the angle  $\theta$  of the tangent and the elastic surface of the plate can also be obtained directly from formulas (2.61). We assume here for a flexible plate

$$\theta = C(\bar{r}^3 - \bar{r}); \quad (5.103)$$

the quantity  $C$  does not depend upon  $\bar{r}$  and is an unknown function of pressure  $p$ . Substituting expression (5.103) into the first equation of the system (5.102), we obtain

$$r \left[ \frac{1}{r} (r\tilde{T})' \right]' = -Eh \frac{C^2}{2} (\bar{r}^3 - \bar{r})^2.$$

We integrate this equation twice. The value of two arbitrary integration constants is obtained from the boundary conditions corresponding to a rigid attachment of the membrane along the outer contour;

when  $r = 0$   $\tilde{T} = 0$ ; when  $r = b$   $\theta = 0$ ,  $v = 0$ ,  $\epsilon_{\varphi} = 0$ .

Then, substituting the result into the second equation of system (5.102), we obtain  $C = 4w_0/b$ , where  $w_0$  is the bend of the plate in the center and the final dependence of the bend of the plate on its parameters:

$$\frac{pb^4}{Eh^4} = \frac{16}{3(1-\mu^2)} \left( \frac{w_0}{h} \right) + \frac{2}{21} \frac{23-9\mu}{1-\mu} \left( \frac{w_0}{h} \right)^3, \quad (5.104)$$

or when  $\mu = 0.3$

$$\frac{pb^4}{Eh^4} = 5.92 \left( \frac{w_0}{h} \right) + 2.76 \left( \frac{w_0}{h} \right)^3.$$

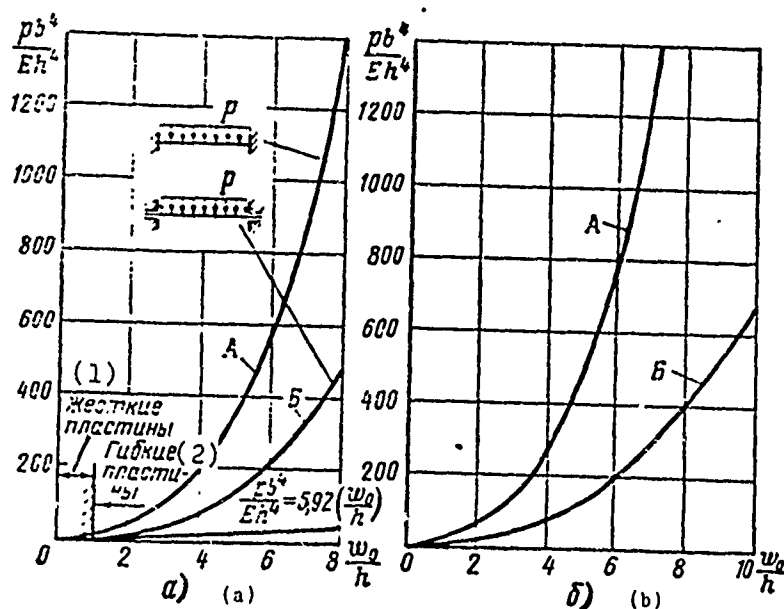


Fig. 5.60. Rigidity of flexible plate.  
KEY: (1) Rigid plates; (2) Flexible plates.

Dependence (5.104) is plotted in Fig. 5.60a. Presented also are the result of the analysis of a plate which can be displaced in a radial direction (without turn) and the result of analysis according to formulas for a rigid plate.

Thus, maximum bend of the membrane and pressure  $p$  are connected by a cubic dependence. With small bends the term containing the third power of ratio  $w_0/h$  can be disregarded; dependence (5.104) converts to the earlier presented dependences for a rigid plate.

The curves in Fig. 5.60a show that with a growth in bend the rigidity of a flexible plate increases. With bends of  $w/h > 1$  the plate should be assumed flexible.

However, this method of analyzing deflections of a flexible plate is not universal. It has good agreement with precise calculation and practice when  $w/h \leq 4$ .

The method requires refinement if the deflections exceed this value. Actually, when examining the elastic surface of a plate, as deflections increase we can note a displacement of the bending point toward the contour and at the limit its agreement with the attachment, which contradicts the basic assumption concerning the similarity of large bends to bends of a rigid plate.

We can prescribe the shape of the elastic surface in the form.  
[43]

$$\theta = C(\bar{r}^2 - \bar{r}). \quad (5.105)$$

This expression differs from expression (5.103) by the fact that here, instead of the exponent 3, there is introduced an undetermined index  $z$  which can be determined each time as a function of the specific relationship between load and plate thickness. Omitting the transformations, we obtain

$$\frac{ph^4}{Eh^4} = \frac{A_1}{1-\mu^2} \left( \frac{w_0}{h} \right) + A_3 \left( \frac{w_0}{h} \right)^3. \quad (5.106)$$



Here  $A_1 = (2)/(3_z)(z + 1)(z + 3)$ ;

$$A_3 = 2 \frac{z+1}{z+3} \left[ \frac{1}{1-\mu} + \frac{2z^3 + 39z^2 + 167z + 174}{6(2z+1)(z+2)(z+5)} \right]. \quad (5.107)$$

In order to solve equation (5.106), we should determine the quantity  $w_0/h$  from expression

$$\left( \frac{w_0}{h} \right)^3 = \frac{B}{1-\mu^2}; \quad (5.108)$$

here B depends upon z:

$$B = \frac{(z^2 - 9)(z + 1)(z + 3)}{z^2} : \left[ \frac{6}{1-\mu} + \frac{16z^6 + 206z^5 + 217z^4 + 7899z^3 + 14533z^2 + 12726z + 4011}{2(z+1)^2(z+2)^2(z+5)^2} \right]. \quad (5.109)$$

Thus, the problem of finding large bends of a plate reduces to the following. If we prescribe parameters z, we find quantity B according to formula (5.109), and then ratio  $w_0/h$  from expression (5.108). Then with known z and  $w_0/h$  from formula (5.106) we determine rigidity  $pb^4/Eh^4$  or pressure p.

Calculation can be shortened if we use Table 5.5 and the graph in Fig. 5.60b for  $\mu = 0.3$ . The table has been compiled for a plate having a rigid attachment. The graph presents results for rigid A and free B attachments.

Experience indicates that the calculated characteristic thus obtained gives a better agreement with experiment during bends on the order of 15-20 thicknesses.

#### Stress in a flexible plate

Maximum stresses arise on the pinched contour:

$$\sigma_r = \frac{\bar{T}_r}{h} \pm \frac{6\bar{M}_r}{h^2}; \quad \sigma_z = \frac{\bar{T}_z}{h} \pm \frac{6\bar{M}_z}{h^2}. \quad (5.110)$$

Table 5.5.

$z$	$w_0/h$	$pb^4/Eh^4$	$z$	$w_0/h$	$pb^4/Eh^4$
4	1,029	8,569	19	5,953	749,9
5	1,488	19,91	21	6,554	989,3
7	2,224	50,88	23	7,151	1273
9	2,384	99,56	25	7,748	1607
11	3,514	159,8	27	8,345	1995
13	4,134	265,4	29	8,942	2442
15	4,759	395,8	31	9,534	2944
17	5,351	552,5	33	10,13	3518

A plus or minus sign is taken depending upon the fact that for each surface of the plate stress is determined.

With a rigid attachment of the plate on its contour

$$\varepsilon_z = \frac{1}{E}(\sigma_z - \mu\sigma_r) = 0, \text{ hence } \sigma_z = \mu\sigma_r.$$

We find  $\sigma_r \max = \sigma_z$  from formula [43]:

$$\sigma_r \max = \frac{Eh^2}{l^2} \frac{z+1}{1-\mu} \left( \frac{w_0}{h} \right) \left[ \frac{1}{1+\mu} + \frac{1}{2(z+3)} \left( \frac{w_0}{h} \right) \right]. \quad (5.111)$$

The order of stress analysis is as follows: based on given pressure  $p$  we calculate quantity  $pb^4/Eh^4$ , then we find from table  $z$  and  $w_0/h$  and, finally, according to formula (5.111) we find the stress.

### Absolutely flexible membrane

If a flexible plate has negligible rigidity during bend, it is called a membrane. In practice, these are flexible plates which have  $w_0/h \geq 10$ . Let us examine a membrane having a rigid attachment along the internal opening and loaded with pressure  $p$  (Fig. 5.61).

A differential steady-state equation for the membrane is obtained from system (5.102), assuming  $D = 0$ :

$$r \left[ \frac{1}{r} (r\tilde{T})' \right]' = -Eh \frac{p}{2}; \quad \tilde{T}\theta = \frac{pr^2}{2}. \quad (5.112)$$

The angle of deflection for a section of the tightened membrane, with sufficient accuracy, can be expressed as

$$\theta = G\bar{r}. \quad (5.113)$$

We substitute this value into the first equation of system (5.112) and integrate it twice.

The integration constants are found from the conditions: when  $r = a$   $\epsilon_r = 0$ ; when  $r = b$   $\epsilon_r = 0$ ; we obtain

$$w = \frac{1}{2} C b (\bar{r}^2 - 1).$$

Substituting the obtained result into the second equation of system (5.112), we obtain

$$C = - \frac{2w_0}{b[1-\bar{a}^2]}, \quad \text{where } \bar{a} = \frac{a}{b},$$

and the dependence between load and bend in the center of the membranes

$$\frac{pb^4}{Eh^4} = A_3 \left( \frac{w_0}{h} \right)^3; \quad (5.114)$$

here

$$A_3 = \frac{1}{(1-\bar{a}^2)^3(1-\bar{a}^4)} \left[ -\frac{2}{3}(1-\bar{a}^6) + \frac{3-\mu}{1-\mu}(1+\bar{a}^2)(1-\bar{a}^4) + \right. \\ \left. + 2 \frac{3-\mu}{1+\mu} \bar{a}^2(1-\bar{a}^2) \right]. \quad (5.115)$$

If  $\bar{a} = 0$ , then when  $\mu = 0.3$   $A_3 = -\frac{2}{3} + \frac{3-\mu}{1-\mu} \approx 3.19$  and

$$\frac{pb^4}{Eh^4} = 3.19 \left( \frac{w_0}{h} \right)^3; \quad w_0 = 0.68b \sqrt[3]{\frac{pb}{Eh}}. \quad (5.116)$$

This result scarcely differs from the precise result

$$\frac{pb^4}{Eh^4} = 3.45 \left( \frac{w_0}{h} \right)^3; \quad w_0 = 0.662b \sqrt[3]{\frac{pb}{Eh}}.$$

The dependence of membrane bend on effective pressure is shown in Fig. 5.62.

Stress in the membrane is

$$\sigma_r = -\frac{Eb}{r} \psi; \quad \sigma_{r, \max} = -\frac{Eb}{a} \psi; \quad \psi = \frac{C_1^2}{16} \left( \bar{r}^3 + C_2 \bar{r} + \frac{C_3}{\bar{r}} \right); \\ C_1 = -\frac{2w_0}{b(1-\bar{a}^2)}; \quad C_2 = -\frac{3-\mu}{1-\mu}(1+\bar{a}^2); \quad C_3 = -\frac{3-\mu}{1+\mu} \bar{a}^2; \\ \bar{r} = \frac{r}{h}; \quad \bar{a} = \frac{a}{h}.$$

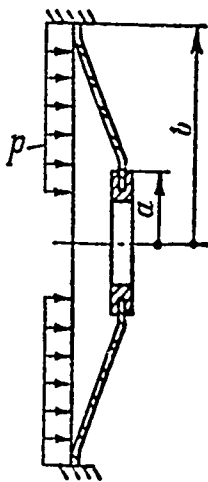


Fig. 5.61. Plate with opening.

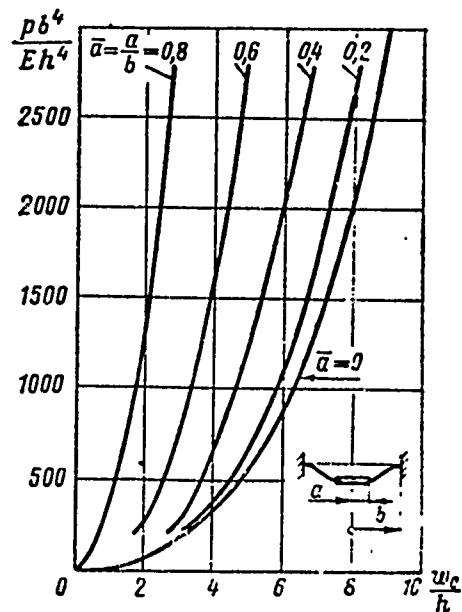


Fig. 5.62. Rigidity of flexible plate with opening.

### Bellows analysis

The bellows, or fluted adapter, is a cylindrical body with wave-shaped folds applied along the circumference. The shapes of the folds or corrugation, in axial cross section and with various designs of bellows are shown in Fig. 5.63. The most widespread shape of corrugation, which has the least rigidity, is shown in Fig. 5.63a. Bellows with such corrugation are called packed bellows. Technologically simpler forms are encountered (Fig. 5.63b, c). If in the internal cavities of the bellows there is a liquid or gas under high pressure, the corrugation is fastened by rigid rings (Fig. 5.63d).

The main advantage of the bellows lies in its ability, under the effect of a small end thrust, to give noticeable elastic elongation or compression depending upon the direction of the effective forces. This has brought about the widespread use of bellows in the most varied elements of motor design.

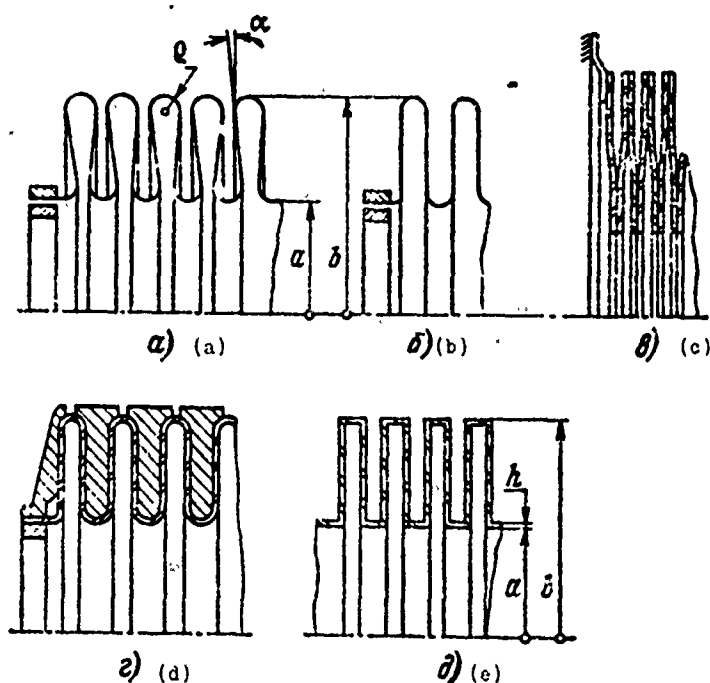


Fig. 5.63. Bellows design.

Most frequently they are used as elastic couplings of piping with angular and axial displacement; they are irreplaceable as temperature compensators for displacements of individual parts of the piping, while preserving the complete seal of the latter.

Bellows are used for sealing movable couplings in taps, valves, and various distributors, and they also serve as the elastic limiters of various media in the compensator, frequently with large variations in the volumes of these media. The walls of the bellows can be both single-layer and multi-layer, simple or armored depending upon the requirements for system sealing or upon the fluid pressure in the pipes or vessel.

Let us discuss some of the general properties of bellows. Obviously the movement of the limiting plane of the bellows under the effect of axial loading, with other conditions remaining constant, is directly proportional to the number of corrugations on its surface and inversely proportional to the cube of the wall thickness  $n$ .

Movement of the bellows also depends on the ratio of its diameters. In the first approximation, this dependence can be assumed equal to the square of the ratios of the diameters:

$$\frac{\lambda_1}{\lambda_2} = \left(\frac{b}{a}\right)_1^2 : \left(\frac{b}{a}\right)_2^2.$$

To calculate strains and stresses in the walls of the bellows, it is considered a system of circular plates bound on the external and the internal contours by cylindrical inserts (Fig. 5.63e).

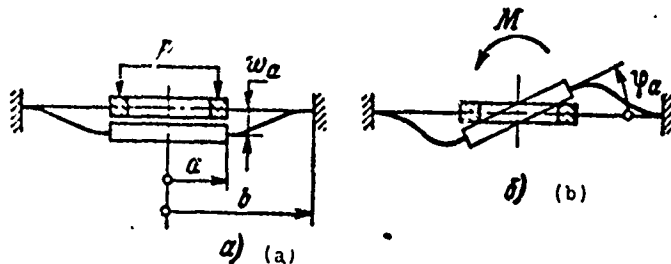


Fig. 5.64. Determining the rigidity of a flexible element.

For the internal diameter of the plates we should take the internal diameter of the bellows  $2a$  and for the external we should take the external diameter of the bellows  $2b$ . Plate thickness  $h$  is assumed constant. We further assume that all plates operate under identical conditions. The angle of turn for the plates on the external and internal contours is zero. Bends of plates are considered small - the bend of any plate does not exceed its thickness  $h$ . This is the first approach to a more accurate solution.

Thus, we seek the stresses and strains of a circular plate with pinched contours under loading by axial force  $P$  (Fig. 5.64a). Using the steady-state equation for the forces of elasticity of a rigid plate, we derive a formula for calculating a circular plate [43]:

$$w_a = \frac{Pa^2}{4\pi D} \left[ \frac{k^2 - 1}{4} - \frac{k^2}{k^2 - 1} \ln^2 k \right], \quad (5.117)$$

where  $w_a$  is the bend of the plate on radius  $a$ ;  $k = b/a$ .

Elongation of the bellows will be greater by a factor of  $2n$  than from formula (5.117)

$$\Delta L = \frac{Pa^2n}{2\pi D} \left[ \frac{k^2 - 1}{4} - \frac{k^2}{k^2 - 1} \ln^2 k \right], \quad (5.118)$$

where  $n$  is the number of complete waves of the corrugation; the number of plates is  $2n$ .

The greatest bending moment occurs in the plate near the internal contour:

$$\overline{M}_{ra} = \frac{P}{4\pi} \left[ 2 \frac{k^2 \ln k}{k^2 - 1} - 1 \right]. \quad (5.119)$$

If we eliminate from equation (5.119) force  $P$ , we can establish the function of bending moment as a function of the axial displacement of the conduits:

$$\overline{M}_{ra} = \frac{\Delta L}{2n} \frac{Eh^3}{12(1-\mu^2)a^2} \frac{4(2k^2 \ln k - k^2 + 1)}{(k^2 - 1)^2 - 4k^2 \ln^2 k}.$$

Bending stress is

$$\sigma_{ra} = \frac{6\overline{M}_{ra}}{h^2} = \frac{\Delta L}{n} \frac{Eh}{(1-\mu^2)a^2} \frac{2k^2 \ln k - (k^2 - 1)}{(k^2 - 1)^2 - 4k^2 \ln^2 k}, \quad (5.120)$$

or

$$\sigma_{ra} = \frac{\Delta L}{n} \frac{Eh}{(1-\mu^2)a^2} k_{1a},$$

where  $k_{1a}$  is the last fraction in the equation (5.120).



The coefficient  $k_{1a}$ , calculated for various values of  $k$ , is presented in Table 5.6. Here and henceforth the obtained stresses are calculated based on the absolute value without a more precise definition of their signs.

Let us introduce the formula for stresses near the external contour:

$$\sigma_{rB} = \frac{\Delta L}{n} \frac{Eh}{(1-\mu^2)a^2} \frac{k^2 - 1 - 2\ln k}{(k^2 - 1)^2 - 4k^2 \ln^2 k}, \quad (5.121)$$

or

$$\sigma_{rB} = \frac{\Delta L}{n} \frac{Eh}{(1-\mu^2)a^2} k_{1b}.$$

The coefficient  $k_{1b}$  is also given in Table 5.6. We introduce the formulas for analyzing a bellows with its angular deformations (Fig. 5.64b).

The angle of turn of the center with a fixed external contour is

$$\Delta\varphi_a = \frac{M}{4\pi D} \frac{(k^2 + 1) \ln k - k^2 + 1}{k^2 + 1}; \quad (5.122)$$

the complete turn of the ends of the bellows is

$$\Delta\Phi_a = \frac{Mn}{2\pi D} \frac{(k^2 + 1) \ln k - k^2 + 1}{k^2 + 1}; \quad (5.123)$$

bending moment in a radial direction on radius  $a$  is

$$\overline{M}_{ra} = \frac{n\Delta\Phi_a}{na} \frac{k^2 - 1}{(k^2 + 1) \ln k - k^2 + 1};$$

bending stress is

$$\sigma_{ra} = \frac{6\bar{M}_{ra}}{h^2} = \frac{\Delta\Phi_a}{n} \frac{Eh}{(1-\mu^2)a^2} \frac{0,5(k^2-1)}{(k^2+1)\ln k - k^2 + 1}, \quad (5.124)$$

or

$$\sigma_{ra} = \frac{\Delta\Phi_a}{n} \frac{Eh}{(1-\mu^2)a} k_{2a},$$

where  $k_{2a}$  is the last fraction in equation (5.124).

Similarly to stresses near the outer contour b

$$\sigma_{rb} = \frac{\Delta\Phi_a}{n} \frac{Eh}{(1-\mu^2)a} \frac{0,5(k^2-1)}{k[(k^2+1)\ln k - k^2 + 1]}, \quad (5.125)$$

or

$$\sigma_{rb} = \frac{\Delta\Phi_a}{n} \frac{Eh}{(1-\mu^2)a} k_{2b}.$$

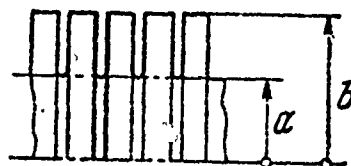
The values of  $k_{1a}$ ,  $k_{1b}$ ,  $k_{2a}$ ,  $k_{2b}$  are presented in Table 5.6.

Table 5.6.

$k$	1,10	1,15	1,20	1,25	1,30	1,35	1,40
$k_{1a}$	155	70,0	39,9	25,9	18,3	13,6	10,57
$k_{1b}$	145	63,7	35,4	22,3	15,33	11,16	8,45
$k_{2a}$	165	76,7	45,2	30,2	21,9	16,8	13,3
$k_{2b}$	150	66,6	37,7	24,1	16,8	12,4	9,50

If, in addition to displacement compensations, the bellows is loaded by pressure and the unloading pressures of the ring have not been established, it is necessary to check the stresses according to the formula for circular stresses arising in a cylindrical shell.

Fig. 5.65. Stress analysis of a bellows.



Experience shows that failure of the bellows under the action of internal force precedes the complete disappearance of the internal curvatures of the corrugation and the unfolding of the external ones (Fig. 5.65).

Circular stresses in the shell are  $\sigma_{\varphi} = ph/b$ . Evaluation of the coefficient of the safety of the bellows in a circular direction is performed as above for cylindrical shells.

## APPENDIX

### STRENGTH CHARACTERISTICS OF MATERIALS USED IN EXTRATERRESTRIAL ENGINES<sup>1</sup>

#### Uranium

Uranium is a light soft metal with high density ( $\rho \approx 18.9 \text{ g/cm}^3$ ); it is easily oxidized in air; however, a brown oxide film of uranium shields metal from further corrosion at room temperature. It melts at  $1133^\circ\text{C}$ . The coefficient of linear expansion  $\alpha = 15.27 \cdot 10^{-6}$ ;  $16.2 \cdot 10^{-6}$ ;  $20.5 \cdot 10^{-6} \text{ } 1/^\circ\text{C}$  at temperatures 25-125; 125-325; 325-650°C respectively. The heat conductivity of uranium can be calculated using the formula  $\lambda \approx 24.4 + 0.23t \text{ W/m}^\circ\text{C}$ . The average indices of elastic properties at room temperature are: the modulus of elasticity  $E = 2.0 \cdot 10^6 \text{ daN/cm}^2$ , the Poisson coefficient  $\mu = 0.2$ , yield strength  $\sigma_{0.2} = 20 \text{ daN/mm}^2$ , ultimate stress  $\sigma_b = 60 \text{ daN/mm}^2$ . Short-term strength of uranium at high temperatures is given in Table A-1.

The spread in the strength values is caused by the various uranium processing techniques used.

The variation in the modulus of elasticity and the Poisson coefficient as a function of temperature is shown in Fig. A.1.

---

<sup>1</sup>V. S. Chirkin. Thermophysical properties of materials in nuclear technology. Handbook, Atomizdat, 1968. High-melting materials in machine building. Handbook, M., "Mashinostroyeniye," 1967. High-melting metal materials for space technology, coll., izd-vo "Mir," 1966.

Table A.1. Mechanical properties of uranium.

Температура, °C (1)	Предел прочности даН/мм <sup>2</sup> (2)	Предел текучести даН/мм <sup>2</sup> (3)	Относительное удлинение, % (4)
20	43—77	17—30	6—13
300	18—43	10—12	33—49
500	7,4—7,8	3,6—3,9	57—60

KEY: (1) Temperature, °C; (2) Ultimate stress даН/мм<sup>2</sup>; (3) Yield strength даН/мм<sup>2</sup>; (4) Relative elongation, %.

Pure uranium can be used in low-temperature reactors. At approximately 660°C its density and mechanical qualities change sharply. At higher temperatures uranium oxide and carbides, which have the best mechanical qualities, are used.

Some strength characteristics of these compounds are presented in Table A.2.

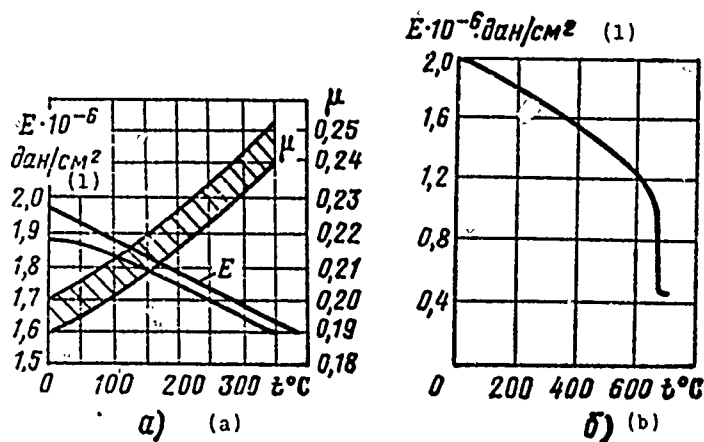


Fig. A.1. Variation in the modulus of elasticity for uranium.  
KEY: (1) даН/см<sup>2</sup>.

Uranium monocarbide UC is one of the materials used. It has the best strength characteristics, heat conductivity, and a greater uranium content than UO<sub>2</sub>. However, it is more subject to oxidation.

Table A.2. Characteristics of uranium compounds.

(1) Соединение	(2) Плотность, г/см <sup>3</sup>	(3) Температура плавления, °C	(4) Содержание U		(5) E · 10 <sup>-6</sup> даH/см <sup>2</sup>		(7) λ вт/м · °C			(6) ε <sub>n</sub> даH/мм <sup>2</sup>		
			%	г/см <sup>3</sup>	t °C	E · 10 <sup>-6</sup> даH/см <sup>2</sup>	t °C	λ вт/м · °C	α · 10 <sup>6</sup> 1/°C	t °C	ε <sub>n</sub> даH/мм <sup>2</sup>	
UO <sub>2</sub>	10,97	2880	88,2	9,68	0—300	1,8	0—200	5,25	0—200	9	20—500	10,2
					300—600	1,75	200—2800	1,25	200—2800	12	900—1000	10—13
					600—900	1,65						
UC	13,63	2350	95,2	13,0			100—400	25,2—22,2	20—1500	10,5—11,6	20—500	8,4
							400—735	22,2—25,2			1000	21
UC <sub>2</sub>	11,68	2470	90,8	10,6			200—2000	11,7—29,3	200—2000	13,1		

KEY: (1) Compound; (2) Density, g/cm<sup>3</sup>; (3) Melting point, °C; (4) Content U; (5) даН/см<sup>2</sup>; (6) даН/мм<sup>2</sup>; (7) W/m°C.

Uranium dicarbide UC<sub>2</sub> has medium properties between UC<sub>2</sub> and UC.

The heat conductivity characteristics, modulus of elasticity, ultimate stress, and rupture strength of UC<sub>2</sub> are shown in Fig. A.2, a, b, and c.

#### Graphite

Graphite has low density ( $\rho = 1.5-1.9$  g/cm<sup>3</sup>), high heat conductivity ( $\lambda = 16.8-33.6$  W/m°C), near that of metals, and high resistivity to thermal loads.

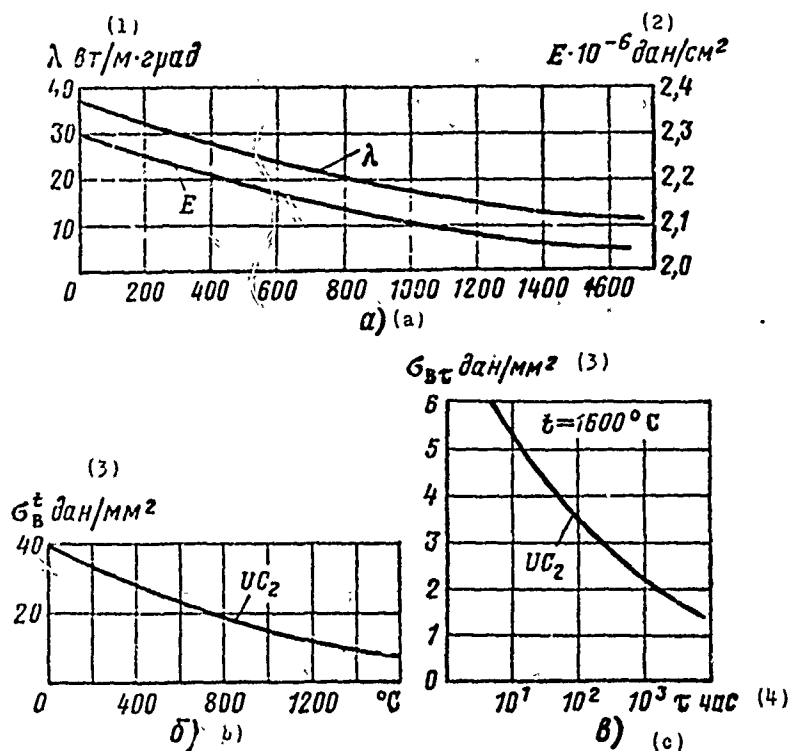


Fig. A.2. Strength characteristics of  $UC_2$ .  
KEY: (1)  $W/m \cdot ^{\circ}C$ ; (2)  $daN/cm^2$ ; (3)  $daN/mm^2$ ; (4) hour.

The main characteristic of graphite is the increase of its strength with an increase in temperature  $2000-2500^{\circ}C$ ; in this temperature range it is stronger than any other known material.

The good mechanical processability makes it possible to manufacture parts of various shapes and dimensions from graphite. Graphite is distinguished by chemical inertness to the effect of many aggressive media, including the vapor of liquid metals.

However, there can be a wide spread in the properties of the same batch of graphite. There is substantial anisotropy of properties in directions parallel and perpendicular to the direction of compression. Its ultimate compressive strength almost doubles the ultimate tensile strength.

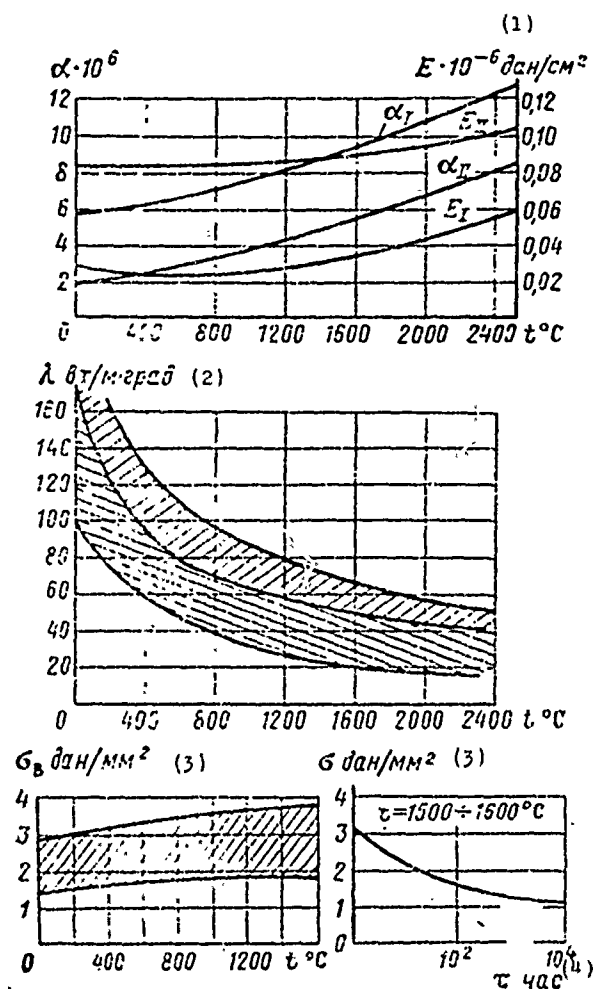


Fig. A.3. Strength characteristics of graphite.

KEY: (1) daN/cm<sup>2</sup>; (2) W/m·deg; (3) daN/mm<sup>2</sup>; (4) hour.

The characteristic of graphite's elastic properties is nonlinear. The modulus of elasticity even under normal conditions grows somewhat with loading. In the temperature range 1000-2200°C this growth is insignificant, as a result of which we can tentatively assume  $E \approx 8 \cdot 10^2 \text{ daN/mm}^2$ .

Graphite has high emissivity. We can assume during calculations that the emissivity factor is  $\epsilon \approx 0.9$ . The coefficient of linear expansion for mean temperatures is  $\alpha = 3.15 \times 10^{-6} \text{ 1/}^\circ\text{C}$ . The coefficient of heat conductivity for the same temperatures can be taken on the average as  $\lambda = 50 \text{ W/m}^\circ\text{C}$ . The Poisson coefficient is  $\mu = 0.34$ .



A shortcoming of graphite is the nonpreservation of properties during reheating, which is the result of sintering and graphitization. Some data on graphite has been given in Fig. A.3.

### Berillium

Berillium is widely used in retarders and reflectors of reactors. It is characterized by the small absorption cross section of thermal neutrons and has good strength qualities and corrosion resistance. A shortcoming of berillium is its toxicity at the stage of technological processing.

The basic strength characteristics of berillium are shown in Figures A.4a, b, and c.

### Stainless steels

Stainless steels are widely used in extraterrestrial engines. The most widely used is Kh18N9T. Its characteristics for short-term and long-term strengths are shown in Fig. A.5. The strain diagram is illustrated in Fig. A.6.

Figure 3.7 in Chapter III presents the graph of  $\alpha$  variation and Figure 3.15 the graph of variation in modulus E based on temperature. Curves of rupture strength and plasticity for this steel are presented in Fig. A.7, a, b, and c.

Figure A.8 shows the curves of rupture strength for other stainless steels having higher strength characteristics.

### Niobium and its alloys

Niobium has many positive properties which enable its use in extraterrestrial electric rocket engines.

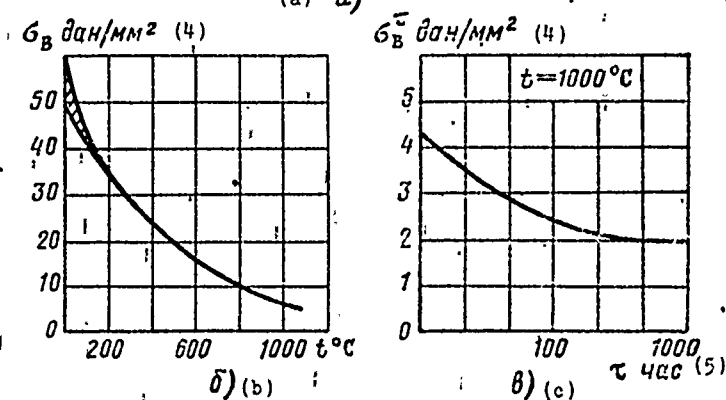
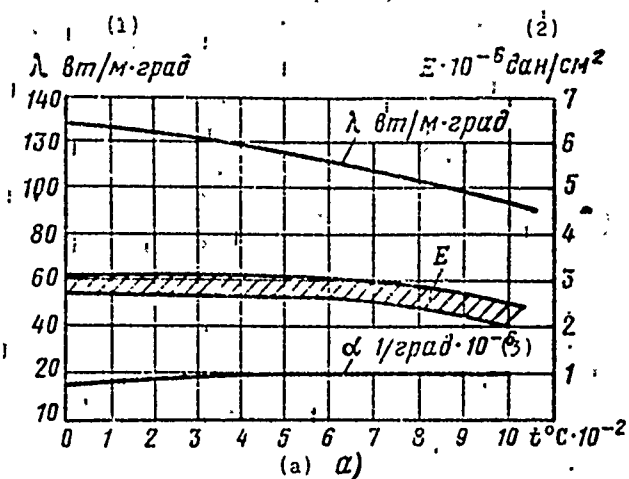


Fig. A.4. Strength characteristics of berillium.

KEY: (1) W/m·deg; (2) daN/cm<sup>2</sup>; (3) 1/deg; (4) daN/mm<sup>2</sup>; (5) hour.

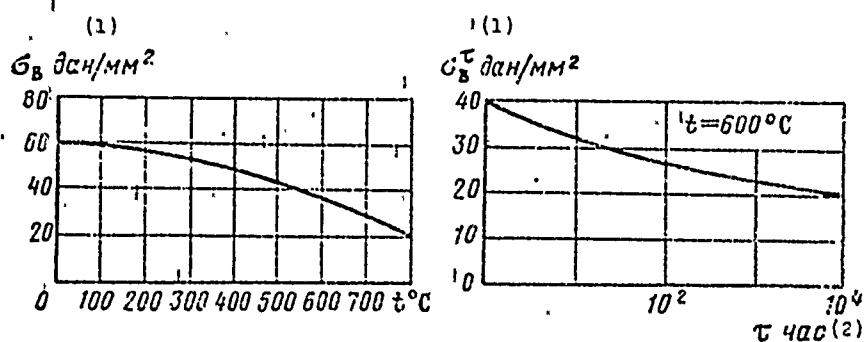


Fig. A.5. Characteristics of Kh18N9T steel.

KEY: (1) daN/mm<sup>2</sup>; (2) hour.

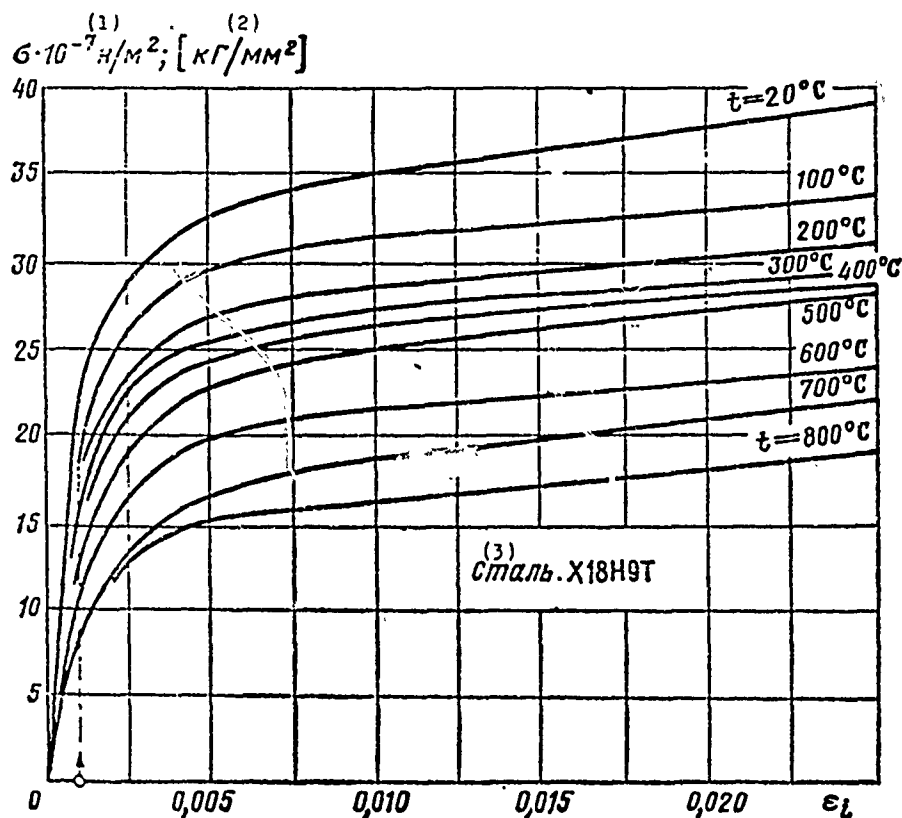


Fig. A.6. Stress diagram of stainless steel.

KEY: (1)  $\text{N/m}^2$ ; (2)  $[\text{kgf/mm}^2]$ ; (3) Steel Kh18N9T.

It has a small thermal neutron capture cross section (1.1 b/atom); high melting point, high strength characteristics, and plasticity; comparatively low specific weight; high chemical stability with respect to aggressive media, for example, lithium.

Niobium alloys have even higher strength properties. Small additions of zirconium, molybdenum, tungsten and other elements appreciably increase the rupture-resistance of niobium.

Table A.3 presents some properties of niobium and its alloys. The content of the main additive is indicated by the digit in front of the formula of the element. For example, 1Zr is a niobium alloy with 1% zirconium. The effect of temperature on 10-hour rupture

strength is shown in Fig. A.9. The digits on this figure correspond to the numbers of the alloys in Table 3.

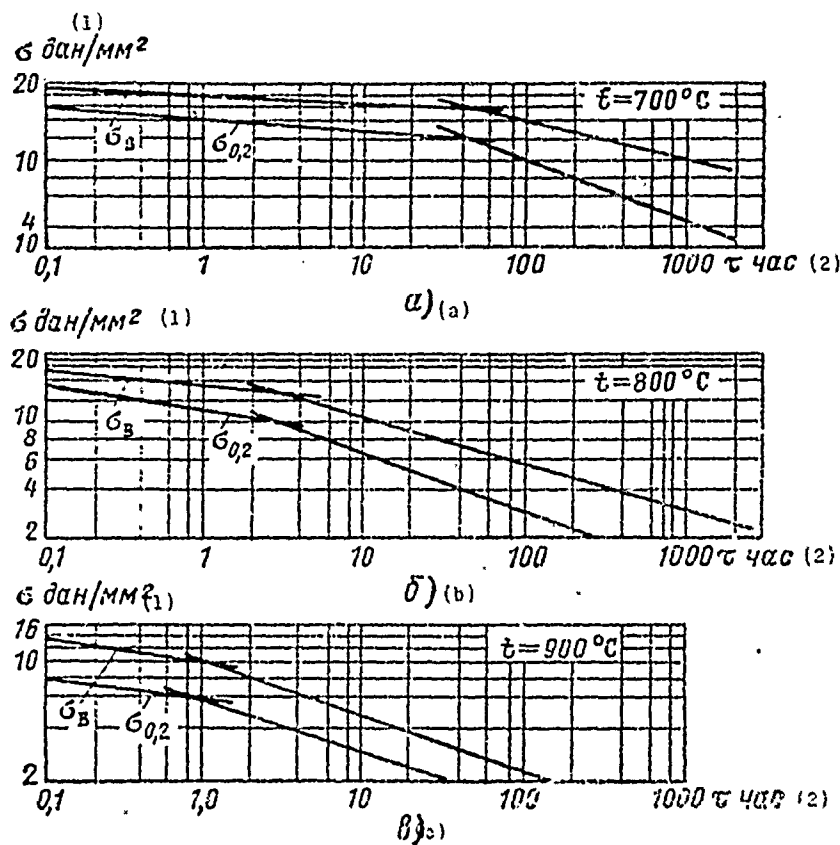


Fig. A.7. Curves of rupture strength for stainless steel: a - 700°C; b - 800°C; c - 900°C.

KEY: (1)  $daN/mm^2$ ; (2) hour.

Figure A.10 presents the strength characteristics for niobium alloy 7, having additives of tungsten and titanium (28W, 7 Ti). This alloy has different characteristics with respect to heat resistance. Figure A.11 shows the rupture strength of this alloy (7) and two other alloys (1, 2).

Some characteristics of niobium are given in Table A.4.

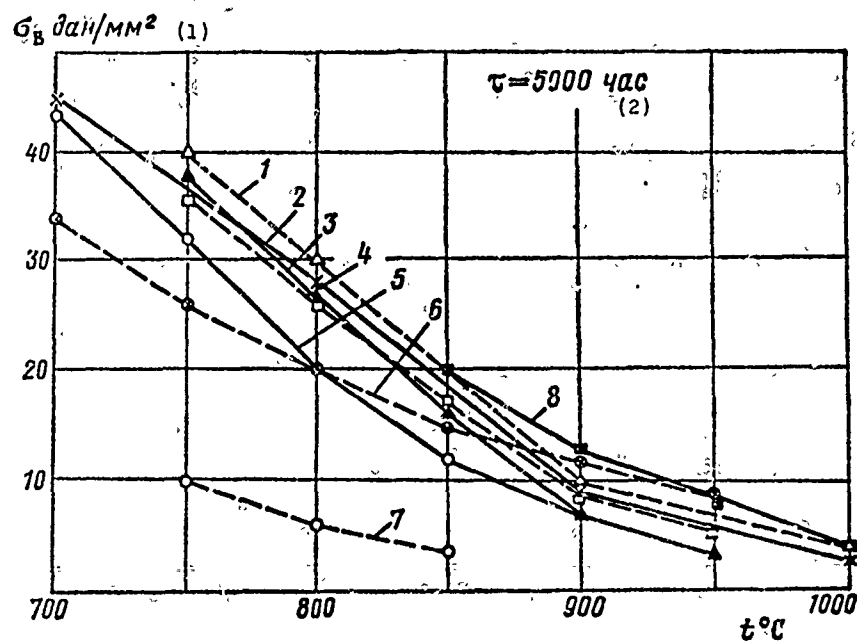


Fig. A.8. Rupture-strength curves for chromium-nickel alloys: 1, 3, 4, 5, 8 - bar; 2, 6 - casting; 7 - sheet.

KEY: (1)  $\text{daN/mm}^2$ ; (2) hour.

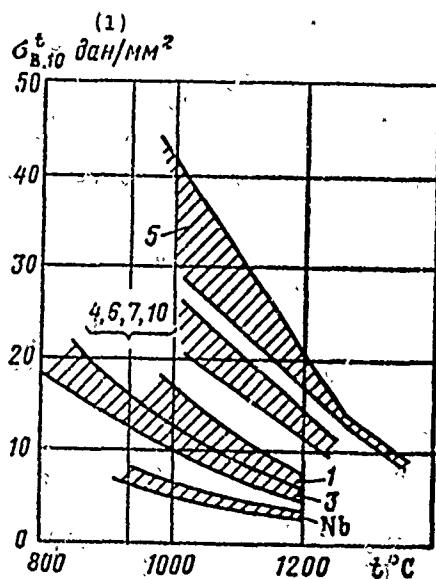


Fig. A.9. Strength curves of niobium alloys.

KEY: (1)  $\text{daN/mm}^2$ .

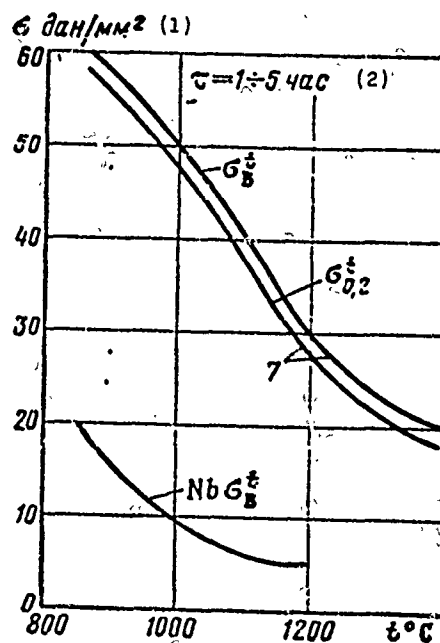


Fig. A.10. High-temperature strength of niobium alloy.

KEY: (1)  $\text{daN/mm}^2$ ; (2) hour.

Table A.3. Properties of niobium alloys.

(1) № сплава	t °C	$\sigma_{0.2}$	$\sigma_B$	$\delta$ %	t °C	$\tau$ час	$\sigma_B$	(2) Содержание добавок %
		(3) дан/мм <sup>2</sup>					(3) дан/мм <sup>2</sup>	
1	21	—	33,1	36	1093	100	13,4	1Zr
	1093	—	16,2	16,2	1093	500	7,7	
	1204	—	13,4	13,4				
2	21	—	38,6	—	1093	10	17,6	0,75Zr; 33Ta
	1093	—	21,1	—	1093	100	12,7	
	1316	—	9,1	9	1093	500	9,8	
3	21	68,9	70,3	15	982	230	10,5	10Mo; 10Ti
	1093	17,2	21,1	25	982			
	1316	6,9	7,1	15	982			
	1427	4,9	4,9	13				
4	21	—	88	10	1093	55	14,1	6Mo; 2W; 10Ti
	1093	37,3	38,2	25				
	1371	—	17,6	35				
5	21	59,8	88	25	1093	10	29,5	1Zr; 5Mo; 15W (5) (Самый проч- ный сплав)
	1093	29,6	45	18	1093	100	24,6	
	1204	21,1	35,2	22	1204	10	16,8	
					1204	100	11,9	
6	21	56,3	85,8	25	1093	10	19,0	1Zr; 5Mo 15W; 5Ti
	1093	24,6	35,2	28	1093	100	14,1	
	1204	19,7	24,6	35		10	11,2	
						100	7,7	
7	1204	29,8	33,8	18	1204	5,6	17,6	38W; 7Ti
	1371	16,9	19,7	33	1204	9	13,7	
8	1204	9,0	9,0	78	999	50	10,5	3V; 3Al
9	21	39,4	46,4	35	1093	10	7,0	0,8Zr; 7Ti
	1093	9,8	11,2	50	1093	100	4,4	

KEY: (1) Alloy no.; (2) Additive content %; (3) daN/mm<sup>2</sup>; (4) hour;  
(5) Strongest alloy.

Table A.3. (Continued)

(1) № сплава	t °C	$\sigma_{0,2}$	$\sigma_n$	$\delta$ %	t °C	$\tau$ час	$\sigma_n$ даН/мм <sup>2</sup>	(2) Содержание добавок %
		даН/мм <sup>2</sup> (3)				(4)	(3)	
10	21	49,2	61,8	26	1204	2,3	17,6	5Zr; 10W
	1204	23,2	27,4	25				
11	23	41,8	57,0	32	1093	0,5	17,7	4V
	1093	21,3	23,0	34				
	1316	9,1	9,6	55,4				
12	23	64,0	80,9	14	1204	0,9	19,3	5V; 5Mo; 1Zr
	1093	40,8	45,7	28				
	1204	24,6	28,1	46				
	1316	19,0	21,8	71				
13	23	74,8	92,7	18	1204	0,55	21,1	5V; 1Zr; 10W
	1316	19,0	21,1	34		1,9	19,3	
						2,4	17,6	
14	21	66,8	73,9	14	1093	158	11,9	0,5Zr; 12W
	1093	28,8	32,3	13	1316	10	9,1	
	1316	—	16,2	40	1427	10	7	
	1538	8,4	9,1	71				
15	21	43,6	54,8	15	1093	100	8,4	5Zr
	1093	19,0	24,6	35	1204	100	3,5	
	1371	8,4	10,5	120				
16	1204	24,0	26,1	—	1499	2,5	5,5	10W; 10Ta
	1427	16,8	18,6	—	1632	2,4	3,5	
	1649	7,4	8,3	—	1760	2,1	2,7	
17	1095	—	7,1		1095	10	3,1	100%Nb
	1205	—	6,5		1095	100	2,18	

KEY: (1) Alloy no.; (2) Additive content %; (3) daN/mm<sup>2</sup>; (4) hour.

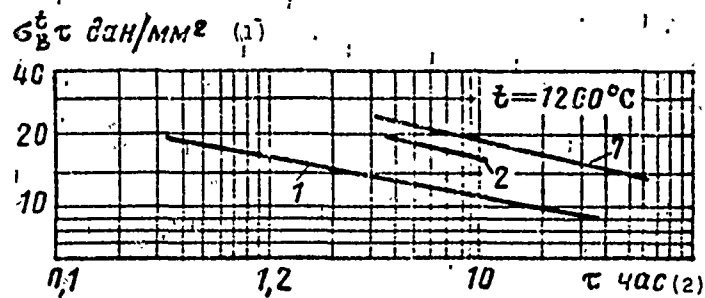


Fig. A.11. Rupture strength of niobium alloy.  
KEY: (1) daN/mm<sup>2</sup>; (2) hour.

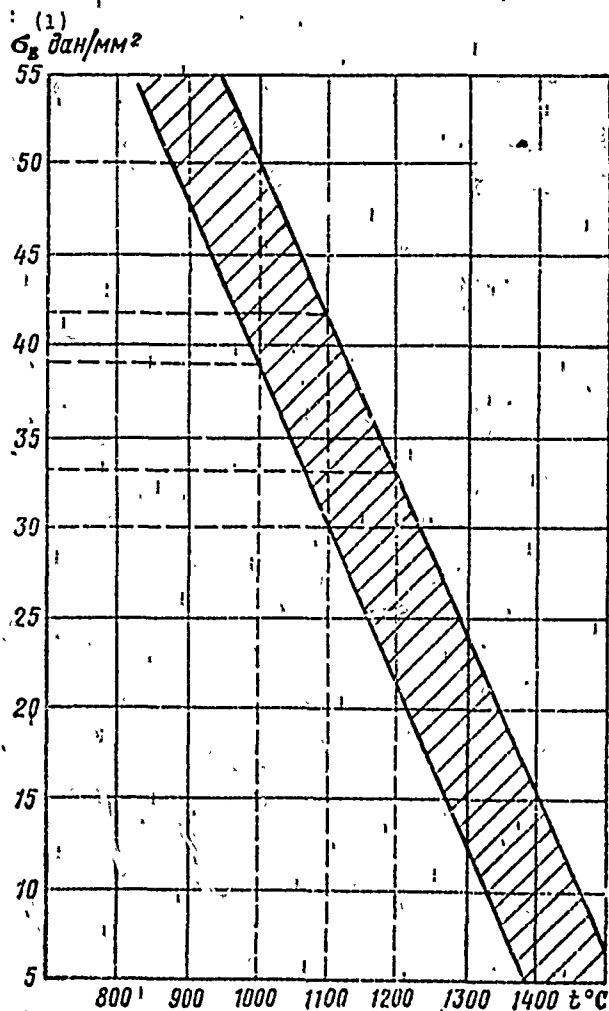


Fig. A.12. Short-term strength of niobium alloys.  
KEY: (1) daN/mm<sup>2</sup>.



Table A.4. Characteristics of niobium.

$t, ^\circ\text{C}$	$\sigma_B$ $\partial a_H / \text{mm}^2$ (1)	$t, ^\circ\text{C}$	$E \cdot 10^{-4}$ $\partial a_H / \text{mm}^2$ (1)	$t, ^\circ\text{C}$	$\alpha \cdot 10^6 \text{ } 1/^\circ\text{C}$
200	23,6	20	1,1	20	7,0
300	24,4	200	1,08	300	7,38
400	23,3	300	1,06	400	7,54
500	25,0	400	1,06	500	7,61
550	22,7	500	1,05	600	7,86
		600	1,07	700	8,02
		700	1,07	800	8,18
		1027	1,07	1027	8,0
				1527	8,6
				2027	9,1

KEY: (1) daN/mm<sup>2</sup>.

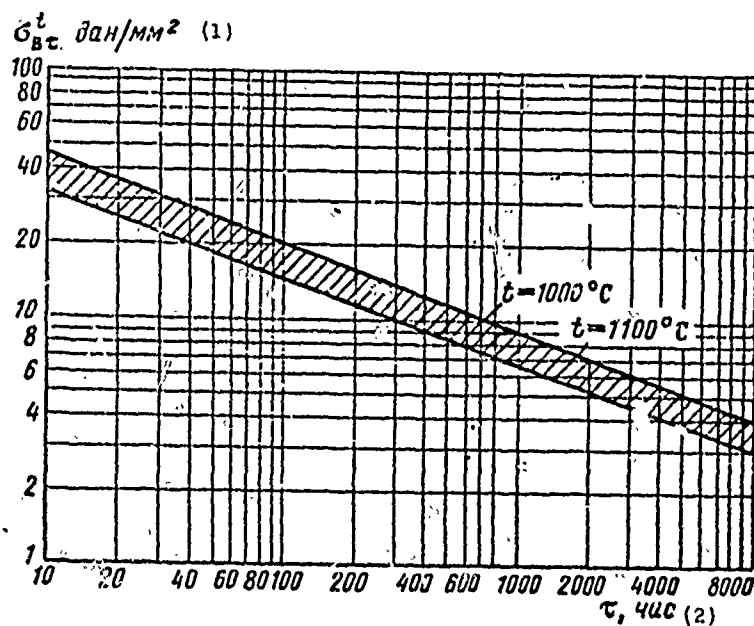


Fig. A.13. Rupture strength of niobium alloys.  
KEY: (1) daN/mm<sup>2</sup>; (2) hour.

Figures A.12 and A.13 present curves of short-term and long-term [rupture] strength of niobium alloys, plotted as a result of processing many literature sources.

#### Molybdenum and its alloys

Table A.5 presents the mechanical properties of molybdenum and some of its alloys, and Table A.6 gives data on the modulus of elasticity and the coefficient of linear expansion.

Figures A.14 and A.15 illustrate the curves of short-term and long-term [rupture] strength for molybdenum alloys.

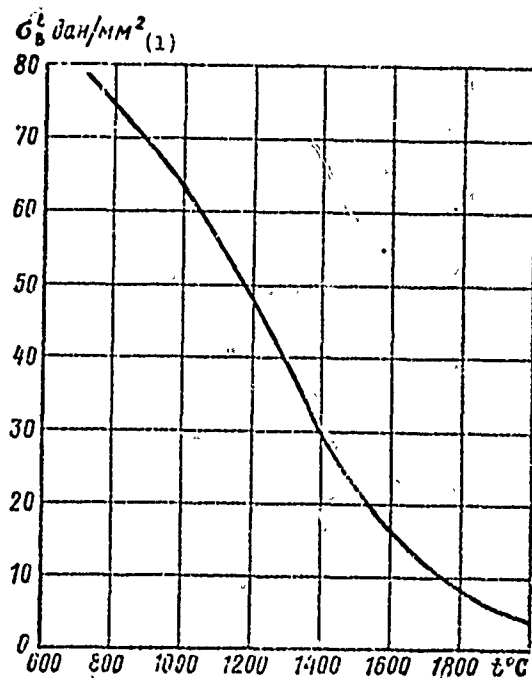


Fig. A. 14. Short-term strength of molybdenum alloys.  
KEY: (1) daN/mm<sup>2</sup>.

Table A.5. Mechanical properties of molybdenum and its alloys.

(1) № сплава	$t$ °C	$\sigma_B$ даН/мм <sup>2</sup> (3)	$t$ °C	$\tau$ час (4)	$\sigma_{\frac{t}{2}}$ даН/мм <sup>2</sup> (3)	(2) Содержание добавок %
1	1095	30,9	1095	100	9,6	100Mo
	1315	9,1				
2	1095	40,0	1095	100	23,9	0,5Ti
	1205	26,0	1205	100	12,7	
	1315	13,4	1315	100	7,0	
3	1095	40,7	1095	100	28,2	1,25Ti; 0,15Zr; 0,15C
	1205	38,0	1205	100	21,8	
	1315	27,4	1315	100	14,7	
4	1095	54,8	1095	100	35,2	0,5Ti; 0,08Zr; 0,08C
	1205	45,7				
	1315	38,0				
5	1095	49,2	1095	100	28,8	0,05Zr; 0,02C
			1205	100	14,4	
		15,5	1315	100	7,3	
6	1095	13,2	1095	100	30,2	25W; 0,1Zr; 0,05C
	1205	57,6	1205	100	23,2	
	1315	51,6	1315	100	8,6	
7	1095	56,2	—	—	—	1,27Ti; 0,29Zr; 0,3C
	1205	49,9	—	—	—	
	1315	42,9	1315	100	13,0	
8	1095	61,8	1095	100	40,1	1,5Nb; 0,25C
	1205	54,1	1205	100	24,6	
	1315	45,0	1315	100	8,6	

KEY: (1) Alloy no.; (2) Additive content %; (3) daN/mm<sup>2</sup>; (4) hour.

Table A.6. Modulus of elasticity and coefficient of linear expansion for molybdenum.

$t$ °C	$E \cdot 10^{-4}$ $\frac{\text{daN}}{\text{mm}^2}$ (1)	$t$ °C	$\alpha \cdot 10^6$ $1/^\circ\text{C}$
20	3,2	20	5,1
527	2,81	527	5,1
1027	2,15	1027	5,5
		1527	6,2
		2027	7,2

KEY: (1) daN/mm<sup>2</sup>.

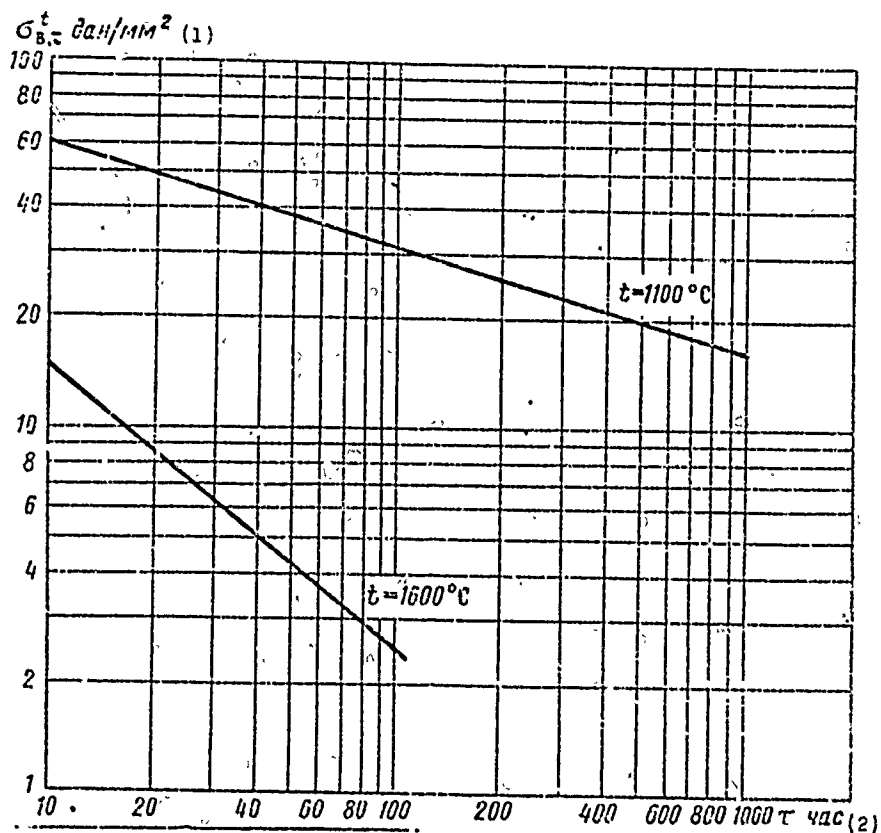


Fig. A.15. Long-term [rupture] strength of molybdenum alloys.  
KEY: (1) daN/mm<sup>2</sup>; (2) hour.

## Tungsten and its alloys

Figure A.16 shows the dependence of ultimate stress in tungsten and its alloys on temperature. As is apparent from the figure, the alloying of tungsten increases its strength at comparatively low temperatures. Table 7 introduces the strength characteristics of tungsten and its alloys, and Table A.8 the modulus of elasticity and coefficient of linear expansion for tungsten.

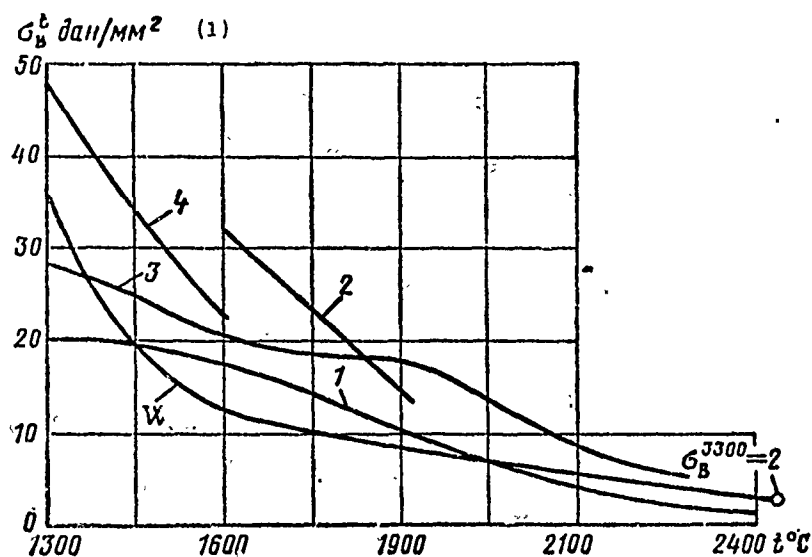


Fig. A.16. Dependence of ultimate stress in tungsten alloys on temperature.  
KEY: (1)  $\text{daN/mm}^2$ .

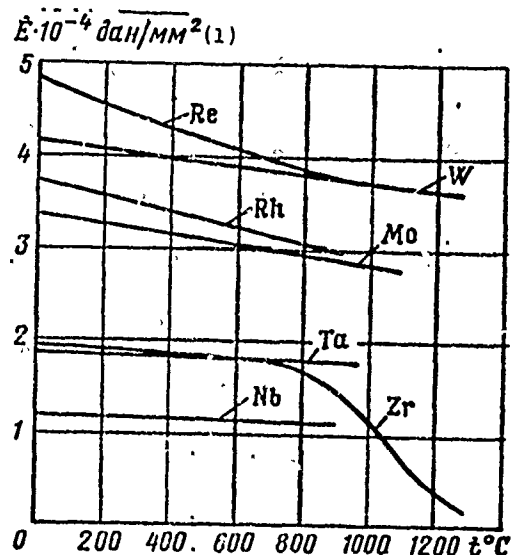


Fig. A.17. Moduli of elasticity for various materials.  
KEY: (1)  $\text{daN/mm}^2$ .

Figure A.17 presents the moduli of elasticity E for various materials, and Table A.9 the properties of several structural materials.

Table A.7. Mechanical properties of tungsten and its alloys.

(1) № сплава	$t$ °C	$\sigma_{\text{в}}$ даН/мм <sup>2</sup> (3)	$t$ °C	$\tau$ час (4)	$\sigma_{\text{в}\tau}$ даН/мм <sup>2</sup> (3)	(2) Содержание добавок %
1	1095	23,9				
	1370	35,1	1203	10	15,4	100W
	1650	14,1	1203	100	13,3	
	1927	7,0	1095	100	15,5	
	2204	4,5	1370	100	7	
2	1370	34,1				1ThO <sub>2</sub>
	1650	26,0				
	1927	19,7				
	2200	9,8				
3	1370	24,9	1370	10	20,4	2ThO <sub>2</sub>
	1650	20,7	1370	100	15,4	
	1927	18,7	—	—	—	
	2200	12,3	—	—	—	
4	1370	30,9	1482	100	7,7	10Mo
	1650	19,7	—	—	—	
	1927	7,7	—	—	—	
	2200	3,5	—	—	—	
5	1370	27,1				15Mo
	1650	17,6				
	1927	9,5				
	2200	4,9				

KEY: (1) Alloy no.; (2) Additive content %; (3) даН/мм<sup>2</sup>; (4) hour.

Table A.8. Modulus of elasticity and coefficients of linear expansion for tungsten.

$t$ °C	$E \cdot 10^{-4}$ $\frac{\text{даН}}{\text{мм}^2}$ (1)	$t$ °C	$\alpha \cdot 10^6$ $1/^\circ\text{C}$
20	4,1	20—327	4,5
527	3,8	20—1027	5,1 (5,2)
1027	3,2	20—2027	5,4 (7,2)
		20—2427	5,8

KEY: (1)  $\text{даН}/\text{мм}^2$ .

Table A.9. Properties of structural materials.

(1) Свойства материала	(2) Температура, °C	(3) Плотность, г/см <sup>3</sup>	(4) Предел прочности, кг/см <sup>2</sup>	(5) Модуль Юнга, 10 <sup>10</sup> кг/см <sup>2</sup>	(6) Коэффициент теплового расширения, 10 <sup>-6</sup> /°C	(7) Температура плавления, °C	(8) Бриггс, кг/см <sup>2</sup>	(9) Химическая стойкость	(10) Химическая стойкость	(11) Атомный вес	(12) Окисление, г/см <sup>2</sup>	(13) Окисление, г/см <sup>2</sup>	(14) Окисление, г/см <sup>2</sup>	(15) Химическая стойкость
(16) Температура плавления, °C	3397	3110	3180	2310	4438	2950	1282	1450	1400	933	2070-2500	2800-3000	2870	30/0
(17) Максимальная температура эксплуатации, °C	2700	2720	—	2020	1720	2070	800	1000	800	~500	1100	1600	—	2500
(18) Плотность, г/см <sup>3</sup>	1,7-2,3	19,3	21	10,2	8,5	46,6	1,65	8,8	8,0	2,08	4,0	3,6	3,02	2,2
(19) Коэффициент теплового расширения, 10 <sup>-6</sup> /°C	—	—	—	—	—	—	—	—	—	—	—	—	—	—
(20) Предел прочности, кг/см <sup>2</sup>	120	165	71	140	50	48-63	100-150	92	12-14	207	—	—	33-150	12,5 (±)
(21) Модуль Юнга, 10 <sup>10</sup> кг/см <sup>2</sup>	70	115	—	110	70	55-74	55-85	56	25	62	6,6	7,6	8,6-24	36,6 (±)
(22) Модуль упругости, 10 <sup>10</sup> кг/см <sup>2</sup>	100	—	—	60	86	92	—	—	—	—	7,0	8,0	1,3-12 (140°)	—
(23) Модуль упругости, 10 <sup>10</sup> кг/см <sup>2</sup>	—	—	—	—	—	—	—	—	—	—	—	—	—	—
(24) Модуль упругости, 10 <sup>10</sup> кг/см <sup>2</sup>	—	—	—	—	—	—	—	—	—	—	—	—	—	—
(25) Модуль упругости, 10 <sup>10</sup> кг/см <sup>2</sup>	—	—	—	—	—	—	—	—	—	—	—	—	—	—
(26) Модуль упругости, 10 <sup>10</sup> кг/см <sup>2</sup>	—	—	—	—	—	—	—	—	—	—	—	—	—	—
(27) Модуль упругости, 10 <sup>10</sup> кг/см <sup>2</sup>	—	—	—	—	—	—	—	—	—	—	—	—	—	—
(28) Модуль упругости, 10 <sup>10</sup> кг/см <sup>2</sup>	—	—	—	—	—	—	—	—	—	—	—	—	—	—
(29) Модуль упругости, 10 <sup>10</sup> кг/см <sup>2</sup>	—	—	—	—	—	—	—	—	—	—	—	—	—	—
(30) Модуль упругости, 10 <sup>10</sup> кг/см <sup>2</sup>	—	—	—	—	—	—	—	—	—	—	—	—	—	—
(31) Модуль упругости, 10 <sup>10</sup> кг/см <sup>2</sup>	—	—	—	—	—	—	—	—	—	—	—	—	—	—
(32) Модуль упругости, 10 <sup>10</sup> кг/см <sup>2</sup>	—	—	—	—	—	—	—	—	—	—	—	—	—	—
(33) Модуль упругости, 10 <sup>10</sup> кг/см <sup>2</sup>	—	—	—	—	—	—	—	—	—	—	—	—	—	—
(34) Модуль упругости, 10 <sup>10</sup> кг/см <sup>2</sup>	—	—	—	—	—	—	—	—	—	—	—	—	—	—
(35) Модуль упругости, 10 <sup>10</sup> кг/см <sup>2</sup>	—	—	—	—	—	—	—	—	—	—	—	—	—	—

KEY: (1) Properties of materials; (2) Graphite; (3) Tungsten; (4) Rhenium; (5) Iridium; (6) Niobium; (7) Tantalum; (8) Beryllium; (9) Nickel; (10) Stainless Steel KhLP; (11) Aluminum; (12) Aluminum oxide; (13) Magnesium oxide; (14) Beryllium oxide; (15) Boron nitride; (16) Melting point; (17) Melting temperature; (18) Density, g/cm<sup>3</sup>; (19) Coefficient of heat conductivity, W/m°C; (20) when; (21) Coefficient of linear expansion α; (22) Modulus of elasticity E; (23) (24) Specific electrical resistance ρ, Ω·m.



## Bibliography

1. Андреев П. А., Гремиллов Д. И., Федорович Е. Д. Теплообменные аппараты ядерных энергетических установок; под ред. Синева Н. М., «Судостроение», 1965.
2. Базовский Н., Надежность. Теория и практика, М., «Мир», 1965.
3. Бассард К. и Де-Лауэр Р., Ракета с атомным двигателем, М., ИЛ, 1960.
4. Безухов Н. И. и др., Расчеты на прочность, устойчивость и колебания в условиях высоких температур, М., «Машиностроение», 1965.
5. Безухов Н. И., Теория упругости и пластичности, М., Гостехиздат, 1953.
6. Бердичевский Б. Б., Оценка надежности аппаратуры автоматики. Методы оценки надежности в процессе разработки, М., «Машиностроение», 1966.
7. Биргер И. А., Круглые пластинки и оболочки вращения, М., Оборонгиз, 1961.
8. Биргер И. А., Шорр Б. Ф., Шнейдерович Р. М., Расчет на прочность деталей машин, М., Машгиз, 1959.
9. Гильзин К. А., Электрические межпланетные корабли, М., «Наука», 1964.
10. Гуров А. Ф., Расчеты на прочность и колебания в ракетных двигателях, М., «Машиностроение», 1966.
11. Гусев Б. М., Расчет тонкостенных цилиндрических аппаратов на устойчивость при осевом сжатии и изгибе. — «Химическое машиностроение», 1961, № 3.
12. Домашнев А. Д., Конструирование и расчет химических аппаратов, М., Машгиз, 1961.
13. Дональд Б., Маккей, Конструирование космических силовых установок, перев. с англ., М., «Машиностроение», 1966.
14. Займовский А. С., Калашников В. В., Головин И. С., Тепловыделяющие элементы атомных реакторов, М., Госатомиздат, 1962.
15. Зубарев Т. Н., Введение в теорию ядерных реакторов, М., 1959.
16. Кан С. Н., Строительная механика оболочек, М., «Машиностроение», 1966.
17. Кинасошвили Р. С., Расчет на прочность дисков турбомашин, М., Оборонгиз, 1954.
18. Контарович Э. Б., Основы расчета химических машин, М., Машгиз, 1960.
19. Корлисс У., Ракетные двигатели для космических полетов, М., ИЛ, 1962.
20. Крюков К. А., Влияние массы вала на критические угловые скорости ротора турбины. Изв. вузов МВО СССР, серия «Авиационная техника», 1958, № 4.
21. Качанов Л. М., Теория ползучести, М., Физматгиз, 1960.
22. Крылов А. Н., Об определении критических скоростей вращающегося вала. Изд-во АН СССР, 1932.

23. Левин А. В., Рабочие лопатки и диски паровых турбин, М., Госэнергоиздат, 1953.
24. Малинин Н. Н., Прочность турбомашин, М., Машгиз, 1962.
25. Материалы для ядерных реакторов. Под ред. Сокурского Ю. Н., М., Госатомиздат, 1963.
26. Мельников Н. П., Конструктивные формы и методы расчета ядерных реакторов, М., Госатомиздат, 1963.
27. Никиреев В. М. и др., Практические методы расчета оболочек, М., Стройиздат, 1966.
28. Никитин В. А., Письменная Г. И., Определение термических напряжений и деформаций при неравномерном распределении температуры. В сб. «Тепловые напряжения в элементах конструкций», вып. 4. Изд-во АН УССР, 1964.
29. Нормы расчета элементов паровых котлов на прочность, М., Машгиз, 1956.
30. Петров П. А., Ядерные энергетические установки, М., Госэнергоиздат, 1958.
31. Писаренко Г. С. и др., Прочность материалов при высоких температурах, Киев, «Наукова думка», 1966.
32. Подгорный Н. Г., Расчет прочности плоских донышек, заглушек и трубных досок, М., Машгиз, 1954.
33. Пономарев С. Д. и др., Расчеты на прочность в машиностроении, т. I; II; III, М., Машгиз, 1958—1959.
34. Преобразование тепла и химической энергии в электроэнергию в ракетных системах, перев. с англ. под ред. В. А. Кириллина и А. Е. Шейдлина, М., ИЛ, 1963.
35. Скубачевский Г. С., Авиационные газотурбинные двигатели, М., «Машиностроение», 1965.
36. Справочник по строительной механике корабля, под ред. Ю. А. Циманского, т. II, М., Судпромгиз, 1958.
37. Сурнов Д. Н., Исследование критических чисел оборотов системы с двумя дисками, вращающимися с различными угловыми скоростями. — Сб. трудов МАИ под ред. Скубачевского Г. С., вып. 74, М., Оборонгиз, 1956.
38. Тимошенко С. П., Пластинки и оболочки, М., Гостехиздат, 1948.
39. Тимошенко С. П., Сопротивление материалов, М., Физматгиз, 1960.
40. Тимошенко С. П., Теория упругости, ОНТИ, 1937.
41. Фаворский О. Н., Установки для непосредственного преобразования тепловой энергии в электрическую, М., «Высшая школа», 1965.
42. Феодосьев В. И., Прочность теплонапряженных узлов жидкостных ракетных двигателей, М., Оборонгиз, 1963.
43. Феодосьев В. И., Сопротивление материалов, М., Физматгиз, 1963.
44. Хоблер Тадеуш, Теплопередача и теплообменники, М., Госхимиздат, 1961.
45. Челиков В. А., Насосы для жидких металлов, М., 1962.
46. Чанг Ш., Преобразование энергии, М., Атомиздат, 1965.
47. Черноусов Н. П., Герметические химико-технологические машины и аппараты, М., «Машиностроение», 1965.
48. Штода А. В. и др., Конструкция авиационных газотурбинных двигателей, М., Воениздат, 1961.
49. Штулингер Э., Ионные двигатели для космических полетов, М., Воениздат, 1966.
50. Энергетические установки для космических аппаратов. — Сб. статей, перев. с англ. под ред. Невировского Д. Д., М., «Мир», 1964.
51. Преобразование тепла и химической энергии в электроэнергию в ракетных системах, перев. с англ. М., ИЛ, 1967.
52. Исследование параметров систем термоэлектронных преобразователей для больших ЯЭУ космических кораблей. — «Вопросы ракетостроения», 1964, № 1.

END